

AD A095096

LEVEL

12

DNA/6501H-4-1

NUCLEAR GEOPLOSICS SOURCEBOOK

Volume IV, Part I, Empirical Analysis of Ground Motion
from Above and Underground Explosions.

General Electric Company—TEMPO
DASIAC
816 State Street
Santa Barbara, California 93102

1 March 1979

Handbook,

CONTRACT No. DNA 001-79-C-0081

DTIC
FEB 1 7 1981

APPROVED FOR PUBLIC RELEASE;
DISTRIBUTION UNLIMITED.

THIS WORK SPONSORED BY THE DEFENSE NUCLEAR AGENCY
UNDER RDT&E RMSS CODE B3370/9464 P99QAXDC00809 H2590D.

Prepared for
Director
DEFENSE NUCLEAR AGENCY
Washington, D. C. 20305

DTIC FILE COPY

81 2 17 036

Destroy this report when it is no longer
needed. Do not return to sender.

PLEASE NOTIFY THE DEFENSE NUCLEAR AGENCY,
ATTN: STTI, WASHINGTON, D.C. 20305, IF
YOUR ADDRESS IS INCORRECT, IF YOU WISH TO
BE DELETED FROM THE DISTRIBUTION LIST, OR
IF THE ADDRESSEE IS NO LONGER EMPLOYED BY
YOUR ORGANIZATION.



UNCLASSIFIED

SECURITY CLASSIFICATION OF THIS PAGE (When Data Entered)

REPORT DOCUMENTATION PAGE		READ INSTRUCTIONS BEFORE COMPLETING FORM																				
1. REPORT NUMBER DNA 6501H-4-1	2. GOVT ACCESSION NO. <i>AD-1095096</i>	3. RECIPIENT'S CATALOG NUMBER																				
4. TITLE (and Subtitle) NUCLEAR GEOPLOSICS SOURCEBOOK Volume IV, Part I - Empirical Analysis of Ground Motion from Above and Underground Explosions		5. TYPE OF REPORT & PERIOD COVERED Handbook																				
7. AUTHOR(s) Jacques E. Schoutens, Editor		6. PERFORMING ORG. REPORT NUMBER DNA 001-79-C-0081																				
9. PERFORMING ORGANIZATION NAME AND ADDRESS General Electric Company — TEMPO DASIAC 816 State St., Santa Barbara, California 93102		10. PROGRAM ELEMENT, PROJECT, TASK AREA & WORK UNIT NUMBERS Subtask P99QAXDC008-09																				
11. CONTROLLING OFFICE NAME AND ADDRESS Director Defense Nuclear Agency Washington, DC 20305		12. REPORT DATE 1 March 1979																				
14. MONITORING AGENCY NAME & ADDRESS (if different from Controlling Office)		13. NUMBER OF PAGES 370																				
		15. SECURITY CLASS. (of this report) Unclassified																				
		15a. DECLASSIFICATION/DOWNGRADING SCHEDULE N/A																				
16. DISTRIBUTION STATEMENT (of this Report) Approved for public release; distribution unlimited.																						
17. DISTRIBUTION STATEMENT (of the abstract entered in Block 20, if different from Report)																						
18. SUPPLEMENTARY NOTES This work sponsored by the Defense Nuclear Agency under RDT&E RMSS Code B337079464 P99QAXDC00809 H2590D.																						
19. KEY WORDS (Continue on reverse side if necessary and identify by block number) <table> <tr><td>Acceleration</td><td>Ejecta</td><td>Hard rock</td><td>Non-linear region</td></tr> <tr><td>Alluvium</td><td>Explosion phenomenology</td><td>HE explosion</td><td>Particle velocity</td></tr> <tr><td>Areal density</td><td>Ground motion</td><td>Hydrodynamic region</td><td>Plastic region</td></tr> <tr><td>Craters</td><td>Granite</td><td>Modeling</td><td></td></tr> <tr><td>Displacement</td><td>Geologic effects</td><td>Nuclear explosion</td><td></td></tr> </table>			Acceleration	Ejecta	Hard rock	Non-linear region	Alluvium	Explosion phenomenology	HE explosion	Particle velocity	Areal density	Ground motion	Hydrodynamic region	Plastic region	Craters	Granite	Modeling		Displacement	Geologic effects	Nuclear explosion	
Acceleration	Ejecta	Hard rock	Non-linear region																			
Alluvium	Explosion phenomenology	HE explosion	Particle velocity																			
Areal density	Ground motion	Hydrodynamic region	Plastic region																			
Craters	Granite	Modeling																				
Displacement	Geologic effects	Nuclear explosion																				
20. ABSTRACT (Continue on reverse side if necessary and identify by block number) <p>This sourcebook is a compendium of nuclear and high-explosive empirical data and analysis of ground motion, cratering, and ejecta. It is a revised and greatly expanded version of the Nuclear Geoplosics Sourcebook published by DNA in 1964 (DASA 1285-IV). It is not meant to be a handbook but rather an authoritative sourcebook on explosion-produced ground-behavior phenomena.</p>																						

UNCLASSIFIED

SECURITY CLASSIFICATION OF THIS PAGE (When Data Entered)

19. KEY WORDS (Continued)

Particle-size distribution
Prediction technique
Salt
Soviet
Strain
Stress
Trajectory
Tuff
Waveforms

Accession For	
NTIS SP&I	<input checked="" type="checkbox"/>
DTIC T/R	<input type="checkbox"/>
Unpublished	<input type="checkbox"/>
Justification	
By	
Distribution/	
Availability Codes	
Avail and/or	
Dist	Special
A	

UNCLASSIFIED

SECURITY CLASSIFICATION OF THIS PAGE (When Data Entered)

PREFACE

This volume of the Nuclear Geoplosics Sourcebook is a revised and greatly expanded version of the previous edition published by DNA in 1964 (DASA 1285-IV). The Nuclear Geoplosics Sourcebook is comprised of five volumes:

- Volume I Theory of Directly Induced Ground Motion
- Volume II-1 Mechanical Properties of Earth Materials - Soils
- Volume II-2 Mechanical Properties of Earth Materials - Rocks
- Volume III Test Sites and Instrumentation
- Volume IV Empirical Analysis of Ground Motion, Cratering and Ejecta
- Volume V Effects of Underground Structures and Equipment

Volume IV consists of two parts and five chapters:

Part I

- Chapter IV-1 Ground Motion from Aboveground Nuclear Explosions
- Chapter IV-2 Ground Motion from Underground Explosions

Part II

- Chapter IV-3 Characteristics of Nuclear and High-Explosive Craters
- Chapter IV-4 Ejecta
- Chapter IV-5 Review of the Soviet Work in Cratering and Associated Ground Motion

The philosophy of the first edition of the Nuclear Geoplosics Sourcebook has been kept. In the words of F. Sauer, author of the original edition, the following quotation remains true in this edition:

"This book is not meant to be a handbook of design specifications. It is meant to be an authoritative sourcebook. Between these two is the difference, for example, between the laboratory course and the lecture course. It contains more philosophy than figures, more hypotheses than certainties. These hypotheses are given whenever possible with the empirical information and the theory upon which they are based so that the reader can make his own judgment of their validity. We strive to avoid the temptation to speculate

intuitively without factual or theoretical foundation for the arguments presented, and we attempt to present objectively all approaches, favored and unfavored, with the reasons for preference of one or another type of analysis or procedure clearly stated. So that the sourcebook need not be classified, a few relevant references are not discussed. In addition new material appearing during the late stages of compilation of the sourcebook is not referenced. It is hoped that these deficiencies will be corrected in future editions."

The Editor wishes to acknowledge the unselfish help and encouragement received from the following individuals:

George Ullrich	HQ DNA (SPSS)
J.R. Stockton	ANSER (formerly DNA COR for this project)
M. Baron	Paul Weidlinger Associates
B.L. Ristvet	Formerly with AFWL
M. Rosenblatt	California Research and Technology
L. Vortman	Sandia Laboratory
A. Chabai	Sandia Laboratory
H.F. Cooper, Jr.	SAFALR (formerly of RDA)
R. Port	R&D Associates
R. Seebaugh	Science Applications Inc.
R.H. Carlson	Boeing
T. Stubbs	Physics International
F. Sauer	Physics International
D. Reitz	GE-TEMPO/DASIAC

The Editor is grateful and wishes to thank these individuals for carefully reviewing the manuscript, for their helpful comments and suggestions, and for the benefit of their invaluable experience in this field, thereby seeing this work brought to a successful conclusion. The Editor assumes the responsibility for any omission, distortion, or other errors that may have crept into this sourcebook despite all the help received.

TABLE OF CONTENTS

<u>Chapter</u>		<u>Page</u>
	PREFACE	IV-i
	LIST OF ILLUSTRATIONS	IV-ix
	LIST OF TABLES	IV-xxvii
IV-1	GROUND MOTION FROM ABOVEGROUND NUCLEAR EXPLOSIONS	IV-1-1
IV-1.0	INTRODUCTION	IV-1-1
IV-1.1	ORIGIN OF GROUND MOTION	IV-1-5
IV-1.2	CORRELATION OF MAXIMUM ACCELERATION DATA	IV-1-26
	IV-1.2.1 Vertical Acceleration Near the Ground Surface . . .	IV-1-28
	IV-1.2.2 Horizontal Acceleration Near the Ground Surface . .	IV-1-41
	IV-1.2.3 Attenuation of Acceleration with Depth	IV-1-48
IV-1.3	CORRELATION OF MAXIMUM PARTICLE VELOCITY DATA	IV-1-55
	IV-1.3.1 Vertical Particle Velocity Near the Surface	IV-1-55
	IV-1.3.2 Variation of Vertical Particle Velocity with Depth	IV-1-62
	IV-1.3.3 Horizontal Particle Velocity	IV-1-73
IV-1.4	CORRELATION OF MAXIMUM DISPLACEMENT DATA	IV-1-81
IV-1.5	CORRELATION OF MAXIMUM STRESS AND STRAIN DATA	IV-1-97
IV-1.6	PREDICTION OF GROUND MOTION WAVEFORMS	IV-1-102
	IV-1.6.1 Vertical and Horizontal Displacement Waveforms for Superseismic Airblast Conditions	IV-1-102
	IV-1.6.2 Vertical Velocity Waveforms for Outrunning Ground Motion	IV-1-105
IV-1.7	VERTICAL VELOCITY RESPONSE SPECTRA	IV-1-108
IV-1.8	GROUND MOTION FROM SURFACE AND NEAR-SURFACE HIGH EXPLOSIVE DETONATIONS	IV-1-112
	IV-1.8.1 Overview of High Explosive Experiments	IV-1-112
	IV-1.8.2 Near-Surface Motions from Surface Detonations on Hard Rock	IV-1-117
	IV-1.8.3 Near-Surface Motions from Surface Detonations on Layered Media	IV-1-133
	IV-1.8.4 Summary	IV-1-163
IV-1.9	REFERENCES.	IV-1-167
IV-1A	OVERPRESSURE WAVEFORMS	IV-1-173
IV-2	GROUND MOTION FROM UNDERGROUND EXPLOSIONS	IV-2-1
IV-2.0	INTRODUCTION	IV-2-1
IV-2.1	UNDERGROUND EXPLOSION PHENOMENOLOGY	IV-2-2
	IV-2.1.1 Environments	IV-2-3

<u>Chapter</u>		<u>Page</u>
	IV-2.1.2 Measurement Techniques	IV-2-5
	IV-2.1.3 Fireball Development	IV-2-11
	IV-2.1.4 Partition of Energy	IV-2-14
	IV-2.1.5 Reflected and Refracted Waves	IV-2-15
	IV-2.1.6 Cavity Decoupling	IV-2-20
	IV-2.1.7 Representative Ground Motion Time Histories	IV-2-23
IV-2.2	STRESS AND MOTION WITHIN THE HYDRODYNAMIC AND PLASTIC REGIONS	IV-2-27
	IV-2.2.1 Measurement Techniques	IV-2-28
	IV-2.2.2 Data Analysis	IV-2-33
IV-2.3	FREE-FIELD GROUND MOTION IN THE NONLINEAR REGION	IV-2-37
	IV-2.3.1 Measurement Techniques	IV-2-37
	IV-2.3.2 Free-Field Ground Motion in Alluvium	IV-2-38
	IV-2.3.2.1 Scaled Acceleration Analysis	IV-2-38
	IV-2.3.2.2 Particle Velocity Analysis	IV-2-40
	IV-2.3.2.3 Scaled Displacement Analysis	IV-2-42
	IV-2.3.2.4 Discussion	IV-2-44
	IV-2.3.3 Free-Field Ground Motion in Dry Tuff	IV-2-45
	IV-2.3.3.1 Scaled Acceleration Analysis	IV-2-46
	IV-2.3.3.2 Particle Velocity Analysis	IV-2-48
	IV-2.3.3.3 Scaled Displacement Analysis	IV-2-48
	IV-2.3.4 Free-Field Ground Motion in Wet Tuff	IV-2-51
	IV-2.3.4.1 Scaled Acceleration Analysis	IV-2-51
	IV-2.3.4.2 Particle Velocity Analysis	IV-2-53
	IV-2.3.4.3 Scaled Displacement Analysis	IV-2-55
	IV-2.3.5 Free-Field Ground Motion in Hard Rock	IV-2-55
	IV-2.3.5.1 Scaled Acceleration Analysis	IV-2-57
	IV-2.3.5.2 Particle Velocity Analysis	IV-2-59
	IV-2.3.5.3 Scaled Displacement Analysis	IV-2-59
	IV-2.3.6 General Discussion	IV-2-59
	IV-2.3.7 Comparisons	IV-2-66
	IV-2.3.7.1 Comparison of Free-Field Motion in Regions of Hydrodynamic and Nonlinear Response	IV-2-66
	IV-2.3.7.2 Comparison of Motion in Different Rocks	IV-2-69
	IV-2.3.8 Scaled Data	IV-2-74

<u>Chapter</u>		<u>Page</u>
IV-2.4	SURFACE ZERO MOTION	IV-2-93
	IV-2.4.1 Peak Vertical Acceleration and Particle Velocity for Detonations in NTS Alluvium	IV-2-93
	IV-2.4.2 Peak Vertical Velocities for Detonations in NTS Granite and Tuff, and in Salt	IV-2-99
IV-2.5	SURFACE MOTION AS A FUNCTION OF SLANT RANGE FROM SHOT POINT . .	IV-2-103
	IV-2.5.1 Peak Vertical Acceleration	IV-2-103
	IV-2.5.2 Peak Vertical Velocity	IV-2-109
	IV-2.5.3 Peak Vertical Displacement	IV-2-112
	IV-2.5.4 Rules for Predicting Vertical Surface Motion . . .	IV-2-113
IV-2.6	OVERVIEW OF GROUND MOTION FROM SUBSURFACE HIGH EXPLOSIVE EVENTS	IV-2-115
IV-2.7	SOME ANALYTICAL MODELS FOR PREDICTING GROUND MOTION PHENOMENA	IV-2-119
	IV-2.7.1 The Butkovich and Lewis Model	IV-2-119
	IV-2.7.2 The BOTE Model	IV-2-140
	IV-2.7.3 The Cooper and Seamon Model	IV-2-147
IV-2.8	REFERENCES	IV-2-148
IV-3	CHARACTERISTICS OF NUCLEAR AND HIGH EXPLOSIVE CRATERS . . .	IV-3-1
IV-3.0	INTRODUCTION	IV-3-1
IV-3.1	CRATER FORMATION MECHANISMS	IV-3-1
	IV-3.1.1 Energy Partition and Transfer	IV-3-2
	IV-3.1.2 Cratering Processes	IV-3-8
IV-3.2	EXPERIMENTAL RESULTS	IV-3-17
	IV-3.2.1 Nuclear Events in the PPG	IV-3-18
	IV-3.2.1.1 IVY-MIKE	IV-3-21
	IV-3.2.1.2 CASTLE-1 (BRAVO)	IV-3-21
	IV-3.2.1.3 CASTLE-3 (KOON)	IV-3-24
	IV-3.2.1.4 LACROSSL	IV-3-24
	IV-3.2.1.5 ZUNI	IV-3-25
	IV-3.2.1.6 SEMINOLE	IV-3-25
	IV-3.2.1.7 TEWA	IV-3-25
	IV-3.2.1.8 CACTUS	IV-3-26
	IV-3.2.1.9 KOA	IV-3-26
	IV-3.2.1.10 OAK	IV-3-26

<u>Chapter</u>		<u>Page</u>
IV-3.2.2	Non-PPG Nuclear Cratering Events.	IV-3-26
	IV-3.2.2.1 SEDAN	IV-3-27
	IV-3.2.2.2 HOLE 1004	IV-3-27
	IV-3.2.2.3 SCHOONER.	IV-3-28
	IV-3.2.2.4 JOHNIE BOY.	IV-3-28
IV-3.2.3	High-Explosive Tests.	IV-3-29
	IV-3.2.3.1 PRAIRIE FLAT, DISTANT PLAIN 6, and DIAL PACK	IV-3-33
	IV-3.2.3.2 MINE SHAFT.	IV-3-33
	IV-3.2.3.3 FLAT TOP I.	IV-3-34
	IV-3.2.3.4 MINE THROW I.	IV-3-35
	IV-3.2.3.5 MIDDLE GUST	IV-3-35
	IV-3.2.3.6 MIXED COMPANY	IV-3-37
	IV-3.2.3.7 ESSEX	IV-3-38
IV-3.2.4	Comparative Geologic Effects on HE Cratering. . .	IV-3-40
IV-3.2.5	Multiple Charge Events—HE and Nuclear Linear Craters	IV-3-45
IV-3.2.6	Repeated Cratering Experiments.	IV-3-52
IV-3.3	EMPIRICAL ANALYSES.	IV-3-56
	IV-3.3.1 Statistical Analyses.	IV-3-63
	IV-3.3.2 Similarity Techniques	IV-3-68
	IV-3.3.3 Small-Scale Experimental Modeling	IV-3-72
	IV-3.3.4 Summary	IV-3-93
IV-3.4	NUMERICAL ANALYSES OF CRATERING	IV-3-95
	IV-3.4.1 Numerical Techniques.	IV-3-96
	IV-3.4.2 Calculation of Buried Explosions.	IV-3-98
	IV-3.4.3 Near-Surface Burst Calculations	IV-3-102
	IV-3.4.4 Summary of Calculations of Explosive and Impact Craters	IV-3-110
IV-3.5	REFERENCES.	IV-3-113
IV-3A	OVERVIEW OF METEOR-PRODUCED CRATERS	IV-3-121
IV-3B	TABULATION OF HIGH-EXPLOSIVE CRATER DATA.	IV-3-127
IV-3C	TABULATION OF SOME NUCLEAR CRATER DATA.	IV-3-143
IV-4	EJECTA.	IV-4-1
IV-4.0	INTRODUCTION.	IV-4-1

<u>Chapter</u>		<u>Page</u>
	IV-4.0.1 Relationship Between TNT and Other Explosives	IV-4-1
	IV-4.0.2 Origin and Compositions of Ejecta	IV-4-3
	IV-4.0.3 Effects of the Environment	IV-4-8
IV-4.1	NUCLEAR EVENTS	IV-4-11
	IV-4.1.1 Near-Surface Events	IV-4-11
	IV-4.1.1.1 The PPG Events.	IV-4-12
	IV-4.1.1.2 JANGLE S and U.	IV-4-13
	IV-4.1.1.3 JOHNIE BOY.	IV-4-15
	IV-4.1.2 Deeply Buried Events.	IV-4-19
	IV-4.1.2.1 CABRIOLET	IV-4-24
	IV-4.1.2.2 DANNY BOY	IV-4-25
	IV-4.1.2.3 SCHOONER.	IV-4-47
	IV-4.1.2.4 SEDAN	IV-4-49
	IV-4.1.2.5 TEAPOT ESS.	IV-4-69
	IV-4.1.3 Summary	IV-4-72
IV-4.2	HIGH-EXPLOSIVE EVENTS.	IV-4-77
	IV-4.2.1 Single-Charge Events.	IV-4-79
	IV-4.2.1.1 STAGECOACH.	IV-4-79
	IV-4.2.1.2 SCOOTER	IV-4-82
	IV-4.2.1.3 AIR VENT I.	IV-4-87
	IV-4.2.1.4 FLAT TOP I.	IV-4-98
	IV-4.2.1.5 FLAT TOP II and III	IV-4-105
	IV-4.2.1.6 MIDDLE GUST	IV-4-120
	IV-4.2.1.7 MIXED COMPANY	IV-4-125
	IV-4.2.1.8 ESSEX	IV-4-131
IV-4.3	SUMMARY OF EJECTA DATA	IV-4-132
	IV-4.3.1 Ejecta Origin	IV-4-132
	IV-4.3.2 Ejecta Areal Density	IV-4-134
	IV-4.3.3 Initial Velocities.	IV-4-144
	IV-4.3.4 Particle Trajectories	IV-4-146
	IV-4.3.5 Post-Impact Particle Statistics	IV-4-148
	IV-4.3.6 Ejecta Deposition	IV-4-152
	IV-4.3.7 Areal Density and Total Ejecta Weight	IV-4-155
	IV-4.3.8 Particle-Size Distribution.	IV-4-159
	IV-4.3.9 Maximum Particle Size	IV-4-166

<u>Chapter</u>		<u>Page</u>
IV-4.4	SUMMARY OF SOME COMPUTATIONAL METHODS.	IV-4-170
IV-4.5	REFERENCES	IV-4-204
IV-4.6	BIBLIOGRAPHY	IV-4-213
IV-5	REVIEW OF THE SOVIET WORK IN CRATERING AND ASSOCIATED GROUND MOTION.	IV-5-1
IV-5.0	INTRODUCTION	IV-5-1
IV-5.1	LARGE YIELD FIELD EXPERIMENTS.	IV-5-3
	IV-5.1.1 Nuclear Cratering Experiments	IV-5-3
	IV-5.1.2 Large Yield High-Explosive Experiments.	IV-5-8
IV-5.3	MODELING EXPERIMENTS	IV-5-33
IV-5.4	EMPIRICAL AND THEORETICAL ANALYSES	IV-5-50
	IV-5.4.1 Basic Theoretical Work.	IV-5-50
	IV-5.4.2 The Method of Characteristics	IV-5-53
	IV-5.4.3 Specialized Problems.	IV-5-54
IV-5.5	SUMMARY.	IV-5-58
IV-5.6	REFERENCES	IV-5-59

LIST OF ILLUSTRATIONS

<u>Figure</u>		<u>Page</u>
IV-1.1	Underground wave systems due to an airblast	IV-1-16
IV-1.2	Typical accelerograms for outrunning ground motion	IV-1-17
IV-1.3	Ray path diagram for determination of critical ray path for two-layer medium	IV-1-20
IV-1.4	Wave transmission through a two-layer system	IV-1-21
IV-1.5	Nomenclature for multilayered systems	IV-1-24
IV-1.6	Construction of arrival time-distance curves in two-layer and three-layer systems	IV-1-25
IV-1.7	Composite maximum negative 5-foot vertical slap acceleration versus maximum surface level air pressure, TUMBLER	IV-1-29
IV-1.8	Airblast-induced acceleration as a function of incident overpressure for shot IVY MIKE	IV-1-30
IV-1.9	Vertical acceleration at Yucca Flat for 5-foot depth	IV-1-31
IV-1.10	Vertical acceleration at Frenchman Flat for 5-foot depth	IV-1-32
IV-1.11	Maximum vertical downward acceleration versus peak overpressure	IV-1-34
IV-1.12	Maximum vertical acceleration versus ground range at NTS	IV-1-36
IV-1.13	Maximum vertical acceleration versus ground range for outrunning ground motion at PPG	IV-1-37
IV-1.14	Maximum scaled vertical acceleration versus scaled ground range for outrunning ground motion at PPG	IV-1-38
IV-1.15	Variation of maximum horizontal acceleration with depth at NTS	IV-1-42
IV-1.16	Vertical and horizontal stress versus time, station 6 (ground range 1050 feet), shot PRISCILLA	IV-1-46

LIST OF ILLUSTRATIONS (Continued)

<u>Figure</u>		<u>Page</u>
IV-1.17	Wave fronts due to superseismic airblast	IV-1-47
IV-1.18	Maximum horizontal acceleration versus ground range for outrunning ground motion at PPG	IV-1-49
IV-1.19	Attenuation of vertical acceleration with depth in superseismic airblast at NTS	IV-1-50
IV-1.20	Predicted attenuation of maximum vertical acceleration from Reference IV-1.23 for the superseismic airblast region	IV-1-52
IV-1.21	Vertical acceleration versus depth for outrunning ground motion at PPG	IV-1-54
IV-1.22	Horizontal acceleration versus depth for outrunning ground motion at PPG	IV-1-56
IV-1.23	Vertical velocity at 5-foot depth. Summary of superseismic data at NTS	IV-1-57
IV-1.24	Maximum vertical velocity versus ground range for outrunning ground motion at PPG	IV-1-60
IV-1.25	Maximum vertical velocity versus ground range at NTS	IV-1-61
IV-1.26	Attenuation of maximum vertical velocity with depth at Frenchman Flat for superseismic blast wave	IV-1-63
IV-1.27	Attenuation factor for maximum vertical stress, maximum strain, and maximum particle velocity	IV-1-65
IV-1.28	Dimensionless initial rate of decay of overpressure versus shock overpressure nuclear airburst	IV-1-67
IV-1.29	Ratio of maximum particle velocity to airblast overpressure versus scaled depth for SMALL BOY and PRISCILLA	IV-1-68
IV-1.30	Ratio of maximum vertical particle velocity to airblast overpressure versus scaled depth for high explosive	IV-1-69
IV-1.31	Vertical particle velocity versus depth for outrunning ground motion at PPG	IV-1-71

LIST OF ILLUSTRATIONS (Continued)

<u>Figure</u>		<u>Page</u>
IV-1.32	Variation of maximum outward horizontal velocity with depth for superseismic blast wave at NTS	IV-1-74
IV-1.33	Variation of maximum inward horizontal velocity with depth for superseismic blast wave at NTS	IV-1-75
IV-1.33a	Comparison of calculated and measured $\Delta P/v$	IV-1-76
IV-1.33b	Comparison of theoretical model and near-surface ground motion data from PRISCILLA	IV-1-78
IV-1.33c	Best estimate of very near-surface vertical motion data from PRISCILLA	IV-1-79
IV-1.33d	Comparison of calculated attenuation rates with normalized peak vertical motion data from PRISCILLA	IV-1-80
IV-1.34	Maximum horizontal velocity versus ground range for outrunning ground motion at PPG	IV-1-82
IV-1.35	Horizontal particle velocity versus depth for outrunning ground motion at PPG	IV-1-83
IV-1.36	Comparison of theoretical model and near-surface ground motion data from PRISCILLA	IV-1-85
IV-1.37	Comparison of simplified model with PRISCILLA peak displacement data	IV-1-86
IV-1.38	Comparison of simplified model with PRISCILLA peak displacement data	IV-1-87
IV-1.39	Best estimate of very near-surface vertical motion data from PRISCILLA	IV-1-88
IV-1.40	Comparison of calculated attenuation rates with normalized peak vertical motion data from PRISCILLA	IV-1-89
IV-1.41	Comparison of overpressure boundary condition with PRISCILLA data	IV-1-90
IV-1.42	Comparison of peak vertical displacements from PRISCILLA with calculations using measured airblast overpressure as a boundary condition	IV-1-91

LIST OF ILLUSTRATIONS (Continued)

<u>Figure</u>	<u>Page</u>
IV-1.43 Comparison of relative displacement data with calculated results using measured overpressure as a boundary condition	IV-1-92
IV-1.44 Comparison of PRISCILLA data with ground motions predicted using Brode's height-of-burst overpressure model	IV-1-94
IV-1.45 Maximum horizontal and vertical displacement versus ground range for outrunning ground motion at PPG	IV-1-96
IV-1.46 Attenuation of maximum vertical strain with depth for superseismic blast wave at NTS	IV-1-100
IV-1.47 Attenuation of maximum vertical stress with depth for superseismic blast wave at NTS	IV-1-101
IV-1.48 Type I superseismic airblast vertical particle velocity waveform and its displacement	IV-1-106
IV-1.49 Illustration of development of outrunning ground motion for TUMBLER, shot 1	IV-1-107
IV-1.50 Type II (outrunning ground motion) vertical particle velocity waveform and its displacement	IV-1-109
IV-1.51 Comparison of predicted and observed outrunning ground motion	IV-1-110
IV-1.52 Correlation of superseismic, nonreflecting vertical velocity response spectra for a 0.5% critical damping	IV-1-111
IV-1.53 Envelope and average undamped response spectra for outrunning ground motion waveforms in alluvium	IV-1-113
IV-1.54 Gauge layout, Event MINERAL ROCK	IV-1-118
IV-1.55 Geometrical scale for a 5 mt contact burst on hard rock compared with MINE ORE/MINERAL ROCK experimental geometry	IV-1-120
IV-1.56 Shock front propagation	IV-1-121

LIST OF ILLUSTRATIONS (Continued)

<u>Figure</u>		<u>Page</u>
IV-1.57	Correlation of near-surface peak particle velocity from cratering bursts in rock	IV-1-122
IV-1.58	Correlation of near-surface peak vertical and horizontal particle displacements	IV-1-124
IV-1.59	Correlation of peak particle velocity at $Z \approx V^{1/3}$ from cratering bursts in rock	IV-1-125
IV-1.60	Correlation of peak particle velocity at $Z \approx 2 V^{1/3}$ from cratering bursts in rock	IV-1-126
IV-1.61	Correlation of peak vertical and horizontal particle displacements at $Z/V^{1/3} \approx 1$	IV-1-128
IV-1.62	Correlation of peak vertical and horizontal particle displacements at $Z/V^{1/3} \approx 2$	IV-1-129
IV-1.63	Estimated peak particle velocity and displacement contours	IV-1-132
IV-1.64	Comparison of PRAIRIE FLAT peak velocity data	IV-1-134
IV-1.65	Peak vertical air slap acceleration and particle velocity for DRES events, 1.5-foot depth	IV-1-136
IV-1.66	Peak vertical air slap acceleration and particle velocity for MIDDLE GUST III and IV and MIXED COMPANY 3, 1.5-foot depth	IV-1-138
IV-1.67	Peak air slap horizontal velocity high explosive test data	IV-1-143
IV-1.68	Comparison of crater-induced peak particle velocities from surface tangent HE events in Cedar City tonolite and DRES silt	IV-1-145
IV-1.69	Crater volume scaled peak displacement correlation for surface tangent high explosive events at DRES and Cedar City	IV-1-147
IV-1.70	Crater volume scaled peak displacement correlation for large surface tangent high explosive events at MIDDLE GUST and MIXED COMPANY	IV-1-148

LIST OF ILLUSTRATIONS (Continued)

<u>Figure</u>		<u>Page</u>
IV-1.71	Crater volume scaled horizontal peak displacement correlation for MIDDLE GUST, wet site calibration events	IV-1-149
IV-1.72	Crater volume scaled peak displacement correlation for top $0.1 V^{1/3}$ for DRES events.	IV-1-151
IV-1.73	Crater volume scaled peak displacement correlation for top $0.1 V^{1/3}$ for MIDDLE GUST IV	IV-1-152
IV-1.74	Crater volume scaled peak displacement correlation for MIDDLE GUST III (Cooper, unpublished data analysis)	IV-1-153
IV-1.75	Peak velocity crater volume scaling correlation for surface tangent DRES events	IV-1-154
IV-1.76	Velocity crater volume scaling correlation for near-surface tangent Cedar City events	IV-1-155
IV-1.77	Near-surface peak velocity geology sensitivity for surface tangent 100-ton high explosive events	IV-1-156
IV-1.78	Near-surface peak velocity geology sensitivity for half-buried 20-ton high explosive events	IV-1-157
IV-1.79	Peak velocity geology sensitivity for one-diameter HOB 100-ton high explosive events	IV-1-158
IV-1.80	High explosive outrunning vertical velocity peak attenuation and nuclear data comparison	IV-1-161
IV-1.81	HOB effects on outrunning peak vertical displacements for NTS events	IV-1-164

LIST OF ILLUSTRATIONS (Continued)

<u>Figure</u>		<u>Page</u>
IV-2.1	Merlin instrumentation	IV-2-9
IV-2.2	PILE DRIVER free-field instrument stations	IV-2-10
IV-2.3	Advance of shock front and growth of fireball or cavity in an atmospheric or underground nuclear explosion	IV-2-13
IV-2.4	Radius versus time relation for an underground nuclear explosion with regard to vaporization, cavity expansion, and inelastic rock deformation	IV-2-15
IV-2.5	Reflection and refraction of plane p- and s-waves at a plane interface	IV-2-17
IV-2.6	Shock geometry at interface	IV-2-19
IV-2.7	Example of free-field radial motion from an underground explosion in NTS granite	IV-2-25
IV-2.8	Example of surface zero motion for a detonation	IV-2-26
IV-2.9	Example of surface motion in the nonspalling region	IV-2-27
IV-2.10	Hugoniot parameters for dry alluvium	IV-2-30
IV-2.11	Pressure and particle velocity attenuation	IV-2-35
IV-2.12	Attenuation of scaled acceleration - dry alluvium	IV-2-39
IV-2.13	Attenuation of particle velocity - dry alluvium	IV-2-41
IV-2.14	Attenuation of scaled displacement - dry alluvium	IV-2-43
IV-2.15	Attenuation of scaled acceleration - dry tuff	IV-2-47
IV-2.16	Attenuation of particle velocity - dry tuff	IV-2-49
IV-2.17	Attenuation of scaled displacement - dry tuff	IV-2-50
IV-2.18	Attenuation of scaled acceleration - wet tuff	IV-2-52
IV-2.19	Attenuation of particle velocity - wet tuff	IV-2-54
IV-2.20	Attenuation of scaled displacement - wet tuff	IV-2-56
IV-2.21	Attenuation of scaled acceleration - hard rock	IV-2-58
IV-2.22	Attenuation of particle velocity - hard rock	IV-2-60

LIST OF ILLUSTRATIONS (Continued)

<u>Figure</u>		<u>Page</u>
IV-2.23	Attenuation of scaled displacement - hard rock	IV-2-61
IV-2.24	Attenuation of particle velocity in the regions of hydrodynamic and nonlinear response	IV-2-68
IV-2.25	Attenuation comparison - scaled acceleration	IV-2-70
IV-2.26	Attenuation comparison - particle velocity	IV-2-71
IV-2.27	Attenuation comparison - scaled displacement	IV-2-73
IV-2.28	Magnitude of first pulse of vertical acceleration at surface zero, scaled to 1 kt, for detonations in NTS alluvium	IV-2-97
IV-2.29	Magnitude of first pulse of vertical velocity at surface zero, scaled to 1 kt, for detonations in NTS alluvium	IV-2-100
IV-2.30	Magnitude of maximum vertical velocity at surface zero, scaled to 1 kt, for detonations in NTS alluvium . .	IV-2-101
IV-2.31	Magnitude of first pulse of vertical velocity at surface zero, scaled to 1 kt, for detonations in NTS tuff and granite, and in salt (GNOME)	IV-2-102
IV-2.32	Magnitude of first vertical acceleration pulse, scaled to 1 kt, as a function of position along the surface for detonations in NTS tuff	IV-2-104
IV-2.33	Magnitude of first vertical acceleration pulse, scaled to 1 kt, as a function of distance along the surface for detonations in NTS granite and in salt	IV-2-106
IV-2.34	Magnitude of first vertical acceleration pulse, scaled to 1 kt, as a function of distance along the surface for detonations in NTS alluvium	IV-2-107
IV-2.35	Magnitude of first vertical velocity pulse, scaled to 1 kt, as a function of distance along the surface for detonations in NTS tuff	IV-2-108
IV-2.36	Magnitude of first vertical velocity pulse, scaled to 1 kt, as a function of distance along the surface for detonations in NTS granite and in salt	IV-2-110
IV-2.37	Magnitude of first pulse of vertical velocity, scaled to 1 kt, as a function of distance along the surface for detonations in NTS alluvium	IV-2-111

LIST OF ILLUSTRATIONS (Continued)

<u>Figure</u>	<u>Page</u>
IV-2.38 Magnitude of vertical displacement prior to spalling, scaled to 1 kt, as a function of distance along the surface	IV-2-114
IV-2.39 <u>In-situ</u> density, porosity, saturation, and water content for rocks of grain density 2.2 g/cm ³	IV-2-123
IV-2.40 <u>In-situ</u> density as a function of compressional velocity for common test and collapse media (rock) at the Nevada Test Site	IV-2-125
IV-2.41 Overburden pressure as a function of depth (to 1250 ft) for various average overburden densities	IV-2-126
IV-2.42 Radius of vaporization as a function of device yield for various <u>in-situ</u> shot-point rock densities	IV-2-127
IV-2.43 Peak radial stress (σ_r) as a function of device yield and distance from the shot point in granite	IV-2-128
IV-2.44 Free-field peak particle acceleration as a function of distance from the shot point in granite	IV-2-129
IV-2.45 Free-field peak particle velocities as a function of distance from the shot point in granite	IV-2-130
IV-2.46 Peak ground-surface acceleration as a function of distance from the shot point in hard rock saturated to the surface	IV-2-132
IV-2.47 Peak vertical free-surface displacement as a function of peak free-surface velocity	IV-2-133
IV-2.48 Cavity volume and radius as a function of device yield (W), and scaled depth of burst for a saturated rock with grain density and <u>in-situ</u> density equal to 2.4 g/cm ³	IV-2-135
IV-2.49 Radial displacement as a function of cavity radius at various distances (R) from the shot point for noncom- pactable rock	IV-2-136
IV-2.50 Horizontal (X) and vertical (Y) components of displace- ment at various distances from the cavity boundary	IV-2-137
IV-2.51 Peak radial stress as a function of scaled radial dis- placement at various depths of burst and distances from the shot point in granite	IV-2-139

LIST OF ILLUSTRATIONS (Continued)

<u>Figure</u>		<u>Page</u>
IV-2.52	Positions of isotherms (lines of constant temperature increase) resulting from the energy deposited by the shock wave generated by a nuclear explosion in relatively dry high-density silicate rock as a function of cavity radius (R_c) for an energy yield of 100 kt.	IV-2-141
IV-3.1	Recommended crater nomenclature.	IV-3-3
IV-3.2	Computed fraction of total energy deposited in the ground from a 100-ton TNT sphere detonated at height \bar{H} (center of mass) above the ground.	IV-3-5
IV-3.3	Fractional energy above ground for slightly buried nuclear devices versus time.	IV-3-7
IV-3.4	Primary types of craters resulting from a variety of burst positions.	IV-3-9
IV-3.5	Scaled crater depth curves	IV-3-10
IV-3.6	Scaled crater radius curves.	IV-3-11
IV-3.7	Estimated relative contribution of various cratering mechanisms to changes in the apparent crater depth	IV-3-12
IV-3.8	Sequential stages of crater formation for buried bursts.	IV-3-13
IV-3.9	Time interval from detonation to formation of subsidence crater versus depth of burst	IV-3-16
IV-3.10	Emplacement geometry for shot SEMINOLE	IV-3-19
IV-3.11	Pre- and post-shot cratering surveys, Event OAK.	IV-3-20
IV-3.12	The SECAN crater	IV-3-28
IV-3.13	Aerial photograph of the PRAIRIE FLAT crater several days after detonation.	IV-3-34
IV-3.14	Test configurations for the MIDDLE GUST HE events.	IV-3-36
IV-3.15	Test configurations for the MIXED COMPANY HE events.	IV-3-39
IV-3.16	Descriptive geologic effect on HE cratering efficiency	IV-3-43
IV-3.17	Comparative cratering efficiency for eleven geologic media	IV-3-44
IV-3.18	BUGGY crater topographic profiles.	IV-3-46
IV-3.19	Regions of line-charge equivalence for crater width as a function of scaled spacing and scaled depth of burst	IV-3-48
IV-3.20	Relative trench depth (a) and ejective index (b) as functions of the relative charge spacing	IV-3-51
IV-3.21	Parameter curves for RCE	IV-3-54
IV-3.22	Crater volume correlation of RCE data.	IV-3-57
IV-3.23	Comparison of crater volume correlations	IV-3-61
IV-3.24	Comparison of crater radius correlations	IV-3-62

LIST OF ILLUSTRATIONS (Continued)

<u>Figure</u>		<u>Page</u>
IV-3.25	Nomograph for predicting crater radius versus charge depth in Nevada alluvium.	IV-3-64
IV-3.26	Plot of apparent crater depth versus depth of burst using $W^{1/3.4}$ scaling	IV-3-65
IV-3.27	Plot of apparent crater radius versus depth of burst using $W^{1/2.4}$ scaling.	IV-3-66
IV-3.28	Crater radius as function of charge depth for desert alluvium	IV-3-68
IV-3.29	Various scaling rules relating depth of burst to crater radius.	IV-3-70
IV-3.30	Logarithmic plot of crater diameter versus gravity for depth of burst > 3.8 cm	IV-3-73
IV-3.31	Logarithmic plot of crater diameter versus gravity for depth of burst > 3.8 cm	IV-3-73
IV-3.32	Effect of atmospheric overpressure on crater radius from shallow explosions.	IV-3-75
IV-3.33	Crater radius versus depth of burst scaled according to Herr.	IV-3-75
IV-3.34	Data of Figure IV-3.33 with scaling length modified to include atmospheric overpressure.	IV-3-77
IV-3.35	Index of ejection n ($n = R_a/D$) as a function of \bar{E}	IV-3-78
IV-3.36	Comparison of crater dimensions in model experiments with field experiments	IV-3-79
IV-3.37	Comparison of the curves for the rate of rise of the free surface above the shot point as a function of time in field experiments	IV-3-80
IV-3.38	Apparent crater radius as a function of charge configuration for the overall series.	IV-3-83
IV-3.39	Apparent crater volume as a function of charge configuration for various density sandbeds.	IV-3-85
IV-3.40	Cratering efficiency as a function of charge configuration for various density sandbeds.	IV-3-86
IV-3.41	Value of Ratio $R_a/V_a^{1/3}$ as a function of charge configuration for various density sandbeds.	IV-3-87
IV-3.42	A comparison of apparent crater volume as a function of charge center HOB or DOB for events detonated using 1.7 gm lead azide and 400-mg equivalent PETN charges	IV-3-88
IV-3.43	Variation of ratio $R_a/V_a^{1/3}$ with HOB or DOB for events in standard data series and 400-mg equivalent PETN series.	IV-3-89
IV-3.44	Apparent crater dimensions as a function of thickness of low-density sand above high-density sand	IV-3-91
IV-3.45	SEDAN crater profile at $t = 2.4$ seconds	IV-3-99
IV-3.46	Calculated crater profile for DANNY BOY at $t = 0.1$ second	IV-3-99
IV-3.47	Calculated and observed ground zero surface velocity for SEDAN.	IV-3-100

LIST OF ILLUSTRATIONS (Continued)

<u>Figure</u>		<u>Page</u>
IV-3.48	Calculated and observed crater profiles for the SCHOONER crater.	IV-3-101
IV-3.49	Apparent crater volume as a function of depth of burst in NTS Area 10 alluvium.	IV-3-102
IV-3.50	Computed particle velocity field at 0.1 second resulting from a 1-MT surface burst.	IV-3-104
IV-3.51	DISTANT PLAIN 6—theoretical calculation: Euler-Lagrange grid at zero time.	IV-3-106
IV-3.52	DISTANT PLAIN 6—theoretical crater calculation: velocity vectors at $t = 220$ msec.	IV-3-107
IV-3.53	DISTANT PLAIN 6—theoretical crater calculation: Lagrange grid at $t = 223$ msec.	IV-3-108
IV-3.54	Geologic cross section of the Sierra Madera Caldera showing the ring depression around the central uplift. . . .	IV-3-109
IV-3.55	Computed crater profile of the Sierra Madera meteor impact event	IV-3-110
IV-4.1	Ejection process for a buried explosion.	IV-4-4
IV-4.2	Ejection process for a near-surface explosion.	IV-4-5
IV-4.3	Ejecta origins and relative ranges for HE detonations. . . .	IV-4-6
IV-4.4	Fraction of total ejecta volume as a function of range from GZ.	IV-4-7
IV-4.5	Maximum missile range for buried charges	IV-4-9
IV-4.6	Crater centerline profile - underground shot, east-west.	IV-4-14
IV-4.7	Crater centerline profile - surface shot, bearing N $62^{\circ}30'W$	IV-4-14
IV-4.8	Apparent crater profiles (two diameters)	IV-4-16
IV-4.9	Ejecta distribution contours	IV-4-18
IV-4.10	Ejecta distribution, JOHNIE BOY.	IV-4-20
IV-4.11	Exponential distribution of ejecta, JOHNIE BOY	IV-4-21
IV-4.12	Dimensionless plot of ejecta deposition versus range for JOHNIE BOY	IV-4-22
IV-4.13	Fraction of total ejecta volume as a function of range from GZ.	IV-4-23
IV-4.14	Post-trenching profiles.	IV-4-26
IV-4.15	Shot geometry and crater dimensions, DANNY BOY	IV-4-28
IV-4.16	Areas selected for measurement of natural throwout material	IV-4-29

LIST OF ILLUSTRATIONS (Continued)

<u>Figure</u>		<u>Page</u>
IV-4.17	Recovery of ideal objects versus azimuth	IV-4-31
IV-4.18	Total distance thrown from initial position for all objects except bricks and lumber	IV-4-32
IV-4.19	Initial velocity versus initial ground range for all objects except bricks and lumber	IV-4-34
IV-4.20	Maximum trajectory height versus initial ground range for all objects except bricks and lumber	IV-4-35
IV-4.21	Total trajectory time versus initial ground range for all objects except bricks and lumber	IV-4-36
IV-4.22	Initial velocities of deep-buried objects and corresponding maximum initial surface velocities	IV-4-37
IV-4.23	Crater lip and equivalent throwout depths.	IV-4-39
IV-4.24	Cumulative distribution of fragment size, Area II.	IV-4-40
IV-4.25	Angular dispersion of ideal objects versus azimuths.	IV-4-41
IV-4.26	Average mass distribution (δ) versus radial distance from GZ (R) for DANNY BOY.	IV-4-43
IV-4.27	Mass distribution contours, in kg/m^2 , for DANNY BOY.	IV-4-44
IV-4.28	Ejecta deposition in the region of the lip for DANNY BOY . . .	IV-4-45
IV-4.29	Ejecta mass distribution curve for DANNY BOY	IV-4-46
IV-4.30	SCHOONER apparent crater cross sections.	IV-4-50
IV-4.31	Apparent crater and continuous ejecta boundary	IV-4-51
IV-4.32	Isopach map of ejecta thickness.	IV-4-53
IV-4.33	SEDAN lip crest.	IV-4-54
IV-4.34	Diagrammatic section of SEDAN crater lip	IV-4-55
IV-4.35	Size distribution of missiles 2 feet by 2 feet and larger	IV-4-56
IV-4.36	Areal density of missiles 2 feet by 2 feet and larger.	IV-4-57
IV-4.37	Grain-size distribution of the two distinct debris layers	IV-4-59
IV-4.38	Mass of material per unit areas as a function of range	IV-4-60
IV-4.39	Areal density versus distance relationships used for computation of ejecta mass	IV-4-62
IV-4.40	Ejecta mass distribution relative to the crater.	IV-4-63
IV-4.41	Sketch of SEDAN crater lip showing mass quantities	IV-4-65
IV-4.42	Distribution of large impact craters	IV-4-67
IV-4.43	Diagrammatic section of impact crater.	IV-4-68

LIST OF ILLUSTRATIONS (Continued)

<u>Figure</u>		<u>Page</u>
IV-4.44	Ejecta areal density as a function of distance and lip profiles for the TEAPOT ESS crater	IV-4-71
IV-4.45	Ejecta mass distribution curve	IV-4-76
IV-4.46	Ejecta density versus distance	IV-4-83
IV-4.47	Comparison of STAGECOACH and SCOOTER effective velocity fields	IV-4-85
IV-4.48	Comparison of crater volume mass and ejecta mass	IV-4-86
IV-4.49	Crater zones	IV-4-88
IV-4.50	Estimated initial velocities of ballistic pellets.	IV-4-92
IV-4.51	Initial velocity magnitudes in ballistic zone.	IV-4-93
IV-4.52	Simple overturning flow of apparent lip source material.	IV-4-95
IV-4.53	Depth and areal density of fallback and ejecta	IV-4-96
IV-4.54	Scaled cumulative distribution of above-grade fallback and ejecta - AIR VENT and FLAT TOP	IV-4-97
IV-4.55	Ejecta areal density as a function of distance for FLAT TOP I	IV-4-99
IV-4.56	Size distribution of total ejecta through 160 meters	IV-4-101
IV-4.57	Distribution of far-out missiles, FLAT TOP I	IV-4-103
IV-4.58	Cumulative frequency distribution of coded cylinder fragments.	IV-4-104
IV-4.59	Computed values of pellet initial velocities, FLAT TOP II.	IV-4-112
IV-4.60	Computed values of pellet initial velocities, FLAT TOP III . .	IV-4-113
IV-4.61	Initial velocities in the ballistic zone, FLAT TOP II.	IV-4-115
IV-4.62	Velocity magnitudes in ballistic zone, FLAT TOP III.	IV-4-116
IV-4.63	Depth and areal density of fallback and ejecta, FLAT TOP II. .	IV-4-117
IV-4.64	Depth and areal density of fallback and ejecta, FLAT TOP III	IV-4-118
IV-4.65	Maximum range of ejecta versus charge yield for the MIXED COMPANY Surface-Tangent (ST) Events with scaled overburden conditions.	IV-4-127
IV-4.66	Ejecta mass density versus range from GZ for MIXED COMPANY III.	IV-4-128
IV-4.67	Impact velocity versus impact distance from all events, all data	IV-4-130
IV-4.68	Ejecta origin/relative range profiles.	IV-4-133

LIST OF ILLUSTRATIONS (Continued)

<u>Figure</u>		<u>Page</u>
IV-4.69	Correlation of ejection velocity and fragment diameter, Event MIDDLE GUST III	IV-4-145
IV-4.70	Terminal velocity (speed) and associated kinetic energy and momentum for ejecta particles	IV-4-149
IV-4.71	Ejecta particle dimensions for explosions in dense rock . . .	IV-4-150
IV-4.72	Ejecta size versus weight for dense rock.	IV-4-151
IV-4.73	Maximum scaled distance for crater ejecta	IV-4-153
IV-4.74	Maximum range versus size for ejecta particles, all data. . .	IV-4-154
IV-4.75	Ejecta areal density parameters	IV-4-156
IV-4.76	Concept of ejecta weight determinations	IV-4-156
IV-4.77	Ejecta distribution in dense rock	IV-4-158
IV-4.78	Ejecta distribution in soft rock and cohesive soil.	IV-4-158
IV-4.79	Ejecta size distributions, near-surface detonations in dense rock.	IV-4-160
IV-4.80	Ejecta size distributions, near-optimum depth of burial, dense rock.	IV-4-160
IV-4.81	Ejecta size distributions, shallow to medium depth of burial, soft rock	IV-4-161
IV-4.82	Size distributions for five NTS shots	IV-4-163
IV-4.83	MIDDLE GUST III size distribution	IV-4-164
IV-4.84	DIAL PACK size distribution	IV-4-165
IV-4.85	Slope of MINERAL ROCK size distributions.	IV-4-167
IV-4.86	Size distribution for PILEDRIVER chimney rubble	IV-4-168
IV-4.87	PILEDRIVER size distribution.	IV-4-169
IV-4.88	Mass of the largest fragment versus total ejected mass for explosive and impact cratering events	IV-4-171
IV-4.89	Ejecta depth as a function of ranges for nuclear bursts . . .	IV-4-182
IV-4.90	Height of burst effects in the near-surface region.	IV-4-185
IV-4.91	Ejecta depth as a function of overpressure.	IV-4-186

LIST OF ILLUSTRATIONS (Continued)

<u>Figure</u>		<u>Page</u>
IV-4.92	Scaled ejecta depth at 1000 psi (689 N/cm^2) and 600 psi (414 N/cm^2) levels as a function of cratering efficiency.	IV-4-187
IV-4.93	Ejecta thickness at 1000-psi (690 N/cm^2) level from high-yield surface burst in layered geology	IV-4-188
IV-4.94	Origin of crater ejecta	IV-4-195
IV-4.95	SHEP velocity distribution for JOHNIE BOY	IV-4-199
IV-4.96	Ejection history for three calculations	IV-4-201
IV-4.97	Calculated MIXED COMPANY ejecta	IV-4-203
IV-5.1	Geologic section of the crater produced by the explosion in hole 1004.	IV-5-5
IV-5.2	Contours of trench and throwout material produced by explosion T-2.	IV-5-6
IV-5.3	Maximum mass velocity of the medium as a function of distance	IV-5-9
IV-5.4	Medium displacement as a function of distance	IV-5-10
IV-5.5	Relationship of maximum velocities on reduced hypocentric distance.	IV-5-12
IV-5.6	Dependence of reduced displacement amplitude in a three-dimensional wave on reduced distance.	IV-5-13
IV-5.7	Peak vertical velocity and displacement	IV-5-15
IV-5.8	Lines of equal scatter of the ground material following the explosion of a 10-ton charge in clay at a depth of 9 meters.	IV-5-18
IV-5.9	Source map of ejecta from tracer pellet data - Event SCOOTER	IV-5-18
IV-5.10	Multiple exposure photograph of trajectories of artificial ejecta (flares) during a nighttime cratering explosion	IV-5-19
IV-5.11	Maximum range of ejecta	IV-5-19
IV-5.12	Ground motion at various epicentral distances	IV-5-21

LIST OF ILLUSTRATIONS (Continued)

<u>Figure</u>	<u>Page</u>
IV-5.13 Ground displacement on the vertical component A_R^z in different phases of the Rayleigh wave versus epicentral distance	IV-5-22
IV-5.14 Peak vertical displacement (A) as a function of yield (C) and range (r) for near optimally buried charges	IV-5-23
IV-5.15 Time-to-peak displacement in compressional wave when scaled according to the Froude (a) and Cauchy (b) rules	IV-5-24
IV-5.16 Maximal ground displacement along the horizontal component and the time of its increase versus epicentral distance in modeling after Cauchy (a) and after Froude (b).	IV-5-25
IV-5.17 The changing frequency spectra of surface wave, R, and total ground movement, K, depending on the scaled distance.	IV-5-28
IV-5.18 Velocity spectra of ground particle in the p-wave at a distance of $r = 100$ meters from the epicenter (a) and in the R-wave at a distance of $r = 200$ meters (b), when the explosions are set off by charges weighing 1000 kg.	IV-5-29
IV-5.19 Lines of equal velocities for linear explosion No. 17	IV-5-32
IV-5.20 Relative trench depth (a) and ejective index (b) as functions of the relative distance between charges.	IV-5-34
IV-5.21 Experimental setup and cross section of ejecta crater in which the explosion, W, is reckoned from the center of the charge	IV-5-36
IV-5.22 Ejective index as a function of the scaled explosion-source emplacement depth.	IV-5-36
IV-5.23 Ejection-crater volume, referred to the unit of blast energy, as a function of the scaled explosion-source emplacement depth	IV-5-37
IV-5.24 Maximum particle velocity (m/sec) as a function of the scaled distance from the center of the explosion ($m/kg^{1/3}$)	IV-5-38
IV-5.25 Comparison of crater dimensions in model experiments (solid line) with experimental results.	IV-5-39
IV-5.26 Comparison of curves for the rate of rise of the free surface above the shot point as a function of time in field experiments and model experiments	IV-5-40

LIST OF ILLUSTRATIONS (Continued)

<u>Figure</u>		<u>Page</u>
IV-5.27	Schematic layout of high explosive experiment area and gauge stations.	IV-5-45
IV-5.28	Shock front contours at various times after detonation.	IV-5-45
IV-5.29	Dependence of the seismic effect of the scaled depth of burst.	IV-5-56
IV-5.30	Energy in transmitted Rayleigh wave, E_R , as a function of height of burst, h	IV-5-56

LIST OF TABLES

<u>Table</u>		<u>Page</u>
IV-1.1	Connecting identities for the elastic constants of isotropic bodies.	IV-1-9
IV-1.2	Relationship between C_R and C_S for some limiting cases	IV-1-12
IV-1.3	Ratio of horizontal to vertical soil pressures	IV-1-45
IV-1.4	Surface burst dry soil peak air slap parameters.	IV-1-139
IV-1.5	Surface burst wet soil peak air slap parameters.	IV-1-140
IV-1.6	Surface burst soft rock peak air slap parameters	IV-1-141
IV-1.7	Surface burst hard rock peak air slap parameters	IV-1-142
IV-1.8	Surface burst close-in peak-DI/CI parameters	IV-1-159
IV-1.9	Surface burst peak ground roll parameters.	IV-1-165
IV-1.A	Idealized and typical waveforms.	IV-1-174
IV-2.1	Geophysical properties of typical rocks.	IV-2-6
IV-2.2	Hugoniot parameters.	IV-2-29
IV-2.3	Scaled free-field ground motion and pressure in the hydrodynamic region - alluvium	IV-2-33
IV-2.4	Scaled free-field ground motion and pressure in the hydrodynamic region - tuff and granite	IV-2-34
IV-2.5	Regression parameters for free-field ground motion	IV-2-65
IV-2.6	Scaled acceleration in nonlinear and linear regions.	IV-2-70
IV-2.7	Particle velocity in nonlinear and linear regions.	IV-2-71
IV-2.8	Scaled displacement in nonlinear and linear regions.	IV-2-73
IV-2.9	Scaled free-field ground motion—alluvium.	IV-2-77
IV-2.10	Scaled free-field ground motion—alluvium.	IV-2-78
IV-2.11	Scaled free-field ground motion—alluvium.	IV-2-79
IV-2.12	Scaled free-field ground motion—tuff.	IV-2-80
IV-2.13	Scaled free-field ground motion—tuff.	IV-2-81
IV-2.14	Scaled free-field ground motion—tuff.	IV-2-82
IV-2.15	Scaled free-field ground motion—wet tuff.	IV-2-83
IV-2.16	Scaled free-field ground motion—wet tuff.	IV-2-84
IV-2.17	Scaled free-field ground motion—wet tuff.	IV-2-85
IV-2.18	Scaled free-field ground motion—wet tuff.	IV-2-86
IV-2.19	Scaled free-field ground motion—wet tuff.	IV-2-87
IV-2.20	Scaled free-field ground motion—granite	IV-2-88

LIST OF TABLES (Continued)

<u>Table</u>	<u>Page</u>
IV-2.21 Scaled free-field ground motion—granite and dolomite	IV-2-89
IV-2.22 Scaled free-field ground motion—granite	IV-2-90
IV-2.23 Scaled free-field ground motion—volcanic breccia and lava . .	IV-2-91
IV-2.24 Scaled free-field ground motion—lava.	IV-2-92
IV-2.25 Scaled free-field ground motion—shale and rhyolite.	IV-2-94
IV-2.26 Scaled free-field ground motion—bedded salt	IV-2-95
IV-2.27 Scaled free-field ground motion—dome salt	IV-2-96
IV-3.1 Partition of energy between air and ground in a contact burst.	IV-3-8
IV-3.2 Comparative reported Pacific nuclear crater dimensions	IV-3-22
IV-3.3 Summary of some HE cratering experiments. Single-charge events (spherical)	IV-3-30
IV-3.4 HE cratering efficiencies for various earth materials at a zero height of burst.	IV-3-42
IV-3.5 Maximum volume linear crater parameters related to optimum single-charge crater dimensions.	IV-3-49
IV-3.6 Normalized crater data from RCE.	IV-3-56
IV-3.7 Crater data from WES and Boeing multiple-cratering experiments.	IV-3-58
IV-3.8 Crater radius versus yield. Vaile scaling exponents	IV-3-65
IV-3.9 Yield scaling exponents for near-surface bursts for crater dimensions.	IV-3-67
IV-3.10 Crater data from high-g linear acceleration sled	IV-3-71
IV-3.11 Comparison of Fulmer, Dillon, and CERF studies	IV-3-92
IV-3.12 Two-dimensional, finite difference codes in use for ground motion and cratering calculations	IV-3-112
IV-3B.1 Single charges, surface bursts (soil).	IV-3-127
IV-3B.2 Single charges, surface bursts (rock).	IV-3-127
IV-3B.3 Single charges, buried bursts (alluvium)	IV-3-128
IV-3B.4 Single charges, buried bursts (other soil)	IV-3-130
IV-3B.5 Single charges, buried bursts (rock)	IV-3-131
IV-3B.6 Single charges, buried bursts (playa).	IV-3-133
IV-3B.7 Line charges	IV-3-134
IV-3B.8 Row charges.	IV-3-136
IV-3C.1 Nuclear crater data.	IV-3-144

LIST OF TABLES (Continued)

<u>Table</u>		<u>Page</u>
IV-4.1	Comparison of explosive cratering efficiency with that of TNT.	IV-4-2
IV-4.2	Summary of near-surface nuclear events	IV-4-11
IV-4.3	Summary of ejecta data available for events listed in Table IV-4.2.	IV-4-12
IV-4.4	JOHNIE BOY crater and ejecta volumes	IV-4-15
IV-4.5	Summary of deeply buried nuclear events.	IV-4-19
IV-4.6	Summary of ejecta and crater data available on events listed in Table IV-4.5.	IV-4-24
IV-4.7	CABRIOLET crater dimensions.	IV-4-25
IV-4.8	Number of objects recovered.	IV-4-28
IV-4.9	SCHOONER crater data and ejecta.	IV-4-48
IV-4.10	Component masses of crater and lip	IV-4-64
IV-4.11	Maximum ejecta range	IV-4-70
IV-4.12	TEAPOT ESS component masses of crater, ejecta, and lip	IV-4-72
IV-4.13	Summary of scaled apparent crater dimensions	IV-4-74
IV-4.14	Summary of ejecta distribution	IV-4-75
IV-4.15	Some ratio of crater masses.	IV-4-77
IV-4.16	Existence of crater and ejecta distribution data	IV-4-78
IV-4.17	Single-charge chemical explosions.	IV-4-80
IV-4.18	Variation of inverse power of R with distance.	IV-4-82
IV-4.19	Comparison between far-out ejecta and masses of corresponding regions of ballistic zone.	IV-4-89
IV-4.20	Mass distribution of crater, fallback, and ejecta zones, FLAT TOP II.	IV-4-107
IV-4.21	Mass distribution of crater, fallback, and ejecta zones, FLAT TOP III	IV-4-109
IV-4.22	Dissociated mass comparison.	IV-4-111
IV-4.23	Similarity in range of throwout.	IV-4-114
IV-4.24	Distribution of ejecta masses.	IV-4-119
IV-4.25	Fallback and ejecta distribution comparisons	IV-4-119
IV-4.26	Apparent and true crater dimensions, MIDDLE GUST Series.	IV-4-121
IV-4.27	MIDDLE GUST Series ejecta characteristics.	IV-4-123
IV-4.28	Ejecta data from explosively formed craters in rock.	IV-4-135
IV-4.29	Ejecta data from explosively formed craters in clay.	IV-4-140

LIST OF TABLES (Continued)

<u>Table</u>		<u>Page</u>
IV-4.30	Ejecta data from explosively formed craters in layered earth.	IV-4-142
IV-4.31	Survey of existing hydrocode calculations.	IV-4-197
IV-4.32	Mass ejection rates.	IV-4-200
IV-5.1	Summary of cratering measurements from reported Soviet single charge nuclear cratering experiments.	IV-5-4
IV-5.2	Results of the T-2 experiments	IV-5-5
IV-5.3	High explosive cratering tests during the 1957 series in southern Kazakhstan.	IV-5-17
IV-5.4	Reduced data from Kazakhstan and Moscow area experiments . . .	IV-5-27
IV-5.5	Variation of spectral maxima and spectral width as functions of yield.	IV-5-30
IV-5.6	Peak velocity and displacements in compression wave.	IV-5-31
IV-5.7	Upward displacement of center of curvature of bottom half of camouflet from center of explosive	IV-5-41
IV-5.8	Partition of energy between air and ground in a contact burst.	IV-5-47
IV-5.9	Crater data from high-g linear acceleration sled experiments.	IV-5-49

CHAPTER IV-1

GROUND MOTION FROM ABOVEGROUND NUCLEAR EXPLOSIONS*

IV-1.0 INTRODUCTION

The ground shock produced by weapons detonated at or near the earth's surface includes all the motions and stresses produced in the earth's surface and below the surface. This Sourcebook deals exclusively with the free-field ground shock which is defined as the ground shock at a point in the absence of structures near that point. The ground shock induced at a point in the free-field by a nuclear detonation depends on the weapon type and yield, the height or depth of burst, the range and depth of the point of interest, and the geology between the detonation point and the point of interest.

The ground shock strength depends on the amount of weapon energy that is coupled directly into the ground at the detonation point and/or the forces induced on the ground surface by the airblast. At one limit, a fully-contained detonation will produce all ground shock by the energy directly coupled to the ground. At the other extreme, all the ground shock will be produced by the airblast from a non-cratering detonation. For a detonation near the ground surface, ground shock will be produced by a combination of airblast and directly coupled energy. Ground shocks are often defined in the following manner (Reference VI-1.1):

Airblast-Induced Ground Shock: The ground stresses and motions caused by the propagating airblast. Airblast-induced ground shock generally produce the high frequency components of the motions.

Direct-Induced Ground Shock: The ground stresses and motions caused by the initial stress wave due to the energy coupled at the burst point in near-surface and underground detonations.

Crater-Induced Ground Shock: The late-time ground stresses and motions produced by crater formation in a cratering detonation.

*Authors: Fred M. Sauer (Physics International Company) and J. E. Schoutens (General Electric Company-TEMPO).

Close-in to ground zero and at early times, the phenomenology from a surface burst is relatively simple (Reference IV-1.2). The airblast arrives first producing strong downward and outward motions. Then compressional motions associated with the direct-induced ground shock and crater forming process arrive and dominate the late-time phenomena, producing a large upward and outward low-frequency component to the ground motion. The relative amplitude of the close-in motions caused by the two loading mechanisms strongly depends on the height-of-burst and to some degree on the near-surface soil and rock properties. As the range increases beyond a few crater radii, the surface motions change from a relatively simple structure to a complex wavetrain of surface waves. The qualitative features of these surface waves appear to be less and less sensitive to details of the explosive energy coupling with the ground as the range increases. The airblast appears to be simply superimposable on a low-frequency wavetrain that could have as easily occurred for a buried cratering burst as for a surface or airburst. The early-time airblast-related phenomena are well understood (Reference IV-1.2). Although qualitative features of the low-frequency ground motions are thought to be known, there remain major uncertainties of causal and propagation phenomena leading to lower confidence in quantitative predictions of late-time motions from large-yield nuclear surface bursts. Existing data show substantial variation in transient ground motion amplitudes by factors of a few and permanent displacement that could be either up or down, out or in, clockwise or counterclockwise depending on the azimuthal location. Variations observed in many experiments are believed larger than systematic or random measurement errors.

The methods of predicting ground shock are based on a combination of nuclear and high explosive test data. The available near-surface detonation data consist of a few nuclear tests conducted at the Nevada Test Site (NTS) and at the Pacific Proving Ground (PPG). The bulk of the unclassified data is presented in this Sourcebook. The data that are available are limited in their direct application for most problems because of the geologies of the NTS and PPG test areas. Generally, the nuclear test geologies are not representative of the sites of practical interest. For example, tests at NTS were carried out in relatively homogeneous sites of alluvium or playa silt. Therefore, reflection and refraction phenomena produced by the presence of major layer interfaces, such as water tables or hard rock, are not represented in NTS data. Moreover, no effects from severe yielding phenomena associated with wet soils having low shear strength under dynamic load are shown in the data.

The large yield nuclear devices were detonated at Enewetak and Bikini Atolls in the Pacific. The geologic constituents of these atolls include coral sand, shells, coral fragments and layers of limestone. This geology is not representative of most sites of practical interest. The fact that the water table is very close to the detonation point in most of the PPG tests introduces a significant complication in the interpretation of these data. The small land areas of these atolls limited the measurements of ground shock and raised numerous questions concerning the channeling of ground shock in the ring configuration of the chain of atoll islands. The Pacific data are generally in the low overpressure range and measuring stations were widely separated.

On the other hand, non-nuclear test data are available from high explosive tests ranging in yield from grams to 500 tons of TNT. The High Explosive Simulation Test (HEST) has provided ground shock data in various geologies under conditions simulating traveling overpressure effects. The Direct-Induced High Explosive Simulation Technique (DIHEST) has provided ground shock data in rock under simulated direct-induced conditions. The use of spheres of high explosives at various heights-of-burst has also provided various combinations of airblast, direct-induced and cratering effects. Although the degree of nuclear simulation achieved by these high explosive tests is somewhat controversial, the non-nuclear data thus obtained provide information on the in-situ behavior of real geologies. Moreover, these data provide the means to evaluate the capabilities of various theoretical methods (Reference IV-1.1).

Theoretical capability in ground shock prediction and phenomenological understanding has made considerable advances through the application of large-scale, two-dimensional axisymmetric continuum computer programs. These computer programs (for example, References IV-1.3, IV-1.4, and IV-1.5) solve finite difference or finite element approximations to the equations of motion for a continuum. They are capable of treating layered media with constitutive relations that simulate the behavior of real geologies.

These large computer programs still have major shortcomings (Reference IV-1.1). For example, these computational tools have been unable to predict late-time phenomena in all materials, in particular phenomena associated with cratering, near-surface effects and effects at large distances from ground zero. Large uncertainties still remain concerning the energy coupling for the surface detonation. Despite these shortcomings, these computer programs provide qualitative

insight into the areas of uncertainties and to some extent insight into the quantitative relationships between the parameters involved in the predictions and the experimental data.

Uncertainty also exists in defining the mode of intense ground shock attenuation when traversing thousands of feet of soil and rock (Reference IV-1.6).

Limitations in understanding of the high-pressure, close-in response of the ground to early-time radiation and bomb debris lead to uncertainties in predicting the subsequent motions for any detonation configuration. These uncertainties are probably less than those produced by our limited ability to predict detailed characteristics of weapons of the future, including their precise yields and intended heights-of-burst. Earth penetrating weapons might significantly enhance ground shock and even if earth penetration is judged to be impractical, a contact burst represents a serious source of ground shock.* The "best estimate" stresses and motions at a given depth below a contact burst are probably less than half those at the same depth below a shallow-buried burst of the same yield, that is, a contact burst requires perhaps four or five times the yield of a shallow penetrating burst to produce the same environment (Reference IV-1.6).

A large-yield, near-surface nuclear explosion produces ground motions with wavelengths that are several thousand feet long. Geologic features with dimensions of tens, or hundreds, or even thousands of feet (such as joints, fissures, lenses, faults, layering, etc.) influence the earth response in ways that are not clearly understood. Even if the response of such geologic structures were known exactly, the burst point of a weapon will not be known in advance.

Considering all possible transmission paths between possible burst points and a given point in the ground, one is likely to find that such inhomogeneities lead to variations in predictions of the ground shock. The limits of these variations are comparable to the data scatter observed azimuthally in well-instrumented large-yield experiments. Scatter in ground motion data from underground nuclear tests and high-explosive simulation tests often approaches a factor of four or five, and generally is greater than a factor of two (Reference IV-1.6). Even after intensive investigation of a specific geologic site, some residual uncertainties of

*Source details that might strongly influence the coupling in a contact burst configuration are masked by the tamping effect of even a shallow burial. Thus, the uncertainties in quantitative understanding of initial coupling phenomena are probably larger for a contact burst than for a shallow-buried burst.

this order will persist and must be superimposed on the understanding of the attenuation characteristics of that medium. For example, the best-estimate peak stress at a given depth below a given explosion might be an order of magnitude less in soft rock than in hard rock, but an inherent uncertainty of a factor of four might exist in both cases.

In considering the uncertainties in predicting ground shock it is helpful to remind the reader of the distinction between early-time and late-time phenomena. By early-time phenomena is meant the stresses and motions in the neighborhood of the peak stress, principally during the loading phase (10 or so milliseconds following the first signal arrival) and within a few tens of milliseconds following the peak stress arrival for megaton size bursts. By late-time phenomena is meant the earth's response many tens, and even hundreds of milliseconds following the peak stress arrival when the stress has decayed about an order of magnitude below its peak amplitude. Early-time phenomena have been the subject of much theoretical and experimental study and most qualitative features are thought to be reasonably well understood. Late-time phenomena have not been studied thoroughly, and are not well understood (Reference IV-1.6).

IV-1.1 ORIGIN OF GROUND MOTION

It is useful to begin the discussion of the ground motion data presented in the next two chapters by calling the reader's attention to a few basic ideas that will help in understanding the origin of ground motion. We begin by describing the types of waves that originate from detonations in a medium as a consequence of basic equations describing the medium behavior. We then proceed to describe the propagation of ground motion as it relates to aboveground and underground nuclear detonations. Although the discussion that follows applies to purely elastic media, the behavior of real media such as soil and rock are far from purely elastic. The materials in which nuclear and high explosive detonation tests were carried out display a considerable amount of hysteresis. The development of equations of motions and the discussion of their solutions for real soils or rock is beyond the scope of this Sourcebook. However, by discussing the equations of motion for purely elastic materials, much useful information can nevertheless be gained that will help the reader in understanding the sections that follow. A useful general discussion on the properties of geologic materials may be found in Section 5.2 of Reference IV-1.1.

An explosion above or below ground will generate extremely high pressures and temperatures that originate from the sudden release of large amounts of energy. This energy release initiates a strong shock in the surrounding medium. For an aboveground explosion an airshock is generated, part of which is transmitted to the ground. For an underground explosion the diverging stress wave can be considered as consisting of four successive regimes which depend on wave pressure. These regimes are hydrodynamic, plastic, crush-up, and elastic (Reference IV-1.7). During the hydrodynamic regime, the stress wave pressure is high enough to classify the wave as a strong shock wave, and its propagation can be described by the use of the Hugoniot jump conditions. During the next three stress wave regimes the strength and porosity of the surrounding medium become important. In particular, their effect upon the variation in sound speed as the wave propagates from the plastic through the crush-up to the elastic regime can have a large effect on the propagation velocity of the wave.

If we now idealize the medium to a perfectly elastic one for simplicity of argument and consider a small amount of material that is subjected to forces resulting in non-equilibrium internal forces, the behavior of that material is described by an equation of motion of the type (Reference IV-1.8).

$$\rho \frac{\partial^2 \bar{u}}{\partial t^2} = (\lambda + \mu) \nabla(\nabla \cdot \bar{u}) + \mu \nabla^2 \bar{u} + \bar{f}_{\text{ext}} \quad (\text{IV-1.1})$$

where λ and μ are the Lame constants (the constant μ is identical with the shear modulus - - the ratio between the shear stress and the shear strain), \bar{u} is the displacement velocity of an element at coordinates x, y, z, ρ in the material density, and \bar{f}_{ext} are external body forces such as gravity. For detonations very near the surface, \bar{f}_{ext} may be neglected. However, for buried explosions \bar{f}_{ext} plays an important part in determining the crater or cavity formation, the venting process, and the coupling of energy to the ground. This equation has the form of a wave equation and for materials whose elastic properties are isotropic a general solution can be found. This equation will be found to have two types of waves. Following Reference IV-1.8, we can set $\bar{u} = \bar{u}_1 + \bar{u}_2$ so that $\nabla \cdot \bar{u}_1 = 0$ and $\nabla \times \bar{u}_2 = 0$. By substituting $\bar{u}_1 + \bar{u}_2$ for \bar{u} in Equation IV-1.1 and eliminating \bar{u}_1 by taking the divergence of that equation there results

$$\rho \frac{\partial^2}{\partial t^2} (\bar{\nabla} \cdot \bar{u}_2) = (\lambda + \mu) \nabla^2 (\bar{\nabla} \cdot \bar{u}_2) + \mu \bar{\nabla} \cdot \nabla^2 \bar{u}_2$$

and since ∇^2 can be interchanged with $\bar{\nabla} \cdot$ we obtain

$$\nabla \cdot \left\{ \rho \frac{\partial^2}{\partial t^2} \bar{u}_2 - (\lambda + 2\mu) \nabla^2 \bar{u}_2 \right\} = 0$$

and since $\nabla \times u_2 = 0$, the curl of the bracket is also zero so that there results the first wave equation

$$\rho \frac{\partial^2 \bar{u}_2}{\partial t^2} = (\lambda + 2\mu) \nabla^2 \bar{u}_2 \quad (\text{IV-1.2})$$

By the same method it can be shown that the second wave equation is

$$\rho \frac{\partial^2 \bar{u}_1}{\partial t^2} = \mu \nabla^2 \bar{u}_1 \quad (\text{IV-1.3})$$

Equations IV-1.2 and IV-1.3 have waves propagating at speeds

$$c_p = \sqrt{(\lambda + 2\mu)/\rho} \quad (\text{IV-1.4})$$

$$c_s = \sqrt{\mu/\rho} \quad (\text{IV-1.5})$$

These are body waves: the first one being called p-waves or compressional waves and the second called s-waves or shear waves.* These names are used synonymously.

*Sometimes the name dilatational wave will be found, and shear waves are sometimes referred to as rotational waves.

The p-waves propagate ahead of the shear waves and arrive at a detector earlier than the shear waves. The p-waves produce material stresses that are along the direction of propagation (radial) while the s-waves produce stresses that are contained in a plane normal to the direction of propagation. Since λ and μ are characteristics of the medium, the values of C_p and C_s apply to all four regimes mentioned above provided the Lamé constants are redefined accordingly. (Alternatively, one can define C_p and C_s in terms of ground characteristics as for example in References IV-1.7 and IV-1.9.) In fact, the most difficult part in the theoretical description of ground media strained by detonations involve the definition of the Lamé constants for the four basic regimes mentioned above. Table IV-1.1 (Reference IV-1.9) shows the relationship between the Lamé constants and other material properties.

Elastic solids can support more than one kind of body wave. The description above applies to isotropic and non-porous solids which transmit compression (p) and shear (s) waves. In stratified solids, these motions are coupled. Mathematically, this coupling arises from the fact that the equations of motion are of fourth order in the space derivatives and have variable coefficients. Physically this means that as the disturbance propagates through the medium the p- and s-wave fields continuously interact and exchange energy. If the interaction forces are weak, the effect is negligible and the equations of motion degenerate into two uncoupled wave equations, one corresponding to p-waves propagating at speed C_p and the other to s-waves propagating at velocity $C_s < C_p$. For porous, liquid-saturated and stratified solids the problem becomes quite complex, the basic equations being of sixth order at least with variable coefficients. On the other hand if the medium is macroscopically homogeneous, these equations degenerate into a second-order, modified shear-wave equation and a fourth-order system representing compressional waves of two kinds with different velocities. The interested reader can find a treatment of the theoretical aspects of this problem in Reference IV-1.10.

Because the media in which detonations occur are not infinite but have boundaries, these boundaries give rise to a second class of waves called surface or boundary waves. The surface of discontinuity or boundary is an intrinsic part of the propagation of such waves. A classic case is that of gravity waves on the surface of an incompressible, homogeneous half-space (for example, water). This case shows that the surface-wave phenomena is unrelated to body-waves as described above. In fact body-waves do not exist for this case (Reference IV-1.10). Of particular importance to ground motion are Rayleigh waves which exhibit large

Table IV-1.1. Connecting identities for the elastic constants of isotropic bodies (Reference IV-1.9).

K	E	λ	v	$\rho_0 c_p^2$	$\rho_0 c_s^2$
$\lambda = \frac{2}{3}\mu$	$\frac{3\lambda + 2\mu}{\mu(\lambda + \mu)}$		$\frac{\lambda}{2(\lambda + \mu)}$	$\lambda + 2\mu$	μ
	$9K\frac{\lambda - \mu}{3K - \lambda}$		$\frac{\lambda}{3K - \lambda}$	$3K - 2\mu$	$\frac{3(K - \lambda)}{2}$
	$\frac{9K\mu}{3K + \mu}$	$K - \frac{2\mu}{3}$	$\frac{3K - 2\mu}{2(3K + \mu)}$	$\lambda + \frac{4}{3}\mu$	
		$\mu \frac{E - 2\mu}{3\mu - E}$	$E/2\mu - 1$	$\frac{4\mu - E}{\mu(3\mu - E)}$	
		$3K\frac{3K - E}{9K - E}$	$\frac{3K - E}{6K}$	$\frac{3K + E}{3K + E}$	$\frac{3KE}{9K - E}$
		$\lambda \frac{(1 + v)(1 - 2v)}{v}$		$\lambda \frac{1 - v}{v}$	$\lambda \frac{1 - 2v}{2v}$
	$\frac{2(1 + v)}{\mu(1 - 2v)}$	$2\mu \frac{2v}{1 - 2v}$		$\mu \frac{2(1 - v)}{1 - 2v}$	
		$3K(1 - 2v)$	$3K \frac{v}{1 + v}$	$3K \frac{1 - v}{1 + v}$	
			$\frac{Ev}{(1 + v)(1 - 2v)}$	$\frac{E(1 - v)}{(1 + v)(1 - 2v)}$	$\frac{E}{(1 + v)^2}$
	$\frac{E}{3(1 - 2v)}$	$\rho(c_p^2 - \frac{4}{3}c_s^2)$	$\rho(c_p^2 - 2c_s^2)$		

a K = bulk modulus, E = Young's modulus, μ = shear modulus, λ = Lame's constant, v = Poisson's ratio.

ρ = density, c_p = compressional velocity, c_s = shear velocity.

amplitudes and long wavelength. (If the solid half-space is homogeneous and isotropic, Rayleigh waves are non-dispersive.) They are generally observed in connection with shallow-focal depth explosions or earthquakes. These waves correspond to two-dimensional spreading of energy from the source and decay exponentially with distance from the source. They arrive after the p- and s-wave arrivals. Rayleigh waves have a horizontal and vertical component contained in a plane perpendicular to the surface along which the waves are traveling and parallel to the direction of propagation. The particle motion follows an ellipse in the plane described and the shape of this ellipse depends upon the value of Poisson's ratio for the medium. Sometimes the vertical component is completely absent (Reference IV-1.11.). For Rayleigh waves, the direction of vibration of the horizontal components should be parallel to the direction of propagation. Horizontal components parallel to the wave front have been observed. These are called Love waves and it can be shown (References IV-1.11, IV-1.12, and IV-1.13) that these waves can be propagated through a layer of the earth without penetrating into the interior. We will not discuss these waves here as the interested reader can consult the references just mentioned. Love waves are part of a more general class of interface waves called Stoneley waves (References IV-1.10 and IV-1.11). Stoneley waves propagate mainly between solid-solid and solid-liquid interfaces. They have been observed at solid-solid and solid-liquid boundaries but not at solid-gas interfaces.

The propagation of surface waves can be obtained from the equation of motion, Equation IV-1.1. The procedure requires the definition of two potential functions to represent the dilatation and the rotation portion of an element of the stressed medium. These functions are substituted in the equation of motion neglecting the external forces. (Eliminating the external forces such as gravity simplifies the solution but yields surface waves that are non-dispersive which implies an isotropic and non-porous solid. Addition of the gravity effect can be made later on to show that such waves then become dispersive. See for example the discussion in Chapter 5 of Reference IV-1.10). There results two uncoupled partial differential equations describing the propagation of the dilatational and the rotational disturbances in the medium. Exponential solutions with variable coefficients are assumed and substituted in these equations. The variable coefficients are amplitude terms depending only on depth from the free surface into the solid. The boundary conditions of zero stress (this is not the case when airblast effects are present, see Section IV-1.5) at the solid surface are then applied to these solutions thereby

yielding the following equations

$$A \left\{ (\lambda + 2\mu) q^2 - \lambda k^2 \right\} - 2B\mu iSk = 0 \quad (IV-1.6)$$

$$2iqkA + (S^2 + k^2)B = 0 \quad (IV-1.7)$$

where A and B are constants to be determined, k is the wave number of the propagating disturbance and

$$q^2 = k^2 - k_p^2$$

$$S^2 = k^2 - k_s^2$$

where k_p and k_s are the compressional (p) wave and the shear (s) wave numbers, respectively. Equations IV-1.6 and IV-1.7 represent a homogeneous system of linear equations in two unknowns A and B. For their solution to be non-trivial, the determinant of the coefficient must vanish. The relationship between p-, s-, and R-wave velocity is obtained by combining Equations IV-1.6 and IV-1.7 to yield (Reference IV-1.11)

$$K^6 - 8K^4 + (24 - 16\alpha^2)K^2 - 16(1 - \alpha^2) = 0$$

where

$$\alpha = \frac{c_s}{c_p}$$

and

$$K = \frac{c_R}{c_s}$$

where C_R is the Rayleigh wave speed. Table IV-1.2 shows the relationship between C_p and C_s for some limiting cases of the value of Poisson's ratio.

Table IV-1.2. Relationship between C_R and C_s for some limiting cases (Reference IV-1.10).

Poisson's Ratio	Rayleigh Wave Speed
$\nu = \frac{1}{2}$ (incompressible solid)	$C_R = 0.955 C_s$
$\nu = \frac{1}{4}$ (typical value)	$C_R = 0.9194 C_s$
$\nu = 0$ (perfectly compressible solid)	$C_R = 0.85 C_s$

These values show that for most solids for which $0.25 \leq \nu \leq 0.5$, that is, over the range from completely incompressible to normal values in rock, the Rayleigh wave velocity is not particularly sensitive to the compressibility of the solid: C_R varies less than 4 percent over the range of ν indicated above.

Since the potential solutions used in solving the equation of motion lead to Equations IV-1.6 and IV-1.7, the particle motion is confined to the vertical xz plane as for the p- and s-waves. The exact shape of the orbit depends upon the value of Poisson's ratio. For example, if $\nu = \frac{1}{4}$, that is, $C_R = 0.9194 C_s$, the ratio of the vertical-to-horizontal displacement of the particle is 1.5 and the motion is counterclockwise if the wave propagates from left to right. At a depth of $Z \approx -1.2/k$, the horizontal displacement vanishes, where k is the wave number as defined above. The details of the derivations of the equations discussed here are given in Chapter 5 of Reference IV-1.10 and Chapter 2 of Reference IV-1.11.

In summary we can say that explosions above or below ground will generate disturbances of at least three types identified as compressional (p) and shear (s) waves and surface or Rayleigh waves. The p- and s-waves are body waves, and the surface waves occur because of the boundary of the solid. The speed of propagation of these waves are related as follows:

$$C_R < C_s < C_p$$

which means that at any detector station at or just beneath the surface, the p-wave arrives first followed by the s-wave and finally the arrival of the Rayleigh wave. The first two decay faster with range and the Rayleigh wave decays rapidly with depth.

Now that the reader has some conception of the types of waves that can be propagated in a solid medium we will consider the actual amplitudes of these waves and their form since they are what is generally measured in field experiments. The magnitude and waveform of ground motion induced by nuclear detonations depend upon the yield of the detonation, the height above or below ground at which the detonation occurs, the physical properties of the ground medium and the ground range to the detector station. For surface detonations (detonations very near or at the ground surface) and for underground detonations, a substantial portion of the energy is directly effective in producing pressures of multimegabar magnitude in the ground immediately adjacent to the weapon case. The fraction of energy coupled in this manner depends upon the construction of the weapon, for example, the radiation opacity of the weapon case. When the detonation is below the ground surface, the energy coupling depends on the degree to which the ground above the weapon provides additional tamping (Reference IV-1.14). As defined in the Introduction, Section IV-1.0, energy coupled by an underground explosion process into the ground results in directly-induced ground motion.

For weapons detonated above, at the surface or just below the surface, energy also appears in the form of an airblast, which induces ground motion by imposing normal pressures and horizontal shear forces on the ground surface. This is the airblast-induced ground motion. Due to the much lower acoustic impedance of air compared to the acoustic impedance of the ground medium, stresses in the ground produced by airblast can be substantially smaller than those generated by a detonation in the ground. However, stress levels at aboveground structures are generally such that airblast induced stresses are equal to or larger than direct induced stresses. The ratio of the average transmitted and reflected power are given by (Reference IV-1.12)

$$\frac{\bar{P}_t}{\bar{P}_i} = \frac{4\rho_2 C_p / \rho_1 C_1}{(1 + \rho_2 C_p / \rho_1 C_1)^2} \quad (\text{IV-1.8})$$

$$\frac{\bar{P}_r}{\bar{P}_i} = \left(\frac{1 - \rho_2 C_p / \rho_1 C_1}{1 + \rho_2 C_p / \rho_1 C_1} \right)^2 \quad (\text{IV-1.9})$$

where ρ_1 and ρ_2 are the air and ground densities respectively, and C_1 and C_p are the air sound speed and the p-wave propagation speed in the ground, respectively. Note that for an air/ground interface $\rho_2 C_p \gg \rho_1 C_1$, which results in $\bar{P}_r \approx \bar{P}_i$, $\bar{P}_t \approx 0$. Consequently for some practical purposes, stresses due to airblast-induced ground motion may be neglected when compared to direct induced ground motion phenomena (Reference IV-1.15). On the other hand, the directly induced stresses attenuate with distance much more rapidly, approximately as the inverse cube of distance so that at some distance from ground zero, these stresses become weaker than the airblast-induced stresses. Thus at any given position, except for a small intermediate region, the major component of the ground stresses and hence ground motion will either be directly induced or airblast-induced but generally not both. In the seismic region, the ground motion attenuates approximately as the inverse of the range from the source (see for example Reference IV-1.16). Estimation of direct-induced ground motion relies primarily on empirical data and the estimation of airblast-induced ground motion, on the other hand, relies primarily, but not entirely, on theory. It should be noted that low frequency components are presently poorly understood for airblast-induced and direct-induced ground motion. We will now discuss the behavior of these waves in different regions from ground zero.

The propagating airblast is a major source of ground shock. The characteristics of the airblast-induced ground shock is governed by the properties of the airblast wave and the properties of the geology. The airblast arrives at a point on the ground surface as a sharply defined shock having a velocity that depends on the peak overpressure. Following the passage of the shock front, the overpressure decreases and soon becomes negative. The overpressure before it becomes negative is called the positive phase of the shock while the other is called the negative phase. As the range from the source increases, the peak overpressure and the shock velocity decrease while the total pulse duration increases. At a point on the ground located immediately beneath the airblast, that point will experience two distinct wave arrivals: the compressive and the shear waves mentioned above. At locations near the surface, a von Schmidt or sp-wave* in addition to a Rayleigh

*von Schmidt waves are also called head waves.

wave are also experienced (Reference IV-1.7). In a homogeneous half-space, the character of the early-time shock is determined by the relative magnitudes of the airblast shock velocity and the wave speed in the half-space medium. Three regions are to be distinguished: the superseismic, the transseismic, and the subseismic. These regions are shown in Figure IV-1.1. The superseismic region is defined as the region where the airblast velocity exceeds the compression and the shear wave velocities in the half-space, thus

$$U > C_p > C_s$$

where U is the airblast shock velocity as shown in Figure IV-1.1a. C_p and C_s are as defined above. Since U is larger than either C_p or C_s in the medium, no disturbance can be propagated ahead of the airblast. The ground shock can therefore only trail the airblast below the surface.

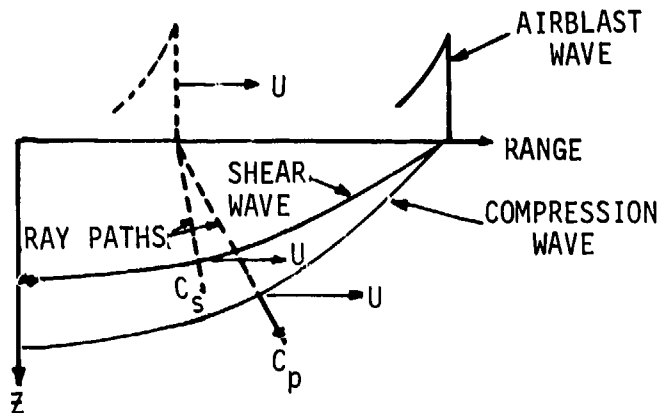
When the airblast shock velocity becomes less than the compression wave velocity, the shear wave velocity or both, disturbances can propagate through the ground ahead of the airblast. Now two cases become possible. The transseismic case shown in Figure IV-1.1b occurs when the airblast shock velocity is smaller than the compression wave velocity but greater than the shear wave velocity or

$$C_p > U > C_s$$

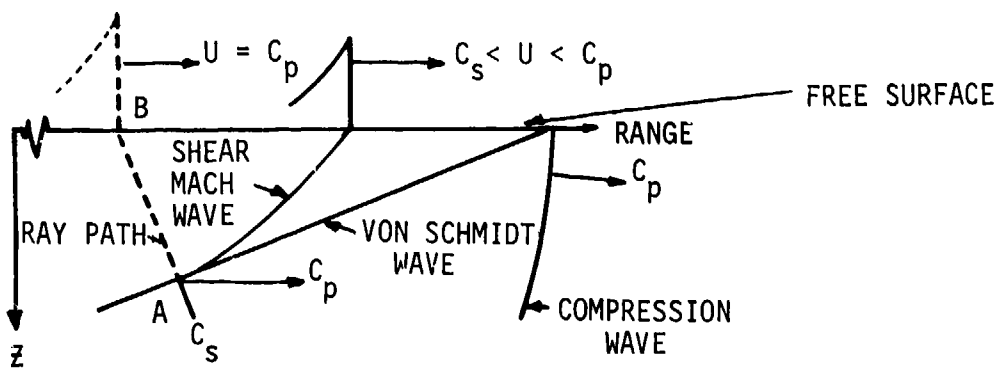
In this case the compression wave propagates ahead of the airblast while the shear wave propagation is controlled by the airblast shock velocity. In the subseismic case shown in Figure IV-1.1c, the airblast shock velocity is now smaller than either the compression or shear wave velocities or

$$U < C_s < C_p$$

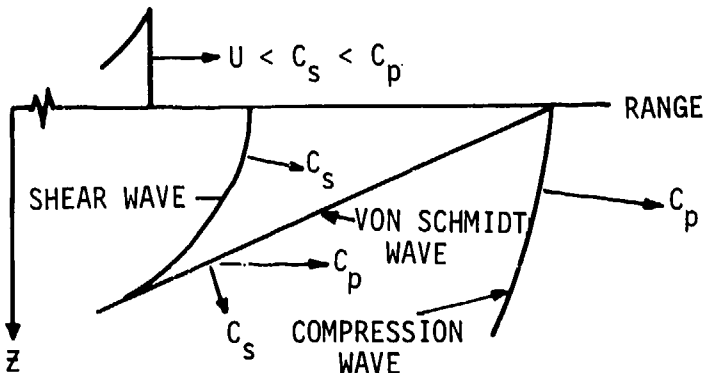
and both propagate ahead of the airblast. In the transseismic and subseismic regions, the ground disturbances arrive at a point before the arrival of the airblast. These regions are therefore often referred to as the outrunning regions because the ground shock outruns the airblast. Ground motions in the outrunning regions are very complex. Typical outrunning ground motion accelerograms are shown in Figure IV-1.2. Note that for (a) the ground motion has just started to outrun the airblast as indicated by the initially slow rise of the acceleration pulse. The time phasing from all overpressure levels can produce reinforcements and oscillations at early and late times. The presence of geologic layering



(a) SUPERSEISMIC AIRBLAST WAVE SYSTEM



(b) TRANSSEISMIC AIRBLAST WAVE SYSTEM



(c) SUBSEISMIC AIRBLAST WAVE SYSTEM

Figure IV-1.1. Underground wave systems due to an airblast.

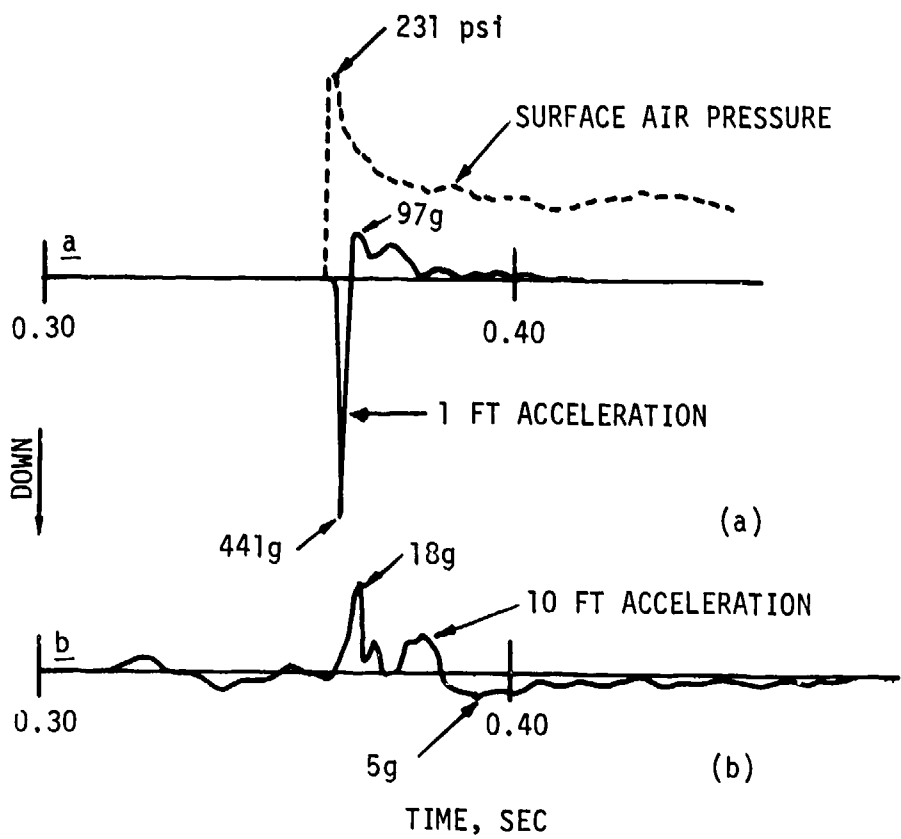


Figure IV-1.2. Typical accelerograms for outrunning ground motion.

introduces additional complications at early and late times. Thus a complex pattern of wavefronts develops because of wave reflections and refractions at layer interfaces. The energy refracted in underlying layers reenter the top layer causing outrunning to occur in the top layer prior to the point where the airblast shock becomes either transseismic or subseismic with respect to the surface layer. Multiple reflections within the top layer can have significant influence on the late time motion.

Figure IV-1.3 shows an example of the wavefront diagram for a two-layer medium in which the compression wave velocity of the substratum equals three times the compression wave velocity of the overburden. The overburden has a thickness h_1 . As previously noted, ray paths in the superseismic region are straight lines. Elements of the wavefront move in the direction of the ray path at the compression wave velocity. Horizontal motion takes place with a velocity equal to the airblast velocity at the point of origin of the ray path. When the wavefront intercepts an interface as shown in Figure IV-1.3a, a fraction of the energy is reflected and a fraction is refracted into the substratum according to Equations IV-1.8 and IV-1.9 with refraction angles according to Snell's law. The refracted energy does not return to the surface unless another deeper stratum with another acoustic impedance is present. For example, if this third layer has $\rho_3 C_p > \rho_2 C_p$ then $\bar{P}_t < \bar{P}_i$ and the wave is entirely reflected. (See for example Reference IV-1.18 for details on the treatment of multilayered media.)

A ray will become totally refracted, that is, refracted in a direction parallel to the interface, when the airblast velocity, U , first becomes equal to the compression wave velocity of the substratum, C_{po} .

Energy then travels along the interface at a velocity equal to C_{po} , or less, resulting in the sequence of wavefront diagrams shown in Figure IV-1.3a. (The wave traveling along EF is an example of a Stoneley wave. This wave is dispersive in a direction normal to the boundary - Reference IV-1.10. Thus, the ray path FG is not the propagation path of the Stoneley wave.) The emergence at the surface of the wave in the upper medium induced by the energy traveling along the interface (point G of Figure IV-1.3a) is the first appearance of the outrunning waveform. Since the initial particle velocity is always in a direction normal to the wavefront, the initial motion is seen to be upward and outward. It is readily determined that the angle of emergence of the critical ray path (FG of Figure IV-1.3a) equals the angle of entrance, of path DE, and hence the theoretical

problem is solved once the time of arrival curve of the airblast is prescribed. As shown in Figure IV-1.3b, a shear wave is also generated at the front of the Stoneley wave at the interface between the overburden and the substratum. The shear wave has approximately twice the velocity amplitude of the outrunning wave.

Comprehensive ground shock analysis in real geologic media has not progressed to the point where simplified techniques are available for use in design and analysis (Reference IV-1.1). Most of the existing prediction techniques are in the development stage and large uncertainties are associated with material properties and the required complexity of the problem. A number of prediction methods are described in Reference IV-1.1. They are based on concepts and data derived from theoretical studies and field test observations.

A sample calculation taken from Reference IV-1.1 is given to illustrate a method of estimating ground shock through a two layer system.

While it is convenient to categorize ground shock according to the source for purposes of discussion and computation, practical problems require an estimate of the complete ground shock environment at a point of interest. The complete environment will result from disturbances arriving from all sources, except in the case of a true air detonation or a fully contained detonation. Although not theoretically correct, a reasonable approximation to the complete ground shock environment may be obtained by superimposing credible airblast-induced, crater-induced and outrunning waveforms according to their relative time-phasing. The airblast arrival time at a given range can be estimated from Reference IV-1.19. The arrival times of disturbances propagated through the ground may be estimated by standard geophysical methods (see for example Reference IV-1.20). Figure IV-1.4 illustrates the paths by which disturbances may travel in a two-layer system. The discussion is restricted to compression waves since they travel with the greatest velocity and will be the first to arrive along any given path. The incident compression wavefront created by an excitation at point S will be hemispherical. The wave paths are represented by rays which are perpendicular to the wavefront and parallel to the direction of wave propagation. One path from the point of excitation to a point a distance x away is a direct path through the top layer. The arrival time for the direct path is simply

$$t_a = \frac{x}{c_{\rho_1}} \quad (\text{IV-1.10})$$

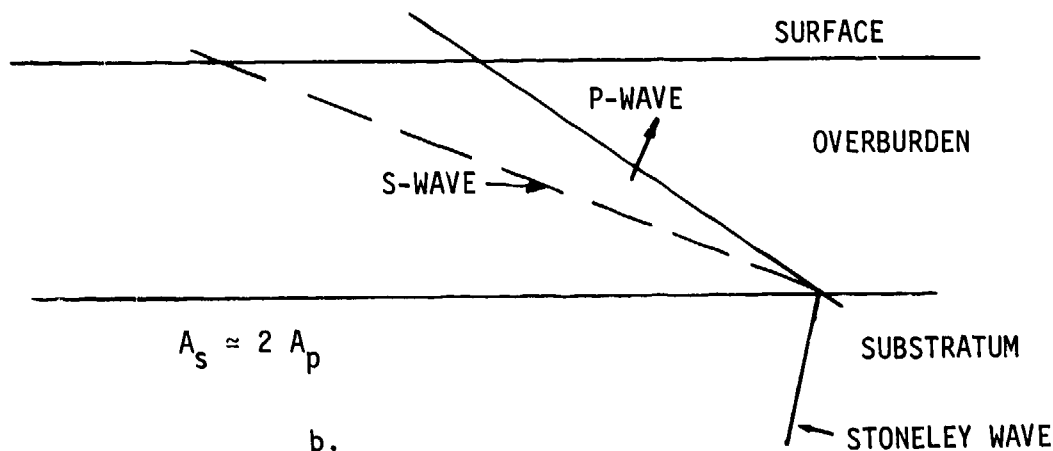
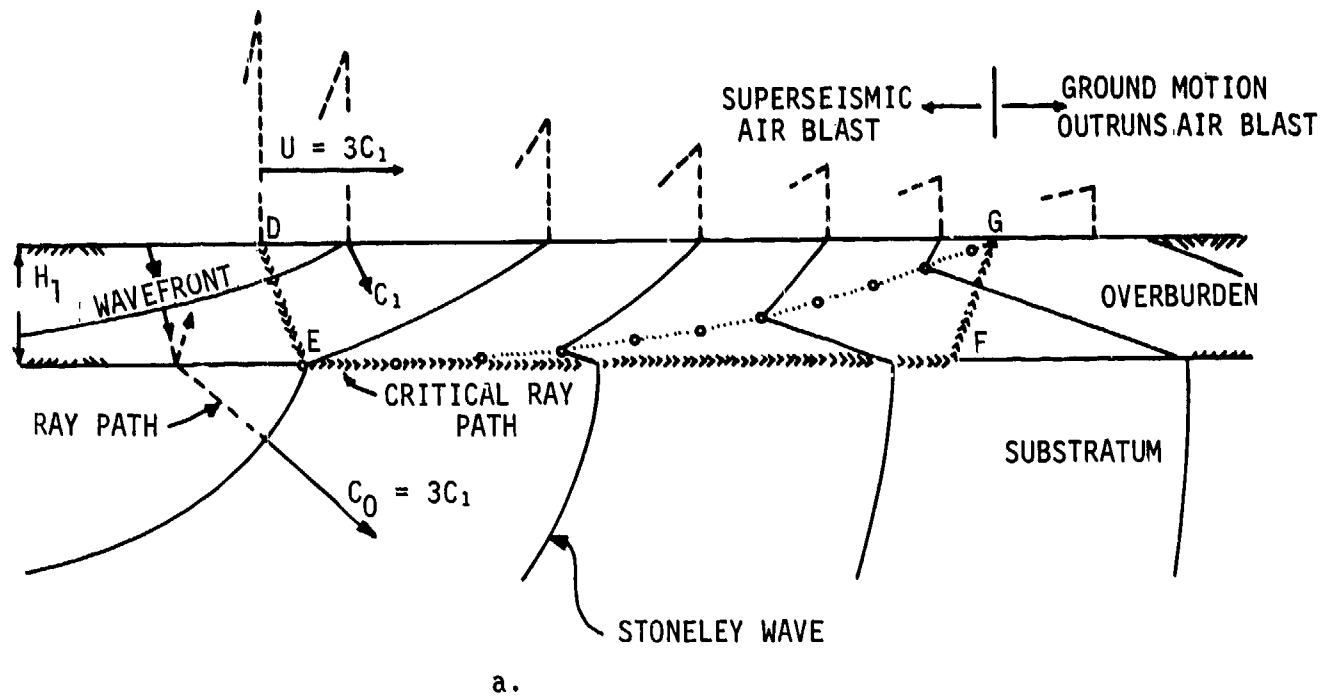
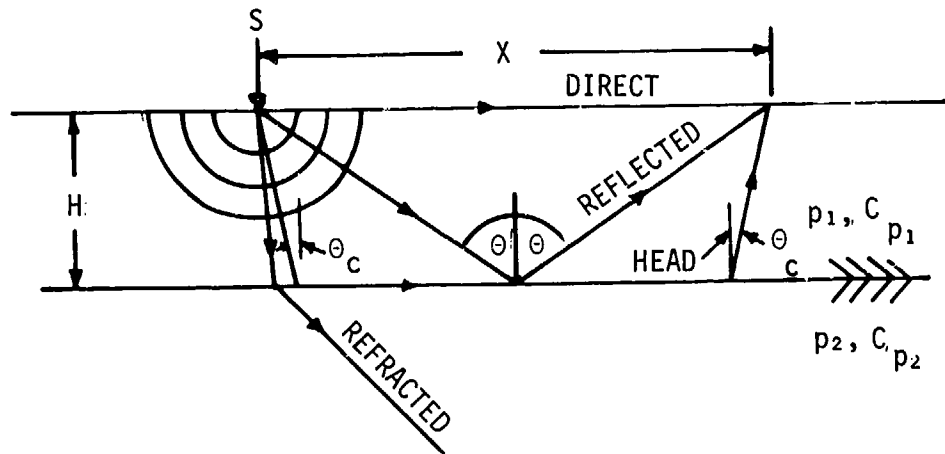
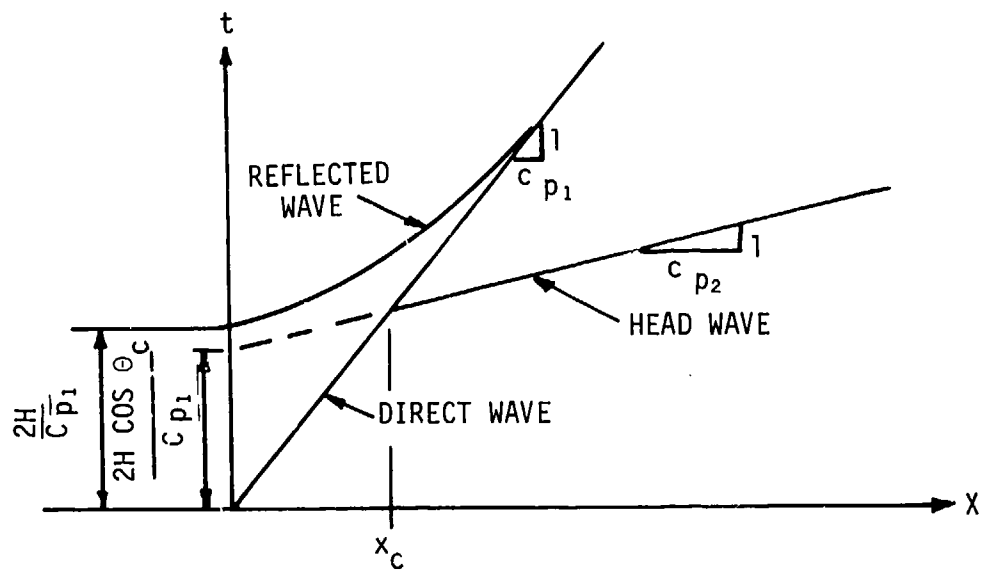


Figure IV-1.3. Ray path diagram for determination of critical ray path for two-layer medium.



(a) Travel Paths



(b) Arrival Time-Distance Curves

Figure IV-1.4. Wave transmission through a two-layer system.

where t_a is the arrival time, x is the distance from the excitation source point of interest, and C_{p_1} is the compression wave velocity in the first layer.

The existence of a layer interface creates two additional paths. The interaction of the incident wave with the layer interface causes reflected waves which travel back toward the surface and refracted waves which continue into the lower medium. The arrival time of the reflected wave at a surface point is

$$t_a = \sqrt{\frac{x^2 + 4H^2}{C_{p_1}}} \quad (\text{IV-1.11})$$

where H is the layer depth. In general, the refracted wave does not return to the surface unless a deeper interface is encountered. However, there is a critical angle of incidence, θ_c , for which the refracted wave travels parallel to the interface in the lower medium. The critically refracted wave causes a disturbance along the interface which, in turn, generates a wave which travels upward into the layer. This new wave is called a Stoneley or head wave and its arrival time at the surface is given by

$$t_a = \frac{x}{C_{p_2}} + \frac{2H \cos \theta_c}{C_{p_1}} \quad (\text{IV-1.12})$$

$$= \frac{x}{C_{p_2}} + 2H \sqrt{\frac{1}{C_{p_1}^2} - \frac{1}{C_{p_2}^2}}$$

where C_{p_1} is the compression wave velocity in the top layer, C_{p_2} is compression wave velocity in underlying half space, and θ_c is the critical angle equal to $\arcsin(C_{p_1}/C_{p_2})$.

The arrival times of the direct, reflected and Stoneley or head waves are shown as a function of distance in Figure IV-1.4b. For distances less than x_c , called the crossover distance, the first arrival will be due to the direct wave. At distances greater than x_c , the Stoneley wave will arrive first. The reflected

wave will lag the direct and Stoneley waves at all distances and, therefore, is not of importance in considering first arrivals.

In multilayered systems, the time of arrival of the Stoneley wave from the n^{th} interface (see Figure IV-1.5) is given by

$$t_a^{(n)} = \left(\sum_{i=1}^n 2H_i \sqrt{\frac{1}{C_{pi}^2} - \frac{1}{C_{pn+1}^2}} \right) + \frac{x}{C_{pn+1}} \quad (\text{IV-1.13})$$

where $t_a^{(n)}$ is the arrival time of head wave from n^{th} interface, H_i is the thickness of the i^{th} layer, C_{pi} is the compression wave velocity in i^{th} layer, and C_{pn+1} is the compression wave velocity in $(n+1)^{\text{th}}$ layer. The use of Equation IV-1.13 for two-layer and three-layer systems is illustrated in Figure IV-1.6. The summation in the parentheses of Equation IV-1.13 is the time axis intercept of the arrival time-distance line for the n^{th} interface Stoneley wave. The summation term is designated by T_n (i.e., T_1 , T_2 , etc.) in Figure IV-1.6.

For the two-layer system of Figure IV-1.6a, it can be seen that the direct wave governs the first arrival at distances less than $x_c^{(1)}$. Between $x_c^{(1)}$ and $x_c^{(2)}$, the Stoneley wave from the first interface is the first to arrive. Beyond $x_c^{(2)}$, the Stoneley wave from the second interface governs.

The general method for determining arrival time-distance curves for ground disturbances may be used with the arrival time-distance curve for the airblast to estimate the time phasing of effects at a point of interest and the ground range at which outrunning first occurs (Reference IV-1.21). In addition, the arrival-time-distance curves may be used to estimate the effective seismic velocity, C_e , used to estimate crater-induced particle velocities and rise times to peak crater-induced horizontal displacement. The effective seismic velocity is simply the inverse slope of the secant line drawn from the origin to the range of interest.

The time of arrival of the airblast wave can be read directly from the airblast time of arrival curve. Also, the arrival time of effects from the source region can be read directly from the ground disturbance curve intersecting the burst point. The ground range at which earliest ground signals and the airblast wave arrive at exactly the same time is the ground range at which outrunning first

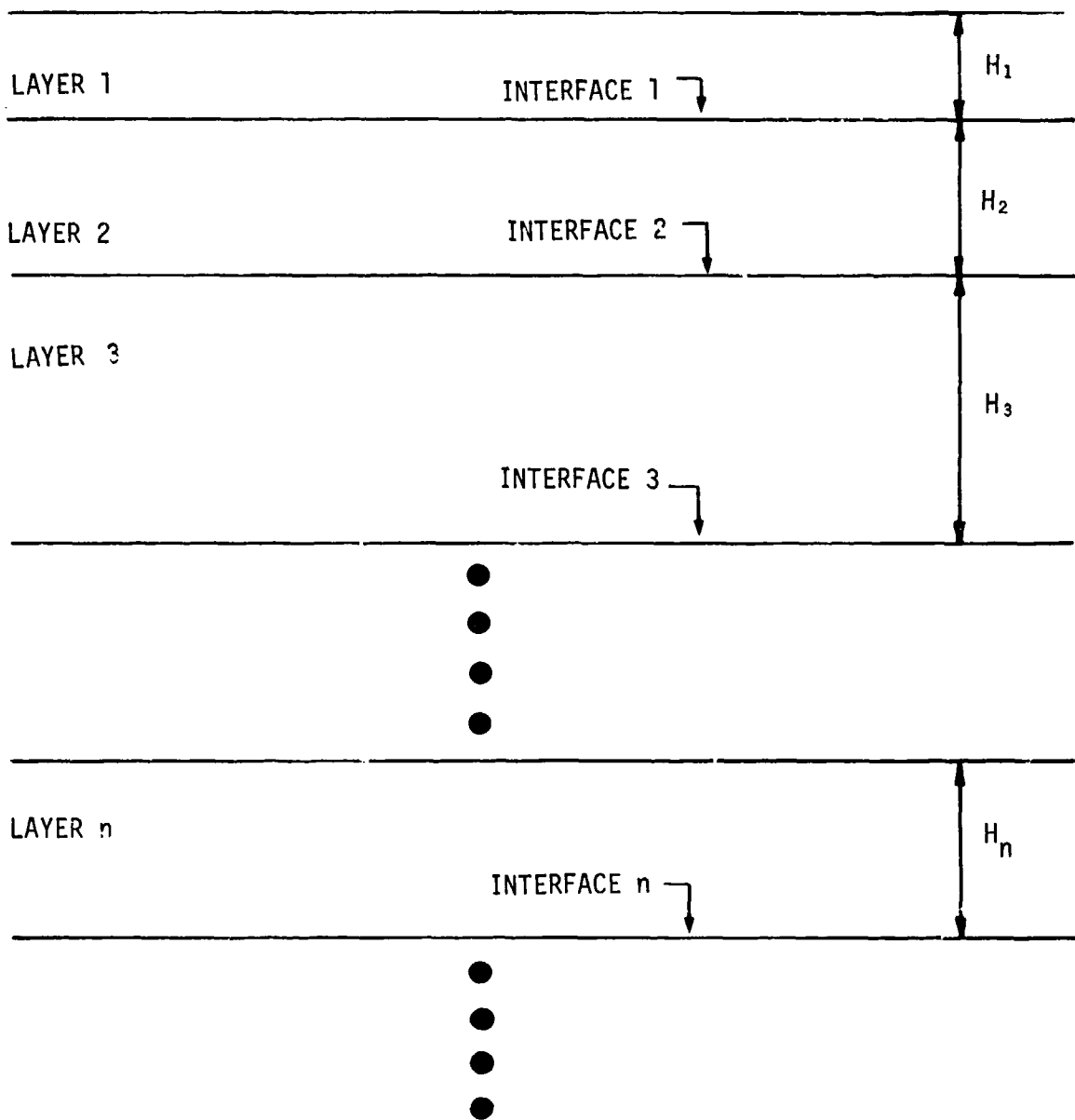


Figure IV-1.5. Nomenclature for multilayered systems.

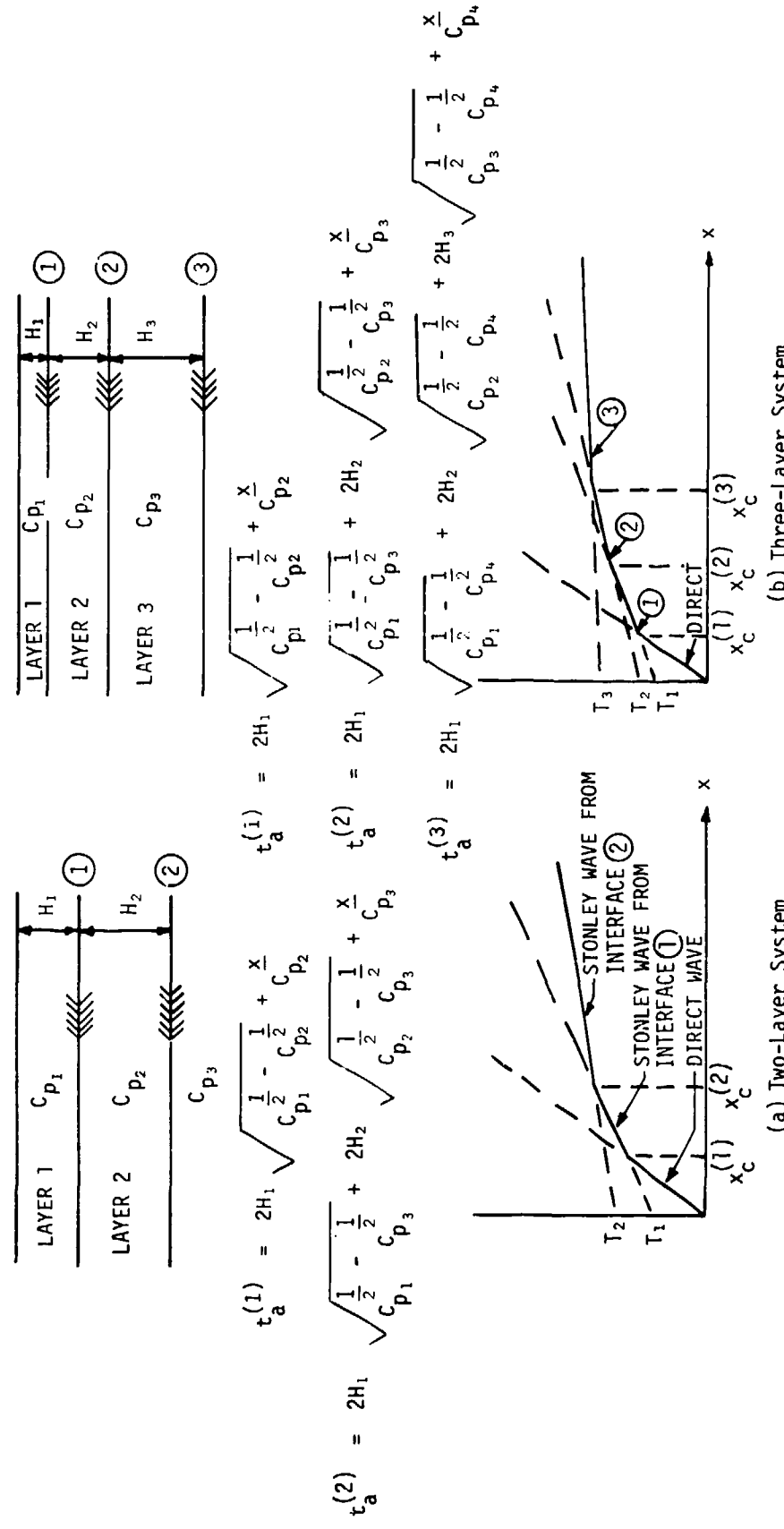


Figure IV-1-6. Construction of arrival time-distance curves in two-layer and three-layer systems.

occurs. The earliest outrunning arrivals can be found by trial and error shifting of the ground disturbance arrival time curve to various origins on the airblast arrival curve, i.e., times and ranges at which energy is imparted to the ground by the expanding airblast. The time at which earliest ground signals arrive at the point of interest prior to the airblast is the time of outrunning arrival.

Given the ground range at which outrunning first occurs, outrunning motions can be predicted. With the arrival times of the various signals, predicted ground shock from all sources can be superimposed to obtain an estimate of the complete ground shock environment.

The discussions and presentations that follow are about experimental data and constitute the primary objectives of this Sourcebook.

IV-1.2 CORRELATION OF MAXIMUM ACCELERATION DATA

This section presents and discusses the maximum horizontal and vertical acceleration data for a number of nuclear tests carried out at the Nevada Test Site (NTS) and the Pacific Proving Ground (PPG). Before discussing the data it is well to preface it with some general remarks.

The maximum vertical downward acceleration is related to the shape of the rise to the maximum velocity. This rise cannot be estimated accurately by analytical methods. Therefore, semi-empirical procedures are used for the prediction of the maximum vertical acceleration. If the rise in vertical velocity is linear, the maximum acceleration is simply

$$a_{\max} = \frac{V_{\max}}{t_r} \quad (\text{IV-1.14})$$

where V_{\max} is the maximum particle velocity and t_r is the linear rise time to V_{\max} . At the ground surface t_r is equal to the rise time of the airblast. Experimental observation shows little dependence of the airblast rise time on the device yield or on the peak side-on overpressure. It is more nearly a function of the ground surface condition (Reference IV-1.24). The value of the rise time that results in accelerations comparable to measured values is on the order of 0.001 sec.

Maximum acceleration attenuates rapidly with depth. This sharp attenuation is due more to the increase in the rise time with increasing depth than to

attenuation of the maximum vertical velocity. As the depth increases, the wave front is seen to stretch because of the nonlinearity of the stress-strain curve for soil. The residual strain that remains at a point in the soil after the load has been removed is

$$\epsilon_r = (1 - r) \frac{\sigma_{\max}}{M_L} \quad (\text{IV-1.15})$$

where r is the strain recovery ratio, σ_{\max} is the maximum vertical stress at the point of interest, and M_L is the uniaxial loading modulus at the same point. The strain recovery ratio is defined as

$$r = \frac{\epsilon - \epsilon_r}{\epsilon} \quad (\text{IV-1.16})$$

where ϵ is the strain corresponding to maximum stress. Because the stress rise time at depth is more nonlinear than at the surface, Newmark and Haltiwanger (Reference IV-1.22) recommend that the peak acceleration at depth be taken as twice the value appropriate to a linear rise time, or

$$a_{\max}(z) = 2 \frac{v_{\max}}{t_r(z)} \quad (\text{IV-1.17})$$

assuming that an airblast rise time of 0.001 sec is used, then value of $t_r(z)$ should be

$$t_r(z) = 0.001 + \frac{z}{C_L} - \frac{z}{C_i} \quad (\text{IV-1.18})$$

where C_L is the loading wave propagation velocity and C_i is the in-situ seismic velocity. Where C_L and C_i are not well defined, the rise time in soil and rock may be taken as (Reference IV-1.23):

$$t_r(z) = \frac{1}{2} \frac{z}{C_L} \quad (\text{IV-1.19})$$

IV-1.2.1 Vertical Acceleration Near the Ground Surface

Maximum vertical acceleration was recognized early to be an almost linear function of airblast overpressure directly over the point of interest (References IV-1.21 and IV-1.24). In the superseismic airblast region, the relationship between acceleration and overpressure was shown to be essentially independent of the weapon yield (Figures IV-1.7 and IV-1.8). In Figure IV-1.7 note that the accelerations for TUMBLER shot 4 are less than those for shots 1, 2, and 3 at the same overpressure. This is due to the decrease in overpressure rise time on shot 4 due to the development of the precursor waveform.* Data points in Figure IV-1.8 are shown with their error bars. The line represents a least square fit to these data points.

Since the maximum vertical acceleration appears proportional to the first power of the airblast overpressure, a rational method of displaying this information is to plot the ratio of the peak acceleration to the overpressure as a function of overpressure (Figures IV-1.9 and IV-1.10). In these figures the influence of the non-ideal overpressure waveforms can be seen by the distribution of the data points.

Overpressure waveforms 1 and 4 shown in Appendix IV-1.B are precursor waveforms exhibiting an increase in rise time as overpressure decreases, consequently, the ratio of acceleration to overpressure decreases as the precursor develops. This is shown on TUMBLER shot 4 and PRISCILLA. The type 7 overpressure waveform represents a flat-topped ideal waveform having the rise time of the near-ideal overpressure waveform and occurs at the end of precursor. Taking into consideration only those values corresponding to ideal or near-ideal waveforms, the ratio of maximum downward acceleration (at a depth of five feet where the instrumentation was located) to the airblast overpressure directly above that point is given in Reference IV-1.26 as 0.45 ± 0.15 (g/psi) for experiments at Frenchman Flat at the Nevada Test Site (NTS). For Yucca Flat, the ratio is given as 0.30 ± 0.10 (g/psi). The effect of weapon yield between 1 kt and 40 kt is not discernible

*For a detailed discussion of precursor phenomena and waveforms, see Reference IV-1.25. Appendix IV-1.B shows various types of waveforms encountered in ground motion measurements.

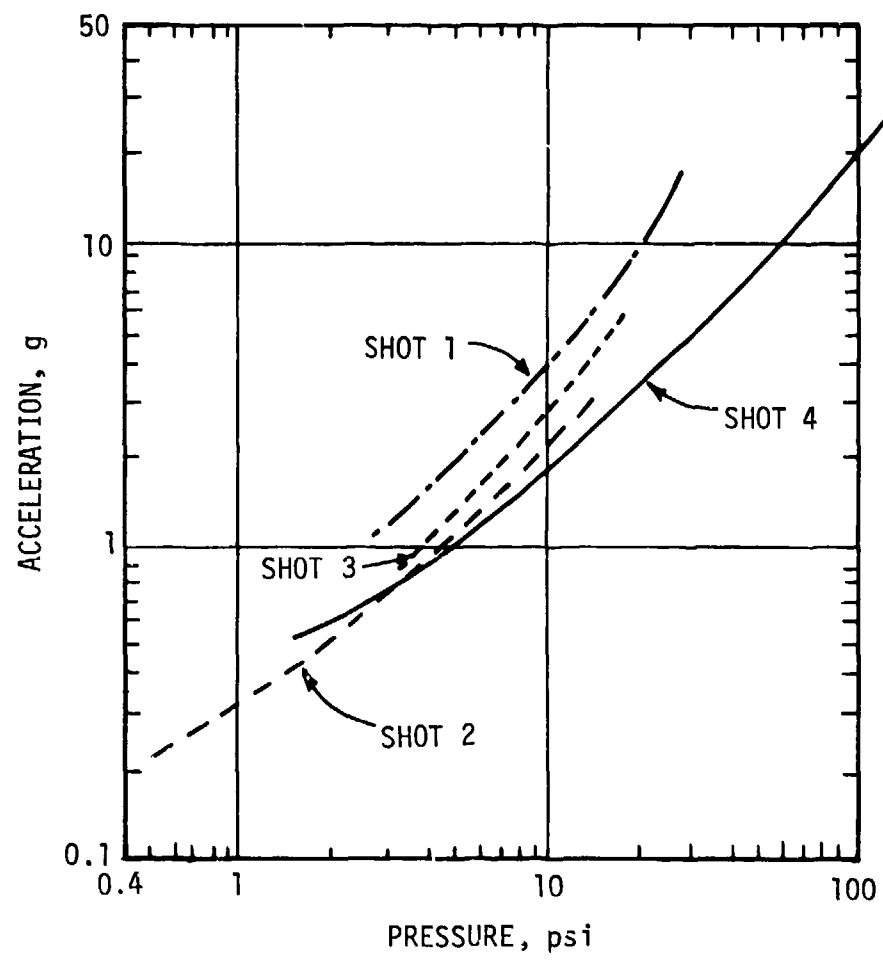


Figure IV-1.7. Composite maximum negative 5-foot vertical
slap acceleration versus maximum surface
level air pressure, TUMBLER (from Reference
IV-1.21).

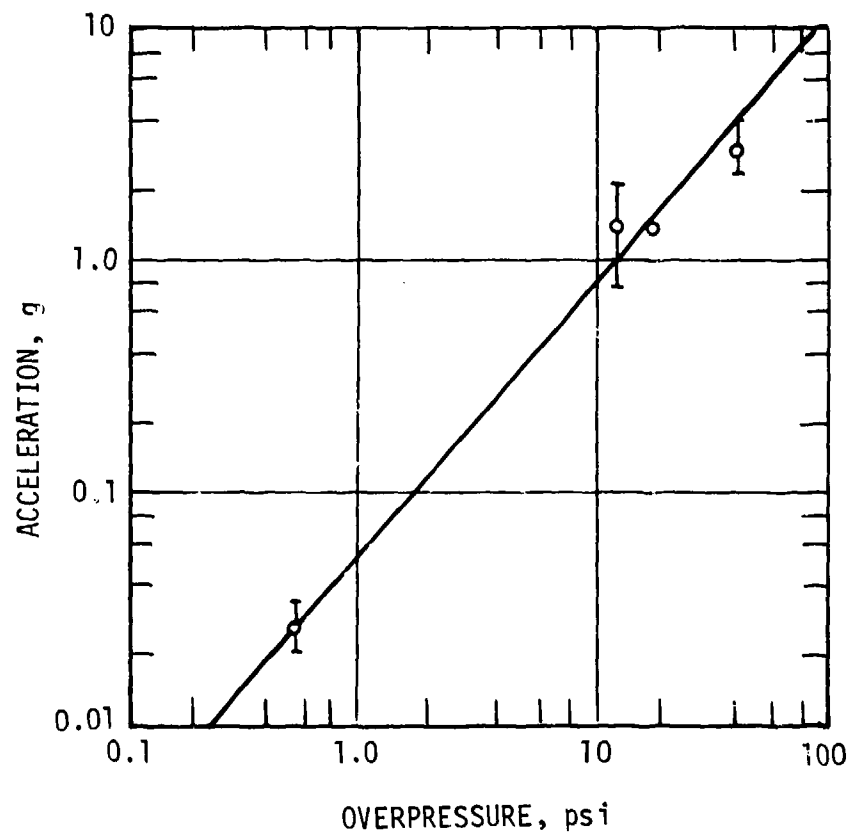


Figure IV-1.8. Airblast-induced acceleration as a function of incident overpressure for shot IVY MIKE.

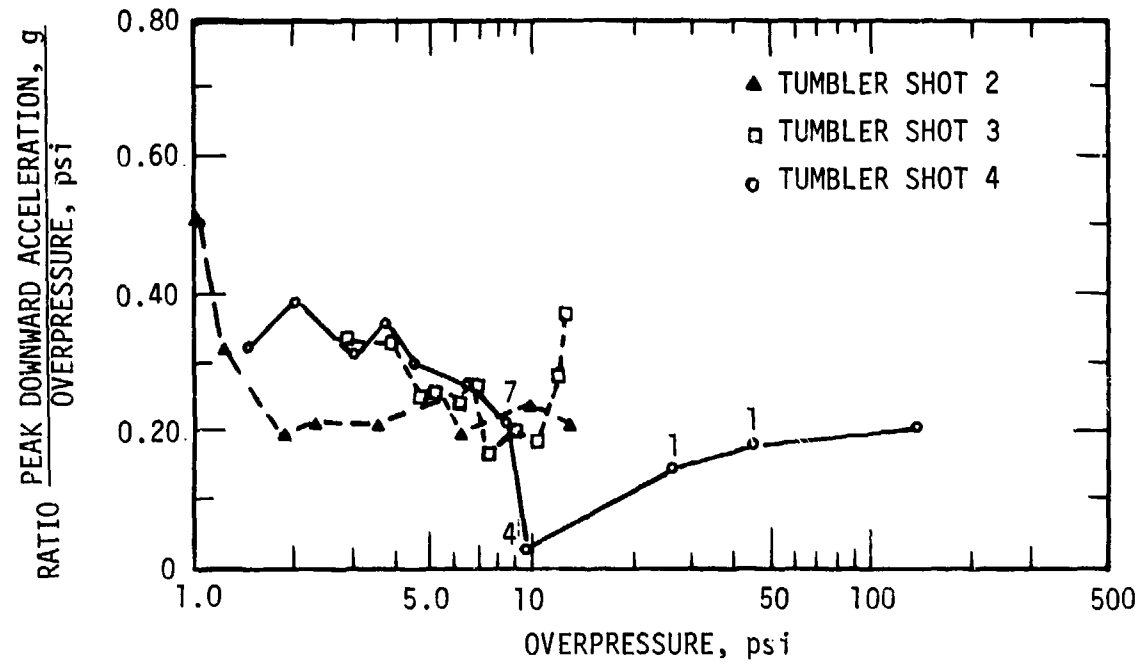


Figure IV-1.9. Vertical acceleration at Yucca Flat for 5-foot depth (numbers indicate overpressure waveform).

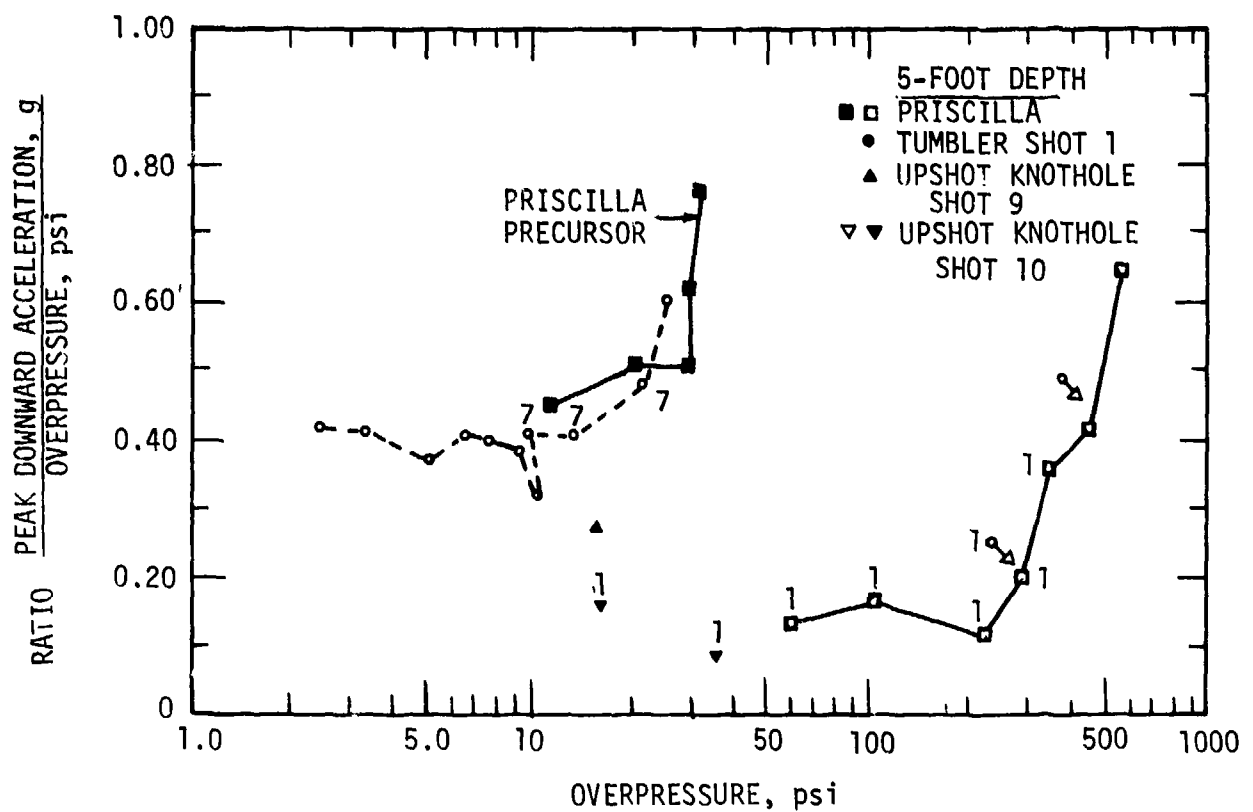


Figure IV-1.10. Vertical acceleration at Frenchman Flat for 5-foot depth (numbers indicate overpressure waveform).

within the scatter of these data.

Newmark and Hall (Reference IV-1.23) suggest a ratio of maximum vertical acceleration at the ground surface, that is, at 1-foot depth, based on the analysis of NTS acceleration data. Using this numerical value and the ratios of acceleration to overpressure at 5-foot depth requires that the ratio of acceleration at 1-foot depth to that of 5-foot depth be equal to 1.7 and 2.5, for Frenchman Flat and Yucca Flat, respectively. This is consistent with Figure IV-1.16 so that the equations recommended in References IV-1.23 and IV-1.26 are compatible. In addition, Newmark and Hall (Reference IV-1.23) suggest that the acceleration be taken inversely proportional to the seismic compressional wave velocity, using as a reference a seismic velocity of 1,000 feet/sec. This is estimated to be the seismic velocity near the surface in the alluvium of NTS (Reference IV-1.23).

They assumed a rise time of about 0.001 sec to attain the peak maximum velocity so that the acceleration at or near the surface could be expressed approximately as

$$a_{\max} \approx 150 \left\{ \frac{P_s}{100} \right\} \left\{ \frac{1000}{C_p} \right\} \quad (\text{IV-1.20})$$

where P_s is the shock, peak overpressure in psi, and C_p is the compressional wave velocity in ft/sec. The numerical factor has dimensions such that "a" is in g's. Since this relationship is for the surface, the surface seismic velocity must be used. They further state that because the surface acceleration is not related solely to the maximum velocity, but is also dependent on weapon yield and other factors, they recommend that $C < 2000$ ft/sec, regardless of the surface acoustic velocity. The above equation is plotted on the NTS data and their graph is reproduced here as Figure IV-1.11. Unfortunately, they do not reference the data points in that figure to the events. Equation IV-1.14 was later modified by Newmark and Haltiwanger (Reference IV-1.22) to include the multiplier $(115/\rho)$, where ρ is the soil density in lb/ft^3 referenced to $115 \text{ lbs}/\text{ft}^3$. Thus, equation IV-1.14 becomes

$$a_{\max} \approx 150 \left\{ \frac{P_s}{100} \right\} \left\{ \frac{1000}{C_p} \right\} \left(\frac{115}{\rho} \right) \quad (\text{IV-1.21})$$

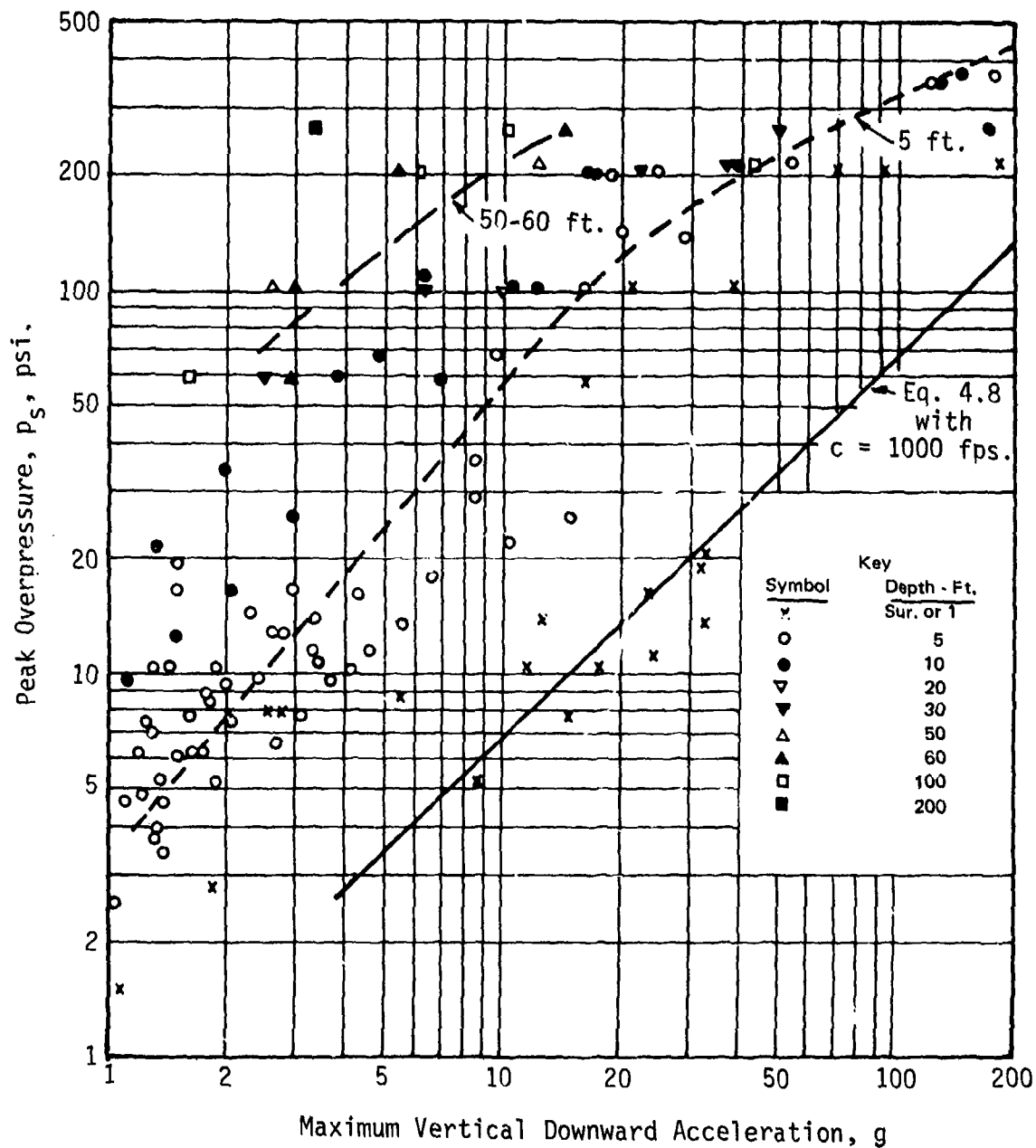


Figure IV-1.11. Maximum vertical downward acceleration versus peak overpressure (NTS - Airblast Component) (Reference IV-1.23).

The inverse relationship between acceleration and wave velocity is deduced from the fact that for an elastic solid the particle velocity is inversely proportional to the compressional wave velocity and that for an ideal airblast wave the rise time of overpressure is essentially a constant independent of yield or overpressure. Since acceleration is the time derivative of velocity, this results in the acceleration being directly proportional to the overpressure (as observed) and inversely proportional to the compressional wave velocity.

When the ground motion becomes of the outrunning type the maximum vertical acceleration is no longer a function of the overpressure immediately above the point of interest but becomes instead a function of the scaled ground range. Figure IV-1.12 shows how this transition takes place for the data at the Nevada Test Site. The data toward the left of the figure do not correlate on the basis of scaled ground range. However, as outrunning occurs (indicated by arrows), the accelerations approach a correlation based on scaled ground range. There appear to be no indications that cube root scaling fails. A demonstration of this correlation may be found by using the acceleration data taken at the Pacific Proving Ground (PPG)* (Figures IV-1.13 and IV-1.14). The accelerations shown in Figure IV-1.14 have been scaled by the cube root of the yield as part of the analysis based on the characteristic results of high explosive and underground nuclear detonations. Note that the scatter in these data is larger for this type of presentation than if the accelerations are left unscaled as shown in Figure IV-1.13. It should be noted that the accuracy of instrumentation used in the 1950's is not available and that comparison of the data may be due entirely to coincidence. The smaller scatter of data in Figure IV-1.13 suggests the use of unscaled acceleration as a function of scaled ground range as a better approach. This is significant in that the accelerations at the same scaled ground range do not decrease as weapon yield increases.

*To assist in the evaluation of figures and discussions involving detonations whose yields are classified the following table has been prepared. Sourcebook shot designations (assigned sequentially in time) and shots have been listed with the largest yield first.

<u>Sourcebook Shot Designation</u>	<u>Operation Name</u>
PPG 4	HARDTACK-I
PPG 1	GREENHOUSE
PPG 3	HARDTACK-I
PPG 2	REDWING

See Part III, Appendix IIIA for list of unclassified yields.

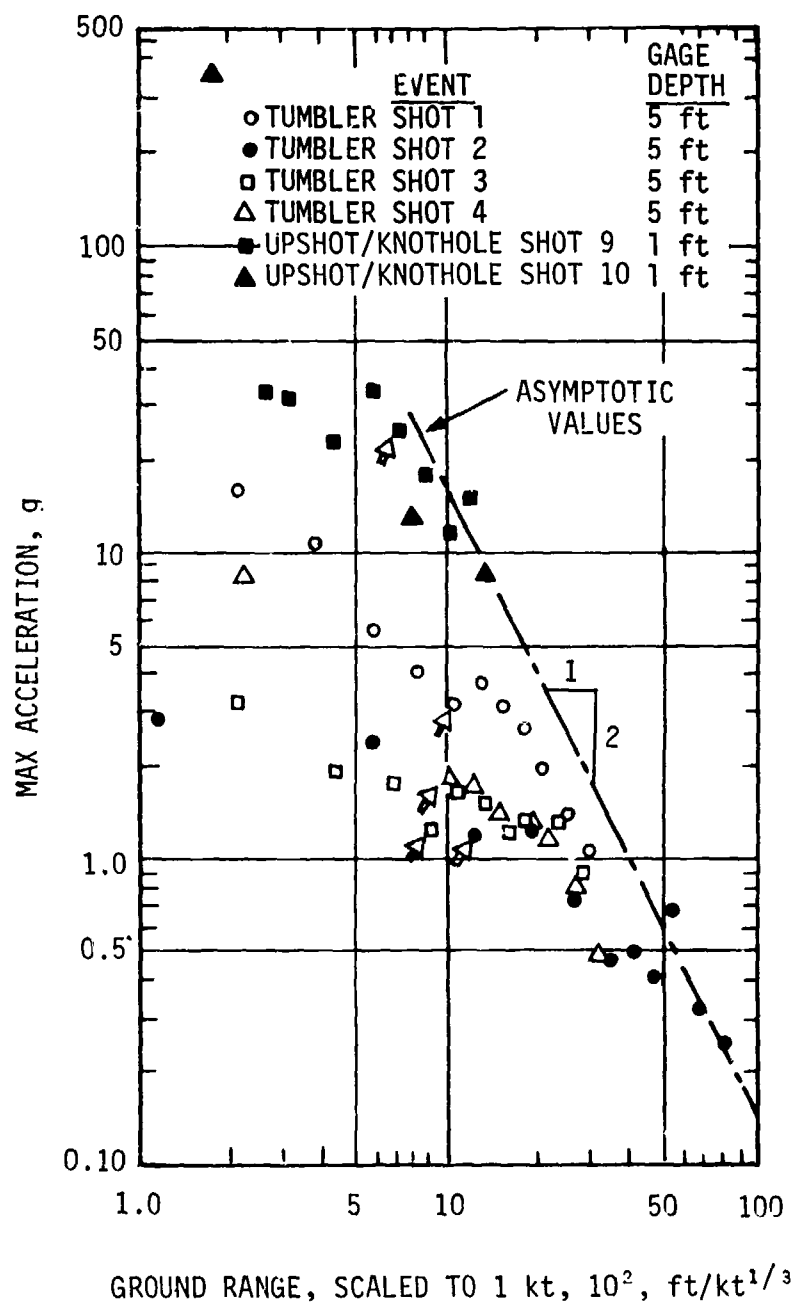


Figure IV-1.12. Maximum vertical acceleration versus ground range at NTS (arrow points to first ground wave outrunning waveform).

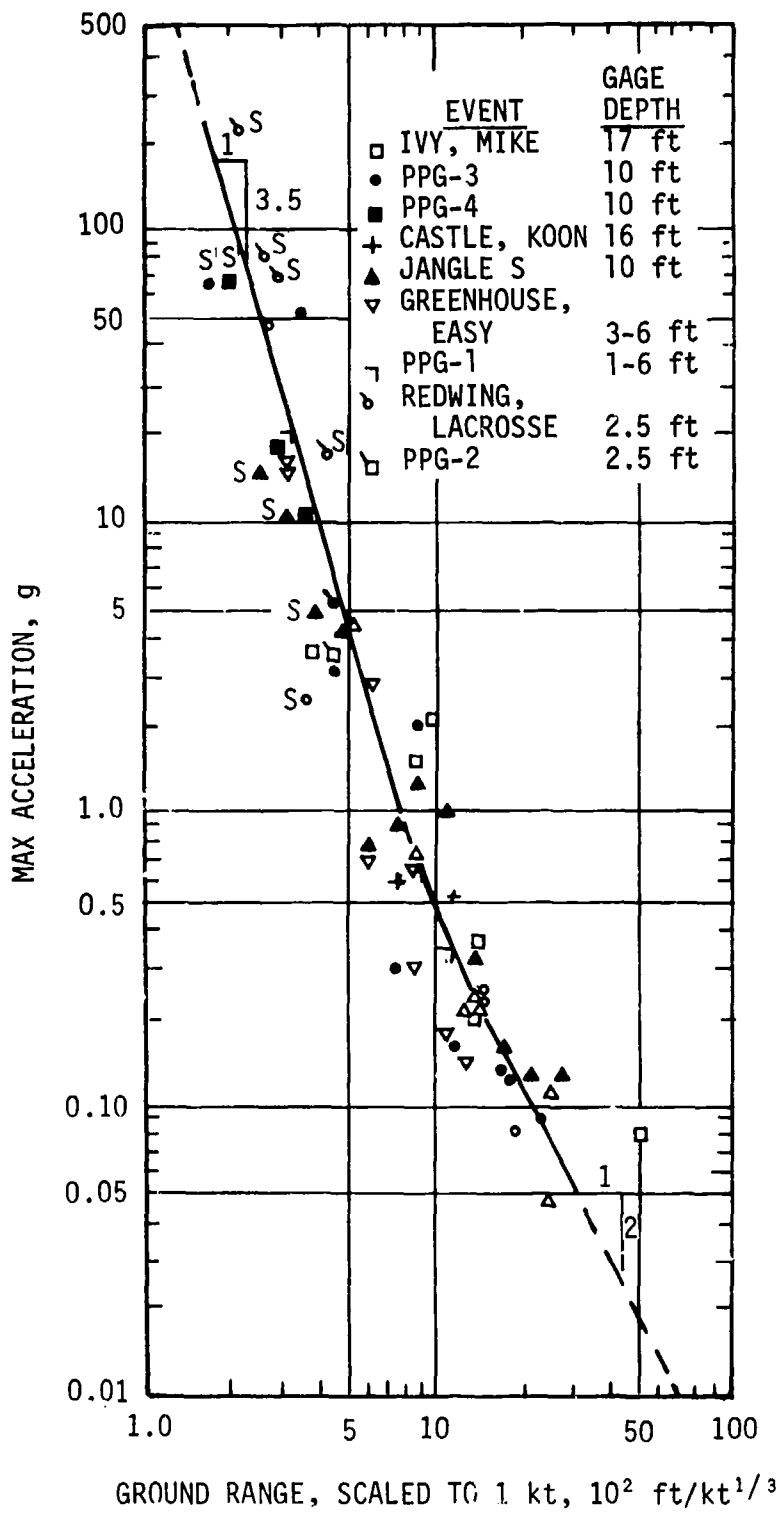


Figure IV-1.13. Maximum vertical acceleration versus ground range for outrunning ground motion at PPG (S indicates superseismic blast wave).

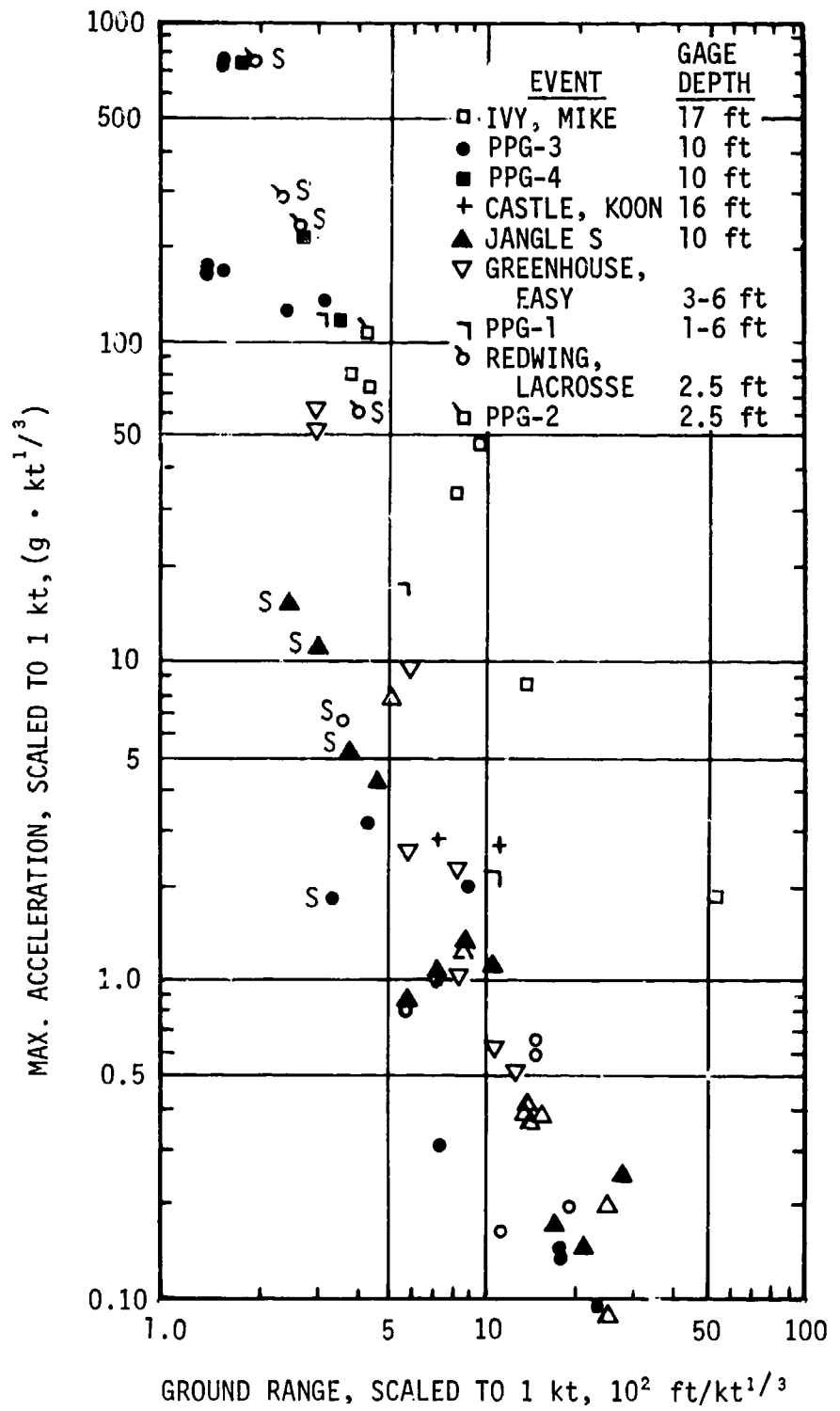


Figure IV-1.14. Maximum scaled vertical acceleration versus scaled ground range for outrunning ground motion at PPG.

Although the scatter of data in Figure IV-1.13 is substantial, note that, with the exception of LACROSSE, data from individual experiments are neither systematically high nor low with respect to the average curve. Moreover, acceleration measurements at the same ground range, but 180 degrees apart, have been known to differ by as much as 300%. Some variation is also to be expected because of the variation in depth of measurement (from the surface to a depth of 17 feet). With a factor of six in the scatter of data, the test site does not appear to be a dominant factor. For example, the data of JANGLE S (approximately 1 kt, Yucca Flat) are in agreement with the PPG data to approximately the same extent that the PPG data agree within themselves. The best evidence in favor of the correlation proposed in Figure IV-1.13 is the correlation of the IVY-MIKE data with the JANGLE S data which represents a ratio of 22:1 in the cube root of the yield.

As a matter of practical application the mean curve through the data of Figure IV-1.13 may be represented by two power law relationships:

$$a_v = 10^{10} \left(\frac{R}{W^{1/3}} \right)^{-3.5}, \quad 150 \leq (R/W^{1/3}) \leq 800 \quad (\text{IV-1.22})$$

with an error range of + 200%, - 70%, and

$$a_v = 5 \times 10^5 \left(\frac{R}{W^{1/3}} \right)^{-2}, \quad 800 < (R/W^{1/3}) \leq 3000 \quad (\text{IV-1.23})$$

with an error range of + 200%, - 70%,

where a_v is the maximum vertical acceleration in g's, regardless of sign, R is the ground range in feet, and W is the detonation yield in kilotons.

The only indication of a dependence of acceleration on soil properties is found from a comparison between the asymptotic value of the acceleration versus scaled ground range for outrunning ground motion at NTS with the outrunning ground motion data at PPG. In Figure IV-1.12 for NTS the vertical acceleration appears to attenuate in the outrunning region as the inverse square of the scaled ground range which is consistent with the trend noted in Figure IV-1.13 for PPG at the larger ground ranges. However, the NTS vertical accelerations are approximately thirty times the values shown in Figure IV-1.13 at the same scaled ground range. A factor of two at most may be accounted for by reducing the 5-foot depth accelerations of Figure IV-1.12 to those at 10-foot depth which are more compatible with Figure IV-1.13. However, the difference is still striking. In addition to the above observation, two measurements of vertical acceleration made below the water table on PPG 2 in the superseismic airblast region indicate a remarkably low acceleration-overpressure ratio (Reference IV-1.27). It would appear then, that vertical acceleration decreases with an increase in compressional wave velocity.*

*It can be shown from an analysis of ground motion given in References IV-1.1 and IV-1.26 that the vertical acceleration is

$$a_v \approx \frac{1}{\rho C_p} \left(\frac{\Delta P_s}{t_r} \right) \quad (\text{IV-1.24})$$

However, the exact nature of this relationship is at present not understood even though it has been suggested by Sauer (Reference IV-1.26) and Newmark and Hall (Reference IV-1.23) that the acceleration varies inversely as the first power of the compressional wave velocity.

IV-1.2.2 Horizontal Acceleration Near the Ground Surface

In data taken at Nevada Test Site, the scatter of maximum horizontal acceleration shown in Figure IV-1.15 is as large if not larger than the scatter of vertical acceleration. It is apparent that at depths less than 10 feet, the data may be divided into two groups. When the airblast is superseismic the horizontal accelerations near the surface vary from 0.2 to 0.5 times the vertical acceleration. For outrunning ground motion, the horizontal accelerations are approximately equal to the vertical accelerations.

Newmark and Hall (Reference IV-1.23) suggest that horizontal acceleration be taken equal to vertical acceleration. In Figure IV-1.15 it is seen that this relationship is conservative for depths less than approximately 20 feet in the superseismic region. For the outrunning ground motion region, the relation is as suggested above.

The one-dimensional methods for vertical ground shock parameters gives little information on horizontal stresses and no information on horizontal motions. Peak horizontal stresses may be estimated on the basis of one-dimensional assumptions (Reference IV-1.1). No consistent method, empirical or otherwise, is presently available for the prediction of horizontal wave forms. Procedures for estimating peak horizontal motions have developed from empirical studies and two dimensional code calculations. Horizontal stress is generally taken as some constant times the vertical stress,

$$\sigma_h = K \sigma_v \quad (\text{IV-1.24})$$

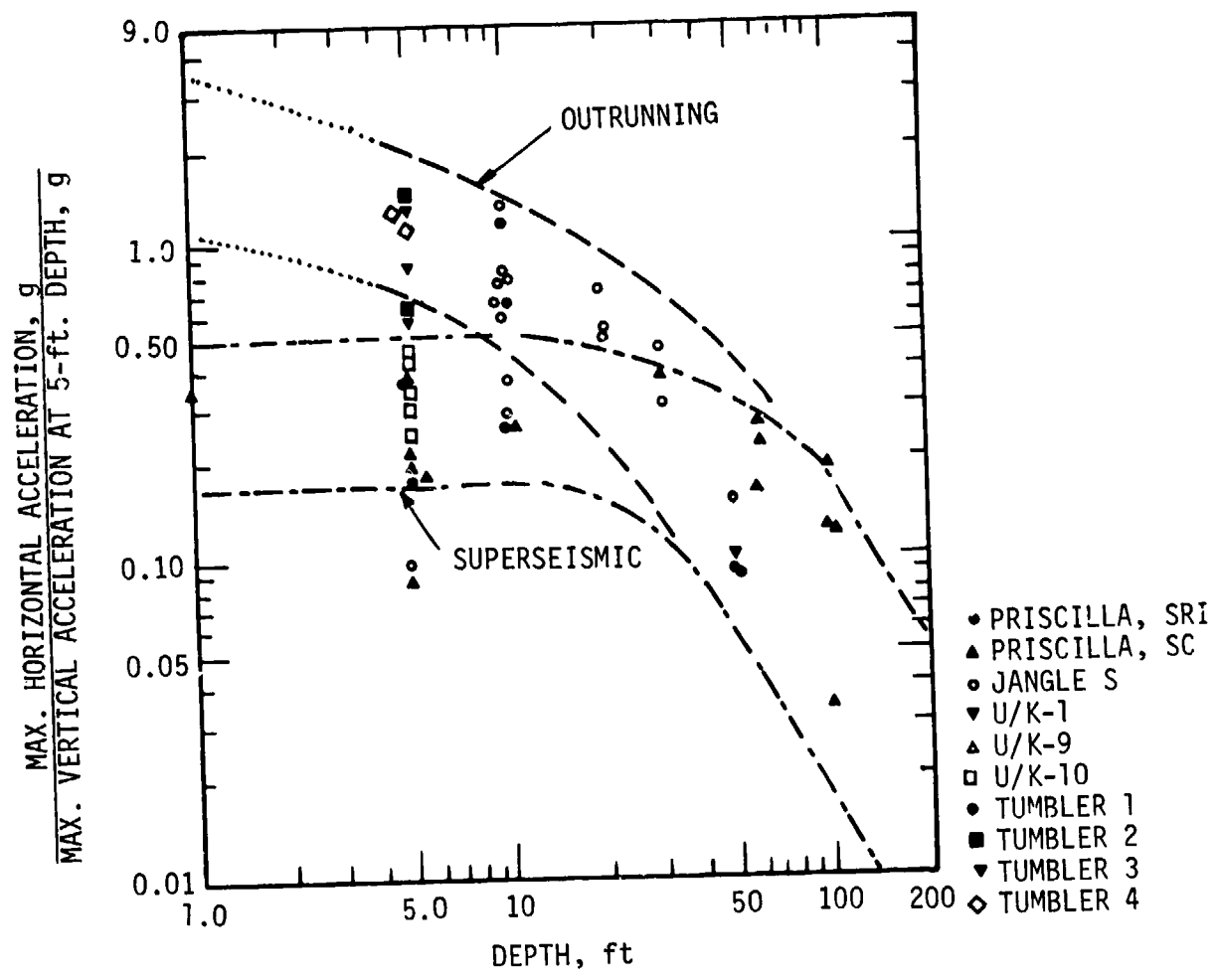


Figure IV-1.15. Variation of maximum horizontal acceleration with depth at NTS.

where σ_h is the horizontal stress, K is the earth pressure coefficient, and σ_v is the vertical stress. The earth pressure coefficient, K , depends upon the properties of the soil, the degree of saturation, the stress level, the condition of lateral restraint, and the previous stress history (Reference IV-1.22).

A soil element under an increment of vertical stress, σ_v , results in a vertical strain increment, ϵ_v . The horizontal strain, ϵ_h , and resulting horizontal stress depend upon the restraint of the confining medium. Under conditions of uniaxial strain, as is assumed under superseismic conditions, the horizontal strain is zero. The earth pressure coefficient corresponding to the condition of zero horizontal strain is called the earth pressure coefficient at rest, usually designated K_0 . In fluids, K_0 is unity, that is, the horizontal stress is equal to the vertical stress. In perfectly elastic materials, K_0 is given by

$$K_0 = \frac{v}{1-v} \quad (\text{IV-1.25})$$

where v is Poisson's ratio. In soils, the in situ values K_0 may be greater or less than unity depending upon the degree of homogeneity, isotropy and prior geologic history. For example K_0 may exceed one in cases where the soil has been heavily pre-loaded in the past by large depths of overburden which have since been eroded. The high horizontal stresses may be envisioned as "locked in." In general, K_0 for soils is not constant but varies with stress level, stress application rate, and whether the soil is being loaded or unloaded. K_0 during unloading generally exceeds the loading K_0 because of the hysteretic nature of soils. A load-unload cycle is similar to the preloading of soil in situ. For the prediction of peak horizontal stresses due to superseismic airblast, K_0 due to an increment of stress, rather than the existing in situ K_0 is necessary. Under dynamic conditions, the value of K_0 depends to a large extent on whether or not the soil is saturated. A stress suddenly applied to an element of a saturated soil is transmitted almost entirely through the water phase because the loading rates are much higher than the rates at which drainage can occur. Therefore, K_0 assumes a value of near unity in most saturated soils. An exception occurs in very stiff cohesive soils, for example, shale of relatively high dry density and low permeability. In stiff cohesive soils, the soil may be stiffer than the water phase; hence, a considerable part of the applied dynamic stress may be transmitted through the soil structure. Therefore, the K_0

value will be less than unity even for complete saturation and may be as low as one-third, a value corresponding to the soil structure without water. For all materials under static loads and drained conditions, K_0 assumes a value corresponding to that of the soil skeleton. Table IV-1.3 presents suggested dynamic K_0 values for several soil categories. Cohesive soils are categorized according to consistency which is defined beneath the table (Reference IV-1.22).

Horizontal stress-time histories for Shot PRISCILLA, conducted in Nevada Test Site alluvium, are compared with corresponding vertical-time histories in Figure IV-1.16. In spite of missing data and significant variations and differences between the available vertical and horizontal waveforms, the horizontal waveforms appear to generally follow the vertical waveforms.

The conclusion of similarity between the vertical and horizontal stress waveforms may be related to the relative homogeneity of the test site. Crawford, et. al. (Reference IV-1.1) recommends that the horizontal waveform be taken similar to the predicted vertical waveform regardless of site conditions. Estimates of horizontal components of acceleration, velocity and displacement must rely upon empirical data and two-dimensional theoretical and code calculation results. At relatively homogeneous sites, the ratios of peak horizontal motion components to peak vertical components appear related to the angle of inclination between the incident wave front and the ground surface. Two dimensional studies of superseismic airblast induced ground shock in elastic unlayered media (Reference IV-1.28) indicate the motions at the wave front occur perpendicular to the wave front. Therefore, the ratio of the horizontal components of motion to the vertical components of motion at the wave front in an elastic medium is equal to the tangent of the angle of inclination of the wave front with respect to the ground surface (see Figure IV-1.17a), or

$$\frac{H}{V} = \tan\beta = \tan (\arcsin \frac{C_p}{U}) \quad (IV-1.26)$$

where H is the horizontal motion component at wave front, V is the vertical motion component at wave front, β is the angle of inclination of wave front, C_p is the compressional wave velocity, and U is the airblast shock front velocity for a

Table IV-1.3. Ratio of horizontal to vertical soil pressures
(Reference IV-1.22).

Soil Description	K_0 , for Stresses Up to 1000 psi (690 N/cm ²)		
	Dynamic	Static	
	Undrained	Undrained	Drained
Cohesionless Soils, Damp or Dry	1/4	1/3-dense 1/2-loose	1/3-dense 1/2-loose
Unsaturated Cohesive Soils of Very Stiff to Hard Consistency*	1/3	1/2	1/2
Unsaturated Cohesive Soils of Medium to Stiff Consistency*	1/2	1/2	1/2
Unsaturated Cohesive Soils of Soft Consistency*	3/4	1/2 to 3/4	1/2 to 3/4
Saturated Soils of Very Soft to Hard Consistency* and Cohesion- less Soils	1	1	1/2-stiff 3/4-soft
Saturated Soils of Hard Consis- tency*	3/4 to 1	1	1/2
Saturated Soils of Very Hard Consistency*	3/4	1	1/2
Rock	Obtain from tests on rock cores and correlate with seismic data		

*Consistency Definitions:

Consistency	Unconfined Compression Strength - q_u - tsf (N/cm ²)	Standard Penetration Test-N-Blows Per ft. (m)
Very Soft	< 0.25	(< 2.4)
Soft	0.25-0.50	(2.4-4.8)
Medium	0.50-1.00	(4.8-9.6)
Stiff	1.00-2.00	(9.6-19.1)
Very Stiff	2.00-4.00	(19.1-38.3)
Hard	4.00-20.00	(38.3-191)
Very Hard	> 20	(> 191)

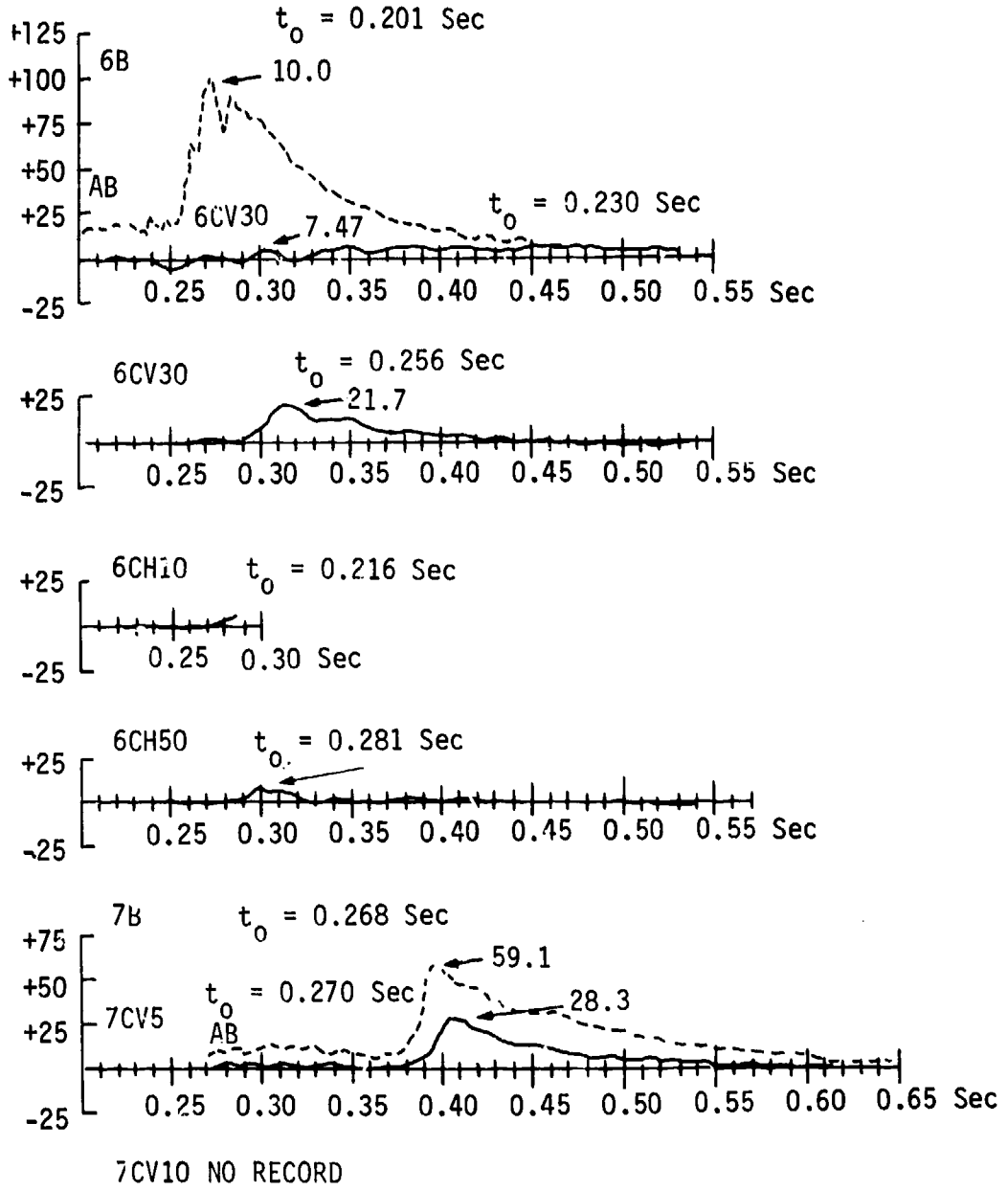
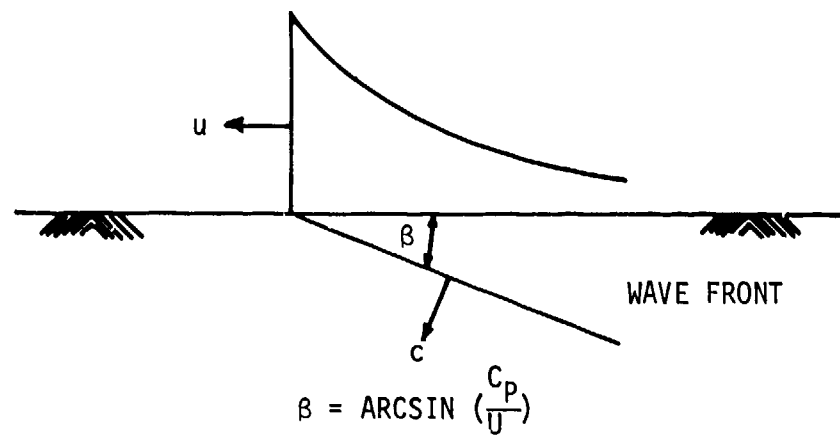
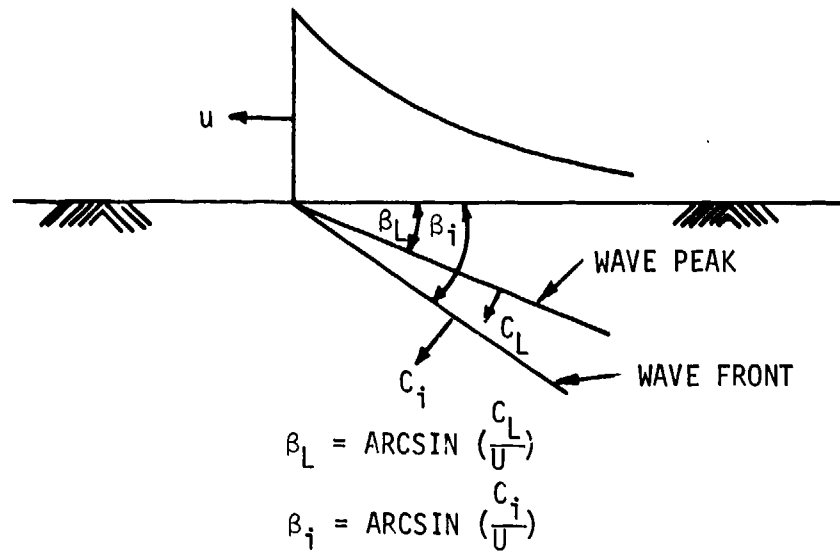


Figure IV-1.16. Vertical and horizontal stress versus time, station 6 (ground range 1050 ft), Shot PRISCILLA (Reference IV-1.27).



(a) Elastic Case



(b) Nonlinear Case

Figure IV-1.17. Wave fronts due to superseismic airblast.

homogeneous site, if $\tan(\arcsin \frac{C_h}{C_v}) > 1$, then the peak horizontal component should be taken as equal to the peak vertical component.

Wave propagation in real geologic materials differs from elastic wave propagation in that lower stress levels propagate at the seismic velocity, C_i , while stress peaks propagate at the velocity associated with the loading modulus, C_L . The wave fronts and inclination angles associated with the two velocities in a homogeneous halfspace are shown in Figure IV-1.17b.

Peak downward vertical accelerations due to the incident wave usually occur with the arrival of the wave front and, therefore, Crawford, et. al. (Reference IV-1.1) recommends that the ratio of peak horizontal acceleration to peak vertical acceleration due to the incident stress wave be estimated by Equation IV-1.26 using $C_p = C_i$.

The horizontal accelerations for the PPG experiments and for JANGLE S are shown in Figure IV-1.18 and are seen to follow the same trend as the vertical accelerations in Figure IV-1.14. On the average, the horizontal accelerations are one-half the vertical accelerations which is in some contrast to the observations at Nevada Test Site noted above.

IV-1.2.3 Attenuation of Acceleration with Depth

While there is no convincing experimental variation with overpressure of the ratio of vertical acceleration to overpressure in the superseismic airblast region, there is a very noticeable variation of acceleration with depth. Based on the data of PRISCILLA, UPSHOT/KNOTHOLE, and TUMBLER/SNAPPER, Swift, Sachs and Sauer (Reference IV-1.27) present the "best fit" power law variation with depth,

$$a_v(y) = 1.5 \Delta p_s y^{-0.83} \quad (\text{IV-1.27})$$

where a_v is the maximum vertical acceleration in g's, Δp_s is the overpressure in psi, and y is the depth in feet. Equation IV-1.27 gives an acceleration-overpressure ratio of 0.4 at 5-foot depth which is consistent with the conclusions drawn from Figures IV-1.9 and IV-1.10. Sauer (Reference IV-1.26) also adopts that power law variation of vertical acceleration with depth. The same data used to develop Equation IV-1.27 are compared in Figure IV-1.19 with that equation. Figure IV-1.19 indicates that the rate of attenuation is somewhat less than that indicated

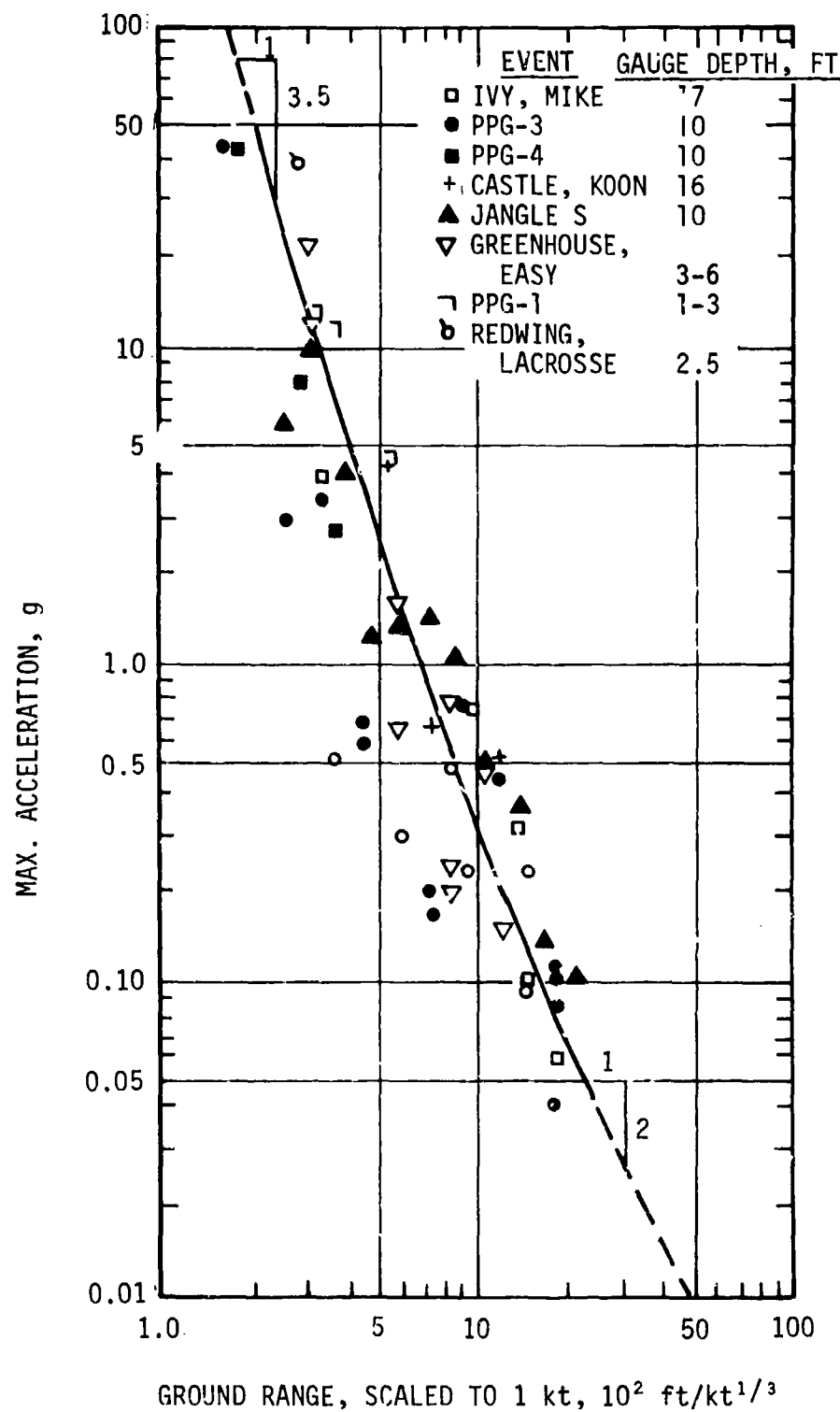


Figure IV-1.18. Maximum horizontal acceleration versus ground range for outrunning ground motion at PPG.

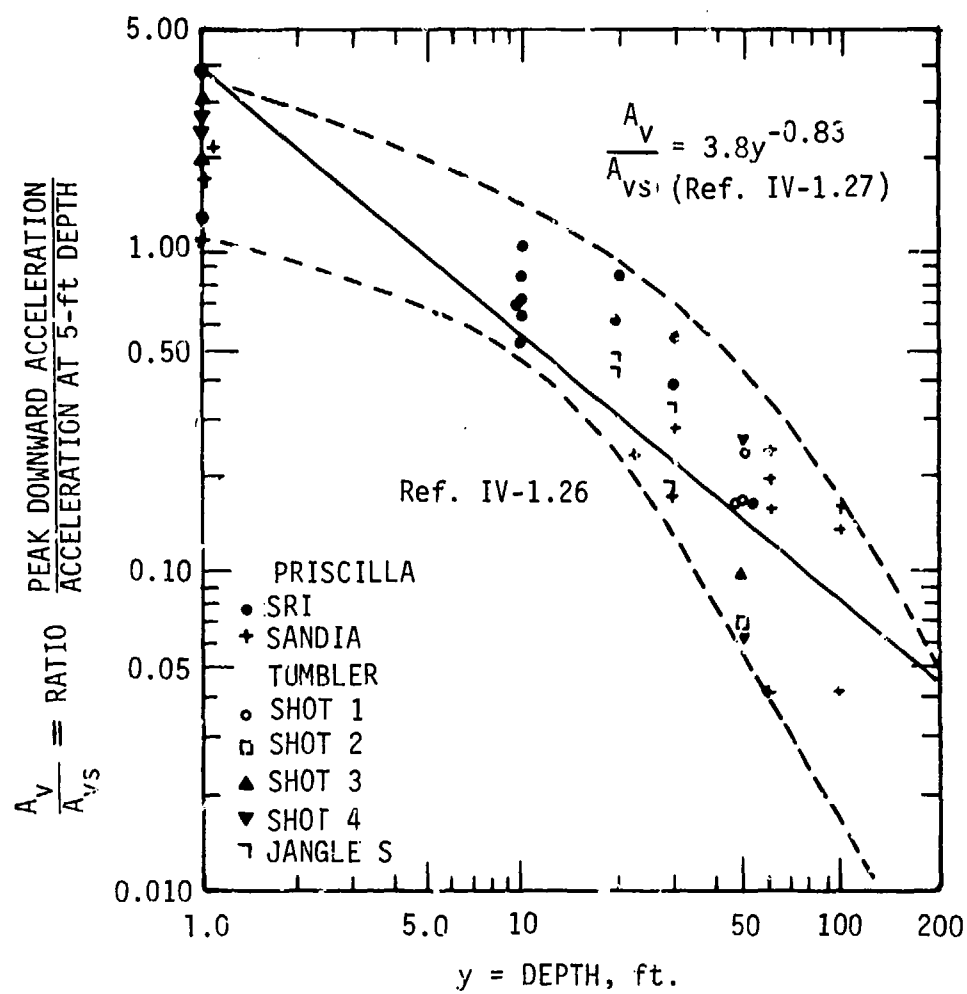


Figure IV-1.19. Attenuation of vertical acceleration with depth in superseismic airblast at NTS.

by Equation IV-1.27 for depths less than 5 . the attenuation is greater than that indicated by Equation IV-1.27 at depths greater than 50 feet, approaching approximately a 3/2 power variation with depth.

Newmark and Hall (Reference IV-1.23) derived the attenuation of vertical acceleration by specifying that the acceleration is approximately equal to the vertical particle velocity divided by the rise time of velocity. The rise time is taken to be half the transit time of the stress wave to reach the depth in question or 2 msec, whichever is greater. Combining the prediction equations of Reference IV-1.23 for the surface particle velocity, the attenuation of particle velocity, and the relationship for the rise time of the particle velocity there results

$$a_v(y) = 2.6\alpha \frac{\Delta p_s \bar{C}_p}{y C_p} \quad (\text{IV-1.28})$$

where a_v is the vertical acceleration in g's. Δp_s is the overpressure in psi, y is the depth in feet, \bar{C}_p is the average of the compressional wave velocities between the surface and the point in question, C_p is the compressional wave velocity at the surface, and α is the attenuation factor for maximum vertical particle velocity (see Figure IV-1.27 and Section IV-1.3.2). Newmark and Hall (Reference IV-1.23) note that this procedure "gives less attenuation in rock than in soil, which is reasonable." For homogeneous media $\bar{C}_p = C_p$ so that the influence of compressional wave velocity cancels in the attenuation of vertical acceleration.

The predictions of Equation IV-1.28 are compared with the data from experiments at NTS (Figure IV-1.19) in Figure IV-1.20. The predictions were calculated for a yield of 40 kt using the soil constants recommended in Reference IV-1.23, $C_p = 1,000$ and $\bar{C}_p = 2,000$ feet/sec for depths greater than approximately 30 feet.*

*In performing these calculations, as shown in Figure IV-1.20, the ratio $a_v(y)/a_v'(5)$ was computed where $a_v'(5)$ is calculated from Equation IV-1.27. A check for 40 kt at a depth of 40 feet for an overpressure of 100 psi shows

$$\frac{a_v(40)}{a_v'(5)} = \frac{7.8}{39.44} \approx 0.2$$

which agrees with Figure IV-1.20. Here, $\alpha = 0.6$ from Figure IV-1.27. The ratio $a_v(y)/a_v'(5)$ plotted as a function depth in Figure IV-1.20 is

$$\frac{a_v(y)}{a_v'(5)} = 6.58 \frac{\alpha}{y} \left(\frac{\bar{C}_p}{C_p} \right) \quad (\text{IV-1.29})$$

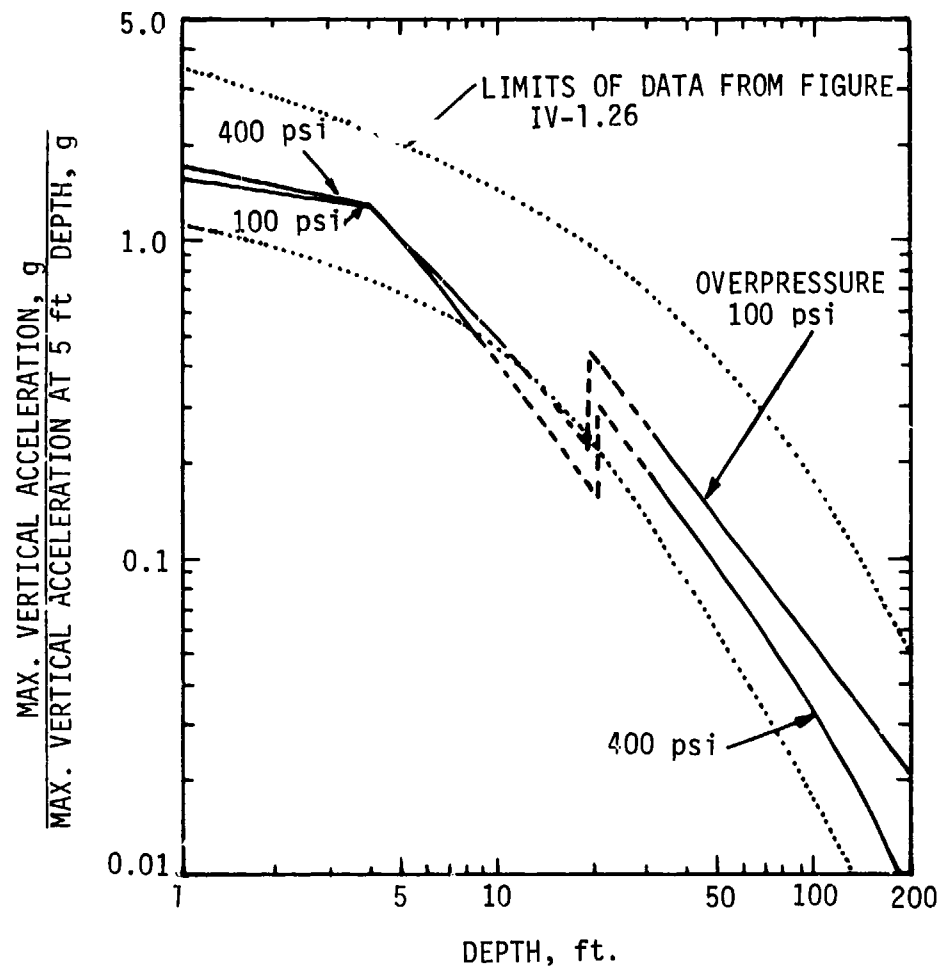


Figure IV-1.20. Predicted attenuation of maximum vertical acceleration from Reference IV-1.23 for the superseismic airblast region.

The seismic compressional wave velocity in Frenchman Flat is known to vary between depth of 10 feet to 30 feet (see Part III) so that the computation proceeded using $\bar{C}_p = C_p = 1,000$ feet/sec for depths less than 10 feet. Hence the prediction is shown dotted in the depth interval of 10 to 30 feet with the transition being arbitrarily taken at a depth of 20 feet. Cusps in the curve at a depth of 4 feet correspond to the use of the minimum value of 2 msec for the particle velocity rise time. The agreement of this prediction method with the data is quite good as evidenced by the comparison shown in Figure IV-1.20. Note that the prediction procedure differs in two fundamental aspects from the presentation of the data in Figure IV-1.19. The attenuation rate increases with increasing overpressure due to dependence of α on overpressure and decreases with increasing yields due to the dependence of α on the scaled depth (see Figure IV-1.27).

The attenuation with depth of vertical acceleration for PPG is shown in Figure IV-1.21 including 19 data points from JANGLE S which were in the outrunning ground motion region. In this plot, the acceleration data are normalized against the acceleration data near the surface using the results in Figure IV-1.13. The attenuation of vertical acceleration with depth at PPG is seen to be similar to that at NTS. Based on the large difference in yield between JANGLE S and PPG 4, it appears that the acceleration does not attenuate proportionately to the scaled depth. This result is probably due to the fact that the magnitude of the acceleration is largely controlled by the nonlinear character of the soil which does not scale with the weapon yield. This argument is in conflict with the results of small underground high explosive detonations. However, it is plausible that effects which play an important role in high explosive detonations do not appear to be a major factor in nuclear detonations.

The attenuation of horizontal acceleration with depth at PPG is shown in Figure IV-1.22. As previously noted, horizontal accelerations near the surface in the superseismic airblast region are approximately 1/3 of the vertical accelerations while those in the outrunning ground motion region are approximately equal to the vertical acceleration. As the depth increases, the horizontal acceleration tends to be equal to the vertical acceleration in both the superseismic airblast and outrunning ground motion regions. In Figures IV-1.21 and IV-1.22, the data from SMALL BOY and JOHNIE BOY were added using Figure IV-1.13. The SMALL BOY and JOHNIE BOY data were taken from References IV-1.29 and IV-1.30, respectively.

*Thus, Equation IV-1.27 fits the data of Figure IV-1.19, while Equation IV-1.29 fits the same data better.

MAX. VERTICAL ACCELERATION
ACCELERATION FROM CURVE OF FIGURE IV-1.12

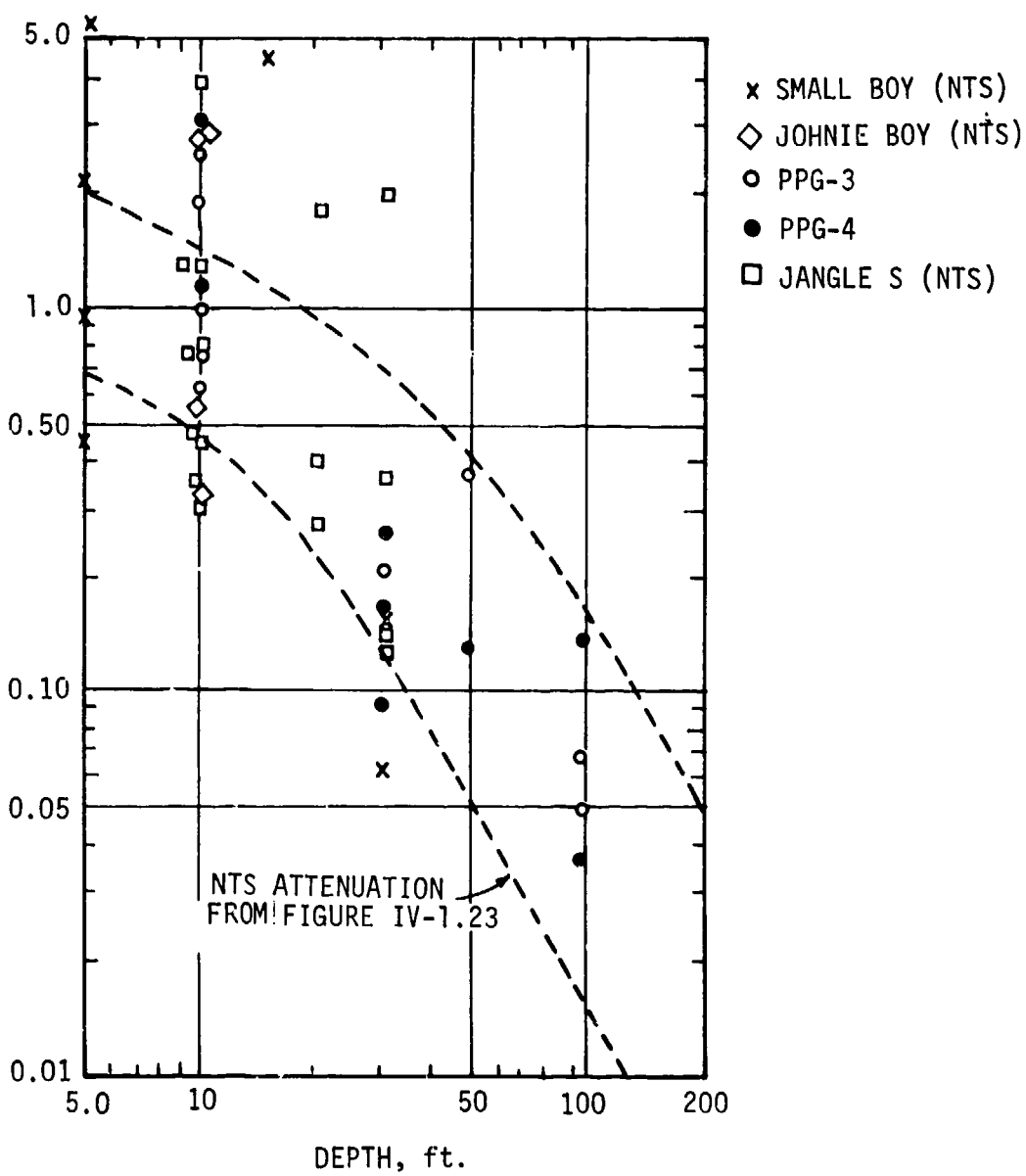


Figure IV-1.21. Vertical acceleration versus depth for outrunning ground motion at PPG.

IV-1.3 CORRELATION OF MAXIMUM PARTICLE VELOCITY DATA

This section presents and discusses the horizontal and vertical particle velocity data for those shots discussed in the previous section.

IV-1.3.1 Vertical Particle Velocity Near the Surface.

Near the ground surface the airblast-induced motion dominates the high-frequency portions of the particle velocity waveforms. For alluvial materials, the airblast is generally sufficiently superseismic that one-dimensional theory offers a good approximation for vertical motion but not for horizontal motion. Using one-dimensional computer codes and given sufficient information on soil properties, it is a comparatively simple task to calculate the vertical airblast-induced ground motion. See, for example, Reference IV-1.31.

The vertical particle velocity at or near the surface in the superseismic airblast region has been shown to be proportional to the overpressure directly above the point of interest (References IV-1.23 and IV-1.26). Figure IV-1.23 shows the ratio of the velocity jump (the sudden increase in velocity due to passage of the overpressure) to the overpressure. This ratio varies between 0.04 and 0.06 ft/sec/psi with a recommended average value of 0.05 ± 20 percent (Reference IV-1.26). Based on the analysis of the same data Reference IV-1.23 gives a ratio of particle velocity to overpressure as 0.042 ft/sec/psi. The 20-percent difference in the ratio is due solely to minor differences in methods of data analysis and should be regarded as trivial in view of the much larger uncertainties involved in extrapolation data from NTS soil to soils of higher or lower compressional wave velocity.*

*If the individual references cited are followed for the calculation of the maximum value of the velocity response spectrum, then the 20-percent difference noted above will almost cancel out. Sauer (Reference IV-1.26) recommends that the maximum response velocity be equal to 1.35 times the maximum particle velocity while Newmark and Hall (Reference IV-1.23) recommend that the maximum response velocity be equal to 1.5 times the maximum particle velocity. Hence the difference in maximum response velocity calculated by the two methods would be less than 8 percent.

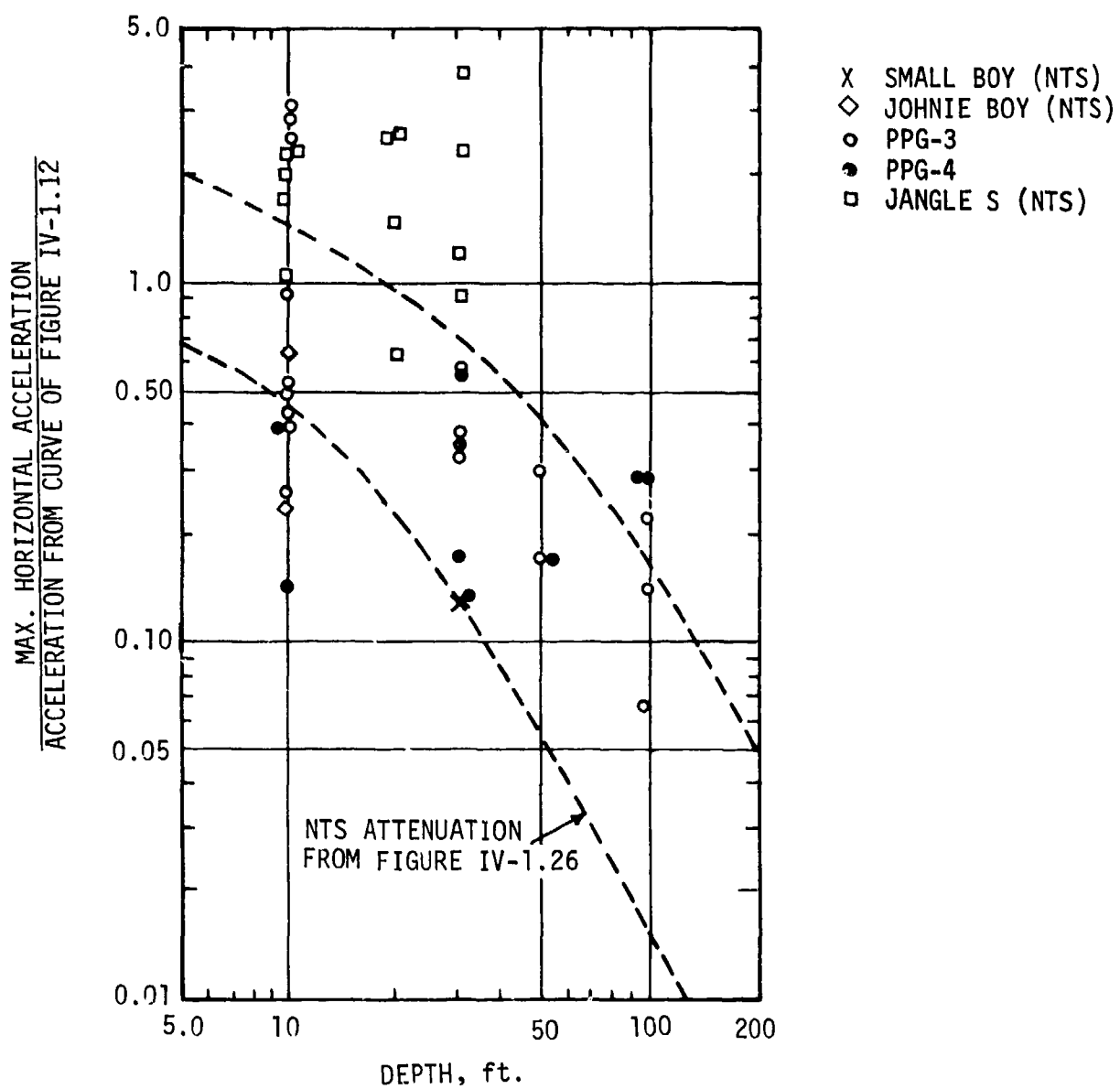


Figure IV-1.22. Horizontal acceleration versus depth for outrunning ground motion at PPG.

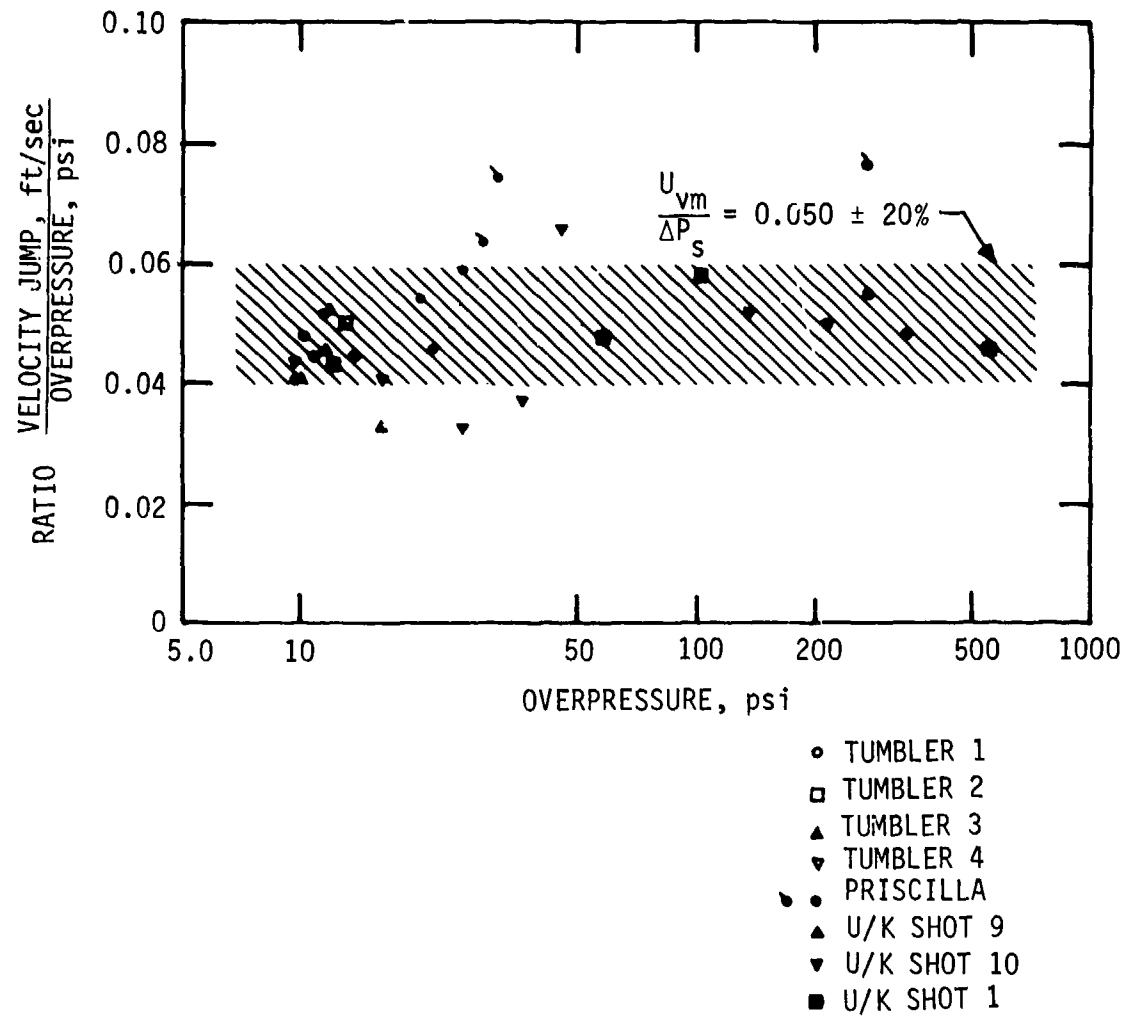


Figure IV-1.23. Vertical velocity at 5-foot depth. Summary of superseismic data at NTS (\blacklozenge = precursor data).

The values mentioned hold for the superseismic region, and still hold for the airslap, and when the ground motion outruns the airblast, the ratio of particle velocity to overpressure may become as high as 0.1. Correlation of maximum velocity data in the outrunning region will be treated later.

Extrapolation of vertical particle velocity data to media whose properties differ from those of NTS may be based on elastic theory. Newmark and Hall (Reference IV-1.23) recommend that the particle velocity be taken inversely proportional to the seismic compressional wave velocity of the medium using a value of 1,000 ft/sec as representative of the NTS alluvium. Sauer (Reference IV-1.26) recommends that the particle velocity be taken inversely proportional to the impedance, ρC_p , where C_p is the compressional wave velocity for the propagation of large stress levels and ρ is the medium density. This latter recommendation is based on the fact that although the seismic velocity equals approximately 1,000 ft/sec near the surface at Frenchman Flat, observations made during a nuclear test show that the compressional wave velocity for the stress levels of interest was approximately 760 ft/sec \pm 15 percent. When this value of compressional wave velocity is inserted along with the in situ soil density then the theoretical value of the vertical velocity-overpressure ratio becomes 0.048 ± 15 percent, almost the exact relationship noted experimentally. Thus, the two sets of prediction relationships are not inconsistent if the recommended procedures are not intermingled. If the recommendations of Reference IV-1.23 are used, then the particle velocity is taken as inversely proportional to the seismic velocity using $C_p = 1,000$ ft/sec for NTS. If the procedure of Reference IV-1.26 is used then the particle velocity is taken as inversely proportional to acoustic impedance of the medium for high-stress waves using the reference values of $128 \text{ lbs}/\text{ft}^3$ for the in situ density and 760 ft/sec for the compressional wave velocity.

Of particular significance in the second prediction method is the concept that the actual compression wave velocity (that corresponding to the propagation of waves of large stress) is not always a constant fraction of the seismic

compression wave velocity. This introduces more complications than are warranted at the present time. However, as dynamic soil mechanics evolves, we should be able to take quantitative account of the differences that are known to exist between the actual compressional wave velocity and the seismic compression wave velocity.

Similar to the behavior of maximum vertical acceleration, maximum vertical particle velocity becomes a function of scaled ground range in the outrunning ground motion region as shown in Figures IV-1.24 and IV-1.25. In Figure IV-1.24, data are presented for weapon yields which range from 1 kt to 10 mt and scaled heights of bursts from the surface to 100 ft/kt^{1/3}. The depth of measurement also varies as indicated in the legend. On a scaled basis, this difference would not appear to be significant except for the presence of the water table. The data plotted represent the measurements made closest to the surface on each shot listed and some measurements appear to be above and below the water table. However, the basic data are not clear in this respect. Within the scatter of the correlation, the data do not exhibit any systematic trend with respect to depth.

Nevada Test Site particle velocity data shown in Figure IV-1.25 are seen to approach asymptotically the same negative slope observed in Figure IV-1.24 for a sufficient range beyond the outrunning region. Maximum particle velocities in the outrunning region for NTS are four times as large as that for PPG.

For fully developed outrunning ground motion, Sauer (Reference IV-1.26) presents the following correlation equations for maximum vertical velocity, v_m , regardless of sign. For NTS it is

$$v_m = 2 \times 10^8 \left(\frac{R}{W^{1/3}} \right)^{-2} , \text{ ft/sec} \quad (\text{IV-1.30})$$

and for PPG it is

$$v_m = 5 \times 10^7 \left(\frac{R}{W^{1/3}} \right)^{-2} , \text{ ft/sec} \quad (\text{IV-1.31})$$

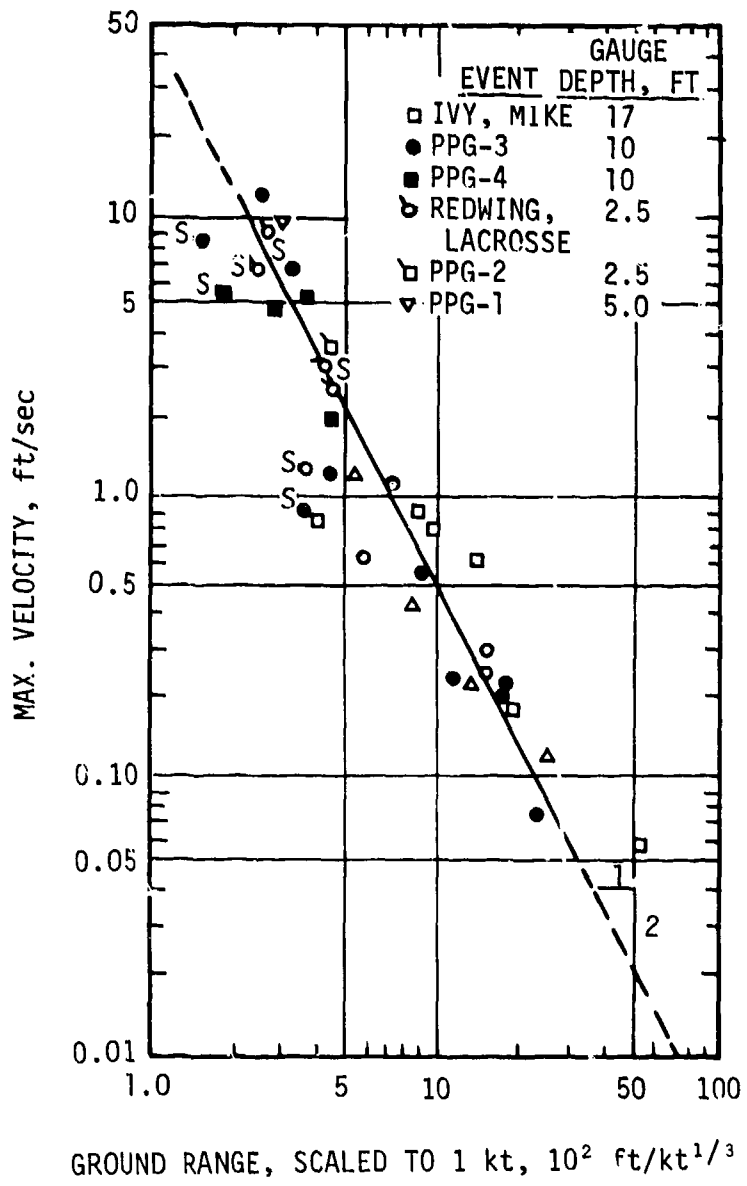


Figure IV-1.24. Maximum vertical velocity versus ground range for outrunning ground motion at PPG (S indicates superseismic blast wave).

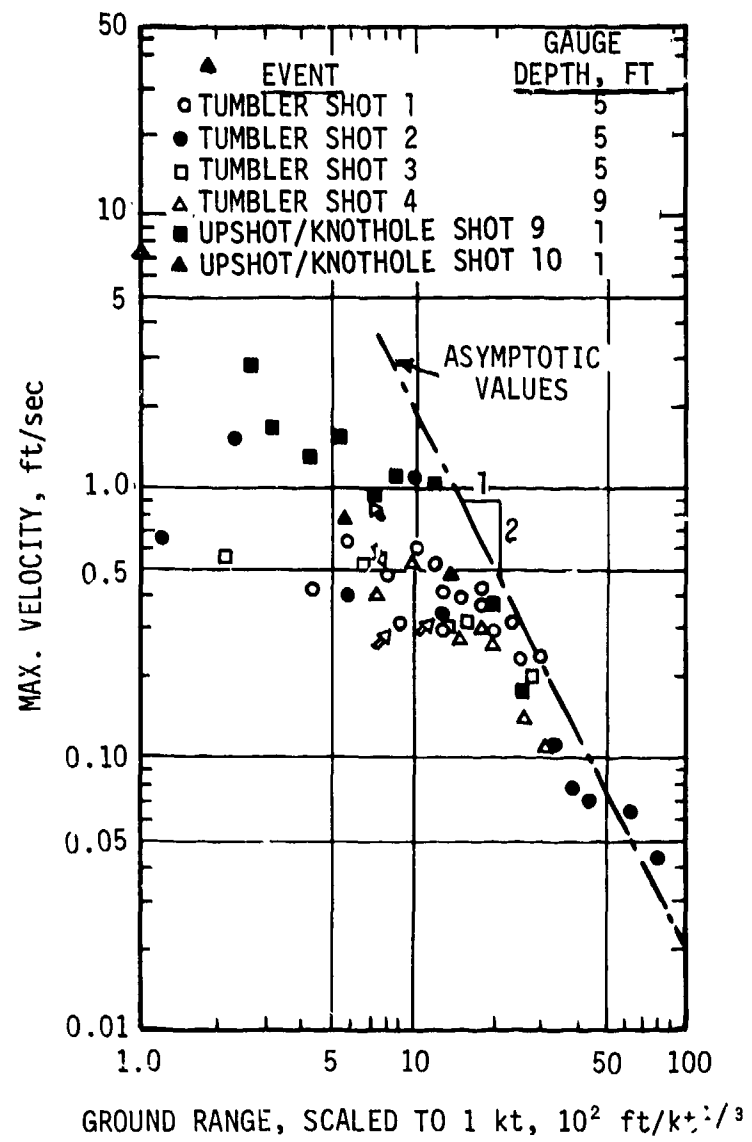


Figure IV-1.25. Maximum vertical velocity versus ground range at NTS.

where v_m is in ft/sec, R is in ft, and W is in mt. The 4:1 difference in the constants of the above equations is evidence that the particle velocity decreases as the compressional wave velocity increases and is consistent with the 5:1 difference in seismic velocity between PPG and NTS.

If it is assumed (Reference IV-1.1) that particle velocity is inversely proportional to the product of the mass density and the seismic velocity, and taking the in situ density of 120 lbs/ft³ for NTS and PPG, and the near-surface seismic velocity of 5500 ft/sec and 1200 ft/sec for PPG and NTS respectively, then there results the following average relation for the peak vertical particle velocity for the outrunning region:

$$v_m = 3.1 \times 10^6 \left(\frac{R}{W^{1/3}} \right)^{-2} \left(\frac{100}{\rho} \right) \left(\frac{1000}{C_p} \right), \text{ ft/sec (IV-1.32)}$$

where v_m , R, and W have the same units as in Equations IV-1.30 and IV-1.31, ρ is in lbs/ft³ and C_p ft/sec.

IV-1.3.2 Variation of Vertical Particle Velocity with Depth

Figure IV-1.26 presents the attenuation of vertical particle velocity as the ratio of the maximum vertical particle velocity at depth to the maximum vertical velocity near the surface (5-ft depth) as a function of a modified scaled depth for data from nuclear events carried out at Frenchman Flat, NTS. The scaled depth is

$$\frac{a}{C_p} = \frac{y}{W^{1/3}} \quad (\text{IV-1.33})$$

where a is the ambient air sound speed, C_p is the compression wave velocity, y is the depth from surface, and W is the weapon yield in kt. This form of depth scaling was derived from correlation of theoretical computations for one-dimensional viscoelastic wave propagation with quasi-steady plane strain wave propagation in an elastic homogeneous half-space. The correlation shown in Figure IV-1.26 was developed using a compressional wave velocity of 760 ft/sec for NTS.

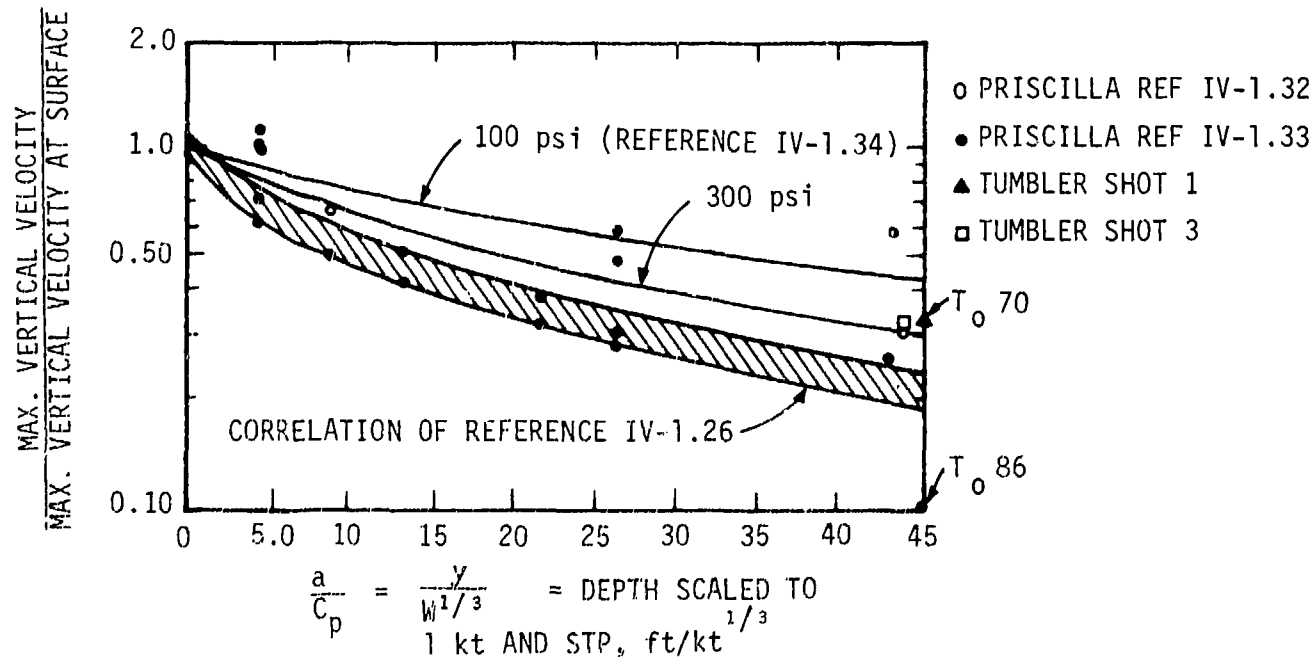
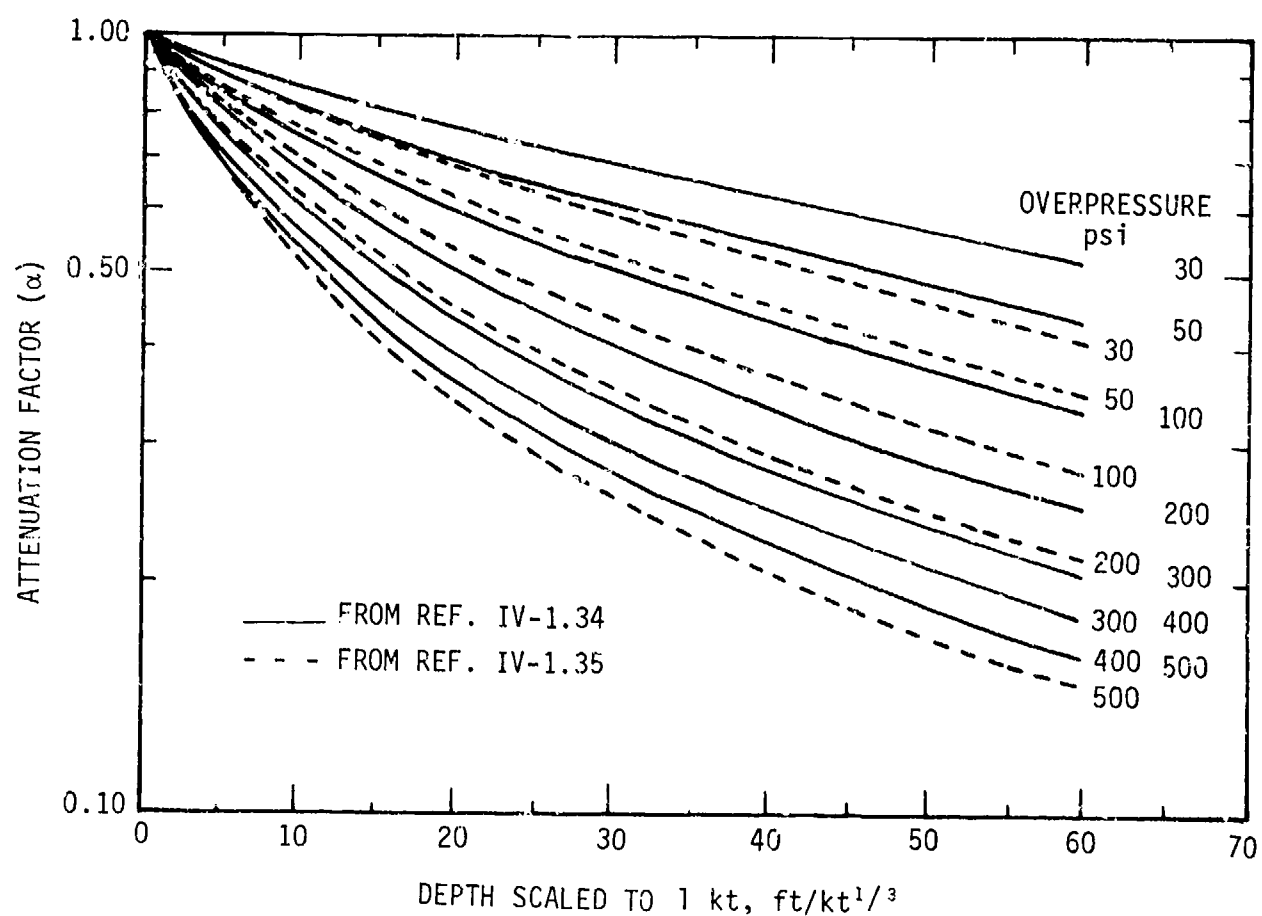


Figure IV-1.26. Attenuation of maximum vertical velocity with depth at Frenchman Flat for superseismic blast wave.

The correlation curve is presumed to represent the best estimate for the variation of maximum velocity with depth. It takes into consideration the fact that velocity should decay somewhat more rapidly than maximum displacement because of the more rapid attenuation of the high-frequency components. The width of the curve does not represent an estimate of error but simply indicates that there is some uncertainty in the specific location of the line. The data do not indicate any correlation with overpressure level or overpressure waveform. It should be noted that all data are for the superseismic airblast region.

Newmark and Hall (Reference IV-1.34) had estimated the attenuation of vertical particle velocity. Maximum vertical velocity was taken to be proportional to maximum vertical stress. The attenuation of vertical stress is found from a solution of the stress field imposed by typical overpressure distributions on the surface of an elastic half-space. Results are given in terms of an attenuation factor, α , which equals the vertical particle velocity (stress) at depth divided by the particle velocity (overpressure) at the ground surface. Figure IV-1.27 shows the attenuation factor as a function of scaled depth and overpressure level computed from equations presented in References IV-1.27 and IV-1.34. The more recent version of Reference IV-1.34 (Reference IV-1.35) shows a somewhat greater attenuation. The difference is not significant in view of the uncertainties that exist in experimental data. The attenuation factor is larger for higher overpressures because the attenuation of stress with depth depends theoretically upon the decay of overpressure with time, which is greater for higher overpressures and for small yields. The yield factor is taken into account by using the depth scaled to 1 kt. Since the overpressure waveform becomes peaked at higher overpressures, the overpressure must enter as an independent parameter. The results of Figure IV-1.27 are shown superimposed on the data in Figure IV-1.26, where the compression wave velocity factor used was the one assumed in Reference IV-1.26 representative of Frenchman Flat ($a/C_p = 1.5$). Overpressures shown are typical of the range of the majority of the PRISCILLA data. The attenuation factor is somewhat smaller than that indicated by the correlation proposed by Sauer (Reference IV-1.26) who favors the data of Reference IV-1.32 over that of Reference IV-1.33. This latter data results from the small amplitude of the primary acceleration. The curves shown on Figure IV-1.26 fall within the spread of the data and it might be argued that the correlation band (Reference IV-1.26) gives an attenuation factor that is too large and, therefore, is not conservative from a protective structure design standpoint. It should be mentioned that in both of the proposed predictions,



$$\alpha = \frac{\text{VERTICAL PARTICLE VELOCITY AT } y}{\text{VERTICAL PARTICLE VELOCITY AT SURFACE}}$$

Figure IV-1.27. Attenuation factor for maximum vertical stress, maximum strain, and maximum particle velocity.

the lack of data prevents substantiation of a critical element of the correlation, namely, the influence of compressional wave velocity in the proposed correlation of Reference IV-1.26 (shaded band in Figure IV-1.26) and the influence of overpressure on the attenuation factor in the correlation of Reference IV-1.34 (curves in Figure IV-1.26).

The maximum overpressure at which ground motion measurements were made was 554 psi on Event PRISCILLA. These measurements lead to the ratios of particle velocity to overpressure discussed in References IV-1.26 and IV-1.34. Subsequent to PRISCILLA, extensive measurements were made on the SMALL BOY Event covering a range from seismic to approximately 2,000 psi equivalent range, and depths from 5 feet to 300 feet in the Frenchman Flat area of NTS (References IV-1.36 and IV-1.37). At the low overpressures, the ratio of particle velocity to overpressure was found to be near 0.1 ft/sec/psi while at the higher overpressures the ratio dropped below the PRISCILLA values. A similar trend is noted in the results of high-explosive experiments over alluvial soils. The lower values of particle velocity to overpressure ratio at high overpressures and/or at low yield is a result of more rapid attenuation of the high frequencies contained in the airblast at these extreme conditions.

Reference IV-1.38 presents an empirical correlation of these data combining in a single parameter, X, the effects of overpressure (expressed in terms of the non-dimensional gradient of overpressure with respect to time just to the rear of the shock front), depth and explosion yield. This correlation is

$$X = \frac{y}{\sqrt{W}} f(\Delta p) \quad (\text{IV-1.34})$$

where y is the depth of measurement in feet, W is the detonation yield in kt, and $f(\Delta p)$ is a function of overpressure. The function $f(\Delta p)$ is shown in Figure IV-1.28 as a function of overpressure scaled to ambient atmospheric pressure. SMALL BOY data plotted against this relationship are shown in Figure IV-1.29 and the data for the events of Figure IV-1.29 are plotted versus X in Figure IV-1.30.

High-explosive data cover a much broader range of detonation yields (256 pounds to 100 tons) than the nuclear data, with overpressures ranging from 4 psi to 1700 psi. These data are shown in Figure IV-1.30. Although the HE data have

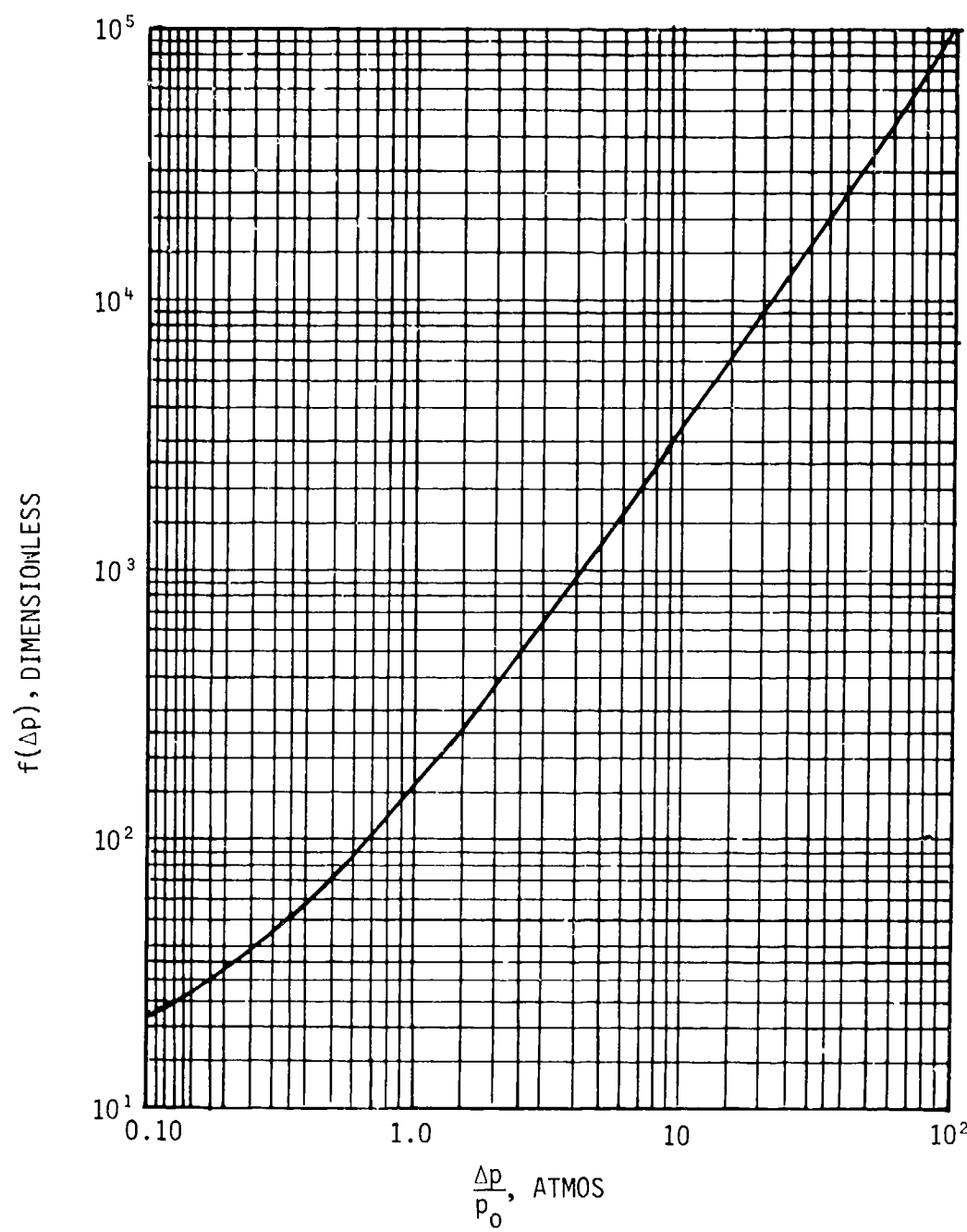


Figure IV-1.28. Dimensionless initial rate of decay of overpressure versus shock overpressure nuclear airburst.

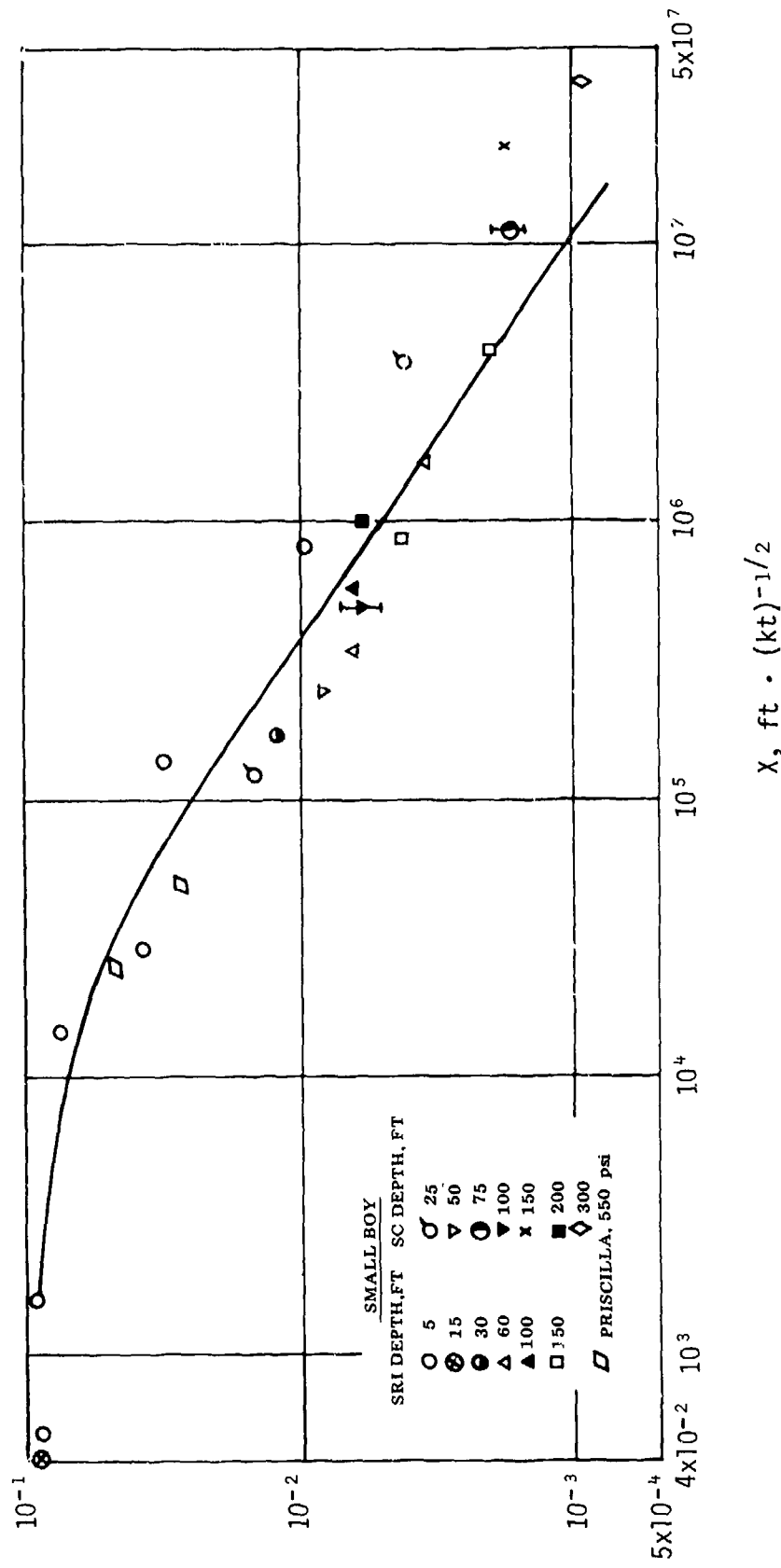


Figure IV-1-29. Ratio of maximum particle velocity to airblast overpressure versus scaled depth for SMALL BOY and PRISCILLA. (SRI = Stanford Research Institute data, SC = Sandia Corporation.)

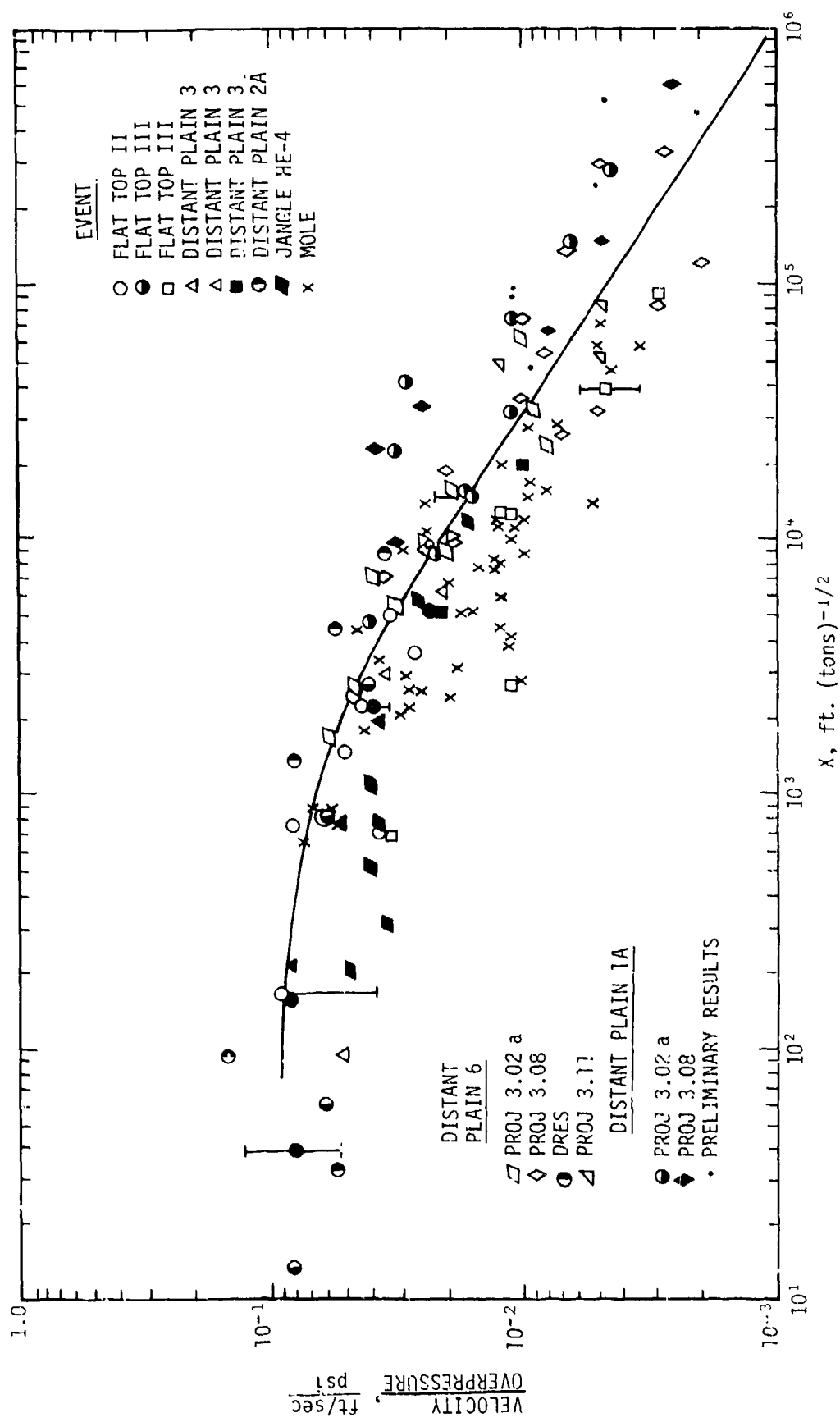


Figure IV-1.30. Ratio of maximum vertical particle velocity to airblast overpressure versus scaled depth for high explosive. (Vertical bars are shown where direct measurement of velocity and integrated acceleration data are available.)

the same trend as the nuclear data, they show a somewhat different correlation. This is most probably due to the fact that the pressure function, $f(\Delta p)$, is based on nuclear overpressure waveforms rather than high-explosive overpressure waveforms.

The only available data on the attenuation of vertical particle velocity for large-yield weapons are from PPG 4. The majority of the HARDTACK-I data (Figure IV-1.31) were in the outrunning ground motion region. In Figure IV-1.31, maximum vertical velocities were normalized by dividing by the values of the mean curve of Figure IV-1.24. The scatter in the correlation is a little greater than the scatter in the data in Figure IV-1.24. Since the yield of PPG 4 is roughly 200 times that of PPG 3, it must be concluded that vertical particle velocities in the outrunning ground motion region attenuate with depth more or less independently of weapon yield. Note that the two superseismic data points (indicated by an X) for PPG 4 do not vary significantly with depth. This is consistent with the correlation suggested in Figures IV-1.26 and IV-1.27. However, the data are too scant to confirm this postulate.

Cooper and Bratton (Reference IV-1.31) reported on a study of vertical air-blast-induced ground motions produced by nuclear explosions over a dry soil medium. Material properties to model Frenchman Flat at NTS for use in first principle calculations were synthesized from very limited dynamic laboratory stress-strain data, various soil characteristics, and seismic data. They performed parametric calculations with a one-dimensional, plane-strain finite difference computer program to define a "theoretical" simplified model that expresses peak vertical velocities and displacements as a function of weapon yield, peak overpressure and depth. The ground motions predicted by this model were then compared to ground motion data from detonations at Frenchman Flat. In particular, predictions of the simplified model were found to be reasonably consistent with the PRISCILLA data. These data were a primary basis for empirical prediction procedures widely used in the design and analysis of strategic structures. The model could be altered in cases where little or no dynamic soil property data exist to provide even better agreement between calculated and measured ground motions. Study of qualitative features of the model results provided insight into the basic wave propagation phenomena at Frenchman Flat which could improve the interpretation of experimental data so that a more consistent comparison between theory and experiment could result.

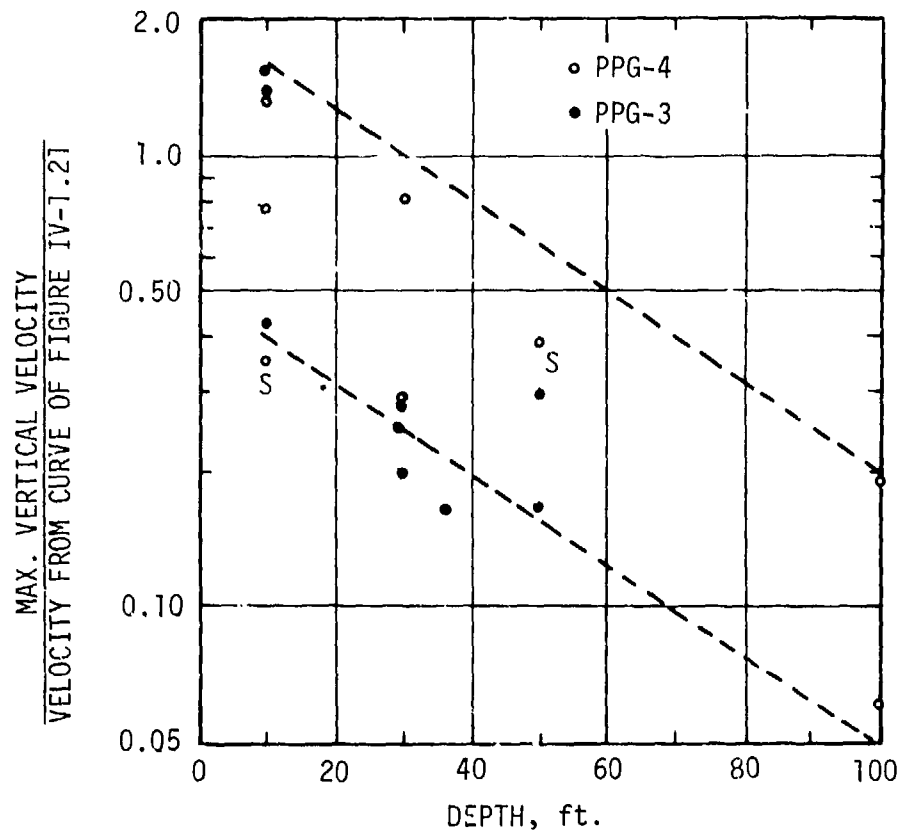


Figure IV-1.31. Vertical particle velocity versus depth for outrunning ground motion at PPG. S indicates superseismic blast wave.

From a series of one-dimensional calculations, Cooper and Bratton (Reference IV-1.31) developed the following expressions for predicting vertical airblast induced velocities as a function of yield, peak overpressures and depth:

$$v = 0.5 \Delta p_s \quad , \quad z = 0 \quad (\text{IV-1.35})$$

$$v = 50 \left(\frac{\Delta p_s}{100} \right)^{0.95} W^\beta e^{-0.0085(z-30)}, \text{ in/sec} \quad (\text{IV-1.36})$$

where

$$\beta = 0.07 \left(\frac{\Delta p_s}{100} \right)^{0.36} \quad (\text{IV-1.37})$$

where v is in inches per sec, z is the depth in feet, W is the weapon yield in mt, and Δp_s is the airblast peak overpressure in psi. Equation IV-1.36 is valid only for $30 \leq z \leq 100$ ft. Equations IV-1.36 and IV-1.37 are valid for 1 kt $\leq W \leq 10$ mt and $100 \leq \Delta p_s \leq 1000$ psi. Cooper and Bratton draw the following conclusions from the study of their model when applied to nuclear test data from Frenchman Flat.

(1) For a given yield, near-surface peak particle velocities are strongly dependent on peak overpressure. For example, at $z = 30$ ft, $v \sim \Delta p_s^{0.95}$ and therefore uncertainties in predicting peak overpressure as a function of range are translated into nearly equivalent uncertainties in predicting near-surface peak vertical airblast-induced ground motions.

(2) For a given peak overpressure, near-surface peak particle velocities are weakly dependent on weapon yield. For example, at $z = 30$ ft, $v \sim W^\beta$ where $0.07 \leq \beta \leq 0.16$ for $100 \leq \Delta p_s \leq 1000$ psi. Thus, uncertainties in specifying the yield are only weakly translated into uncertainties in predicting the peak near-surface vertical ground motions.

(3) Peak vertical particle velocities below about 30 ft attenuate exponentially, but at a rate that is usually less rapid than at shallower depths. In general, the attenuation rates increase with increasing peak overpressure or decreasing yield.

(4) The response of the softer layers below about 30 ft leads to a downward acceleration of the surface so that a residual downward velocity remains, even after the overpressure positive phase is over for low yields. This downward motion is reversed by reflected compressional waves from either the fourth (170 ft) or fifth (650 ft) interface, depending on the yield and peak overpressure.* Such downward coasting phenomena could easily be misinterpreted as a base line shift in the analysis of test data.

IV-1.3.3 Horizontal Particle Velocity

Sauer (Reference IV-1.26) recommends that the maximum horizontal velocity be taken equal to two-thirds of the maximum vertical velocity in the superseismic airblast region. Figures IV-1.32 and IV-1.33 present the relatively small number of data on maximum horizontal velocity in a manner similar to that for vertical particle velocity.

Conner and Bratton compared the ground motions predicted by their simplified model with those measured on several nuclear events in Frenchman Flat. They emphasized the comparison with PRISCILLA data because they were the primary basis of empirical prediction procedures developed in the early 1960's and applied to develop criteria for many existing strategic systems (Reference IV-1.22).

Figure IV-1.33a compares the calculated in situ "impedance" of the very near surface soils data from five nuclear tests in Frenchman Flat. Both the calculated and experimental data were derived by dividing the peak overpressure by the peak particle velocity at the indicated depths ($\rho_c = \Delta P/v$). Thus, the term impedance strictly applies only for the free surface because peak particle velocity and stress attenuate with increasing depth. This attenuation, which is less significant at the low overpressures and high yields, is the cause of the variation between $\Delta P/v$ for 0 and 10 ft depths and for the yield variation between 1 and 100 kilotons. Outrunning conditions exist for peak overpressures less than about 25 psi in Frenchman Flat. Nevertheless, a jump in particle velocity is caused by the arrival of the airblast so that the low overpressure near-surface data in Figure IV-1.33a may be appropriate even though outrunning conditions exist. In any case, the calculated $\Delta P/v$ appears to be somewhat higher than the analogous nuclear test data from the upper 10 ft of soil in Frenchman Flat. This result implies that the loading stress-strain curve assumed for the 0-10 ft layer of Frenchman Flat in

*See Reference IV-1.31 for a description of the Frenchman Flat layers and their properties used in the model.

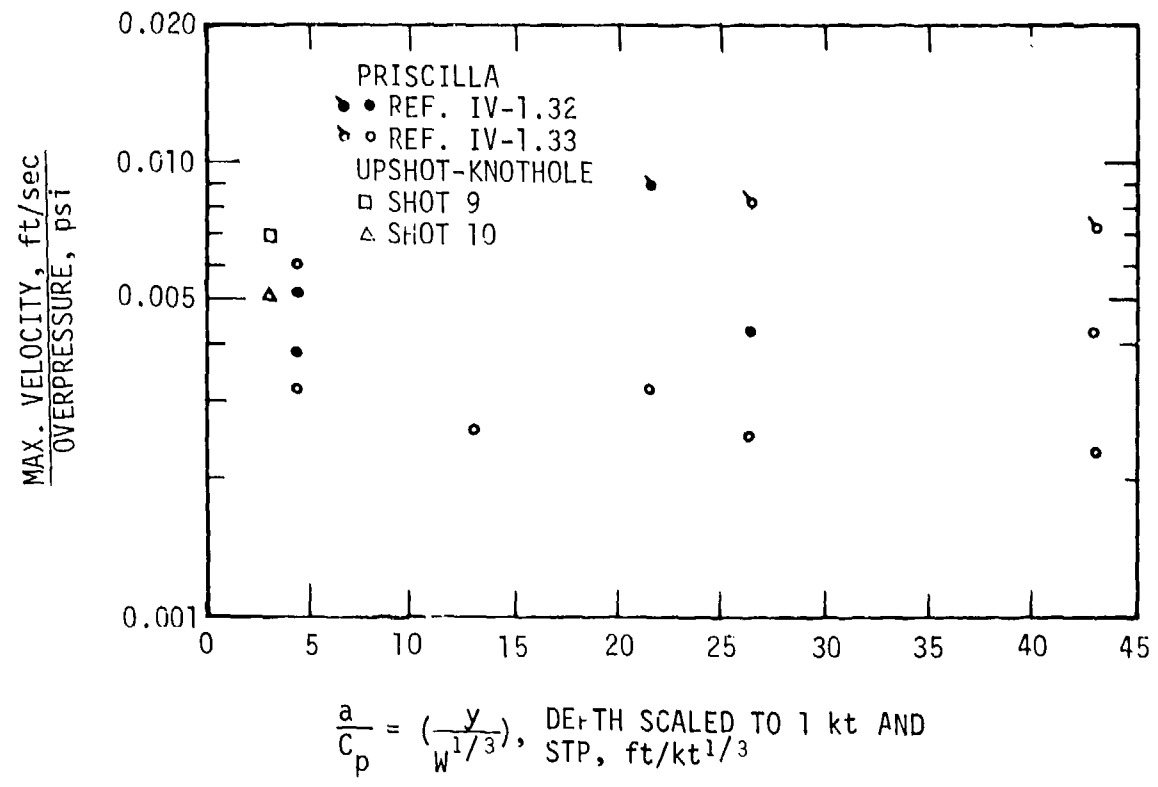


Figure IV-1.32. Variation of maximum outward horizontal velocity with depth for superseismic blast wave at NTS (• = precursor data).

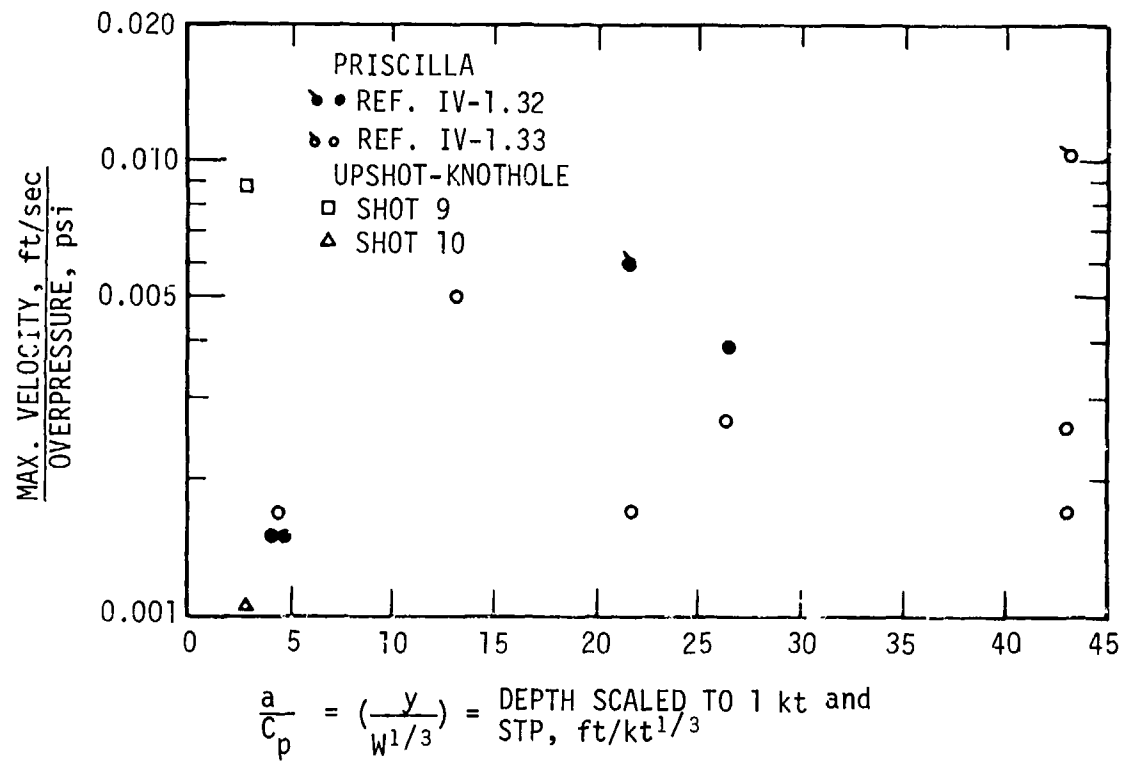


Figure IV-1.33. Variation of maximum inward horizontal velocity with depth for superseismic blast wave at NTS
 (• = precursor data).

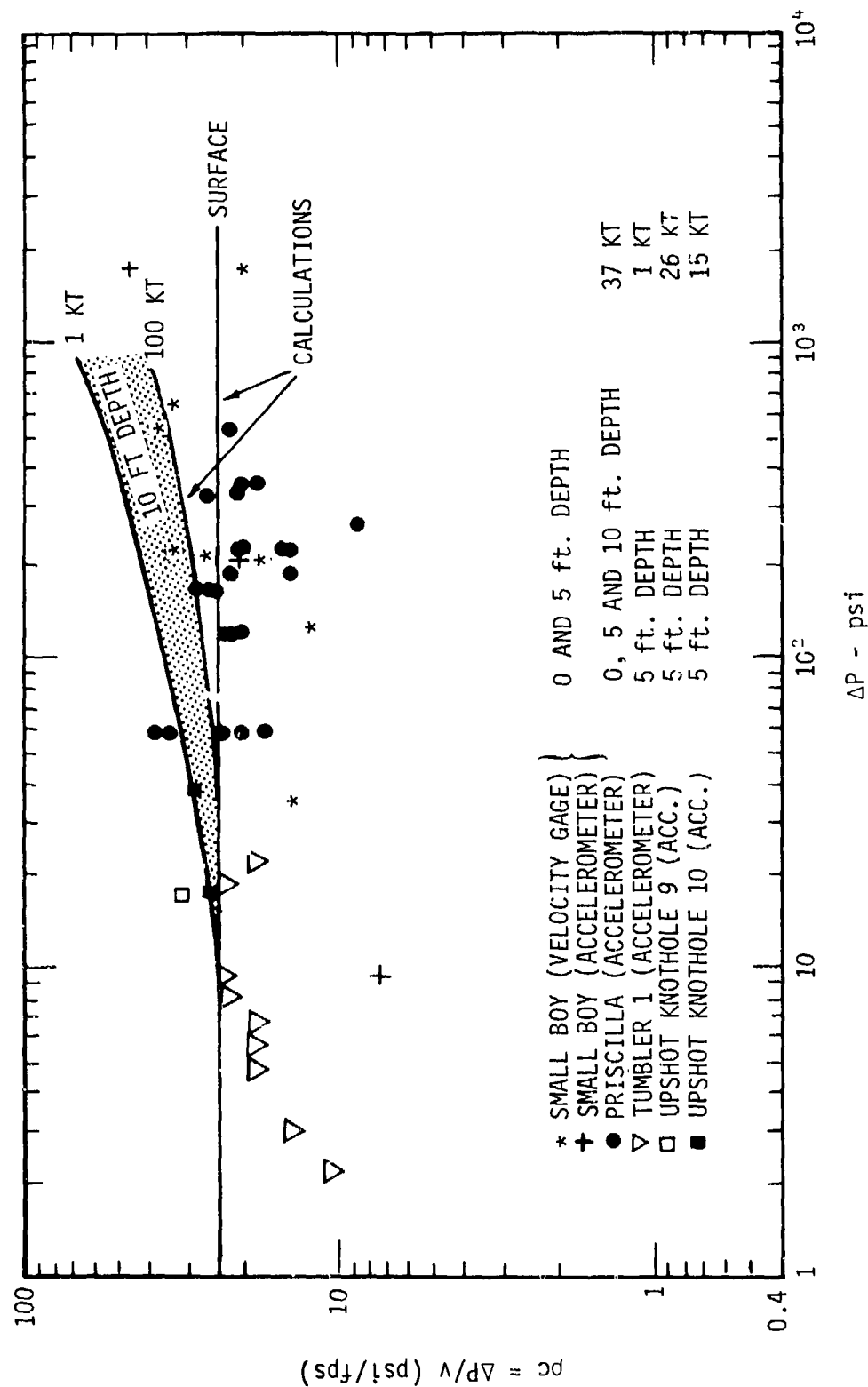


Figure IV-1.33a. Comparison of calculated and measured $\Delta P/V$.

their model may have been too stiff. The experimental data suggest that $\Delta P/v \approx 20$ psi/fps as opposed to the calculated surface impedance of 24 psi/fps (or even larger values at 5 and 10 ft depths). Thus, the calculations would be more consistent with the experimental data if the modulus of the surface layer, for the peak pressures of concern, were reduced by about 30 to 50 percent; an alteration that would produce only a minor increase in the surface displacements and no change in displacements below 10 feet.

The comparison of peak particle velocities predicted by the simplified theoretical model for a yield of 37 kilotons detonated at 700 ft altitude with the experimental data from PRISCILLA was made. Although the equations summarized above could be used as a basis for comparison, they interpolated between the peak displacement and particle velocity attenuation curves for the case of a 37 kt near surface burst. Figure IV-1.33b compares measured near-surface peak particle velocities with predictions from the simplified model. As noted previously, the model tends to underestimate the near-surface peak particle velocity experimental data. To present the data in a form that allows a more representative comparison, the reported vertical motion data were normalized by the best estimate fit to the experimental surface data shown in Figure IV-1.33c. Note that the estimate from the simplified model is about 20 percent lower than the peak particle velocity data. The normalized data are compared with the predicted attenuation of vertical peak particle velocity and displacement, as shown in Figure IV-1.33d.

The simplified model was based on the overpressure boundary condition predicted for a surface burst, and prediction formulae were expressed in terms of peak overpressure. To reduce the possible ambiguity in interpreting discrepancies between the results of theoretical calculations and experimental data from other than surface bursts, they calculated the ground motions directly for the 650 ft and 1,050 ft ranges on PRISCILLA, utilizing fits to the measured overpressure. The calculated particle velocity waveforms are qualitatively similar to those measured, but some quantitative discrepancies exist. The calculations underestimate the near-surface peak particle velocity data. Perhaps of greater importance, the calculated positive phase durations are consistently longer than those reported by SRI (and sometimes significantly shorter than those reported by Sandia).

Note that with the exception of single datum points for Shots 9 and 10 of UPSHOT-KNOTHOLE, respectively, the data on horizontal velocity is limited to PRISCILLA. In Figure IV-1.32, the horizontal velocity-overpressure ratio is

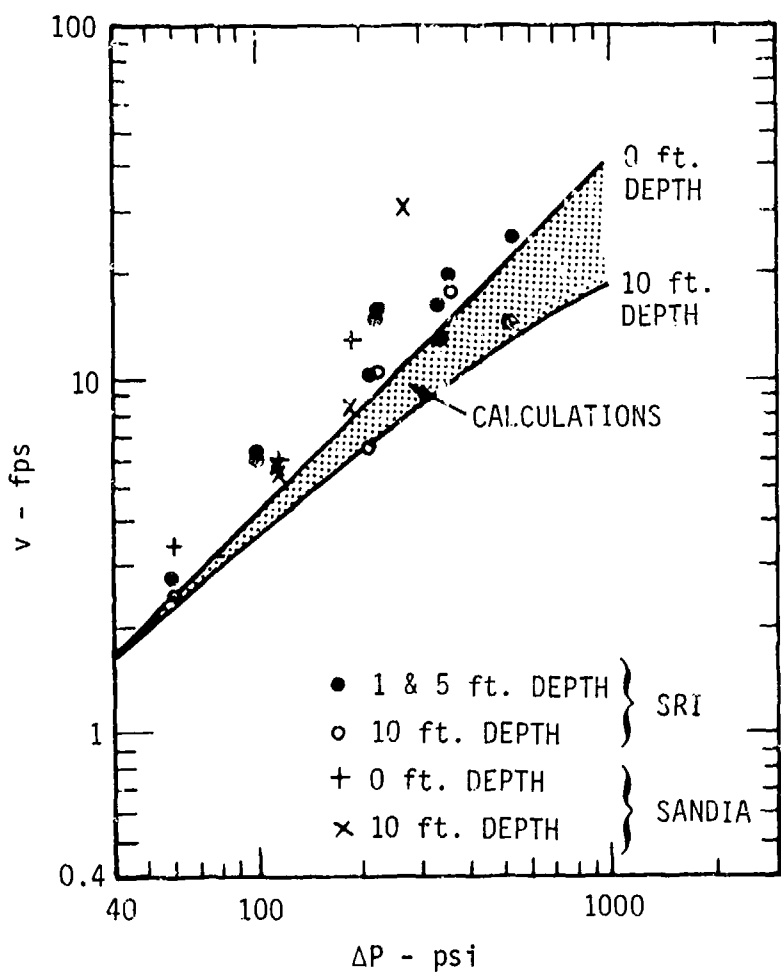


Figure IV-1.33b. Comparison of theoretical model and near-surface ground motion data from PRISCILLA.

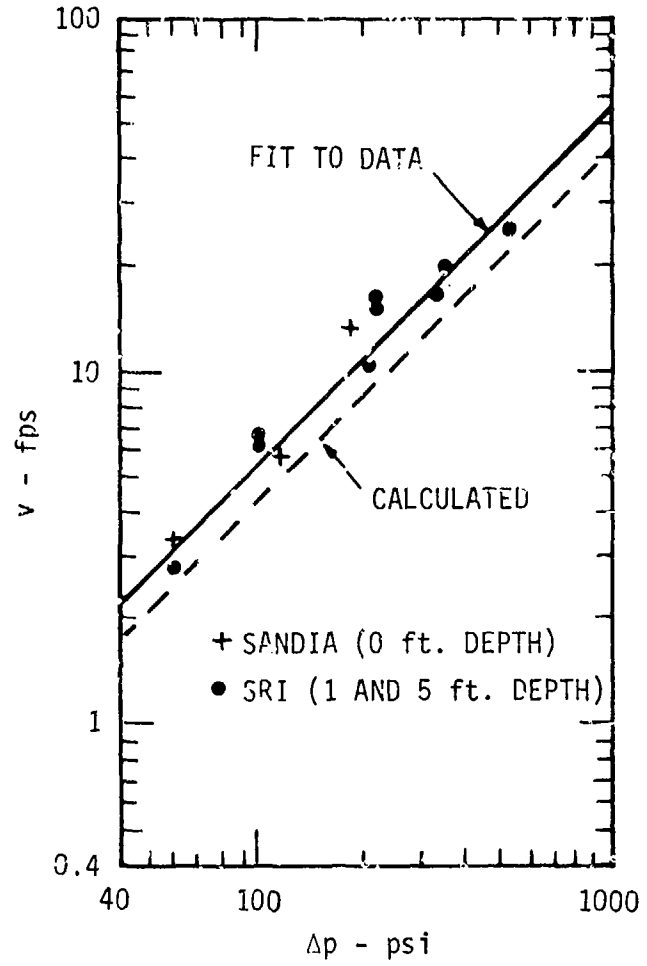


Figure IV-1.33c. Best estimate of very near-surface vertical motion data from PRISCILLA.

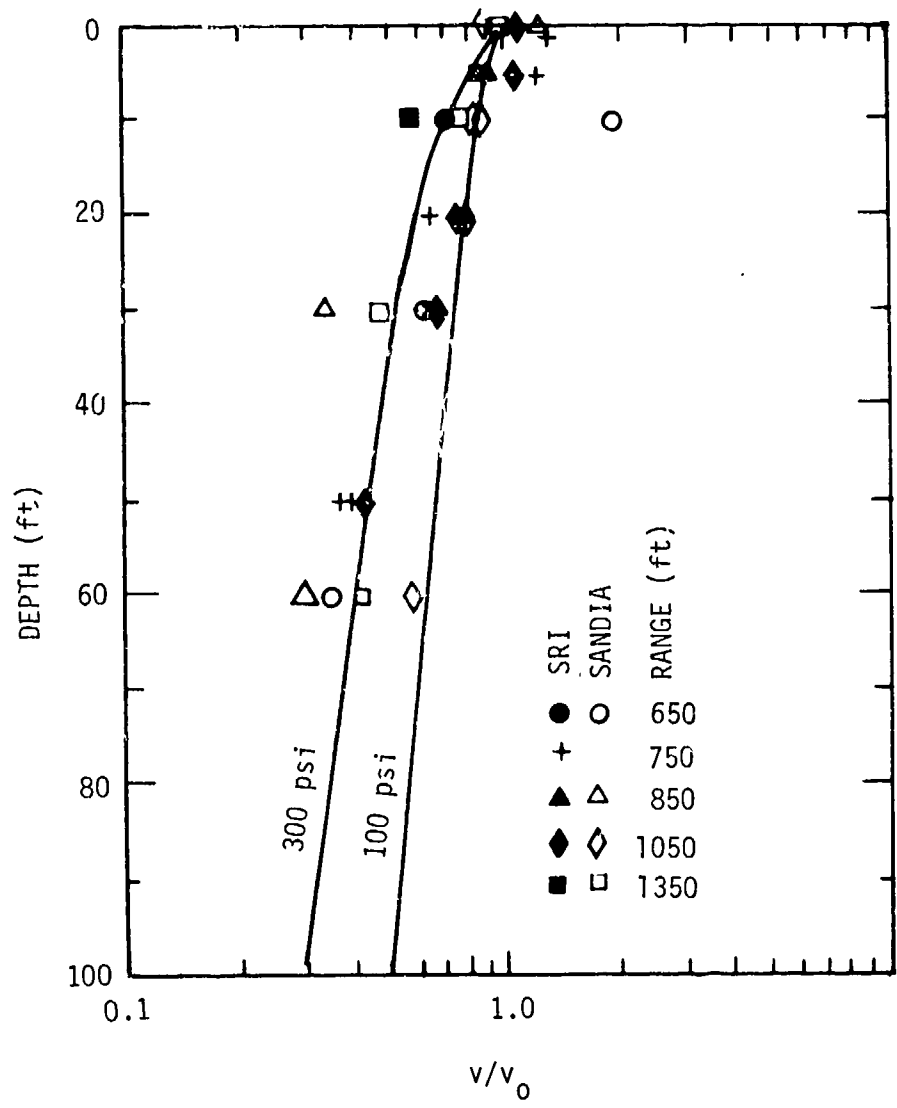


Figure IV-1.33d. Comparison of calculated attenuation rates with normalized peak vertical motion data from PRISCILLA.

approximately 0.005 ft/sec/psi \pm 50 percent. The second maximum in Figure IV-1.33 is somewhat smaller and inward with a velocity-overpressure ratio of 0.003 ft/sec/psi \pm 70 percent. Although the scatter in the data is considerably larger than for the vertical velocity data, the impression given by Figures IV-1.32 and IV-1.33 is that the maximum horizontal particle velocity does not attenuate with depth below the surface, at least not to the depth at which the data cease. Moreover, it appears that the ratio of maximum horizontal particle velocity to maximum vertical particle velocity near the surface is about 1/10 and certainly not larger than 1/4.

Horizontal velocity data near the surface in the outrunning ground motion region are presented in Figure IV-1.34 and were taken from Reference IV-1.35. These data show a larger scatter than the vertical particle velocity data. It is in fact difficult to ascribe a mean line for these data. It appears that the decay of horizontal velocity with ground range lies somewhere between a slope of -1.5 and -2, the -1.5 slope being applicable for scaled ground range greater than 700 ft (overpressure less than approximately 20 psi). At smaller ground ranges (overpressures greater than 20 psi) the maximum horizontal particle velocity appears to be about 1/4 to 1/2 of the maximum vertical particle velocity.

Data on the variation of horizontal particle velocity with depth in the outrunning ground motion region are limited to the data from HARDTACK-I. In Figure IV-1.35, the horizontal particle velocities have been divided by the mean particle velocity near the surface determined from the average values of the curve of Figure IV-1.34. In view of the uncertainty in the correlation of the data of Figure IV-1.34, both mean curves have been used for normalization. The vertical lines of Figure IV-1.35 represent the limits of the results for these two calculations. Horizontal velocity in the outrunning ground motion region does not appear to have any significant attenuation with depth down to 100 ft. This is similar to the situation observed at NTS for the superseismic airblast region (see Figures IV-1.32 and IV-1.33).

IV-1.4 CORRELATION OF MAXIMUM DISPLACEMENT DATA.

In this section is presented a discussion of the data on surface displacements in the superseismic region and data on variations of maximum displacements with depth.

Comparison is made of the ground motions predicted by the simplified model developed by Cooper and Bratton (Reference IV-1.31) with those measured on several nuclear events at Frenchman Flat. Emphasis is placed on the comparison with

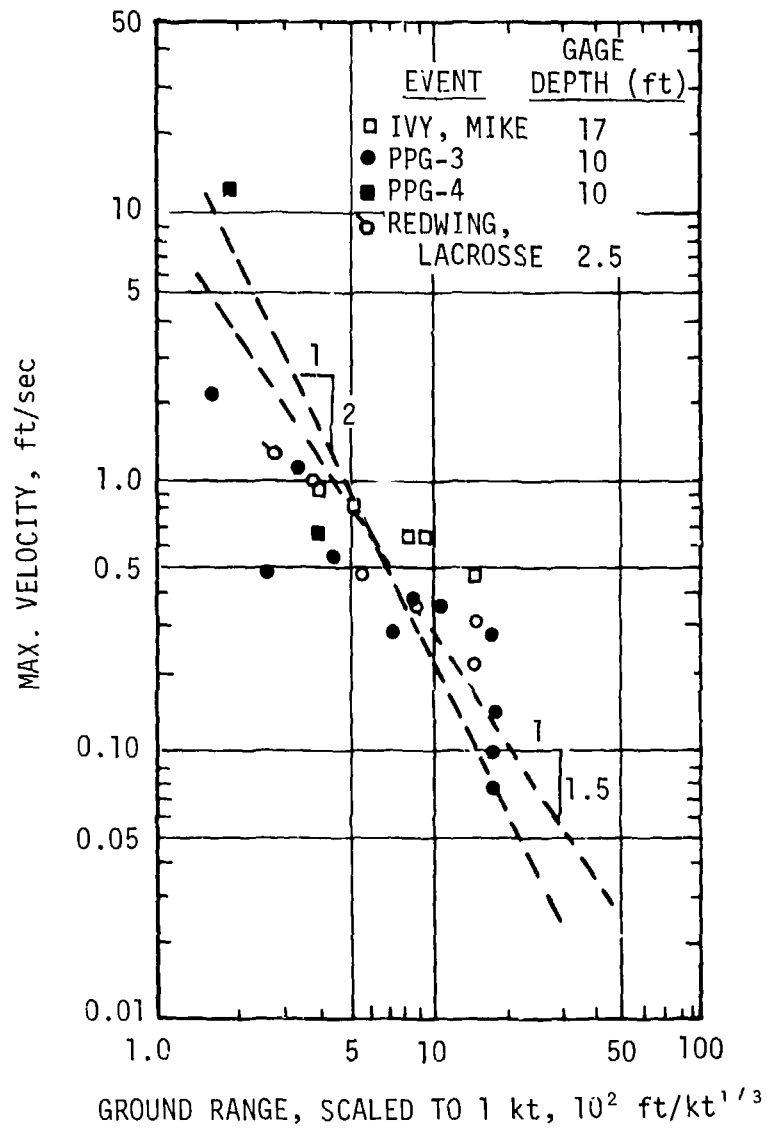


Figure IV-1.34. Maximum horizontal velocity versus ground range for outrunning ground motion at PPG.

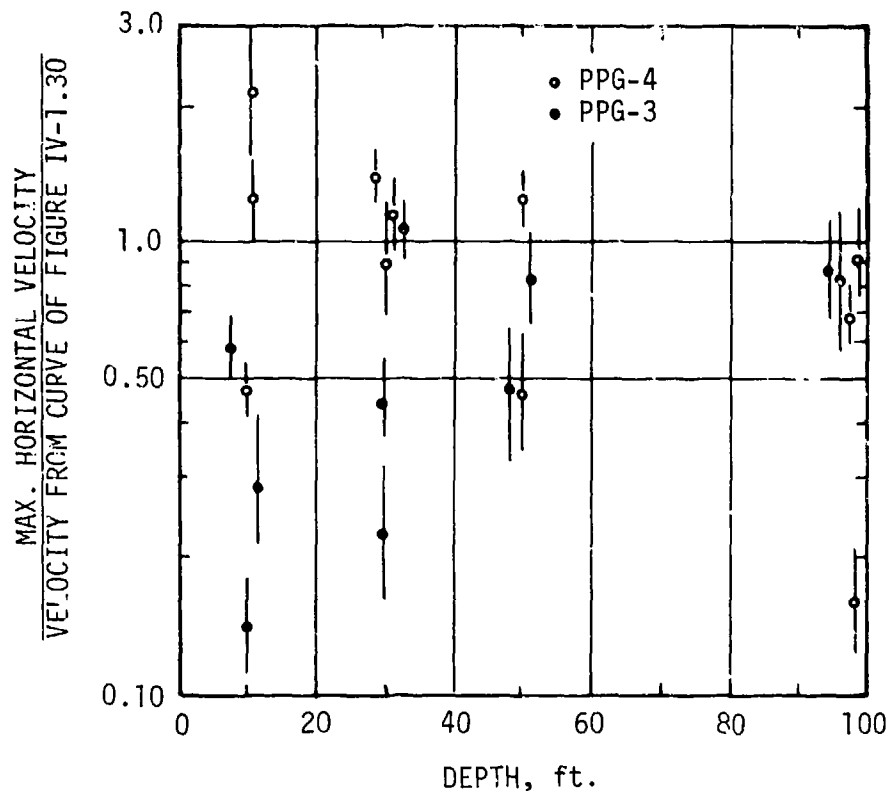


Figure IV-1.35. Horizontal particle velocity versus depth for outrunning ground motion at PPG (vertical lines indicating extent of uncertainty in correlation of Figure IV-1.34).

PRISCILLA data because they were the primary basis of empirical prediction procedures developed in the early 1960's and applied to develop criteria for many existing strategic systems (Reference IV-1.22).

Figure IV-1.36 compares measured near-surface peak displacements with predictions from the simplified model. As noted previously, peak displacements predicted by the simplified model lie more in the center of the data scatter.

Figures IV-1.37 and IV-1.38 compare peak displacement data at depth with predictions from the simplified model procedures. In cases where independent peak overpressure data were reported by Sandia and SRI, the simplified model is unfolded for both cases. It is difficult to evaluate the accuracy of the predicted attenuation characteristics from these plots because insufficient data exist at each range to define the inherent data scatter as a function of depth. To present the data in a form that allows a more representative comparison, Cooper and Bratton normalized the reported vertical motion data by the best estimate fit to the experimental surface data shown in Figure IV-1.39. Note that the estimate from the simplified model is an adequate fit for peak displacements. The normalized data are compared with the predicted attenuation of vertical peak displacement, as shown in Figure IV-1.40.

The simplified model was based on the overpressure boundary condition predicted for a surface burst, and prediction formulae were expressed in terms of peak overpressure. To reduce the possible ambiguity in interpreting discrepancies between the results of theoretical calculations and experimental data from other than surface bursts, Cooper and Bratton calculated the ground motions directly for the 650 ft and 1,050 ft ranges for event PRISCILLA, utilizing fits to the measured overpressure as shown in Figure IV-1.41. The calculated particle velocity waveforms are qualitatively similar to those measured, but some quantitative discrepancies exist. The calculations underestimate the near-surface peak particle velocity data. Perhaps of greater importance, the calculated positive phase durations are consistently longer than those reported by SRI and sometimes significantly shorter than those reported by Sandia. The calculated and measured peak displacements in Figure IV-1.12 differ by at most a factor of 2, that is, less than discrepancies between some of the SRI and Sandia data.

Figure IV-1.43 compares relative displacement data with calculated results for the 650 and 1,050 ft ranges, assuming the measured overpressure as a boundary condition. The calculated results underestimate the data at shallow depths

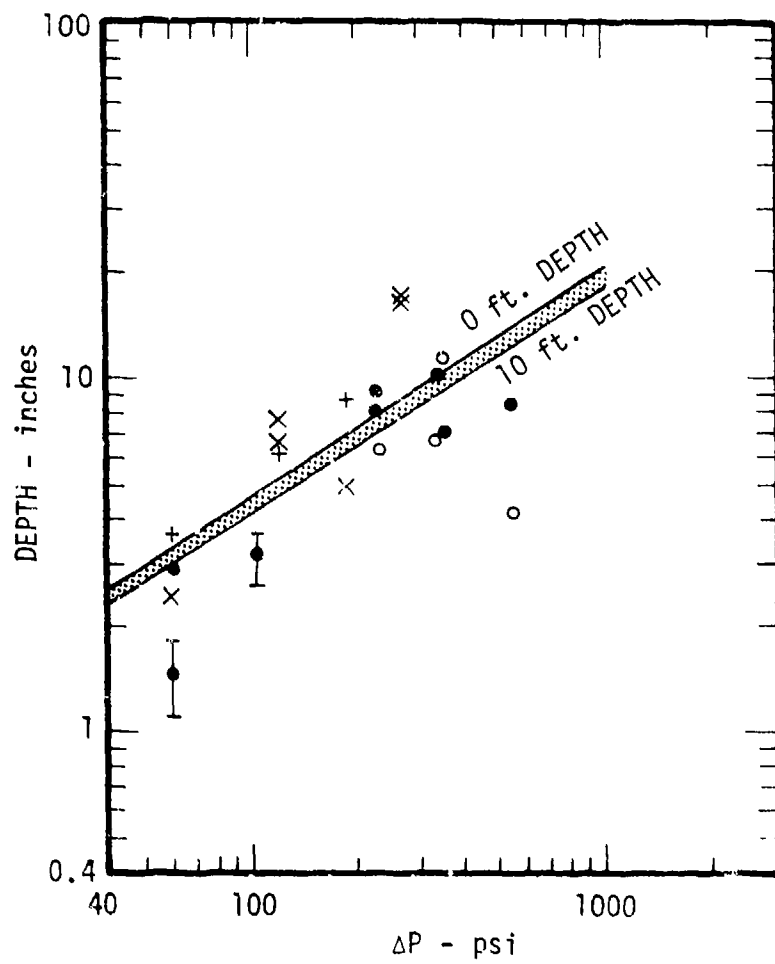


Figure IV-1.36. Comparison of theoretical model and near-surface ground motion data from PRISCILLA.

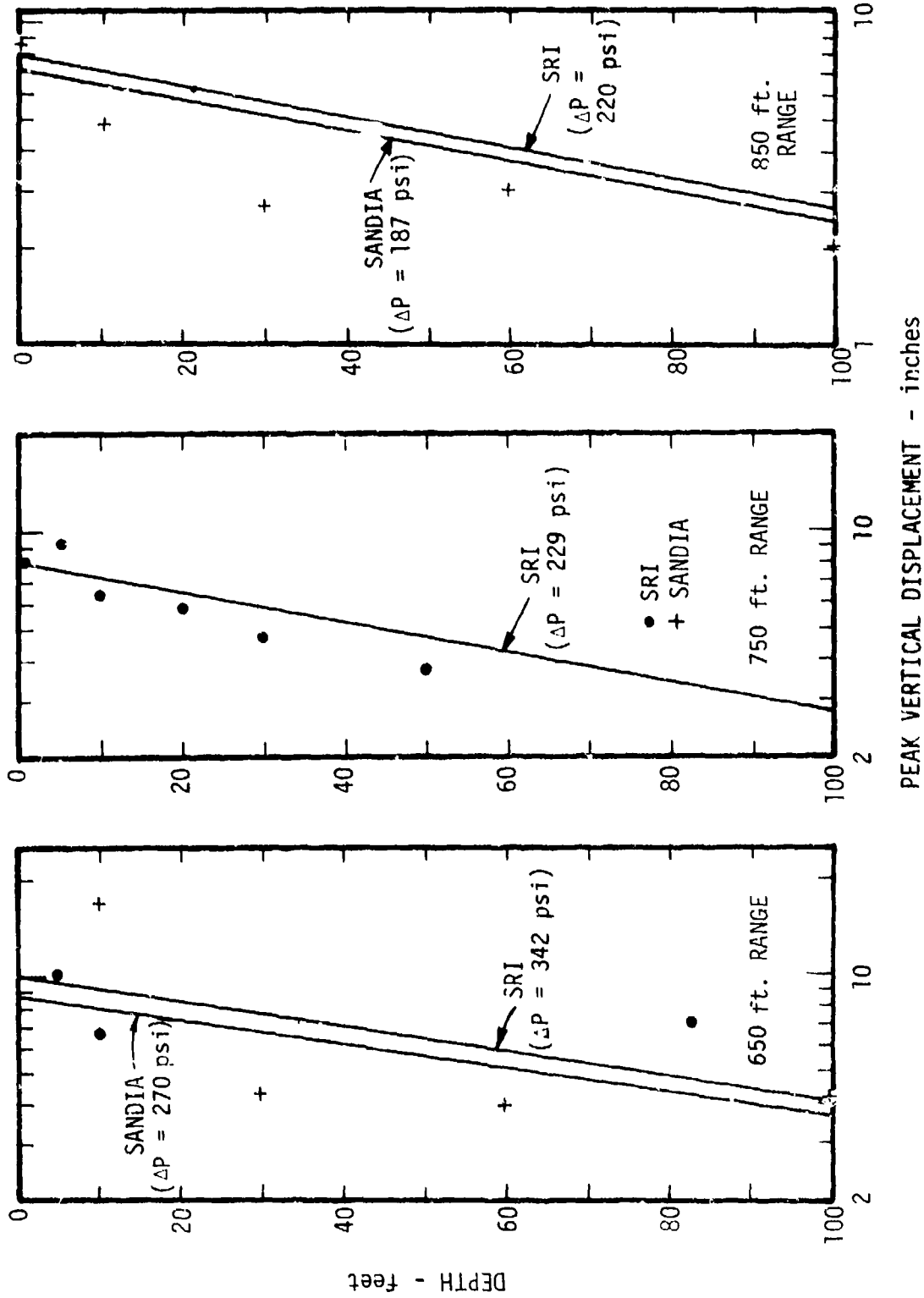


Figure IV-1-37. Comparison of simplified model with PRISCILLA peak displacement data.

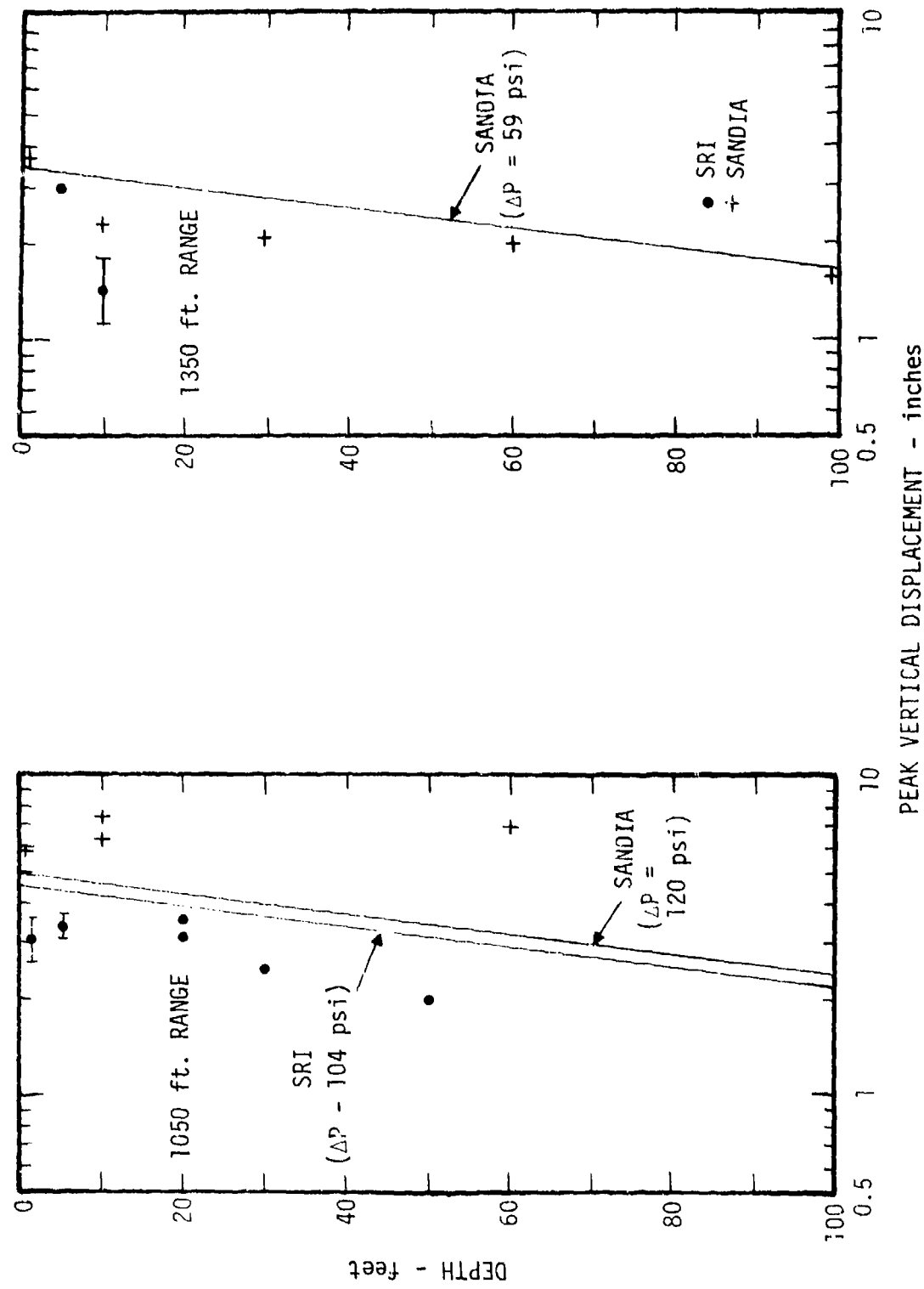


Figure IV-1-38. Comparison of simplified model with PRISCILLA peak displacement data.

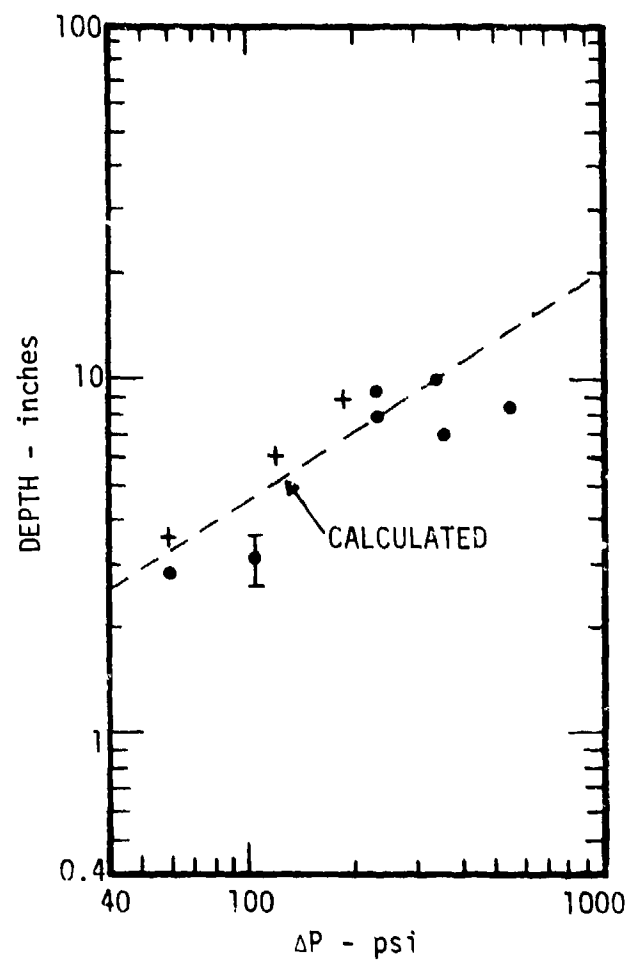


Figure IV-1.39. Best estimate of very near-surface vertical motion data from PRISCILLA.

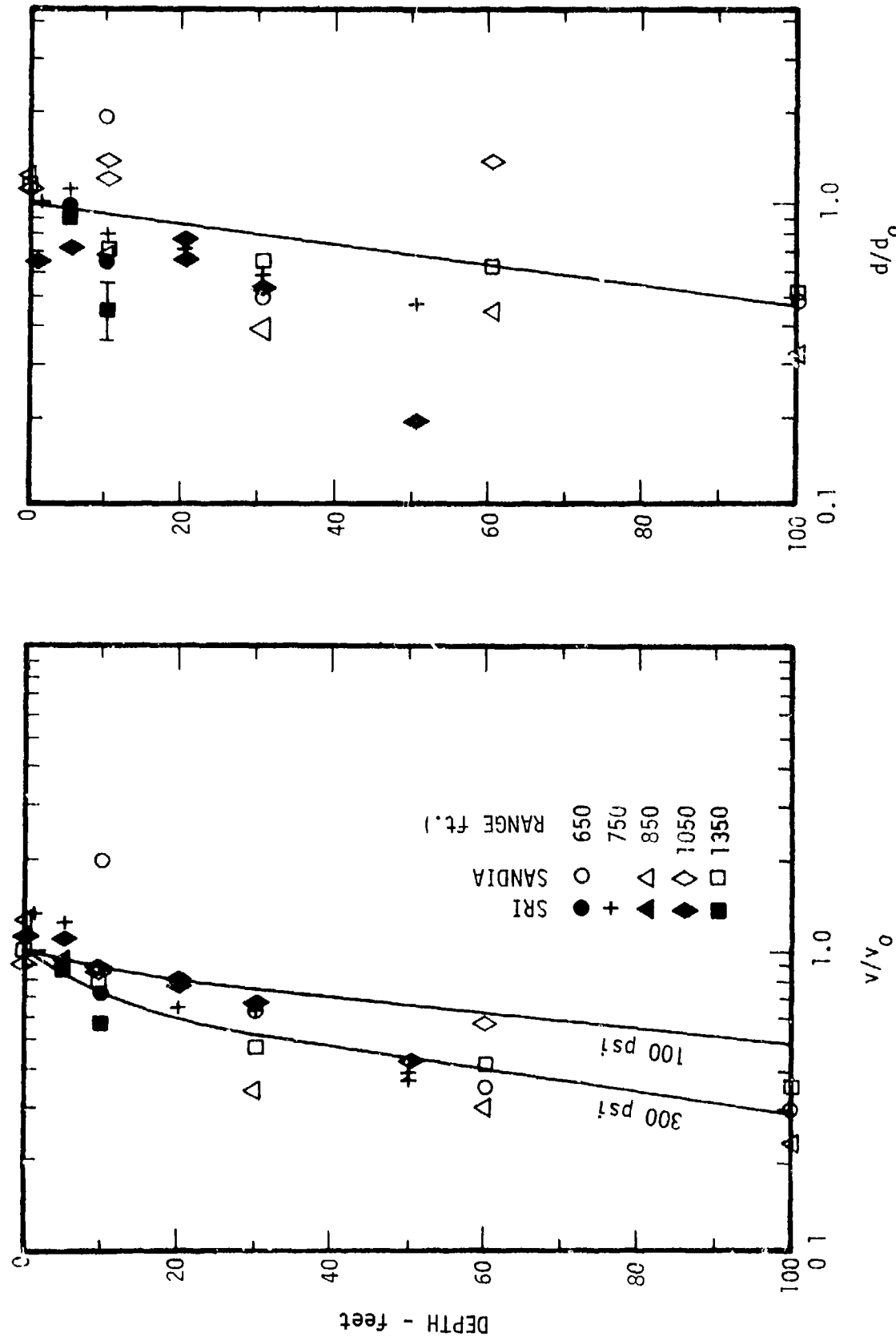


Figure IV-1.40. Comparison of calculated attenuation rates with normalized peak vertical motion data from PRISCILLA.

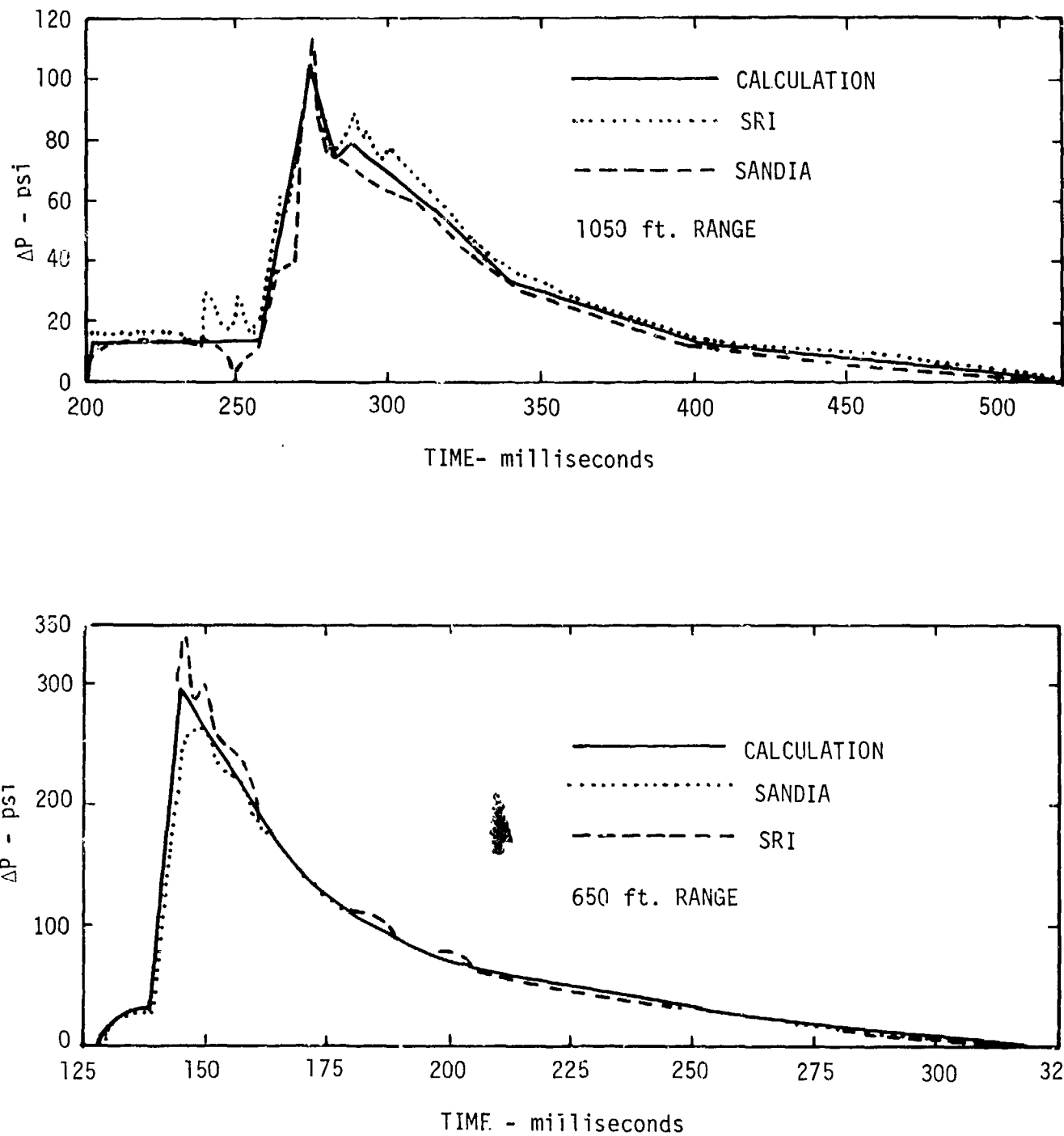


Figure IV-1.41. Comparison of overpressure boundary condition with PRISCILLA data.

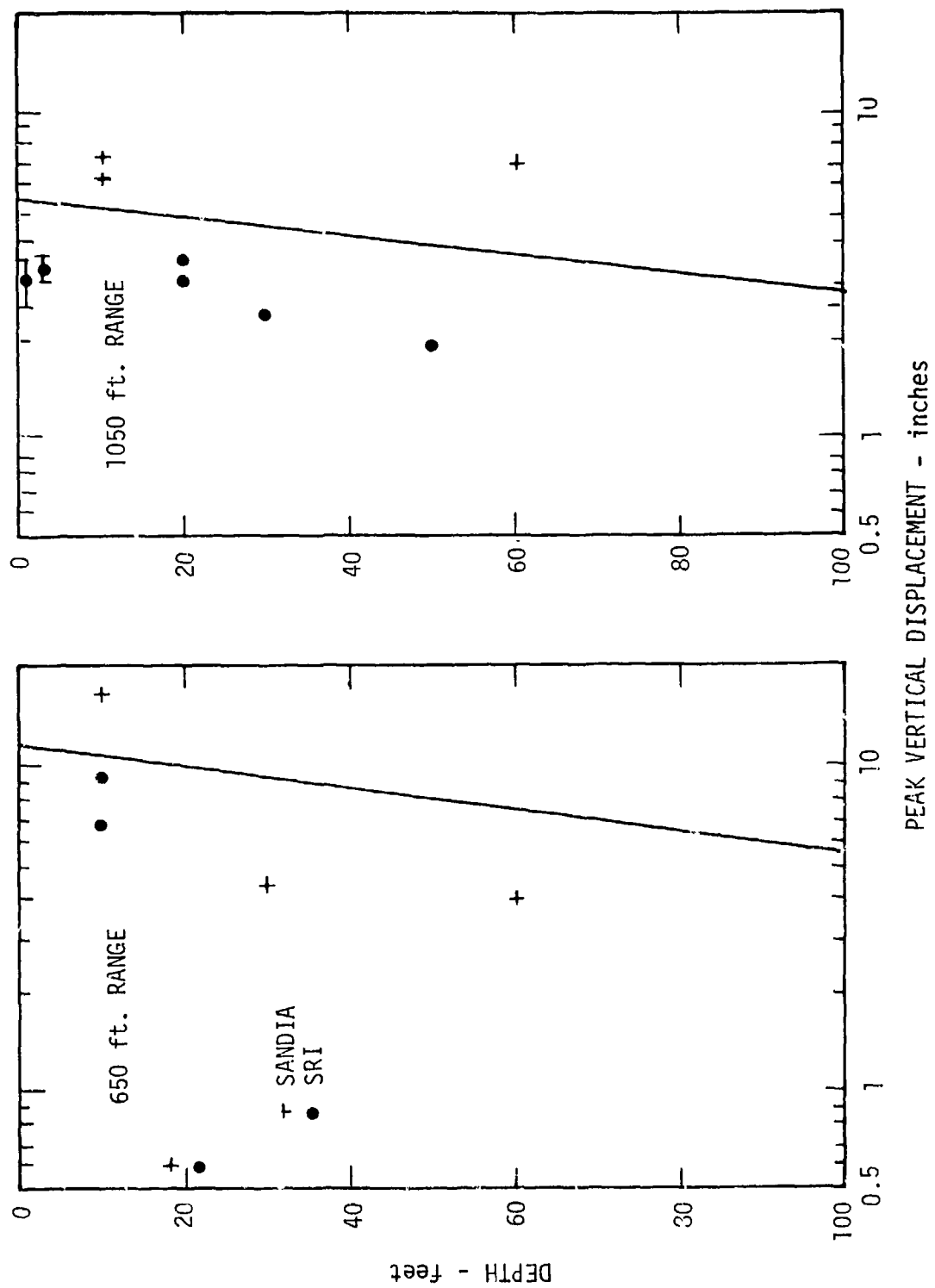


Figure IV-1.42. Comparison of peak vertical displacements from PRISCILLA with calculations using measured airblast overpressure as a boundary condition.

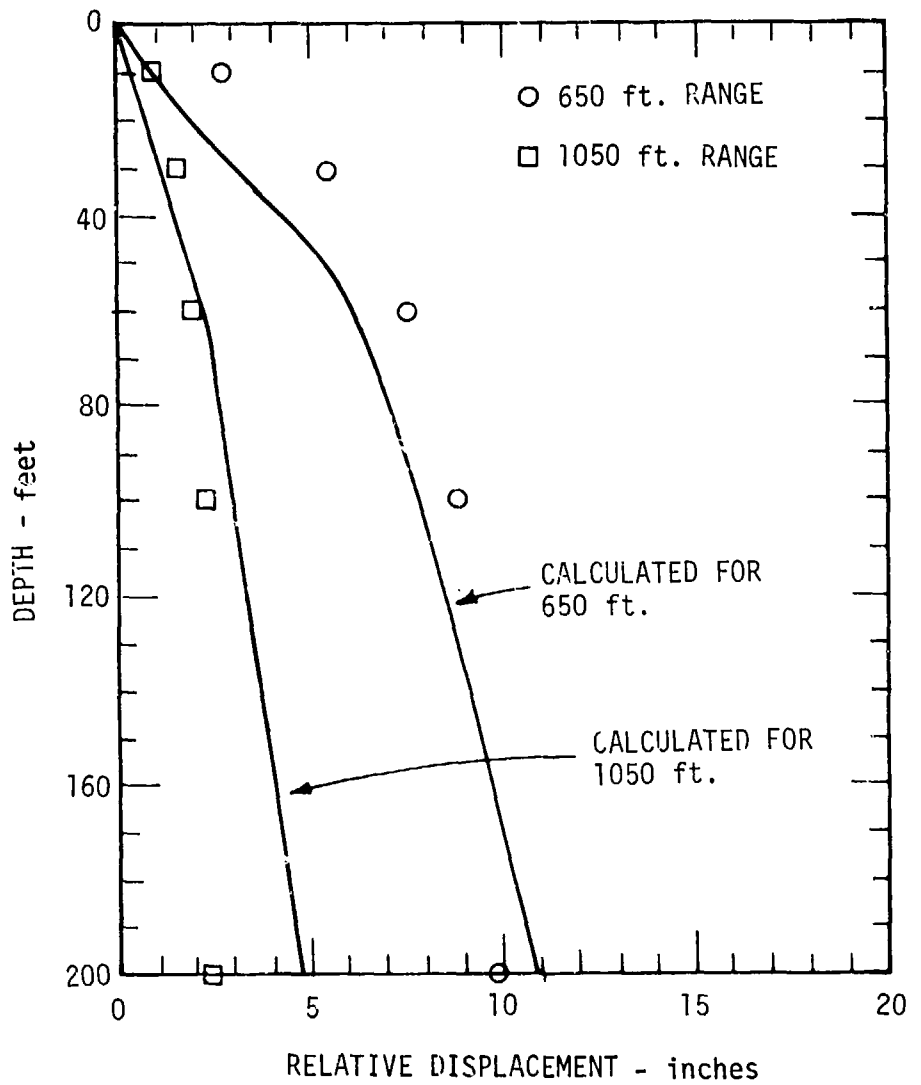


Figure IV-1.43. Comparison of relative displacement data with calculated results using measured overpressure as a boundary condition.

suggesting that the surface layer may be more compressible than was assumed in the model. On the other hand, the measured relative displacements between the surface and 50 ft depth and between the surface and 200 ft depth differ by significantly less than calculated, suggesting that Cooper and Bratton's model for the soils between 50 and 200 ft may be too compressible. The reasonable comparison between calculated and measured peak wave speeds suggests that this discrepancy in peak relative displacements results from differences between calculated and measured late-time phenomena rather than phenomena associated with the arrival of the particle velocity peak.

Surface peak displacements are proportional to $\Delta P^{0.78}$ (Reference T-1.31). Therefore, discrepancies between predictions of peak pressure and PRISCILLA airblast data cause comparable discrepancies between ground motion data and predictions using the model. The comparisons between Cooper and Bratton's model for Frenchman Flat and PRISCILLA data assumed that the overpressure was known at the range of interest. Thus, one must predict the overpressure as a function of range to apply the prediction model in predicting ground motions at a given range from a given yield explosion. Hence, an evaluation of the overall predictive capabilities requires an assessment of the accuracy of theoretical predictions of both airblast and ground motion phenomena. Brode's predictions (Reference IV-1.39) for the peak pressure and impulse from a 700 ft height-of-burst, 37 kilotons event overestimate the PRISCILLA data at the close-in ranges. For overpressures less than about 200 psi, the PRISCILLA data and theoretical predictions are more consistent; perhaps with the peak impulse data falling somewhat above the theory.

Figure IV-1.44 shows that near-surface ground motions are consistently less than predicted on the basis of Brode's height-of-burst theoretical predictions of the PRISCILLA airblast. In other words, first principle calculations, starting with only the yield, height-of-burst, and Cooper and Bratton's estimates of the soil properties for Frenchman Flat, would overestimate surface peak particle velocities and displacements measured at a given range on PRISCILLA. The largest portion of this discrepancy appears to result from the difference between predicted and measured blast overpressure, rather than discrepancies between predicted and measured ground motions once the blast overpressure boundary condition is known. One should not generalize this observation from the comparison with PRISCILLA to other cases because the source of the airblast discrepancy has not been evaluated and therefore its reproducibility is not known.

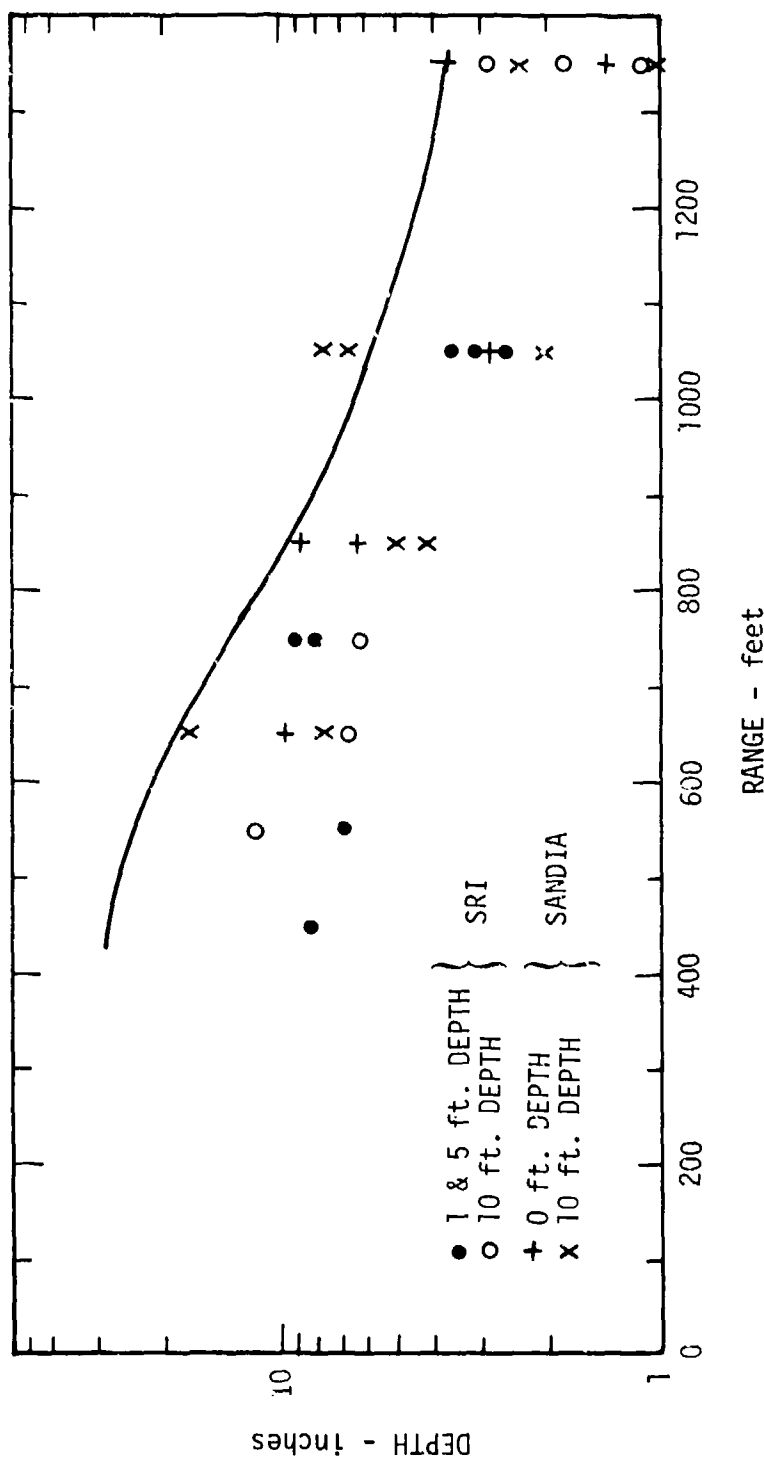


Figure IV-1-44. Comparison of PRISCILLA data with ground motions predicted using Brode's height-of-burst overpressure model.

Data on maximum vertical and horizontal displacement in the Pacific are limited to five shots (Figure IV-1.35). The figure shows a large scatter in the data, primarily due to the deviation of six individual points, which may be caused by integration errors. This possibility is illustrated by the duplicate integration of accelerograms, for example, PPG 2 (SRI) and PPG 2 (SC). Both sets of integrations use the same IBM tabulation and the maximum velocities are within 10 percent of each other and hence are not shown separately in Figure IV-1.24. The LACROSSE vertical displacements agree quite well. However, the displacements for the two vertical accelerograms on PPG 2 differ by ratios of 5:1 and 10:1. This is the result of slightly different baseline corrections in the data for the two cases.

The most recent data on maximum displacements in the outrunning ground motion region were obtained from HARDTACK-I. This was the first series of experiments in which accelerometers were supplemented by long span vertical displacement gauges and reed gauges at the same overpressure level. A comparison of the results of these three methods of determining maximum vertical displacements eliminates, to some degree, uncertainties due to integration errors. On the basis of such a comparison Reference IV-1.27 gives maximum displacements of 2 to 2-1/2 inches for the largest detonation of the HARDTACK-I series. For the smaller yield detonation, the displacements at the closest stations to the burst could only be estimated within the range of 2 to 6 inches, and the displacements at the farthest ground range could only be estimated within 1 to 1-1/2 inches. For both detonations, the maximum horizontal displacements were estimated to be on the order of 2 to 6 inches. The data from HARDTACK-I are shown in Figure IV-1.45 along with their respective uncertainties as stated in Reference IV-1.27. The range of uncertainty in the horizontal displacement is encompassed by the dotted boxes in that figure.

The data of Figure IV-1.45, with the exception of the data from PPG 4, appear to be in general agreement although the scatter is quite large. Horizontal displacements appear to be approximately equal to the vertical displacements and the mean line through the data appears to follow an inverse square law attenuation with ground range.

The scaled displacements on PPG 4 are noticeably lower than the remainder of the data. In fact, at the closest station to ground zero, they are about 1/10 that which would be predicted on the basis of previously obtained data. This

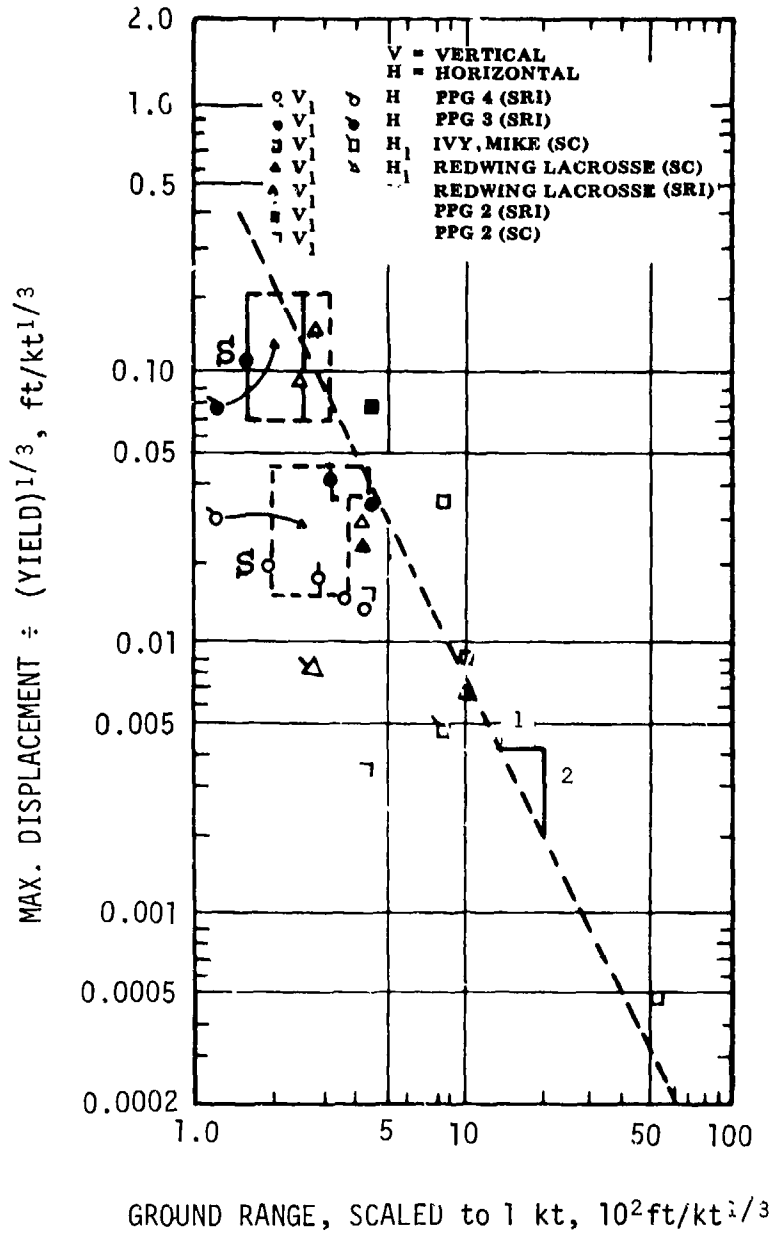


Figure IV-1.45. Maximum horizontal (H) and vertical (V) displacement versus ground range for outrunning ground motion at PPG.

could be interpreted as a failure of the scaling criterion or due to the influence of local geology since the overburden on both HARDTACK shots was only 8 to 10 ft deep. The influence of geology can be thought of in two ways. The shallow depth of overburden underlain by the fairly incompressible water-saturated coral produces a reflected wave which tends to cancel out the downward motion caused by the airblast (Figure IV-1.2a) in a manner identical to that previously discussed for truncation of maximum displacements in the superseismic airblast region. The other way of looking at it is to consider that the average strain in the overburden approached the locking strain for the medium and hence the overburden became essentially incompressible after a very short time subsequent to shock arrival. In any event, it is believed by the authors that the small scaled maximum displacements on PPG 4 are due to a failure to scale the experiment, namely, to scale the depth of overburden, rather than to any failure of the correlation scaling criterion.

IV-1.5 CORRELATION OF MAXIMUM STRESS AND STRAIN DATA.

At the soil surface the vertical stress must equal the overpressure and therefore the maximum vertical stress must equal the maximum overpressure. When the airblast wave is highly superseismic, it can be shown that for an elastic solid the maximum radial stress $\sigma_r(o)$ and the maximum tangential stress $\sigma_\theta(o)$ at the surface are related to the shock overpressure by the relation*

$$\frac{\sigma_r(o)}{\Delta P_s} = \frac{\sigma_\theta(o)}{\Delta P_s} = \frac{v}{1-v} = K_0 \quad (\text{IV-1.38})$$

where v is Poisson's ratio and K_0 is the zero horizontal strain pressure coefficient or the earth pressure coefficient at rest (see Equation IV-1.25). K (unsubscripted) is the bulk modulus.

*In general the stress and strain are tensorial quantities. The strain tensor is related to the stress tensor according to (Reference IV-1.40)

$$\epsilon_{ik} = \frac{1}{9K} \sigma_{ll} \delta_{ik} + \frac{1}{2\mu} (\sigma_{ik} - \frac{1}{3} \sigma_{ll} \delta_{ik})$$

where all subscripts i , k , l run from one to three, ϵ_{ik} is the stress tensor element i , k , K is the bulk modulus, μ is the shear modulus (Lamé constant), and δ_{ik} is the Kronecker delta.

The relationship between vertical stress σ_v and vertical strain ϵ_v for a three-dimensional elastic solid if both the maximum stress and strain occur at the same time is (Reference IV-1.26).

$$\frac{\epsilon_v}{\Delta P_s} = \frac{1}{E} \left(\frac{\sigma_v}{\Delta P_s} \right) \quad \left\{ 1 - v \frac{\sigma_r + \sigma_\theta}{\sigma_v} \right\} \quad (\text{IV-1.39})$$

where ϵ is Young's modulus. If $\sigma_r + \sigma_\theta > 0$, then for a one-dimensional wave propagation in an elastic solid

$$\rho C_p^2 \frac{\epsilon_v}{\Delta P_s} = \frac{\sigma_v}{\Delta P_s} \quad (\text{IV-1.40})$$

so that

$$\frac{(1+v)(1-2v)}{(1-v)} \rho C_p^2 \frac{\epsilon_v}{\Delta P_s} < \frac{\sigma_v}{\Delta P_s} < \rho C_p^2 \frac{\epsilon_v}{\Delta P_s} \quad (\text{IV-1.41})$$

and at the ground surface, the vertical stress must be equal to the overpressure so that

$$1 \leq \rho C_p^2 \frac{\epsilon_v(0)}{\Delta P_s} \leq \frac{(1-v)}{(1+v)(1-2v)} \quad (\text{IV-1.42})$$

Using the average value of $v = 0.39$ for Frenchman Flat (Reference IV-1.26) there results

$$\frac{1}{2} \leq \rho C_p^2 \frac{\epsilon_v(0)}{\Delta P_s} \leq 1 \quad (\text{IV-1.43})$$

If $\rho C_p^2 \epsilon_v(0)/\Delta P_s \equiv 1$, then ν must be zero which corresponds to a perfectly compressible solid and $\rho C_p^2 \epsilon_v(0)/\Delta P_s = 0.5$ corresponds to the average value of $\nu = 0.39$ used above.

Figures IV-1.45 and IV-1.47 show all data for maximum vertical strain and stress, respectively taken from Reference IV-1.26. The correlations are constructed using the same modified scaled depth parameter used to correlate the attenuation of maximum displacement and maximum velocity. The majority of the observations were made on UPSHOT-KNOTHOLE, shots 1, 9, and 10 at overpressures ranging from 15 to 36 psi, and on shot PRISCILLA at overpressures of 100 to 275 psi. Superimposed on the data are the correlations presented in References IV-1.23 and IV-1.26. In constructing the prediction curve for strain from Reference IV-1.23 the relation between stress and strain was chosen as the confined compression modulus in accordance with the case of $\rho C_p^2 \epsilon_v(0)/\Delta P_s = 1$.

In both figures it can be observed that the scatter of data is quite large and that the correlations recommended in Reference IV-1.26 result in more attenuation of both stress and strain than the prediction methods recommended in Reference IV-1.23. Both recommended prediction procedures are reasonably consistent with the strain data of Figure IV-1.46. It might be argued that if as many data existed at a scaled depth of 22 feet/ $kt^{1/3}$ as exist at a scaled depth of 3 feet/ $kt^{1/3}$, then the correlations would be in good agreement with the data.

The situation is somewhat different for maximum vertical stress. It would seem from the data of Figure IV-1.47 that the attenuation of stress is actually much greater than predicted. However, if one is influenced by the lower data of Figure IV-1.47, a calculation of effective moduli (maximum stress divided by maximum strain) leads to values which are exceedingly low. As pointed out in Reference IV-1.26 the variation in vertical stress near the surface is, say at 2-feet/ $kt^{1/3}$ scaled depth, more or less indicative of the inherent errors in the over-all method of stress measurements. These errors can be the result of (1) mismatch in the soil and gauge impedance characteristics, and (2) disturbances of the soil during planting and backfilling around the gauge. The first source of error may be theoretically eliminated or at least made to be constant; the second type of error represents an unknown quantity which may never be eliminated from this measurement in its present form. It is probable that the attenuation of stress will never be adequately described on an empirical basis and hence one must rely upon theory to give information in this particular area. Since the data

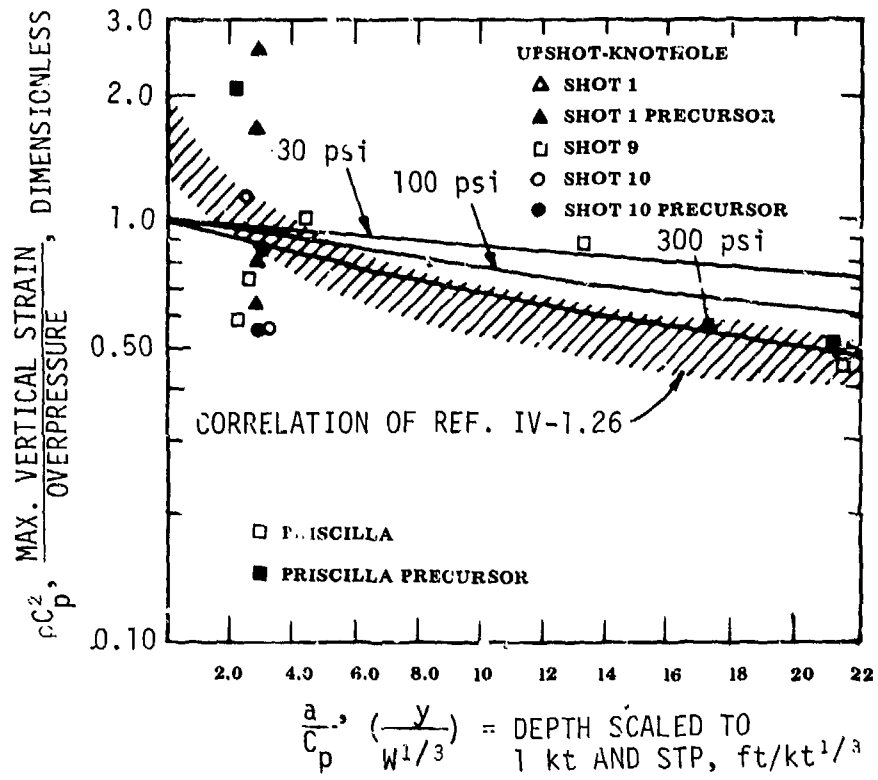


Figure IV-1.46. Attenuation of maximum vertical strain with depth for superseismic blast wave at NTS.

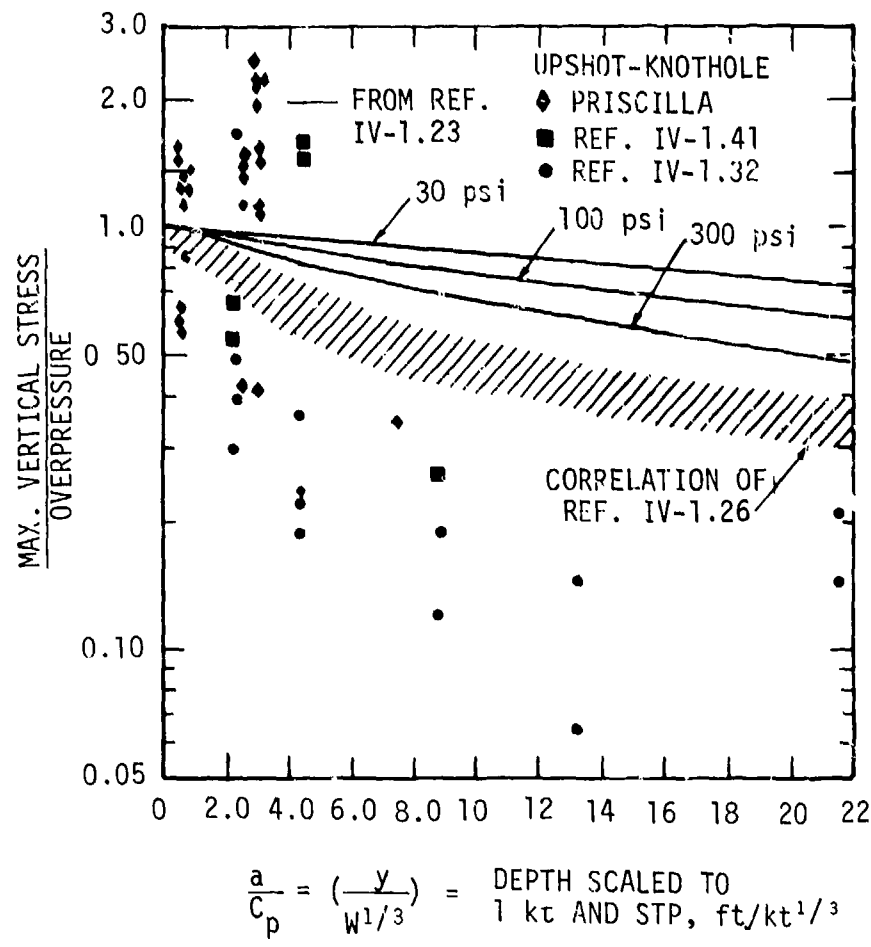


Figure IV-1.47. Attenuation of maximum vertical stress with depth for superseismic blast wave at NTS.

themselves are suspect, empirical checks of theoretical descriptions of the attenuation of stress must rely upon comparison with other quantities such as velocity, displacement, strain, or a combination of these.

IV-1.6 PREDICTION OF GROUND MOTION WAVEFORMS .

This section presents a discussion of vertical and horizontal displacement waveforms in the superseismic region and vertical velocity waveforms in the outrunning region.

IV-1.6.1 Vertical and Horizontal Displacement Waveforms for Superseismic Airblast Conditions

The subject of airblast-induced ground motion in layered, nonelastic media is complex and Wilson and Sibley (Reference IV-1.42) developed a method for finding maximum displacement that takes into account laboratory measurements of the confined compression modulus, but which neglects any ability of soil to sustain shear (negligible shear modulus). From laboratory studies, Wilson and Sibley concluded that for values of stress due to overpressure loading (overstress) equal to or less than the overburden stress, the soil behaves elastically. Moreover, they concluded that it has a constrained modulus approximately equal to that derived from laboratory vibration tests at the overburden pressure. As the ratio of overstress to overburden pressure increases, it has been further concluded that the constrained modulus decreases and attains a minimum value at an overstress ratio between 3 and 5. This minimum modulus is approximately the same as the upper limit of modulus defined by laboratory dynamic confined compression tests under fast loading conditions. Consequently, the constrained modulus in the soil is presumed to vary with depth even though the medium may be otherwise homogeneous. The initial arrival of the stress pulse travels at higher velocity (defined by the modulus from vibration tests) than the velocity of the maximum stress wave (defined by the dynamic modulus). This results in an increase in rise time of the stress pulse. Since the analysis does not define the attenuation of maximum stress, this relationship is obtained from Reference IV-1.23. The trailing portion of the stress pulse is attenuated by the same factor. On the basis of constrained modulus determinations and the nature of the soil, values of elastic vertical compression (the percentage of elastic recovery) are assigned to the geologic profile. A range of 70 to 80% elastic vertical compression is assigned to overburden soils, the smaller values are applied to weathered residual clays and loose granular soils and the larger values applied to dense, competent, granular soils and to very stiff to hard clays.

Where the permanent water table is encountered, the elastic vertical compression is considered to be 100%. Between the above limits, values in elastic compression vary in accordance with the overstress. For overstress ratios greater than unity, the strain relaxes linearly from the strain defined by the maximum stress to that defined by the percent elastic vertical compression.

With the dynamic stress-strain curve defined by the preceding rules, it is then possible to compute the strain-time histories at a particular depth from the stress-time histories. Vertical displacement-time history, $d(t)$, is then obtained by an integration of the strains according to the relationship

$$d(t) = \int_{\infty}^z \varepsilon_z(t) dz \quad (\text{IV-1.44})$$

where $\varepsilon_z(t)$ is the time-dependent vertical strain, t is time, and z is the vertical coordinate. The entire procedure is given in detail in Reference IV-1.22.

If the medium is considered to be bilinear so that a residual strain ε_r remains after all loads have been removed, then

$$\varepsilon_r = (1 - r) \frac{\sigma_{\max}}{M_L} \quad (\text{IV-1.45})$$

where r is the strain recovery ratio and M_L is the uniaxial loading modulus. Integration of Equation IV-1.1 from infinity to the depth of interest gives the total residual displacement or

$$d_r = \int_{\infty}^z \varepsilon_r dz \quad (\text{IV-1.46})$$

By treating the depth in increments, the residual displacement in a particular increment is (Reference IV-1.1)

$$\Delta d_r = (1 - r) \frac{\overline{\sigma_{max}}}{M_L} \Delta z \quad (\text{IV-1.47})$$

where $\overline{\sigma_{max}}$ is the average maximum vertical stress in the increment Δz . The total residual displacement at a particular point is computed by summing the residual displacements in all underlying increments.

An approximate expression can also be used to calculate the peak vertical displacements if the soil properties are not well defined and time histories are not important (Reference IV-1.1). If the medium below a particular point can be assumed to be reasonably uniform to a depth equal to the wavelength of the stress wave in the medium, the maximum transient absolute displacement of the point considered is obtained from the airblast impulse as

$$d_{max} = \frac{I}{\rho C_p} \quad (\text{IV-1.48})$$

where I is the total airblast impulse.

Horizontal displacements are determined from computed vertical displacements assuming that the displacement vector at any time is in the direction normal to the compression wave (Figure IV-1.1a). This assumption is only true at the wave-front itself. This method, particularly the choice of moduli as a function of overstress, was developed as a result of a comparison with displacement data obtained from the PLUMBBOB Event. Although it is quite sophisticated in its treatment of the role of soil properties, it may only be applicable to soils existing at Frenchman Flat. The apparent weaknesses of this method are best described by paraphrasing the conclusions of Reference IV-1.42:

- The attenuation of stress pulses is obtained from a quasi-static elastic solution for a homogeneous medium and hence is subject to all the weaknesses of that method of stress prediction.
- Horizontal displacements are predicted from vertical displacements by considering the local inclination of the normal to the

compression wavefront to the local vertical. This is contrary to both theory and observation.

In addition, the effect on the propagating stress wave of the varying impedance of the medium has been neglected.

The displacement and particle velocity-time histories developed using the methods of Reference IV-1.42 are similar to those shown in Figure IV-1.48. Particle velocity and acceleration are obtained by differentiation of the displacement-time history. These quantities are more accurately determined from the correlations of Sections IV-1.2 and IV-1.3, respectively. The velocity pulse characteristic time, T_1 , of Figure IV-1.48 and the approximate ratio of maximum rebound velocity to maximum downward velocity may be determined also from the displacement-time calculations. The pulse duration is approximately equal to the overpressure duration for small detonation yields over fairly homogeneous ground media. For increasingly larger yields the velocity pulse duration does not increase as rapidly as the overpressure duration. This occurs because of the general increase with depth of the constrained modulus of the ground medium. The resulting velocity pulse has been called a Type I pulse (Reference IV-1.43).

IV-1.6.2 Vertical Velocity Waveforms for Outrunning Ground Motion

For a particular geologic composition, the larger the detonation yield, the higher the overpressure at which outrunning ground motion is first observed (Reference IV-1.21). Outrunning ground motion is first observed at Frenchman Flat at overpressure levels of about 10 psi. At PPG, outrunning ground motion commences at overpressure levels of several hundred psi. One of the better examples of the development of the outrunning ground motion waveform is illustrated by TUMBLER I data (Figure IV-1.49). For the station just preceding the four shown in Figure IV-1.49, the vertical particle velocity waveform was definitely superseismic. The arrival of the airblast at the station is indicated by the letters AB. Note that the waveform begins to depart from the essentially one-sided waveform associated with the superseismic airblast region almost immediately as outrunning begins and the waveform becomes more oscillatory as the ground range increases. Also note that the direction of first motion is upward in contrast to the downward motion associated with the superseismic airblast region.

Assuming that the total outrunning ground motion waveform is the superposition of a Type I waveform and an oscillatory Type II waveform, it is possible to abstract from the data a composite Type II vertical velocity waveform (Reference

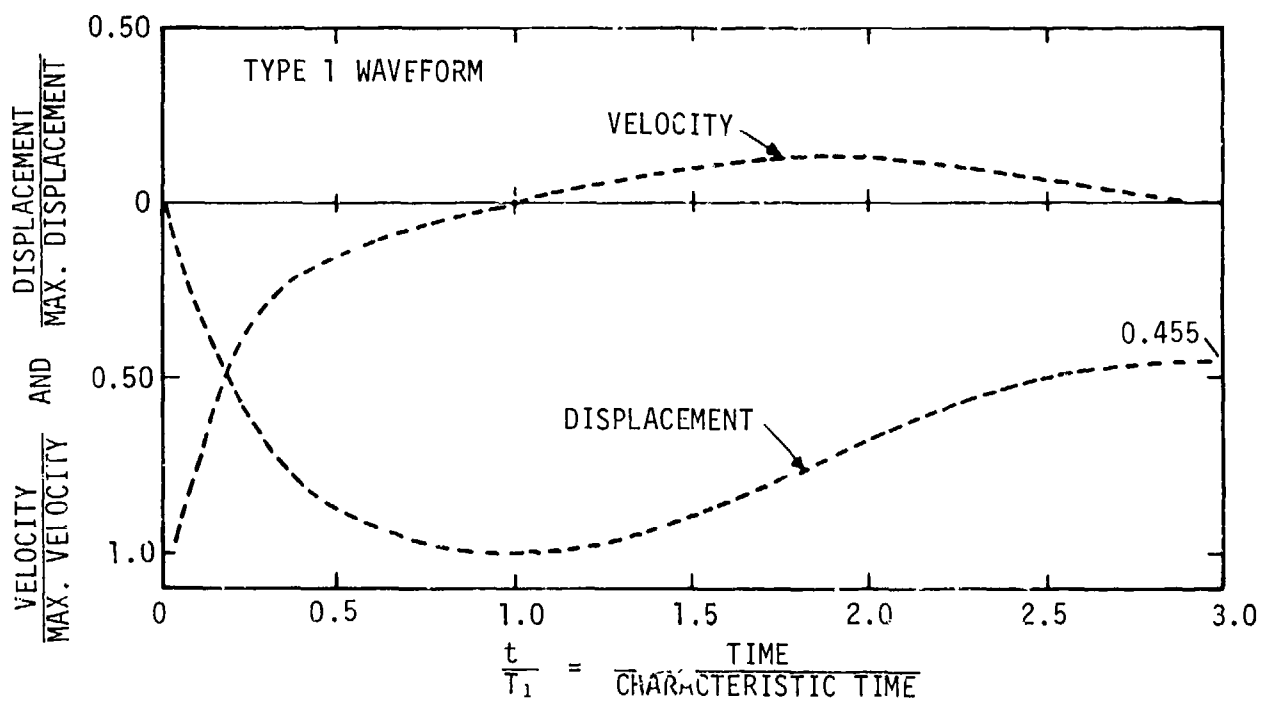


Figure IV-1.48. Type I superseismic airblast vertical particle velocity waveform and its displacement.

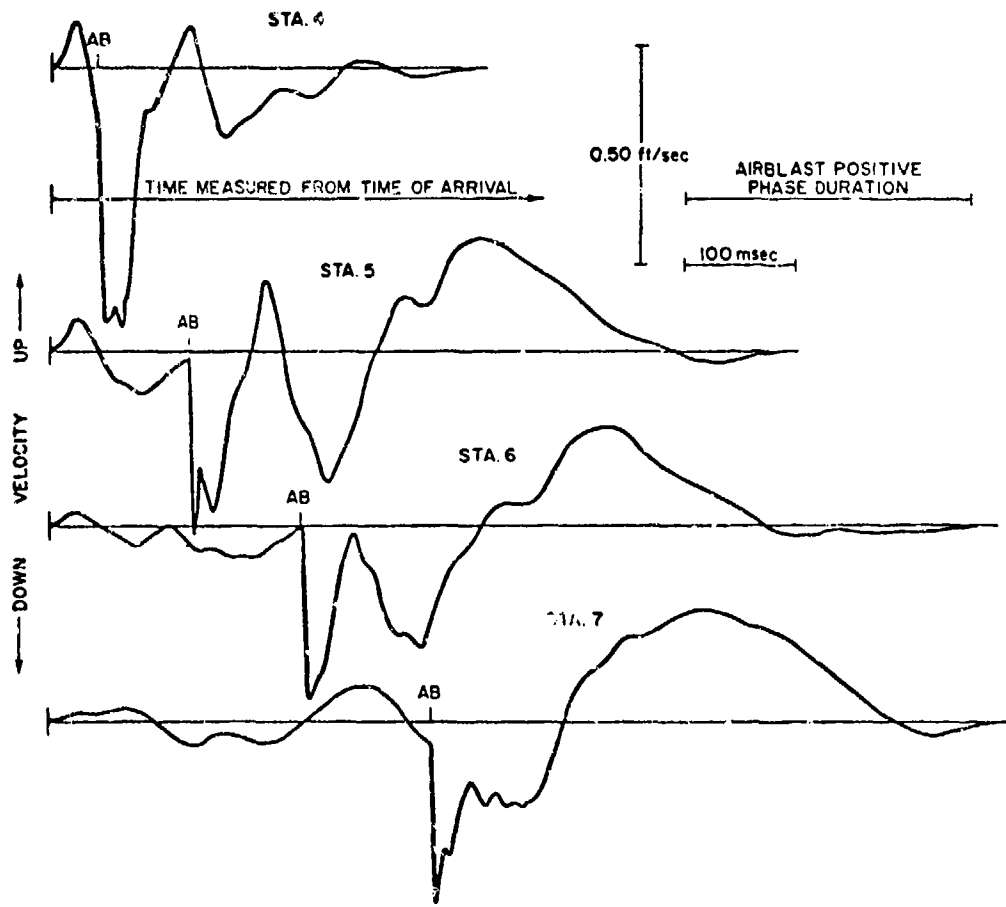


Figure IV-1.49. Illustration of development of outrunning ground motion for TUMBLER, shot 1.

IV-1.43). The Type II waveform shown in Figure IV-1.50 is an average of about one dozen observations. The high frequency portions of the ground motion have been filtered out. Any residual displacement of the Type II waveform has been arbitrarily taken as zero due to conflicting data on this point. The characteristic time, T_2 , does not appear to scale in the usual manner, that is, proportional to the one-third power of the yield, but appears to be related to the difference between the ground range and the ground range at which outrunning first occurs, ΔR , in the following manner:

$$T_2(\text{msec}) = 100 + \frac{\Delta R}{4} \quad (\text{IV-1.49})$$

where ΔR is in feet. Thus the dominant frequency of the Type II waveform decreases as the ground range increases.

The phase between Type I and Type II waveforms and their relative amplitudes may be determined once the detonation yields and the lithographic structure are known (Reference IV-1.43). Simple superposition of the two waveforms, although theoretically incorrect, is seen in Figure IV-1.51 to lead to a reasonable approximation of the complete outrunning ground motion waveform profile. The data shown in this figure represent two extremes: the surface motion on TUMBLER I (1 kt), and the motion at depth from the much larger yield of PPG 4.

IV-1.7 VERTICAL VELOCITY RESPONSE SPECTRA*

A summary of the response spectra calculated from accelerograms and measured directly by reed gauges is contained in Reference IV-1.26. A presentation of some of these data in dimensionless form is shown in Figure IV-1.52. Response spectra were computed using 0.5% critical damping because this amount of damping was ascribed to the reed gauges used for direct measurement of response spectra at NTS. Ground motions corresponding to these response spectra were in the super-seismic airblast region and consequently the response spectra have the characteristic shape associated with a one-sided pulse. Note that good correlation is achieved at low frequency. At high frequencies, the spectra tend to disperse since spectra magnitudes at high frequencies are determined by maximum accelerations.

*For background information on the calculation and the use of response spectra, see Part V, Chapter V-4, or Reference IV-1.1.

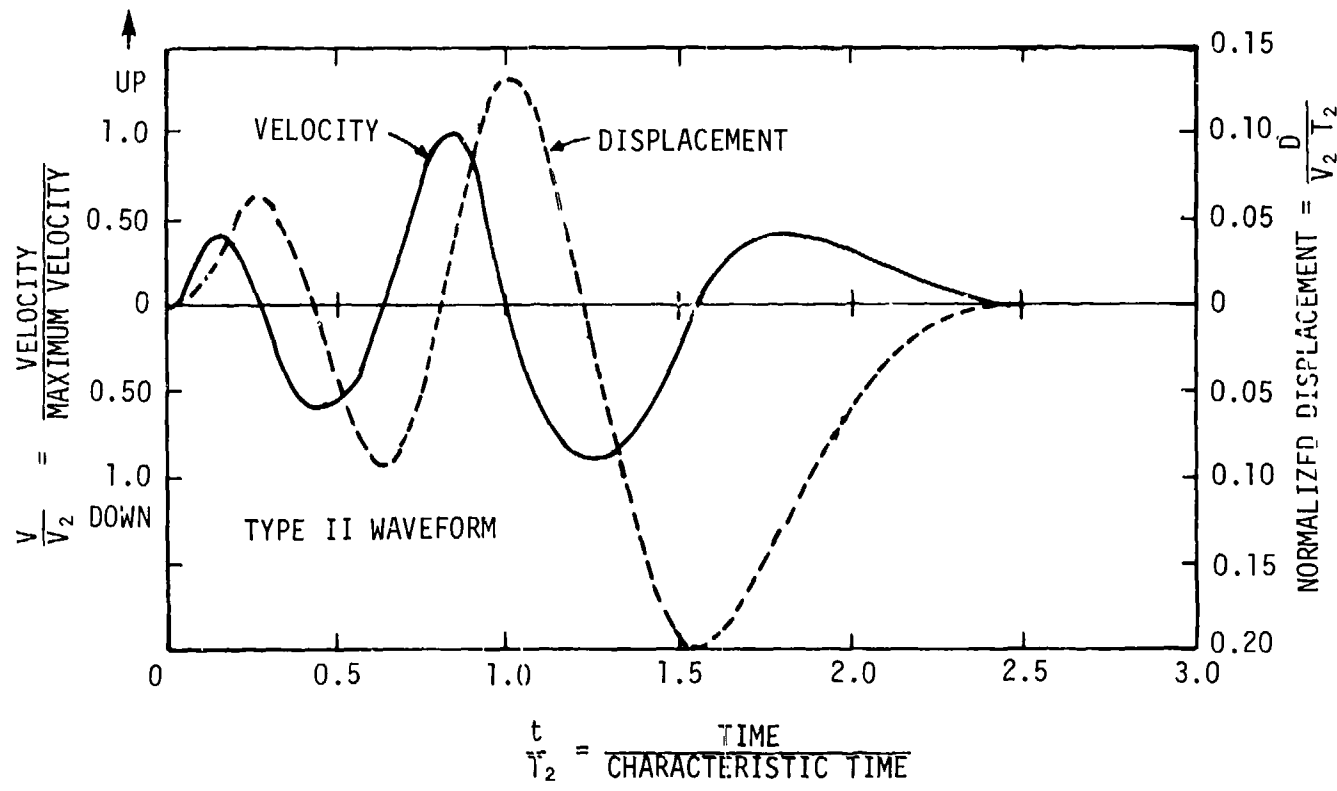


Figure IV-1.50. Type II (outrunning ground motion) vertical particle velocity waveform and its displacement.

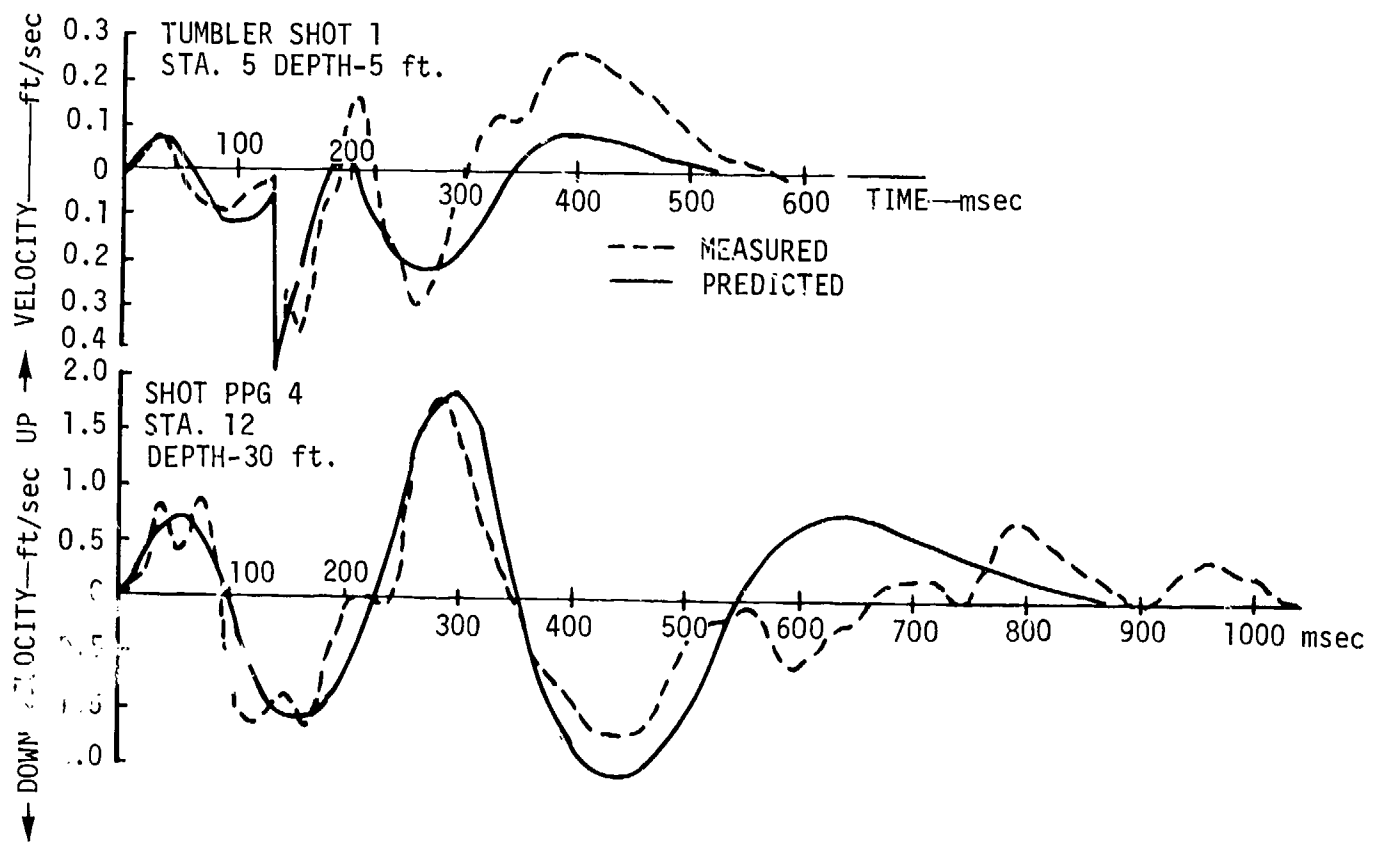


Figure IV-1.51. Comparison of predicted and observed outrunning ground motion.

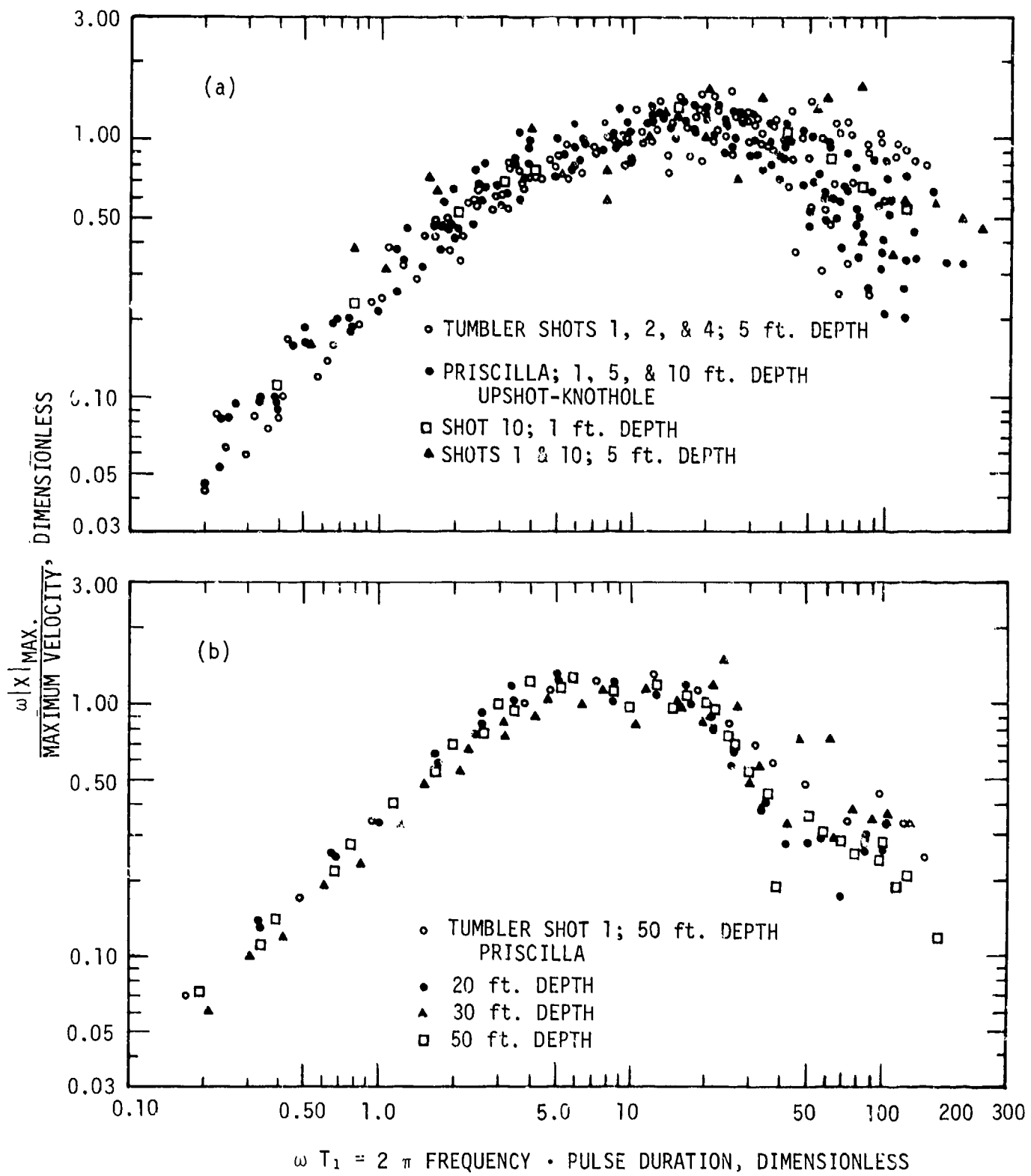


Figure IV-1.52. Correlation of superseismic, nonreflecting vertical velocity response spectra for a 0.5% critical damping. (a) 1- to 10-foot depths, (b) 20- to 50-foot depths. These data are for NTS.

Also, since the maximum acceleration decreases faster with depth than maximum particle velocity, the magnitude of the velocity response spectra at high frequency exhibits the same dispersion.

Response spectra were computed for outrunning ground motion pulse shapes and presented in Reference IV-1.43. In addition to five measured pulse shapes, a parametric study has been made of the response to 29 possible combinations of Type I and Type II waveforms. A summary of these results is shown in Figure IV-1.53. The upper curve is the envelope of the extremes of the 34 spectra. At low frequency, the velocity response shown by the envelope and the average curve increases with frequency at a rate greater than the first power of frequency. This is characteristic of multiple sided velocity pulses. Note that the maximum amplification factor for the envelope is approximately 4 and for the average it is approximately 2 compared with the much lower values of 1.5 and 1.25, respectively, for the superseismic airblast ground motions of Figure IV-1.52.

IV-1.8 GROUND MOTION FROM SURFACE AND NEAR-SURFACE HIGH EXPLOSIVE DETONATIONS

We begin with an overview of ground motion experiments with high explosives (HE) covering a period from the beginning of 1972 to the end of 1975. It does not list all reports dealing with the subject over the stated period as that would make this section rather voluminous. The material is presented in the form of abstracts derived from the references listed. The reader is urged to consult that list of references for specific information. This section is only intended to provide the interested readers with a place to start their search. For those interested in acquiring an understanding of the physical development and the chemical processes of an HE detonation, the physics and chemistry of detonations and their computations, they should consult Reference IV-1.44.

IV-1.8.1 Overview of High Explosive Experiments

Joachim, in January 1972 (Reference IV-1.45) reported on two events of the MINE SHAFT Series. This series provided free-field ground motion data from high-explosive detonations near the surface of hard rock. The first experiments in this series, MINE UNDER and MINE ORE, were 100-ton spherically shaped TNT charges detonated at heights of burst of 2 and 0.9 charge radii above the surface, respectively. For the MINE UNDER Event, 88 data channels were installed at ranges varying from 39 to 400 feet and at nominal depths between 2 and 18 feet. For the MINE ORE Event, 108 channels were installed at ranges varying from 28 to 125 feet. In addition, near-surface (depth of 2 feet) vertical gauges installed for the MINE

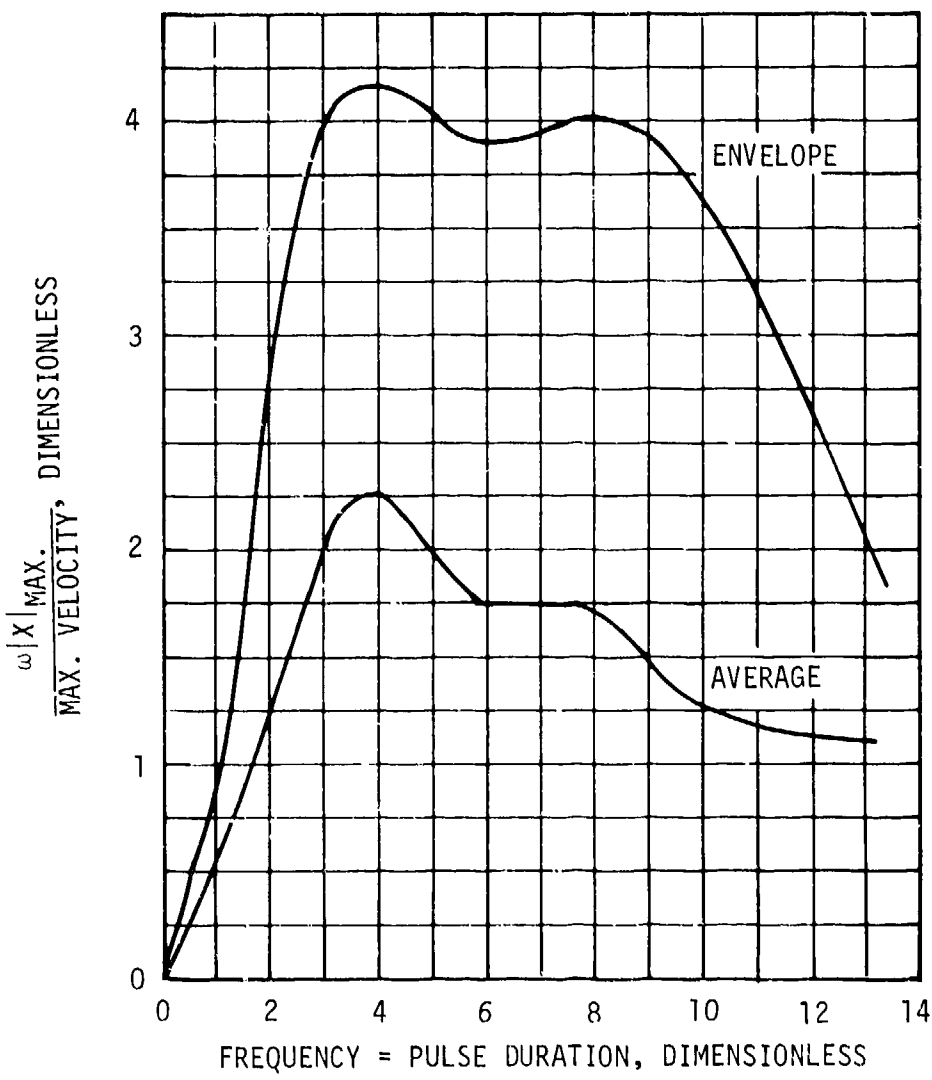


Figure IV-1.53. Envelope and average undamped response spectra for outrunning ground motion waveforms in alluvium.

UNDER Event were used for recording data during the MINE ORE detonation. Measurements included acceleration, velocity, and rock strain. The MINE UNDER and MINE ORE peak downward acceleration data can be directly correlated to peak airblast overpressure. Accurate integrated accelerations were obtained during the high-frequency airblast-induced shock, but poor accuracy was noted during the low-acceleration cratering-induced motions which followed. Velocity measurements are poor for the high-frequency portion of the time history and very good for the low-acceleration cratering-induced motion portion of the time history. The effect of jointing is indicated by a comparison of the peak upward velocity measurements between two perpendicular MINE ORE gauge lines. It is believed that differences are related to horizontal jointing near the surface where the lack of upward confinement allows more rebound in the jointed material. A similar difference in the horizontal direction was noted.

Murrell, in April 1972 (Reference IV-1.46), reported on the far-out ground motion of the MINERAL ROCK Event of the MINE SHAFT Series. The objectives of this experiment were to measure all ground motions in the outrunning region. The MINERAL ROCK Event was a duplication of the MINE ORE Event of the same series, and consisted of a 100-ton sphere of TNT placed with the center of gravity 0.9 charge radius (about 7.7 feet) above the ground surface. Accelerometers and velocity gauges were installed from 200 to 500 feet from ground zero at depths of 2, 10, and 18 feet. Time histories of all successfully recorded gauges are presented in an appendix of that report along with integrals of each record. The outrunning acceleration data were partially obscured by cable noise. This noise was induced by blast overpressure and unfortunately was present during the significant part of the onset of outrunning motion, that is, before airblast arrival at the gauge locations. Although these data are limited, Murrell discusses them together with the outrunning velocity data. Airblast-induced motions are treated in some detail. Vertical airblast-induced accelerations were found to attenuate rapidly with distance and depth from the maximum downward acceleration of 32 g's at the 200-foot range and 2-foot depth. These accelerations were correlated with overpressure, and, for the depth of 2 feet, acceleration-to-overpressure ratios averaged 0.2 g/psi, which is considerably less than for a similar detonation over soil. Vertical particle velocities also attenuated with distance and depth from the maximum value of 1.3 ft/sec at the 200-foot range and a depth of 2 feet. Horizontal velocities followed much the same pattern, with a peak value of 2 ft/sec at the same location. Outrunning motion was noted on all horizontal velocity gauge records. For the

vertical component, outrunning motion was not apparent at the 250-foot range, but was of significant magnitude at the 500-foot range. Vertical downward displacements of a high confidence level were limited to the 250-foot range and were found to be 0.0060 to 0.0075 foot. Horizontal displacements were successfully computed from acceleration and velocity records, and at the 250-foot range were three to four times as large as the vertical displacements.

Reference IV-1.47 describes some of the tests conducted under the MIDDLE NORTH Series. MIXED COMPANY was the third HE TNT blast and shock experiment of this series. The primary objectives of this test, which was conducted near the Glade Park area in western Colorado, was to obtain ground motion data in layered medium (silty sand over sandstone). Three shots were fired: one 20-ton shot on 1 June 1972, one 20-ton shot on 13 July 1972 and one 500-ton shot on 13 November 1972. The MIDDLE GUST Series was also part of the MIDDLE NORTH program. Its primary purpose was to obtain ground motion data from a clay-over-shale environment for use in empirical predictions and for evaluation of computer prediction techniques. The MIDDLE GUST Series, conducted between 16 September 1971 and 10 August 1972, consisted of two 20-ton and three 100-ton shots of various configurations. These tests were conducted near Ordway in southeastern Colorado. A profusion of test data obtained during the MIDDLE GUST Series is documented in Reference IV-1.48. This reference presents an analysis of the airblast and ground motion data. The explosive yields and heights of burst chosen for the MIDDLE GUST Series were selected to provide direct experimental comparison with previous cratering and ground motion experiments conducted in different geologic media. The MIDDLE GUST data and data from similar previous events are compiled and evaluated with respect to the influence of the degree of water saturation and geologic layering on the resulting ground motions and stress fields.

Also in May 1973, Murrell (Reference IV-1.49) published a report dealing with some ground motion measurements during the DIAL PACK Event, Project LN305. The objective of this project was to measure and analyze ground shock in the outrunning region produced by a 500-ton detonation at the surface. Motions and stresses were measured at a ground range of 645 and 840 feet and at depths of 1.5, 5, 10, and 20 feet. Thirty-one of thirty-two gauges produced good records of time histories and frequency response spectra. Peak outrunning accelerations and velocities showed little attenuation over the instrumented range. The vertical peaks did not show any consistent relationship with depth, but the horizontal

motions increased with depth. Since the deeper gauges were close to the refractive layer, the motions emanating from this layer were stronger at depth. Vertical accelerations were greater than horizontal accelerations by a factor of 4, and vertical velocities showed a tenfold increase over horizontal velocities. Similar patterns of attenuation were noted for the displacements. Due to additive effects of the airblast-induced motion, horizontal displacements were greater than vertical displacements by a factor of 1.9. Airblast-induced accelerations and velocities were compared with the outrunning motions and were found to be dominant at the depths of 1.5 and 5 feet. At the depths of 10 and 20 feet, accelerations and velocities from the two sources were about equal.

In April 1974, Murrell also published a report dealing with measurements carried out during the DIAL PACK Event, Project LN302 (Reference IV-1.50). The objectives of this project were to measure and to analyze the earth motions and stresses produced by the DIAL PACK 500-ton TNT detonation. Particle acceleration, particle velocity, and soil stress gauges were installed to measure the ground motions and stresses in the 1,500- to 50-psi predicted airblast overpressure region (83 to 540 feet from ground zero) at depths below the ground surface of 1.5 to 30 feet. Ground shock arrival time data indicated the occurrence of outrunning ground motion at the ground surface at a distance of about 600 feet from ground zero, or the 35-psi overpressure level. Peak vertical particle accelerations varied from 1,400 g's near ground zero to 8 g's at the extremes of the instrumented region, attenuating sharply with both distance and depth. An equation was developed to describe the peak acceleration as a function of both pressure and depth. Downward vertical particle velocities varied from 72 to 0.88 ft/sec over the area instrumented, also attenuating rapidly with distance and depth. An equation similar to that for acceleration was developed to express velocity as a function of pressure and depth. The downward velocity pulse was followed by an upward motion of generally longer duration and, except at the lesser ranges and 5- and 10-foot depths, lesser magnitude. Peak horizontal particle velocities varied from about 20 to 0.35 ft/sec over the range instrumented, attenuating as the -2.1 power of distance. These did not vary with depth. Both horizontal and vertical displacements were calculated from measured velocities. Maximum transient displacements were 20 feet upward and 20 feet outward at the 83-foot range and 1.5-foot depth. The upward displacement attenuated more rapidly than the outward displacement with distance, so that at 540 feet it was only about one-half of the outward displacement.

In January 1975, Ferritto and Forrest published a document presenting data from four instrumented 1,000-pound spherical TNT shots detonated at the Pacific Proving Ground as part of the Pacific Cratering Experiments (PACE) (Reference IV-1.51). In two tests the charge was tangent to and above the ground, and in two tests the charge was half-buried in the ground. A discussion of the site properties is presented in their report. There is a discussion of the ground motion data accompanied by graphs and scaling laws. The data are compared with previous nuclear test data and with Event MIDDLE GUST data. A supplement to this reference contains the data plots for all the shots.

IV-1.8.2 Near-Surface Motions from Surface Detonations on Hard Rock

The content of this section was taken from Reference IV-1.6. Predictions for near-surface ground motions from nuclear surface bursts must be derived by some means other than direct empiricism because there have been no nuclear surface bursts on hard rock. First principle calculations of the surface-burst problem provide some insight into the basic phenomena, but until these prediction procedures are validated only low confidence can be placed in their quantitative results. Therefore, Cooper suggests that we are well advised to also consider experimental data in deriving quantitative criteria. This section discusses near-surface ground motion data from two high-explosive experiments in hard rock and suggests some generalizations that might be applied to estimate the near-surface ground motions from a nuclear contact burst.

We will consider some of the ground motion data from MINERAL ROCK and MINE ORE, two 100 ton high-explosive experiments conducted in the Three Peaks area of southwestern Utah, approximately 10 miles northwest of Cedar City (References IV-1.45, IV-1.46, IV-1.52, IV-1.53). The ground zeros were at about 5900 ft elevation on an iron-rich quartz monzonite intrusion covered with a veneer of sandy silt and somewhat weathered rock. The rock is classified as tonolite, and results of laboratory analysis give a specific gravity of 2.6, a compression wave velocity of 13,000 ft/sec, a shear wave velocity of 7500 ft/sec, a porosity of 5 percent which is relatively high compared to hard rock such as granite, dolomite, etc., and non-linear stress-strain behavior.

Both experiments used 100 ton spherical TNT charges, detonated at 0.9 charge radius height-of-burst as indicated in Figure IV-1.54. This test geometry was chosen to approximate the partitioning of energy between the airblast-induced and direct-induced ground shock expected from a high-yield nuclear contact burst.

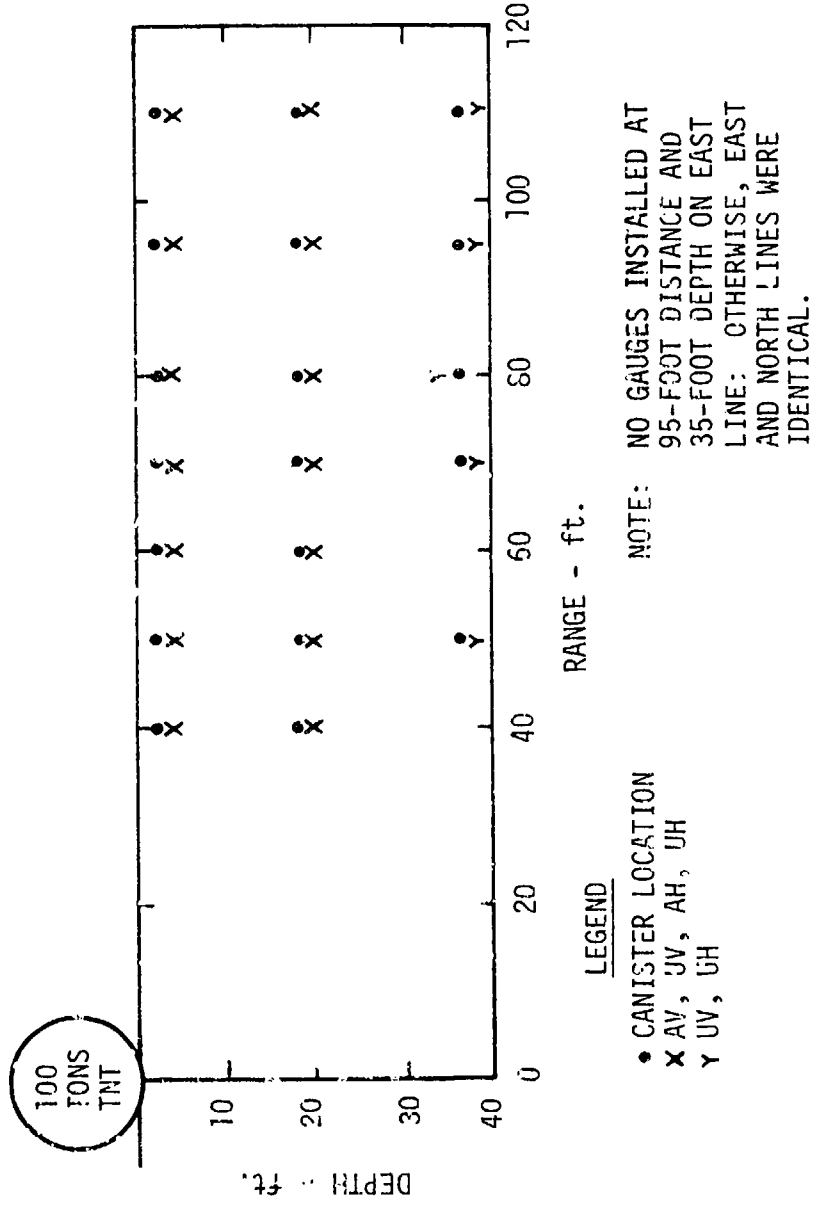


Figure IV-1.54. Gauge layout, Event MINERAL ROCK.

As shown in Figure IV-1.54, ground motion measurements by means of acceleration and velocity sensing gauges were made along two radial lines at depths of 2, 18, and 36 ft.

To use these data in predicting ground motions from a nuclear contact burst, some scaling procedure must be adopted. Cooper (Reference IV-1.6) assumed that the cube-root of the crater volume is a characteristic length that can be used to correlate the close-in, near-surface direct-induced ground motions from both high-explosive and nuclear cratering bursts. By close-in is meant ground ranges less than about $7.5 V^{1/3}$ where V is the apparent crater volume. Such a geometrical scaling avoids arguments over the differences between nuclear and high-explosive sources by hypothesizing that the direct-induced ground motions can be directly correlated with the size of the crater in both cases. In other words, it is hypothesized that whatever physical phenomenon causes a large crater also causes correspondingly larger close-in ground motions independent of details of the explosive source. An estimate of the crater volume from a megaton surface burst on hard rock is required to apply these scaling procedures. He then assumed that the cratering efficiency of a nuclear contact burst on hard rock is $3 \times 10^7 \text{ ft}^3/\text{mt}$ and that the crater radius and depth are given by $1.2 V^{1/3}$ and $0.5 V^{1/3}$.

As indicated in Figure IV-1.55, the gauge depths on MINERAL ROCK and MINE ORE correspond to approximately $0.1 V^{1/3}$, $1 V^{1/3}$, and $2 V^{1/3}$.

Figure IV-1.56 shows arrival time contours computed from the MINERAL ROCK and MINE ORE data. These results indicate that outrunning ground motions began at a range of about 90 ft ($R/V^{1/3} \approx 4.5$) and a peak overpressure of about 700 psi. Outrunning ground motions would be expected closer-in for hard rock, at ranges consistent with a few thousand psi. However, because the direct-induced ground motions are thought to dominate the close-in ground response, relatively small variations in the ground range to where outrunning begins is not expected to affect the main qualitative features of the ground motions for ranges less than about $7.5 V^{1/3}$.

The attenuation of near-surface peak horizontal and vertical particle velocity with range is indicated in Figure IV-1.57. As suggested by the boundary lines, the peak particle velocity attenuates approximately as $(R/V^{1/3})^{-2}$. Figure IV-1.57 also shows that the horizontal peak particle velocity tends to be about twice the vertical peak particle velocity.

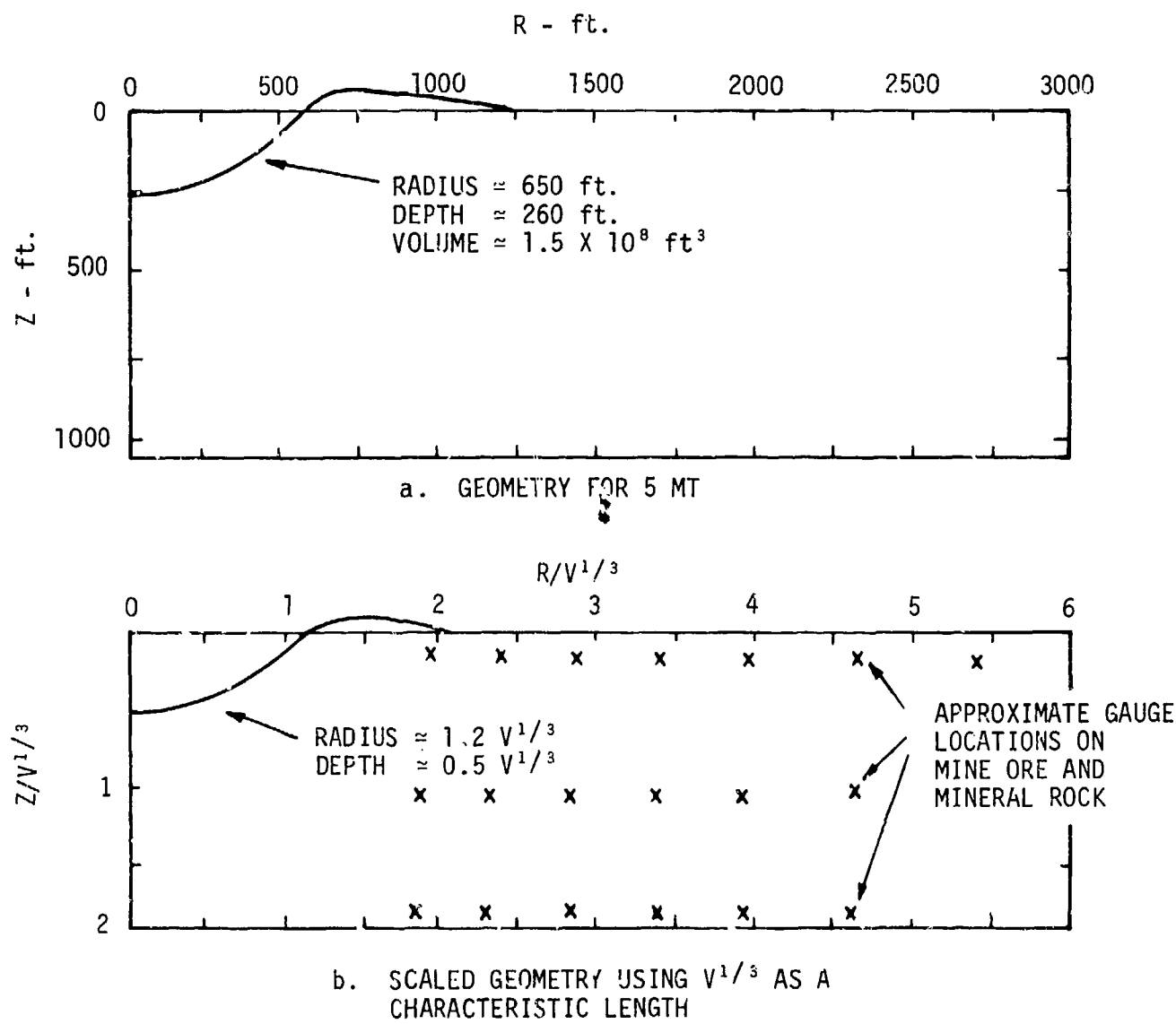


Figure IV-1.55. Geometrical scale for a 5 mt contact burst on hard rock compared with MINE ORE/MINERAL ROCK experimental geometry.

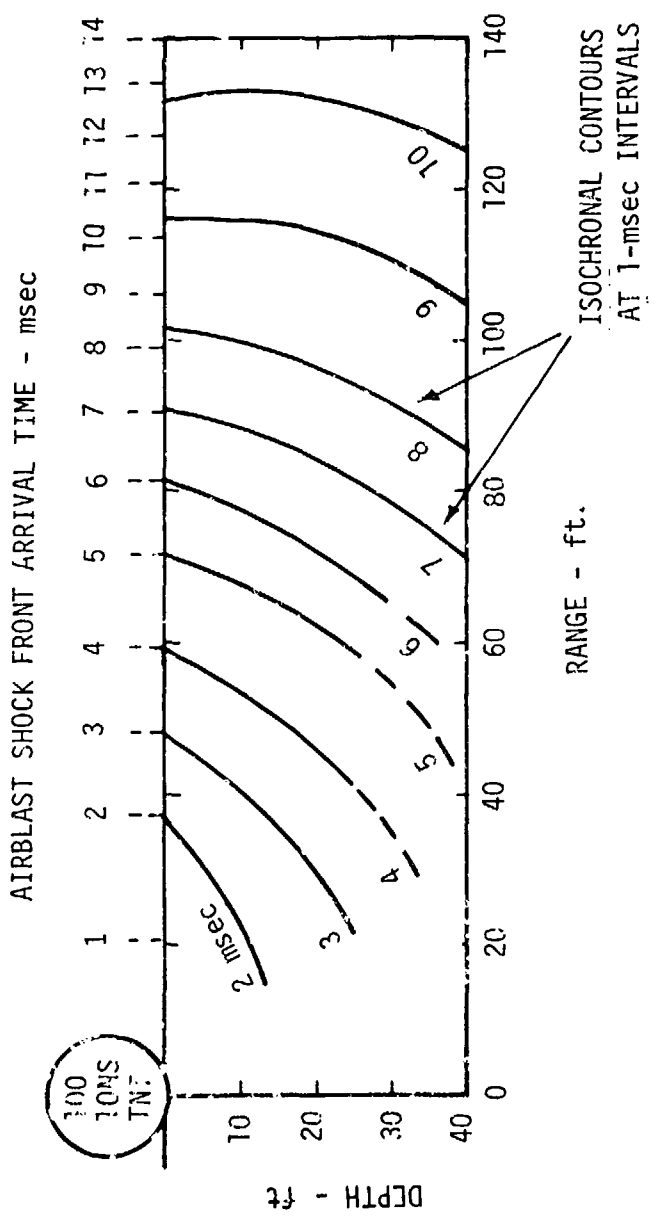


Figure IV-1.56. Shock front propagation.

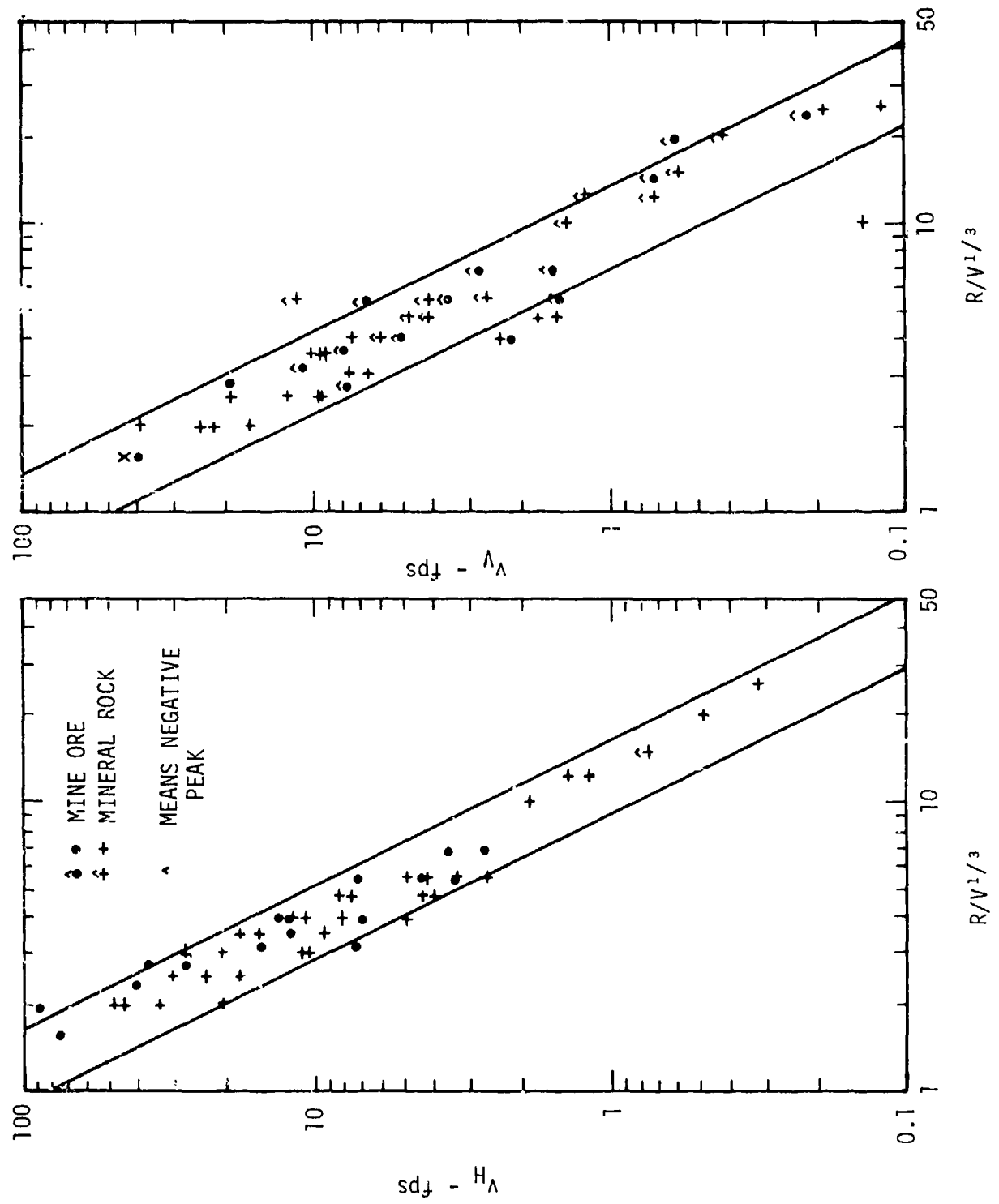


Figure IV-1-57. Correlation of near-surface peak particle velocity from cratering bursts in rock.

IV-1-122

Figure IV-1.58 shows the correlation of vertical and horizontal peak particle displacements from MINERAL ROCK and MINE ORE compared to a best estimate line obtained from correlating the near-surface peak displacements from above-surface high explosive cratering experiments in several soil and rock "uniform" geologies. Beyond a range of about $6 V^{1/3}$, the near-surface ground motions become increasingly oscillatory and the attenuation of peak displacements becomes less rapid than R^{-3} .

Figures IV-1.59 and IV-1.60 compare the peak particle velocity data at $Z/V^{1/3} \approx 1$ and $Z/V^{1/3} \approx 2$ with two lines that bound the data from the shallow gauges. It appears that the peak horizontal particle velocity does not attenuate appreciably for $0 \leq Z/V^{1/3} \leq 1$, but does decrease by almost a factor of two between $Z/V^{1/3} \approx 1$ and $Z/V^{1/3} \approx 2$. On the other hand, the peak vertical particle velocity decreases by almost a factor of two between the surface and $Z/V^{1/3} \approx 1$, and by another factor of almost two between $Z/V^{1/3} \approx 1$ and $Z/V^{1/3} \approx 2$. It should be noted that the data at $Z/V^{1/3} \approx 2$ are really too sparse to define an attenuation rate. Based on geometrical considerations, one might expect that the attenuation rates (as a function of $R/V^{1/3}$ for a fixed $Z/V^{1/3}$) would decrease with increasing depth and increasing range. However, the data scatter at $Z/V^{1/3} \approx 1$ is too great to suggest an attenuation rate different from the near-surface data. In any case, within the range of these data ($2 \leq R/V^{1/3} \leq 6$), the peak horizontal and vertical particle velocities in ft/sec may be estimated by

$$\left. \begin{array}{l} V_H \approx 150 (V^{1/3}/R)^2 \\ V_V \approx 100 (V^{1/3}/R)^2 \end{array} \right\} Z/V^{1/3} \approx 0 ;$$

$$\left. \begin{array}{l} V_H \approx 150 (V^{1/3}/R)^2 \\ V_V \approx 50 (V^{1/3}/R)^2 \end{array} \right\} Z/V^{1/3} \approx 1 ;$$

$$\left. \begin{array}{l} V_H \approx 80 (V^{1/3}/R)^2 \\ V_V \approx 30 (V^{1/3}/R)^2 \end{array} \right\} Z/V^{1/3} \approx 2 . \quad (IV-1.50)$$

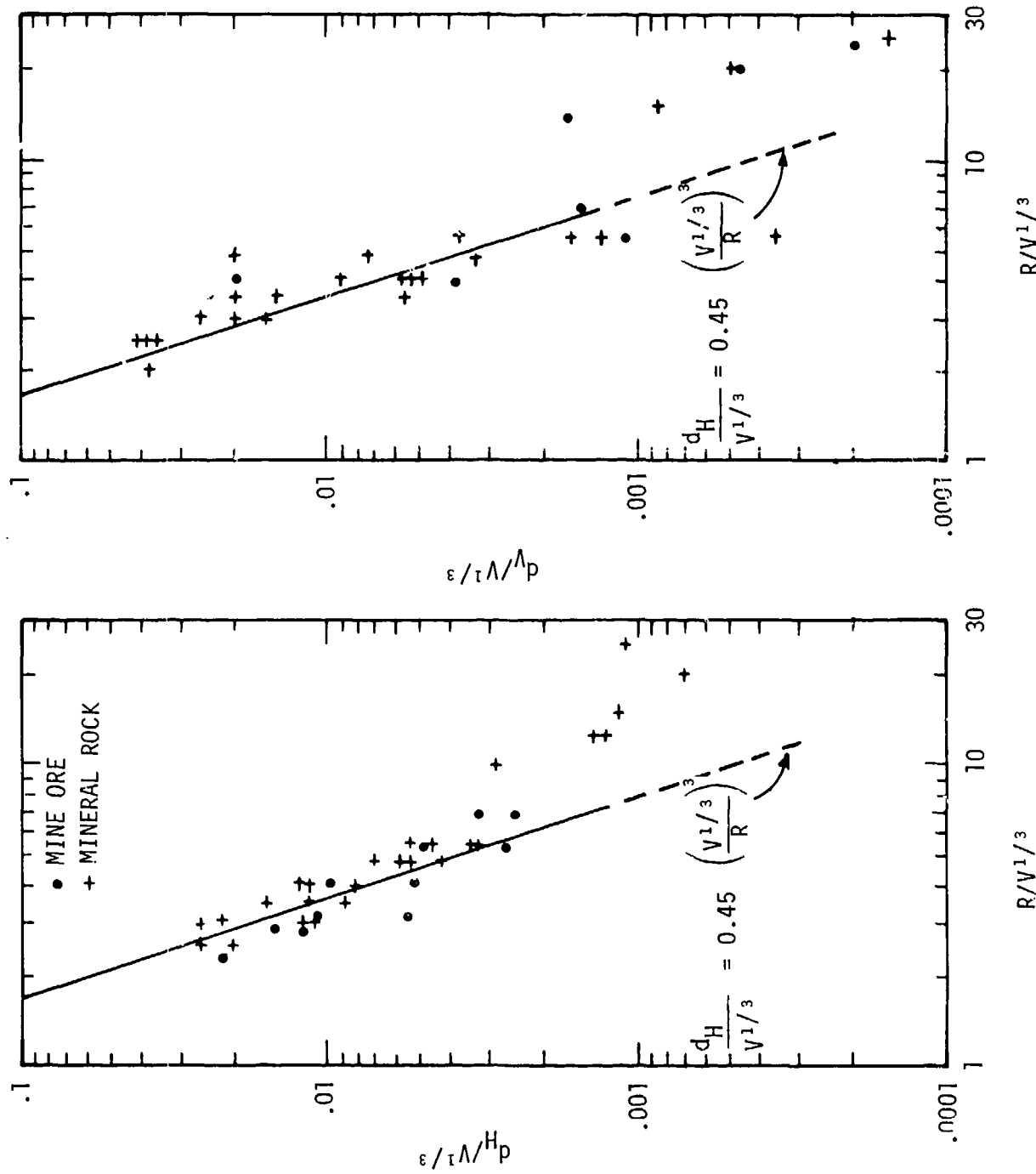


Figure IV-1.58. Correlation of near-surface peak vertical and horizontal particle displacements.

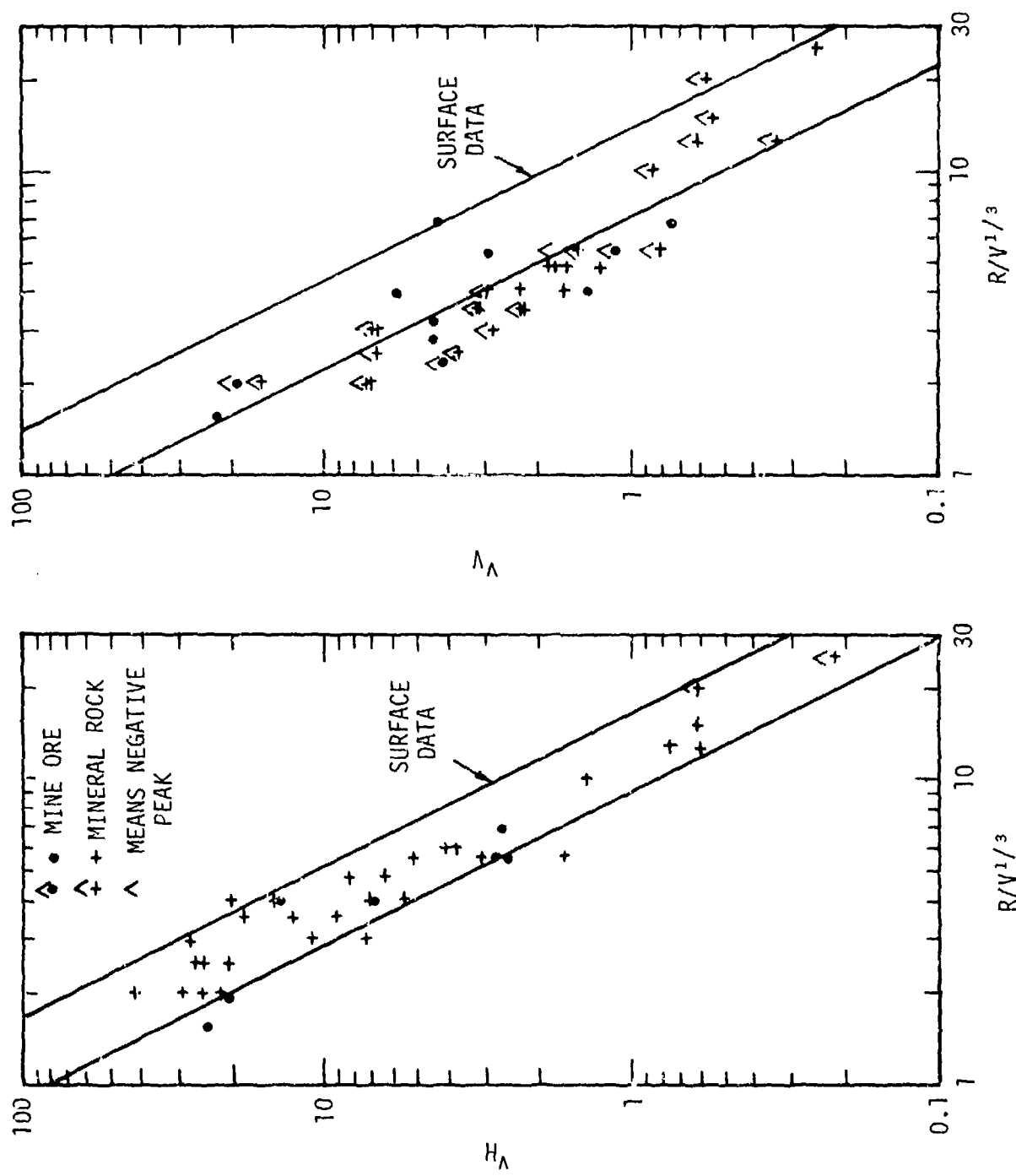


Figure IV-1-59. Correlation of peak particle velocity at $Z \approx V^{1/3}$ from cratering bursts in rock.

IV-1-125

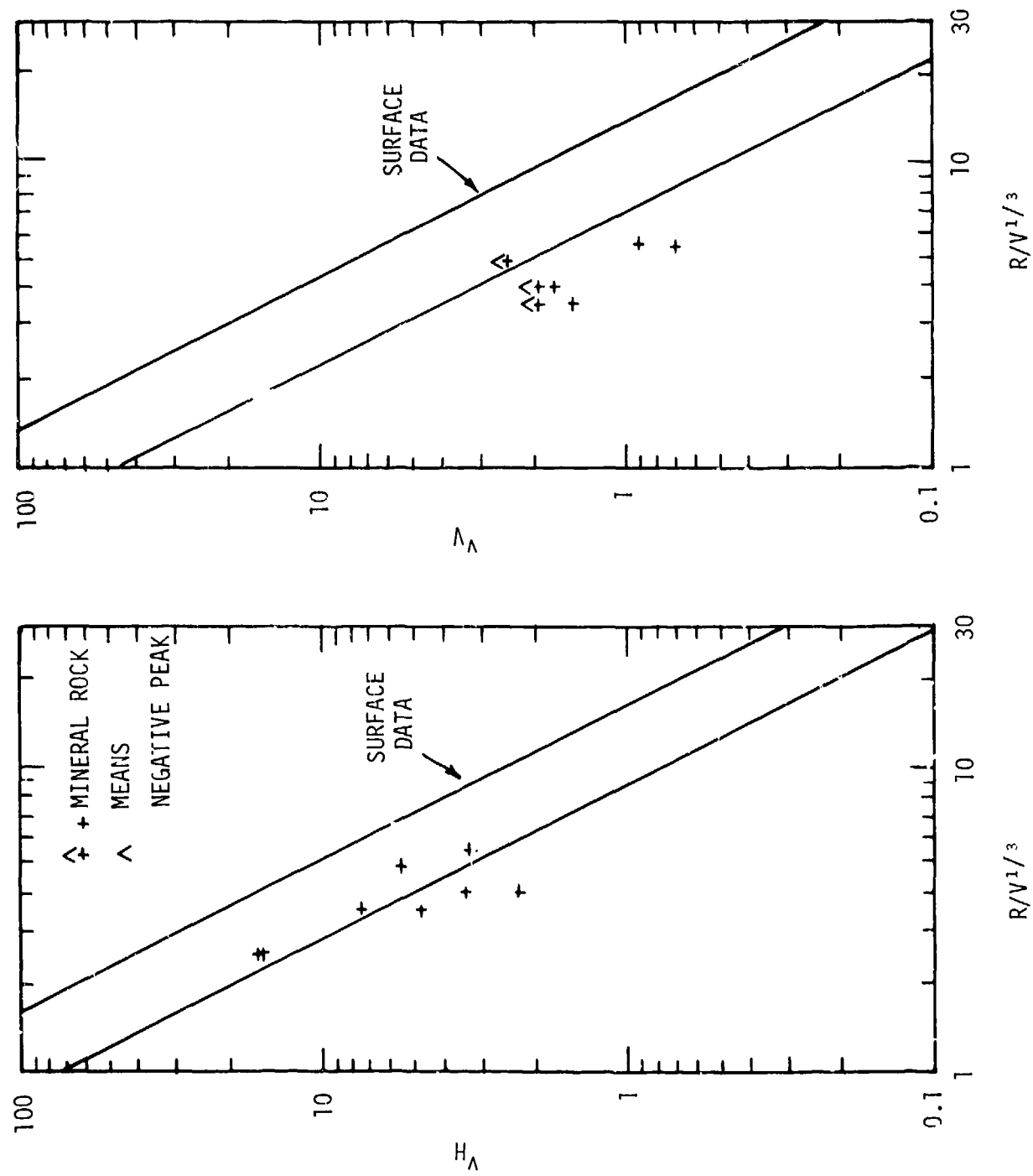


Figure IV-1.60. Correlation of peak particle velocity at
 $Z \approx 2 V^{1/3}$ from cratering bursts in rock.

These expressions represent best estimates to the peak particle velocity data from MINERAL ROCK and MINE ORE. To obtain upper and lower bound estimates, they should be multiplied or divided by about 2.

Figure IV-1.61 shows that the peak vertical particle displacement decreases to about one-half the surface value at $Z/V^{1/3} \approx 1$ while the peak horizontal displacements at that depth do not appear to differ appreciably from the surface values. Figure IV-1.62 shows that the peak vertical and horizontal displacements decrease by a factor of about two between $Z/V^{1/3} \approx 1$ and $Z/V^{1/3} \approx 2$. Based on these results, Cooper's best estimates of the peak displacements for $2 \lesssim R/V^{1/3} \lesssim 6$ are (Reference IV-1.6):

$$d_h \approx d_v \approx 0.45 V^{4/3} R^{-3} \quad \text{for } Z/V^{1/3} \approx 0 ;$$

$$\left. \begin{array}{l} d_h \approx 0.45 V^{4/3} R^{-3} \\ d_v \approx 0.2 V^{4/3} R^{-3} \end{array} \right\} \quad \text{for } Z/V^{1/3} \approx 1 ;$$

$$\left. \begin{array}{l} d_h \approx 0.2 V^{4/3} R^{-3} \\ d_v \approx 0.1 V^{4/3} R^{-3} \end{array} \right\} \quad \text{for } Z/V^{1/3} \approx 2 .$$

(IV-1.51)

Estimates of the upper and lower bounds can be obtained by multiplying and dividing by a factor of about 2.

Equations IV-1.50 and IV-1.51 summarize the peak particle velocity and displacement data from MINERAL ROCK and MINE ORE. It should be understood that the inverse square and inverse cube attenuation rates assigned in these formulae are not least-square fits to the data. Rather, they were assumed as reasonable "eyeball" representations. In Cooper's opinion, the quality of the experimental data does not justify a more rigorous statistical treatment.

The tonalite in which the MINERAL ROCK and MINE ORE experiments were conducted is not really a hard rock. As indicated earlier, it has a porosity of about 5 percent and a seismic compressional wave speed of about 12,000 - 13,000 ft/sec. Therefore, it is expected that the peak particle velocities measured on

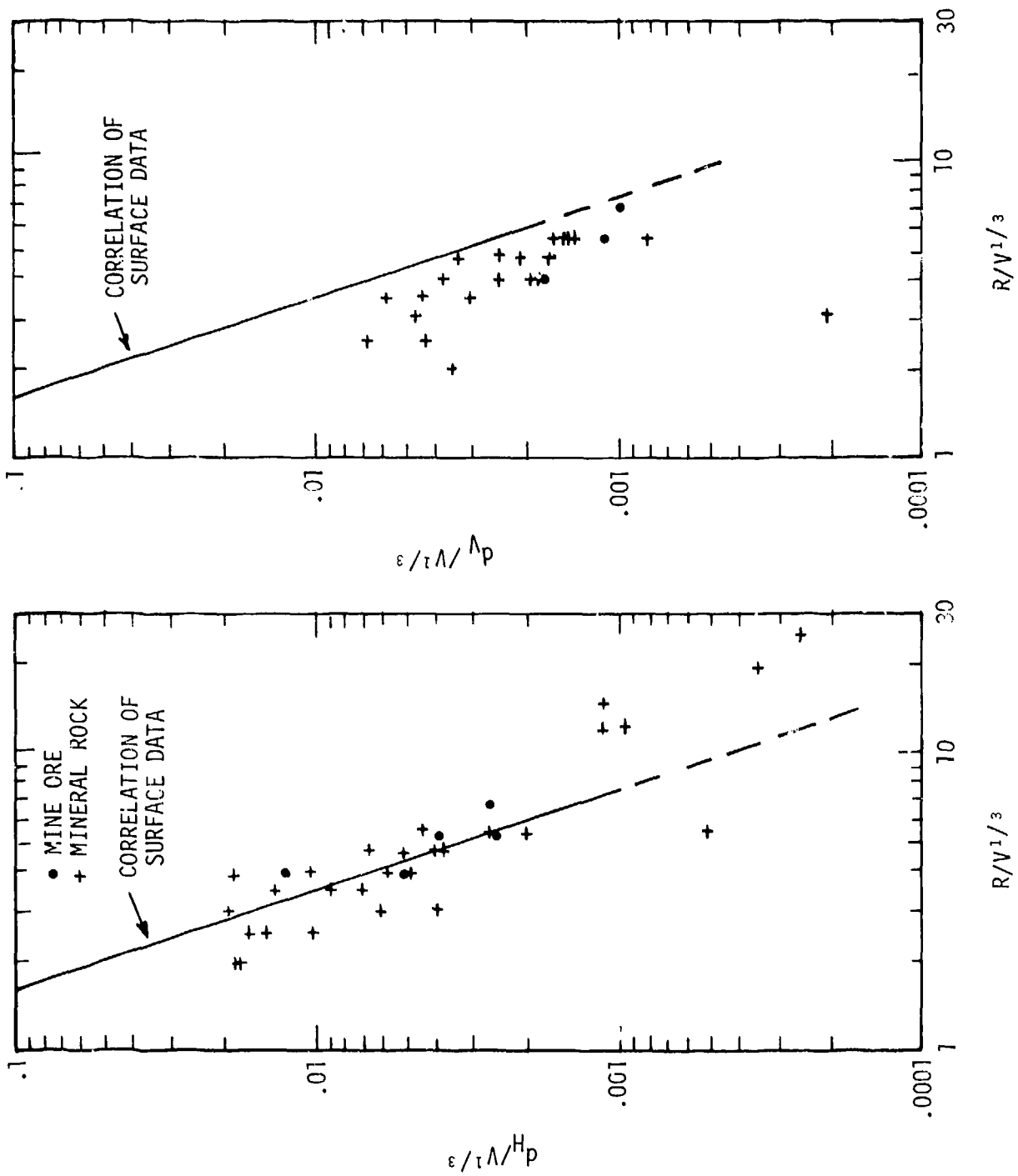


Figure IV-1-61. Correlacion of peak vertical and horizontal particle displacements at $Z/V^{1/3} \approx 1$.

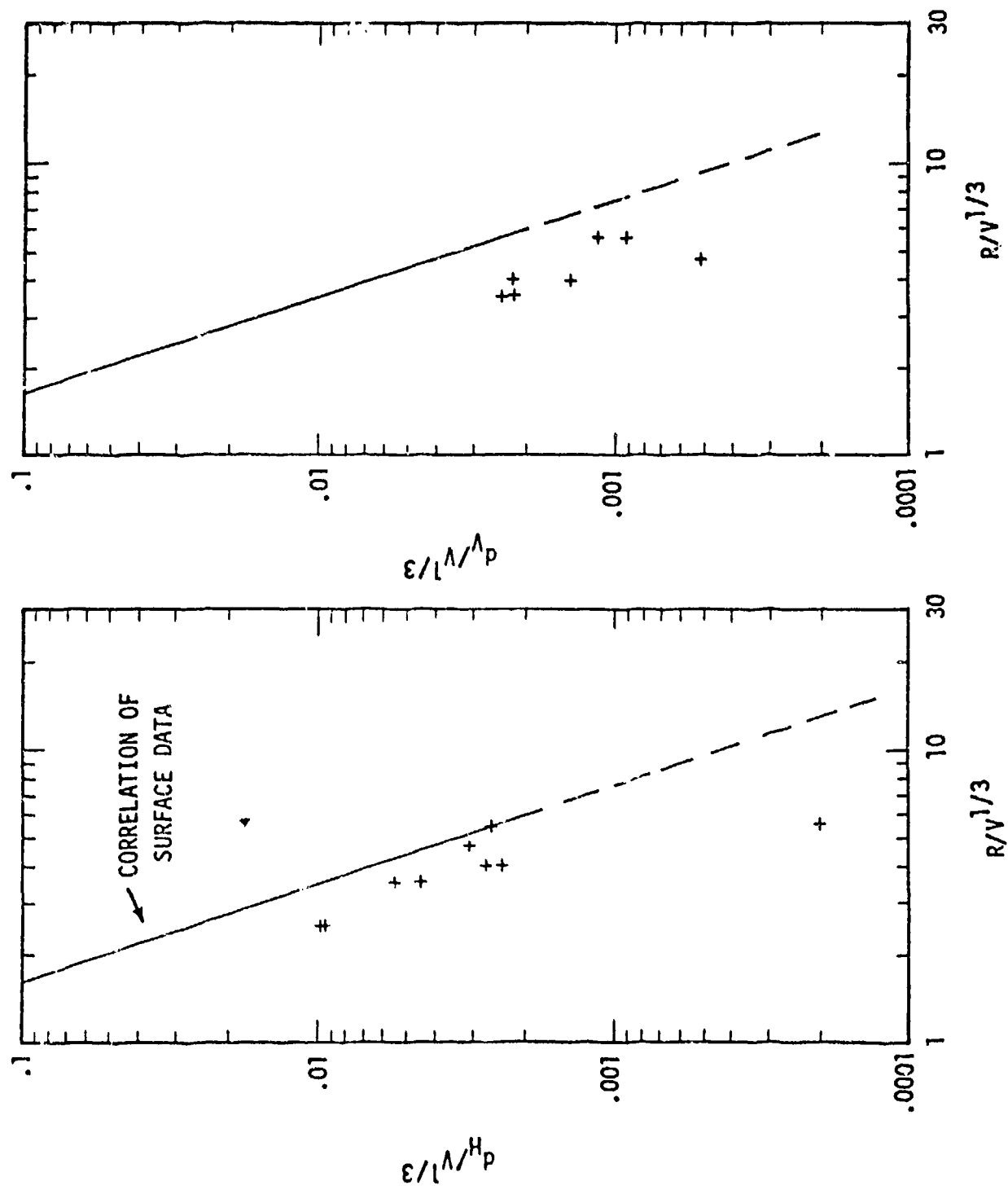


Figure IV-1-62. Correlation of peak vertical and horizontal particle displacements at $Z/V^{1/3} \approx 2$.

MINERAL ROCK and MINE ORE were somewhat less than would occur if the experiments had been conducted on a harder rock. If we assume that the seismic velocity of a hard rock is 18,000 ft/sec and increase the peak particle velocity amplitudes by the ratio of seismic velocities (References IV-1.54 and IV-1.55), we would have for "hard rock":

$$\left. \begin{array}{l} v_H \approx 225 (V^{1/3}/R)^2 \\ v_V \approx 150 (V^{1/3}/R)^2 \end{array} \right\} Z/V^{1/3} \approx 0 ;$$

$$\left. \begin{array}{l} v_H \approx 225 (V^{1/3}/R)^2 \\ v_V \approx 75 (V^{1/3}/R)^2 \end{array} \right\} Z/V^{1/3} \approx 1 ;$$

$$\left. \begin{array}{l} v_H \approx 120 (V^{1/3}/R)^2 \\ v_V \approx 45 (V^{1/3}/R)^2 \end{array} \right\} Z/V^{1/3} \approx 2 . \quad (IV-1.52)$$

These equations will be assumed to provide reasonable estimates of the peak particle velocities in hard rock for $2 \leq R/V^{1/3} \leq 6$. The peak particle displacements given by Equation IV-1.51 are assumed to be appropriate for the near-surface displacements in hard rock.

Cooper then attempted to synthesize these formulae with those developed for the ground motion from nuclear detonations on hard rock below the surface. For the ground motions directly below the burst point, the best-estimate peak particle velocities and displacements was derived as

$$v_z \approx 24 \frac{W^{2/3}}{mt} \frac{Z^{-2}}{kft};$$

$$d_z \approx 0.25 \frac{W^{5/6}}{mt} \frac{Z^{-3/2}}{kft} \quad (IV-1.53)$$

where Z_{kft} is the depth below ground zero in kft, w is the yield in mt and where v_z is in ft/sec and d_z is in ft. Assuming that the cratering efficiency of a contact burst on hard rock is $V/W_{mt} = 3 \times 10^7 \text{ ft}^3/\text{mt}$, there results

$$v_z \approx 250 (V^{1/3}/Z)^2 ;$$

$$d_z/V^{1/3} \approx 0.0047 (V^{1/3}/Z)^{3/2} \quad (\text{IV-1.54})$$

where v_z is in ft/sec. Some interesting comparisons were then made by Cooper between these estimates of peak ground motions below ground zero and those along the earth's surface. The peak particle velocities are estimated to attenuate as the inverse square of the distance from ground zero in both cases, but the square of the distance from ground zero in both cases, but the close-in peak displacements below the burst point are estimated to attenuate much less rapidly with increasing depth than do the near-surface displacements with increasing range from ground zero. The close-in peak particle velocities below the burst point are estimated to be comparable to the near-surface peak particle velocities at the same range from ground zero. For example, at a depth of $Z/V^{1/3} = 3$, Equation IV-1.54 gives a peak particle velocity of about 28 ft/sec, corresponding to a peak stress of about 1 kilobar. On the earth's surface at a range of $R/V^{1/3} \approx 3$, Equation IV-1.52 give $v_H \approx 25$ ft/sec and $v_y \approx 17$ ft/sec. On the other hand, these formulae suggest that close-in peak displacements below ground zero are significantly less than the near-surface peak displacements at a comparable scaled range. At $Z/V^{1/3} = 3$, Equation IV-1.54 gives $d_z/V^{1/3} \approx 0.0009$, but Equation IV-1.51 gives $d_H/V^{1/3} \approx d_y/V^{1/3} \approx 0.017$, that is, over an order of magnitude greater displacement at the earth's surface.

Figure IV-1.63 presents some results of a rather loose synthesis of the MINERAL ROCK and MINE ORE data with the analysis in Reference IV-1.6. Contours of constant peak particle velocity and displacement were derived by interpolating (with a fair amount of liberty) Equations IV-1.51, IV-1.52, and IV-1.54. It was assumed that vertical and horizontal peaks occurred simultaneously in which case equations such as $|v| \approx [(225)^2 + (150)^2]^{1/2} (V^{1/3}/R)^2 \approx 270 (V^{1/3}/R)^2$ for $Z/V^{1/3} = 0$ can be developed. As suggested above, the estimated contours of constant peak

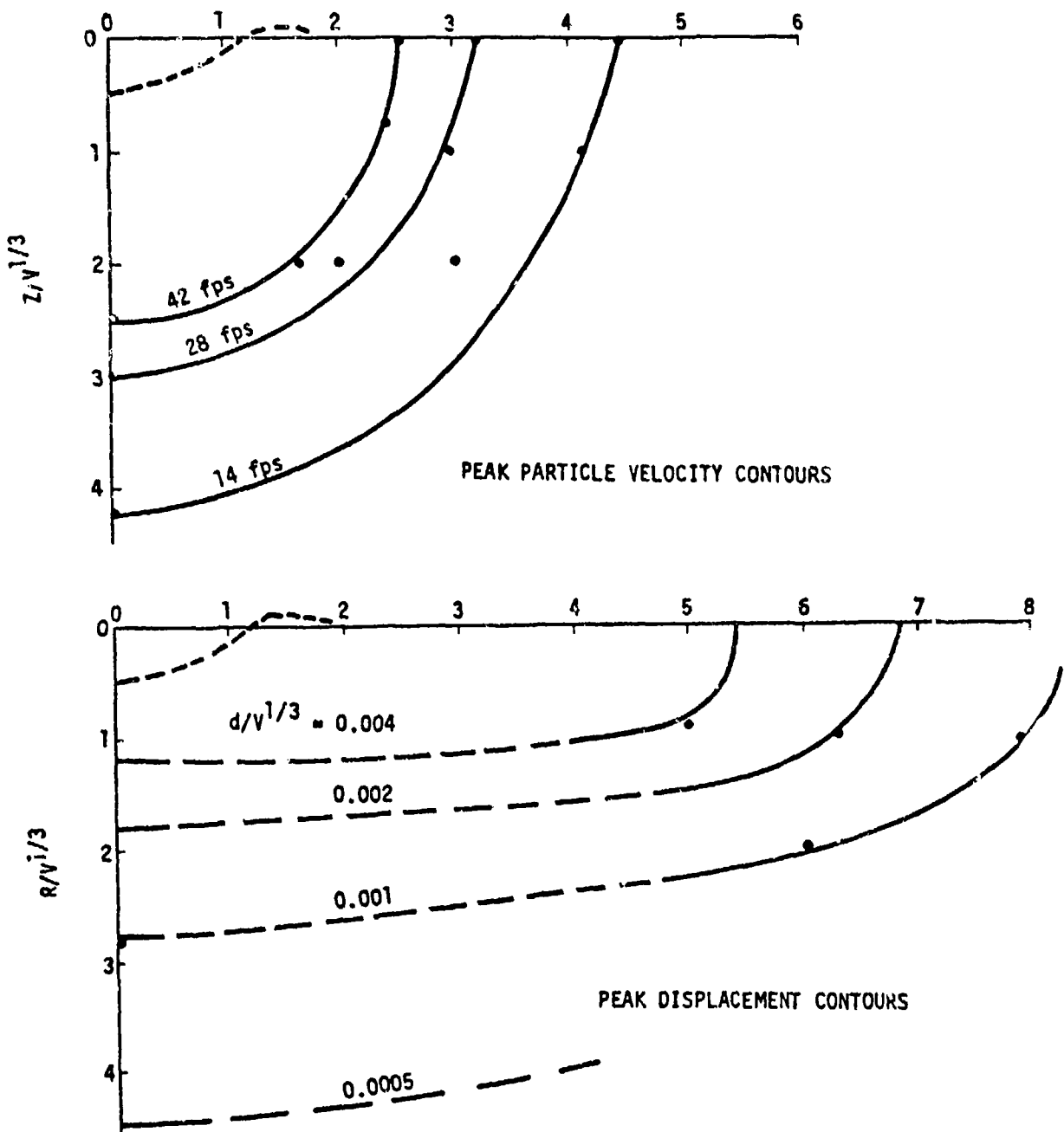


Figure IV-1.63. Estimated peak particle velocity and displacement contours.

particle velocity are almost hemispherical. On the other hand, the estimated peak displacement contours are rather peculiarly shaped, suggesting much larger near-surface displacements than at depth beneath ground zero. This estimate for the nuclear case is somewhat inconsistent with permanent displacement contours measured on MINERAL ROCK where displacements below the burst point were more comparable to surface values at a given range. As stated previously, the displacement equivalent yield obtained from the cavity experiment may be somewhat low because the influence of the joints on the late-time motions may not have been properly modeled. These estimated contours of peak particle velocity and displacement are very speculative because of the sparsity of data at depth, because of the uncertainty in predicting the crater volume from surface bursts on hard rock, and because of the unproven assumption that one can so simply combine the analysis for nuclear explosions (Reference IV-1.6) with the analysis of high-explosive data. Furthermore, some apparent inconsistencies were ignored in plotting these data; for example, some MINERAL ROCK data suggest the displacement at $Z/V^{1/3} \approx 2$ (and $2 \leq R/V^{1/3} \leq 6$) are greater than those suggested by the analysis of ground motion from nuclear detonations below ground in hard rock at the same depth below ground zero. In this case, the on-axis displacement from nuclear data was connected with a monotonically varying smooth line to the appropriate displacement along $Z/V^{1/3} \approx 1$. Cooper suggests that further study is required to resolve the apparent inconsistencies.

IV-1.8.3 Near Surface Motions from Surface Detonations on Layered Media

In this section we briefly mention some of the ground motion data obtained from high explosive detonations over layered media.

The most extensively instrumented test series to date are MIDDLE GUST, PRAIRIE FLAT and MIXED COMPANY also contained redundant measurements. It should be recalled that the PRAIRIE FLAT, DISTANT PLAIN 6, and DIAL PACK Events were executed at the Canadian test range on a bed of layered clay on sandy loam. Figure IV-1.64 shows a comparison of peak velocity data for the 500-ton PRAIRIE FLAT Event (References IV-1.56 and IV-1.57). Both the airblast-induced (AI) and the initial peaks following the direct-induced (DI) arrival are shown. The figure compares integrated accelerometer data with velocity gauge data for measurements in close proximity to one another. The comparison is also made between the Waterways Experiment Station (WES) and the Stanford Research Institute (SRI) measurements for azimuths that are 120 degrees apart. These data show that the accelerometer results are about 20 percent higher than the velocity gauge

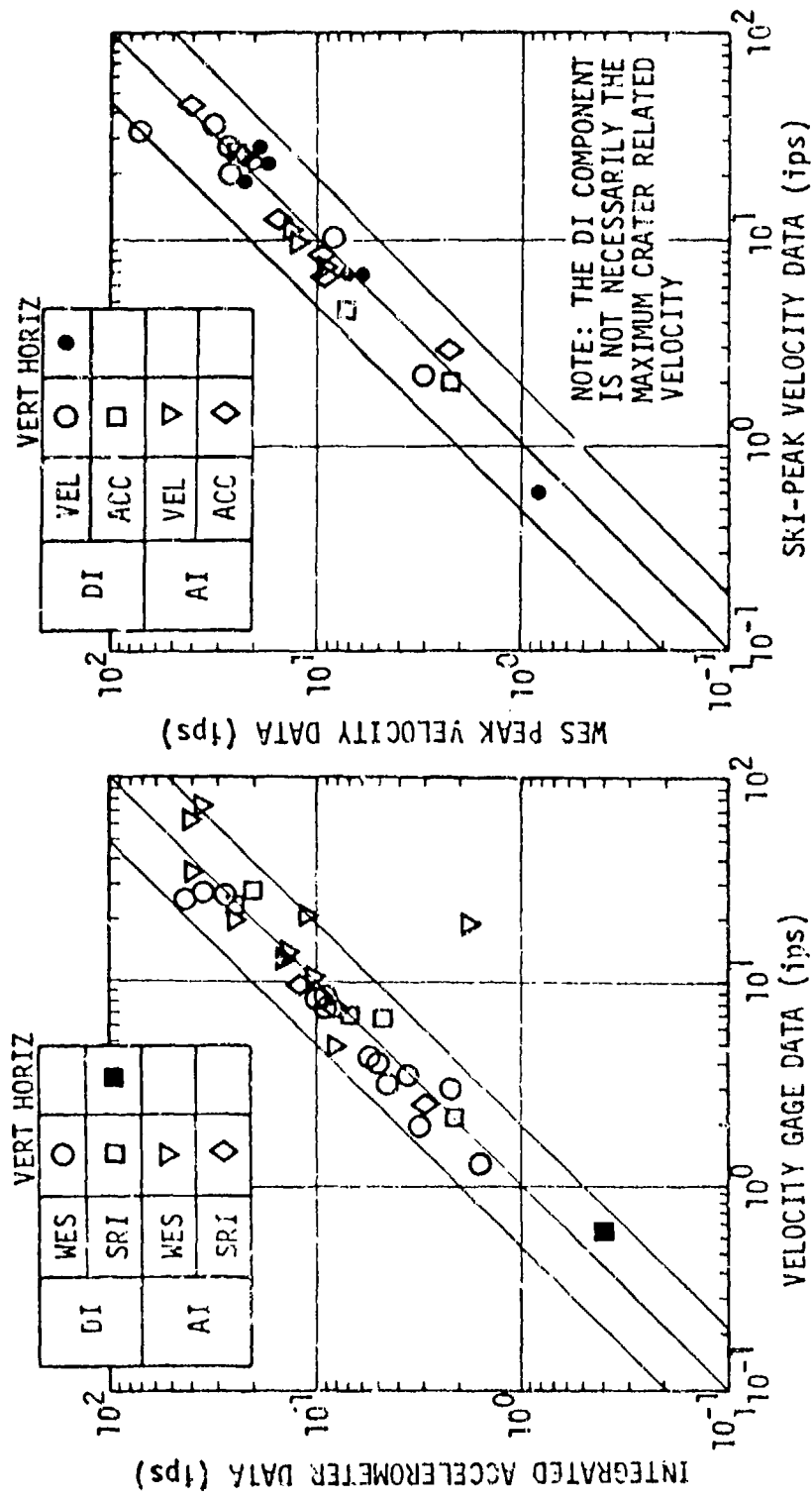


Figure IV-1-64. Comparison of PRAIRIE FLAT peak velocity data.

results and the majority of the WES and SRI data are within 30 percent of each other (Reference IV-1.58).

The MIXED COMPANY III Event consisted of the detonation of a 500-ton TNT charge, spherical in shape, placed tangent above the ground surface. The geology consisted of sandstone overlayed by 5.5 feet of soil. The detonation took place at Grand Junction, Colorado. the MIDDLE GUST III and IV Events were 100-ton TNT charges, spherical in shape, placed tangent above the ground surface. These charges were detonated over a layered medium near Crowley, Colorado. The medium over which MIDDLE GUST III was detonated consisted of shale with a 9-foot thick overburden of clay and a water table that came within 4 feet of the ground surface. This site is referred to in the literature as the "wet" site. MIDDLE GUST IV was detonated over a medium consisting of shale overlayed by 2 feet of clay and not water. This is referred to in the literature as the "dry" site.

Figure IV-1.65 shows the peak near-surface air slap vertical acceleration and velocity for high explosive events at the Defence Research Establishment Suffield (DRES), formerly known as the Suffield Experimental Station (Reference IV-1.2). It is generally possible to separate the air slap near-surface peak vertical acceleration and velocity from the rest of the data, with a primary exception occurring when the air slap and refracted wave effects arrive at a point at about the same time. The scatter of the acceleration data is on the same order for individual events as for all DRES events. The 500-ton PRAIRIE FLAT and DIAL PACK Events tend to have higher velocities at the 1.5-ft depth than the other events which have lower yields of 20 or 100 tons. The scatter of the velocity data is slightly larger than for acceleration data, probably because of the higher yield sensitivity of peak velocity. However, both sets of data essentially fall within bands about a factor of five apart. The root-mean-square of these bands, given by the following expressions, reasonably represent the data (Reference IV-1.58):

$$a_V = 950 \text{ g's} \left(\frac{P}{1000 \text{ psi}} \right) \quad (\text{IV-1.55})$$

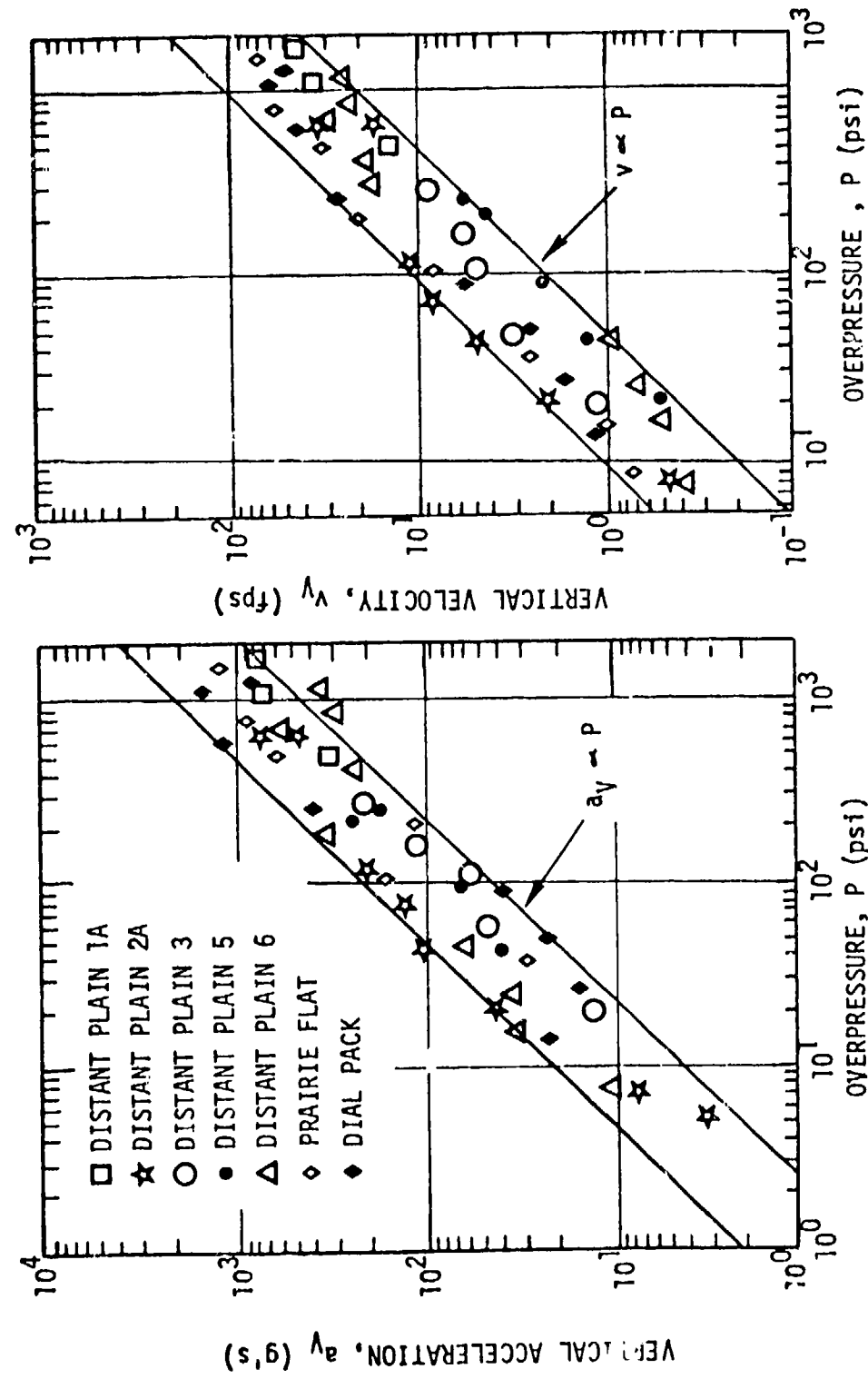


Figure IV-1.65. Peak vertical air slap acceleration and particle velocity for DRES events, 1.5-ft. depth (Reference IV-1.2).

$$v_V = 540 \text{ ips} \left(\frac{P}{1000 \text{ psi}} \right) \quad (\text{IV-1.56})$$

The near-surface peak vertical acceleration and velocity data for MIXED COMPANY 3 and MIDDLE GUST III and IV are shown in Figure IV-1.66 (Reference IV-1.2) and compared with the DRES data band. Between 10 and 300 psi, the MIDDLE GUST data are within the DRES scatter bands but tend to be lower at higher pressure. For MIXED COMPANY, all the data are within the DRES bands. Thus the near-surface material for these high explosive test sites apparently does not have significant impedance differences for stress levels at least up to 300 psi.

The air slap ground shock parameters recommended by Lipner, et. al. (Reference IV-1.58) for dry soil, wet soil, and soft and hard rock are summarized in Tables IV-1.4 through IV-1.7, respectively. According to Lipner, et. al., these relations give the best estimate peak values for displacements, velocities, accelerations, and stresses, including scaling with yield, overpressure, and depth. Additionally, 2σ uncertainty factors are also shown.

The accuracy of horizontal air slap velocity measurements is not as good as the vertical response since the direct shear wave which follows the compressional wave causes an inward component resulting in a short pulse width (higher frequency) response. For a low value of Poisson's ratio, the shear wave component is quite large and the elastic solution produces inward displacements. This type of response has been observed in test events such as MINERAL ROCK, where the medium has a high shear strength and modulus (Reference IV-1.58). The near-surface peak air-slap-induced horizontal velocity for high explosive test events is shown in Figure IV-1.67. The expression $P/\rho U$ is somewhat on the high side of the data for sites other than Cedar City. Velocity attenuation caused by the compaction hysteresis of soft material near the surface would be expected at the 1.5-foot depth for the very low yield airblast loading. The data for the Cedar City events are for the transition region and are above the $P/\rho U$ curve. The symbol s_a is the integral of the acceleration. Figure IV-1.68 shows a comparison of crater-induced peak particle velocities from surface tangent high explosive events in Cedar City tonolite and DRES silt.

For surface burst conditions, the close-in near-surface vertical response consists of downward motion brought about by the air slap and followed by the

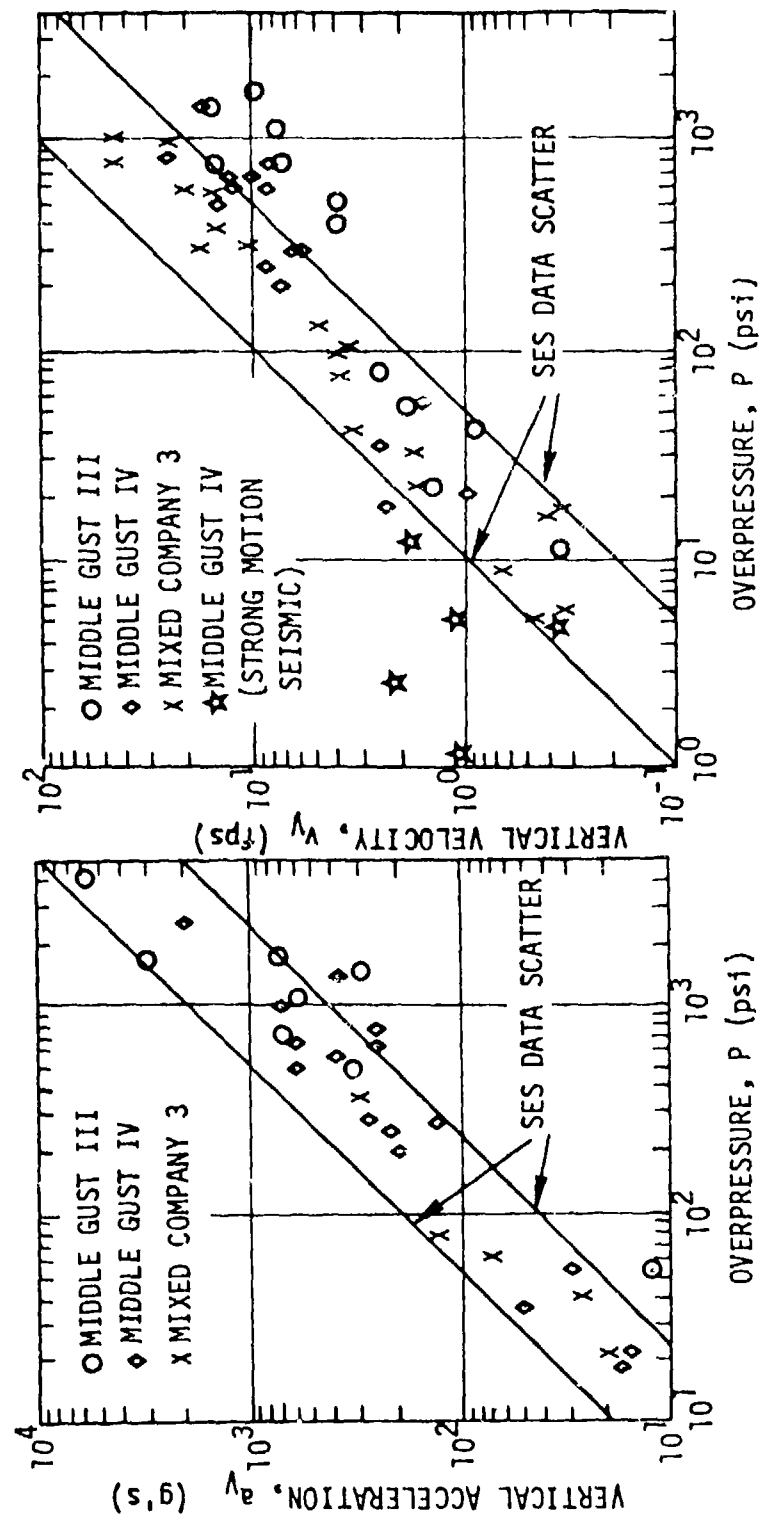


Figure IV-1.66. Peak vertical air slap acceleration and particle velocity for MIDDLE GUST III and IV and MIXED COMPANY 3, 1.5 ft. depth (Reference IV-1.2).

Table IV-1.4. Surface burst dry soil peak air slap parameters (Reference IV-1.58).

$$\text{Environment Value} = \left(\frac{\text{Value}}{\text{Reference Value}} \right) \left(\frac{W}{1 \text{ mt}} \right)^A \left(\frac{P}{1000 \text{ psi}} \right)^B \exp \left[-\frac{z}{L_0} \right]$$

ENVIRONMENT PARAMETER	REFERENCE VALUE	SCALING FACTORS*			2 σ UNCERTAINTY FACTOR**
		A	B	L ₀ (ft)	
d _V (in)	42	(1)	2/3	150	2.5
d _H (in)	7	(1)	1/3	500	3.0
v _V (ips)	540	0	1	(2)	2.5
v _H (ips)	80	0	0.6	∞	2.5
a _V (g's)	2800	0	1	(3)	3.0
a _H (g's)	400	0	0.6	(3)	3.5
σ_V (psi)	1000	0	1	∞	2.0
σ_H (psi)	350	0	0.8	∞	3.0

*Scaling Range: $20 \text{ kt} \leq W \leq 50 \text{ mt}$
 $10 \text{ psi} \leq P \leq 5000 \text{ psi}$
 $z \leq 50 \text{ ft}$

$$(1) A = \frac{1}{6} \left(\frac{P}{1000 \text{ psi}} \right)^{0.23}$$

$$(2) L_0 = 50 \text{ ft} \left(\frac{P}{1000 \text{ psi}} \right)^{-1/4} \left(\frac{W}{1 \text{ mt}} \right)^{1/12}$$

$$(3) a_{V,H} = \frac{5v_{V,H}}{\left(1 + \frac{z}{4 \text{ ft}} \right)} \text{ g's/ips, } z > 0$$

**When ranges of values are given, the uncertainties are largest for the lower overpressure, outrunning region; and smallest for the high overpressure, superseismic region.

Table IV-1.5. Surface burst wet soil peak air slap parameters
(Reference IV-1.58).

$$\text{Environment Value} = \left(\frac{\text{Reference Value}}{1 \text{ mt}} \right)^A \left(\frac{P}{1000 \text{ psi}} \right)^B \exp \left[- \frac{z}{L_0} \right]$$

ENVIRONMENT PARAMETER	REFERENCE VALUE	SCALING FACTORS*			2 σ UNCERTAINTY FACTOR**
		A	B	L ₀ (ft)	
d _V (in)	12	(1)	2/3	250	2.5
d _H (in)	15	(1)	2/3	∞	3.0
v _V (ips)	160	0	1	250	2.5
v _H (ips)	60	0	0.6	∞	2.5
a _V (g's)	830	0	1	(2)	3.0
a _H (g's)	420	0	0.6	(2)	3.5
σ_V (psi)	1000	0	1	∞	2.0
σ_H (psi)	1000	0	1	∞	2.0

*Scaling Range: $20 \text{ kt} \leq W \leq 50 \text{ mt}$
 $10 \text{ psi} \leq P \leq 5000 \text{ psi}$
 $z \leq 50 \text{ ft}$

$$(1) A = \frac{1}{6} \left(\frac{P}{1000 \text{ psi}} \right)^{0.23}$$

$$(2) a_{V,H} = \frac{5v_{V,H}}{\left(1 + \frac{z}{9 \text{ ft}} \right)} \text{ g's/ips, } z > 0$$

**When ranges of values are given, the uncertainties are largest for the lower overpressure, outrunning region; and smallest for the high overpressure, superseismic region.

Table IV-1.6. Surface burst soft rock peak air slap parameters (Reference IV-1.58).

$$\text{Environment Value} = \left(\frac{\text{Reference Value}}{1 \text{ mt}} \right)^A \left(\frac{P}{1000 \text{ psi}} \right)^B \exp \left[-\frac{z}{L_0} \right]$$

ENVIRONMENT PARAMETER	REFERENCE VALUE	SCALING FACTORS*			2σ UNCERTAINTY FACTOR**
		A	B	L_0 (ft)	
d_V (in)	4	1/3	0.4	400	2.5
d_H (in)	4	1/3	0.4	400	3.0
v_V (ips)	65	0	1	600	2.5
v_H (ips)	40	0	0.6 ⁺	∞	2.5 to 3.5
a_V (g's)	330	0	1	30	3.0
a_H (g's)	330	0	1	30	3.5 to 4.5
σ_V (psi)	1000	0	1	∞	2.0
σ_H (psi)	1000	0	1	∞	3.0 to 4.0

*Scaling Range: $20 \text{ kt} \leq W \leq 50 \text{ mt}$
 $10 \text{ psi} \leq P \leq 5000 \text{ psi}$
 $z \leq 50 \text{ ft}$

⁺ $v_H = v_V$ for $P < 300 \text{ psi}$

**When ranges of values are given, the uncertainties are largest for the lower overpressure, outrunning region; and smallest for the high overpressure, superseismic region.

Table IV-1.7. Surface burst hard rock peak air slap parameters (Reference IV-1.58).

$$\text{Environment Value} = \left(\frac{\text{Reference Value}}{\text{Value}} \right) \left(\frac{W}{1 \text{ mt}} \right)^A \left(\frac{P}{1000 \text{ psi}} \right)^B \exp \left[- \frac{z}{L_0} \right]$$

ENVIRONMENT PARAMETER	REFERENCE VALUE	SCALING FACTORS*			L_0 (ft)	2σ UNCERTAINTY FACTOR**
		A	B			
d_V (in)	1.3	1/3	0.4		∞	2.5
d_H (in)	1.3	1/3	0.4		∞	3.0
v_V (ips)	23	0	1		∞	2.5
v_H (ips)	30	0	1		∞	2.5 to 3.5
a_V (g's)	120	0	1		60	3.0
a_H (g's)	120	0	1		60	3.5 to 4.5
σ_V (psi)	1000	0	1		∞	2.0
σ_H (psi)	1000	0	1		∞	3.0 to 4.0

*Scaling Range: $20 \text{ kt} \leq W \leq 50 \text{ mt}$
 $20 \text{ psi} \leq P \leq 5000 \text{ psi}$
 $z \leq 50 \text{ ft}$

** When ranges of values are given, the uncertainties are largest for the lower overpressure, outrunning region; and smallest for the high overpressure, superseismic region.

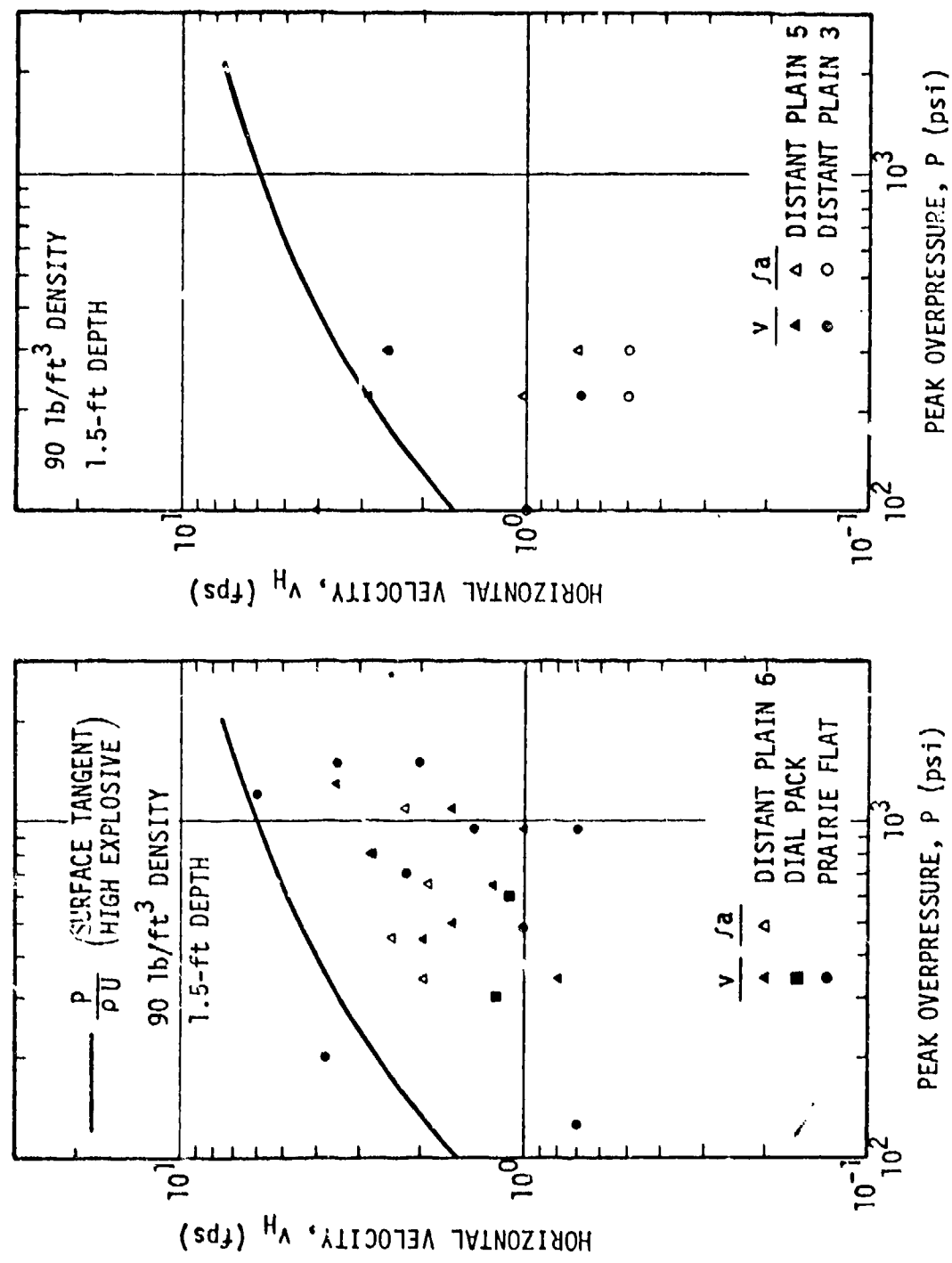


Figure IV-1-67. Peak air blast horizontal velocity high explosive test data.

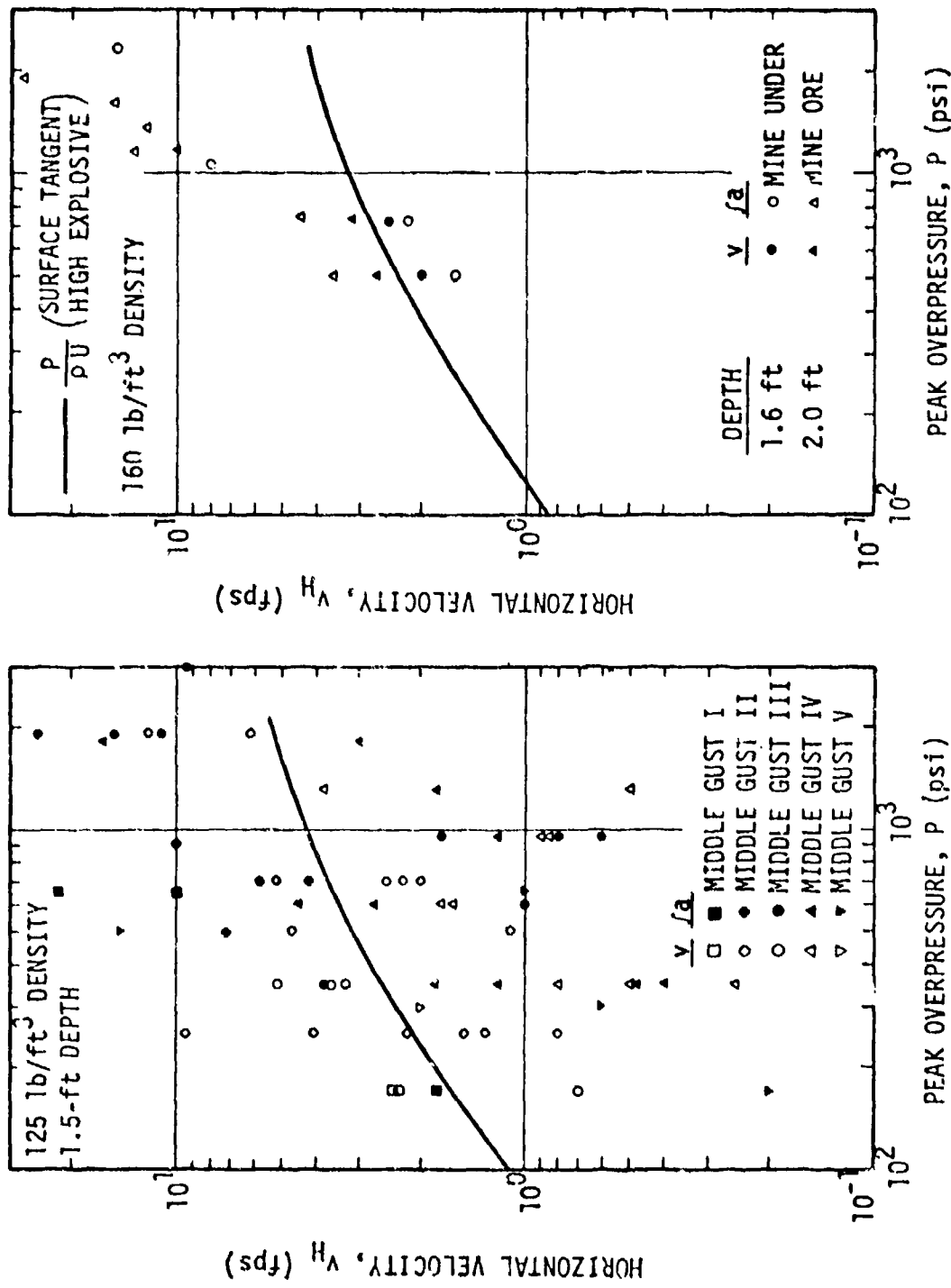


Figure IV-1.67. Peak air slap horizontal velocity high explosive test data (concluded).

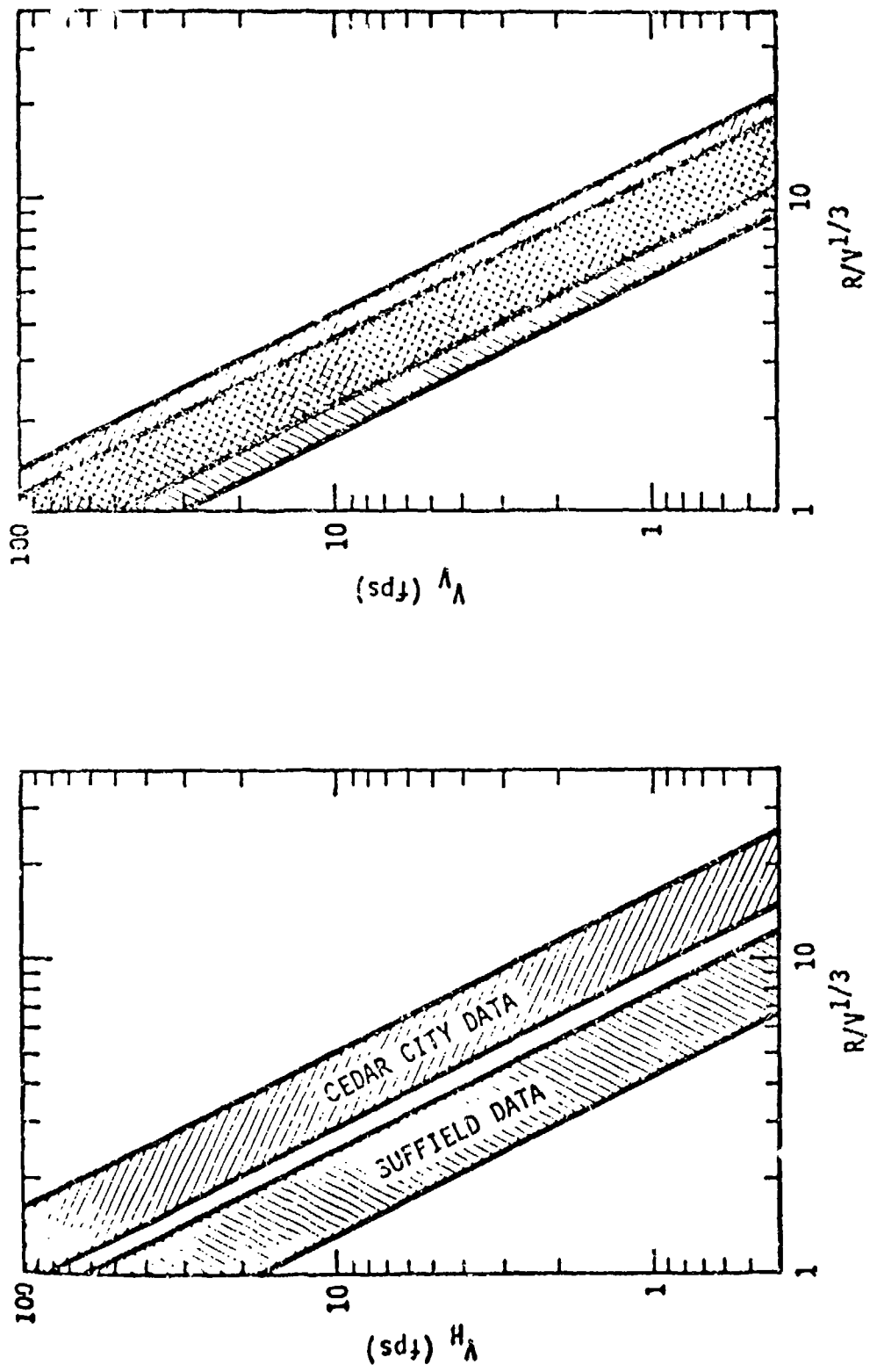


Figure IV-1-68. Comparison of crater-induced peak particle velocities from surface tangent HE events in Cedar City tonolite and DRES silt (Reference IV-1-2).

upward motions associated with direct induced and crater induced effects. Figure IV-1.69 (Reference IV-1.2) shows a comparison between vertical and horizontal scaled displacement data for DRES and Cedar City high explosive events, where close-in the crater-related effects dominate the response. The Cooper crater volume scaled peak horizontal displacement data are on the high side of the equation for the solid line in Figure IV-1.69. The vertical and horizontal peak displacements are approximately equal, with both data sets being essentially within scatter bands a factor of ten apart. Analysis of nuclear data, by Cooper, for above-surface bursts in the PPG shows much scatter in limited data, but the trend is consistent with horizontal and vertical displacements being equal.

Figure IV-1.70 shows the vertical and horizontal scaled displacements for the two 100-ton MIDDLE GUST (III and IV) and the 500-ton MIXED COMPANY surface tangent high explosive Events. Also shown, for comparison, are the scatter bands for the DRES and Cedar City data. These horizontal displacement data on the average agree with the prediction equation; however, a marked geology dependence is shown. The scaled displacements for MIXED COMPANY 3 (dry hard sandstone overlayed with soil) are the largest, with the MIDDLE GUST dry clay/shale site having nominal values and the MIDDLE GUST wet clay/shale site having the smallest values. The peak vertical displacements are about a factor of two lower than the horizontal with the same geological separation.

The MIDDLE GUST and MIXED COMPANY Events are the first significant tests in medium with strong near-surface impedance mismatches. Since many strategic sites of interest have strong layering features at comparable scaled depths, it is important to better define the effects of layering on ground shock response. Possibly geological correction factors to crater volume scaling could be determined.

Scaled displacement data for five of the eight 1000-lb calibration shots fired at various depths in the MIDDLE GUST wet site are shown in Figure IV-1.71. Surface tangent and half-buried conditions were obtained by excavating down to the depths of interest. The site is not as strongly layered, in a scaled sense, for these smaller high explosive charges; and data for the surface tangent events are slightly lower than, but in reasonable agreement with, the prediction equation. However, the half-buried event data are high compared with the prediction equation. Actually, the calibration data do not exhibit a difference in crater volume scaling between half-buried and surface tangent events (References IV-1.2 and 1.58).

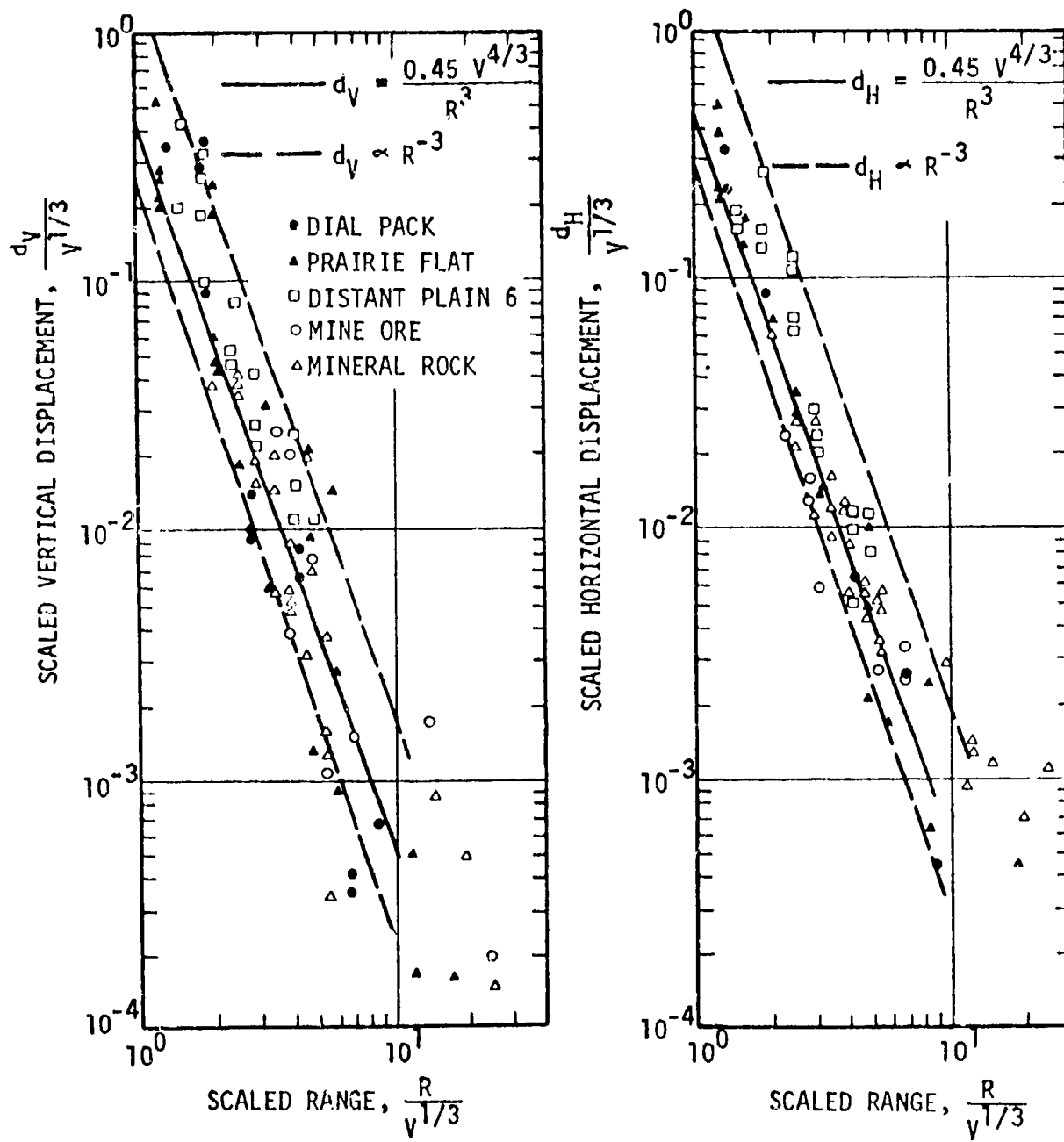


Figure IV-1.69. Crater volume scaled peak displacement correlation for surface tangent high explosive events at DRES and Cedar City (Reference IV-1.2).

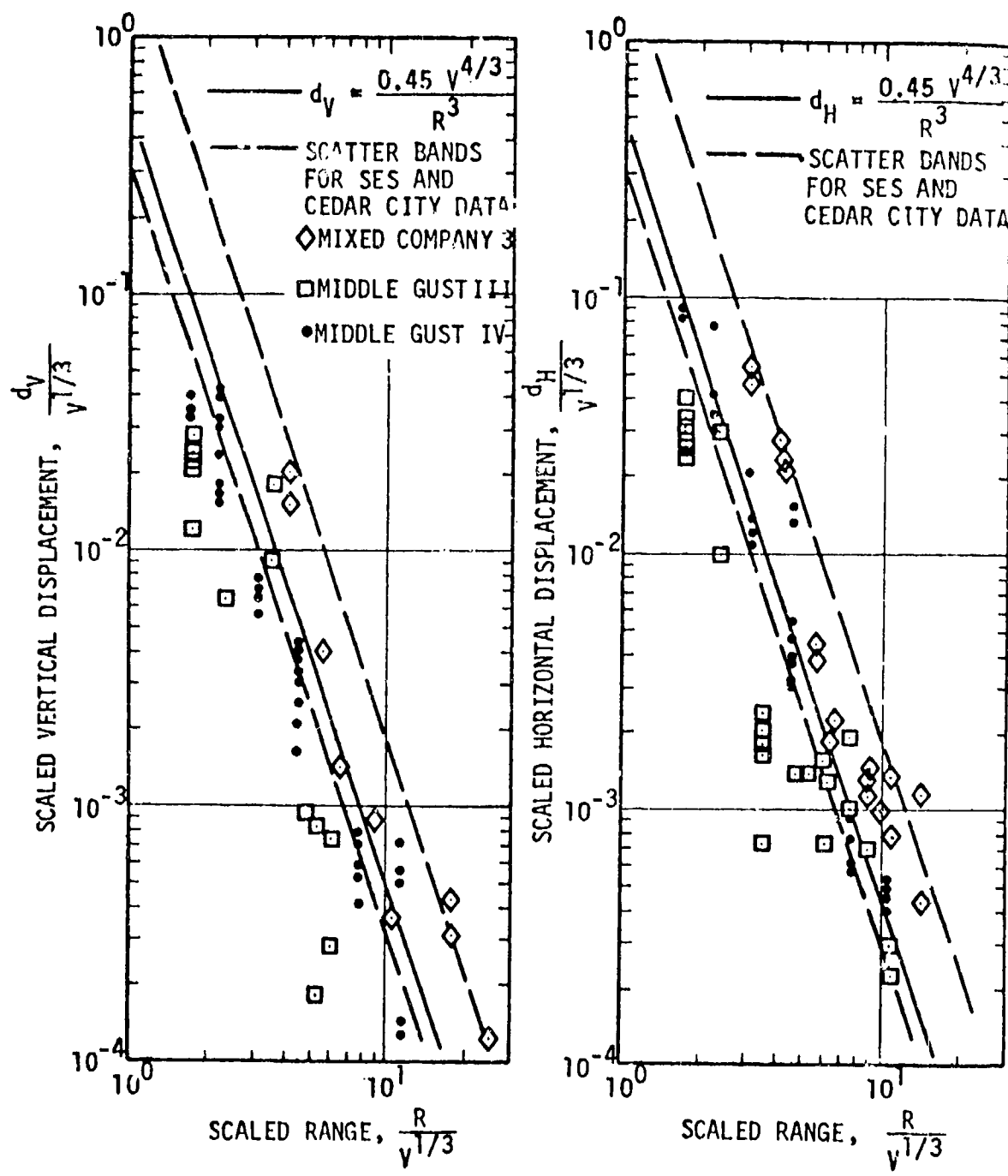


Figure IV-1.70. Crater volume scaled peak displacement correlation for large surface tangent high explosive events at MIDDLE GUST and MIXED COMPANY.

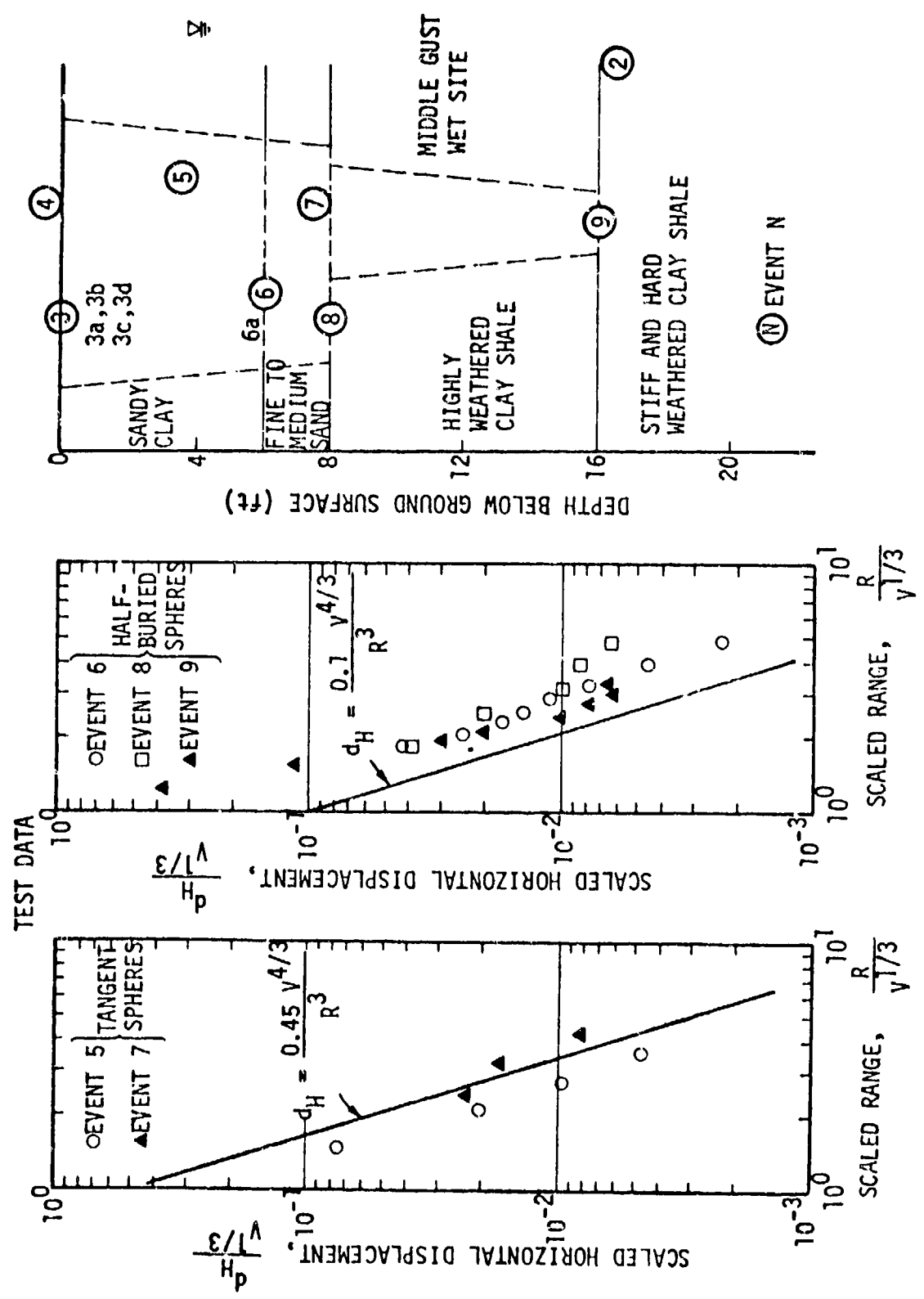


Figure IV-1-71. Crater volume scaled horizontal peak displacement correlation for MIDDLE GUST, wet site calibration events (Cooper, unpublished data analysis).

Test events generally have data for gauges from various depths. However, dimensional scaling considerations indicate that if the response is a function of depth, then it is more appropriate (for at least nearly homogeneous sites) to compare data from similar scaled depths. Figure IV-1.72 (Reference IV-1.59) shows that when DRES data for only the top $0.1 V^{1/3}$ are considered, then the scatter about the best fit line is considerably reduced. Figures IV-1.73 and IV-1.74 show these data for MIDDLE GUST IV and MIDDLE GUST III, respectively.

The vertical and horizontal near-surface ($<0.1 V^{1/3}$) velocity data for surface tangent events at DRES are shown in Figure IV-1.75 (Reference IV-1.2), plotted against scaled range. No trend separates the 500-ton PRAIRIE FLAT and DIAL PACK data from the 100-ton DISTANT PLAIN 6 data. In addition, vertical velocities are about a factor of two higher than the horizontal velocities. This difference is possible due to the fact that the direct-induced and crater-induced motions are initially caused by a refracted wave which has a front directed primarily upward. The Cedar City near-surface-tangent event velocity data are shown in Figure IV-1.76 along with the DRES data scatter bands. The horizontal velocity is larger than the vertical for these events, fielded in the much stiffer medium.

In order to determine geological effects, it is useful to compare data for events with comparable explosive sources and differing geological conditions (Reference IV-1.58). Figure IV-1.77 shows the velocity data for 100-ton surface tangent and near-surface-tangent events for conditions from soft soil to rock. The peak horizontal velocity for this charge configuration is not very dependent on geology, a trend also observed for air-slap-induced motions. Vertical velocities do depend on geology, being largest for the softest medium. The 20-ton half-buried events data (Figure IV-1.78) show horizontal velocities to be higher in the stiffer MIDDLE GUST sites. As the HOB decreases, this trend is expected since higher velocities have been observed in stiffer medium for fully buried detonations. However, the geological separation of the horizontal half-buried data is not large. The corresponding data for 1.0- and 0.9-diameter HOB 100-ton events are given in Figure IV-1.79.

The ground shock parameters recommended by Lipner, et. al. (Reference IV-1.58) for the four types of media discussed are shown in Table IV-1.8. This table gives Lipner's best estimate of the peak values for displacements, velocities, accelerations, and stresses, and includes scaling with weapon yield and ground range. Since scaled depths are within about $0.3 V^{1/3}$ for most of the conditions

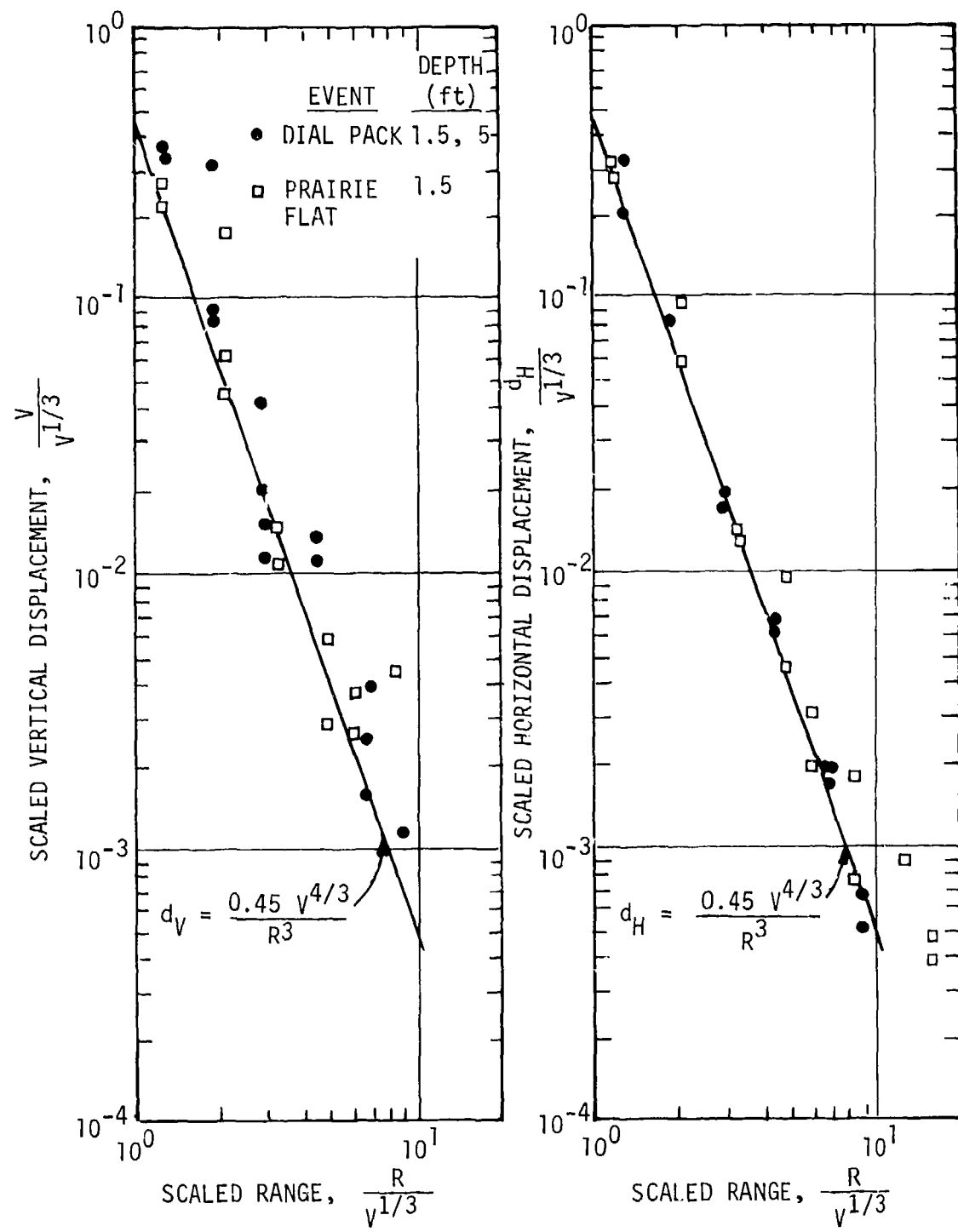


Figure IV-1.72. Crater volume scaled peak displacement correlation for top $0.1 V^{1/3}$ for DRES events (Reference IV-1.59).

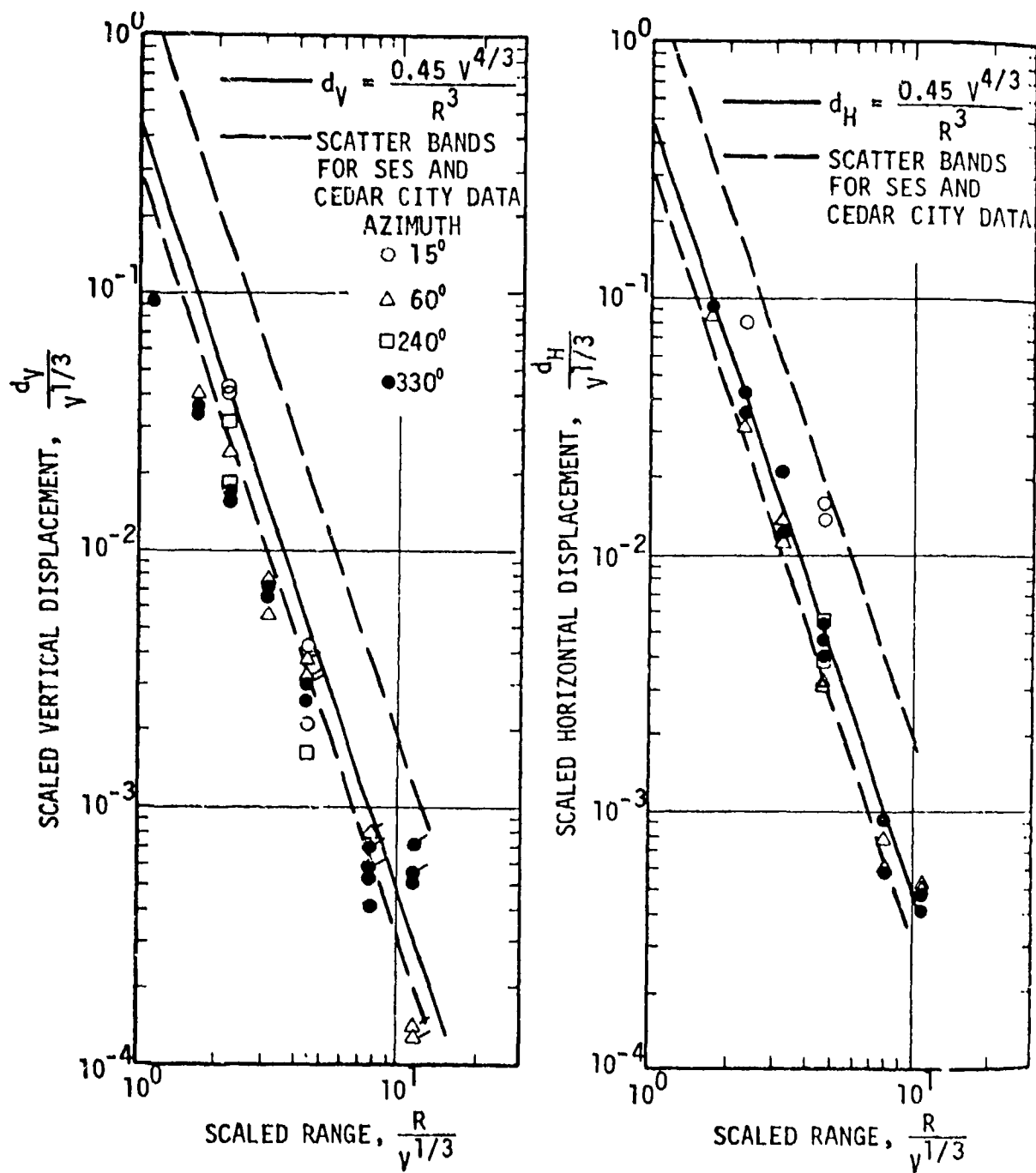


Figure IV-1.73. Crater volume scaled peak displacement correlation for top $0.1 V^{1/3}$ for MIDDLE GUST IV (Cooper, unpublished data analysis).

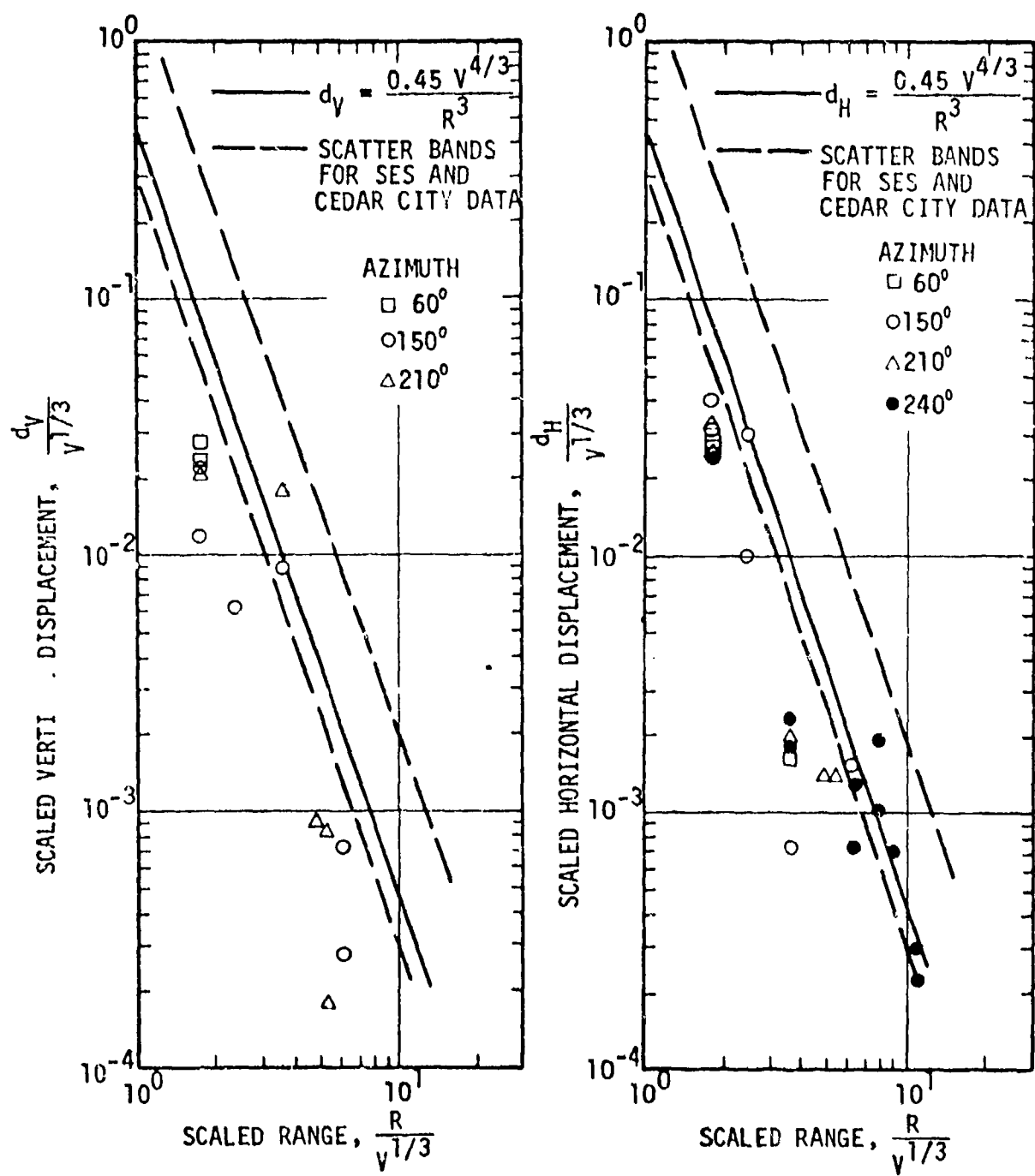


Figure IV-1.74. Crater volume scaled peak displacement correlation for MIDDLE GUST III (Cooper, unpublished data analysis).

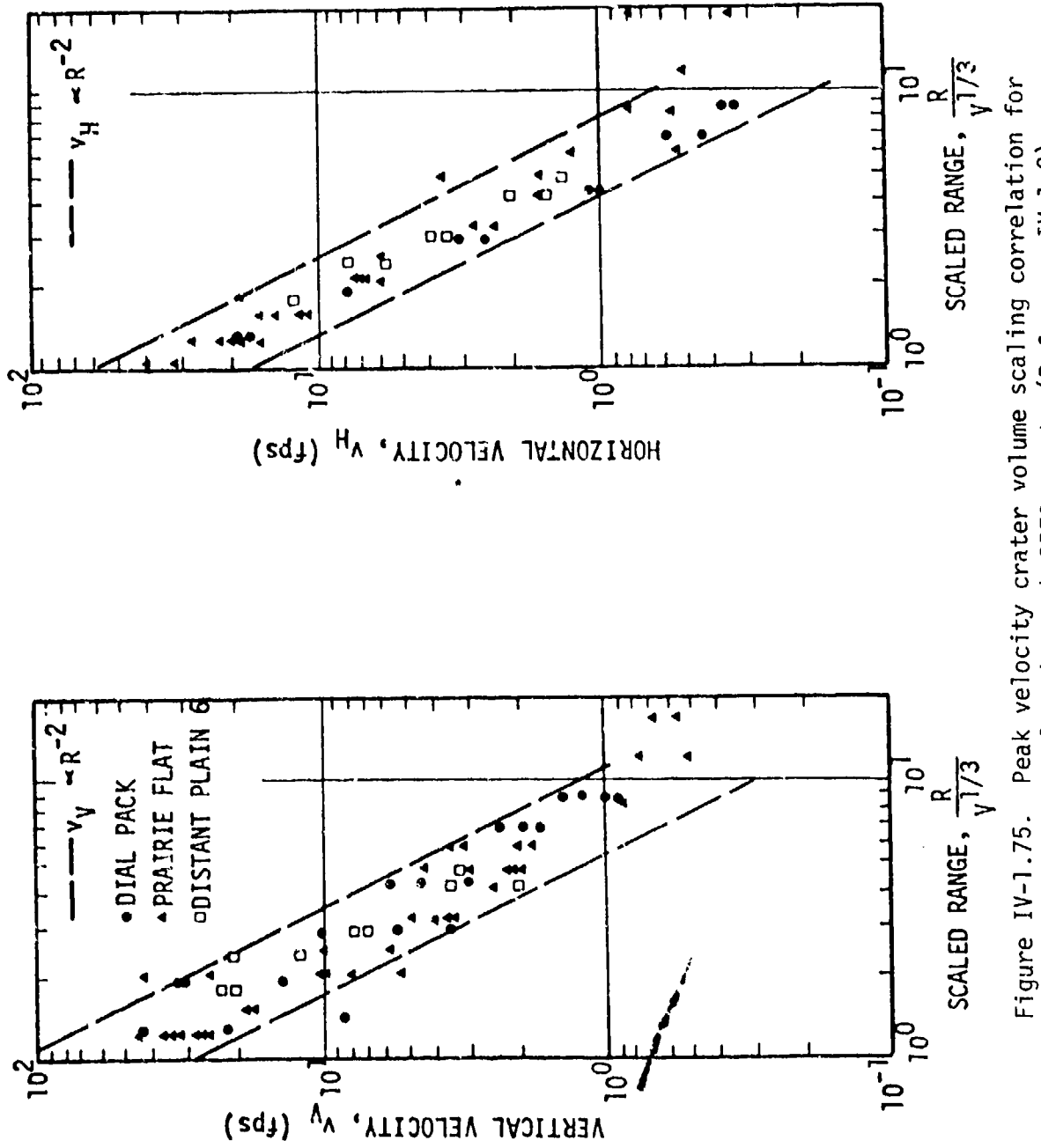


Figure IV-1.75. Peak velocity crater volume scaling correlation for surface tangent DRES events (Reference IV-1.2).

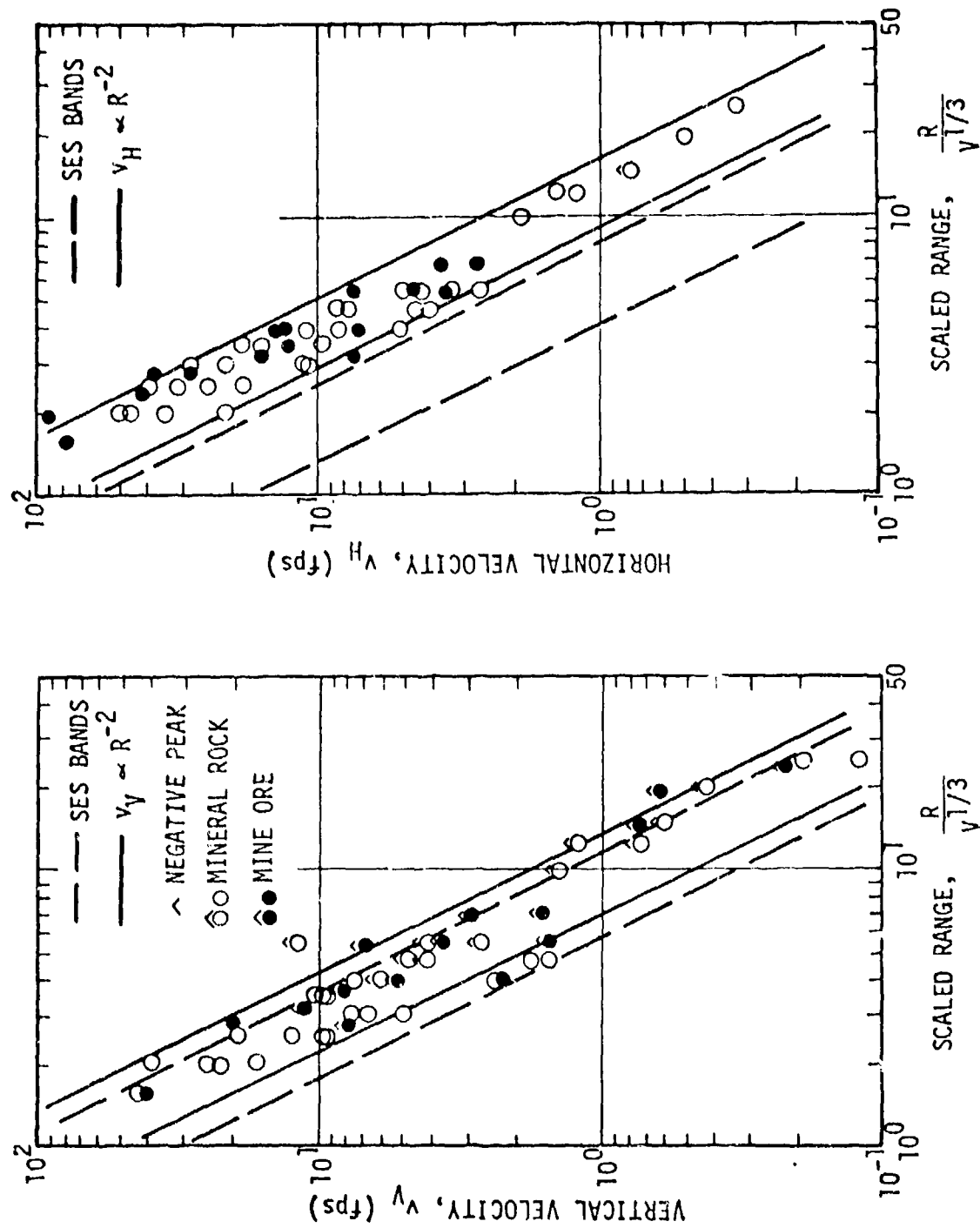


Figure IV-1.76. Velocity crater volume scaling correlation for near-surface tangent Cedar City events (Reference IV-1.2).

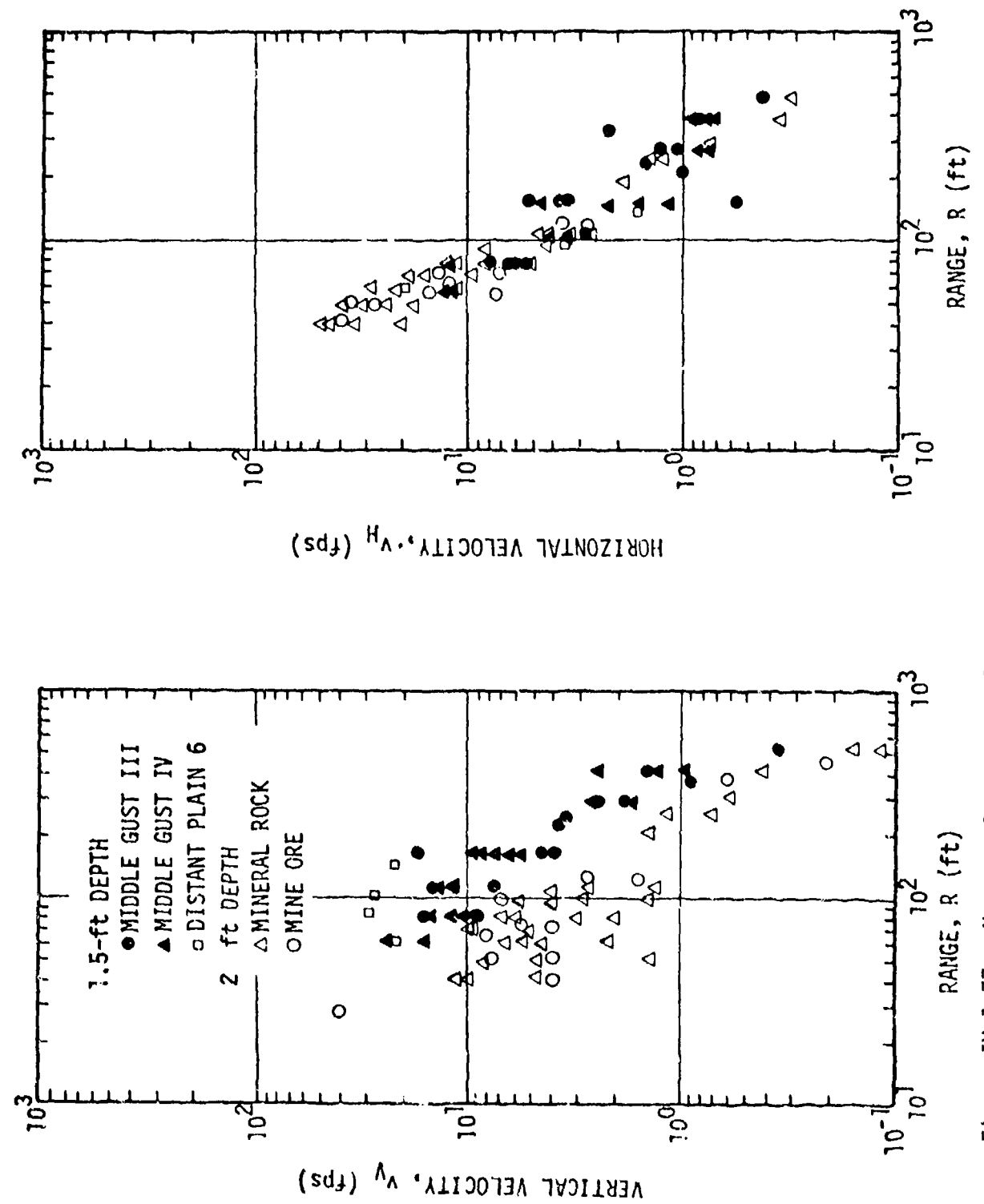


Figure IV-1.77. Near-surface peak velocity geology sensitivity for surface tangent 100-ton high explosive events (Reference IV-1.48).

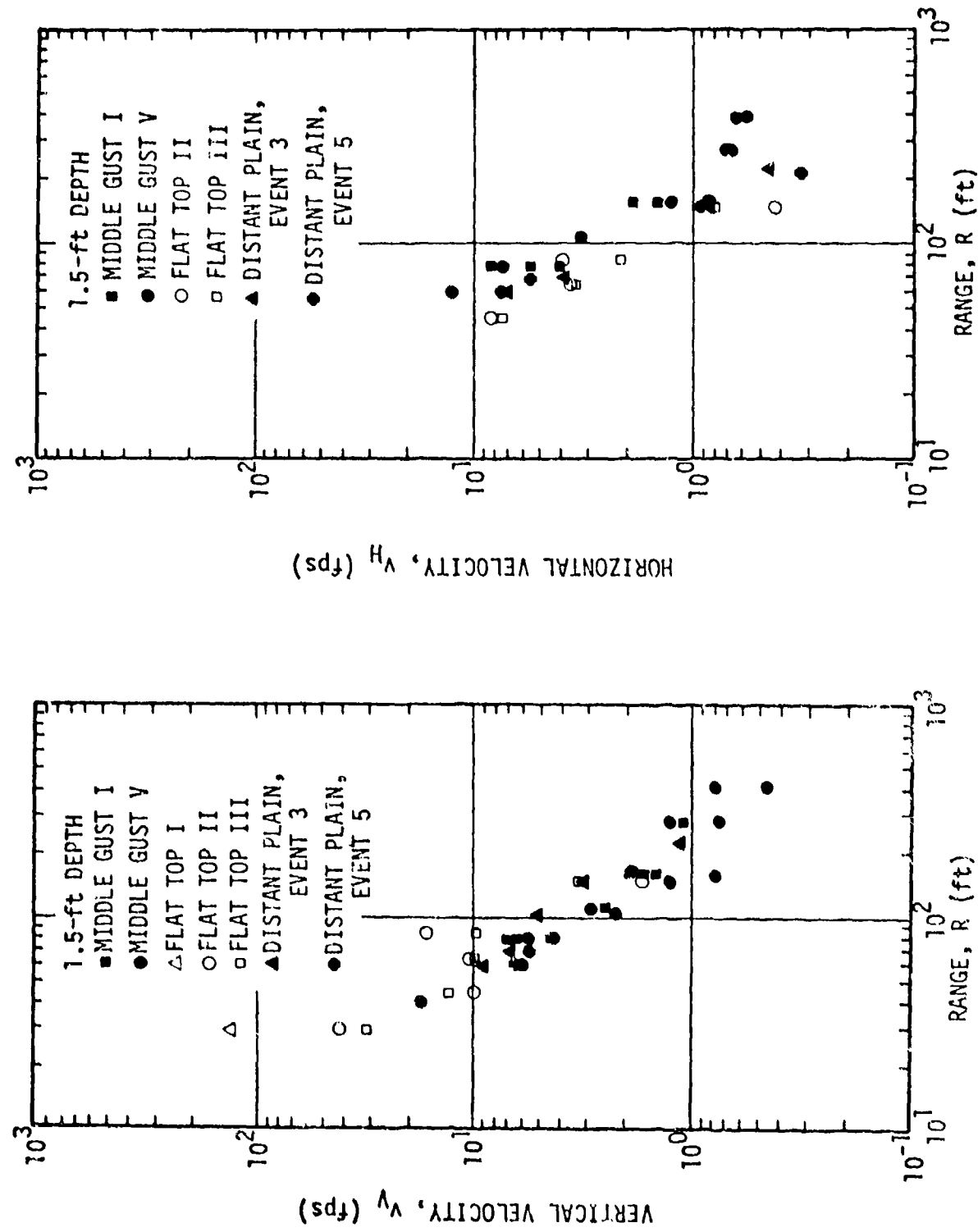


Figure IV-1-78. Near-surface peak velocity geology sensitivity for half-buried 20-ton high explosive events (Reference IV-1.48).

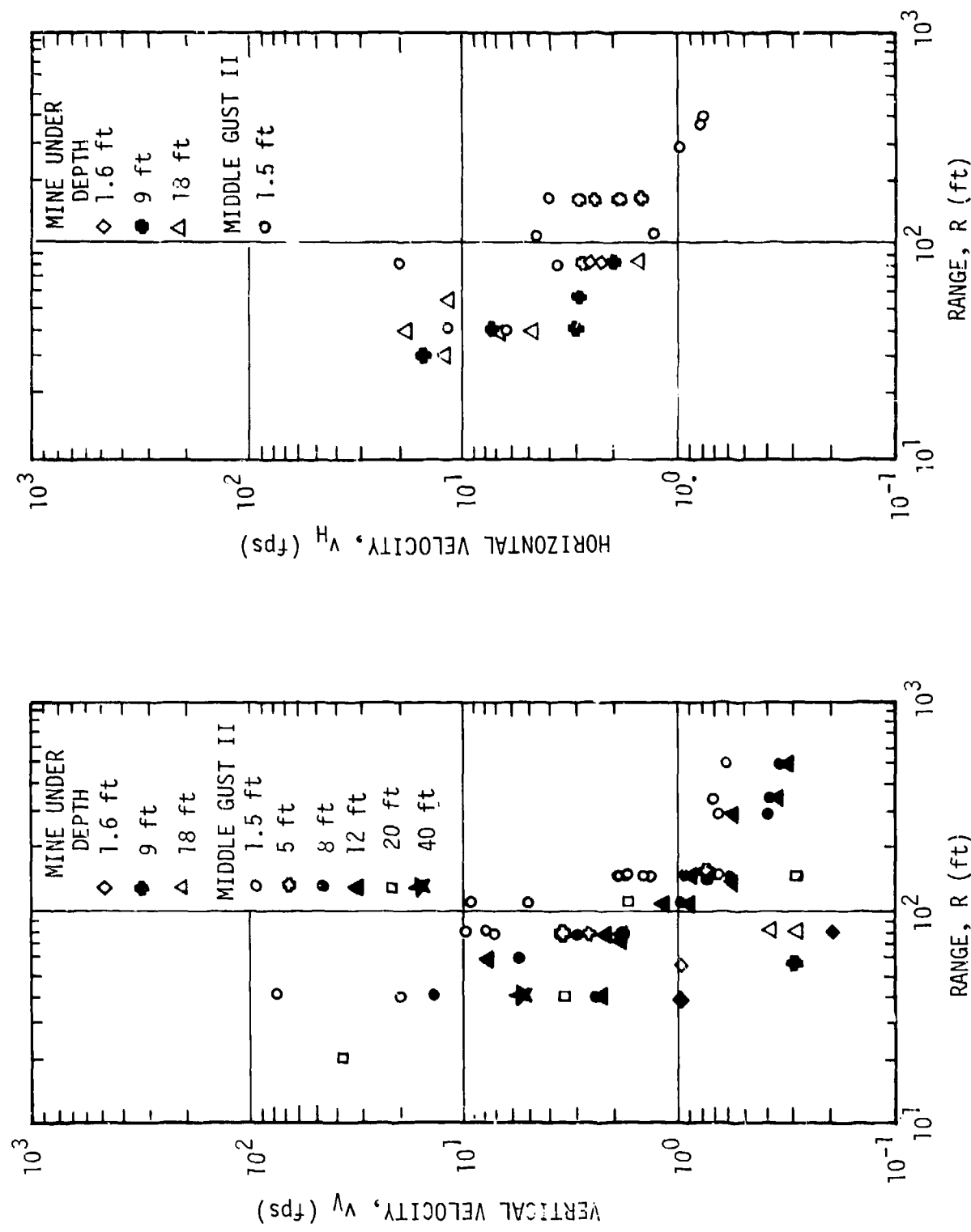


Figure IV-1.79. Peak velocity geology sensitivity for one-diameter 100-ton high explosive events (Reference IV-1.48).

OF
A
95096

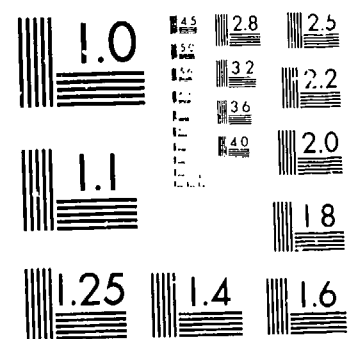


Table IV-1.8. Surface burst close-in peak-DI/CI parameters (Reference IV-1.58).

$$\text{Environment} = \left(\frac{\text{Value}}{\text{Reference Value}} \right) \left(\frac{W}{1 \text{ mt}} \right)^A \left(\frac{1000 \text{ ft}}{R} \right)^B$$

ENVIRONMENT PARAMETER	REFERENCE VALUE			SCALING FACTORS		2σ UNCERTAINTY FACTOR	
	Dry Soil	Wet Soil	Soft Rock	Hard Rock	A	B	
Crater Volume (10^6 ft^3)	50	170	40	30	1	0	1.8
Displacement (in)	100	510	75	50	4/3	3	3.5
Velocity (ips)	50	180	110	150	2/3	2	3.5
Acceleration (g's)	5	15	25	140	1	4	5
Stress (psi)	75	750	880	5000	2/3	2	4

considered in this study, no variation with depth is specified. The table also specifies 2σ uncertainty factor estimates.

Analysis of data from the high explosive events suffers from the difficulty of separating airblast-induced ground roll effects from direct-induced and crater-induced ground roll effects (Reference IV-1.5). Separation is particularly important if scaling techniques to predict nuclear motions are to be developed from the data, since source coupling effects are significantly enhanced in the high explosive tests. As previously discussed, the initial response in the outrunning region, for layered media, is usually associated with a refracted wave caused by upstream airblast sources. However, for relatively homogeneous media, outrunning occurs when the airblast slows down below the ground shock speed and the initial response is associated with a near-surface wave path. In both cases, the initial motion is upward and outward.

Analysis of the initial upward vertical velocity (v_1) for high explosive events at DRES, MIDDLE GUST, MIXED COMPANY, and Cedar City indicated the data to correlate best with cube root of yield scaling of range (Reference IV-1.60). The reference shows the specific data points for the individual events which indicate scatter bands varying from a factor of about 1.5 up and down for MIDDLE GUST II and III to a factor of about 2.5 for MIXED COMPANY 2 and 3. Separating near-surface from deeper gauge data did not help reduce the scatter. The DISTANT PLAIN 6 100-ton-event data were significantly lower than the 500-ton DRES events and were not included in the best fit. However, the scatter bands for MIXED COMPANY contained most of the DISTANT PLAIN 6 data. The initial peak decay with range varies from $R^{-1.5}$ to $R^{-1.65}$. Higgins and Schreuer (Reference IV-1.60) indicate that an $R^{-1.5}$ decay is representative of most of the data. Figure IV-1.80 shows the fits to the data of Reference IV-1.60.

For the layered sites, the initial peak velocity is approximately proportional to the propagation velocity (phase velocity) of outrunning motions. These phase velocities (References IV-1.58 and IV-1.60) are about 11,000 fps for the MIDDLE GUST wet site; 10,500 to 13,500 fps for the MIXED COMPANY site; and 5,500 fps for the DRES site.

The initial peak velocities for the Cedar City events are significantly below the MIXED COMPANY and MIDDLE GUST data even though the outrunning propagation velocities are comparable. The Cedar City site is a fairly homogeneous medium with outrunning being initiated at the surface. Therefore, the initial peak upward

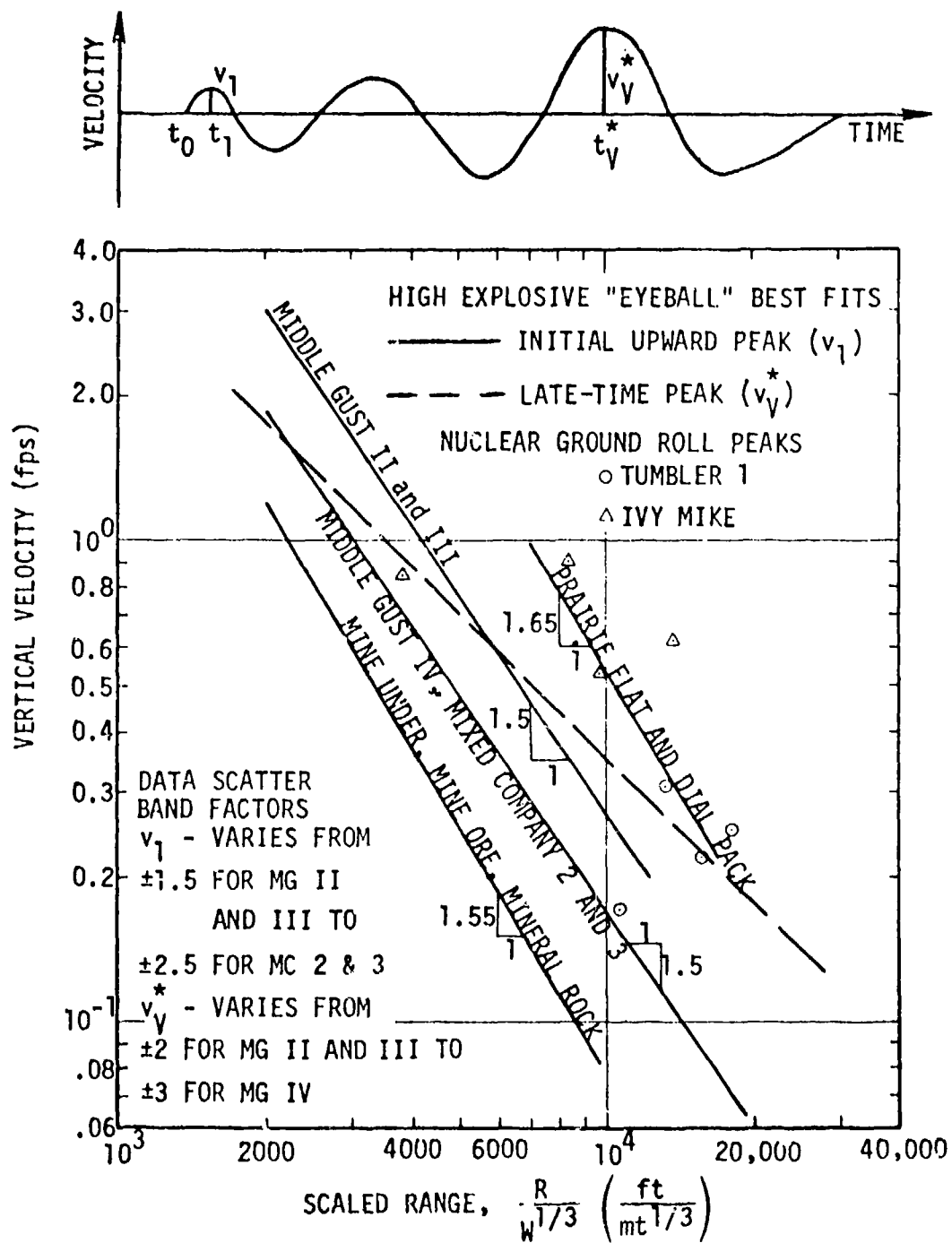


Figure IV-1.80. High explosive outrunning vertical velocity peak attenuation and nuclear data comparison (Reference IV-1.60).

velocity may not be as large as if it were due to a refracted wave whose wave front normal is more vertical. The jointing of the medium at Cedar City resulted in direction-dependent wave speeds of 8800 fps for propagation perpendicular to the jointing and 11,000 fps in the parallel direction. The direction of propagation did not appear to significantly affect the initial peak vertical velocity, however, the horizontal response exhibited propagation direction-associated differences. Additional analysis of vertical refracted wave velocity peaks for MIDDLE GUST is presented in Reference IV-1.61. This analysis indicates that the velocities normalized to a layer impedance factor correlate well with wave path length for a given event.

The analysis of Reference IV-1.60 indicates that the late-time peak ground roll velocities were not very geology dependent. The late-time peak vertical velocities attenuate slightly faster than R^{-1} and the data scatter varies from a factor of about 2 up and down for MIDDLE GUST II and III to a factor of about 3 for MIDDLE GUST IV and the Cedar City events, as discussed in the reference. A comparison of data for approximately surface tangent and one-diameter HOB conditions at the MIDDLE GUST wet site (Events II and III) with the Cedar City (MINE UNDER and MINE ORE or MINERAL ROCK) site did not show a significant HOB dependence for the vertical response at a given test site.

The horizontal ground roll response is more complex than the vertical and has not been analyzed quite as extensively in References IV-1.58 and IV-1.60. The horizontal ground roll velocity response at MIDDLE GUST III was more severe and more rapidly attenuating than the corresponding response at MIDDLE GUST II, indicating a probable HOB effect associated with the close-in coupling for this motion component. A similar behavior was also observed for the Cedar City events.

The analysis of the high explosive data in Reference IV-1.60 considers only the peak velocity, which generally occurred on the initial pulse rather than both the initial and late time peaks. The analyses of both References IV-1.60 and IV-1.62 indicate that the initial peak horizontal velocity in the outrunning region is due to both airblast-induced and direct-induced effects; therefore, it would have an HOB dependence (Reference IV-1.58).

At the maximum scaled range of interest ($10^4 \text{ ft}/\text{mt}^{1/3}$) the peak horizontal velocities for all events are on the order of 0.3 ft/sec except for the 0.9 diameter HOB MINE UNDER Event which was about a factor of two lower. The horizontal and vertical late time peak velocities are about equal for this maximum scaled

range with the primary differences between the two components occurring in the initial peaks. The maximum horizontal velocity decayed with range ($R^{-1.4}$ to $R^{-2.0}$ for various events) more steeply than the initial vertical velocity ($R^{-1.5}$ to $R^{-1.65}$ for various events) possibly because the faster attenuating direct-induced effects had more influence on the horizontal.

Peak displacement data for the outrunning region for NTS events are analyzed in Reference IV-1.16. The analysis indicates that the displacements shown in Figure IV-1.81 follows $W^{1/3}$ scaling. In the outrunning region data for airbursts, surface contact bursts, and optimum depth-of-burial bursts all attenuated as R^{-1} . The airburst data are about a factor of 1.8 lower than the surface contact burst data, with the depth-of-burial burst data a factor of 2.6 higher. Thus, in each of these cases the phenomenology should be similar since the attenuation rates are the same, the primary difference being the amount of energy causing the motions.

The ground roll motion predictions recommended by Lipner, et. al. (Reference IV-1.58) for the four types of media discussed are given in Table IV-1.9. Again 2σ uncertainty factor estimates are specified.

IV-1.8.4 Summary

The data creditability and repeatability depend on:

- (1) Instrumentation reproducibility,
- (2) Variations in gauge placement, recording, data reduction, etc.,
- (3) Repeatability of experiments, and
- (4) Azimuthal variations around ground zero.

Although measurement errors contribute to the scatter in the data, in situ inhomogeneties probably are the dominant source of observed variations on a given well instrumented experiment. This implies that since experiments and test sites are usually carefully selected, previously observed scatter in the data may be less than could occur for randomly selected test sites. Therefore, the uncertainty implied by the scatter in the data (factor of 2 to 4) is probably a lower bound estimate of the variation that might be expected from nuclear surface bursts on sites of strategic interest (Reference IV-1.2).

A substantial data base exists for the evaluation of near-surface, early-time, airslap-induced vertical motions in soil and rock. At the earth's surface, $a_v \approx \Delta P_s$, where a_v is the vertical acceleration in g's and ΔP_s is the overpressure

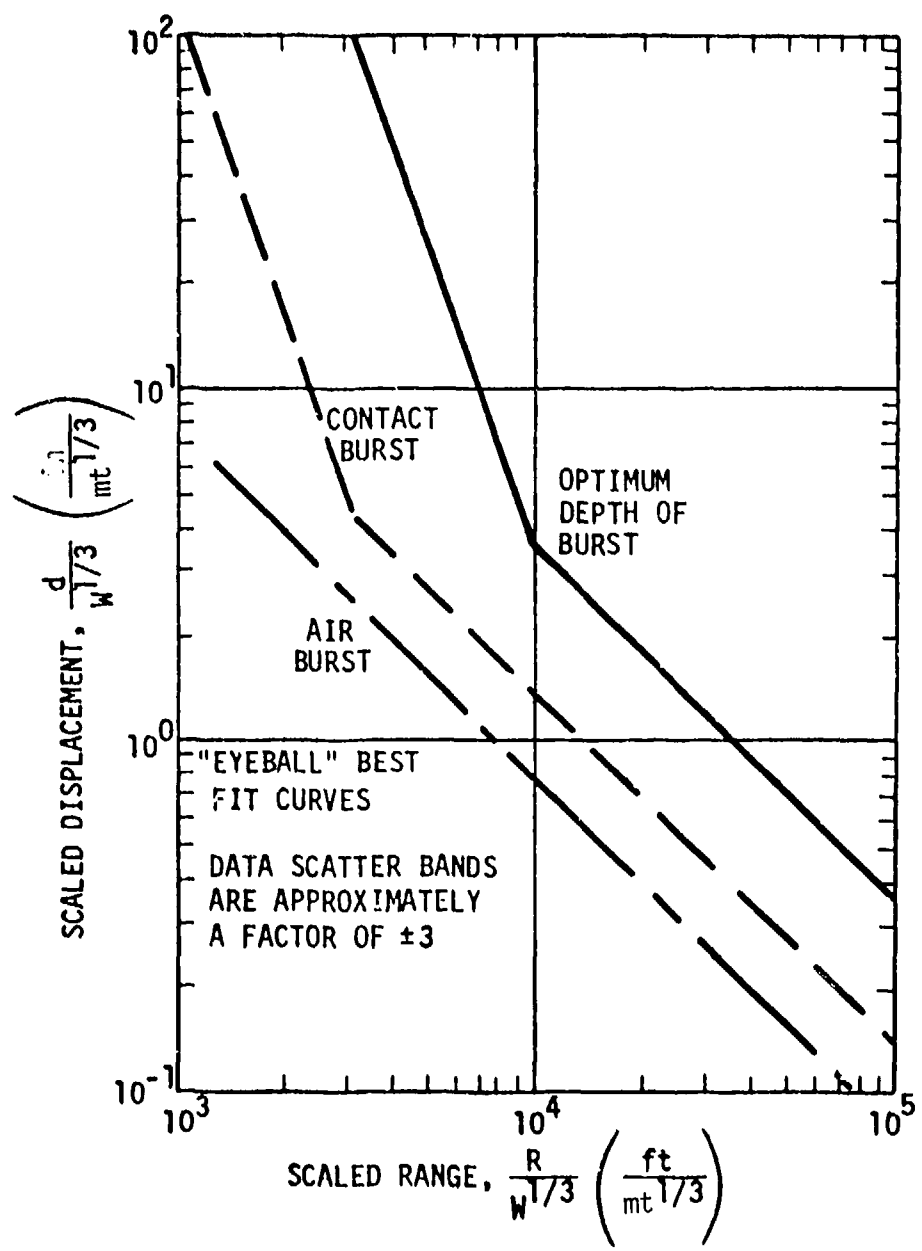


Figure IV-1.81. HOB effects on outrunning peak vertical displacements for NTS events
(Reference IV-1.16).

Table IV-1.9. Surface burst peak ground roll parameters (Reference IV-1.58).

$$\text{Environment} = (\text{Reference}) \left(\frac{\text{Value}}{\text{Value}} \right)^A \left(\frac{W}{R} \right)^B$$

PREDICTION PARAMETER	ENVIRONMENT PARAMETER	GENERIC SITE			SCALING FACTORS
		Dry Soil	Wet Soil	Soft Rock	
REFERENCE VALUE	Displacement (in)	1.5	1.5	0.6	0.6
	Velocity (ips)	6.0	6.0	2.4	2/3
2 σ UNCERTAINTY FACTOR	Displacement	3.5	4.0	5.0	1/2
	Velocity	3.5	3.5	4.0	3/2

in psi, and $v \approx \Delta P_s / \rho C_p$. One dimensional wave propagation theory should be used to predict peak displacements, waveforms, and depth-attenuation rates. Airslap-induced vertical motions are thought to be predictable to within a factor of 2 (Reference IV-1.2).

Qualitative low-frequency features for close-in ($R \leq 5V^{1/3}$) near-surface particle velocity waveforms from cratering explosions do not appear to vary as a function of the geology. The crater-induced peak particle velocities attenuate approximately as R^{-2} with the exception of MINE THROW IV. The crater-induced peak displacements attenuate approximately as R^{-3} . The greatest uncertainty in predicting crater-induced ground motions is associated with scaling the velocity amplitudes and the time characteristics.

Many qualitative features of low-frequency ground motion in the outrunning and ground roll regions appear to be relatively independent of details of the source geometry. Ground motion waveforms consist of a low-frequency surface wavetrain on which is superimposed the high-frequency airslap-related signals. There appears to be a transition region between the close-in region where crater-induced phenomena dominate and the farther-out region where classical surface-wave phenomena exist. The attenuation of the ground motion with increasing range in this transition region is substantially less than in the close-in or far-out regions. In fact, the ground motion amplitudes sometimes appear to increase with increasing range in this transition region.

IV-1.9 REFERENCES

- IV-1.1 Crawford, R. E., C. J. Higgins, and E. H. Bultman, The Air Force Manual for Design and Analysis of Hardened Structures, Civil Nuclear Systems Corporation, Albuquerque, New Mexico, Report No. AFWL-TR-74-102, October 1974.
- IV-1.2 Cooper, H. F., Jr., A Review of Ground Motion from Nuclear and High-Explosive Experiments, Strategic Structures Review Meeting held at SRI, Menlo Park, California, 19-20 February 1975.
- IV-1.3 Bertholf, L. D., and S. E. Benzley, Toody II, A Computer Program for Two-Dimensional Wave Propagation, Sandia Laboratories, Albuquerque, New Mexico, Report No. SC-PR-68-41, 1968.
- IV-1.4 Trulio, J. G., Theory and Structure of the AFTON Codes, Air Force Weapons Laboratory, Albuquerque, New Mexico, Report No. AFWL-TR-66-19, June 1966.
- IV-1.5 Belytochko, R. L. Chiapetta, and J. D. Rouse, A Computer Code for Dynamic Stress Analysis of Structure-Media Problems with Nonlinearities (SAMSON), 4 Vols, Air Force Weapons Laboratory, Albuquerque, New Mexico, Report No. AFWL-TR-72-104, February 1973.
- IV-1.6 Cooper, H. F., Jr., Empirical Studies of Ground Shock and Strong Motions in Rock, R&D Associates, Marina Del Rey, California, Report No. DNA 3245F (RDA-TR-3601-002), October 1973.
- IV-1.7 Kurtz, S. R., "A Back-of-the-Envelope Approach to Predicting Ground Motion Phenomena," J.G.R., Vol. 80, No. 32, 4449-4460, November 10, 1975.
- IV-1.8 Feynman, R. P., R. B. Leighton, and M. Sands, The Feynman Lectures on Physics, Vol. II, Chapter 39, Addison Wesley, Massachusetts, 1964.
- IV-1.9 Butkovich, T. R., and A. E. Lewis, Aids for Estimating Effects of Underground Nuclear Explosions, UCRL-50929, Rev. 1, February 23, 1973.
- IV-1.10 Tolstoy, I., Wave Propagation, McGraw-Hill Book Company, 1973.
- IV-1.11 Kolsky, H., Stress Waves in Solids, Dover Publications, Inc., New York, 1963.
- IV-1.12 Lindsay, R. B., Mechanical Radiation, McGraw-Hill Book Company, Inc., 1960.

- IV-1.13 Rodean, H. C., Nuclear-Explosion Seismology, U.S. Atomic Energy Commission, Division of Technical Information, Report TID-25572, 1971.
- IV-1.14 Brode, H. L., Initial Cratering and Ground Shock Action-Some Implications for High Yield Weapon Employment and Superhard Design, RAND (Unpublished).
- IV-1.15 Brode, H. L., and R. L. Bjork, Cratering from a Megaton Surface Burst, June 20, 1960.
- IV-1.16 Cooper, H. F., Jr., Height-of-Burst Effects on Strong-Motion Seismic Ground Motions from Nuclear Air Burst Explosions, R&D Associates, Marina Del Rey, California, Report No. RDA-TR-063-DNA, June 1972.
- IV-1.17 Whitman, R. V., The Response of Soils to Dynamic Loadings, U.S. Army Engineer Waterways Experiment Station, Vicksburg, Mississippi, Report No. 3-26, May 1970.
- IV-1.18 Ewing, Jaredetsky, and Press, Elastic Waves in Layered Media, New York, McGraw Hill Book Co., Inc., 1957.
- IV-1.19 Brode, H. L., "Review of Nuclear Weapons Effects," Annual Review of Nuclear Science, Vol. 18, 1968.
- IV-1.20 Grant, F. S., and G. F. West, Interpretation Theory in Applied Geophysics, McGraw-Hill Book Company, New York, New York, 1965.
- IV-1.21 Salmon, V., and S. R. Hornig, Earth Acceleration vs Time and Distance, SRI, Operation TUMBLER, WT-517, February 1953.
- IV-1.22 Newmark, N. M., and J. D. Haltiwanger, Principles and Practices for Design of Hardened Structures, Air Force Weapons Laboratory, Albuquerque, New Mexico, Report No. SWC-TDR-62-133, December 1962.
- IV-1.23 Newmark, N. M., and W. J. Hall, Preliminary Design Methods for Underground Protective Structures, Air Force Special Weapons Center, Albuquerque, New Mexico (Unpublished).
- IV-1.24 Perret, W. R., Ground Motion Studies on Operation IVY and CASTLE, Sandia Corporation (Unpublished).
- IV-1.25 Moulton, James F., et al., Nuclear Weapons Blast Phenomena (Unpublished).
- IV-1.26 Sauer, F. M., Ground Motion Produced by Aboveground Nuclear Explosions, SRI (Unpublished).

- IV-1.27 Swift, L. M., D. C. Sachs, and F. M. Sauer, Ground Motion Produced by Nuclear Detonations, SRI (Unpublished).
- IV-1.28 Neidhard, G. L., Analysis of Free-Field Data in a Half-Space Under Dynamic Loads, Air Force Weapons Laboratory, Albuquerque, New Mexico, Report No. AFWL-TR-64-143, April 1964.
- IV-1.29 Swift, L. M., and J. D. Eisler, Close-In Earth Motion, SRI (Unpublished).
- IV-1.30 Pinkston, J. M. , Jr., Earth Motion Measurements, WES (Unpublished).
- IV-1.31 Cooper, H., and J. Bratton, Calculation of Vertical Airblast-Induced Ground Motions from Nuclear Explosions in Frenchman Flat, AFWL-TR-73-111, October 1973.
- IV-1.32 Swift, L. M., D. C. Sachs, and F. M. Sauer, Ground Acceleration, Stress and Strain at High Incident Overpressures, SRI, Operation PLUMBOB, WT-1404, May 10, 1960.
- IV-1.33 Perret, W. R., Ground Motion Studies at High Incident Overpressure, Sandia Corporation, Operation PLUMBOB, WT-1405, 1960.
- IV-1.34 Newmark, N. M., and W. J. Hall, Preliminary Design Methods for Underground Protective Structures, University of Illinois (Unpublished).
- IV-1.35 Newmark, N. M., and W. J. Hall, Preliminary Design Methods for Underground Structures, University of Illinois (Unpublished).
- IV-1.36 Swift, L.M., and J. D. Eisler, Close-In Earth Motion, Operation SUNBEAM, Shot SMALL BOY, SRI (Unpublished).
- IV-1.37 Perret, W. R., Ground Motion Induced by a Near-Surface Explosion, Operation SUNBEAM, Shot SMALL BOY, Sandia Corporation (Unpublished).
- IV-1.38 Sauer, F. M., An Improved Prediction Method for the Attenuation of Vertical Airblast-Induced Particle Velocity in Alluvium (Unpublished).
- IV-1.39 Brode, H. L., Height of Burst Effects at High Overpressures, The RAND Corporation, Report No. RM-6301-DASA, DASA 2506, July 1970.
- IV-1.40 Landau, L. D., and E. M. Lifshitz, Theory of Elasticity, Vol. 7 of Course in Theoretical Physics, Second Edition, Pergamon Press, 1970.
- IV-1.41 Bultman, E. H., G.F. McDonough, and G.K. Sinnamon, Loading on Simulated Buried Structures at High Incident Overpressure, University of Illinois and AFSWC (Unpublished).

- IV-1-42 Wilson and Sibley, "Ground Displacements from Air-Blast Loading," Proc. ASCE, Vol. 88, No. SM6, December 1962, Part 1, pp 1-31.
- IV-1-43 Epure, S. T., J. Dastor, and R. Frankian, A Guide for the Design of Shock Isolation Systems for Underground Protective Structures, Ralph M. Parsons Corporation, Project 1080, Task 10803, AF 29(601)-4551, AFSWC-TDR-62-64, December 1962.
- IV-1-44 Cook, M. A., The Science of High Explosives, Robert E. Krieger Publishing Co., Inc., Huntington, New York, 1971.
- IV-1-45 Joachim, C. E., Mine Shaft Series, Events Mine Under and Mine Ore: Subtask SS222, Ground Motion and Stress Measurements, U.S. Army Engineer Waterways Experiment Station, Vicksburg, Mississippi, Technical Report N-72-1, January 1972.
- IV-1-46 Murrell, D. W., Operation Mine Shaft - Mineral Rock Event, Far-Out Ground Motions from a 100-ton Detonation over Granite, U.S. Army Engineer Waterways Experiment Station, Vicksburg, Mississippi, Technical Report N-72-6, April 1972.
- IV-1-47 Proceedings of the MIXED COMPANY/MIDDLE GUST Results Meeting 13-15 March 1973, - Volume II, Sessions 2B and 3B, Defense Nuclear Agency, Report No. DNA 3151P2, 1 May 1973.
- IV-1-48 Jaramillo, E. E., and R. E. Pozega, MIDDLE GUST Free-Field Data Analysis, Air Force Weapons Laboratory, Report No. AFWL-TR-73-251, April 1974.
- IV-1-49 Murrell, D. W., Operation DIAL PACK - Project LN 305: Earth Motion and Stress Measurements in the Outrunning Region, U.S. Army Engineer Waterways Experiment Station, Technical Report No. N-73-4, May 1973.
- IV-1-50 Murrell, D. W., Earth Motion and Stress Measurements, Project LN 302, Operation DIAL PACK, U.S. Army Engineer Waterways Experiment Station, Technical Report No. N-74-3, April 1974.
- IV-1-51 Ferritto, J. M., and J. B. Forrest, Ground Motions from Pacific Cratering Experiments 1,000-Pound Explosive Shots, U.S. Naval Civil Engineering Laboratory, Naval Construction Battalion Center, Port Hueneme, California, Technical Report R 808, January 1975.

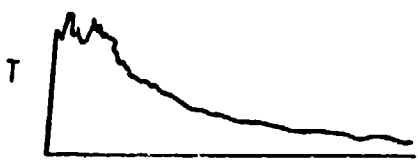
- IV-1.52 Murrell, D. W., and H. D. Carlton, Operation MINE SHAFT, Ground Shock from Underground and Surface Explosions in Granite, U.S. Army Engineer Waterways Experiment Station, Report Nos. MS-2159 and MS-2160, April 1973.
- IV-1.53 Ingram, L. F., Ground Motions from High Explosive Experiments, U.S. Army Engineer Waterways Experiment Station, Miscellaneous Paper N-72-10, December 1972.
- IV-1.54 Cooper, H. F., H. L. Brode, and G. G. Leigh, Some Fundamental Aspects of Nuclear Weapons, Presented at NATO Defense Research Group Seminar on System Concepts for Hardening of Military Installations, Bodo, Norway, 14-16 September 1971.
- IV-1.55 Cooper, H. F., H. L. Brode, and G. G. Leigh, Some Fundamental Aspects of Nuclear Weapons, Air Force Weapons Laboratory, Albuquerque, New Mexico, Report No. AFWL-TR-72-19, March 1972.
- IV-1.56 Murrell, D. W. Operation PRAIRIE FLAT, Project LN-302: Earth Motion and Stress Measurements, U.S. Army Engineer Waterways Experiment Station, Vicksburg, Mississippi, Report No. TR-N-72-2, February 1972.
- IV-1.57 Hoffman, H. V., F. M. Sauer, and B. Barclay, Operation PRAIRIE FLAT, Project LN-308: Strong Ground Measurements, Stanford Research Institute, Menlo Park, California, Report No. POR-2108, 5 April 1971.
- IV-1.58 Lipner, N., D. C. Anderson, and P. K. Dai, Ground Motion Environments for Generic Site Conditions, TRW, Redondo Beach, California, Report No. 26128-6004-RU-00, 31 December 1975.
- IV-1.59 Cooper, H. F., On the Prediction of Crater Volumes and Crater-Induced Ground Motions from Nuclear Explosions, R&D Associates, Marina Del Rey, California, Report No. RDA-TR-193-DNA, 23 April 1973.
- IV-1.60 Higgins, C. J., and H. L. Schreyer, An Analysis of Outrunning Ground Motions, Air Force Weapons Laboratory, Albuquerque, New Mexico, AFWL-TR-72-220, July 1974.
- IV-1.61 Palaniswamy, K., and J. L. Merritt, Inferred In-Site Uniaxial Stress-Strain Curves for MIDDLE GUST, CIST and Related Sites, Consulting and Special Engineering Service, Inc., Redlands, California, Report No. 74-003-71, 17 July 1975.

IV-1.62 Hadala, P. F., Effects of Constitutive Properties of Earth Media on Out-running Ground Shock from Large Explosions, U.S. Army Engineer Waterways Experiment Station, Vicksburg, Mississippi, Report No. TR-S-73-6, August 1973.

APPENDIX IV-1A
OVERPRESSURE WAVEFORMS

This Appendix presents a number of overpressure waveforms. They are ranked according to profile and given a type number because actual waveform traces have been found to fit these categories. The waveforms are plotted in Table IV-1.A as amplitude versus time. First, the idealized pulse profile is shown which presents the general aspect seen on recorder traces. Shown below is the typical or actual waveform found on recorder traces. The next column of the table identifies the type number. The last column provides a description of the waveforms and their relationship to other waveforms in the table.

Table IV-1.A. Idealized and typical waveforms.

Waveform profile*	Type	Description of waveform and relation to lower ranking waveforms
 	0	In its ideal form, it is the classical single-peaked shock wave. It is usually recorded as a double peak. The waveform shows a sharp initial rise to a double-peaked maximum. The peaks are close together in time and their amplitudes are approximately equal.
 	1	A sharp rise to a first peak followed by a plateau or slight decay in amplitude, then followed by a second increase to a peak higher than the first and terminating by a rapid decay. The time interval between the first and second peak varies significantly. The first peak indicates the presence of a disturbance traveling faster than the main wave front. This type of waveform is nonclassical.
 	2	The general feature is the same as for Type 1 except that the second peak has a lower amplitude than the first. Each peak is characterized by a steeper rise than for Type 1 followed by rounded maxima, which in the typical form, are less distinct. The second peak decays more slowly than for Type 1.

*I stands for idealized while T stands for typical waveform.

Table IV-1.A. (Continued)

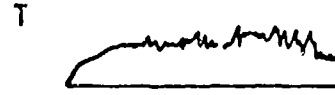
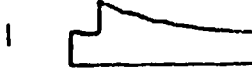
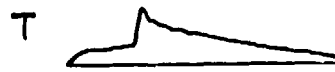
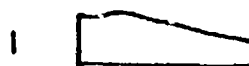
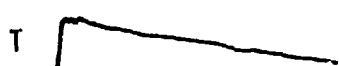
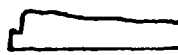
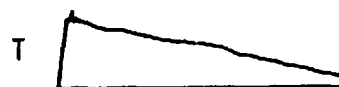
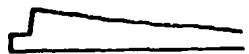
Waveform profile	Type	Description of waveform and relation to lower ranking waveforms
 	3	At first there appears a pointed first peak preceded by a slow rounded rise (labeled 1). Then a decay in amplitude followed by second peak (labeled 2) terminating in slow decay. The rise to maximum may be slower than for Type 2 and the secord maximum has a lower amplitude than the first peak.
 	4	A rise to broad and flat maximum exhibiting a long and slow decay. The relatively sharp twin-peaked amplitude rise of the Type 3 waveform by a slow rise with only one maximum. The actual trace shows noise or what may be called "grass."
 	5	A slow rounded rise steepening to a cusp of maximum amplitude. This is followed by a decay, fast at first, slowing later. The single grassy plateau of Type 4 develops a compression-type main peak. This may be the first indication of the return of the main wavefront.
 	6	A rounded rise to a plateau followed by a steep rise to a maximum, then a slow decay in amplitude. This is a clean-up (grassless) Type 5 waveform with the compression-type peak becoming a shock.

Table IV-1.A. (Continued)

Waveform profile	Type	Description of waveform and relation to lower ranking waveform
 	7	A steep rise to a peak followed by a gentle rise or a plateau to a broad maximum followed by a slow decay. In its typical form this type of waveform is similar to the classical Type 0 waveform.
	7R	The ideal and typical are nearly identical in appearance. This type of waveform refers to Type 7 in a region of regular shock reflection (pre-Mach stem) where the second (reflected) shock front is evident.
 	8	This is a classical waveform characterized by a sudden rise followed by an exponential-like decay. The single peak is sharp, typically slightly "grassy," followed by a slow decay.
	8R	This is a classical Type 8 waveform in a region of regular shock reflection. The second rise is due to the reflected shock front. This waveform is very similar in profile to Type 7R.

CHAPTER IV-2

GROUND MOTION FROM UNDERGROUND EXPLOSIONS*

IV-2.0 INTRODUCTION

Over a period of more than 15 years, beginning with the RAINIER underground nuclear explosion in 1957, the Department of Energy (DOE)[†] has detonated a considerable number of nuclear devices underground in connection with weapon tests, PLOWSHARE program objectives, and VELVA UNIFORM seismic detection studies. Observation of the ground motion produced by many of these explosions has been undertaken by various agencies for numerous purposes.

Ground motion induced by underground nuclear explosions involves four typical domains of mechanical response of the rock to energy released. These are:

1. In the immediate vicinity of an underground nuclear explosion, within a few meters to a few tens of meters depending on the energy released and the type of rock, stresses induced in the rock are extremely high, a megabar and greater, the macro and crystalline structure of rocks exercise little influence on their reaction to the stress, and the result is a hydrodynamic response. Energy lost or trapped in this region and spherical divergence results in decreased stresses at increased distance so that beyond the hydrodynamic regime rock structure begins to control the response.
2. Where stresses are still high, tens of kilobars to hundreds of kilobars, energy is lost to dissipative processes and the response to loading is nonlinear.
3. At still more remote regions as stress levels decrease to a few bars and less, response of the rock becomes linear or quasi-linear and continues in this mode to the limits of detection.
4. Finally, the fourth response is characterized by the influence of the free surface on motion. This includes ballistic effects at the ground surface directly above the explosion and the generation of surface waves near that area.

*Authors: F. M. Sauer (Physics International Company), J. E. Schoutens (General Electric Co.-TEMPO), W. R. Perret and R. C. Bass (Sandia Laboratories).

[†]Formerly Energy Research and Development Administration (ERDA) and Atomic Energy Commission(AEC).

Ground motion measurements are generally segregated into two regional classes, the free-field and the surface motions. The domain of the free-field motion is defined as the region within the earth surrounding an explosion but sufficiently remote from both the free ground surface and other major rock interfaces or fault zones that perturbations of the motion by such discontinuities are either negligible or affect only late-time portions of the motion. The degree of approximation of any real detonation environment to this definition ranges from good in relatively uniform massive geologic formations to very poor in highly stratified formations that include appreciable thicknesses of alluvium, tuff, and carbonate rocks. In the domain of hydrodynamic response, these differences have little or no influence on the motion.

Surface motion measurements are considered to represent motion of the free surface of the earth. However, for practical reasons of instrumentation installation and general classification, such motion is characteristic of a surface layer a few meters in thickness.

IV-2.1 UNDERGROUND EXPLOSION PHENOMENOLOGY

Before beginning the discussion of ground motion data obtained from underground nuclear explosions, it is well to familiarize the reader with the concepts and terminology of this subject. The presentation covers a number of areas and is purposefully brief in each as the reader will be referred to detailed discussions given elsewhere. Two points should be made at this time. First, underground nuclear explosions are unlike underground high-explosive detonations in that the former involves the release of energy in the form of radiation in addition to the development of very high temperatures and pressures. Second, the present discussion is narrowed to detonations producing a closed cavity in the ground, that is, none of the explosion products such as radioactive gases are vented to the surface. Device detonations such as those resulting in craters and the ejection of ground material from them will be discussed in the next two chapters of this Sourcebook.

The discussion begins with a general description of the environment in which various nuclear tests were conducted, measuring techniques employed in detecting free-field and surface motions, and proceed through a brief description of underground nuclear explosion phenomenology associated with the formation of a cavity, a discussion of the energy distribution or partition, wave propagation and attenuation, cavity decoupling, and concluding with a brief discussion of ground motion time histories.

IV-2.1.1 Environments

As indicated in the Introduction, the geologic environment of an underground explosion exercises considerable control over the character of ground motion within the more remote regions where response is either nonlinear or linear. Specific differences in characteristics of the rock surrounding an explosion are not particularly significant to motion in the hydrodynamic region, with the possible exception of the degree of water saturation of porous rocks. However, because mechanical properties of the rock in the more remote regions influence energy absorption and transmission strongly at the lower stress levels, the geologic environment will affect ground motion there significantly.

Those underground events from which free-field data were derived occurred in a variety of geologic environments which have been classified into four general geological types: dry alluvium, dry tuff, wet tuff, and hard rock. All four of these geologic types are present at the Nevada Test Site (NTS), and several exist at the Supplemental and Special Event sites. These specific environments are described in some detail in the following paragraphs.

Dry alluvium applies to the valley fill in the Yucca Flat valley at NTS. It consists of sandy and gravelly detritus from the surrounding mountains composed principally of tuffs and carbonate rocks. It forms about 300 m or more of surface fill and is generally well above the water table. Within this alluvium there may occur masses of unweathered tuff ranging in size from cobbles to boulders. In this valley alluvium lies over various tuff strata, ranging from welded tuff to extremely friable ash flows and varying in thickness from 300 to 700 meters. Water table depths vary from 500 to 600 m, and consequently tuffs occur in both dry and saturated states. Beneath the tuffs lie formations paleozoic shale and carbonate rocks. This cross section is roughly characteristic of those portions of NTS designated as Areas 1, 3, 4, 7, 8, 9, and 10.

Rainier Mesa, NTS Area 12, is composed almost entirely of tuffaceous strata of which the top consists of 10 to 50 m of a dense welded tuff overlying nearly 600 m of relatively soft tuff strata which in turn lie upon thick paleozoic carbonate rocks. Several localized perched water tables occur in this mesa, and the degree of saturation in some parts of the mesa is highly variable.

Hard rocks at NTS include the paleozoic carbonates mentioned above, granitic intrusive rock in Area 15, and some of the rhyolitic flows among the volcanic rock of Pahute Mesa, Areas 19 and 20. The Climax Stock in Area 15 outcrops and, as an

intrusive mass, extends to great depth. It is comprised of large masses of granodiorite and quartz monzonite bordered by metamorphosed carbonates. It includes several nearly vertical fault zones of significant thickness as well as at least three uniformly developed fissure systems. Pahute Mesa includes over a thousand meters of volcanic ash and lava flows within a large caldera, with the consequent pattern of numerous and extensive vertical faults.

At the DOD Supplemental Test Sites, the geologic environments are roughly similar to some areas at NTS. The Central Nevada Supplemental Test Site (CNSTS) includes part of a caldera in which several hundred meters of typical alluvium overlie tuff, andesites, rhyolites, and sedimentaries to a depth of more than two kilometers. At this site the water table is about 100 m below the surface and normal underground shot depths imply a saturated tuff environment.

Amchitka Island in the Aleutian Islands is composed of numerous lava and ash flows and thick volcanic breccia strata, essentially all of submarine origin and extending to a depth of more than 2 kilometers. The lavas are primarily basaltic or andesitic.

The geologic environments of those PLOWSHARE and VELVA UNIFORM Events from which data were derived differ considerably from those at NTS. GNOME was a PLOWSHARE experiment detonated within a thick series of evaporites in southern New Mexico. These flat-lying salt strata range from less than 10 cm to several meters in thickness and are composed principally of halite, sylvite, and polyhalite, with thin brine-saturated clay seams in bedding planes. The evaporites are overlain by about 150 m of anhydrite and red bed strata and about 60 m of alluvium.

GASBUGGY, another PLOWSHARE Event, occurred in the San Juan Basin of northwest New Mexico. It was detonated near the top of the 500-m thick Lewis shale within a 1600 m series of Cretaceous sandstones and shales. These are overlain by 1200 m of Tertiary and Recent sedimentary rocks.

The VELA UNIFORM Event SHOAL was located in a tunnel within the Sand Spring Range of Central Nevada. This range consists of an intrusive granitic mass cut by numerous dikes and thick fault zones filled with wet clay gouge.

The second VELA UNIFORM experiment, SALMON, was detonated within the Tatum Salt Dome in central Mississippi. This dome, composed of more than 90 percent halite, is about 1.5 km in diameter at shot depth, extended to a depth of about 8 km and was capped by 200 m of anhydrite and limestone beneath about 250 m of Recent sediments.

These descriptions of the sites suggest the multiplicity of environments possible, and in one sense it has appeared that there might be nearly as many specific environments as events. However, various characteristics of the free-field motion data and theoretical studies suggest that the four geologic categories chosen provide a reasonable division of source environments for this study. There are a few exceptions in which the best geological description of an explosion site differs from that in which the data fit most readily. Such cases are noted, and an attempt is made to rationalize differences in discussion of the data.

The dry alluvium category includes principally those events which occurred at depths between 300 and 500 m within Yucca Flat at NTS. The dry tuff classification includes some events in Rainier Mesa and in the outer edges of Yucca and Frenchman Flats. The third group, wet tuff, includes events detonated at the CNSTS, in Yucca Flat below the water table, and some in Rainier Mesa. Finally, the fourth category, hard rock, covers all those events which were detonated in granitic, volcanic, or carbonate rocks or in sandstone, shale, or salt (References IV-2.1 through IV-2.26 and IV-2.45 through IV-2.79).

Geophysical properties of the various rocks are particularly significant to their response to explosive loading in the linear and nonlinear regions. The values listed in Table IV-2.1 are generally applicable to the rock types described here and serve to indicate differences in response of such rocks. The wave velocity quoted for bedded salt is probably high as is the density because of a layer of dense polyhalite directly below the shot point.

IV-2.1.2 Measurement Techniques

Mechanical effects of an underground explosion include transient pressure, strain, and particle motion. Observation of any of these parameters must depend upon compatibility of an instrumentation system with conditions in the vicinity of the observation point. In the region of hydrodynamic response pressure levels, rise times and temperatures restrict such instrumentation systems to those responsive to shock front velocities, from which pressure levels may be deduced. Near the outer limits of the hydrodynamic region where rocks begin to respond plastically, gauges have been devised which yield a signal relatable to the whole transient disturbance. The primary limiting factor in this region is the very brief survival of instruments and cables, because of the very high stress levels and large mass velocities behind the shock front. These conditions prevent acquisition of data

Table IV-2.1. Geophysical properties of typical rocks (Reference IV-2.27).

Rock	Natural Density (gm/cm ³)	Porosity (% Vol)	Water Saturation (%)	Compressive Wave Velocity (m/sec)		Seismic Impedance (gm/m ² sec)
				(m/sec)	(ft/sec)	
Alluvium (NTS)	1.78±0.19	36±6	61±16	1800±310	5900±1000	32.0±8.9
Dry Tuff (NTS)	1.72±0.19	36±6	61±16	1800±310	5900±1000	32.0±8.9
Wet Tuff (NTS)	1.86±0.05	38±3	92±6	2350±440	7700±1450	43.7±9.4
Rainier Mesa Tuff (NTS)	1.90±0.12	35±7	96±9	2500±275	8203±900	47.5±8.2
Dry Volcanics Pahute Mesa (NTS)	2.06±0.22	23±5	50 (est)	3091±795	10,142±2600	63.7±23.1
Wet Volcanics Pahute Mesa (NTS)	2.25±0.19	20.1±6	100 (est)	3374±743	11,070±2440	75.9±23.1
Bedded Salt	2.30±0.16	2.9±2.2	79±65	4839±968	15,877±3175	111.3±30
Dome Salt	2.23±0.10	nil	nil	4669±25	15,319±82	104.1±5.2
Breccia (Amchitka)	2.30±0.2	22.5	100 (est)	3833±201	12,577±659	88.2±12.3
Lava (Amchitka)	2.48±0.2	8.1	100 (est)	4677±53	15,346±174	116.0±9.5
Granite	2.67±0.04	0.76±0.66	100 (est)	5722±430	18,774±1410	152.8±13.8

after shock arrival within the hydrodynamic regime and often terminate data during later portions of the stress transient in the plastic regime.

Cable survival and maintenance of cable integrity is also a limiting factor in the forward portion of the nonlinear response region. This problem is generally limited to stress levels above one kilobar, although permanent cable damage may occur at lower stress levels where gross displacements occur at bedding planes or faults intersected by the cables. There is, however, a very different restraint imposed on measuring techniques in the lower stress regions as a consequence of impedance matching problems between the rock and the instruments. As a consequence of this problem, it has been found that measurement of motion in terms of particle acceleration or its time integrals is more reliable than observation of either stress or strain. Response of instrumentation for measuring stress or strain appears to be much more sensitive to disturbance of the environment by gauge emplacement or to mismatch of rock and gauge impedance than is response of motion gauges. Consequently, data from the hydrodynamic domain are shock front velocities translated to peak pressure levels by means of experimentally determined rock properties, and data from the nonlinear and linear or quasi-linear domains are motion data recorded as time-histories of acceleration or particle velocity.

Contained underground nuclear explosions are placed at depths of the order of 250 m or deeper. Emplacement is either in a deep vertical borehole from the ground surface or in a horizontal tunnel or drift extending either from the face of a mesa or from the bottom of a vertical access shaft, depending upon the terrain and specific objectives of the test. Regardless of the type of explosive emplacement, the preferred pattern of free-field ground motion instrument stations is in a radial line from the explosive at distances dependent upon instrumentation and feasible positions. Such instrument arrays are generally on horizontal radii at shot depth or on the vertical radius through surface zero directly above the explosive. In special cases vertical arrays may also be offset horizontally from surface zero at various distances and horizontal arrays may be above or below shot level.

Emplacement of the explosive in a deep vertical hole requires that horizontal instrument arrays be emplaced in a series of vertical holes drilled at specified distances along a radius and that vertical arrays be located in a boring offset about 10 m or more from the shot hole. The MERLIN Event in NTS Area 3 included instrument arrays of this type, Figure IV-2.1. Events for which distant offset

vertical arrays were required, such as SALMON and HANDCAR used similar series of instrumentation borings; but these borings usually extended to depths appreciably below shot level.

Free-field instrumentation arrays for nuclear explosions emplaced in tunnels were usually installed at or near shot level in borings extending from the floor or walls of the tunnel to depths of 3 or more tunnel diameters and in vertical borings from surface zero, Figure IV-2.2. In tunnel installations where stations were required at distances or in directions beyond the tunnel complex, offset vertical borings were also used for shot level stations.

It is pertinent here to describe the method of handling data from measurements for the analysis which forms the basis for this chapter. Peak values of stress and particle velocity were derived from measurements made in the hydrodynamic region, and corresponding peak values of acceleration, particle velocity, and displacement were derived from ground motion measurement records obtained within the nonlinear response domain. These peak data were from numerous events involving explosively released energy which ranged over several orders of magnitude and from gauges placed at distances ranging from a few meters to a few kilometers. Comparison of such data requires normalization to some logical base by means of dimensional analysis. Such analysis has shown that, normalized to an energy release equivalent to that of one kiloton of TNT explosive, pressure or stress and particle velocity vary inversely with the n^{th} power of the distance from source to measurement station reduced by the cube root of the yield or energy released in equivalent kilotons of TNT. Similar power law relationships are derived from accelerations normalized by multiplying by the cube root of yield and for displacement divided by the cube root of yield. General equations for these normalization or scaled relationships are:

$$p = p_0 \left(\frac{R}{W^{1/3}} \right)^{-n} \quad (IV-2.1)$$

$$u = u_0 \left(\frac{R}{W^{1/3}} \right)^{-n} \quad (IV-2.2)$$

$$a \cdot W^{1/3} = \left(a \cdot W^{1/3} \right)_0 \left(\frac{R}{W^{1/3}} \right)^{-q} \quad (IV-2.3)$$

$$d/W^{1/3} = \left(d/W^{1/3} \right)_0 \left(R/W^{1/3} \right)^{-r} \quad (\text{IV-2.4})$$

where p , u , a and d are respectively pressure, particle velocity, acceleration, and displacement, R is the distance or range between source and measurement station, and W is the energy yield in equivalent kilotons of TNT. The subscript zero refers to the value of the normalized quantity for $(R/W^{1/3})$ equal to one.

It is convenient for all free-field ground motion data presented in this chapter to be normalized to a value of W equal to 1 kt. The resulting linear fits and plots are compared and discussed in the remainder of this part of this chapter.

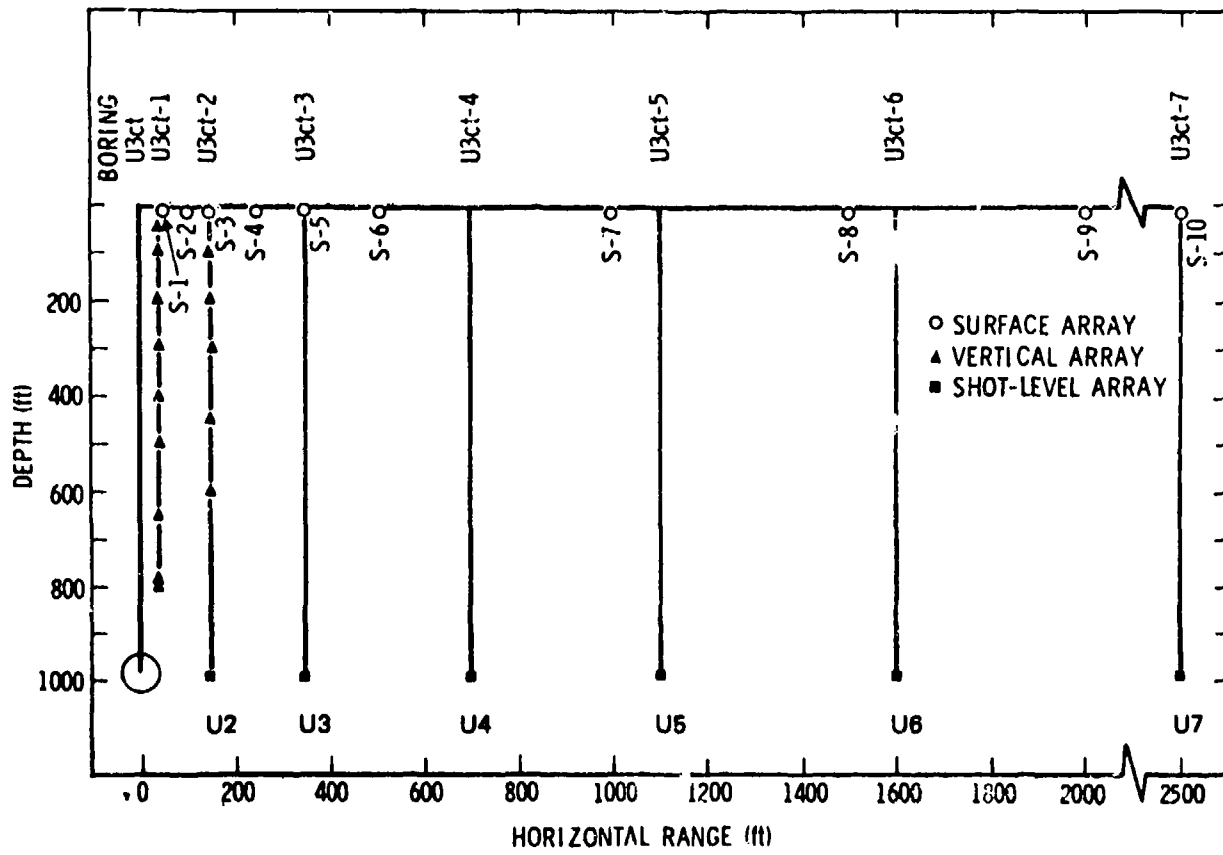


Figure IV-2.1. Merlin instrumentation (Reference IV-2.27).

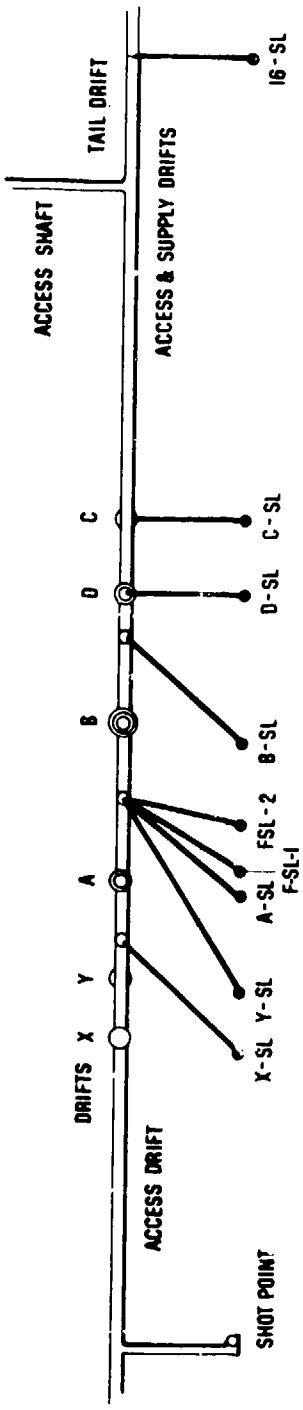


Figure IV-2.2. PILE DRIVER free-field instrument stations (Reference IV-2.27)

IV-2.1.3 Fireball Development

A good description of the disassembly of a nuclear device is given in Reference IV-2.28. The description is applicable to the explosion in the atmosphere including the atmosphere contained in a cavity large enough to decouple the detonation from the cavity. For the purpose of this section we quote the following descriptive paragraph from Reference IV-2.28, p. 71.

In the earliest stage of the expansion of the weapon residues, the temperature is extremely high and the mean free path of the radiation is long compared to the dimensions of the volume of expanding residues. Consequently, the transfer of energy by radiation takes place rapidly within the mass of hot gas and the temperature throughout the material is uniform. This mass is, therefore, referred to as the "isothermal sphere" and represents the early stages of the fireball. Provided the ambient air is cold and has an appreciable density, the soft X-rays and ultraviolet radiation, constituting the major part of the thermal radiation emanating from the isothermal sphere are absorbed or degraded in energy within a short distance. The surrounding air thus becomes extremely hot, with the result that the dimensions of the fireball increase rapidly. At first, the shock front lags behind the radiation front, i.e., the surface of the fireball, because the mean free path of the radiation in the hot gas is so long that the transfer of energy by radiation is more rapid than by mass motion. As the fireball expands and the energy is deposited in an ever-increasing volume (and mass) of air, the temperature within the isothermal sphere falls. As a result, the mean free path of the radiation decreases and transfer of energy by radiation becomes less rapid. The shock front then begins to advance faster than the radiation front and soon the two coincide. The shock front continues to advance more rapidly than the radiation front and moves ahead of it at the time when the temperature of the isothermal sphere has fallen to about 300,000°C. This phenomenon is called "hydrodynamic separation."

Johnson, Higgins and Violet (Reference IV-2.29) have noted that in the case of the 1.7 kt shot RAINIER, the explosion took place in a cavity having a volume of about 7 m^3 and containing a mass of material of about 1000 kg. They estimated that a few microseconds after explosion time the pressure in the room was around $7 \times 10^6 \text{ atm}$ and the temperature at about 10^6°C . These represent conditions equivalent to having the fireball filling the cavity. For a full decoupling of an explosion in a cavity, the cavity size must be such that the explosion-produced pressure at the cavity wall does not produce stress in excess of the elastic limit of the surrounding medium. This pressure is about 150 atm (0.15 kilobar)* according to Latter et al (Reference IV-2.30). From this we conclude that the RAINIER shot was essentially tamped. Had that shot been decoupled, the fireball would have expanded beyond the cavity dimensions before the shock front moved out beyond the radiation front. It is, therefore, appropriate to continue quoting from Reference IV-2.28, pp. 71 to 76.

As the shock front moves ahead of the isothermal sphere it causes a tremendous compression of the ambient air and the temperature is thereby increased to an extent sufficient to render the air incandescent. The fireball now consists of two concentric regions. The inner (hotter) region is the isothermal sphere of uniform temperature, and this is surrounded by a layer of luminous, shock-heated air at a somewhat lower, but still high, temperature. The surface of separation between the very hot core and the somewhat cooler outer layer is the radiation front. For some time the fireball continues to grow in size at a rate determined by the propagation of the shock front in the surrounding air. During this period the temperature of the shocked air decreases steadily so that it becomes less opaque. Eventually, it is transparent enough to permit the much hotter and still incandescent interior of the fireball to be seen through the faintly visible shock front. The temperature at this time is considerably lower than that of the isothermal sphere but the radius is larger. As the temperature of shocked air approaches 1800°C it absorbs (and reradiates) less rapidly. Then the shock front becomes increasingly transparent to the radiation from the isothermal sphere and there is a gradual unmasking of the still hot isothermal sphere, representing breakaway.

*1 bar = 1.013 atmosphere = 14.7 psi.

At the instant of breakaway the shock front pressure is approximately 50 atm (Reference IV-2.31). The relative positions of the shock front and the fireball are shown in Figure IV-2.1 (Reference IV-2.32). This figure shows that after shock breakaway, the fireball growth or the cavity growth reaches a maximum value while the shock front continues to expand radially outward.

As indicated in Reference IV-2.32, the shock front overtakes the radiation front earlier if the nuclear explosion takes place in a ground medium instead of the atmosphere. The fireball for an underground explosion can extend some distance into the surrounding medium but is significantly smaller than for a comparable atmospheric detonation. In a tamped explosion the fire ball can extend a considerable distance beyond the isothermal sphere because the shock front is initially sufficiently strong to vaporize the surrounding rock. In this case, the fireball boundary coincides with the shock front out to the radius of vaporization (where the shock energy is just sufficient to vaporize the rock). Beyond this radius the shock front breaks away from the vapor-filled cavity and successively melts (some materials such as dolomite will decompose and sublime) and inelastically deforms the surrounding rock by plastic deformation, shear failure, and crushing, if porous, before decaying into an elastic wave. The motion of the shock front and the growth of a cavity produced by an underground nuclear explosion are analogous to the shock-front motion and fireball growth of an atmospheric nuclear explosion as shown in Figure IV-2.3 (Reference IV-2.32).

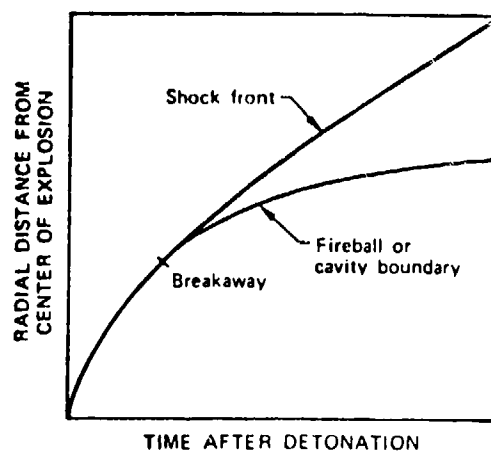


Figure IV-2.3. Advance of shock front and growth of fireball or cavity in an atmospheric or underground nuclear explosion (Reference IV-2.32).

Using Figure IV-2.4 from Reference IV-2.32 we can then describe the processes involved in the formation of a cavity during an underground nuclear explosion. Consider an underground nuclear explosion to occur in rock with the initial cavity the size of the device (tamped explosion). As the detonation begins the intense shock wave will vaporize the rock out to a radius R_v ; R_v corresponds to the shock breakaway time. The cavity now continues to expand until it attains its final radius R_c . This is the condition at which the cavity pressure is in equilibrium with the resisting stress at the cavity wall. The cavity now has a radius R_c that corresponds to the cavity boundary as shown on Figure IV-2.4. The shock front continues to move out radially until the inelastic stress wave decays to an elastic wave at radius R_σ . The inelastic stress wave produces permanent rock deformation. The radial stress at the elastic radius R_σ has a peak value corresponding to the elastic limit stress of the rock. For most media this corresponds to about 150 atm (0.15 kilobar).

IV-2.1.4 Partition of Energy

We can briefly examine what energy remains in the cavity after the detonation and how much is available for production of seismic waves. For ground motion to be minimized, the energy dissipation in the inelastic region should be maximized. For a fully decoupled explosion, the cavity has the size corresponding to R_σ of the inelastic region where a large fraction of the explosive energy is dissipated and remains trapped in the form of cavity gases. This gas is hot and contains the air originally in the cavity in addition to the vaporized weapon. For a tamped explosion, the inelastic region extends into the surrounding rock where the rock has vaporized, melted, cracked, crushed and undergone plastic deformation. The energy partition values given below refer to a tamped explosion.

Heckman (Reference IV-2.33) analyzed the data from postshot rock temperature for eight nuclear detonations. His analysis indicated that 90 to 95 percent of the energy released remains as residual thermal energy in the vicinity of the explosion assuming complete containment is achieved. More detailed studies of SALMON Event has shown that approximately 90 percent of the total yield energy was deposited within a 50-m radius from the center of the explosion. This value does not take account of the energy dissipated in crushing and fracturing the salt out to 90 m from the cavity edge whose radius is 17 m (Reference IV-2.32). From these figures one can conclude that less than 10 percent of the device energy is available to generate seismic waves.

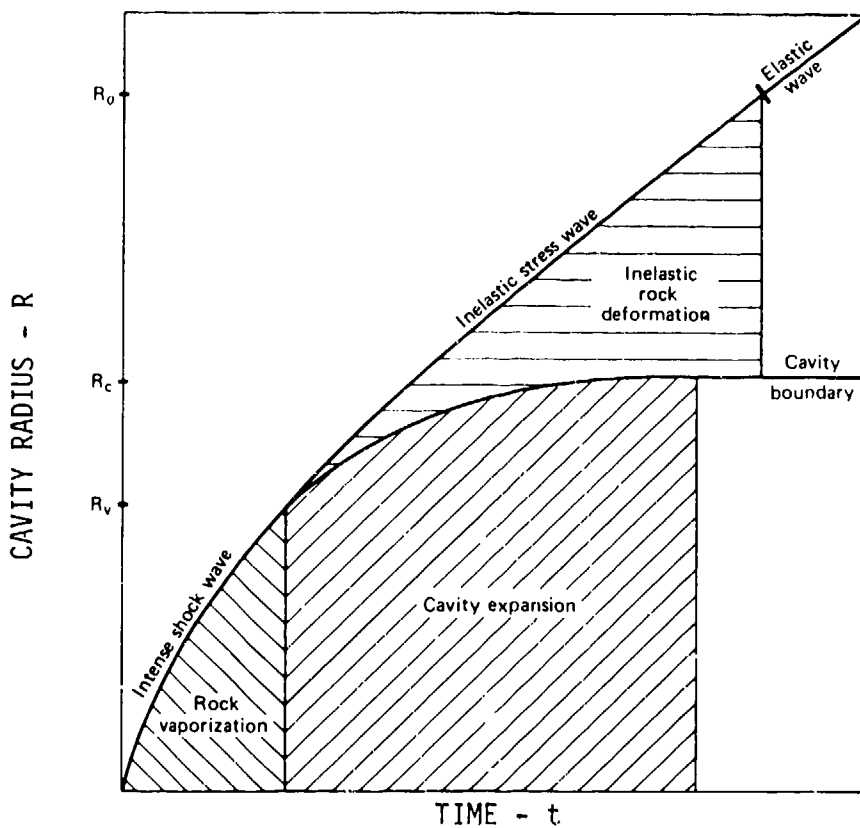


Figure IV-2.4. Radius versus time relation for an underground nuclear explosion with regard to vaporization, cavity expansion, and inelastic rock deformation (Reference IV-2.32).

IV-2.1.5. Reflected and Refracted Waves

As we have seen in Chapter IV-1, there are two types of body waves: the compressional or p-wave and the shear or s-wave. The reflection and transmission of these body waves at a single or at multiple boundaries in elastic solids is quite complex even in the limiting case of an homogeneous, isotropic and nonporous solid. This complexity arises from the transformation of energy from p- to s- or s- to p-waves; that is, an incident wave train gives four kinds of waves. In the case of a medium consisting of two semi-infinite half-spaces, each with different acoustic impedance properties, which are "welded" together at the plane interface, four boundary conditions are imposed on the solution of the wave equation. These boundary conditions require that the normal and tangential displacements and stresses on each side of the interface be equal. If one of the half-spaces is a

vacuum, the plane interface is a free surface and the four boundary conditions reduce to two; the normal and tangential stresses at the free surface are equal to zero (References IV-2.32, IV-2.34, IV-2.35, and IV-2.36). An analysis will show that if either a p- or an s-wave are incident on an interface or a free surface, these additional boundary conditions cannot be satisfied by the reflection and refraction of the same type of wave. An additional type of wave is reflected and refracted. Assuming that the plane interface is horizontal we can describe these waves as (Reference IV-2.32):

Incident p —————→ reflected (p + sv) + refracted (p + sv)

and

Incident sv —————→ reflected (p + sv) + refracted (p + sv)

where sv is a vertically polarized shear wave (normal to interface plane). If the incident wave is a horizontally polarized shear wave, sh, parallel to the free surface, then there is no additional wave reflected and refracted at the interface. Thus

Incident sv —————→ reflected sh + refracted sh.

Figure IV-2.5 shows these cases of reflection and refraction. Note that the angles of incidence, reflection, and refraction can have values ranging from zero to $\pi/2$. The angles of incidence and reflection of a given type of wave are of course equal. Snell's Law can be used to relate the angles of incidence, reflection, and refraction to the wave propagation velocities (Reference IV-2.32 or IV-2.34)

$$\frac{\sin \theta_{p1}}{C_{p1}} = \frac{\sin \theta_{s1}}{C_{s1}} = \frac{\sin \theta_{p2}}{C_{p1}} = \frac{\sin \theta_{s2}}{C_{s1}} = \frac{\sin \theta_{p3}}{C_{p2}} = \frac{\sin \theta_{s3}}{C_{s2}} \quad (\text{IV-2.5})$$

where C_p is the compressional wave velocity and C_s is the shear wave velocity. Where the incident compressional wave propagates in a direction normal ($\theta_{p1} = 0$) to an interface, the ratios of the displacement amplitudes for the transmitted and reflected p-wave are given by (Reference IV-2.37)

$$\frac{A_{pr}}{A_{pi}} = \frac{1 - \rho_2 C_2 / \rho_1 C_1}{1 + \rho_2 C_2 / \rho_1 C_1} \quad (\text{IV-2.6})$$

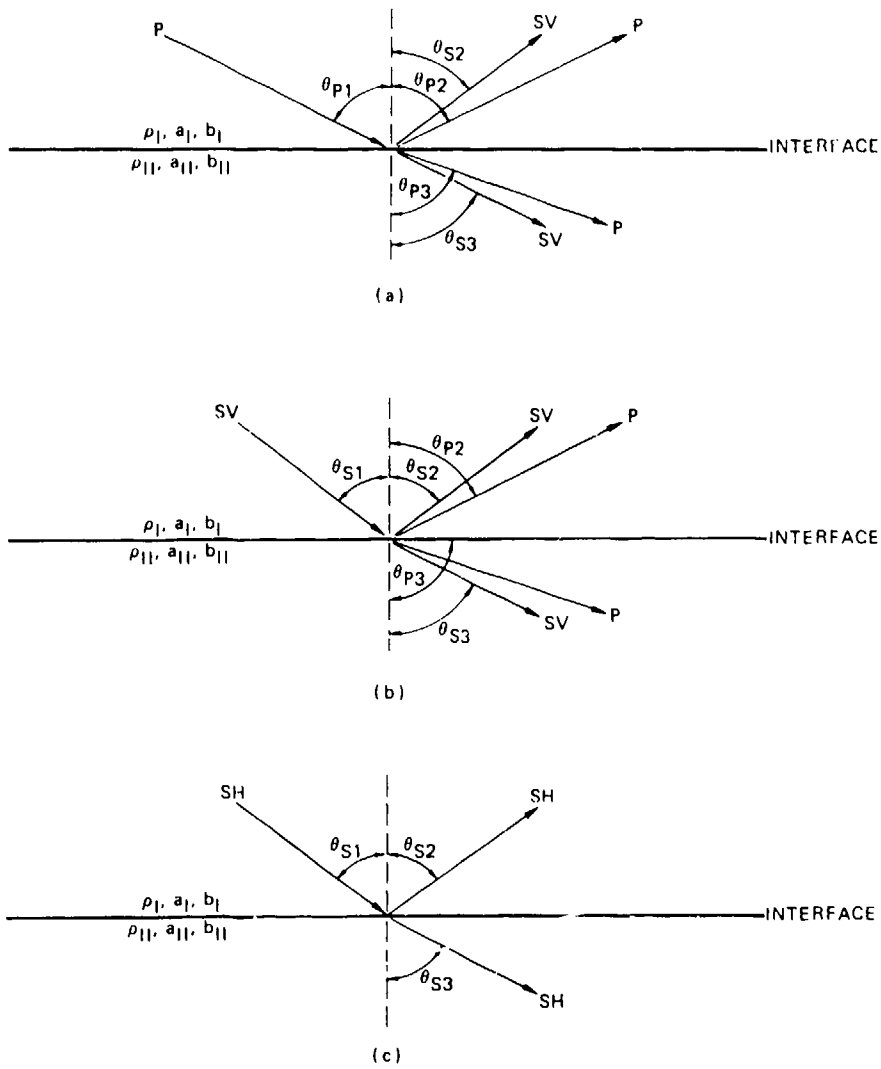


Figure IV-2.5. Reflection and refraction of plane p- and s-waves at a plane interface. (a) Incident p-wave and reflected and refracted sv-waves. (b) Incident sv-wave and reflected and refracted p- and sv-waves. (c) Incident sh-wave and reflected and refracted sh-waves (Reference IV-2.32).

$$\frac{A_{pt}}{A_{pi}} = \frac{2}{1 + \rho_2 C_2 / \rho_1 C_1} \quad (\text{IV-2.7})$$

where the wave propagates from medium 1 having an acoustic impedance $\rho_1 C_1$ into medium 2 having an acoustic impedance $\rho_2 C_2$. These equations have already been discussed in Chapter IV-1. Suffice it to add here that if the acoustic impedances of the two semi-infinite half-spaces approach a common value as a limit, the interface will disappear and so will the reflected wave. (In the limit, this corresponds to an imaginary interface in a continuous medium, thus $\rho_2 C_2 = \rho_1 C_1$ and therefore $A_{pr}/A_{pi} = 0.$) The opposite occurs when the second half-space becomes a vacuum. This results in the disappearance of the refracted wave and the incident wave is completely reflected. Mention may be made in passing that if the incident wave fronts, either p- or sv-waves, are not planar, but have a finite radius of curvature, the zero-stress condition at the free surface is not satisfied by the reflection of two types of waves. Three types of waves are now generated (Reference IV-2.32). They are

$$p \longrightarrow p + sv + R \quad \text{and} \quad sv \longrightarrow sv + p + R$$

where R is the Rayleigh wave mentioned in Chapter VI-1. Nakano (Reference IV-2.38) has shown that the Rayleigh waves vanish when the incident wave front curvature approaches zero (see also Reference IV-2.36).

Analysis of wave reflection and refraction in real geology becomes extremely complex. Many computational methods have been developed, some extremely time-consuming to use and others fairly simple. We present a brief description of a graphical method developed by Chaszyka (Reference IV-2.39). This method is used to predict all the elements required to follow the behavior of the explosion, that is, the position and velocity of the shock front and the associated particle velocity. The solution is restricted to three- and two-shock geometry shown on Figure IV-2.6. There is an incident shock at angle θ_i to the original surface, a reflected shock at angle θ_r , a transmitted shock at angle θ_t , and a new position of the interface at angle θ_s .

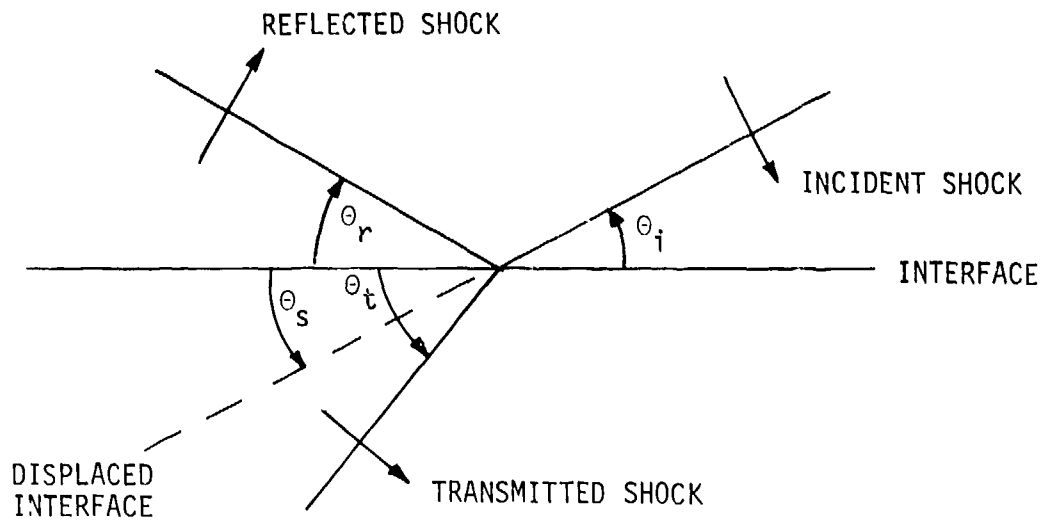


Figure IV-2.6. Shock geometry at interface.

The conditions assumed for the analysis are the following:

1. The shock intersection remains at the interface.
2. The components of particle velocity normal to the interface are equal across the interface.
3. Attention is restricted to a small region such that the flow can be considered uniform in each region and pressure is continuous across the interface.
4. The hydrodynamic transport velocity behind the reflected waves is such that the reflected wave cannot overtake the incident wave intersection at the interface.

The solution is valid whether the reflection process results in a rarefaction or a shock wave in the original medium and is applicable for any equation of state in the media involved. The method lends itself well to keeping track of all possible solutions which satisfy the boundary conditions. Consequently, the physically unreal solutions can be discarded.

IV-2.1.6 Cavity Decoupling

The problem of cavity decoupling has its origin in the possibility of concealing an underground nuclear explosion from seismic detection. The method of concealing a nuclear detonation by enlargement of the underground cavity was at first discarded because it was erroneously concluded that a cavity would not be effective in decoupling the signal. Later on it was correctly reasoned and experimentally verified that it does pay to have detonation occur in a large enough cavity to eliminate any nonelastic behavior of the rock. Nonelastic behavior of rock is undesirable because the medium can flow and thereby undergo large displacements. Therefore, an estimate of the effectiveness of this method indicates that a yield of more than 300 kt could be made to appear seismically like a yield of 1 kt (Reference IV-2.40).

Consider a nuclear explosion of yield W to occur in an underground cavity of radius $r = R_\sigma$ sufficiently large that the pressure on the wall of the cavity does not exceed the elastic limit of the medium (approximately 150 atm). Moreover, we assume the energy W to be suddenly released and uniformly distributed in the cavity volume producing a step-function pressure increase on the wall. This pressure then is

$$p = \frac{3(\gamma - 1) W}{4\pi R_\sigma^3} \quad (\text{IV-2.8})$$

where $\gamma = 1.2$ (Reference IV-2.32) is a constant characterizing the gas mixture in the cavity.

The Fourier transform of the elastic displacement produced by the step-pressure p at a range r in the wave zone is (Reference IV-2.41)

$$\xi(\omega) = \frac{PR_0}{8\pi\mu r} \left\{ \frac{C_p}{\omega_0^2 + i\omega_0\omega - \frac{\lambda + 2\mu}{4\mu}\omega^2} \right\} \quad (\text{IV-2.9})$$

where λ and μ are the Lamé constants, C_p is the compressional wave speed and ω is the angular frequency, and

$$\omega_0 = C_p / R_\sigma \quad (\text{IV-2.10})$$

If one's interest is confined to those values of ω for which elastic displacements are propagated to large distances with negligible attenuation in the earth, that is, for ω ranging from zero to about 6 sec^{-1} , then the first term in the denominator of Equation IV-2.9 dominates so that

$$\xi(\omega) = \frac{P R_\sigma^3}{8\pi\mu r C_p} = \frac{3(\gamma - 1) W}{32\pi^2 \mu r C_p} \quad (\text{IV-2.11})$$

This equation shows that the amplitude of the distant seismic signal is proportional to W . The amplitude is independent of the initial cavity radius R_σ (R_σ is the cavity radius corresponding to wall pressures equal to or below the elastic limit of the medium, see Figure IV-2.4).

To determine the advantages of initiating the explosion in a large cavity, an analysis of the measurements made on the RAINIER Event is given. RAINIER was a 1.7 kt nuclear device detonated at a depth of 900 ft in Nevada tuff. Acceleration measurements were made in a vertical direction at 371 ft and 451 ft from the zero position. These measurements are particularly useful because the medium is homogeneous and appears to be elastic in this region, and the records were relatively free of extraneous reflections. Using Equation (4) of Reference IV-2.41 for the Fourier transform of the displacement at a range r

$$\xi(\omega) = \frac{\hat{P} \bar{R}_\sigma}{8\pi\mu} \left(\frac{1}{r^2} + \frac{i\omega}{r C_p} \right) \left\{ \frac{C_p^2}{\omega_0^2 + i\omega_0\omega - \frac{\lambda + 2\mu}{4\mu} \omega^2} \right\} \quad (\text{IV-2.12})$$

where \bar{R}_σ is the unknown radius at which the medium begins to behave elastically and \hat{p} is the unknown Fourier transform of the pressure acting at \bar{R}_σ and ω_0 is defined as before by Equation IV-2.10. Latter, et al (Reference IV-2.40) have fitted the experimental data by choosing various values of \bar{R}_σ and different forms of \hat{p} . They found that the best value for \bar{R}_σ is approximately 280 ft so that $\omega_0 \approx 25$ and is essentially independent of the form of \hat{p} . Moreover, for an explosion of any yield in the RAINIER environment, the angular frequency ω_0 must scale as $W^{-1/3}$ and hence

$$\omega_0 = 25 \left(\frac{1.7}{W} \right)^{1/3}, \text{ sec}^{-1} \quad (\text{IV-2.13})$$

where W is in kt. Using Equation IV-2.12 and the RAINIER experimental data, a Fourier transform of the displacement in the wave zone was determined. The result was then compared with the transform given for the case of a cavity specified by Equation IV-2.11. The result, after some mathematical manipulation given in Reference IV-2.40, leads to the equation for the decoupling factor, or

$$\frac{\xi(\omega)}{\xi_h(\omega)} = 2.4 \mu_h \frac{C_{hp}}{C_p} \quad (\text{IV-2.14})$$

where the shear modulus μ is given in kilobars. The subscript h refers to the quantities associated with the cavity. For a cavity in the RAINIER medium, $C_{hp} = C_p$ and $\mu_h \approx 20$ kilobars so that the decoupling factor is approximately 50. According to Equation IV-2.14, to increase the decoupling factor the cavity should be made in a stronger medium for which μ and C_p are large. For example, in salt where a number of the events of the COWBOY Series were fired (Reference IV-2.42) $C_{hp} \approx 2.5 C_p$ and $\mu_h \approx 100$ kilobars. This gives a decoupling factor of about 600. This number should be reduced somewhat because the stronger medium will couple eventually to softer media and overshoot will occur. Assuming this overshoot to be on the order of 2, the decoupling factor becomes at least 300. Thus a 300 kt detonation can appear as a 1 kt detonation.

In conclusion it is worth noting that Cherry, Bache and Patch have performed computations (Reference IV-2.43) that suggest that detonating a nuclear explosion

in a tunnel may be a viable evasion technique in terms of the M_s/m_b discriminant. (For a detailed discussion on the various techniques of discriminating between a nuclear explosion and an earthquake see Reference IV-2.44.) M_s is the surface wave magnitude while m_b is the body wave magnitude.* The authors performed computer modeling of sources as well as conducted experimental tests. They carried out measurements of 37 small scale detonations inside 14 different tunnel configurations. They concluded from their analysis that with the source at an orientation close to the horizontal, the teleseismic signatures became much more like those of earthquakes. Especially at 45 degrees orientation, significant Love waves were generated. For a linear source the most favorable orientation is the horizontal with values of M_s enhancement ranging up to 0.34 with about an average over the entire radiation pattern of 0.2. Unlike the linear source, the most favorable orientation of the nonlinear source for M_s enhancement is at 45 degrees to the vertical. The difference between the 45 degree and horizontal orientation is large with the horizontal actually leading to a negative M_s enhancement at most azimuths. For the linear source, the 45 degree orientation gives slightly less M_s enhancement than the horizontal orientation. On balance, considering both Love and Rayleigh waves, cylindrical source orientations between the vertical and horizontal would seem most likely to exhibit earthquake-like surface wave behavior in the teleseismic range. The computed Rayleigh wave amplitude for the nonlinear 45 degree source is as much as an order of magnitude greater than that from an equivalent spherical explosion. They also noted that body wave (magnitude of m_b) excitation remained almost unaffected by the source orientation.

IV-2.1.7 Representative Ground Motion Time Histories

Because of symmetry, motions in the vicinity of a detonation contained in a homogeneous medium are theoretically radial only. However, as the absolute distance from ground zero increases secondary motions arise from inhomogeneity of the medium or from refraction and reflection processes. These secondary motions are

*In general, the magnitude values M_s and m_b are determined from empirical expression of the form

$$m = a + \log_{10} \frac{A}{T} + n \log_{10} \Delta \quad (\text{IV-2.15})$$

where m is the magnitude, a and n are empirical constants, A is the signal amplitude, T is the signal period, and Δ is the epicentral distance (see References IV-2.32 and IV-2.44).

usually accompanied by a substantial amount of tangential motion. Because these secondary motions are associated with a particular geological formation they are considered a perturbation on the main radial motion when considering correlation of data. For this reason, motion of the free-field is inferred to be radial, although in some circumstances this is not necessarily the case. Where substantial secondary motions occur, thereby giving rise to substantial tangential motions, these data have been eliminated from the analysis.

An illustration of typical free-field radial motion is given in Figure IV-2.7. As indicated, motions in the free field near an underground explosion are similar to the wave motion from a detonation in free air.* Initially, there is a large outward radial velocity followed by a much smaller inward radial velocity. Therefore, the permanent (residual) displacement is a large fraction of the maximum transient displacement. At large ranges the outward and inward radial velocities become more nearly equal, so that the permanent displacement tends toward zero more rapidly than the maximum transient displacement.

At the ground surface directly above ground zero (surface zero) the incident compression wave is reflected from the free surface causing an increase in the magnitudes of the peak acceleration and velocity. Because of the low tensile strength of soils and rock formations, reflection of the compressive wave causes a single or multiple spall to form below the surface. The motion of the surface is then as if it were given an initial velocity equal to a multiple between 1 and 2 of the free-field velocity which existed at that range, followed by a period of the free fall of the spalled material (Figure IV-2.8). The fallback and subsequent collision of the slat with the surface below the spall gap produces a second peak of acceleration whose magnitude usually is larger than that of the first. The second peak is judged to be unpredictable in magnitude and time of occurrence and is not included in analysis of surface motions. This sequence of events may be repeated several times, as it occurred at surface zero for the GNOME Event (Figure IV-2.8), depending to a great extent on the number of spalls or the degree of bulking that occurs in the surface layers. Hence, the maximum and permanent displacements of the surface are unpredictable since spalling phenomena are not yet completely understood.

*By "free air" is meant well above the ground surface so that the ground plane does not interfere with the shock propagation.

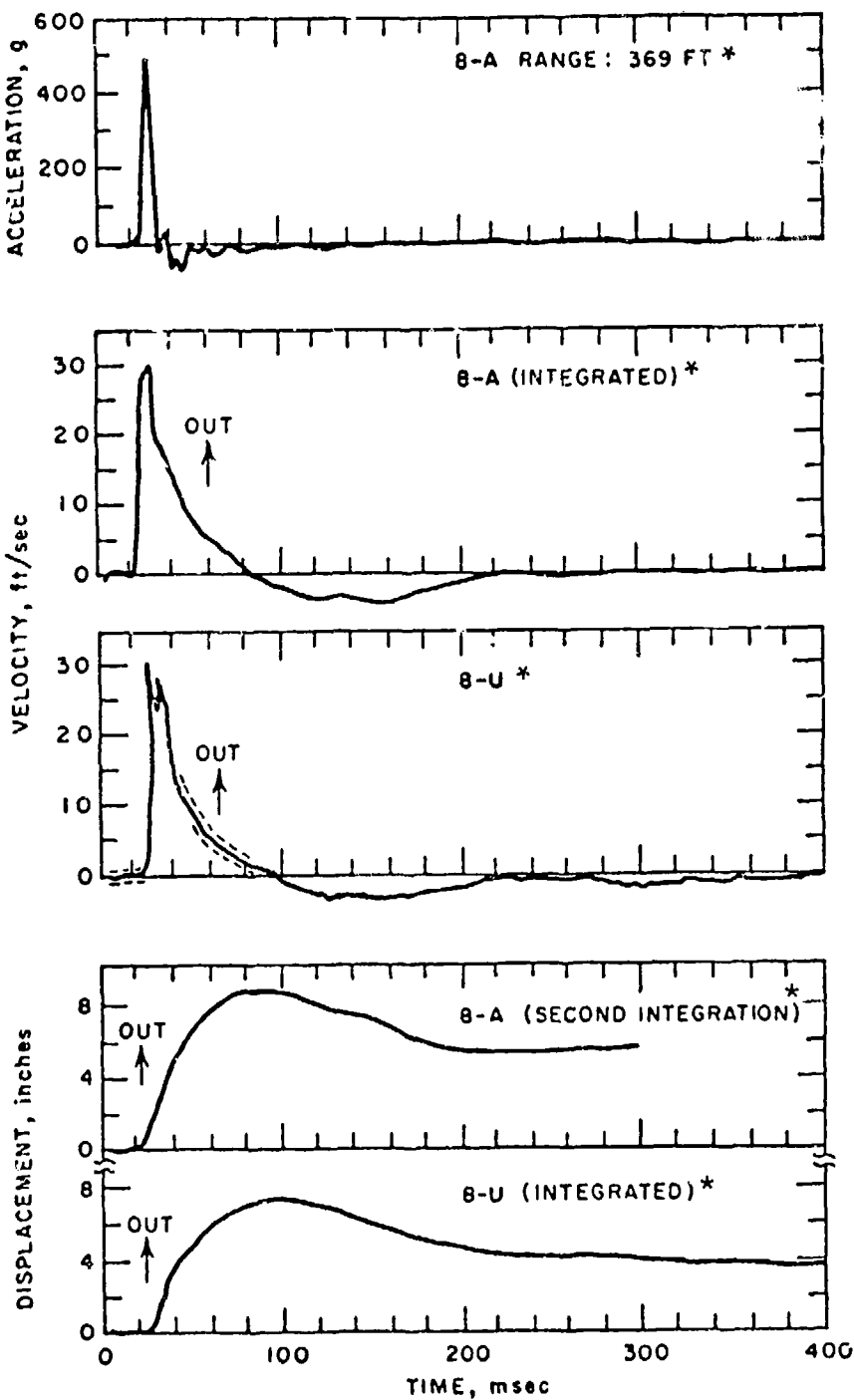


Figure IV-2.7. Example of free-field radial motion from an underground explosion in NTS granite (data from HARDHA1).

*B-A and like designations on these graphs refer to the station number where the data were taken.

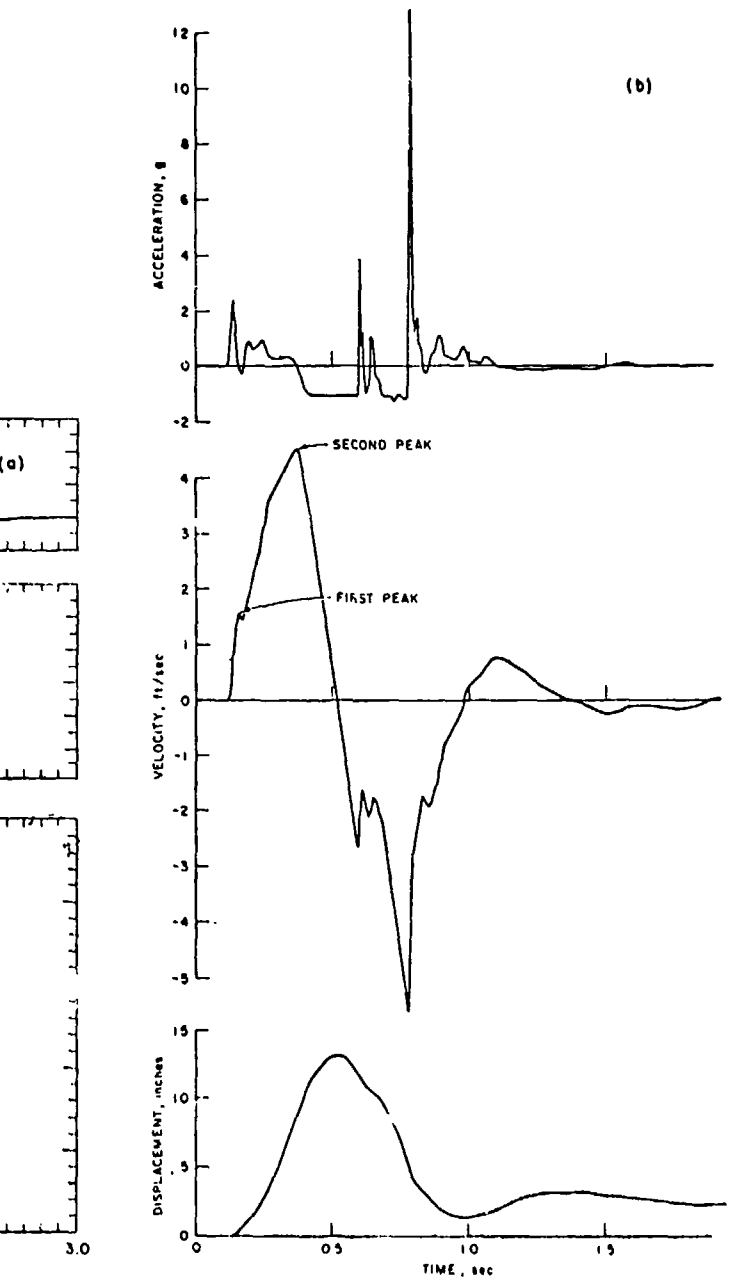
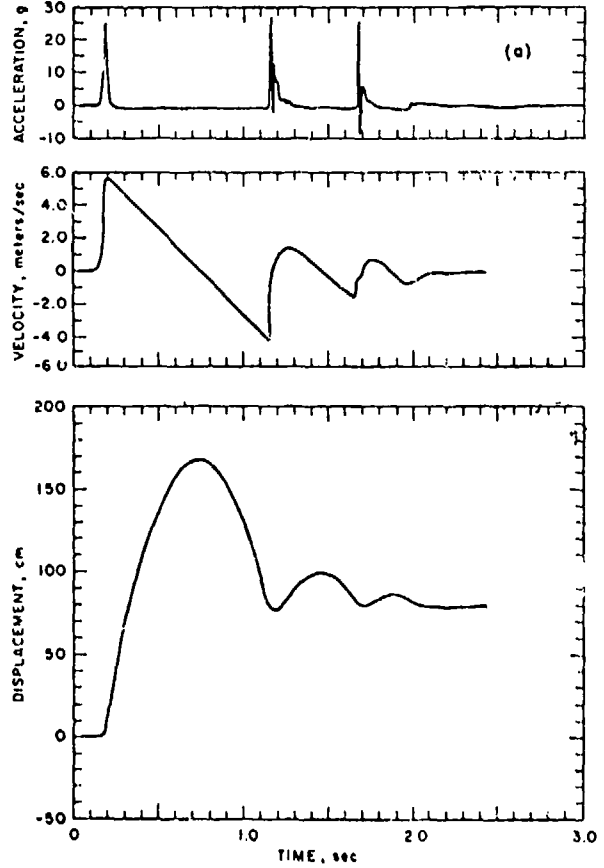


Figure IV-2.8. Example of surface zero motion for a detonation,
 (a) salt (data from GNOME) and (b) NTS
 alluvium (data from CHINCHILLA).

At some distance from ground zero, spalling ceases and the character of the motions changes as illustrated in Figure IV-2.9. The magnitudes of the various peaks of acceleration and velocity become more nearly equal and the motion stretches out in time as the various modes of surface motion develop.

For example, Event HANDCAR, (Reference IV-2.64) was detonated in a thick dolomite section. Surface data were obtained in the overlying desert alluvium while free-field data were collected in the dolomite body. It was indicated in Reference IV-2.64 that the vertical component of the surface velocity fell squarely on similar data of Event RAINIER. The peak free-field velocity data also closely approximated those for competent tuff as calculated by Werth and Herbst (Reference IV-2.65).

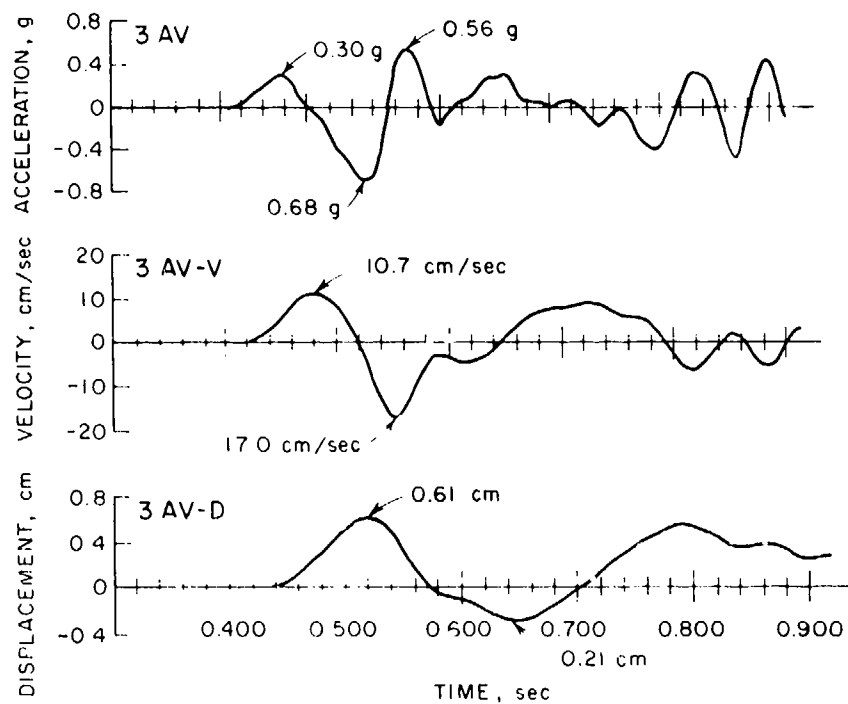


Figure IV-2.9. Example of surface motion in the nonspalling region (data from GNOME).

IV-2.2. STRESS AND MOTION WITHIN THE HYDRODYNAMIC AND PLASTIC REGIONS

This section has been adapted from Reference IV-2.27.

IV-2.2.1 Measurement Techniques

In the immediate vicinity of underground explosions temperatures and pressures are so great that rock responds hydrodynamically to the load. Such response is more strongly dependent upon the chemical elements in the rock than upon its crystalline or macrostructure. Only limited means exist for experimental studies of shock front characteristics under these conditions. Conventional instruments or systems for measuring stress or motion in the rock would be destroyed under the extremely high stress levels and large mass velocities which exist behind the shock front in this region. However, it is feasible to derive certain parameters of the shock front which, combined with the equation of state for the geologic material that surrounds an explosion, can provide information about the maximum stress in the shock front and particle velocities immediately behind it. In an environment of hydrodynamic shock, the equation of state of a material may be described by the Hugoniot equation (see for example Reference IV-2.31). This is a special form of the equation of state which involves neither temperature nor volume directly but is formulated in terms of the dynamic characteristics of a shock front. These parameters include initial pressure and density ahead of the shock, p_0 and ρ_0 , shock propagation velocity, U_s , and pressure and particle velocity immediately behind the shock front, p and u_p . The Hugoniot equation for this condition (Reference IV-2.80) is:

$$p - p_0 = \rho_0 U_s u_p \quad (\text{IV-2.16})$$

In addition to Equation IV-2.16, a second relationship expresses the shock front velocity as a linear function of particle velocity behind the front

$$U_s = C + S u_p \quad (\text{IV-2.17})$$

where C and S are respectively the intercept and slope of a linear segment of a plot of U_s versus u_p for a specific range of pressure levels. For some materials, the full range of pressure levels within the hydrodynamic region may be represented

by a single linear plot. For others, such as alluvium shown in Figure IV-2.10, the curve is not linear, but several linear segments serve as a practical approximation for application to the Hugoniot equation of state.

Laboratory studies of a particular rock within which an explosion is planned provide values of C and S characteristic of the material over the applicable range of pressures, and it is sufficient to determine only the velocity with which the shock front is propagated from field measurements at a point near the explosion in order that both pressure level and particle velocity there may be determined. Such field measurements are customarily made by recording the times at which the shock arrives at two closely spaced and accurately positioned detectors. These shock front arrival measurements may be made either through part of the rock itself or within a sample of a different material, the Hugoniot parameters for which have been experimentally established.

Data reported here were obtained by Sandia Laboratories (Reference IV-2.27) and include results of measurements near 30 underground nuclear explosions in alluvium, tuff, and granite. Hugoniot parameters used in reduction of these data were derived from laboratory experiments reported elsewhere (References IV-2.81, IV-2.82, and IV-2.83), and are listed in Table IV-2.2. Different field measurement schemes were devised for different geometries of explosive emplacement. These techniques are described briefly in conjunction with the types of rock to which each was best adapted.

Table IV-2.2 Hugoniot parameters (Reference IV-2.27).

Rock	Pressure Range (Kilobars)	Density (gm/cm ³)	C (cm/ μ sec)	S
Alluvium	<90	1.54	0.062	1.875
	>90 - <183	1.54	0.247	0.722
	>183 - <354	1.54	0.016	1.577
	>354	1.54	-0.46	2.84
Dry Tuff	<85	1.46	0.068	1.80
	>85 - <210	1.46	0.22	0.86
Partially Saturated Tuff	<108	1.74	0.34	0.74
Saturated Tuff	>20 - <86	2.00	0.223	1.328
Granite	>350	2.65	0.41	0.96

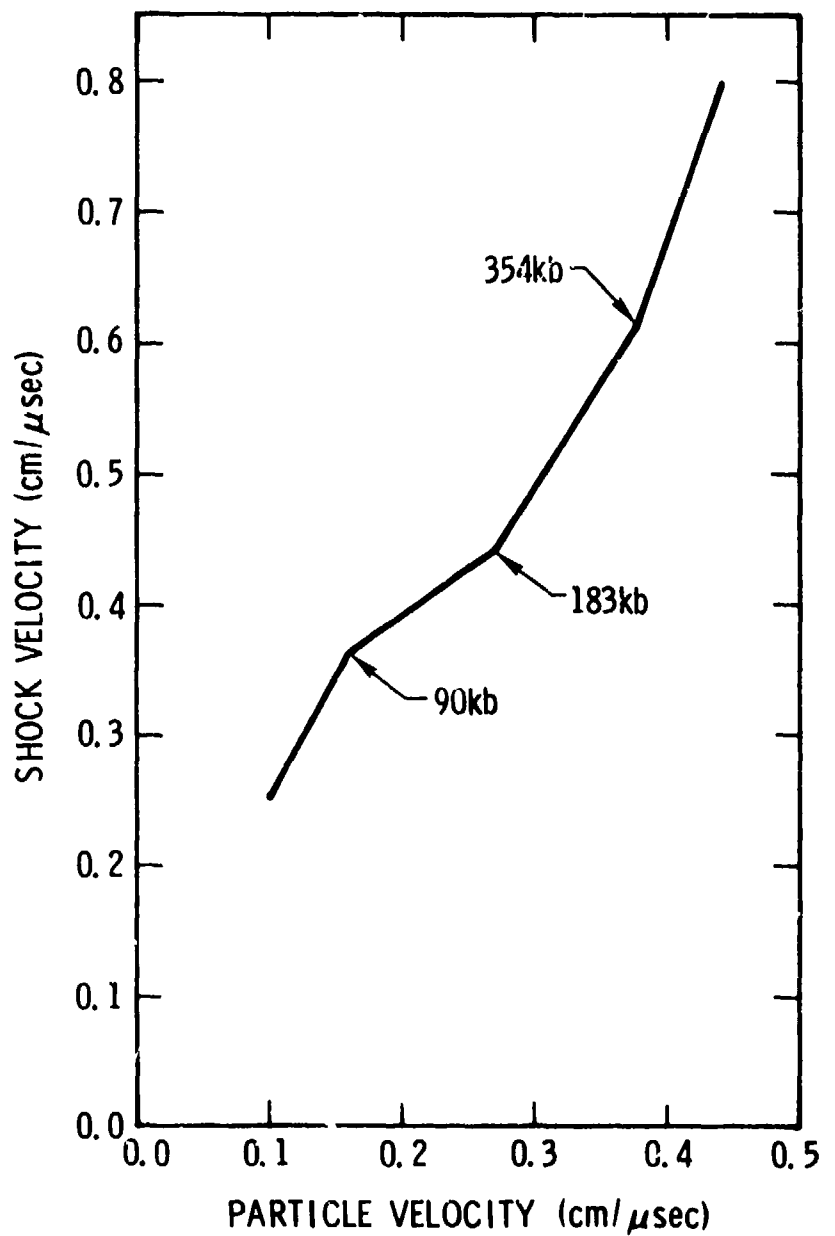


Figure IV-2.10. Hugoniot parameters for dry alluvium
(Reference IV-2.27).

Underground nuclear explosion tests in alluvium are typically conducted in deep, vertical drill holes. Emplacement of gauges for shock front measurements in the hydrodynamic region for these explosions must be accomplished from the surface, which is often more than a thousand feet above the prescribed gauge position. Three techniques for these deep hole measurements have been employed by Sandia Laboratories. The first system used as the shock front velocity gauge a plexiglass slab about 5 cm thick with PZT (lead zirconate titanate) ferroelectric crystals mounted on opposite surfaces. This slab was oriented by remote control so that the path of the shock front through it corresponded to that between the PZT crystals. A remote indicating gyroscope system permitted orientation of the gauge with an angular precision of $\pm 1^\circ$ at depths of 1000 ft, and configuration of the arrival-time matrix was such that positioning error always resulted in positive error in derived pressures. Each hole containing a gauge was backfilled with alluvium after final orientation of the gauge to minimize perturbation of the shock front. Shock velocities observed within the plexiglass were related to pressures by means of known Hugoniot parameters for plexiglass. This pressure corresponded essentially to the driving pressure in the alluvium because Hugoniot parameters for alluvium and plexiglass are very similar. Difficulty and expense of gauge orientation at these depths led to the development of a ring-type or "nondirectional" gauge (Reference IV-2.84). Active elements of these gauges were a pair of PZT crystal rings about 5 cm and 10 cm in diameter, each having square cross sections about 6 mm on a side. The rings were mounted 10 cm apart coaxially on the axis of a thin-walled plexiglass tube which was filled with alluvium. The gauge was placed at shot horizon with its axis vertical. Arrival of the shock front at each ring produced a signal from which shock front velocity was deduced. A third method and rarely used technique utilized a quartz crystal embedded in a plexiglass blank. This type of gauge required precise orientation similar to that for slab gauges. Proper uniform backfill of gauge emplacement holes with local alluvium and special care to prevent bridged voids in the backfill is essential to successful operation of all three types of gauges. All three systems also required precise time and high speed oscilloscopic recording of shock arrival signals.

Underground nuclear detonations in tuff have been conducted both in deep vertical borings and in tunnel and drift complexes mined into mesas surrounding some of the broad valleys at the Nevada Test Site. Those tests conducted in vertical wells were instrumented in the hydrodynamic region in the manner described for explosions in alluvium. Those tests conducted in tunnel complexes permitted

more sophisticated measurement systems. In tunnel systems it is usually feasible to reach desired gauge positions within the hydrodynamic region by means of horizontal instrument borings 30 m or less in length. In such configurations, gauge orientation is readily and accurately controllable and measurement of the range from shot point to the gauge is accurate to a few centimeters in several meters. This type of installation also permits bonding gauges to the surrounding rock with a cement grout which is matched to the rock in acoustic impedance. Gauges of significantly larger size may be used in such tunnel installations. Shock velocity data for shots in tuff were obtained primarily with PZT-ring gauges. It was also found feasible to obtain some direct pressure-history data in lower pressure regions with piezoresistive gauges formed of manganin wire grids embedded in epoxy. These gauges have a useful pressure range of from 10 to 500 kilobars.

The region of hydrodynamic response in granite is considerably smaller than in alluvium or tuff, with the consequent requirement that shock arrival gauge systems for explosions in granite must be emplaced much closer to the shot point. Fortunately, nuclear explosion tests in granite have been located in deep tunnel complexes which permit precise close-in gauge emplacement. The applicable improved gauge installation procedures also permit use of other, more precise devices, such as impedance-match gauges with which pressures ranging from a megabar to 100 kbars can be measured. This system relates transit velocities measured in calibrated samples of two materials which are driven by the shock in granite to the shock velocity in granite. Sample materials are chosen for well established shock response characteristics and are typically aluminum and brass. This technique generates in situ Hugoniot data for granite. However, its use is limited by a required complex transmission and recording system.

Stress histories may be measured more readily in the lower pressure region just beyond the hydrodynamic region where rock is deformed plastically. Gauges have been devised for use in this region which, though stronger than the surrounding rock and capable of withstanding the shock front, do not severely distort the front and develop a signal relatable to the driving disturbance. Gauge systems for such measurements include active elements of ytterbium, quartz or PZT. Ytterbium gauges, which employ a foil of ytterbium embedded in epoxy, are suitable for recording pressures between 1 and 15 kilobars. In regions of somewhat lower stress, PZT gauges were found suitable. Quartz gauge systems (Reference IV-2.84) also have been used for stress measurements in granite.

IV-2.2.2 Data Analysis

Data derived from measurements of shock front velocity in the hydrodynamic region surrounding nuclear explosions in alluvium are listed in Table IV-2.3 and similar data for explosions in tuff and granite are listed in Table IV-2.4. These data are plotted as a function of scaled range in Figure IV-2.11. In this figure, solid lines represent linear regression fits to the data and dashed lines represent 90-percent confidence limits for these fits. Two sets of pressure data, identified as Tuff (nonlinear) and Granite (nonlinear) in the figure, were omitted from regression analysis for reasons discussed in Reference IV-2.27.

Table IV-2.3. Scaled free-field ground motion and pressure in the hydrodynamic region - alluvium (Reference IV-2.27).

Scaled Range m/kt ^{1/3}	Scaled Range ft/kt ^{1/3}	Pressure kilobar	Particle Velocity m/sec	Velocity ft/sec	Gauge Type
2.39	7.84	565±10	4404	14450	Ring
2.76	9.06	295±25	3475	11400	Ring
2.85	9.35	475±50	4148	13610	Ring
3.19	10.47	196±20	2734	8970	Ring
3.26	10.70	120±20	1948	6390	Ring
3.44	11.29	300±30	3505	11500	Plexiglass
3.50	11.48	188±15	2658	8720	Ring
3.78	12.40	162±15	2402	7880	Plexiglass
3.91	12.83	140±15	2170	7120	Ring
4.00	13.12	167±15	2451	8040	Plexiglass
4.06	13.32	130±15	2060	6760	Ring
4.22	13.85	90±10	1554	5100	Plexiglass
4.30	14.11	187±15	2646	8680	Plexiglass
4.34	14.24	56±5	1225	4020	Ring
4.55	14.93	78±10	1454	4770	Ring
4.72	15.49	80±5	1475	4840	Ring
4.80	15.78	81±5	1487	4880	Ring
5.25	17.23	72±5	1393	4570	Ring
5.34	17.52	27±5	811	2660	Ring
5.43	17.81	37±5	988	3240	Ring
5.60	18.37	76±5	1403	4700	Plexiglass
5.90	19.36	75±5	1420	4660	Plexiglass
6.14	20.14	45±5	1094	3590	Plexiglass
6.25	20.51	20±5	661	2170	Quartz
6.27	20.57	30±5	872	2860	Ring
6.63	21.75	25±5	771	2530	Ring
6.69	21.95	13±5	274	900	Ring
6.77	22.21	20±5	661	2170	Ring
6.85	22.47	26±5	792	2600	Plexiglass
7.58	24.87	15±5	335	1100	Ring
7.66	25.13	22±5	707	2320	Ring
7.88	25.85	54±5	1201	3940	Plexiglass
8.25	27.07	22±5	707	2320	Ring

Table IV-2.4. Scaled free-field ground motion and pressure in the hydrodynamic region - tuff and granite (Reference IV-2.27).

Scaled Range m/kt ^{1/3}	Pressure kilobar	Particle Velocity m/sec	Particle Velocity ft/sec	Gauge	Rock Moisture
TUFF					
3.14	10.3	212±20	2301	7550	Ring
3.63	11.9	140±10	1750	5740	Ring
3.89	12.8	125±15	2079	6820	Ring
4.88	16.0	40±10	1049	3440	Ring
8.05	26.4	14±5*	719	2360	Ring
8.71	28.6	28*	472	1550	Manganin
14.6	48	8*	180	590	Ferroelectric
16.2	53	5*	96	315	Ferroelectric
29.0	95	2.2*	44	144	Ytterbium
30.2	99	2.4*	48	157	Ytterbium
35.1	115	1.8*	35	115	Ytterbium
41.1	135	1.2*	24	79	Ferroelectric
43.3	142	1.4*	28	92	Ytterbium
45.7	150	1.1*	21	69	Ytterbium
49.7	163	0.8*	16	52	Ferroelectric
GRANITE					
2.50	8.2	620±48	3300	10830	Impedance Match
2.83	9.3	660	3400	11155	Impedance Match
3.05	10.0	300±80	1900	6235	Impedance Match
3.23	10.6	450±50	2600	8530	Impedance Match
3.60	11.8	137	900	2955	Impedance Match
10.2	33.6	41±5*	276	906	Quartz
15.4	50.4	14±5*	94	309	Quartz
23.5	77.0	7.5*	53	175	Quartz
35.7	117	4.0*	28	93	Quartz
51.3	168	1.25*	8.8	29	Quartz

*Data omitted from hydrodynamic response regression analysis.

Regression equations for these data were obtained by Perret and Cass (Reference IV-2.27).

$$p = 7.71 \times 10^3 \left(\frac{R}{W^{1/3}} \right)^{-2.96 \pm 0.19} \quad (\text{IV-2.18})$$

where p is the pressure in kilobars, R is the radial distance in meters, and W is the explosive energy in equivalent kilotons of TNT; and

$$u = 2.43 \times 10^4 \left(\frac{R}{W^{1/3}} \right)^{-1.87 \pm 0.05} \quad (\text{IV-2.19})$$

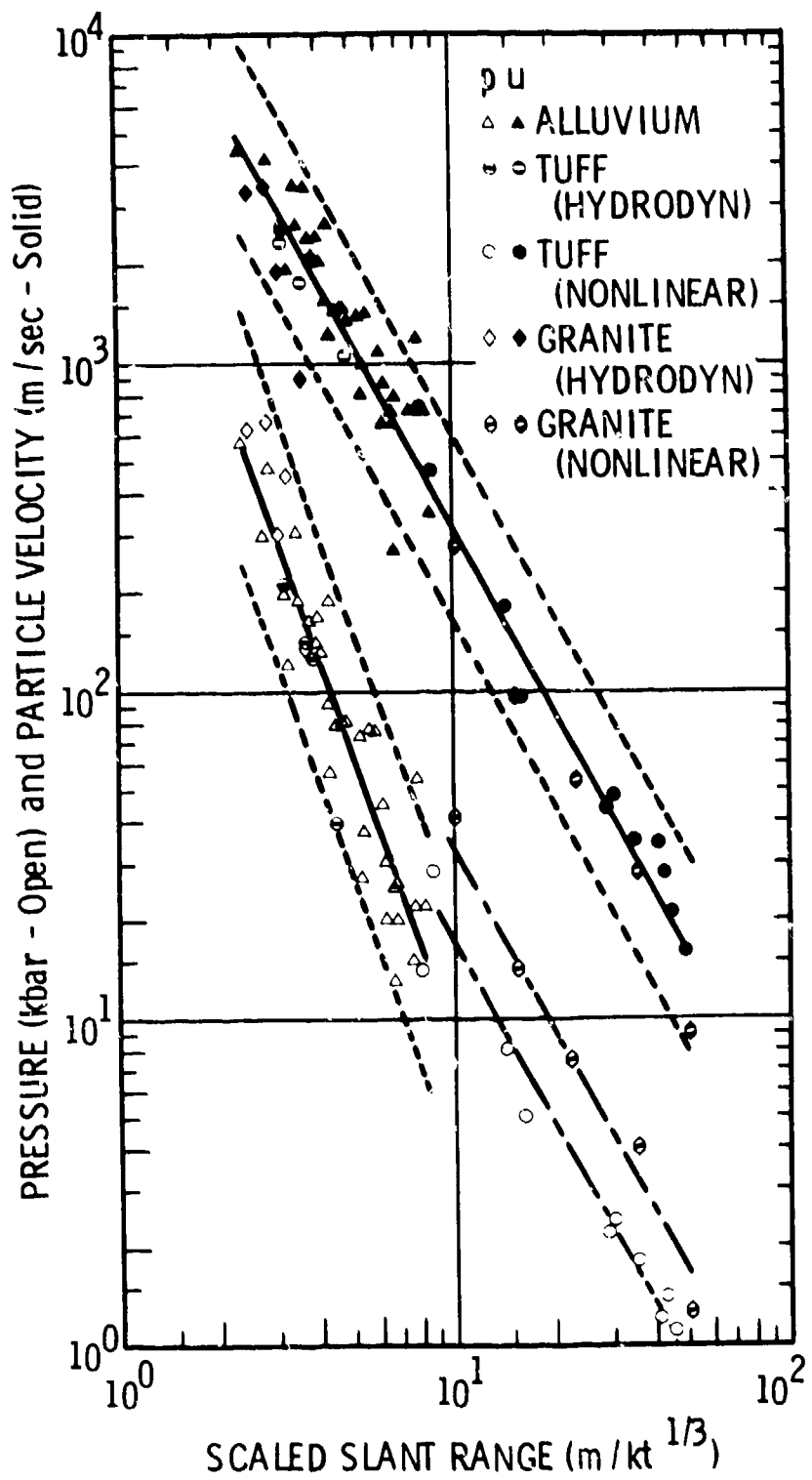


Figure IV-2.11. Pressure and particle velocity attenuation (Reference IV-2.27).

where u is the particle velocity in m/sec and R and W are as defined above. The fractional standard deviation for the exponent in Equation IV-2.18 is 6.4 percent; in Equation IV-2.19 it is 2.7 percent. Variance factors for the coefficients are 1.34 and its reciprocal for Equation IV-2.18, and 1.11 and its reciprocal for Equation IV-2.19. The variance of the coefficient is defined by the standard deviation of the common logarithm of the coefficient. The antilog of this deviation and the reciprocal antilog are the applicable variance factors.

This analysis of pressure data indicates that in the range from 700 to about 10 or 20 kilobars, the pressure decreases as the inverse 2.96 power of scaled distance in good agreement with the theoretical attenuation for hydrodynamic response as the inverse cube of distance. It also indicates that particle velocity derived from hydrodynamic region pressures by the Hugoniot equation of state is attenuated as the inverse 1.87 power of range or roughly as the inverse square of range.

Pressure data from both the transition region between the hydrodynamic and the plastic response and from the plastic response region are represented in Figure IV-2.11 by the points below 10 kilobars. Of these data, those from explosions in granite are greater than those from shots in tuff by a factor of about 2.2, but the attenuation rate is essentially the same as that for all particle velocity data as indicated by the dash-dot lines which have been drawn through these pressure data parallel to the velocity regression curve. Evidently, pressures below 10 kilobar must be related to particle velocities by a constant factor, but above that stress level there is a variable relationship which changes with pressure. However, both the Hugoniot equation of state for the hydrodynamic region, that is, at pressures above 10 to 20 kilobars, and the relationship between shock front velocity and particle velocity indicate that, in hydrodynamic shock, pressure and particle velocity are not related by a simple factor because the propagation velocity, U_s , varies with pressure, and density behind the shock front must also depend on pressure.

Beyond the hydrodynamic response region and in fact into the region of non-linear and linear response, both the propagation velocity and the density remain constant at least through the initial peak levels, and stress throughout this region is related to particle velocity by a constant factor, the seismic impedance, which is the product of density and propagation velocity.

The differences in pressure levels in different types of rock previously noted in data below 10 kilobars are absent in the higher pressure data. The explanation of these phenomena lies in the different porosities and strengths of the rocks and in the fact that at stress levels sufficiently high to cause hydrodynamic response to the loading, neither porosity nor strength, which derive from the crystalline and macrostructure of the rock, exist to differentiate response of the rock to hydrodynamic shock. However, in the regions of lower stress beyond that of hydrodynamic response, these properties of the rocks exercise strong control over response to transient loading.

IV-2.3 FREE-FIELD GROUND MOTION IN THE NONLINEAR REGION

IV-2.3.1 Measurement Techniques

It was noted earlier that in regions of nonlinear and linear response of rock, measurement of motion rather than stress provides more reliable results. Measurements of transient stress in a rock environment require a continuous, good bonding between the gauge and rock and a good match of seismic impedance as well. In the region of hydrodynamic response, this requirement must be met for extremely short periods during an early portion of the rise to the shock wave peak for time-of-arrival measurements. In the transition zone between hydrodynamic and nonlinear response where stress-history gauges may survive passage of part or all of the transient, the duration time is still very short and gross motions produced by the stress wave have only a minor effect on the match between the gauge and the rock impedance during the period.

However, in the regions of nonlinear and linear response, rise times increase from fractional milliseconds to tens of milliseconds, and both dispersive effects and absorption of high frequency components broaden the peaks and the decay portions of the transient. A consequence of this is that gross motions, which can be adequately registered by motion sensitive gauges bonded securely to the rock, result in variations in gauge-rock bonding and impedance match with questionable stress gauge response. In general, motion-histories derived from the more sophisticated theoretical calculations agree reasonably with records from motion gauges such as accelerometers or particle velocity gauges. This discussion does not imply that impedance matching between rock, bonding material, and gauge may be ignored in free-field motion measurements in the regions of nonlinear or linear response, but simply that such measurements are much less sensitive to mechanical consequences of passage of the broadened stress wave than are stress measurements.

Both accelerometers and particle velocity gauges used in the Sandia Laboratory measurements were simple mass-spring or pendulum systems suitably damped to produce the desired response and equipped with electronic devices to translate motion to electric output corresponding directly to the motion within a frequency band broader than that of the relevant motion. Accelerometer mass-spring systems were damped to about 0.7 times critical and responded with constant sensitivity over a frequency range bounded by zero Hz and half the natural frequency of the mass-spring system. This latter gauge parameter ranged from about 50 Hz for low range (about 1-g full scale) to more than 10 kHz for high range (more than 10^3 -g full scale) accelerometers. Particle velocity gauges employed pendulums grossly over-damped, about 100 times critical, and capable of sensitivity adjustment from 15 cm/sec to more than 30 m/sec full scale over a frequency range from about 0. 1z to 200 Hz (Reference IV-2.32 - Appendix A).

IV-2.3.2 Free-Field Ground Motion in Alluvium

Free-field ground motion has been recorded for seven contained underground nuclear explosions in desert alluvium at the Nevada Test Site and for one underground chemical cratering explosion at NTS. Horizontal shot level instrument arrays were used for five of these events: SCOOTER (Reference IV-2.16), FISHER, HOGNOSE, HAYMAKER (Reference IV-2.59), and MERLIN (Reference IV-2.12) and vertical radius arrays were used in four of them, MERLIN, VULCAN, HUPMOBILE (Reference IV-2.18), and PACKARD (Reference IV-2.26). In two cases, HOGNOSE and HAYMAKER, gauge arrays were near but not at shot depth. Because alluvium events all involved emplacement of explosives at the bottom of deep borings or shafts, the vertical instrument arrays nearest surface zero were in borings offset about 10 m from the emplacement boring.

IV-2.3.2.1 Scaled Acceleration Analysis. Scaled acceleration data from alluvium events are plotted in Figure IV-2.12. Data from each event is distinguished by a specific symbol. Data from the MUD PACK Event (Reference IV-2.11) are included in this figure and the corresponding alluvium plots of particle velocity and displacement for apparent reasons which are discussed later. The MUD PACK Event was detonated in a dry tuff environment. In Figure IV-2.12 and the succeeding data plots, linear regression fits to the data are plotted as solid lines and 90 percent confidence limits for the fit are shown as dashed lines. In many cases, certain data were omitted from the regression analysis because of anomalous conditions either in the instrumentation or the recorded motion. Such omitted points are indicated by underlining of the symbol.

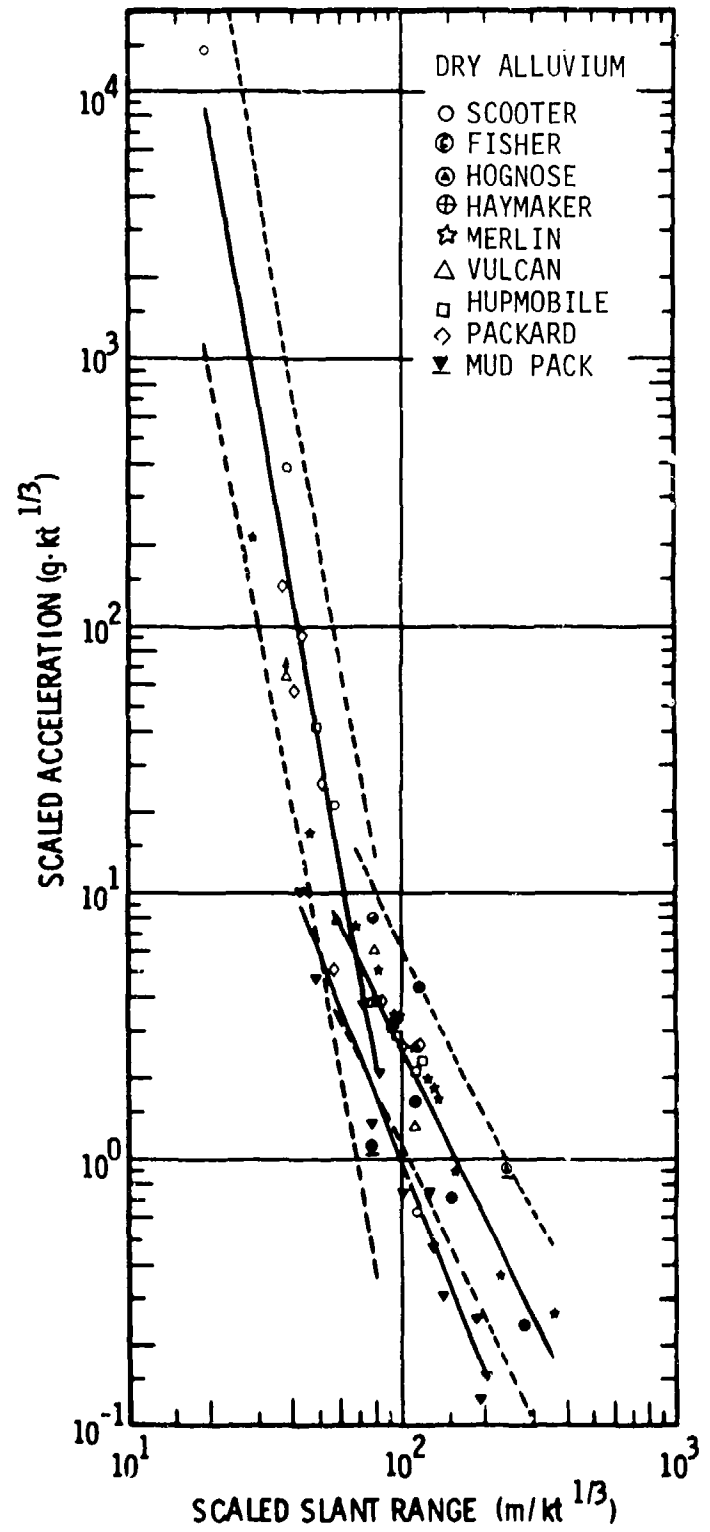


Figure IV-2.12. Attenuation of scaled acceleration - dry alluvium
(Reference IV-2.27).

Where a complete set of data have been omitted from analysis, as were the MUD PACK data in Figure IV-2.12, the symbol in the legend block has been underlined. In some cases, a separate regression fit for an omitted event is plotted without confidence limits, as in Figure IV-2.12.

Alluvium acceleration data in Figure IV-2.12 fall into two groups; those at scaled distances less than $80 \text{ m}/\text{kt}^{1/3}$ are attenuated at a much faster rate than those at scaled distances greater than $60 \text{ m}/\text{kt}^{1/3}$. The overlap recognizes that any transition in attenuation pattern is not a discontinuous process and that the use of linear fits to the data represents a simplifying approximation. Over a scaled range interval from 20 to $80 \text{ m}/\text{kt}^{1/3}$, scaled acceleration peaks fall off according to the equation

$$a \cdot W_1^{1/3} = 2.24 \times 10^{11} \left(R/W_1^{1/3} \right)^{-5.78 \pm 0.47} \quad (\text{IV-2.20})$$

where scaled acceleration, $a \cdot W_1^{1/3}$, is in $\text{g} \cdot \text{kt}^{1/3}$, scaled slant range, $R/W_1^{1/3}$, is in $\text{m}/\text{kt}^{1/3}$, and W is the explosive energy yield in equivalent kilotons of TNT. The coefficient of this equation, which represents the intercept of the fit at $R/W_1^{1/3}$ equal to unity, has a variance defined by the factors 6.39 and its reciprocal; hereafter in quotation of variance factors the reciprocal is understood. The exponent has a fractional standard deviation of 8.1 percent.

Over the interval from 60 to $350 \text{ m}/\text{kt}^{1/3}$ in slant range, the regression equation is

$$a \cdot W_2^{1/3} = 4.79 \times 10^4 \left(R/W_2^{1/3} \right)^{-2.13 \pm 0.18} \quad (\text{IV-2.21})$$

Variance of the coefficient is described by the factor 2.34. Fractional standard deviation of the exponent is 8.4 percent.

IV-2.3.2.2 Particle Velocity Analysis. Particle velocity data from the alluvium events are plotted as a function of scaled slant range in Figure IV-2.13. Here, some individual MUD PACK data were not included in the analysis so that only omitted points are underscored rather than the legend symbol. These underscored MUD

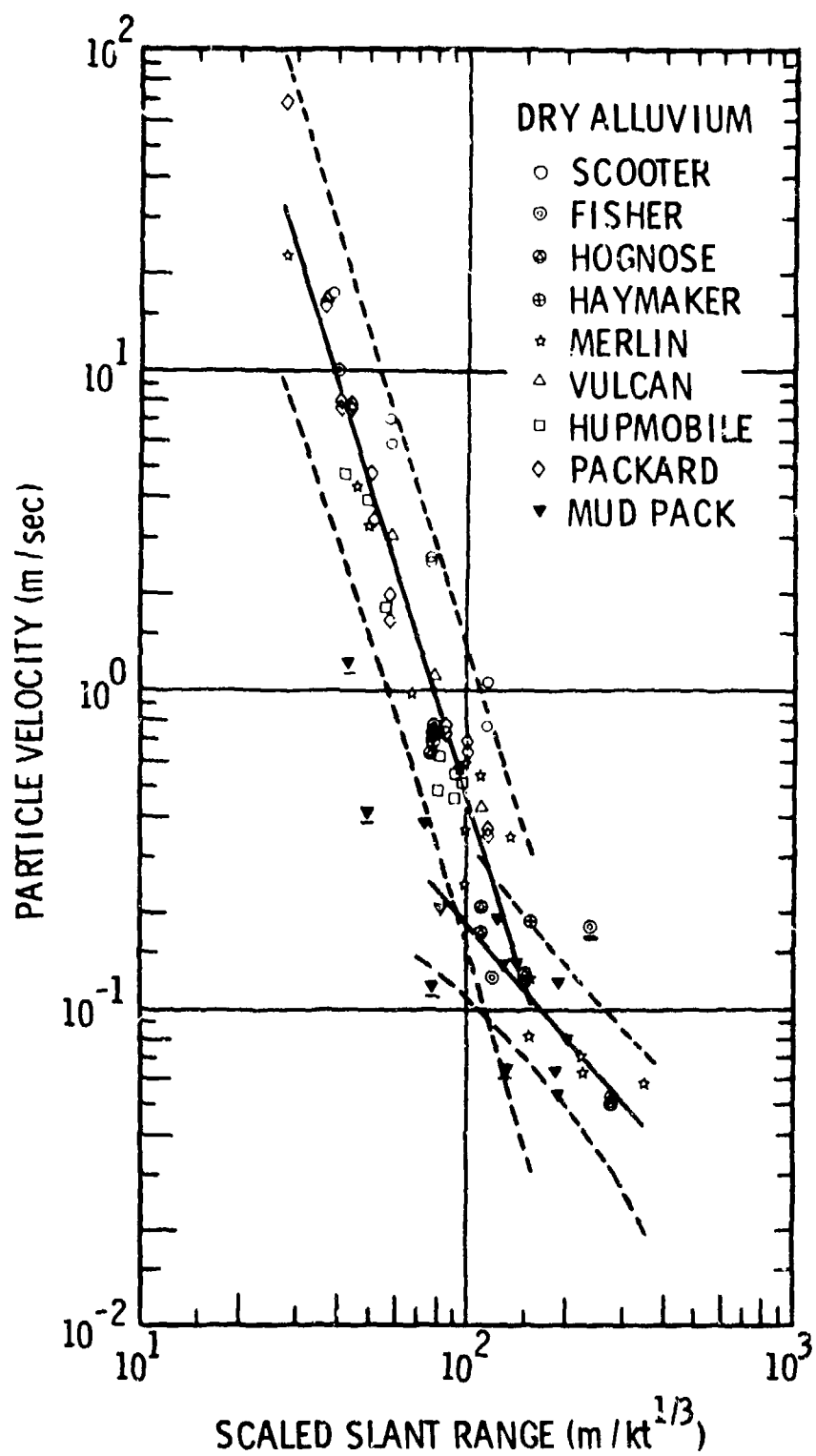


Figure IV-2.13. Attenuation of particle velocity - dry alluvium (Reference IV-2.27).

PACK points represent data recorded at stations in carbonate rock beneath the tuff shot environment.

In this plot there are again two phases in the regression fit. In the first, at scaled ranges between 30 and 150 m/kt^{1/3}, the least-squares fit is represented by the equation

$$u_1 = 1.52 \times 10^6 \left(R/W^{1/3} \right)^{-3.27 \pm 0.16} \quad (\text{IV-2.22})$$

where u_1 represents particle velocity in m/sec and other terms are as previously defined. The variance of the coefficient is given by the multiplier 1.96. Fractional standard deviation of the exponent is 4.9 percent.

The second segment of these data, which covers the scaled slant range interval from 100 to 350 m/kt^{1/3} and includes some of the MUD PACK data in the analysis, is described by the regression equation

$$u_2 = 3.86 \times 10^1 \left(R/W^{1/3} \right)^{-1.16 \pm 0.14} \quad (\text{IV-2.23})$$

where the coefficient variance multiplier is 2.09 and fractional standard deviation of the exponent is 12 percent.

IV-2.3.2.3 Scaled Displacement Analysis. Scaled displacement data from the alluvium events are plotted against scaled range in Figure IV-2.14. In this plot, all SCOOTER scaled displacements and specific MUD PACK data have been excluded from the regression analyses. Again, there are two phases in the analysis, of which the first, representing scaled ranges between 40 and 150 m/kt^{1/3}, fits the equation

$$d/W_1^{1/3} = 3.44 \times 10^6 \left(R/W^{1/3} \right)^{-3.04 \pm 0.20} \quad (\text{IV-2.24})$$

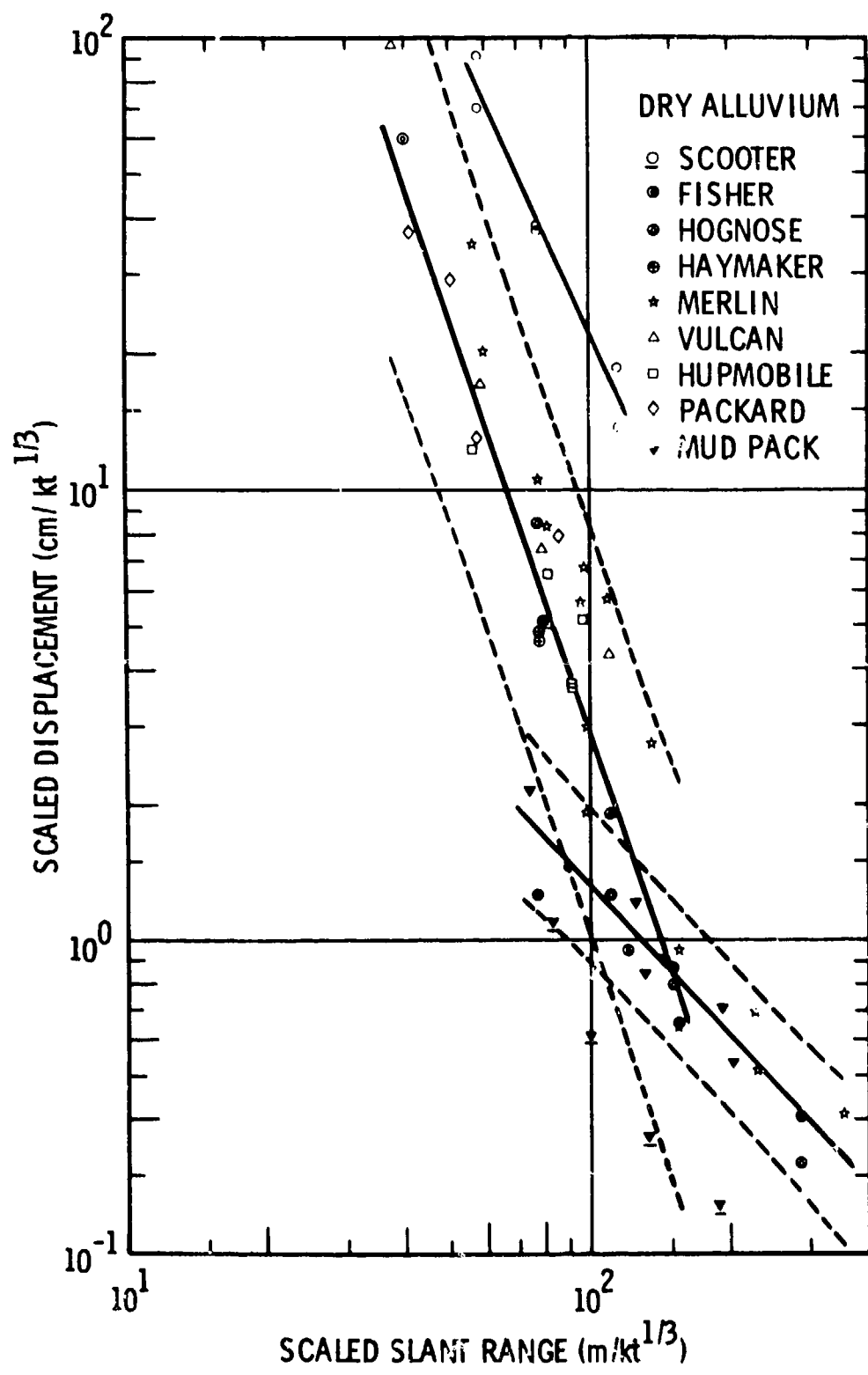


Figure IV-2.14. Attenuation of scaled displacement - dry alluvium (Reference IV-2.27).

where $d/W^{1/3}$ is the scaled displacement peak in $\text{cm}/\text{kt}^{1/3}$. Variance of the coefficient is defined by the factor 2.42 and fractional standard deviation of the exponent is 6.6 percent.

The more remote scaled displacement data for alluvium within scaled ranges between 100 and 350 $\text{m}/\text{kt}^{1/3}$ and including more than half of the MUD PACK data yield the equation

$$d/W^{1/3} = 2.22 \times 10^2 \left(R/W^{1/3} \right)^{-1.11 \pm 0.11} \quad (\text{IV-2.25})$$

where the variance factor for the coefficient is 1.72 and fractional standard deviation of the exponent is 9.9 percent.

IV-2.3.2.4 Discussion. A few pertinent facts which are evident in these plots and analyses merit discussion at this point. It is evident that SCOOTER accelerations fall among those observed during the other events, that SCOOTER particle velocities are in general higher near the upper 90 percent confidence limit, and that scaled displacements from SCOOTER exceed all others at the same slant range by a factor of at least two and fall well beyond the confidence limit plotted in Figure IV-2.14. The explanation for this probably is related to the fact that SCOOTER depth of burst is roughly 10 percent of that of the contained explosions. Consequently, for SCOOTER geostatic pressure is considerably less, bulk density is low and in the looser particulate material greater particle velocities and displacements may develop. Scaled rise times show that, in general, for accelerations this parameter is roughly the same for all events, for particle velocities it is greater for SCOOTER, and for displacements scaled rise times are even greater for the shallow event. It is also possible that the difference in explosives may have contributed to this difference, because of residual gases from the TNT explosion, but this effect would be somewhat mitigated by venting of SCOOTER as it cratered.

MUD PACK data do not belong in the alluvium analysis because that explosive was placed in dry tuff 30 m above the paleozoic rock in Area 8 at NTS. However, cores from instrument borings adjacent to the MUD PACK shot hole included several units of extremely friable, porous ash-flow tuff which probably responds much more like alluvium in the nonlinear domain than would the more common zeolitized tuffs of NTS. These very weak tuff cores were from the vicinity of the MUD PACK shot

depth. Scatter in MUD PACK data is large, but it tends to correlate with geologic materials at specific instrument locations. Thus, stations in the carbonate paleozoic rock show motions much smaller than those in tuff at comparable scaled range, in keeping with both rock response and with energy losses due to reflection at the tuff-carbonate interface. The MUD PACK data appear to follow a pattern similar to those from SCOOTER in that scaled accelerations are all distinctly lower than those from the other alluvium events, and particle velocities and scaled displacements fall generally among the alluvium data from the other nuclear events.

IV-2.3.3 Free-Field Ground Motion in Dry Tuff

Seven events from which free-field ground motion data were obtained were considered to have been detonated in "dry tuff." This definition of the shot environment is at best arbitrary. The category might more precisely have been called "not very wet tuff" since laboratory and theoretical studies of response of porous rocks to high stress transients differs little as moisture content is increased up to about 90 percent of saturation but changes radically between 90 and 100 percent saturation, where saturation implies that all pores are filled with liquid water. Dry tuffs may, therefore, be within the moist zone but well above the water table.

Examination of cores and outcrops of tuff at NTS indicates that this type of rock ranges from extremely friable grainy material hardly distinguishable mechanically from weakly cemented or consolidated sandy alluvium through varying degrees of cementation and vitreous bonding to dense welded tuffs which have seismic impedance similar to that of limestone and dolomite. Consequently, events assigned to the dry tuff category are limited to those detonated in tuff well above the water table, and none was located in high impedance welded tuff.

All dry tuff events were detonated at NTS either in Area 12, Rainier Mesa, or in Area 8. All three types of instrument station array were used: shot level, vertical radius, and offset vertical arrays.

Classified yields of some events have required that their identification be limited to a letter rather than the event name to permit unclassified use of the scaled data in this report.

Identification of the DISCUS THROWER shot environment as dry tuff prompts some explanation as a consequence of the BANEERRY Event. The latter explosion was much more effectively coupled to the rock than expected and produced much more

vigorous motion. Subsequent investigation indicated the presence of a significant quantity of saturated montmorillonite within the tuff surrounding the BANEERRY explosion. It is noted, however, that DISCUS THROWER, in addition to being some 300 m north of and deeper than the BANEERRY shot, was in tuff appreciably beyond the limits of the montmorillonite bearing formation and that water content of the tuff at and near the DISCUS THROWER shot point was significantly below the 95 percent saturation which would have influenced rock response toward that typical of the wet tuff classification.

IV-2.3.3.1 Scaled Acceleration Analysis. Scaled acceleration data were available from only four of the dry tuff events because only velocity gauges were employed at free-field motion stations for the other three. These acceleration data are plotted versus scaled range in Figure IV-2.15. Data from the RAINIER (Reference IV-2.7), EVANS (Reference IV-2.6), and DISCUS THROWER (Reference IV-2.17) Events are treated separately from those from the MUD PACK Event because the latter are generally lower by an order of magnitude.

Regression analysis of the data from the first three events was performed in two linear phases. The first, applied to the scaled slant range interval between 40 and 150 m/kt^{1/3}, resulted in the equation

$$a \cdot W_1^{1/3} = 4.90 \times 10^{10} \left(R/W_1^{1/3} \right)^{-4.77 \pm 0.33} \quad (\text{IV-2.26})$$

where variance of the coefficient is given by the factor 4.33 and fractional standard deviation of the exponent is 6.9 percent.

The second phase linear regression to these data covers the scaled range interval from 100 to 500 m/kt^{1/3} and is described by the equation

$$a \cdot W_2^{1/3} = 7.71 \times 10^4 \left(R/W_2^{1/3} \right)^{-1.92 \pm 0.14} \quad (\text{IV-2.27})$$

where the multiplier 2.12 defines variance of the coefficient and 7.4 percent is the fractional standard deviation of the exponent.

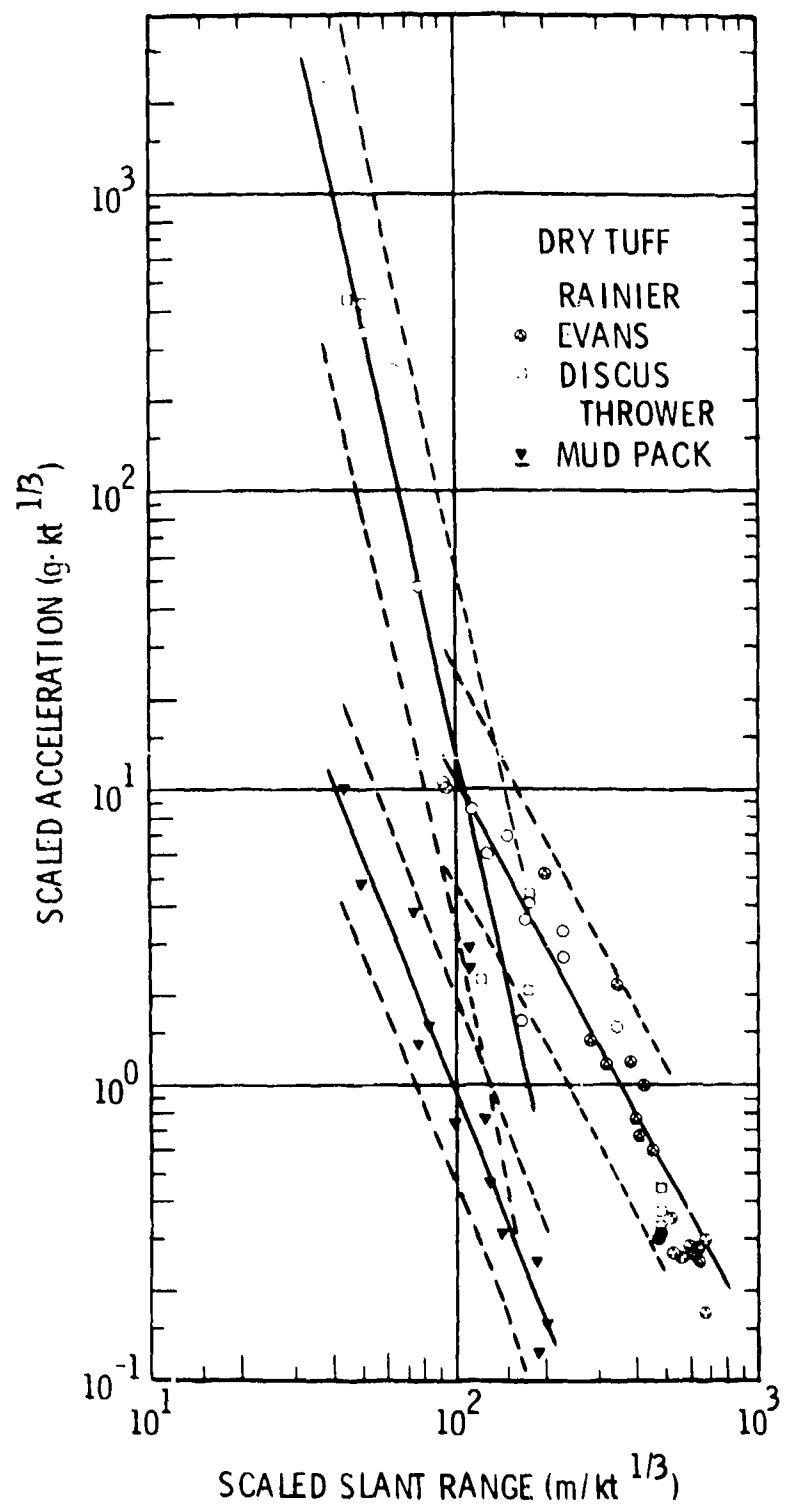


Figure IV-2.15. Attenuation of scaled acceleration - dry tuff (Reference IV-2.27).

IV-2.3.3.2 Particle Velocity Analysis. Particle velocity data plotted in Figure IV-2.16 are available from all seven dry tuff events, but those from MUD PACK are again about an order of magnitude below those from the other events and are analyzed separately. Linear regression of data from the remaining six dry tuff events yielded the equation

$$u = 1.85 \times 10^4 \left(R/W^{1/3} \right)^{-1.98 \pm 0.11} \quad (\text{IV-2.28})$$

over the full span of scaled range from 40 to 500 m/kt^{1/3}. The multiplier 1.81 defines variance of the coefficient and fractional standard deviation of the exponent is 5.6 percent.

IV-2.3.3.3 Scaled Displacement Analysis. Data plotted in Figure IV-2.17 represent all available peak displacements from the underground explosions in dry tuff. Scatter is unusually great, as indicated by the 90 percent confidence limits which span about an order of magnitude near the midpoint of the slant range data. MUD PACK data are again low by an order of magnitude and are analyzed separately.

Linear regression of scaled displacement data from the dry tuff events, omitting MUD PACK, leads to the equation

$$d/W^{1/3} = 3.80 \times 10^5 \left(R/W^{1/3} \right)^{-2.20 \pm 0.21} \quad (\text{IV-2.29})$$

where the fractional standard deviation of the exponent is 9.6 percent and variance of the coefficient is encompassed by the multiplier 3.11 and its reciprocal. This applies to the span of scaled slant range between 100 and 500 m/kt^{1/3}.

Displacement data from six of the DISCUS THROWER stations are lower by a factor of nearly 10 than those from either the other DISCUS THROWER stations at about the same scaled range or from other events in dry tuff. These low data points represent motion within the carbonate rock below the tuff or from the tuff-carbonate interface and reflect the decreased pore volume and greater rigidity in the underlying paleozoic rock. This effect is hardly discernible in the acceleration data, Figure IV-2.15, and is considerably smaller by a factor of about 1.5 in the particle velocity plot, Figure IV-2.16, than in the scaled displacement data, Figure IV-2.17.

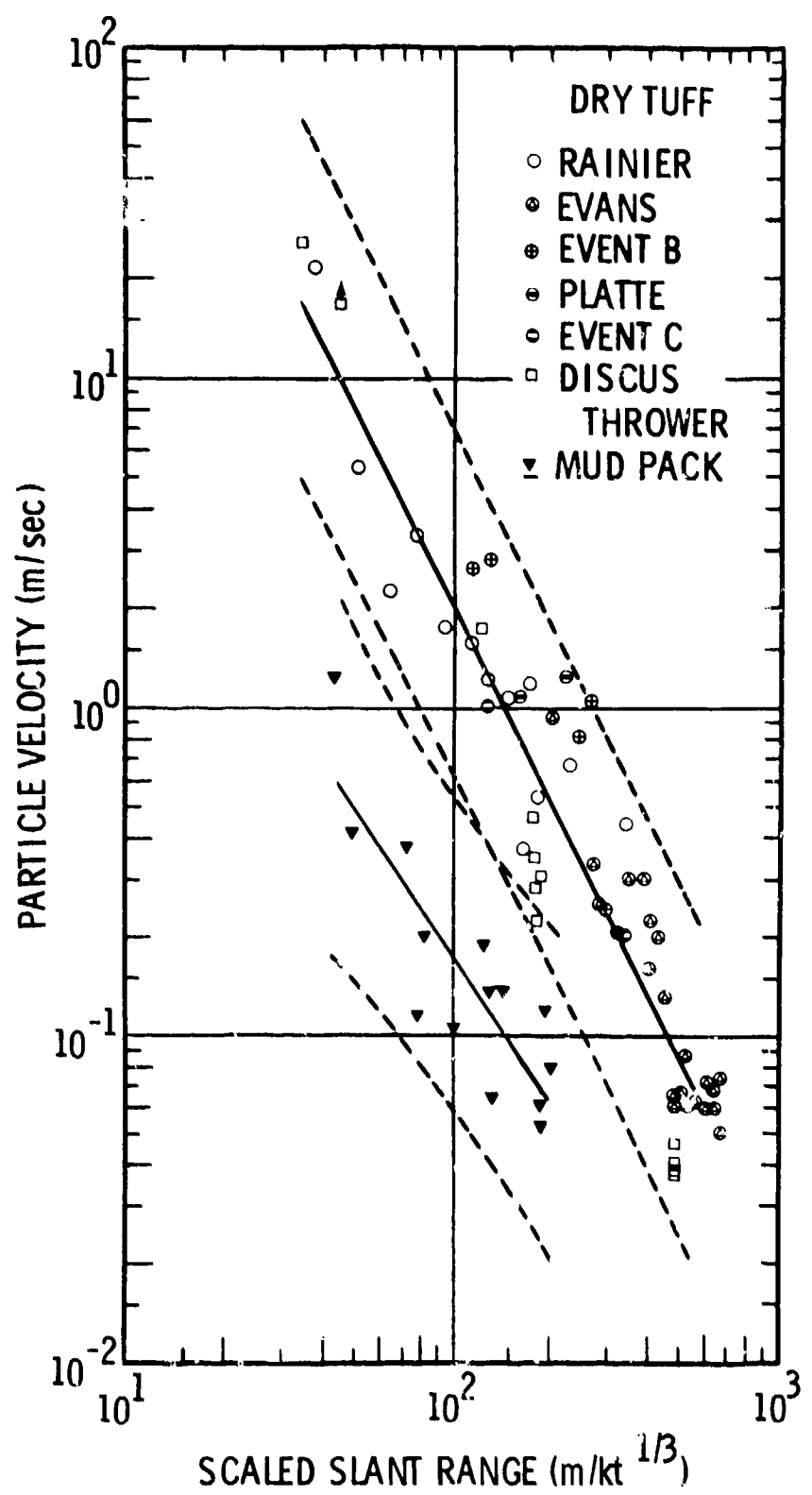


Figure IV-2.16. Attenuation of particle velocity - dry tuff (Reference IV-2.27).

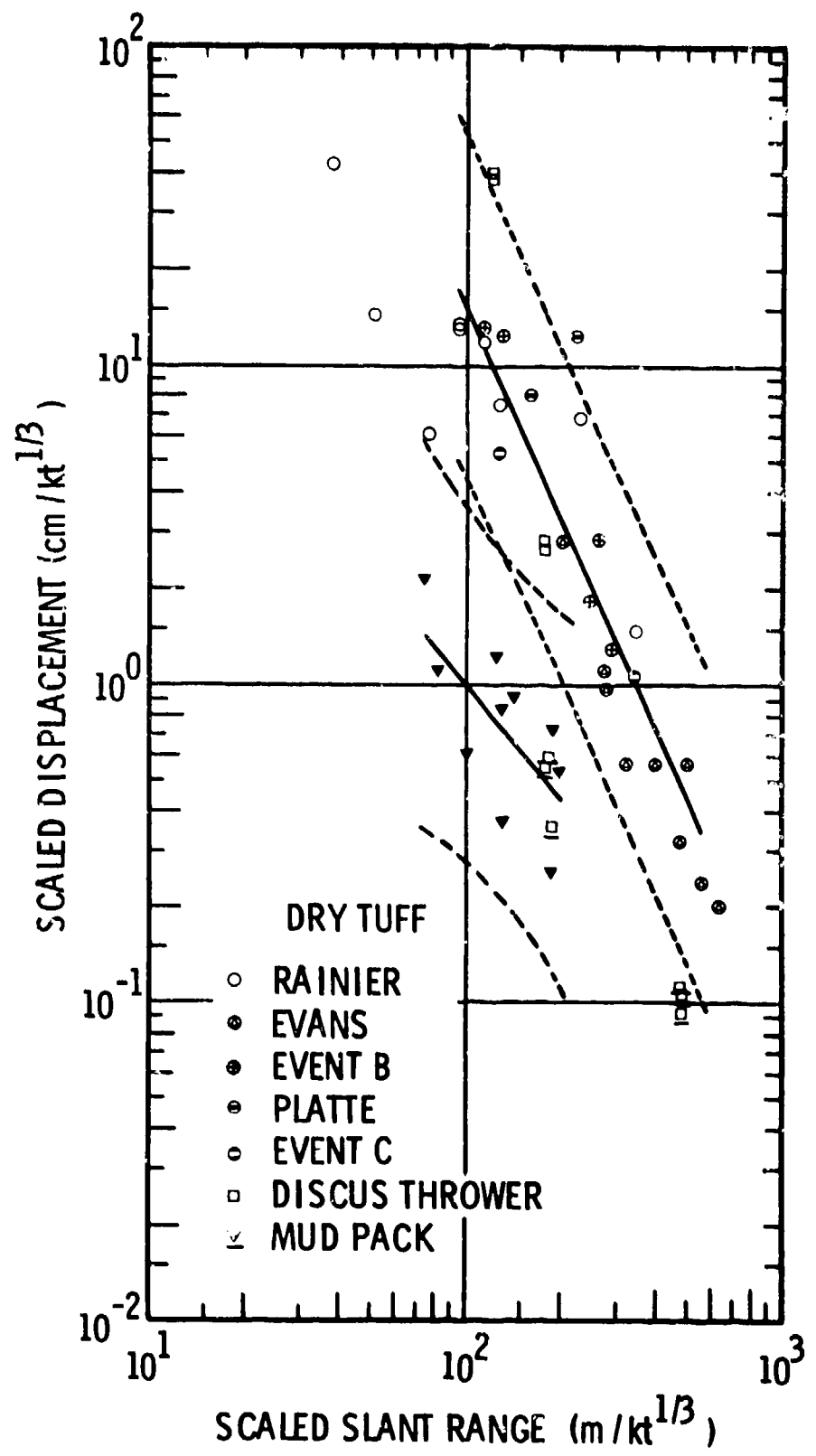


Figure IV-2.17. Attenuation of scaled displacement - dry tuff (Reference IV-2.27).

These differences also reflect the relatively shorter scaled rise times for displacements at the DISCUS THROWER paleozoic rock stations than at stations in tuff. The very distant DISCUS THROWER stations in tuff show rise times similar to those in the denser rocks, probably because early portions of the signal are transmitted over a refracted path through the underlying, higher impedance carbonate rocks.

IV-2.3.4 Free Field Ground Motion in Wet Tuff

Of the 14 contained underground nuclear explosions in wet tuff for which free-field ground motion data are available, eight were detonated in deep borings in tuff below the water table in Areas 2 and 9. At CNSTS, one was above the water table in drier tuff and the remainder were in tunnel complexes within Rainier Mesa. In one case, Event L, the water content was probably at or just below the critical range, and data suggest response more nearly like dry than wet tuff. Tuff at that site was also unusually porous. However, at the nearby site of Event M saturation of the tuff was almost complete. Event I, above the water table, probably should have been included with the dry tuff events.

Data from seven of the events in deep borings were derived from offset vertical instrumentation arrays which included stations above shot level in dry tuff, near shot level in wet tuff, and, in four cases, one station in deeper carbonate rocks. A few events involved one or two shot level stations. Six events included vertical radial arrays in adjacent borings. Many of the stations in these vertical arrays were in dry tuff or dry alluvium.

Data from all events in Rainier Mesa tunnels were derived from shot level stations.

IV-2.3.4.1 Scaled Acceleration Analysis. Scaled acceleration data are available from only 10 events detonated in wet tuff. These data, plotted in Figure IV-2.18 versus scaled slant range, appear to lie in two groups, one approximately an order of magnitude below the other. This separation of data suggested separate regression analyses because it appears that, with two exceptions, Events H and L, those data which fall in the lower group derive from offset vertical array stations either above the water table or in underlying carbonate rocks. The linear regression fit to wet tuff acceleration data (uppermost group) resulted in the equation for scaled ranges between 30 and 600 m/kt^{1/3}

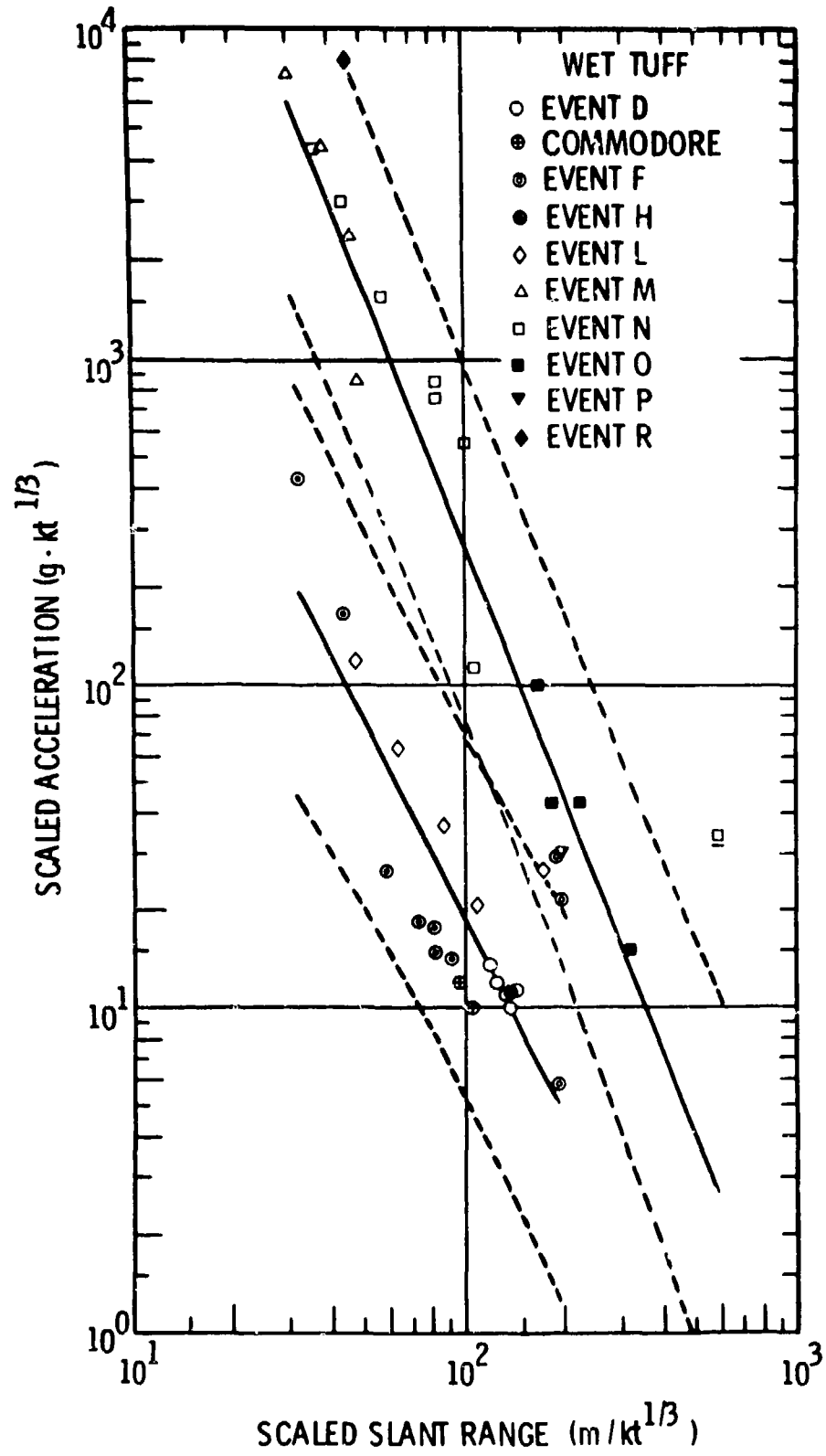


Figure IV-2.18. Attenuation of scaled acceleration - wet tuff (Reference IV-2.27).

$$a \cdot W_1^{1/3} = 4.31 \times 10^7 \left(R/W_1^{1/3} \right)^{-2.61 \pm 0.17} \quad (\text{IV-2.30})$$

Variance of the coefficient is expressed by the factor 2.21 and fractional standard deviation is 5.8 percent.

A similar regression fit to the lower set of data yielded, for the scaled slant range span of 30 to 200 m/kt^{1/3}, the equation

$$a \cdot W_2^{1/3} = 2.05 \times 10^5 \left(R/W_2^{1/3} \right)^{-2.02 \pm 0.29} \quad (\text{IV-2.31})$$

where variance of the coefficient is given by the factor 3.66 and fractional standard deviation of the exponent is 14.3 percent.

Data for this second analysis represent stations from dry tuff above the saturated tuff shot environment, from Event L, which was in exceptionally porous wet tuff that may have been near the lower limit of saturation for that classification, and from stations above Event H, which were in a region above the water table in tuff and alluvium. Comparison of Equation IV-2.31 and Equation IV-2.27 for dry tuff at a somewhat more remote spread of scaled ranges indicates that the exponents -2.02 and -1.92 differ by less than either standard deviation and the intercepts (coefficients) differ by a factor of about 2.6, greater than the variance in Equation IV-2.27, but much less than that in Equation IV-2.31.

High frequency components of motion are attenuated by absorption in dry porous or particulate materials at a considerably higher rate than in similar water saturated materials, and acceleration transients are much more sensitive to the loss of high frequency components of motion than are particle velocities or displacements. Consequently, it seems likely that the data represented by Equation IV-2.31 were derived either from explosions which were within tuff of water content below 90 percent saturation or from stations sufficiently remote in dry tuff or alluvium to receive acceleration transients similar to those from explosions in dry tuff.

IV-2.3.4.2 Particle Velocity Analysis. Particle velocity data from all wet tuff events, as plotted in Figure IV-2.19, do not suggest the definite segregation

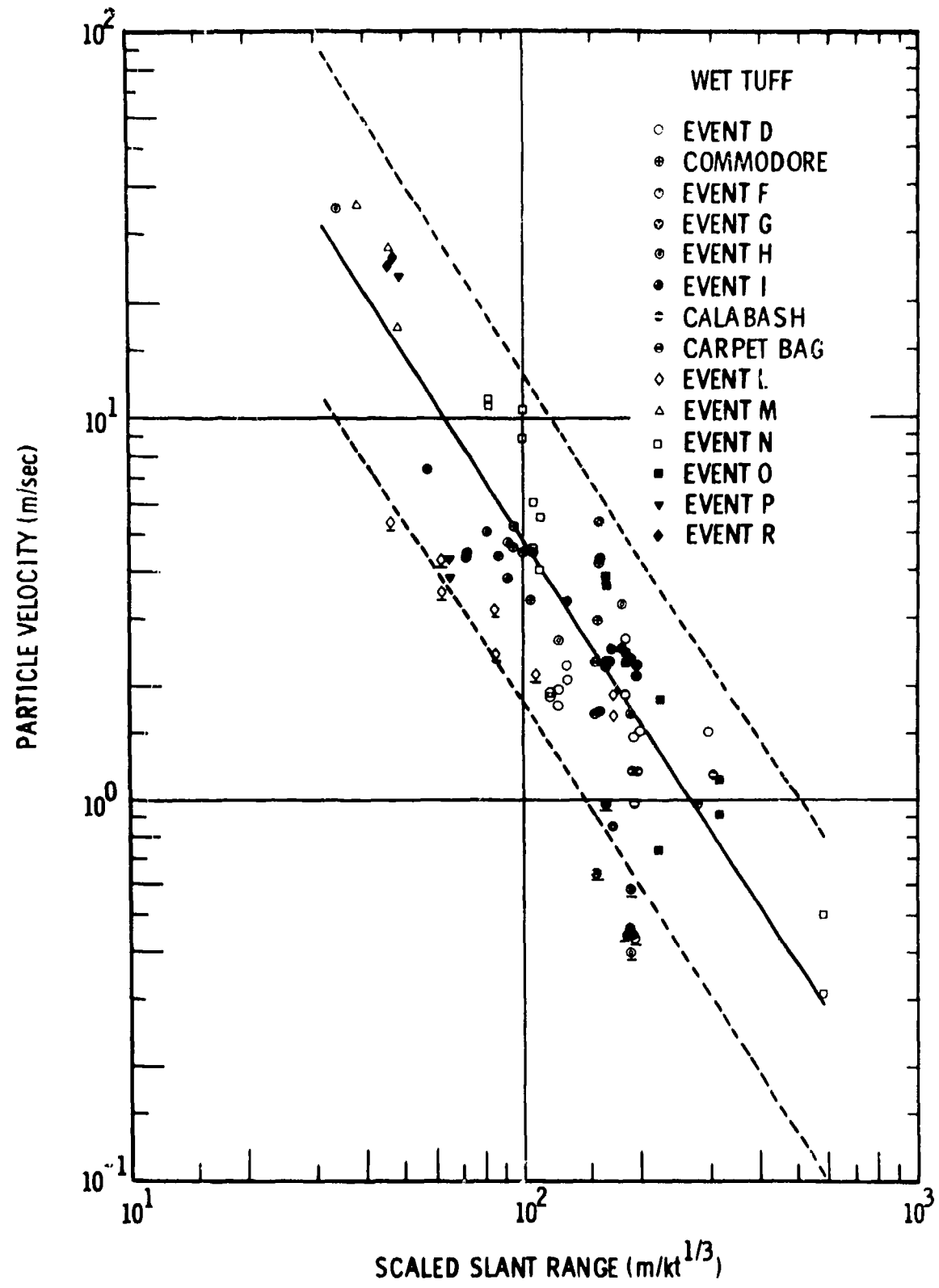


Figure IV-2.19. Attenuation of particle velocity - wet tuff (Reference IV-2.27).

indicated by the acceleration data. However, there are a number of individual points, data from Event I and the shorter range velocity data from Event L, which are significantly low. These low points, especially those representative of stations in carbonate rock or dry tuff, have been omitted from the regression fit to velocity data which yielded, for the scaled ranges between 30 and 600 m/kt^{1/3}, the equation

$$u = 6.61 \times 10^3 \left(R/W^{1/3} \right)^{-1.56 \pm 0.09} \quad (\text{IV-2.32})$$

In this equation, the coefficient variance is relatively low, the multiplier is 1.56, and fractional standard deviation of the exponent is only 5.8 percent. However, the span of the 90-percent confidence zone is nearly an order of magnitude, roughly comparable to those for the dry alluvium and dry tuff velocity data.

IV-2.3.4.3 Scaled Displacement Analysis. Like the particle velocity data, the scaled displacement data from wet tuff events, Figure IV-2.20, fail to show a significant differentiation such as that indicated by acceleration data. A few low data points and those from Event L have been omitted from the regression analysis of scaled displacements which resulted in the equation

$$d/W^{1/3} = 4.90 \times 10^6 \left(R/W^{1/3} \right)^{-2.63 \pm 0.19} \quad (\text{IV-2.33})$$

for which fractional standard deviation of the exponent is 7.2 percent and variance of the coefficient is expressed by the factor 2.63. This fit to the scaled displacement data covers scaled ranges between 50 and 600 m/kt^{1/3}.

IV-2.3.5 Free-Field Ground Motion in Hard Rock

The term "hard rock" as noted earlier is a catchall term for rocks of high seismic impedance, about 100 to 150 gm/m² sec, and generally occurs in massive, though often stratified deposits. Of the eleven hard rock underground nuclear explosions, four, HARD HAT (Reference IV-2.58), SHOAL (Reference IV-2.25), PILE DRIVER (Reference IV-2.8), and GNOME (Reference IV-2.24). were in deep tunnel complexes reached through access shafts and all were instrumented with both

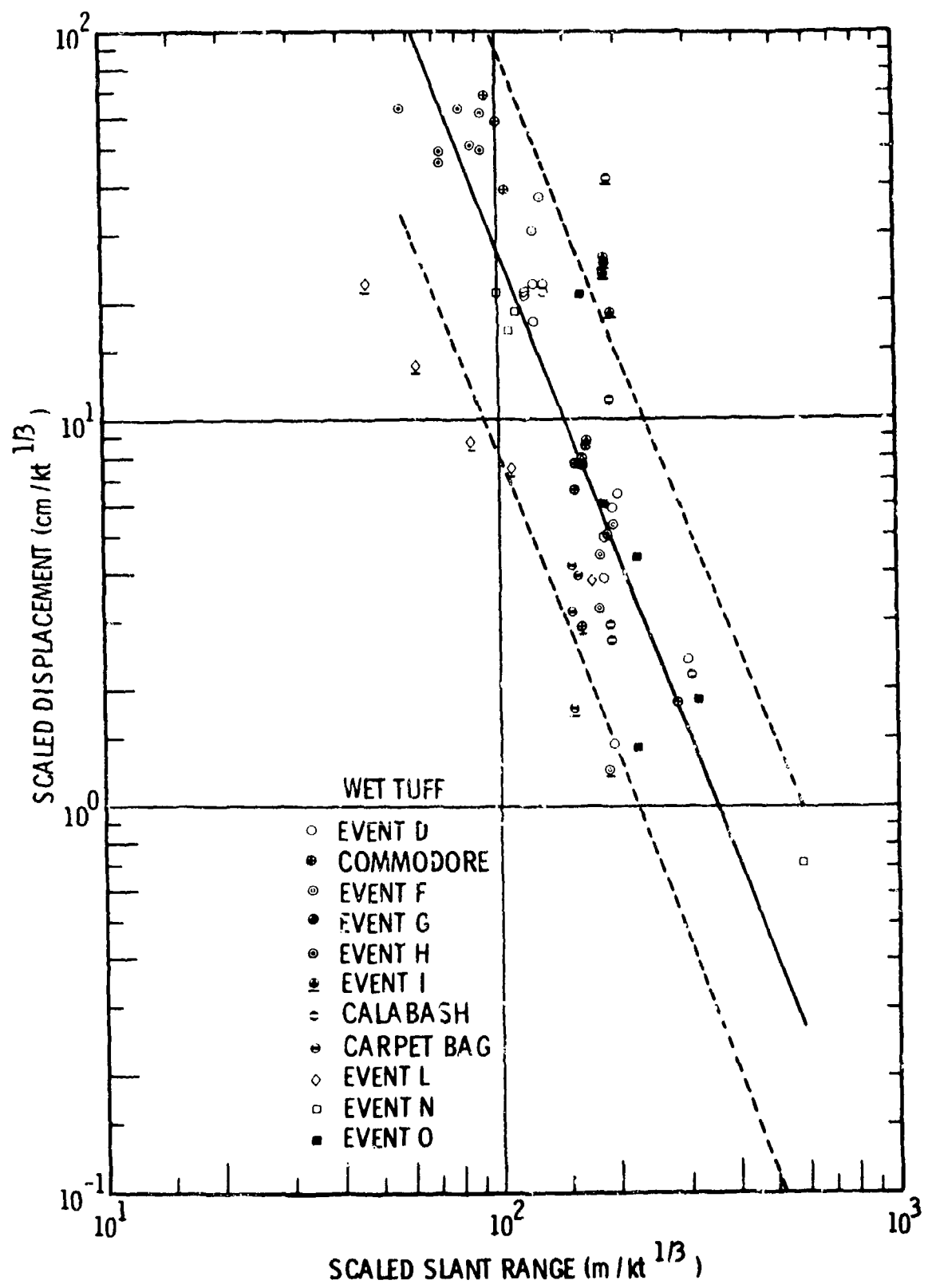


Figure IV-2.20. Attenuation of scaled displacement - wet tuff
(Reference IV-2.27).

shot level and vertical radius station arrays. The others, all emplaced in deep borings, were instrumented with vertical radial arrays. SALMON (Reference IV-2.62) and HANDCAR (Reference IV-2.10) instrumentation included offset vertical arrays which incorporated a shot level gauge station array, and that for BOXCAR included two remote shot level stations. Because of the wide variety of rock included in this category, or because a few events included stations installed in lower impedance rocks than that in which the explosion occurred, or because such things as low impedance strata or thick fault zones filled with clay gouge occurred between the explosion and some stations, there are sets of data or individual points which differ sufficiently from the general trend of more numerous data to suggest their omission from the regression analysis or their separate analysis. In particular, the SALMON and HANDCAR Events indicated both separate analysis of the data set and omission of specific points.

IV-2.3.5.1 Scaled Acceleration Analysis. Scaled acceleration data from the hard rock events, Figure IV-2.21, were divided into two sets, and the SALMON free-field data were analyzed separately. The regression equation for hard rock acceleration in the scaled range from 40 to 200 m/kt^{1/3} is

$$a \cdot W_1^{1/3} = 6.20 \times 10^{10} \left(R/W_1^{1/3} \right)^{-4.35 \pm 0.32} \quad (\text{IV-2.34})$$

with coefficient variance expressed by the factor 4.06 and fractional standard deviation of the exponent given by 7.3 percent. The data in this analysis included many relatively low points from the HANDCAR and BOXCAR Events but did not include SALMON data.

Regression analysis of the hard rock scaled acceleration data within the interval from 90 to 2200 m/kt^{1/3} but exclusive of SALMON data and the points underscored in Figure IV-2.21 gave the equation

$$a \cdot W_2^{1/3} = 9.29 \times 10^6 \left(R/W_2^{1/3} \right)^{-2.32 \pm 0.08} \quad (\text{IV-2.35})$$

where the fractional standard deviation of the exponent is 3.4 percent and the variance factor for the coefficient is 1.56.

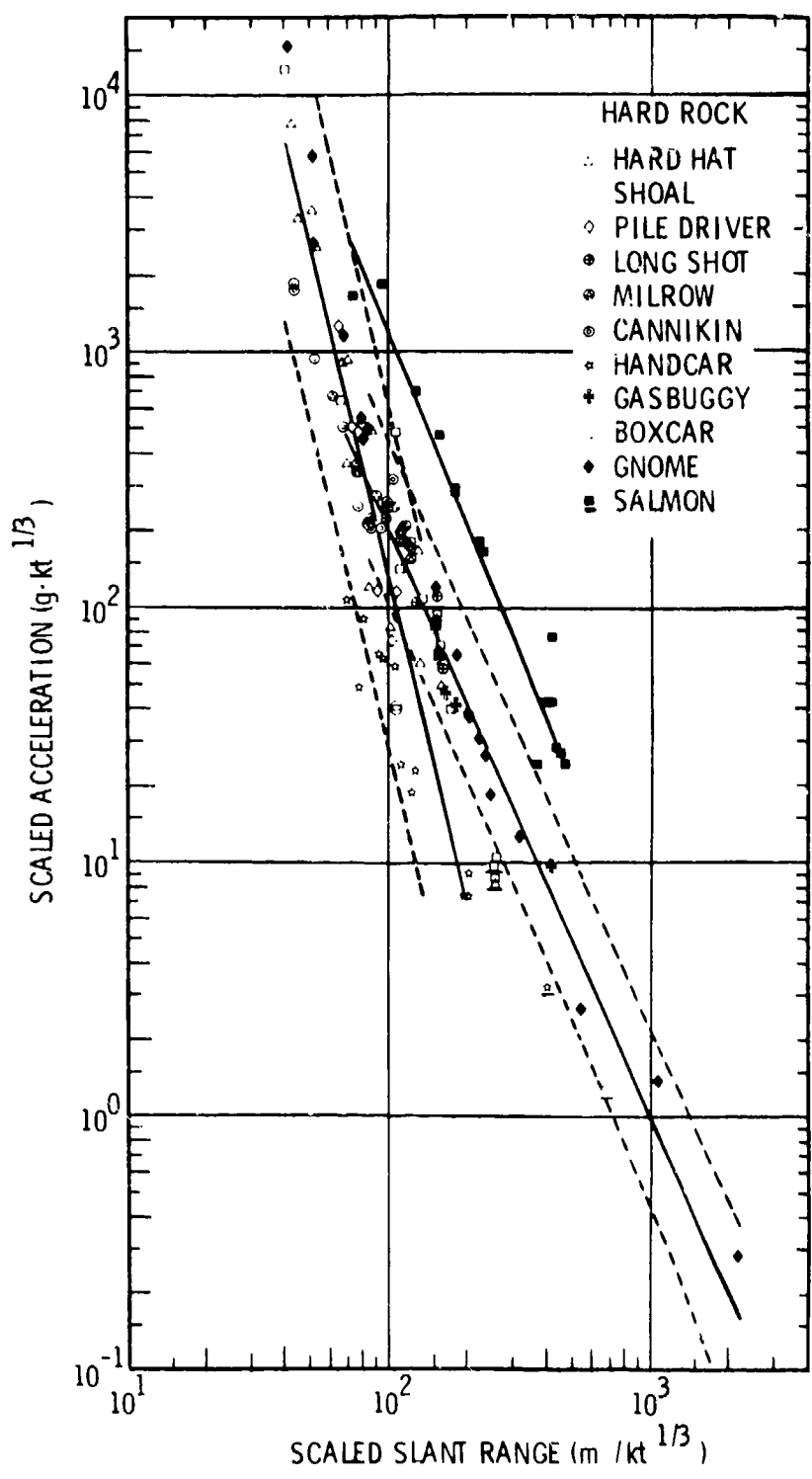


Figure IV-2.21. Attenuation of scaled acceleration - hard rock (Reference IV-2.27).

IV-2.3.5.2 Particle Velocity Analysis. Hard rock free-field particle velocity data appear to be more closely packed than do similar data from explosions in the lower seismic impedance rocks. However, HANDCAR data are generally lower and SALMON data higher than those from other events and, together with the underscored points in Figure IV-2.22, have been omitted from regression of the general data set. HANDCAR particle velocity data were analyzed separately, but SALMON velocity data were not. Regression analysis of the remaining hard rock velocity data yielded the equation

$$u = 1.81 \times 10^4 \left(R/W^{1/3} \right)^{-1.72 \pm 0.07} \quad (\text{IV-2.36})$$

where coefficient variance is defined by the multiplier 1.39; fractional standard deviation of the exponent is 4.1 percent. This equation holds for the scaled slant range span from 40 to 2200 m/kt^{1/3}.

IV-2.3.5.3 Scaled Displacement Analysis. Scaled displacement data from all hard rock events are plotted in Figure IV-2.23. SALMON displacements fall well within the scatter of other data sets, and only a few HARD HAT and HANDCAR points have been underscored for omission from the regression analysis. The equation for this analysis, which holds for scaled ranges between 70 and 2200 m/kt^{1/3}, is

$$d/W^{1/3} = 8.72 \times 10^4 \left(R/W^{1/3} \right)^{-1.88 \pm 0.14} \quad (\text{IV-2.37})$$

for which the coefficient variance is defined by the factor 2.08 and fractional standard deviation of the exponent is 7.5 percent.

IV-2.3.6 General Discussion

Review of the data plots, Figures IV-2.12 through IV-2.23, and of the regression equations pertinent to these data indicates that the most extreme scatter of data and consequently greater variances occur for events in which either some gauge stations were emplaced in rock of very different seismic impedance from that in which the explosive was emplaced or the environmental rock at the shot point was probably transitional between two categories, as in the case of the dry friable

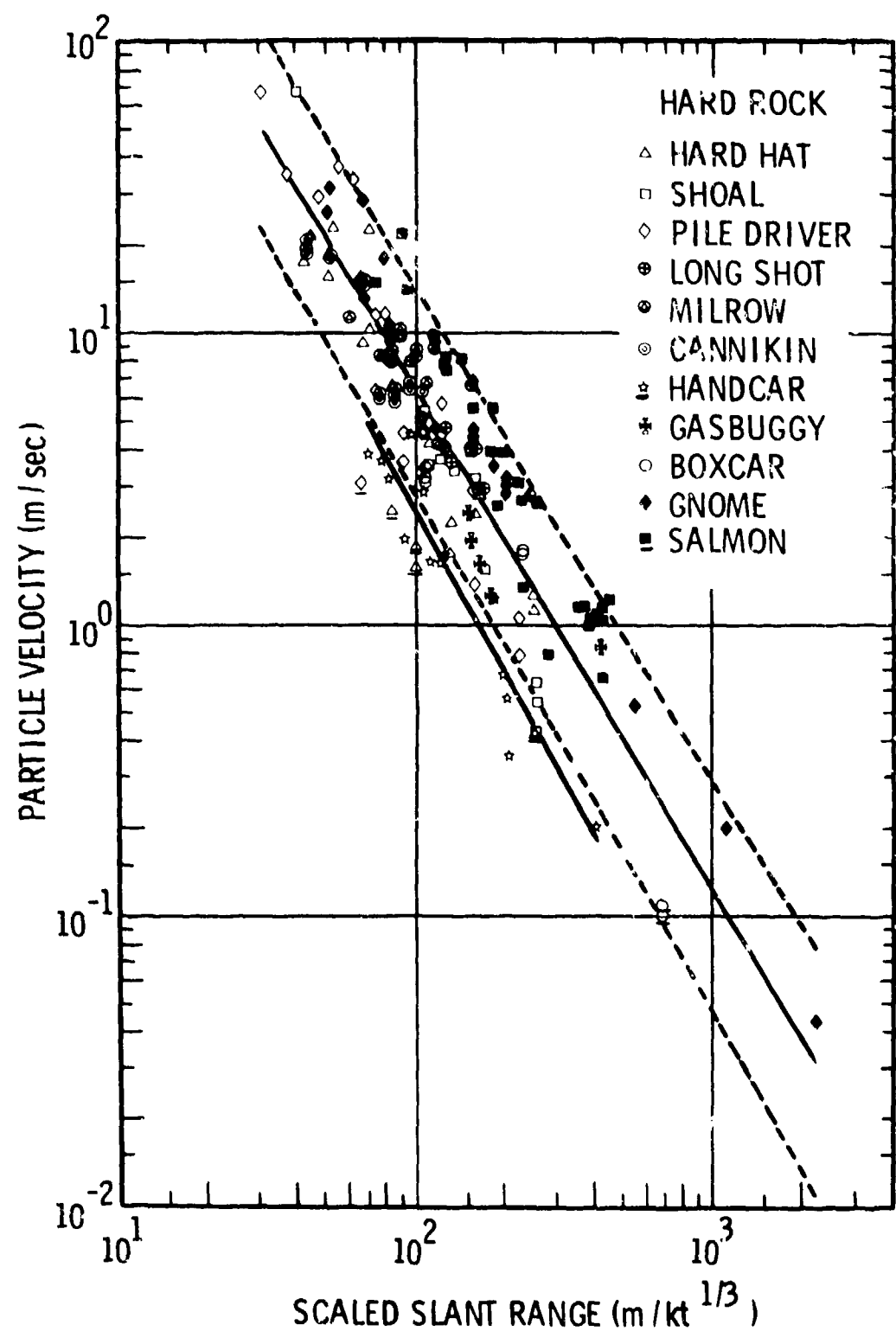


Figure IV-2.22. Attenuation of particle velocity - hard rock
(Reference IV-2.27).

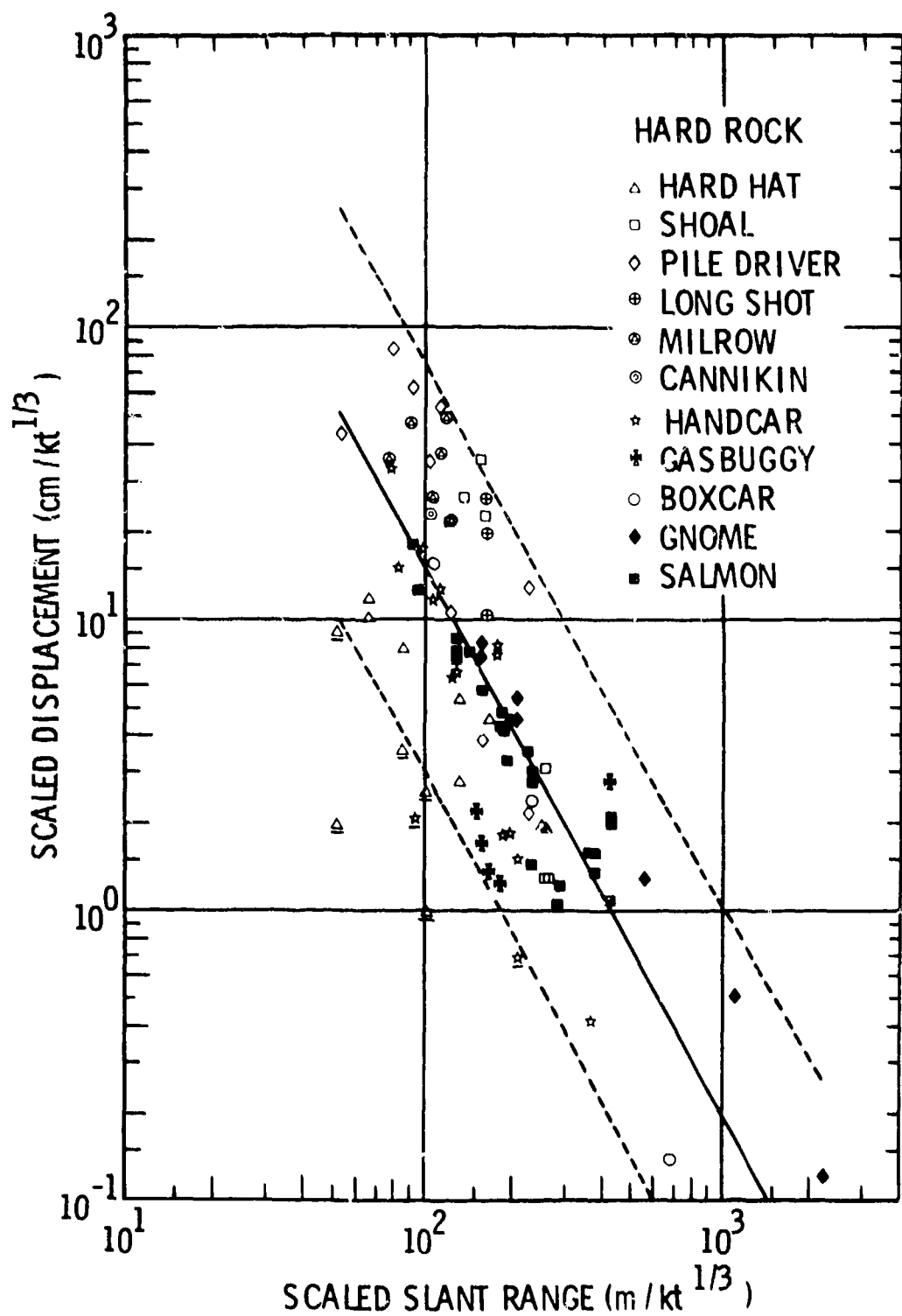


Figure IV-2.23. Attenuation of scaled displacement - hard rock
(Reference IV-2.27).

tuff at the MUD PACK site and the incompletely saturated wet tuff at the Event L location. In many cases, data which derived from such conditions were omitted from analysis, but in others knowledge of the real situation at a gauge station or shot point was not sufficient to justify deletion of the data from analysis. In some cases where a complete set of data has been omitted from analysis, a separate regression has been undertaken to those data sets.

The SCOOTER displacement data, Figure IV-2.14, were found to fit the equation

$$d/W^{1/3} = 8.79 \times 10^5 \left(R/W^{1/3} \right)^{-2.30 \pm 0.21} \quad (\text{IV-2.38})$$

with a 9.2 percent fractional deviation of the exponent and a coefficient variance multiplier of 2.55.

MUD PACK data, in addition to being derived from some stations in much higher impedance rock than the shot point material and evidently fitting the dry alluvium category better than the dry tuff one, are characterized by very broad scatter. Regression equations for MUD PACK peak motion data are

$$a \cdot W^{1/3} = 1.83 \times 10^5 \left(R/W^{1/3} \right)^{-2.64 \pm 0.17} \quad (\text{IV-2.39})$$

where the variance multiplier for the coefficient is 2.26 and fractional deviation of the exponent is 6.5 percent, Figure IV-2.15;

$$u = 1.48 \times 10^2 \left(R/W^{1/3} \right)^{-1.47 \pm 0.26} \quad (\text{IV-2.40})$$

with a coefficient variance factor of 3.42 and a fractional standard deviation of the exponent of 17.7 percent, Figure IV-2.16, and

$$d/W^{1/3} = 2.35 \times 10^2 \left(R/W^{1/3} \right)^{-1.19 \pm 0.49} \quad (\text{IV-2.41})$$

with a coefficient variance multiplier of 9.34 and a fractional standard deviation of the exponent equal to 38.6 percent, Figure IV-2.17. It is evident in the figures that scatter is least among MUD PACK scaled accelerations where the variances are not very different from those of the other dry tuff data although magnitudes are significantly below other dry tuff values, but scatter is very broad in both the particle velocity and displacement data from MUD PACK and variances are exceptionally large in both regression fits.

Separate analysis of SALMON scaled acceleration data, Figure IV-2.21, yielded the regression equation

$$a \cdot W^{1/3} = 1.33 \times 10^8 \left(R/W^{1/3} \right)^{-2.52 \pm 0.11} \quad (\text{IV-2.42})$$

where the variance factor for the intercept is 1.79 and fraction standard deviation of the exponent is 4.2 percent.

Finally, separate analysis of HANDCAR particle velocity data gave the equation

$$u = 1.35 \times 10^4 \left(R/W^{1/3} \right)^{-1.87 \pm 0.18} \quad (\text{IV-2.43})$$

with an intercept variance factor of 2.39 and an exponent fractional standard deviation of 9.5 percent.

It must be recognized that, although throughout this analysis and discussion of free-field ground motion data, apparently anomalous results have been considered a consequence of environmental anomalies. It is also possible, where complete sets of data such as those just analyzed are above or below the general family of data for a particular environment, that an erroneous value of explosive yield has been used in scaling data. A low yield will shift scaled quantities toward higher values and a high yield toward lower ones. This argument does not serve very well where only one motion parameter, such as the SCOOTER scaled displacement or SALMON scaled acceleration, is anomalous, but it can find support in the MUD PACK analysis where all three data sets are lower than the dry tuff data from other events. The second criterion for comparison of these data is the slope of the linear fit, that

is, the exponents. If these are closest to those of the assumed or prescribed environment, then the assumed yield and consequently the scaling factor may again be in doubt. However, energy yields of most explosions are established by diagnostic measurements well within a factor of 2 and the change in scaling factor for doubling or halving yield is only about 26 percent, so that anomalies in scaled data of the order of 2 or more are most likely caused by differences or uncertainties in environmental characteristics.

It is of interest to tabulate the intercept coefficients and exponents of the regression equations for the various motion parameters and their variance factors, Table IV-2.5. In this tabulation, scaled accelerations have been separated into those derived from the shorter scaled ranges and those from the more remote stations. The wet tuff scaled accelerations characterized earlier as being derived from events in rock of transitional water content have been omitted from the table. The equations for shorter range fits to particle velocities and scaled displacements have not been separately listed because such separation was undertaken for the alluvium environment only and even there its justification for particle velocity is questionable.

Evidently exponents of scaled accelerations in the shorter ranges are considerably greater than for the more remote data in all but the wet tuff events. This implies that in each of these environments loss of higher frequency components was significantly greater near the beginning of the region of nonlinear response than throughout the remainder. Fractional standard deviation of exponents for close-in scaled acceleration is comparable with those from most of the other data, but since the exponents are larger, the intercept variances for these acceleration data are greater than for any others.

The more remote scaled accelerations appear to be attenuated as the inverse square of scaled range in alluvium and dry tuff and as the inverse 2.5 power in wet tuff and hard rock. Average variance of the exponents is a little over 5 percent, and the mean intercept variance factor is about 2.1.

Particle velocity data for most environments are attenuated nearly as the inverse square of the scaled range, but the short and long range portions of the alluvium data are very different from each other and from the other rock categories. The exponent variance for long range alluvium data is unusually high, 12 percent. For the tuff and hard rock data, particle velocities fall off as the inverse 1.75

Table IV-2.5 Regression parameters for free field ground motion.

Motion	Rock	Intercept Coefficient	Variance Factor	Exponent	Standard Deviation (%)	Applicable Range (m/kt ^{1/3})
$a \cdot W^{1/3}$	Alluvium	2.24×10^{11}	6.39	-5.78	8.1	20-80
$a \cdot W^{1/3}$	Dry Tuff	4.90×10^{10}	4.33	-4.77	6.9	40-150
$a \cdot W^{1/3}$	Hard Rock	6.20×10^{10}	4.06	-4.35	7.3	40-200
$a \cdot W^{1/3}$	Alluvium	4.79×10^4	2.34	-2.13	8.4	60-350
$a \cdot W^{1/3}$	Dry Tuff	7.71×10^4	2.12	-1.92	7.4	100-500
$a \cdot W^{1/3}$	Wet Tuff	4.31×10^7	2.21	-2.62	5.8	30-600
$a \cdot W^{1/3}$	Hard Rock	9.29×10^6	1.56	-2.32	3.4	90-2200
u	Alluvium	1.52×10^6	1.96	-3.27	4.9	30-150
u	Alluvium	3.86×10^1	2.09	-1.16	12.0	100-350
u	Dry Tuff	1.85×10^4	1.81	-1.98	5.6	40-500
u	Wet Tuff	6.61×10^3	1.56	-1.56	5.8	30-600
u	Hard Rock	1.81×10^4	1.39	-1.72	4.1	40-2200
$d/W^{1/3}$	Alluvium	3.44×10^6	2.42	-3.04	6.6	40-150
$d/W^{1/3}$	Alluvium	2.22×10^2	1.72	-1.11	9.9	100-350
$d/W^{1/3}$	Dry Tuff	3.80×10^5	3.11	-2.20	9.6	100-500
$d/W^{1/3}$	Wet Tuff	4.90×10^6	2.63	-2.63	7.2	50-600
$d/W^{1/3}$	Hard Rock	8.72×10^4	2.08	-1.88	7.5	70-2200
$a \cdot W^{1/3}$	Mud Pack	1.85×10^5	2.26	-2.64	6.5	40-200
$a \cdot W^{1/3}$	Salmon	1.33×10^6	1.79	-2.52	4.2	70-450
u	Mud Pack	1.48×10^2	3.42	-1.47	17.7	40-200
u	Hamcar	1.35×10^4	2.39	-1.87	9.5	70-400
$d/W^{1/3}$	Mud Pack	2.35×10^2	9.34	-1.19	38.6	70-200
$d/W^{1/3}$	Scooter	8.79×10^5	2.55	-2.30	9.2	19-120

power with an average standard deviation of about 5.2 percent and a mean intercept variance factor of about 1.6.

Scaled displacement for all environments is attenuated at an average rate of roughly the inverse 2.2 power of scaled range, with a mean standard deviation of 8.2 percent. Again, omission of the alluvium data results in scaled displacement attenuation for the tuff and hard rock environments equal to the inverse 2.2 power of scaled slant range, with a mean standard deviation of 8.1 percent. Mean intercept variance factor for all four environments is 2.4, and for the last three materials it is 2.6.

The apparent anomalous behavior of the alluvium data in both particle velocity and displacement may be a consequence either of the fact that the particulate nature of the alluvium emphasized the difference in reaction at short versus longer scaled ranges or that greater scatter in the other media resulted in masking of real but small differences in attenuation rates in the tuff and hard rock data. However, it is also possible that the evident, more rapid attenuation of particle velocity, and consequently of stress, in alluvium resulted in the onset of linear or quasi-linear response within the scaled range of available data. This argument is based on the assumption that within the region of linear elastic response particle velocity and stress will decrease as a consequence of spherical dispersion only and consequently with the inverse first power of distance.

IV-2.3.7 Comparisons

IV-2.3.7.1 Comparison of Free-Field Motion in Regions of Hydrodynamic and Non-linear Response. Attenuation of free-field particle velocity in the region of hydrodynamic response for all rocks, Figure IV-2.10, occurred as the inverse 1.87 power of scaled range. Similar data from the domain of nonlinear response for dry tuff, wet tuff, and hard rock indicated attenuation as the inverse 1.98, 1.56, and 1.72 power, respectively. Intercept coefficients in the corresponding regression equations were roughly similar, 2.43×10^4 , 1.85×10^4 , 6.61×10^3 , and 1.81×10^4 . However, the dry tuff regression equation within the span of pertinent data is significantly below those for wet tuff and hard rock; at a scaled range of $100 \text{ m}/\text{kt}^{1/3}$, the dry tuff fit is 2.11 m/sec as compared to 4.96 and 6.51 m/sec at the same distance in wet tuff and hard rock. Consequently, a logical comparison of particle velocities in the hydrodynamic and nonlinear regions should be limited to data from wet tuff and hard rock in

the latter region. All particle velocity data corresponding to Figures IV-2.10, IV-2.19, and IV-2.24 were plotted in Figure IV-2.24 as a function of scaled range, and a linear regression was performed on these data, omitting the underscored points as in the previous analyses.

The data in Figure IV-2.24 evidently follow a single trend; there is no obvious change in slope or transitional offset, and data from the three sets overlap through one decade of velocity values. In general, the principal difference between the data sets is the greater scatter in the nonlinear region where differences in physical characteristics of the rock can influence data significantly.

The linear fit to these data is shown in Figure IV-2.24 and is described by the equation

$$u = 1.85 \times 10^4 \left(R/W^{1/3} \right)^{-1.76 \pm 0.02} \quad (\text{IV-2.44})$$

where the intercept variance factor is 1.12 and fractional standard deviation of the exponent is 1.4 percent. The extent of data represented by this equation is suggested by the fact that the nearly 350 particle velocity data range between 4.4×10^3 and 4.3×10^{-2} m/sec and the corresponding range of stress, from nearly one megabar to about one bar, is over five orders of magnitude.

Therefore, throughout both the hydrodynamic and nonlinear response domains surrounding contained underground nuclear explosions in competent rock, particle velocity decreases as the inverse 1.76 power of scaled distance, and can be very roughly approximated by inverse square attenuation. It has been noted previously that in the domain of hydrodynamic response, although stress is attenuated roughly as the inverse cube of distance, variability of density and shock velocity with stress in the equation of state results in inverse square attenuation of particle velocity. At lower stress levels within the domain of nonlinear response, both stress and particle velocity are attenuated at similar rates since the seismic impedance, i.e., the product of density by propagation velocity, remains essentially constant beyond the hydrodynamic regime. In this region, particle velocities in competent rocks (high impedance) were found to be attenuated roughly as the inverse square of scaled distance. The significant result derived from this analysis is the strong evidence that a single continuous rate describes

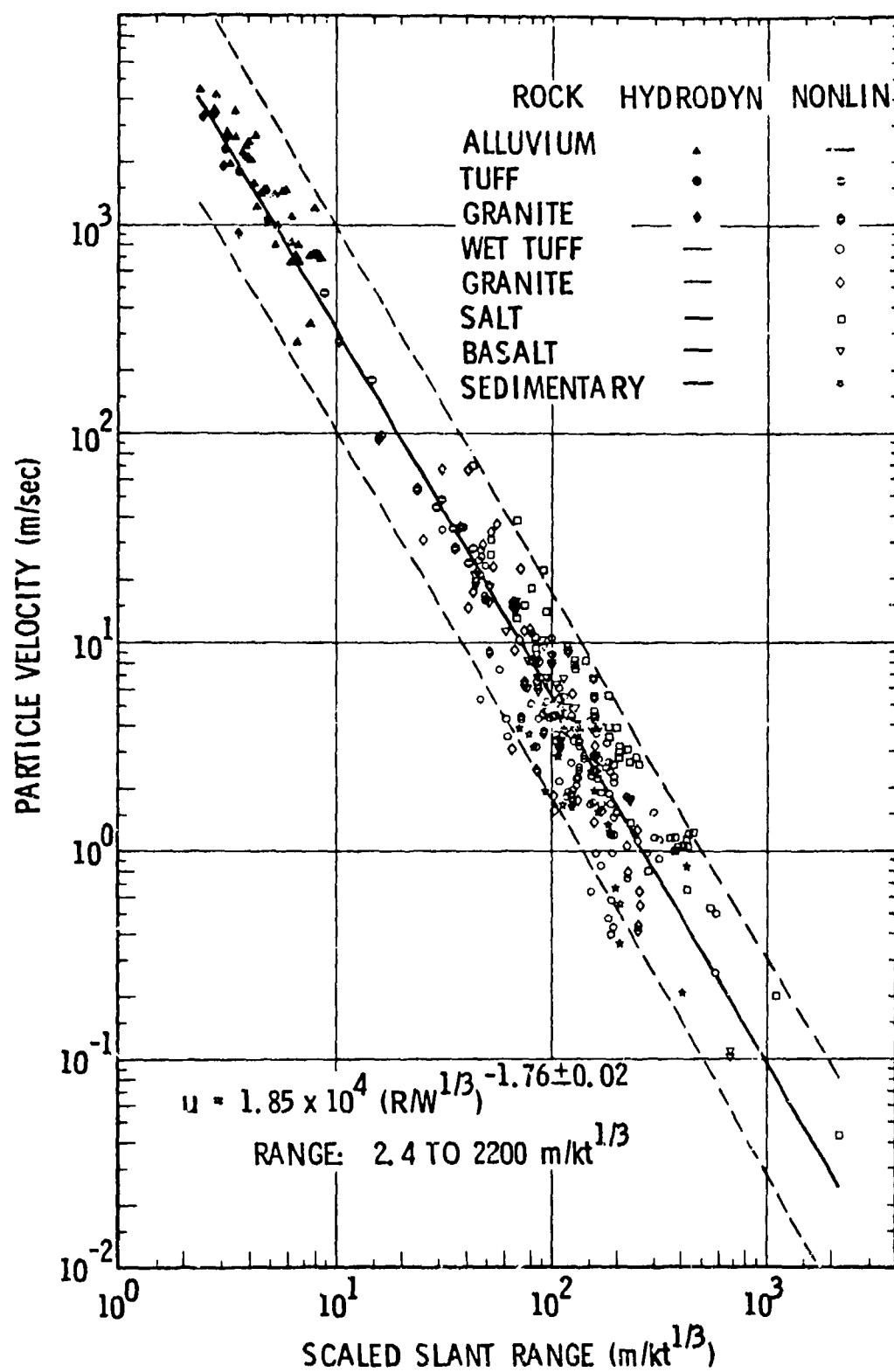


Figure IV-2.24. Attenuation of particle velocity in the regions of hydrodynamic and nonlinear response (Reference IV-2.27).

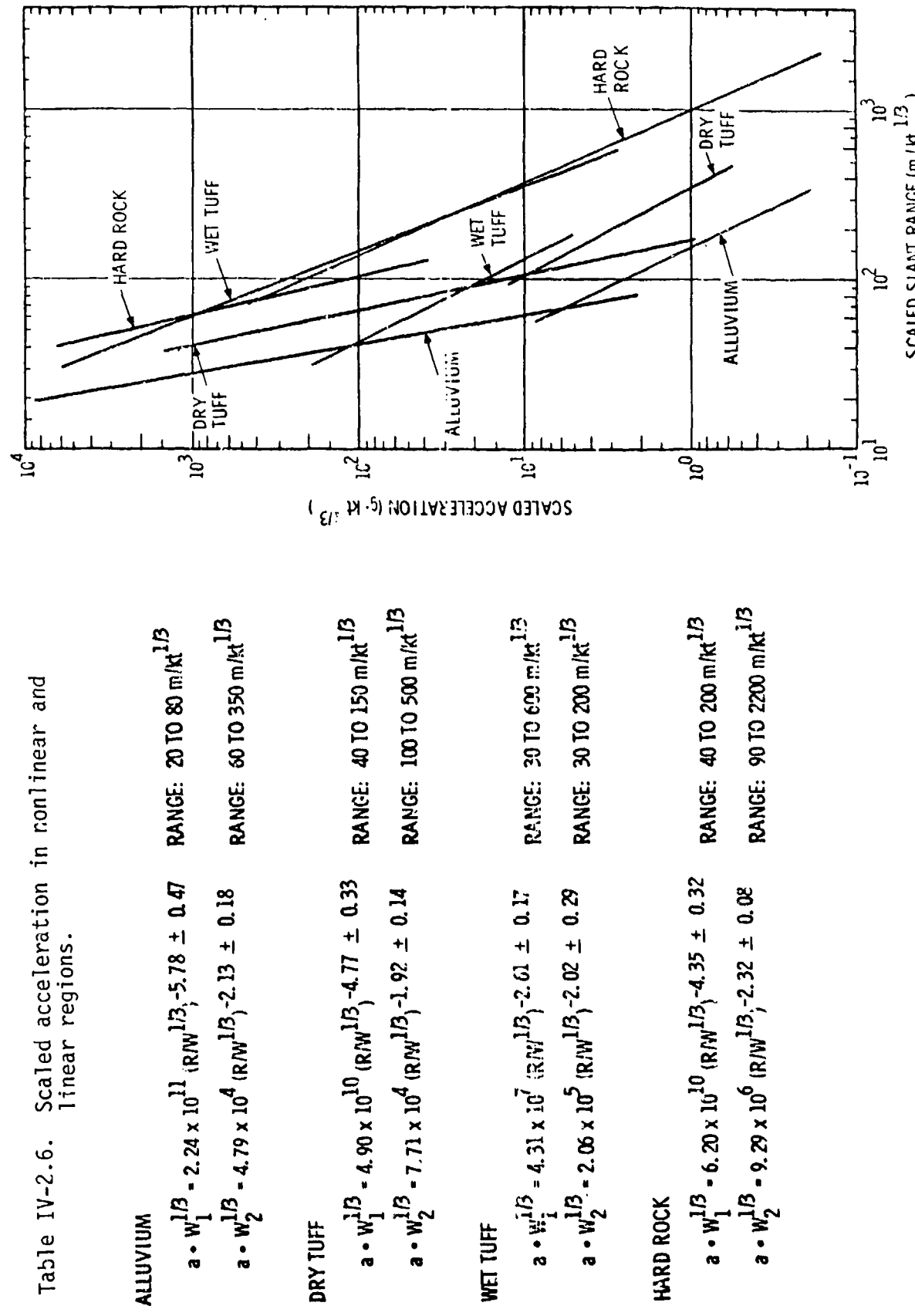
attenuation of particle velocity over a peak stress range from a megabar to a bar in a number of competent rock environments.

IV-2.3.7.2 Comparison of Motion in Different Rocks. More meaningful interpretation of differences in attenuation between a particular motion parameter in different rock environments should be available from comparison of the regression curves and equations. For this purpose, plots which include each regression fit for a single parameter, as scaled acceleration, for the four rock environments were assembled. Corresponding regression equations are grouped in tables. These plots aid in identifying the influence of general rock characteristics on response to the explosion induced motion.

Figure IV-2.25 includes the regression curves for scaled acceleration data from alluvium (Figure IV-2.12), from dry tuff (Figure IV-2.15), from wet tuff (Figure IV-2.18), and from hard rock (Figure IV-2.21). Equations for these curves are listed in Table IV-2.6. In each rock type there are two linear regression phases; however, those for wet tuff data differ from the others, and the lower one is probably anomalous. Both phases of the alluvium and dry tuff lines are roughly parallel, but the tuff lines and their intersection represent higher acceleration levels than the alluvium ones for identical scaled ranges. This situation is very likely a consequence of greater energy absorption, particularly of the high frequency components at high stress levels in the unbonded porous alluvium. The wet tuff curve and both phases of the hard rock curve are roughly similar and at much higher acceleration levels than the dry tuff and alluvium ones. This fact confirms the anticipated lower energy losses in the competent, higher impedance rocks.

The curves plotted in Figure IV-2.26 are those fitted to particle velocity data from alluvium (Figure IV-2.13), from dry tuff (Figure IV-2.16), from wet tuff (Figure IV-2.19), and from hard rock (Figure IV-2.22). The equations for these curves are presented in Table IV-2.7. Included in Figure IV-2.26 is the general linear fit to particle velocity data from Figure IV-2.24. Only the alluvium curve includes two phases, of which the second with an attenuation rate near the inverse first power suggests linear or elastic propagation beyond a scaled range of about $150 \text{ m}/\text{kt}^{1/3}$. Again, the alluvium curves are considerably lower than the others, a fact which, in conjunction with the lower seismic impedance in alluvium, implies much lower stress levels at similar scaled ranges. Of the remaining four regression curves, that for dry tuff falls below the more competent rock although

Table IV-2.6. Scaled acceleration in nonlinear and linear regions.



IV-2-70

Figure IV-2.25. Attenuation comparison - scaled acceleration.

Table IV-2.7. Particle velocity in nonlinear and linear regions.

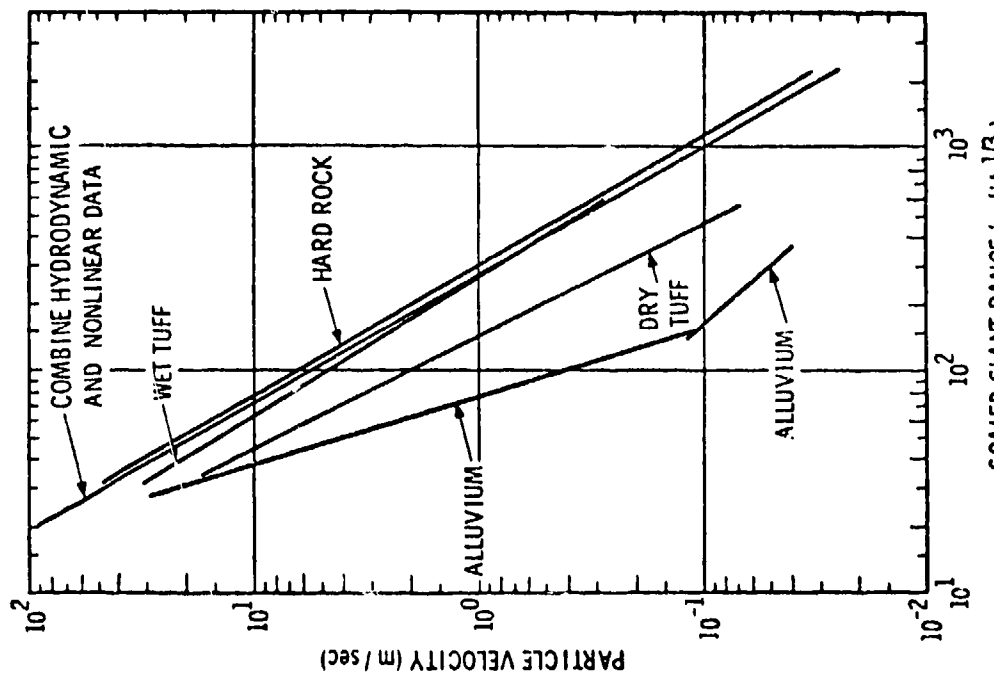


Figure IV-2.26. Attenuation comparison - particle velocity.

ALLUVIUM	$u_1 = 1.52 \times 10^6 (R/W)^{1/3}, -3.27 \pm 0.16$	RANGE: 30 TO 150 m/kt ^{1/3}
	$u_2 = 3.86 \times 10^1 (R/W)^{1/3}, -1.16 \pm 0.14$	RANGE: 100 TO 350 m/kt ^{1/3}
DRY TUFF	$u = 1.35 \times 10^4 (R/W)^{1/3}, -1.98 \pm 0.11$	RANGE: 40 TO 500 m/kt ^{1/3}
WET TUFF	$u = 5.51 \times 10^3 (R/W)^{1/3}, -1.56 \pm 0.09$	RANGE: 30 TO 60 m/kt ^{1/3}
HARD ROCK	$u = 1.81 \times 10^4 (R/W)^{1/3}, -1.72 \pm 0.07$	RANGE: 40 TO 2200 m/kt ^{1/3}

its slope is comparable, as noted in the preceding section. The significant factor in this difference is probably the much larger proportion of gas-filled pore volume as compared with the wet tuff and the much stronger interparticle bonding as compared with alluvium which may have porosity comparable to tuff. Propagation of motion through the dry tuff is inhibited by its porosity, but the stronger bonding in the tuff also inhibits some of the losses which occur in the unbonded porous alluvium. The wet tuff and hard rock curves lie near each other and obviously near the curve for composite data. As previously noted, in these higher impedance rocks attenuation seems to occur, in general, at a constant rate over a very wide range of pressures.

Regression curves for scaled displacement data presented in Figure IV-2.27 are those derived from alluvium data (Figure IV-2.14), dry tuff data (Figure IV-2.17), wet tuff data (Figure IV-2.20), and hard rock data (Figure IV-2.23). The equations for these curves are assembled in Table IV-2.8. Of the three motion transients generated by underground explosions, displacement is not only an appreciably longer duration phenomenon than particle velocity or acceleration but it is the only one which may have residual nonzero values as a result of irreversible processes. Curves for both types of tuff and for hard rock are closely grouped and, although slopes of these lines differ, within the range of data scaled displacements are not very different in the three rock types. However, scaled displacements in alluvium not only appear to include two phases within the range of data, but are lower than those in higher impedance rock by factors of 5 to 10. The corresponding particle velocity factors coupled with a factor of 3 difference in seismic impedance between alluvium and hard rock indicate that in the region of nonlinear response stresses in hard rock are between 9 and 30 times those in alluvium at the same scaled range. Further, because the alluvium is a much more dispersive material than is hard rock, the lower stress transients are broadened and a relatively larger portion of this transient is too small to exceed intergranular friction and thus contribute to significant displacement.

Studies of seismic source energies of contained nuclear underground explosions (Reference IV-2.13) in various geologic materials indicate that near the onset of linear or elastic response the ratio of available seismic energy to released explosive energy is less than 0.1 percent in alluvium and between 2 and 3 percent in hard rock and wet tuff. Energy from an explosion in alluvium is less effectively coupled to the environment than is that for one in higher impedance rock. This

Table IV-2.8. Scaled displacement in nonlinear and linear regions.

ALLUVIUM	
$\delta N^1\beta = 3.44 \times 10^6 (RN^1\beta)^{-3.04 \pm 0.20}$	RANGE: 40 TO 150 m/kt ^{1/3}
$\delta N^2\beta = 2.22 \times 10^2 (RN^1\beta)^{-1.11 \pm 0.11}$	RANGE: 100 TO 350 m/kt ^{1/3}
DRY TUFF	
$\delta N^1\beta = 3.80 \times 10^5 (RN^1\beta)^{-2.20 \pm 0.21}$	RANGE: 100 TO 500 m/kt ^{1/3}
WET TUFF	
$\delta N^1\beta = 4.90 \times 10^6 (RN^1\beta)^{-2.63 \pm 0.19}$	RANGE: 50 TO 600 m/kt ^{1/3}
HARD ROCK	
$\delta N^1\beta = 8.72 \times 10^4 (RN^1\beta)^{-1.83 \pm 0.14}$	RANGE: 70 TO 2200 m/kt ^{1/3}

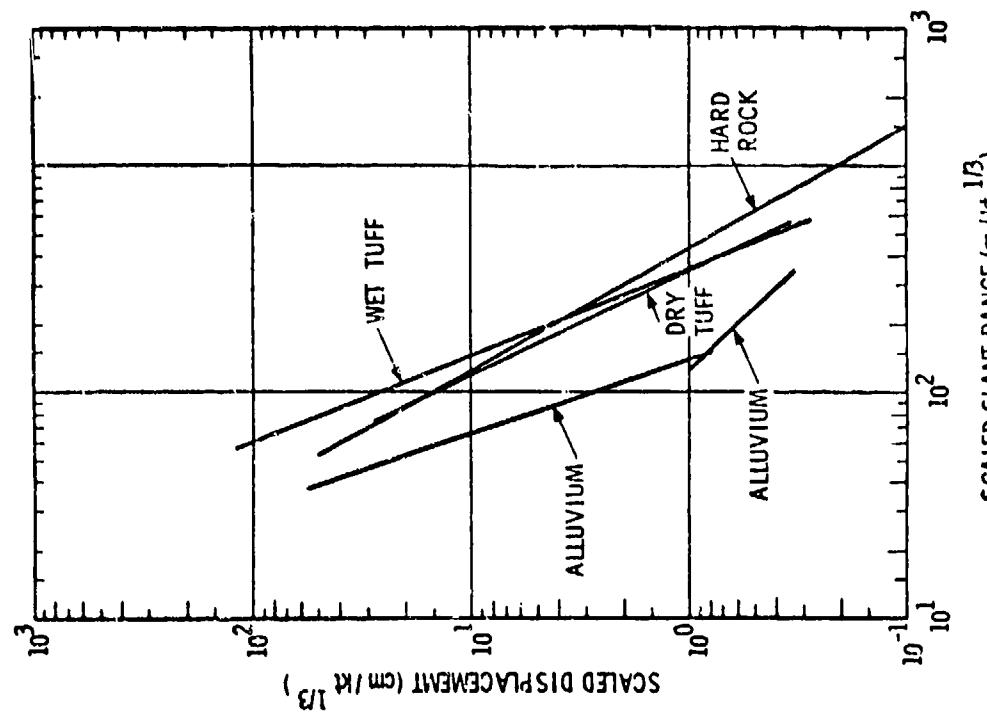


Figure IV-2.27. Attenuation comparison - scaled displacement.

energy has been more rapidly dissipated in transit through the alluvium to the seismic region. The consequence must be reduced motion throughout the same region in alluvium compared to motion in higher impedance rocks.

IV-2.3.8. Scaled Data

The problem of direct comparison of ground motion data induced by underground explosions of widely differing energy yield requires that some form of normalization to a common explosive energy base be applied to all data. Dimensional analysis indicates that necessary and sufficient conditions for such normalization or scaling are met by use of the cube-root of actual energy yield as the scaling factor for both free-field motion parameters and distances or ranges between the measuring station and explosion. The result of such scaling, using the explosive energy, W , in terms of equivalence to energy released by a kiloton of TNT, in that normalized acceleration is the actual acceleration multiplied by $W^{1/3}$. Stress, strain, and particle velocity are unaltered. Distances, displacements, and times are divided by $W^{1/3}$. The results of these operations are equivalent to motion or stress produced by one kiloton equivalent energy. It is noted here that free-field conditions satisfy such scaling, but phenomena which depend upon such factors as gravity or density require considerably more sophisticated procedures for analytical comparison.

All free-field stress and motion data used have been assembled in Table IV-2.3, IV-2.4, and IV-2.9 through IV-2.27. All tables include dimensions in both metric and British systems; meters and feet are used in all cases except displacements where centimeters and inches apply. In general, the tables are self-explanatory. The gauge numbers quoted in Tables IV-2.9 through IV-2.27 are significant only in identifying data with record traces or gauge stations in referenced reports. In a few cases, special comments will be referenced to a table where it seems pertinent.

The energy yields of some of the events included in these tables are classified information and might be compromised if the scaled data were associated with the event name. However, all of these events have unclassified coded yields; i.e., "L" indicates a low yield, less than 20 kt; "L-I" refers to a low-intermediate yield of between 20 and 200 kt; and "I" indicates an intermediate yield of between 200 and 1000 kt (1 megaton). Those events for which only coded yields have been released are designated alphabetically, but not in chronological sequence, to provide a means for easier reference in discussion.

The first two tables present data from the regions of hydrodynamic and plastic response. None of these data has been identified here with a specific event. Table IV-2.3 already mentioned earlier includes only data obtained from underground nuclear explosions in desert alluvium at NTS. Table IV-2.4 also mentioned earlier includes data from similar explosions in tuff and granite. Data from quartz, man-ganin, ytterbium, and ferroelectric gauges represent measurements from the region of plastic response.

Data in all remaining tables are from ground motion gauges. When a report is pertinent to an event, it is referenced in the tables, and the agencies responsible for the data are indicated for each event. These agencies include Sandia Laboratories, Stanford Research Institute (SRI); Lawrence Radiation Laboratory (LRL) or, more recently, Lawrence Livermore Laboratory (LLL); Edgerton, Germeshausen, and Grier (EG&G); Defense Nuclear Agency (DNA); Physics International Company (PI); and U.S. Army Engineers Waterways Experiment Station (WES). In addition to scaled ranges, accelerations, particle velocities, and displacements, scaled rise times are noted where available. Rise time is defined here as the time interval between onset of motion and the first peak in a record. Residual displacements refer to apparent stable displacement levels in those records where such a term is definable for a period several times the transient displacement duration. Those record numbers which include the letter "S" in the various tables represent data from stations on the ground surface directly above the explosion. These data obviously do not represent free-field motion. However, essentially total reflection of the stress at the free surface doubles the motion amplitude. Such "surface zero" data have been included at half-value in some of the analyses, and in general the corrected values fall within normal scatter of the actual free-field data from the same event.

The sign convention in these measurements is as follows: for vertical gauges upward motion is positive, for radial gauges outward motion is positive, and for tangential gauges clockwise motion is positive. The standard coordinate system is cylindrical, with the vertical axis through the shot point. The exceptions to this are the radial vector measurements or vectorially derived records which correspond to a spherical coordinate system.

For all events which have unclassified numerical yields, that yield, the shot depth, environmental rock, and type of installation is given. For those events designated alphabetically, only the location, rock type, and type of installation are given.

Table IV-2.9 includes data from SCOOTER (Reference IV-2.16), the only non-nuclear explosion included in this review. This was a cratering shot, as previously noted, and was included for comparison of both cratering versus contained and chemical versus nuclear explosion effects. Tables IV-2.9, IV-2.10, and IV-2.11 include all events detonated in alluvium which have been included in this review.

Tables IV-2.12, IV-2.13, and IV-2.14 include data from all events detonated in dry tuff. Note that for Event N several values of peak acceleration carry the prefix for "greater than" as an indication that the record peak indicated system saturation and in general that no true peak appears on the record, as indicated by the uncertainty in the scaled risetime and absence of velocity data from those gauges.

In Tables IV-2.17 and IV-2.18, certain of the measurements from COMMODORE and Events D, F, and G were obtained from the same gauge stations in one particular boring, U2Z-1. These stations at depths of 1100 ft (335 m), 1400 ft (427 m), 2200 ft (670 m), 2600 ft (792 m), and 3400 ft (1036 m) were in various types of rock, as indicated by the foot notes to these tables. It is also noteworthy that the deepest station, Z34, was probably not securely bonded to the carbonate rock although direct evidence of this fact is lacking.

A similar situation holds for CALABASH, CARPETBAG, and Event I in Table IV-2.18 where similarly positioned stations in borings U2Z-2 and U2Z-3 were used for several events. Depths to these stations were 1400 ft (427 m), 1800 ft (549 m), 2000 ft (610 m), and 2400 ft (732 m), with similar identification of the rock surrounding each station.

Data presented in Tables IV-2.20, IV-2.21, and IV-2.22 were derived from nuclear explosions in granite and in dolomite. All three events in granite occurred in tunnel complexes. The explosive for the dolomite event (HANDCAR) was emplaced in a deep boring and the ground motion stations were positioned at various depths in instrument borings in different types of rock, as indicated by superscripts and the footnote to Table IV-2.21.

The Aleutian Island of Attu was the locale of the three events included in Tables IV-2.23 and IV-2.24. These events were all detonated in volcanic rocks, and all free-field motion gauge stations were along approximately vertical radii, that is, in vertical arrays offset a short distance from the shot hole. For the MILROW (Reference IV-2.15) and CANNIKIN (Reference IV-2.14) Events, station numbers include the approximate distance above the explosion in hundreds of feet, except

Table IV-2.9. Scaled free-field ground motion—alluvium.

Record Number	Scaled Slant Range ft/kt 1/3	Scaled Acceleration Peak g.kt 1/3	Particle Velocity Peak ft/sec	Risetime sec/kt 1/3	Peak cm/kt 1/3	Scaled Dispacement Risetime sec/kt 1/3	Residual in/kt 1/3
SCOOTER: 0.5 kt TNT, 38 m (125 ft) deep in Area 10 NTS ALLUVIUM—Boring, Sandia (Reference IV-2.16).							
Shot level array							
A-50	19.2	63	0.0029	>1200	0.0049	--	--
A-100	38.4	126	0.0365	16.2	0.0403	~134	--
A-150	57.6	189	0.0189	5.85	0.1084	69.4	+18.9
BV-150				6.98	0.1096	90.2	+27.7
A-200	76.8	252	0.0214	2.61	0.1471	37.4	+0.378
BV-200				8.55	0.1474	38.7	+0.966
A-300	115	378	0.0428	2.51	0.2003	13.7	+1.26
BV-300				0.77	0.2003	5.39	+4.79
				1.05	0.1902	7.32	0.79
				3.44	0.1902	0.3414	0.0
FISHER: "L" kt at 363 m (1190 ft) in Area 2 NTS ALLUVIUM—Boring.							
6-UR	39.8	130	--	9.91	32.5	59.8	23.5
8-UR	79.0	259	--	0.762	2.50	5.16	2.05
4-UR	119	389	--	0.125	0.41	0.0324	0.376
2-AR	237	778	0.926	--	--	--	0.1210
2-UR				0.183	0.60	0.0307	+0.22
7-AV-S	158	517	5.09	--	1.01	0.397	--
				0.61	2.0	1.48	--
					3.76	0.1529	--
HOGNOSE: "L" kt at 239 m (784 ft) in Area 3 NTS ALLUVIUM—Boring.							
4-AR	76.2	250	1.10	0.057	0.610	2.1C	0.0820
4-JR				0.174	0.57	0.0445	1.27
2-AR	110	360	1.66	0.008	0.174	0.57	0.0365
2-iR				0.204	0.67	0.0350	1.27
6-AR	150	493	0.72	0.009	0.119	0.39	0.0620
6-UR				0.128	0.42	0.0630	0.864
8-AR	281	923	0.24	0.012	0.049	0.16	0.0600
8-UR				0.055	0.18	0.0600	0.318
						0.125	0.0900
HAYMAKER: 46 kt at 408 m (1340 ft) in Area 3 NTS ALLUVIUM—Boring.							
2-AR	77.7	255	7.99	0.0276	0.732	2.4C	0.0472
2-UR				--	0.701	2.30	0.0466
4-UR	154	504	--	0.189	0.62	0.0307	4.61
1-AV-S	114	373	8.96	--	1.05	3.45	0.659
						12.2	4.80

Table IV-2.10. Scaled free-field ground motion—alluvium.

Record Number	Scaled Slant Range m./kt $^{1/3}$	Scaled Acceleration Peak ft./kt $^{1/3}$	Scaled Velocity Peak g. kt $^{1/3}$	Risetime sec./kt $^{1/3}$	Particle Velocity Peak m./sec. ft./sec.	Risetime sec	Peak cm./kt $^{1/3}$	Peak in./kt $^{1/3}$	Scaled Displacement Risetime sec./kt $^{1/3}$	Residual cm./kt $^{1/3}$
m./kt	$^{1/3}$	ft./kt	$^{1/3}$	sec./kt	ft/sec	sec	cm	in	cm./kt	in./kt
MERLIN: 10 kt, 296 m (972 ft) deep in Area 3 NTS ALLUVIUM—Boring, Sandia (Reference IV-2.12).										
Shot level array										
3-UR	49.4	162	--	--	3.26	10.7	0.0939	20.2	7.96	+17.9
4-UR	98.7	324	3.52	0.0102	0.363	1.19	0.0495	2.97	1.17	+ 0.532
4-UR	155	509	--	--	0.241	0.790	0.0472	1.94	0.76	+ 1.35
5-UR	226	741	--	0.0120	0.122	0.400	0.0319	0.952	0.375	+ 0.426
5-UR	7-AR	353	11.38	0.367	--	0.082	0.270	0.0338	0.254	--
6-UR	1-AV1	27.9	91.6	2162	0.0263	22.6	74	--	0.235	+ 0.093
6-UR	1-AV2	46.0	151	16.9	0.0537	4.30	14.1	0.0897	0.273	+ 0.046
1-AV3	67.0	220	7.50	0.0217	0.963	3.16	0.0736	10.7	4.20	+ 0.056
1-AV4	80.9	266	5.10	0.0208	0.716	2.35	0.0638	8.31	3.27	+ 0.23
1-AV5	95.0	312	3.52	0.0435	0.561	1.84	0.0652	5.62	2.21	+ 0.59
2-AV4	97.0	318	3.35	0.0430	0.576	1.89	0.0652	6.76	2.66	+ 0.28
1-AV7	109	328	2.59	0.0509	0.552	1.81	0.0773	5.71	2.25	+ 2.08
1-AV5	123	404	2.01	0.0523	0.719	2.36	0.0703	6.08	2.39	+ 0.42
1-AV10	130	427	1.88	0.0402	0.674	2.21	0.0731	5.49	2.16	+ 0.35
S-LAV2	136	448	3.39	0.0161	0.707	2.32	0.0628	5.37	0.1579	+ 0.60
VULCAN: "L" kt at 322 m (1057 ft) in Area 2 NTS ALLUVIUM—Boring, LRL/Nortronics.										
7-AV	37.4	123	> 64	0.0363	--	16.5	54	--	96.9	38.2
7-JV	--	--	--	0.0267	--	--	0.0482	--	--	0.158
6-AV	58.2	191	8.01	--	--	--	--	--	--	--
6-DV	--	--	--	0.0171	3.05	10	0.0886	17.1	6.73	0.1535
5-AV	79.0	259	6.14	--	--	--	--	--	--	--
5-JV	--	--	--	0.0103	1.10	3.6	0.1235	7.40	2.91	0.2117
4-AV	89.4	293	8.77	0.0133	1.80	5.9	0.1026	--	--	--
8-AV	105	344	3.22	0.0103	1.13	3.7	0.0619	--	--	--
15-AV-S	110	360	2.63	--	0.853	2.8	0.0612	8.65	3.41	0.1566
15-JV-S	--	--	--	--	--	--	--	--	--	--

Table IV-2.11. Scaled free-field ground motion—alluvium.

Record Number	Scaled Slant Range m/kt 1/3 ft/kt 1/3	Scaled Acceleration			Particle Velocity			Scaled Displacement			Residual
		Peak g·kt 1/3	Risetime sec/kt 1/3	Peak ft/sec	Peak sec/kt 1/3	Risetime sec/kt 1/3	Peak cm/kt 1/3	Risetime sec/kt 1/3	Peak cm/kt 1/3	Risetime sec/kt 1/3	
HUMMOBILE: "L" kt, 247 m (810 ft) deep in Area 2 NTS ALLUVIUM—Boring, LLL/EG&G.											
Shot level array											
19-AR	91.7	301	3.12	0.0046	0.457	1.50	0.0626	3.64	1.43	0.1062	---
19-UR	--	--	0.549	1.80	0.0585	3.74	1.47	0.1037	+1.64	+	+0.647
Vertical array											
9-AV-UV	11.9	138	46.7	0.0492	4.72	15.5	0.0826	--	--	--	--
10-UV	49.9	164	--	--	3.94	12.8	0.0780	--	--	--	--
11-UV	56.0	184	--	--	1.80	5.91	0.0934	16.3	4.83	0.1319	--
12-AV	80.7	265	3.90	0.0056	0.482	1.58	0.0641	5.08	2.00	0.1421	--
12-UV	--	--	--	--	0.610	2.00	0.0590	6.48	2.55	0.1432	--
13-AV	96.2	316	2.92	0.0062	0.515	1.69	0.0739	5.19	2.04	0.1473	--
14-AV	112	366	2.14	0.0082	0.625	2.05	0.0713	5.83	2.30	0.1478	--
14-UV	--	--	--	--	0.664	2.18	0.0693	6.07	2.39	0.1442	--
15-AV	119	389	2.34	0.0082	0.573	1.88	0.0698	4.93	1.94	0.1432	--
15-UV	--	--	--	--	0.561	1.84	0.0677	5.00	1.97	0.1421	--
PACKARD: 10 kt at 247 m (810 ft) in Area 2 NTS ALLUVIUM—Boring, LLL/EG&G (Reference IV-2.26).											
Shot level array											
23-AR	40.7	134	57.1	0.0371	7.83	25.7	0.0529	--	--	--	--
23-UR	--	--	7.32	24.0	0.0497	37.1	14.6	0.1068	--	--	--
Vertical array											
15-JV	27.7	91.0	--	--	69.5	228	0.0167	--	--	--	--
16-AV-UV	36.9	121	142	0.0353	15.8	52	0.0357	--	--	--	--
17-AV	43.6	143	91.6	0.0501	7.56	24.8	0.0696	--	--	--	--
17-JV	--	--	--	--	7.92	26.0	0.0696	--	--	--	--
18-AV	50.8	167	25.9	0.0603	3.41	11.2	0.0845	--	--	--	--
18-UV	--	--	--	--	4.75	15.6	0.0863	29.0	11.4	0.1420	--
19-AV	57.3	188	5.17	0.0608	1.98	6.5	0.0919	--	--	--	--
19-JV	--	--	--	--	1.65	5.4	0.1030	13.0	5.12	0.1448	--
20-AV	85.7	281	3.88	0.0116	0.741	2.43	0.1137	--	--	--	--
20-JV	--	--	--	--	0.777	2.55	0.1219	7.92	3.12	0.1685	--
21-AV	100	328	2.71	0.0125	0.671	2.20	0.0752	--	--	--	--
21-UV	--	--	--	--	0.716	2.35	0.0789	8.12	3.20	0.1644	--
22-AV-S	114	375	5.39	0.0241	0.732	2.4	0.0789	--	--	--	--
22-UV-S	--	--	--	--	0.701	2.3	0.0757	75.0	29.5	0.2172	--

Table IV-2-12. Scaled free-field ground motion—tuff.

Record Number	Scaled Slant Range m./kt. 1/3 ft./kt. 1/3	Scaled Acceleration Peak g./kt. 1/3	Scaled Velocity Peak sec./kt. 1/3	Particle Velocity Peak m./sec	Risetime sec./sec	Peak cm./kt. 1/3	Peak in./kt. 1/3	Scaled Displacement Risetime sec./kt. 1/3	Residual cm./kt. 1/3 in./kt. 1/3
RAINIER: 1.7 kt, 274 m (896 ft) deep in Area 12 NTS (Rainier Mesa) TUFF—Tunnel, Sandia (Reference IV-2.7).									
Shot level array									
AHP-2	37.8	124	2228	0.0017	21.6	71	0.0017	42.6	16.8
AHP-3	50.8	167	421	0.0017	5.2 ^b	17.2	0.0034	2.25	0.017
AHP-3X	50.8	167	334	0.0025	5.36	17.6	0.0042	5.64	0.032
AHP-4	63.8	210	251	0.0025	2.22	7.29	0.0034	1.04	0.021
AHP-5	76.6	251	47.7	0.005	3.29	10.8	0.015	2.40	0.029
AHP-6	128	420	5.97	0.023	1.20	3.95	0.035	7.49	2.95
AHP-7	230	755	2.67	0.026	1.66	2.18	0.035	6.81	2.68
AR	346	1135	1.55	0.046	0.44	1.45	0.061	1.92	0.75
Vertical array									
AVS-1	93.5	307	10.3	0.010	1.73	5.67	0.048	13.5	5.31
AVS-1X	94.7	311	10.1	0.008	1.72	5.64	0.047	13.3	5.22
AVS-2	114	374	8.47	0.013	1.56	5.13	0.036	11.9	4.68
AVS-3	171	562	3.58	0.018	1.17	3.83	0.109	17.6	6.93
AVS-4	178	585	4.08	0.023	1.41	4.64	0.091	21.7	8.55
AVS-6-S	229	751	6.56	0.0385	2.35	7.72	0.072	30.4	12.0
SRI (Swift, Sechi 1956a)									
OAP-320	148	486	6.90	0.015	1.05	3.46	0.034	--	--
OAP-250	166	544	1.62	0.017	0.37	1.20	0.064	--	--
OAP-180	184	603	1.74	0.018	0.53	1.73	0.065	--	--
EVENT B: "L" kt, in Area 12 NTS—TUFF—Boring, SRI.									
OVW5	113	372	--	--	2.65	8.7	0.025	13.0	5.11
OVW4	130	425	--	--	2.80	9.2	0.032	12.4	4.89
3VH5	244	799	--	--	0.805	2.64	0.010	1.82	0.715
3VH4	263	864	--	--	1.05	3.45	0.018	2.86	1.13
3VW2	293	963	--	--	0.24	0.80	0.017	1.30	0.511
PLATTE: 1.85 kt, 191 m (628 ft) deep in Area 12 NTS—TUFF—Tunnel, Sandia unreported.									
6500UH	161	529	--	--	1.07	3.5	0.0461	3.16	0.082
9000UH	223	733	--	--	1.22	4.0	0.3880	4.94	0.085
EVENT C: "L" kt in Area 12 NTS—TUFF—Tunnel, SRI.									
VR-9	128	420	--	--	0.999	3.28	0.0407	5.31	6.21
VR-12	340	1115	--	--	0.205	0.672	0.259	1.04	9.31
									+ 2.44
									+ 3.67
									0.0 0.0
									c.o. c.o.

Table IV-2.13. Scaled free-field ground motion—tuff.

Record Number	Scaled weight in/kt	Scaled Slant Range 1/3 ft./kt	Scaled Acceleration Peak	Particle Velocity Peak	Risetime	Peak	Scaled Displacement
	1/3	1/3	g•kt 1/3	m/sec	sec/kt 1/3	cm/kt 1/3	in/kt 1/3
			g•kt 1/3	ft/sec	sec	in	in/kt
EVANS: 0.055 kt, 260 m (850 ft) deep in Area 12 NTS (Rainier Mesa) TUFF—Tunnel (Reference IV-2.6).							
Vertical array							
A-550	349	1143	2.2	0.042	0.30	1.0	0.053
A-500	389	1275	1.2	0.018	0.30	1.0	0.029
AX-350	410	1344	0.68	0.045	0.22	0.72	0.100
A-450	429	1407	0.99	0.029	0.20	0.64	0.037
AX-300	450	1475	0.61	0.024	0.13	0.42	0.037
AX-250	490	1607	0.32	0.024	0.06	0.21	0.055
A-350	509	1570	0.26	0.019	0.067	0.22	0.050
AX-200	530	1738	0.27	0.039	0.06	0.20	0.053
AX-150	570	1870	0.26	0.032	0.06	0.19	0.050
AX-100	610	2001	0.27	0.033	0.06	0.21	0.076
A-200	629	2064	0.26	0.032	0.06	0.20	0.050
AX-50	550	2130	0.25	0.032	0.06	0.21	0.047
A-0-S	680	2232	0.34	0.042	0.10	0.32	0.098
AX-0-S	680	2232	0.60	0.047	0.15	0.50	0.068
SRI (Reference IV-2.23).							
DAV 10	200	657	5.21	0.013	0.923	3.03	0.029
DAV 7	273	894	--	0.335	1.10	0.024	1.12
DAV 8	281	920	1.42	0.018	0.252	0.828	0.029
DAV 7	321	1052	1.18	0.024	0.205	0.672	0.032
DAV 6	401	1315	0.772	0.024	0.162	0.531	0.034
DAV 5	481	1578	0.299	0.026	0.066	0.215	0.039
DAV 4	521	1709	0.359	0.029	0.087	0.285	0.039
DAV 3	561	1841	0.264	0.031	0.063	0.207	0.042
DAV 2	601	1972	0.292	0.026	0.072	0.236	0.045
DAV 1	641	2104	0.282	0.034	0.068	0.223	0.047

Table IV-2.14. Scaled free-field ground motion—tuff.

Record Number	Scaled Slant Range ft/kt $^{1/3}$	Scaled Acceleration Peak g-kt $^{1/3}$	Scaled Risetime sec/kt $^{1/3}$	Particle Velocity			Peak cm/kt $^{1/3}$	Risetime sec/kt $^{1/3}$	Scaled Displacement Risetime sec/kt $^{1/3}$	Residual displacement cm/kt $^{1/3}$
				Peak ft/sec	Rise time sec	Peak in/kt $^{1/3}$				
MUDPACK: 2.7 kt, 156 m (510 ft) deep in Area 8 NTS—TUFF—Boring, Sandia (Reference IV-2.11).										
Off-set vertical array										
NS-AV1-S	111	365	5.78	0.0180	1.63	5.35	0.0905	20.3	11.1	+ 1.09
NS-AV2-S			4.89	0.0165	1.42	4.65	0.0898	22.4	8.83	-11.9
B5-10TR	1	43.6	143	9.93	0.0007	1.20	3.94	0.0539	--	--
B5-20TR	2	49.3	162	4.68	0.0029	0.408	1.34	0.0582	--	--
B5-30TR	3	77.3	254	1.35	0.0065	0.113	0.37	0.0582	--	--
B5-40TR	3	187	614	--	--	0.061	0.20	0.0531	--	--
B5-40TR	2	73.8	242	3.79	0.0057	0.378	1.24	0.0517	2.13	0.3840
N1-10TR	1	82.3	270	1.57	0.0129	0.201	0.66	0.0481	1.09	0.431
N1-20TR	2	100	328	0.738	0.0086	0.104	0.34	0.0409	0.602	0.237
N1-30TR	3	132	434	0.460	0.0108	0.064	0.21	0.0553	0.365	0.144
N1-40TR	3	125	411	0.752	0.0180	0.189	0.62	0.0632	1.20	0.474
B4-10TR	2	130	426	0.460	0.0230	0.134	0.44	0.0661	0.839	0.330
B4-20TR	3	142	465	0.306	0.0165	0.134	0.44	0.0603	0.912	0.359
B4-30TR	3	188	618	0.251	0.0661	0.052	0.17	0.0754	0.257	0.101
B2-10TR	1	192	629	0.125	0.0632	0.119	0.39	0.0847	0.711	0.280
B2-20TR	2	201	661	0.153	0.0136	0.079	0.26	0.0819	0.529	0.208
DISCUS THROWER: 21 kt, 338 m (1106 ft) deep in Area 8 NTS—TUFF—Boring, Sandia (Reference IV-2.17).										
LS-AV1-S	122	400	4.50	0.0204	3.35	11.0	0.2305	80.1	31.5	0.3066
LS-UV-S			--	--	3.41	11.2	0.2215	77.3	30.4	0.3048
4E-UV	3	34.4	113	--	-25.6	-84	0.0018	--	--	--
5B-TR	1	44.9	147	436	0.0022	>16.5	>54	0.0051	--	--
9A-TR	1	177	581	2.07	0.0069	0.460	1.51	0.0402	2.82	1.11
9B-TR	1	178	584	4.41	0.0185	0.351	1.15	0.0308	2.69	1.06
9B-TR	4	180	591	--	--	0.280	0.918	0.0109	0.549	0.216
9D-TR	3	183	599	--	--	0.223	0.730	0.0178	0.591	0.233
9E-TR	3	189	621	--	--	0.304	0.998	0.0120	0.359	0.141
9F-TR	3	1591	1591	0.3117	0.0221	0.046	0.150	0.0250	0.110	0.043
12B-TR	1	485	1592	0.3767	0.0087	0.037	0.120	0.0188	0.092	0.0453
12D-TR	3	485	1594	0.331	0.0040	0.038	0.125	0.0232	0.106	0.042
12E-TR	3	486	1599	0.441	0.0072	0.040	0.130	0.0294	0.109	0.043
12F-TR	5	487	--	--	--	--	--	--	--	--

NOTE: Superscripts indicate rock at gauge station as follows: 1. tuff, 2. shale, 3. carbonate, 4. tuff-carbonate interface, 5. argillite.

Table IV-2.15. Scaled free-field ground motion—wet tuff.

Superscript 1 indicates gauge stations below water table.

Table IV-2.16. Scaled free-field ground motion—wet tuff.

Record Number	Scaled Slant Range mi/kt $^{1/3}$	Scaled Acceleration			Particle Velocity			Scaled Displacement		
		Peak g·kt $^{1/3}$	Risetime sec/kt $^{1/3}$	Peak m/sec	Peak ft/sec	Risetime sec/kt $^{1/3}$	Peak cm/kt $^{1/3}$	Risetime sec/kt $^{1/3}$	Peak in/kt $^{1/3}$	Risetime sec/kt $^{1/3}$
EVENT D: "L-1" kt in Area 2 NTS—WET TUFF—Boring, Sandia unreported.										
Vertical array										
V5-AV	11.8	386	13.3	0.0061	1.92	6.3	0.0852	20.9	8.21	0.1632
V5-UV			--	--	1.89	6.2	0.0872	21.1	8.31	0.1652
V4-AV	12.4	406	11.8	0.0041	1.95	6.4	0.0781	22.1	8.72	0.1683
V4-UV			--	--	1.77	5.8	0.0760	17.8	6.99	0.1551
V3-AV	13.0	426	10.9	0.0061	2.07	6.8	0.0416	21.1	8.31	0.1612
V3-UV			--	--	2.26	7.4	0.0405	22.1	8.72	0.1531
V2-AV	13.6	447	9.86	0.0061	2.53	8.3	0.0426	22.9	9.02	0.1581
V2-UV			--	--	2.44	8.0	0.0365	20.6	8.11	0.1480
V1-AV	14.2	467	11.3	0.0243	2.68	8.8	0.0426	19.6	7.70	0.1480
V1-UV			--	--	2.90	9.5	0.0426	19.6	7.70	0.1521
Offset Vertical array										
Z11-JR	200	655	--	--	1.52	5.0	0.0203	6.39	2.51	0.0993
Z14-JR	2	634	--	--	1.46	4.8	0.0120	5.87	2.31	0.0852
Z22-JR	3	184	603	--	2.65	8.7	0.0101	4.94	1.95	0.0710
Z26-JR	3	184	604	--	1.89	6.2	0.0207	3.84	1.51	0.0801
Z34-JR	4	194	636	--	0.427	1.4	0.0034	1.54	0.608	0.1032
Shot level array										
X24-JR	3	298	978	--	1.52	5.0	0.0245	2.37	0.933	0.1050
COMMODORE: 250 kt, 749 m (2449 ft) deep in Area 2 NTS—WET TUFF—Boring, Sandia unreported.										
Vertical array										
M5-AV	95.2	312	11.8	0.0048	4.60	15.1	0.1006	--	--	0.2221
M5-UV			--	--	5.24	17.2	0.0998	68.7	27.0	0.2164
M4-UV	100	328	--	--	4.48	14.7	0.0982	58.0	22.8	0.2164
M3-AV	105	345	9.94	0.0097	4.51	14.8	0.0949	--	--	0.2164
M3-UV			--	--	3.35	11.0	0.1006	39.0	15.3	0.2164
M1-AV	115	377	18.0	0.0145	4.82	15.8	0.0636	--	--	--
M1-UV			--	--	5.00	16.4	0.0620	66.2	26.1	0.2084
Offset Vertical array										
Z11-JR	168	551	--	--	2.32	7.6	0.0137	8.42	3.31	0.1142
Z14-JR	2	163	535	--	2.32	7.6	0.0145	7.60	2.99	0.0893
Z22-JR	3	156	511	--	4.21	13.8	0.0217	7.77	3.06	0.0708
Z26-JR	3	156	511	--	2.93	9.6	0.0257	6.54	2.57	0.0901
Z34-JR	4	162	533	--	0.975	3.2	0.0080	2.94	1.16	0.0869
Shot level array										
X24-JR	3	280	918	--	0.975	3.2	0.0386	1.84	0.724	0.0949

Superscripts indicate rock at gauge station as follows: 1 dry tuff, 2 welded tuff, 3 tuff below water table, 4 carbonate rock.

Table IV-2.17. Scaled free-field ground motion—wet tuff.

Record Number	Scaled Slant Range m/kt 1/3	Scaled Acceleration Peak g-kt 1/3	Scaled Acceleration Risetime sec/kt 1/3	Particle Velocity Peak m/sec	Risetime sec/kt 1/3	Peak cm/kt 1/3	Scaled Displacement Risetime sec/kt 1/3	Residual cm/kt 1/3 in/kt 1/3
EVENT F: "L-I" kt in Area 2 NTS—WET TUFF—Boring, Sandia unreported.								
Vertical array								
X3-UV	123	4.04	--	2.65	8.7	0.0669	30.6	0.1644
X2-UV	129	4.24	--	3.35	11.0	0.0501	37.1	0.1725
X1-AV	135	4.33	17.2	0.0103	3.35	0.0494	32.6	0.1751
X1-UV*		--		3.20	10.5	0.0494	31.1	0.1727
Offset vertical array								
Z11-AR 1	195	64.0	21.3	0.0148	2.13	0.0182	--	--
Z11-TR 1		--		2.26	7.4	0.0188	5.31	2.09
Z11-AR 2	189	62.0	28.9	0.0122	2.38	7.8	--	--
Z11-TR 2		--		1.68	5.5	0.0150	5.01	1.97
Z22-AR 3	180	590	--	--	3.29	10.8	0.0061	4.46
Z22-TR 3	180	591	--	--	2.50	8.2	0.0071	3.26
Z23-AR 4	189	62.0	5.98	0.0034	0.396	1.3	0.0154	--
Z23-TR 4		--		0.579	1.9	0.0197	1.23	0.484
EVENT G: "L-I" kt in Area 2 NTS—WET TUFF—Boring, Sandia unreported.								
Z11-TR 1	168	550	--	2.50	8.2	0.0276	8.66	3.41
Z11-TR 2	163	535	--	2.23	7.3	0.0239	7.77	3.06
Z22-TR 3	157	514	--	5.39	17.7	0.0071	--	--
Z22-TR 3	158	520	--	4.27	14.0	0.0081	--	--
Z23-TR 4	170	558	--	0.853	2.8	0.0199	--	--
							0.0367	+ 0.401
								+ 0.158

Subscripts indicate rock at gauge stations as follows: 1 dry tuff, 2 welded tuff, 3 tuff below water table, 4 carbonate rock.

Table IV-2.18. Scaled free-field ground motion—wet tuff.

Record Number	Scaled Siant Range			Scaled Acceleration			Particle Velocity			Scaled Displacement		
	m/kt 1/3	ft/kt 1/3	g·kt 1/3	Peak	Risetime	Peak	Risetime	Peak	Risetime	sec/kt 1/3	in/kt 1/3	sec/kt 1/3
EVENT H: "L-I" kt in Area 9 NTS—WET TUFF—Boring, LLL/EG&G.												
Vertical array												
16-AV-UV	31.4	103	436	0.0225	34.7	114	0.0301	--	--	--	--	--
15-AV	43.0	141	163	0.0375	--	--	--	--	--	--	--	--
14-AV-UV	57.6	189	26.3	0.0032	7.41	24.3	0.0659	62.7	24.7	0.2140	--	--
13-AV	72.1	236	18.4	--	4.45	14.6	0.1001	45.8	18.0	0.1873	--	--
13-DV					4.33	14.2	0.1007	49.3	19.4	0.2235	--	--
12-AV	80.8	265	17.1	0.0061	5.06	16.6	0.1043	62.7	24.7	0.2280	--	--
11-AV	86.6	284	14.7	0.0057	4.36	14.3	0.1037	50.5	19.9	0.2046	--	--
10-AV	92.4	303	14.2	0.0067	4.75	15.6	0.1089	61.5	24.2	0.2202	--	--
10-DV					3.81	12.5	0.1060	49.9	19.6	0.2202	--	--
EVENT I: "I" kt in Area 2 NTS—WET TUFF—Boring, Sandia/LLL unreported.												
Offset vertical array												
Z3-11UTR ¹	188	618	--	--	0.445	1.46	0.0091	25.0	9.85	0.0699	-3.6	-1.4
Z3-18UTR ¹	187	615	--	--	0.442	1.45	0.0190	23.7	9.33	0.0837	+16	+6.4
Z3-20UTR ²	188	618	--	--	0.460	1.51	0.0130	25.9	10.2	0.0888	+7.2	+2.8
Z3-24UTR ³	192	631	--	--	0.442	1.45	0.0095	18.8	7.41	0.0736	+1.8	+0.7
CALABASH: 110 kt 626 m (2050 ft) deep in Area 2 NTS—WET TUFF—Boring, Sandia/LLL unreported.												
Z2-14UTR ¹	197	646	--	--	1.19	3.9	0.0159	41.6	16.4	0.0756	+13	+5.0
Z2-18UTR ²	193	632	--	--	0.975	3.2	0.0140	12.1	4.76	0.0597	--	--
Z2-20UTR ³	192	631	--	--	1.19	3.9	0.0121	2.93	1.15	0.0538	--	--
Z2-24UTR ³	193	634	--	--	1.8	6.2	0.0284	2.67	1.05	0.0447	--	--
Z3-20UTR ²	304	997	--	--	1.16	3.8	0.0380	2.16	0.852	0.0860	--	--
CARPETBAG: 220 kt 663 m (2171 ft) deep in Area 2 NTS—WET TUFF—Boring, Sandia/LLL unreported.												
Z3-14UTR ¹	158	519	--	--	1.71	5.6	0.0232	3.91	1.54	0.0629	+2.4	+1.0
Z3-18UTR ¹	154	505	--	--	0.64	2.1	0.0172	1.79	0.706	0.0394	--	--
Z3-20UTR ²	153	502	--	--	1.68	5.5	0.0137	4.19	1.65	0.0480	+1.5	+0.6
Z3-24UTR ³	153	502	--	--	2.32	7.6	0.0129	3.18	1.25	0.0444	--	--

Superscripts indicate rock at gauge stations as follows: 1 dry tuff, 2 welded tuff, 3 tuff below water table.

Table IV-2.19. Scaled free-field ground motion—wet tuff.

Record Number	Scaled Weight 1/3 ft./kt	Scaled Slant Range 1/3 ft.	Scaled Acceleration Peak g·kt ^{1/3}	Risetime sec/kt ^{1/3}	Particle Velocity Peak m/sec	Risetime sec/kt ^{1/3}	Scaled Displacement Peak cm/kt ^{1/3}	Risetime sec/kt ^{1/3}
EVENT O: "L" kt in Area 12 NTS (Rainier Mesa) WET TUFF-Tunnel, Sandia/DNA unreported.								
Shot level array								
AR00 164	539	100	0.0093	3.87	12.7	0.3111	--	--
UR00	--	--	3.63	11.9	0.0111	20.9	8.22	0.1295
AR13 183	599	42.4	0.0074	2.44	8.0	0.0149	--	--
UR13	--	--	2.35	7.7	0.0158	6.01	2.37	0.0427
AR40 224	736	43.1	0.0074	1.83	6.0	0.0088	4.36	0.0483
UR40	--	--	0.732	2.4	0.0046	1.41	0.557	0.2553
AR110 319	1047	14.9	0.0097	1.13	3.7	0.0172	--	--
UR110	--	--	0.914	3.0	0.0181	1.89	0.743	0.0404
EVENT P: "L" kt in Area 12 NTS—WET TUFF—Tunnel, SRI/PI.								
270UR1 48.9	160	--	--	23.2	76	0.0107	--	--
640UR1 114	374	--	--	3.78	12.4	0.0134	--	--
640UR2 113	372	--	--	4.24	13.9	0.0116	--	--
1110AR1 197	646	30.5	0.0122	--	--	--	--	--
1110UR1	--	--	0.223	0.73	0.0290	--	--	--
EVENT R: "L" kt in Area 12 NTS—WET TUFF—Tunnel, Sandia.								
AR-35 45.4	149	602	0.0028	--	--	--	--	--
UR-35	--	--	--	24.4	80	0.0041	--	--
UR-38 47.0	154	--	--	25.9	85	0.0024	--	--

Table IV-2.20. Scaled free-field ground motion—granite.

Record Number	Scaled Slant Range mi/kt ^{1/3}	Scaled Acceleration			Particle Velocity			Scaled Displacement		
		Peak	Risetime sec/kt ^{1/3}	g/ft	Peak	Risetime sec/kt ^{1/3}	ft/sec	Peak	Risetime sec/kt ^{1/3}	cm/kt ^{1/3}
HARD HAT: 5.9 kt, 290 m (950 ft) deep in Area 15 NTS—GRANITE—Tunnel, Sandia (Reference IV-2.58).										
Shot Level	ARRAY									
4-A	43.2	142	76.36	0.0006	17.2	56.5	0.0007	8.99	3.54	0.0089
6-A	51.6	169	3516	0.0012	18.5	60.6	0.0075	1.97	0.77	—
6-U	—	—	—	—	15.6	51.3	—	—	—	—
8-A	66.8	219	891	0.0014	9.17	30.1	0.0039	11.9	4.70	0.039
8-U	—	—	—	—	9.14	30.0	—	9.98	3.93	—
9-A	85.2	279	119	0.0017	6.52	21.4	0.0048	7.87	3.10	0.033
9-U	—	—	—	—	2.44	8.0	—	3.51	1.38	—
11-AR	1.02	334	83.1	0.0024	1.83	6.0	0.0069	2.53	0.996	0.041
11-UR	1.32	434	59.1	0.0028	1.58	5.2	—	0.984	0.387	—
12-AR	—	—	—	—	1.74	5.7	0.0061	2.78	1.10	0.045
12-UR	—	—	—	—	2.26	7.4	—	3.65	1.14	—
SRI										
22VR-1	168	553	—	—	2.78	9.13	0.0039	4.54	1.79	0.038
2ARS-1	251	825	8.04	0.0014	0.418	1.37	0.0080	—	—	—
2VRS-1	—	—	—	—	1.26	4.12	0.013	1.93	0.758	0.052
3VR-1	253	830	—	—	1.11	3.65	0.0004	1.88	0.742	0.045
Vertical Array										
CAV-6	45.5	149	3234	0.0019	21.4	70.1	0.0022	—	—	—
CAV-5	54.0	177	2533	0.0022	22.8	74.9	0.0026	—	—	—
CAV-4	70.8	232	361	0.0025	10.1	33.3	0.0055	—	—	—
CAV-3	87.7	288	905	—	22.2	72.9	—	—	—	—
CAV-2	113	371	484	0.0033	8.02	26.3	0.0045	—	—	—
CAV-1	130	426	204	2.0039	4.18	13.7	0.0055	—	—	—
CAV-S	150	526	164	0.0044	3.93	12.9	0.0064	—	—	—
		96.5	96.5	0.012	4.79	15.7	0.024	—	—	—

Table IV-2.21. Scaled free-field ground motion—granite and dolomite.

Record Number	Scaled Range ft./kt ^{1/3}	Scaled Acceleration Peak g./kt ^{1/3}	Risetime sec./kt ^{1/3}	Particle Velocity Peak m/sec	Risetime sec./kt ^{1/3}	Peak cm/kt ^{1/3}	Risetime sec./kt ^{1/3}	Scaled Displacement Residual cm/kt ^{1/3}	Risetime sec./kt ^{1/3}
SHOAL: 12 kt, 318 m (11205 ft) deep in Central Nevada—GRANITE—Tunnel, Sandia (Reference IV-2.25).									
	VUF 2001								
Shot Level Array									
PH-7	10.3	132	12.477	0.0006	67.1	220	0.0026	-	-
PH-6	66.6	21.8	64.1	0.0022	14.9	49.0	0.0044	-	-
PH-5	111	363	24.0	0.0031	3.54	11.6	0.0052	-	-
PH-4	173	568	38.9	0.0052	1.55	5.10	0.0072	-	-
PH-3	258	84.7	8.59	0.0055	0.640	2.10	0.0148	3.11	+0.655
PH-2	256	84.0	9.62	0.0043	0.430	1.43	0.0141	1.22	+0.066
PH-1	260	853	10.3	0.0037	0.546	1.79	0.0088	0.507	-0.052
Vertical Array									
PH-8-8	108	355	4.81	0.0032	5.39	17.7	0.0041	>24.4	-
PH-8-9	122	401	1.79	0.0038	3.86	12.7	0.0053	21.6	-0.44
PH-8-10	136	446	10.8	0.0031	3.33	11.1	0.0061	26.1	+5.33
PH-8-11	154	504	93.9	0.0062	3.90	12.8	0.0104	34.9	+4.43
PH-8-12	160	525	14.0	0.0032	6.40	21.0	0.0133	44.9	+6.12
HANDCAR: 12 kt, 402 m (1319 ft) deep in Area 8 NTS—DOLOMITE—Boring, Sandia (Reference IV-2.10).									
Offset Vertical Arrays									
Bl-SAV 175	575	9.75	0.0095	2.07	6.80	0.0376	15.2	5.98	+3.66
Bl-SAV ₁	78.1	256	9.62	0.0026	3.69	12.1	0.0214	16.0	+8.88
B1-1UR ₁	70.2	230	109	0.0017	3.87	12.7	0.0105	12.8	+3.49
B2-1UR ₁	107	350	58.4	0.0017	2.85	9.35	0.0144	-	+10.5
B2-2UR ₂	97.6	320	63.0	0.0017	4.42	14.5	0.0114	11.6	-
B2-3UR ₃	82.5	271	90.0	0.0017	3.11	10.2	0.0149	17.2	+9.76
B4-1UR ₁	12.8	422	23.1	0.0048	1.73	5.66	0.0144	6.77	+3.84
B4-2UR ₂	12.3	404	19.0	0.0031	1.65	5.40	0.0183	6.26	+6.20
B4-3UR ₃	11.3	372	24.3	0.0044	1.66	5.44	0.0175	12.3	+4.85
B4-4UR ₃	93.6	307	65.0	0.0026	1.98	6.49	0.0070	2.05	+8.88
B5-1UR ₁	20.8	683	9.09	0.0087	0.354	1.16	0.0166	0.677	-0.262
B5-2UR ₂	20.6	675	7.28	0.0087	0.561	1.84	0.0323	0.266	+0.666
B5-3UR ₃	19.8	650	7.37	0.0074	0.671	2.20	0.0170	1.50	+0.999
B5-4UR ₃	1.86	612	-	-	1.423	4.03	0.0144	0.590	+0.393
B6-1UR ₃	41.2	1352	3.27	0.0175	0.201	0.650	0.0236	1.86	+1.44
								0.734	+0.569
								1.81	+0.666
								0.712	+0.262
								0.366	0.0
								0.144	0.0
								0.0555	0.0

Superscripts indicate rock at gauge stations as follows: 1 tuff, 2 shale, 3 carbonate.

Table IV-2.22. Scaled free-field ground motion—granite.

Record Number	Scaled Siant Range			Scaled Acceleration			Particle Velocity			Scaled Displacement			Residual in/kt ^{1/3}
	m/kt ^{1/3}	fr/kt ^{1/3}	g-kt ^{1/3}	Peak	Risetime	Peak	Risetime	sec/kt ^{1/3}	ft/sec	cm/kt ^{1/3}	in/kt ^{1/3}		
PILE DRIVER: 56 kt 453 m (1518 ft) deep in Areas 15 NTS—GRANITE—Tunnel, SRI (Reference IV-2.61).													
Vertical Array													
9UV	47.8	157	—	—	29	95	0.0026	—	—	—	—	—	—
8UV	55.8	183	—	—	36.6	120	0.0024	—	—	—	—	—	—
6AV	79.7	261	51.6	0.0021	8.23	27	0.0034	—	—	0.2381	+77	+30	—
6UV	60.6	—	—	—	11.6	38	0.0029	83.7	—	—	—	—	—
5AV	91.6	301	115	0.0014	3.66	12	0.0099	—	—	0.2250	+39.8	+15.7	—
5UV	104	340	—	—	4.57	15	0.0091	61.7	24.3	—	—	—	—
3AV	353	—	73	0.0091	4.57	15	0.0139	—	—	0.2159	+18.6	+7.3	—
3UV	108	366	—	—	3.35	11	0.0128	34.5	13.6	—	—	—	—
2AV	112	366	353	0.0089	4.57	—	0.0115	—	—	0.2141	+23	+9.1	—
1UV	121	397	—	0.0091	4.88	16	0.0183	53.1	20.9	—	—	—	—
OAV-S	—	—	—	—	7.62	25	0.0128	—	—	—	—	—	—
Shot Level Array													
1403 UR	159	523	—	—	2.93	9.6	0.0065	—	—	—	—	—	—
2403 UR	159	523	—	—	1.65	5.41	0.0067	3.86	1.52	0.0565	+2.31	+0.91	—
1503 UR	225	740	—	—	1.05	3.44	0.0084	12.8	5.04	0.0371	+0.32	+0.13	—
2503 UR	225	740	—	—	0.787	2.58	0.0105	2.16	0.851	0.0709	+0.96	+0.96	—
Sandia (Reference IV-2.81).													
X-SLRAR-UR	25.3	85.1	2.3x10 ⁵ *	0.0004	30.5	100	0.0004	—	—	—	—	—	—
Z-SLRUR	30.8	101	—	—	67.1	220	0.0007	—	—	—	—	—	—
A-SLRUR	37.7	124	—	—	35.4	116	0.0013	—	—	—	—	—	—
F-SLRUR	40.5	133	—	—	14.6*	48	0.0058	—	—	—	—	—	—
E-SLRUR	44.9	147	—	—	65.2*	214*	0.0013	43.2	17.0	0.0503	—	—	—
B-SLRUR	53.2	175	—	—	33.5	110	0.0014	—	—	—	—	—	—
D-SLRAR	66.4	218	1247	0.0014	15.2	50	0.0021	—	—	—	—	—	—
E-SLRUR	—	—	—	—	3.05	10	0.0017	—	—	—	—	—	—
—RAR	74.3	244	501	0.0015	6.25	20.5	0.0022	—	—	—	—	—	—
C-SLRUR	123	403	—	—	11.4	37.5	0.0022	—	—	—	—	—	—
15-SLRUR	—	—	—	0.0018	4.48	14.7	0.0055	—	—	10.4	4.10	0.0452	—
16-SLRUR	—	—	—	—	5.73	18.8	0.0055	—	—	—	—	—	—

*Saturated record peaks.

Table IV-2.23. Scaled free-field ground motion—volcanic breccia and lava.

Record Number	Scaled Slant Range m/kt ^{1/3}	Scaled Peak ft/kt ^{1/3}	Scaled Acceleration Peak		Particle Velocity Peak		Scaled Displacement Risetime		Scaled Displacement Risetime	
			g/kt ^{1/3}	sec/kt ^{1/3}	ft/sec	m/sec	sec/kt ^{1/3}	in/kt ^{1/3}	cm/kt ^{1/3}	sec/kt ^{1/3}
LONGSHOT: 81 kt, 701 m (2300 ft) deep in Amchitka—VOLCANIC BRECCIA—Boring, WES (Reference IV-2.4).										
Vertical Array										
6A	84.5	277	215	0.0025	7.99*	26.2*	0.0051	—	—	—
6V	—	—	—	—	8.81	28.9	0.0046	—	—	—
5A	98.6	324	225	0.0028	8.02	26.3	0.0051	—	—	—
5V	—	—	—	—	7.04*	23.1*	—	—	—	—
4A-V	113	370	132*	0.0049	7.71*	25.3*	0.0055	—	—	—
3A	127	416	103	0.0032	4.05	13.3	0.0058	—	—	—
3V	—	—	—	—	4.85	15.9	0.0051	—	—	—
9V	134	436	—	—	3.63	11.9	0.0063	—	—	—
2A	155	508	106	0.0042	6.68	21.9	0.0125	—	—	—
2V	—	—	—	—	3.99	13.1	0.0116	—	—	—
8V	161	527	—	—	3.96	13.0	0.0136	26.2	10.3	0.141
1AV-S	162	532	114	0.0042	5.76	18.9	0.0079	39.6	15.6	0.145
1V-S	—	—	—	—	5.64	18.5	0.0067	51.8	20.4	0.174
MILROW: ~1 Mt, 1220 m (4000 ft) deep in Amchitka—PILLOW LAVA—Boring, Sandia (Reference IV-2.15).										
Vertical Array										
II-20AV-TV	61.5	202	673	0.0023	11.2	36.9	0.0035	—	—	—
II-25AV-TV	76.7	252	335	0.0011	8.35	27.4	0.0037	35.3	13.9	0.1393
II-25AV-UV	—	—	361	0.0012	10.1	35.2	0.0063	—	—	+25.9
II-30AV-10	91.9	302	273	0.0014	9.57	31.4	0.0052	46.5	18.3	0.0081
II-30AV-UV	—	—	272	0.0014	5.09	16.7	0.0017	25.9	10.2	0.1366
II-35AV-UV	107	351	245	0.0024	—	—	—	—	—	+16.8
II-37AV-hi	113	371	181	0.0016	6.71	22.0	0.0016	36.8	14.5	0.1051
II-37AV-hi	—	—	196	0.0018	9.69	31.8	0.0092	—	—	+14.0
12-37AV-UV	119	391	207	0.0037	—	8.87	0.0128	49.3	19.4	0.1027
12-39AV	—	—	—	—	—	—	—	—	—	+17.3
12-39UV	—	—	—	—	—	—	—	—	—	+6.80
SO-AV hi	122	400	355	0.0037	—	—	—	—	—	—
SO-AV-UV	—	—	303	0.0035	8.41	27.7	0.0140	43.2	17.0	0.1051
										+11.9

*Indeterminant peak.

Table IV-2.24. Scaled free-field ground motion—lava.

Record Number	Scaled Slant Range m/kt ^{1/3}	Scaled Acceleration Peak g·kt ^{1/3}	Scaled Velocity Peak ft/sec	Particle Velocity		Scaled Displacement Risetime sec/kt ^{1/3}	Residual displacement in/kt ^{1/3}
				Rise time sec/kt ^{1/3}	Peak ft/sec		
CANNIKIN: ~5 kt, 1750 m (5875 ft) deep in Amchitka—PILOW LAVA—Boring, Sandia (Reference IV-2.14).							
Vertical Array							
I25-AVhi	44.1	145	1830	0.0021	21.0	69	0.0026
I25-AVLo			1710	0.0020	18.9	62	0.0027
I25-UV			—	—	19.2	63.0	>11.9
I30-AV	53.0	174	940	0.0025	18.3	60	0.0027
I40-AVhi	68.5	225	513	0.0020	14.8	48.6	0.0044
I40-AVLo			513	0.0020	15.4	50.4	0.0046
I40-UV			—	—	14.6	48.0	0.0044
I45-AV	77.4	254	248	0.0014	6.04	19.8	0.0040
I45-UV			—	—	6.10	20.0	0.0038
I50-AVhi	86.4	283	210	0.0011	6.16	20.2	0.0049
I50-AVLo			222	0.0012	6.61	21.7	0.0049
I50-UV			—	—	5.88	19.3	0.0047
I55-AV	95.3	313	202	0.0012	6.46	21.2	0.0058
I55-UV			—	—	6.71	22.0	>12.2
I57-AVhi	99.5	326	258	0.0007	8.69	28.5	0.0094
I57-AVLo			243	0.0008	8.60	28.2	0.0095
I57-UV			—	—	7.83	25.7	0.0094
I58-AVhi	101	332	313	0.0036	11.9	39.0	0.0065
I58-AVLo			305	0.0034	13.0	42.7	0.0063
I58-UV			—	—	11.0	36.2	0.0063
I59-AV	103	338	336	0.0032	10.9	35.7	0.0057
I59-UV			—	—	10.3	33.8	0.0057
SG-AV-UV	105	343	608	0.0011	12.6	41.2	0.0054

that the uppermost stations for CANNIKIN were somewhat deeper as a consequence of a change in shot depth. For both events, the uppermost 2 or 3 stations produced records seriously perturbed by the surface reflection and were omitted from the analysis.

Data in Table IV-2.25 represent two events in very different hard rock environments. The GASBUGGY (Reference IV-2.9) stations were in a single boring offset about 460 m from the shot hole. These stations were at nominal depths of 3200 ft (975 m), 3600 ft (1097 m), 4100 ft (1250 m), and 4600 ft (1402 m) in the several rocks noted in the foot note. The two free-field stations associated with the BOXCAR Event in Pahute Mesa at NTS were in deep borings approximately at shot level and offset laterally, about 8000 ft (2438 m) and 24,000 ft (7315 m), from the BOXCAR shot hole.

Finally, the data in Tables IV-2.26 and IV-2.27 were obtained from the two nuclear detonations in salt: GNOME in a tunnel complex in horizontally bedded salt and SALMON in a salt dome.

IV-2.4 SURFACE-ZERO MOTION

In this section we discuss the differences in peak vertical acceleration and particle velocities for detonations in NTS alluvium, granite and tuff, and in salt, obtained at the surface directly above the shot point.

IV-2.4.1 Peak Vertical Acceleration and Particle Velocity for Detonations in NTS Alluvium*

Surface-zero motions from detonations in alluvium differ in some detailed aspects from those associated with more competent materials as shown for example in Figures IV-2.8a and IV-2.8b. The most important differences are a slower rate of decay in alluvium from peak acceleration to minus 1 g. Another important difference is the appearance of a second peak of acceleration, although of lesser magnitude, that has a longer duration than the first pulse and hence contributes substantially to the maximum particle velocity. This second acceleration pulse is probably a reflection from the bottom of the surface spall or from a second spall. The example chosen for Figure IV-2.8b (CHINCHILLA) displays this characteristic most predominantly whereas for some detonations, for example, PLATYPUS, SHREW, and ERMINE, this secondary acceleration pulse is not evident in the data.

*Maximum vertical displacement is discussed in Section IV-2.5.3.

Table IV-2.25. Scaled free-field ground motion—shale and rhyolite.

Record Number	Scaled Slant Range m/kt ^{1/3}	Scaled Peak Acceleration g·kt ^{1/3}	Scaled RiseTime sec/kt ^{1/3}	Particle Velocity Peak ft/sec	RiseTime sec/kt ^{1/3}	Peak cm/kt ^{1/3}	Scaled Displacement Risetime sec/kt ^{1/3}	Residual cm/kt ^{1/3}
GASBUGGY: 29 kt, 1290 m (4240 ft) deep in San Juan Basin—LEWIS SHALE—Boring, Sandia (Reference IV-2.9).								
Offset Vertical Array								
U1-UR ₁	152	499	83.0	0.0029	2.42	7.94	0.0052	2.23
U46-UR ₂	156	510	63.6	0.0036	1.96	6.43	0.0052	1.70
U36-UR ₃	166	544	45.5	0.0039	1.59	5.21	0.0062	1.36
U32-UR ₄	181	594	40.9	0.0029	1.33	4.36	0.0049	1.23
SI-AV	422	1383	19.2	0.0133	1.67	5.48	0.0218	5.57
BOXCAR: 1.2 Mt, 1165 m (3822 ft) deep in Area 20 NTS—RHYOLITE—Boring, Sandia unreported.								
Shot Level Array								
UB-AR	231	756	21.3	0.0141	1.77	5.8	0.0191	—
JB-UR			—	1.80	5.9	0.0188	2.37	0.93
UB-AR	685	2247	1.28	0.0028	0.107	0.35	—	—
UB-UR			—	0.101	0.33	0.0094	0.139	0.0254
SO-Avh ₁	109	358	78.6	0.0015	6.10	20.0	0.0245	—
SO-Avh ₂			81.8	0.0019	6.89	22.6	0.0245	—
SO-UV		—	—	6.40	21.0	0.0245	30.8	12.1
							0.0922	—
							+6.69	+2.63

Superscripts indicate rock at gauge station as follows: 1 Pictured Cliffs sandstone, 2. Lewis Shale, 3. Ojo Alamo sandstone, 4. Nacimiento shale and sandstone.

Table IV-2.26. Scaled free-field ground motion—bedded salt.

Record Number	m/kt ^{1/3}	Scaled Slant Range ft/kt ^{1/3}	Peak g'ft/kt ^{1/3}	Scaled Acceleration Rise-time sec/kt ^{1/3}	Particle Velocity Peak m/sec ft/sec	Rise-time sec/kt ^{1/3}	Peak cm/kt ^{1/3} in/kt ^{1/3}	Scaled Displacement Residual cm/kt ^{1/3} in/kt ^{1/3}
GNOME: 3.1 kt, 366 m (1200 ft) deep in BEDDED SALT—Tunnel, Sandia (Reference IV-2.24).								
Vertical Array								
18A	80.2	263	554	-	18.0	59.1	-	-
23A	154	504	117	0.012	6.7	22.0	0.013	-
24A	184	605	64.2	0.011	3.5	11.5	0.020	25.7
25A	206	675	36.5	0.016	3.2	10.5	0.033	0.350
26A	226	743	40.8	0.013	4.1	14.4	0.039	27.0
27A	237	779	26.2	0.023	4.8	15.7	0.043	0.357
20A-S	247	810	36.5	0.030	5.6	18.4	0.047	0.438
								0.419
								0.366
Shot Level								
1A	42.5	140	15,602	0.0013	70.1	230	-	-
2A-hi	52.1	171	5,687	0.0019	31.1	102	0.0034	-
2A-10			3,645	-	26.0	85.3	-	-
3A	68.6	225	1,137	0.0021	13.0	42.7	0.0040	-
4A-hi	83.7	275	496	0.0043	38.1	125	0.0049	-
4A-10			452	-	10.5	34.4	0.0069	-
4U-hi			-	-	10.3	33.8	-	-
4U-10			-	-	9.3	30.5	-	-
5A	119	389	175	0.0071	9.5	31.2	-	-
5U			-	-	4.8	15.7	0.0082	-
6A-hi	157	515	87.5	0.0102	9.0	29.5	-	-
6A-10			65.6	-	4.7	15.4	-	7.54
6U			-	-	4.2	13.8	-	2.97
7A	204	671	37.9	0.0117	4.4	14.4	0.0138	8.37
7U			-	-	2.8	9.19	-	4.46
21A	327	1073	12.7	0.0191	3.0	9.84	0.0165	3.29
					4.49	14.7	0.0233	1.75
								0.0494
SRI (Reference IV-2.20)								-
2 AR	552	1811	2.64	0.0089	0.528	1.73	0.0288	1.28
3 AR	1103	3620	1.37	0.0130	0.198	0.650	0.0336	0.505
4 AR	2208	7243	0.280	0.0377	0.043	0.140	0.0453	0.0524
5 AR	6481	21263	0.0223	0.0617	0.0042	0.0138	0.0720	0.049
								0.0665

Table IV-2.27. Scaled free-field ground motion—dome salt.

Record Number	Scaled Slant Range ft./kt ^{1/3}	Scaled Acceleration Peak g·kt ^{1/3}	Particle Velocity Peak ft./sec	Risetime sec/kt ^{1/3}	Scaled Displacement Risetime sec/kt ^{1/3}	Residual cm/kt ^{1/3}
	m/kt ^{1/3}	g·kt ^{1/3}	m/sec	sec/kt ^{1/3}	cm/kt ^{1/3}	in/kt ^{1/3}
SALMON: 5.3 kt, 828 m (2717 ft) deep in Tatum SALT DOME—Boring, Sandia (Reference IV-2.62).						
Offset Vertical Array						
14C-27ARH	95.1	31.2	0.0041	14.0	46.1	0.0047
14C-22AR	129	42.4	0.0058	7.52	24.7	12.5
14C-22UR				8.17	26.8	7.32
14C-32AR	129	42.4	0.0057	7.70	25.3	8.55
14C-32UR				5.19	18.0	0.0071
14-20AR	158	51.9	0.0070	3.90	12.8	0.0083
6-27ARH	183	59.9	0.0079	5.18	18.0	0.0094
6-27URH				5.18	18.0	0.0087
14C-36UR	184	60.4	0.0082	3.85	12.6	0.0099
6-20UR	223	73.0	0.0101	3.05	10.0	0.0115
14C-39AR	230	75.6	0.0101	2.68	8.79	0.0118
14C-39UR				2.67	8.76	0.0110
11-27URH	357	117.0	0.0116	1.16	3.82	0.0166
11-20UR	375	122.9	0.0117	1.15	3.77	0.0178
11-34UR	378	124.1	0.0117	0.990	3.25	0.0192
5-27URH	427	140.0	0.0117	0.652	2.14	0.0186
SRI (Reference IV-2.5).						
Shot Level Array						
2V RL	192	629	—	2.6	8.5	0.0109
26V RL	198	650	—	3.9	12.8	0.0109
13V RL	258	846	—	2.6	8.5	0.0152
14V RL	282	924	—	0.8	2.62	0.0161
Vertical Array						
15AV-6	71.2	24.3	0.0017	15.0	49.2	0.0029
15V-4	91.5	300	—	22.0	72.2	0.0046
15V-3	14.3	468	—	8.20	26.9	0.0057
15V-1	231	757	—	1.35	4.43	0.0115
16UV-6	388	1274	—	1.04	3.42	0.0115
16AV-5	405	1330	41.8	0.0092	1.05	0.0144
16AV-4	423	1387	41.5	0.0086	1.12	0.0115
16W-4			—	1.04	3.41	0.0115
16AV-3	436	1430	27.9	0.0109	1.20	0.0115
16AV-2	449	1473	17.8	0.0103	1.07	0.0161
16W-2			—	1.29	4.23	0.0178
16AV-1	458	1502	26.9	0.0120	1.22	0.0149
16AV-VI-S	475	1559	48.8	0.0195	3.60	11.8

Data are available on near surface-zero motions (generally within 50 ft of surface zero) on 17 detonations in NTS alluvium. These include four shots for which subsurface radial motion data are available. For near normal incidence of a compression wave with a free surface one would expect the free-field acceleration and velocity to be doubled at the surface. In Figure IV-2.28 a comparison is made between this theoretical deduction and near surface zero vertical acceleration data. It can be seen in Figure IV-2.28 that a considerable number of the measured accelerations are substantially larger than given by doubling the composite radial acceleration curve.

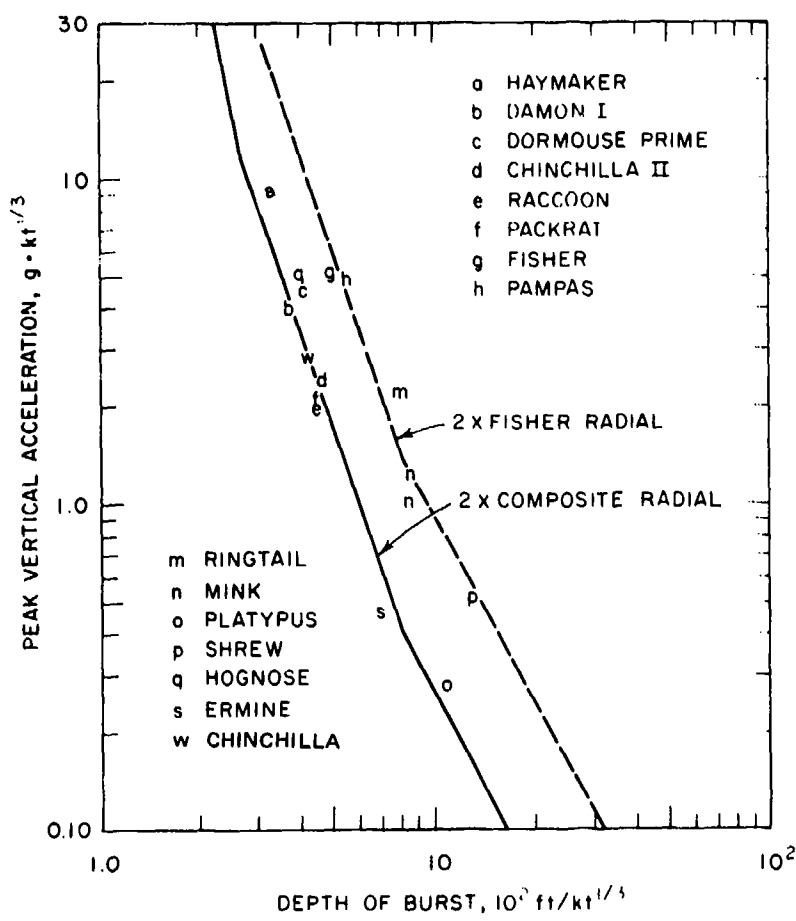


Figure IV-2.23. Magnitude of first pulse of vertical acceleration at surface zero, scaled to 1 kt, for detonations in NTS alluvium.

It should be pointed out that, although the lone FISHER acceleration datum of Figure IV-2.12 has some uncertainty in magnitude, its mean value is some three and one-half times the magnitude indicated by the composite curve. Assuming that the FISHER datum is representative of the extent of variations in material properties within what is generically termed NTS alluvium and in accord with the hypothesis which leads to the establishment of the composite acceleration curve; a second curve has been drawn parallel to the composite curve of Figure IV-2.28 at an amplitude seven times that of the free field, that is, twice the hypothesized free-field radial acceleration curve through the FISHER datum. The data of Figure IV-2.28 fall between the two constructed curves with the FISHER surface zero datum (point g) falling close to the doubled FISHER curve and the HOGNOSE datum (point q) falling close to the doubled composite (HAYMAKER/HOGNOSE) radial curve. More precisely, one group of data (the A group) appears to scatter around the HAYMAKER/HOGNOSE curve and the second group of data (the B group) appears to scatter around the FISHER curve. Thus, it would seem that only two sets of material properties are involved corresponding to a grouping of test areas. It appears then that the scatter in data observed in Figure IV-2.28 is the result of variations in material properties rather than a failure of the scaling rules.

Figure IV-2.29 displays peak vertical velocities corresponding to the first peak acceleration pulse shown in Figure IV-2.28. It is worth noting that the extreme variation in the yield represented by the data of Figures IV-2.28 and IV-2.29 is nearly 20:1 in the 1/3 power of the yield. This is the largest difference in yield for any set of data available on nuclear ground motion in a single medium. Also shown are the doubled HAYMAKER/HOGNOSE and FISHER correlations of Figure IV-2.13. The reason for constructing the FISHER velocity curve of Figure IV-2.13 through the $233 \text{ m}/\text{kt}^{1/3}$ datum is now apparent since it corresponds to the only FISHER acceleration data. As noted for the acceleration data, the doubled HAYMAKER/HOGNOSE and FISHER radial correlations are lower and upper bounds, respectively, for surface-zero peak vertical velocities. Without a comparison with the free-field data one would have been tempted to draw a curve through the surface-zero velocities at a reduced slope (approximately the inverse first power of depth) resulting in a variable reflection coefficient at the surface. There is the converse argument that the rate of attenuation of radial velocity in the free-field should be based on the apparently lesser rate of attenuation with depth of the surface-zero velocities. A combination plot of surface and free-field data could be

obtained by dividing surface motion data by two. However, this is tricky as will be shown in the following section.

As previously noted, surface zero velocities generally consist of two peaks: data pertaining to the first peak as shown in Figure IV-2.29, and data for the second or maximum peak as shown in Figure IV-2.30. For the 17 detonations in alluvium only three deviate markedly from the doubled FISHER radial velocity curve. The data of Figure IV-2.30 are presented not only because of their usefulness in range settings for field experiments, but also to demonstrate how an inconsistent comparison (surface-zero second peaks of velocity compared to free-field first peaks of velocity) leads to greater apparent consistency than a rigorously consistent comparison such as that made in Figure IV-2.29. The maxima of Figure IV-2.30 depend significantly on spall mechanics and hence may vary by a factor greater than that shown.

IV-2.4.2 Peak Vertical Velocities for Detonations in NTS Granite and Tuff, and in Salt

The only other "homogeneous" media for which surface motions are available is that HARDHAT Event in granite. The data consist of accelerogram. The peak vertical acceleration is almost exactly double that given by the composite curve for granite. The peak velocity (Figure IV-2.31) is within 15 percent of the doubled granite radial velocity correlation. The surface-zero motion for PILE DRIVER is substantially less than that of HARDHAT. Taking these data at face value would indicate a reflection coefficient very close to 1.0 for PILE DRIVER.

Surface-zero motions for detonations in NTS tuff (Figure IV-2.31) are strongly influenced by the rhyolite cap rock and the intermediate transition layers. The data are fairly sparse compared to that in alluvium and consist of three measurements (RAINIER and ANTLER mesa surface-zero and RAINIER slope surface-zero) and two photometric measurements of displacement (BLANCA and NEPTUNE). The photometric measurements (Reference IV-2.58) are the result of superposition of data from several cameras and the solid data points of Figure IV-2.31 represent the derivative of the average displacement curve. The upper limit of the plotted data is indicative of the maximum velocity obtained by point-to-point differentiation. The lateral extent of the data points represents the uncertainty in yield. The three mesa surface-zero velocity data are consistent with an apparent reflection factor of 5 (4.5 for RAINIER and 6 for ANTLER) based on the tuff composite radial velocity curve extrapolated to the surface. The slope

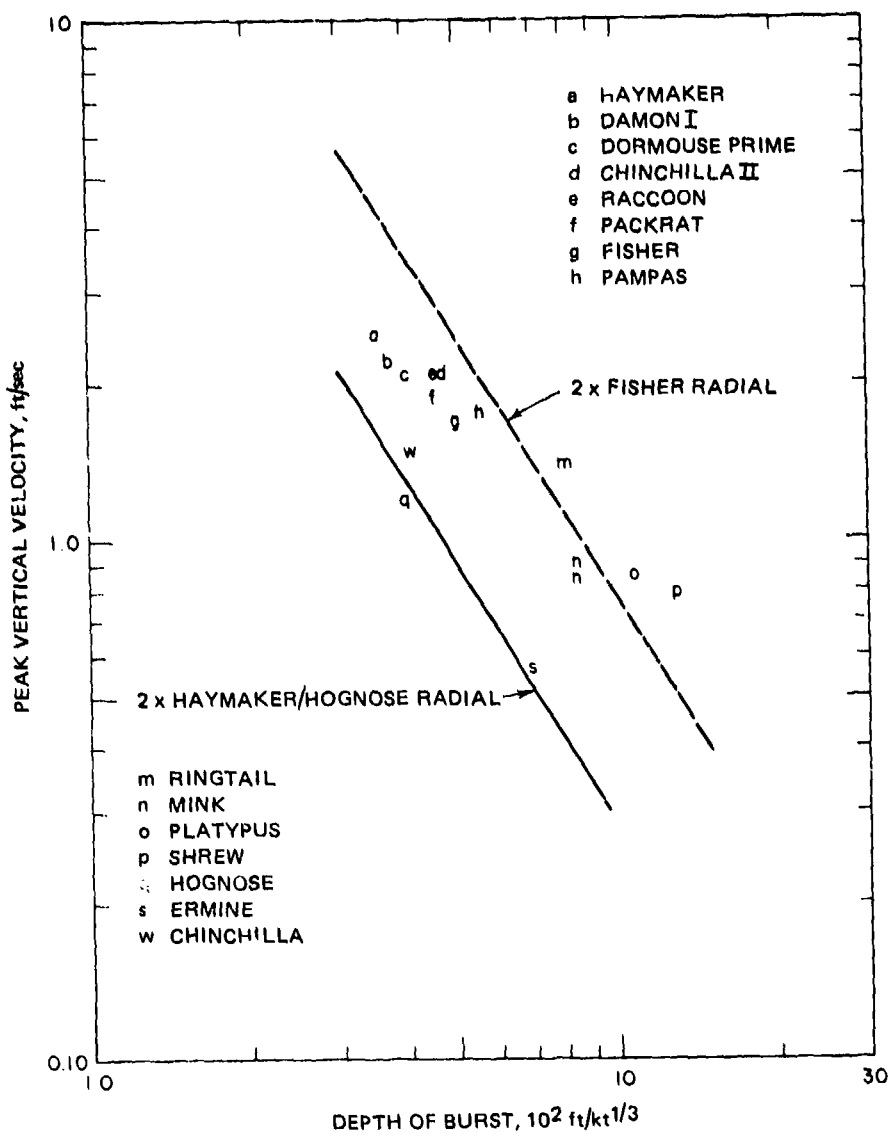


Figure IV-2.29. Magnitude of first pulse of vertical velocity at surface zero, scaled to 1 kt, for detonations in NTS alluvium.

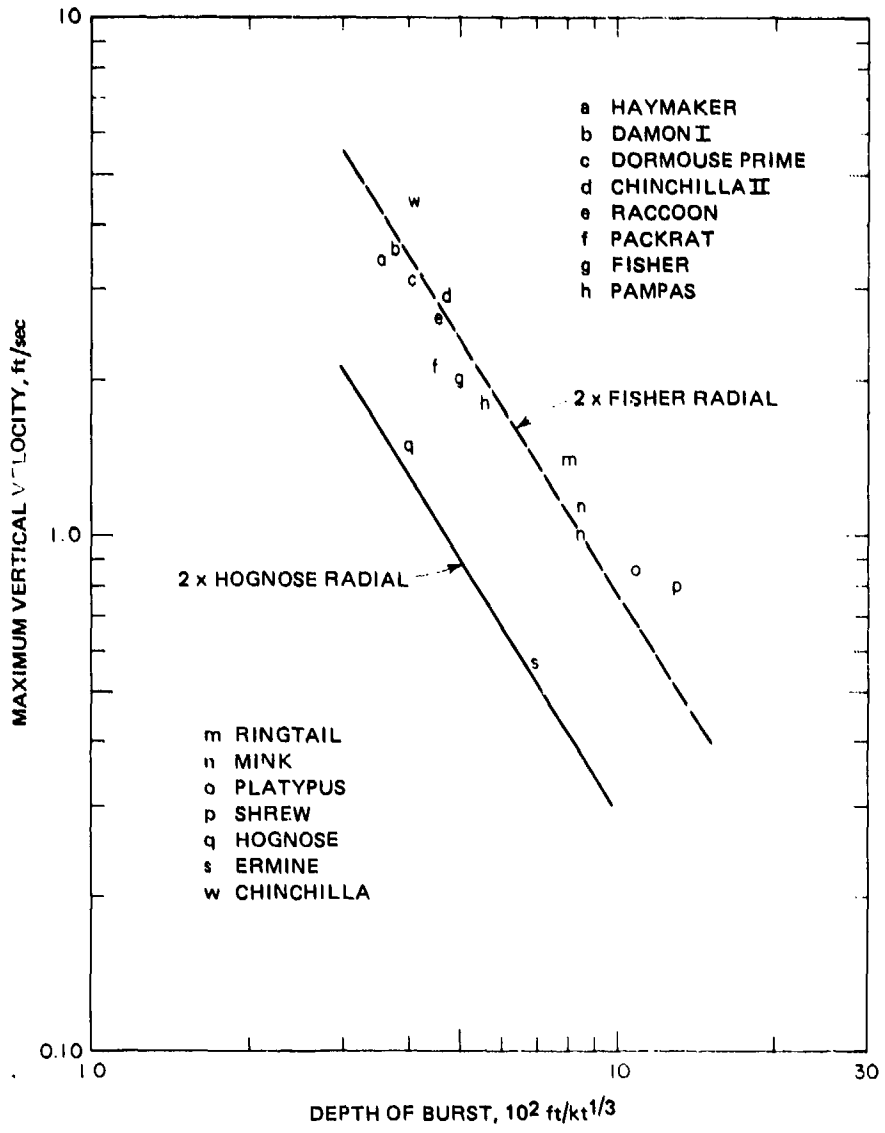


Figure IV-2.30. Magnitude of maximum vertical velocity at surface zero, scaled to 1 kt, for detonations in NTS alluvium.

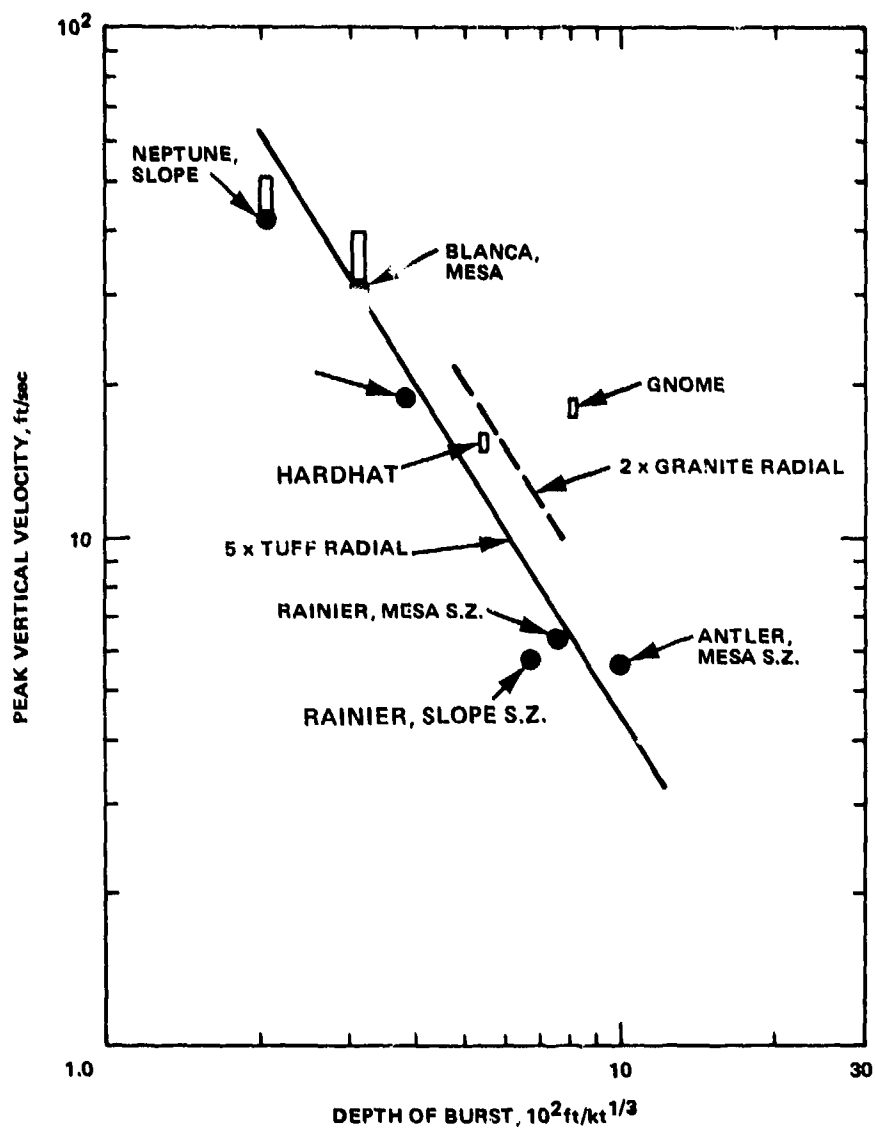


Figure IV-2.31. Magnitude of first pulse of vertical velocity at surface zero, scaled to 1 kt, for detonations in NTS tuff and granite, and in salt (GNOME).

surface-zero velocity data indicate an apparent reflection factor slightly larger than 3.* As will be seen later in Section IV-2.5.1, an apparent reflection factor of 5 applied to the peak radial acceleration is also approximately correct for the surface-zero vertical accelerations on RAINIER and ANTLER. The reflection factors quoted are fictitious values based on what would have occurred in tuff at the slant range equal to the depth of burst. They are increased over the theoretical value of two by the decreasing seismic velocity above the shot points. Their only usefulness is to indicate the degree of consistency to be found between a comparison of peak radial velocity and the corresponding motion at surface-zero.

The surface motions on GNOME are influenced by the lithologic discontinuities overlaying the salt. The GNOME datum point is plotted as a matter of interest. It should be noted that the apparent reflection factor of 3 is taken with respect to the composite correlation for radial velocity in salt.

IV-2.5 SURFACE MOTION AS A FUNCTION OF SLANT RANGE FROM SHOT POINT

In this section we present a brief discussion of the peak vertical acceleration, velocity and displacement as a function of the slant range to the shot point. Some simple rules for predicting vertical motion are presented. Some recent events of the ROUND ROBIN Program, Events LATIR and TYBO (References IV-2.85 and IV-2.86) will not be presented here as the yields are classified and therefore the surface motion data cannot easily be compared to the data discussed in this section.

IV-2.5.1 Peak Vertical Acceleration

Measurements of surface motion above detonations in NTS tuff, which include surface-zero motion, are limited to the RAINIER and ANTLER Events. Peak vertical acceleration data for these two detonations are shown in Figure IV-2.32. Also plotted for comparison is the scaled free-field acceleration data for tuff multiplied by 2 obtained from the curves of Figure IV-2.15 or IV-2.25. The scaled acceleration data used for this comparison is for the scaled range of 100 to 500 $\text{m}/\text{kt}^{1/3}$ or

$$a \cdot W_2^{1/3} = 7.71 \times 10^4 (R/W^{1/3})^{-1.92 \pm 0.14} \quad (\text{IV-2.27})$$

*For the slopes, the "vertical velocity" was taken as that in the direction normal to the slope.

which when multiplied by 2 gives

$$a \cdot W_2^{1/3} = 1.54 \times 10^5 \left(\frac{R}{W} \right)^{1.92 \pm 0.14} \quad (\text{IV-2.45})$$

The apparent reflection factor of 2 was based on an analysis of surface-zero vertical particle velocity data. An eye-ball fit through the RAINIER data with an apparent reflection factor of 1.7 would seem to fit the data better. For the ANTLER data, not only a higher apparent reflection factor is required but also a change in slope. These large differences in the apparent reflection factors may be caused by the layering of the media near the shot point, and between the shot point and the surface.

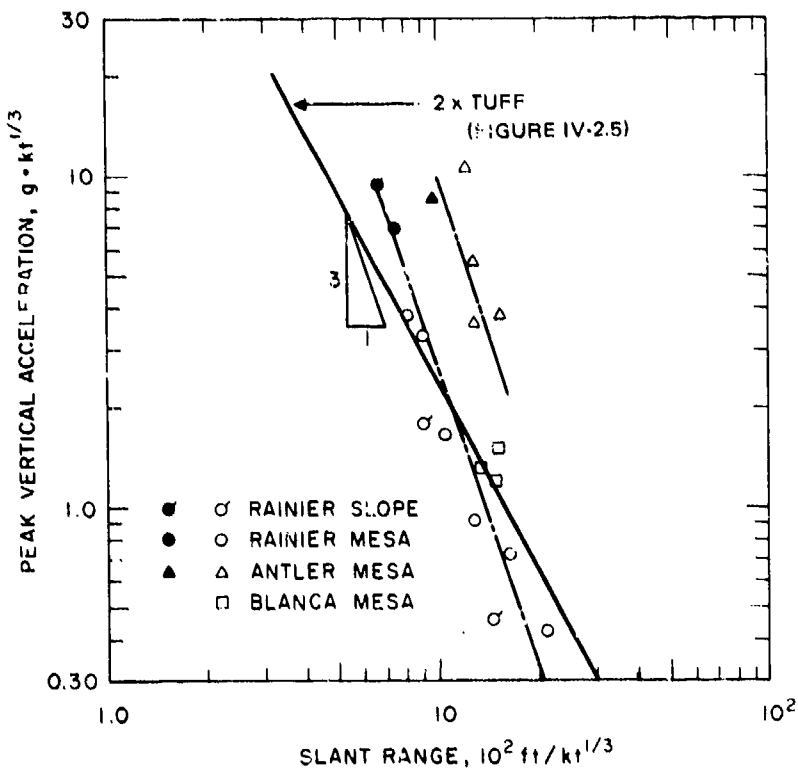


Figure IV-2.32. Magnitude of first vertical acceleration pulse, scaled to 1 kt, as a function of position along the surface for detonations in NTS tuff. Closed symbols are surface-zero data.

It is to be expected that the vertical surface motion would attenuate more rapidly with slant range than would the free-field motion since the former is diminished both by the attenuation of the free-field and the geometry of the wave-front intersecting the free surface.

This does in fact appear to be the case, with the vertical accelerations attenuating at approximately the inverse cube of the slant range whereas the free-field accelerations attenuate approximately as the inverse square of the slant range (see Equation IV-2.45). The few first peak data from BLANCA appear to be consistent with this conclusion.*

It is to be expected that the vertical surface motion would attenuate more rapidly with slant range than would the free-field motion since the former is diminished both by the attenuation of the free-field and the geometry of the wave-front intersecting the free surface.

The inverse cube attenuation with slant range of vertical acceleration is also consistent with the surface motion above detonations in granite and salt, Figure IV-2.33, and for detonations in alluvium, Figures IV-2.34a and IV-2.34b. For alluvium we have the situation of a larger number of detonations but fewer data points per detonation (a maximum of four). To examine these data in more detail, they have been separated into two groups. The data of Figure IV-2.34a correspond to the "A group" of Figure IV-2.28 and the data of Figure IV-2.34b correspond to the "B group" of Figure IV-2.28. On the average, the magnitude of the peak vertical acceleration of Figure IV-2.34b are 3 times the magnitude of those of Figure IV-2.34a, which is consistent with the separation noted in the surface-zero data. As previously discussed, this scatter in data is believed to be due to the variation in properties of the alluvium rather than to any breakdown of the scaling rules. Data of Figure IV-2.34a (with the exception of HAYMAKER-46 kt at 408 m depth) are in very good agreement with the inverse cube attenuation rule proposed for surface vertical accelerations. Moreover, the scatter of data is exceptionally small considering the nearly 20:1 variation in 1/3 power of the detonation yields. The data of Figure IV-2.34b show a somewhat poorer correlation even though the variation in the 1/3 power of yield is only 13:1. The set of data which deviates from the inverse cube prescription (HAYMAKER) corresponds to a yield in the nominal range.

*The maximum accelerations quoted in the listing of Reference IV-2.68 are second peaks and are three to four times larger than the first peak.

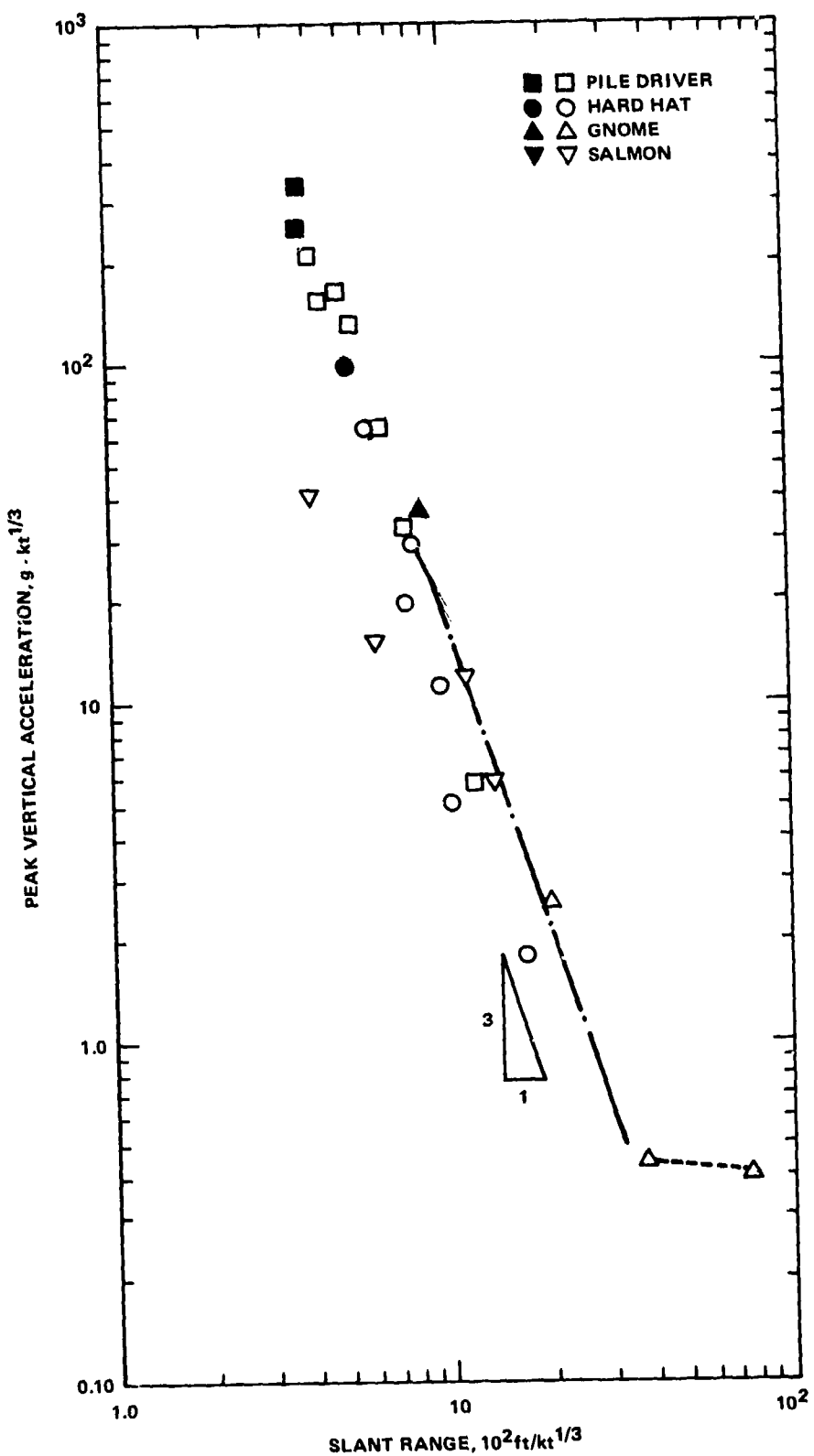


Figure IV-2.33. Magnitude of first vertical acceleration pulse, scaled to 1 kt, as a function of distance along the surface for detonations in NTS granite and in salt. Closed symbols are surface-zero data.

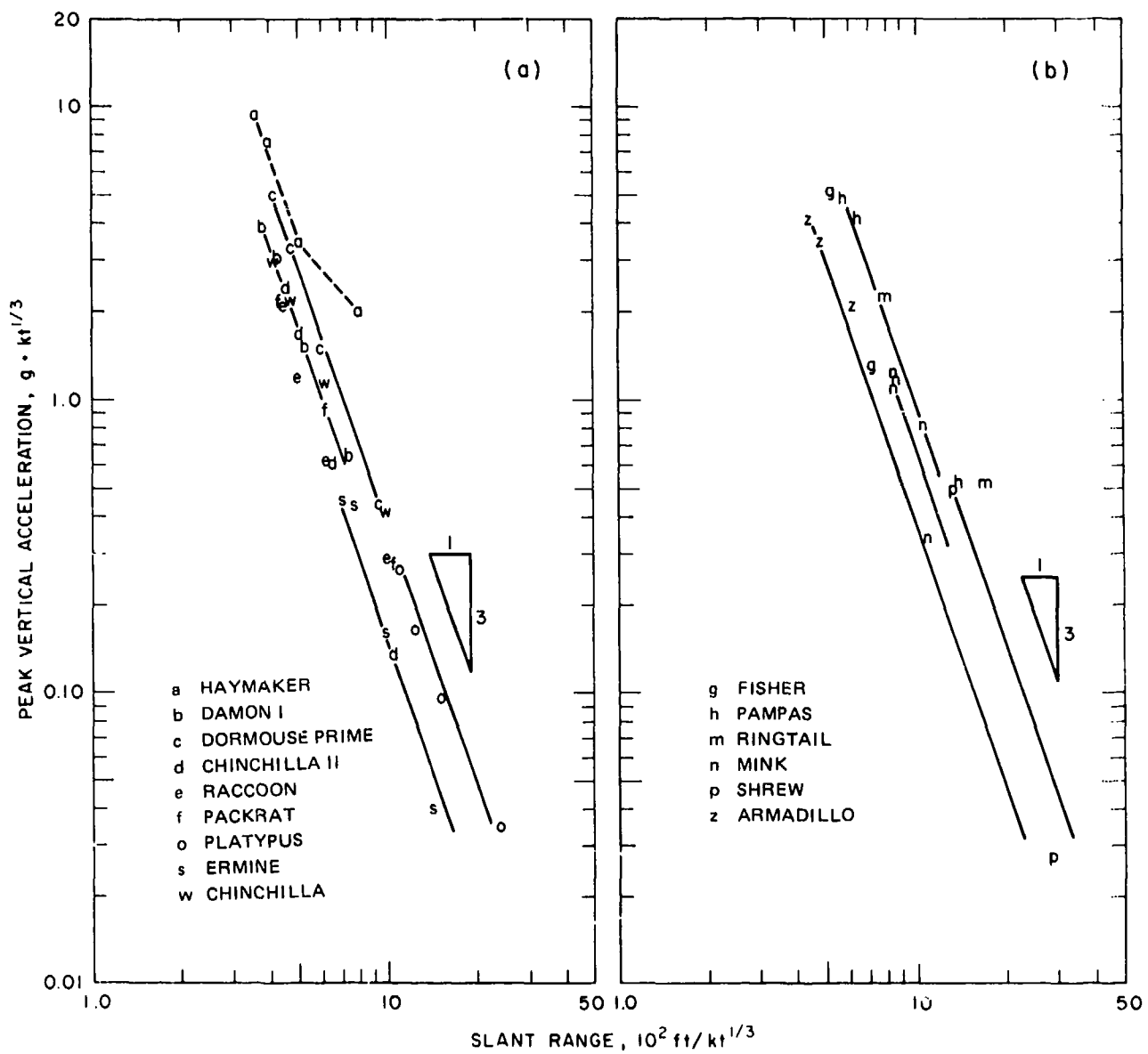


Figure IV-2.34. Magnitude of first vertical acceleration pulse, scaled to 1 kt, as a function of distance along the surface for detonations in NTS alluvium. (a) "A group" of Figure IV-2.28; (b) "B group" of Figure IV-2.28.

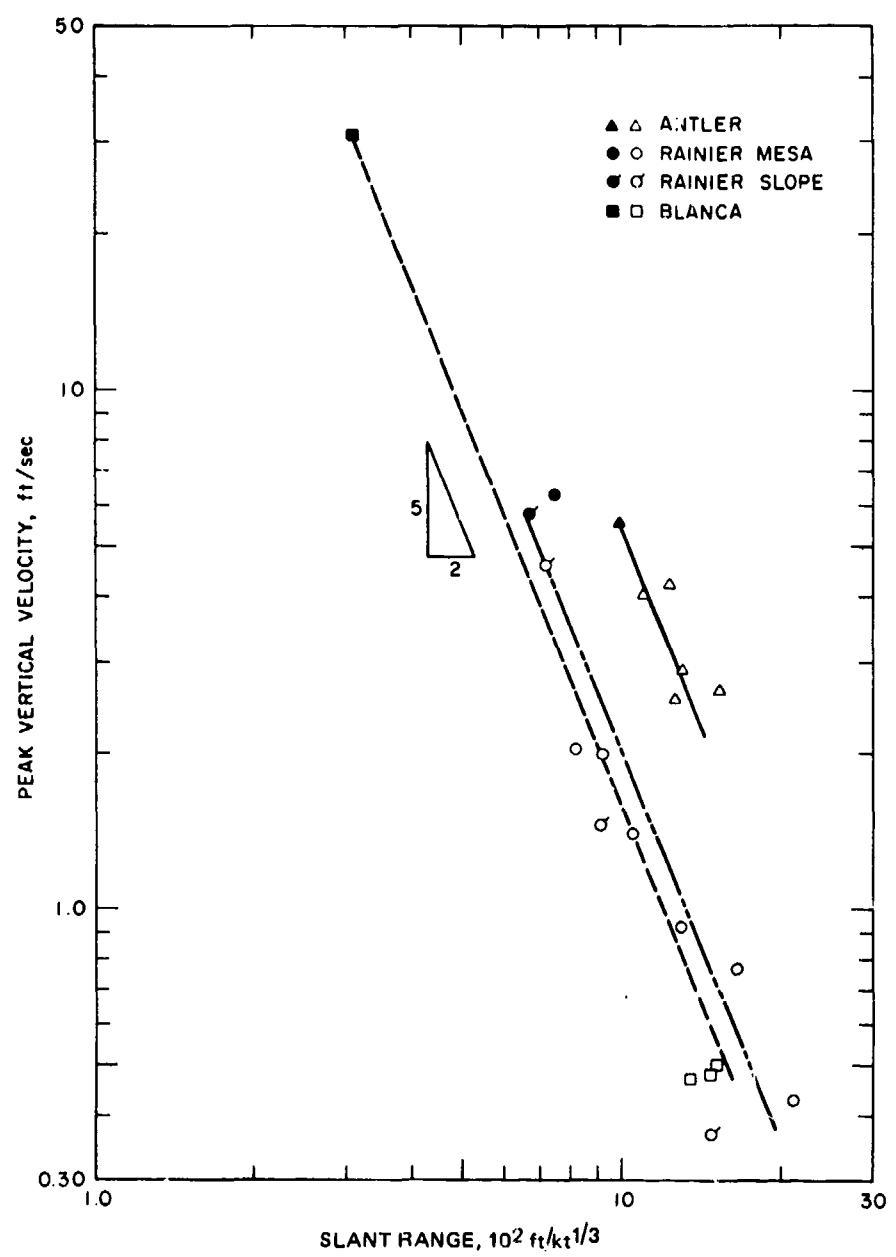


Figure IV-2.35. Magnitude of first vertical velocity pulse, scaled to 1 kt, as a function of distance along the surface for detonations in NTS tuff. Closed symbols are surface-zero data.

Hence, the absolute distances, corresponding to the scaled slant range shown, are much greater than for the remainder of the detonations. It is believed that the departure of the HAYMAKER data from inverse cube attenuation is due to reflections resulting from nonhomogeneity of the media. Note the influence of refraction at the farthest stations on GNOME shown in Figure IV-2.33 as a dashed line connecting two datum points.

Peak vertical acceleration of both HARDHAT and PILE DRIVER are almost coincident (Figure IV-2.33). The attenuation rate of the surface vertical motion from SALMON appears to be at variance with all the other data for scaled ranges less than about $700 \text{ ft}/\text{kt}^{1/3}$. At greater scaled ranges, data from salt and granite are nearly identical. The extreme layering above the Tatum Salt Dome undoubtedly has a profound influence on the surface motion.

IV-2.5.2 Peak Vertical Velocity

Peak vertical velocities for detonations in NTS tuff are shown in Figure IV-2.35. These peaks correspond to integration of the first acceleration pulse, the peaks of which are shown in Figure IV-2.32. Corresponding data for the HARDHAT Event in granite and for GNOME are shown in Figure IV-2.36 and for NTS alluvium in Figure IV-2.37. In all three figures the vertical velocity attenuates as the inverse 2.5 power of surface range which is consistent with the data. The degree of conformity with this attenuation rule varies, however, with the experiment. for HARDHAT, PILE DRIVER, and GNOME*, agreement is quite good over the entire range covered by the experiments. Again, the data from SALMON appear to have been altered by the layering above the relatively flat (but limited in lateral range) dome cap. The granite and SALMON data are very nearly the same for ranges greater than $700 \text{ ft}/\text{kt}^{1/3}$. Data from ANTLER (which do not cover a sufficient range to weigh heavily in the selection of an attenuation rate) and data from RAINIER (which contain considerable scatter) do not invalidate the inverse 2.5 power of surface range attenuation rule for detonations in tuff. Data from BLANCA are in agreement with this attenuation rule, but the surface zero vertical velocity is subject to some uncertainty (see Figure IV-2.31).

The greatest mass of evidence in favor of the inverse 2.5 power attenuation rule comes from data for detonations in NTS alluvium (Figure IV-2.37). Several detonations, DORMOUSE PRIME, ERMINE, CHINCHILLA II and PLATYPUS give extremely

*Except for data at the largest distance where, as previously noted, energy appears to have arrived by a refracted path.

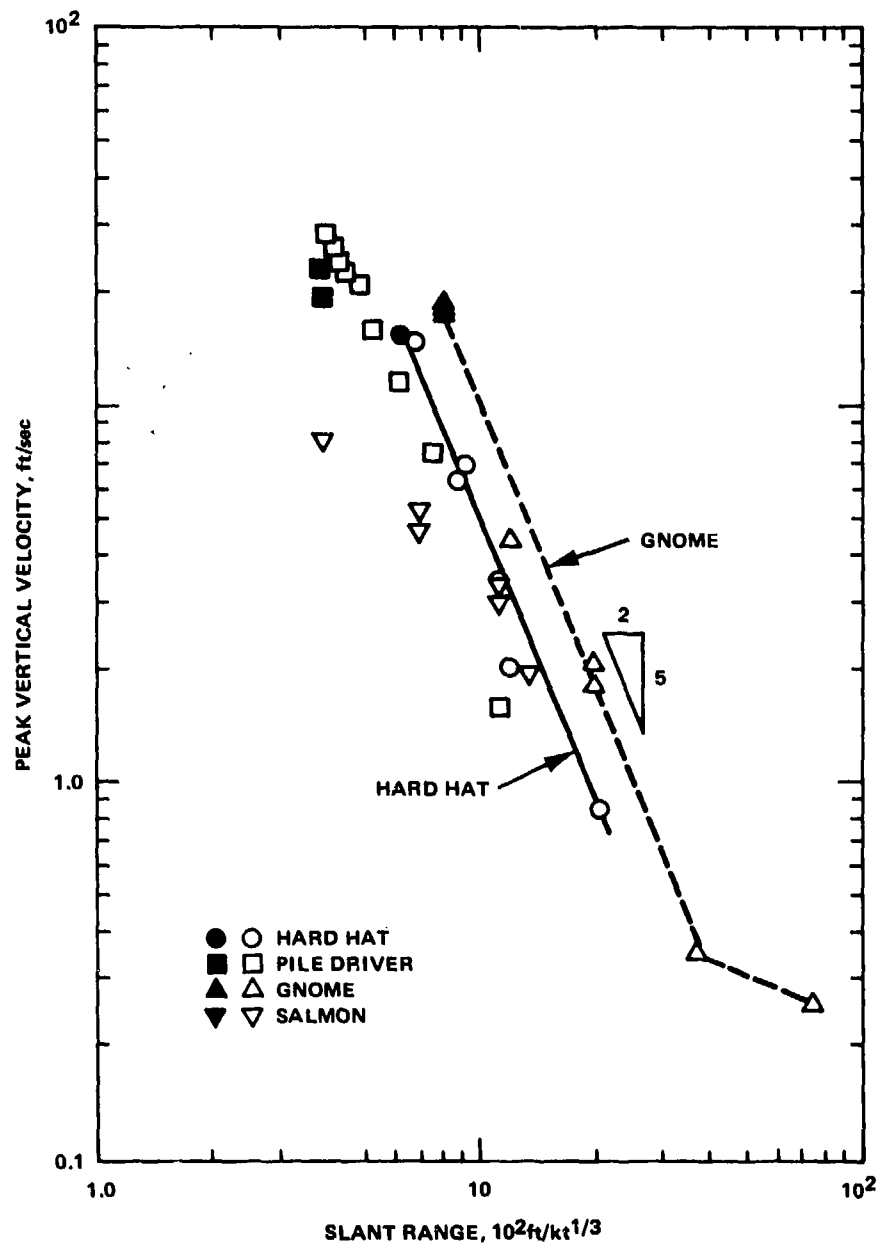


Figure IV-2.36. Magnitude of first vertical velocity pulse, scaled to 1 kt, as a function of distance along the surface for detonations in NTS granite and in salt. Closed symbols represent surface zero data.

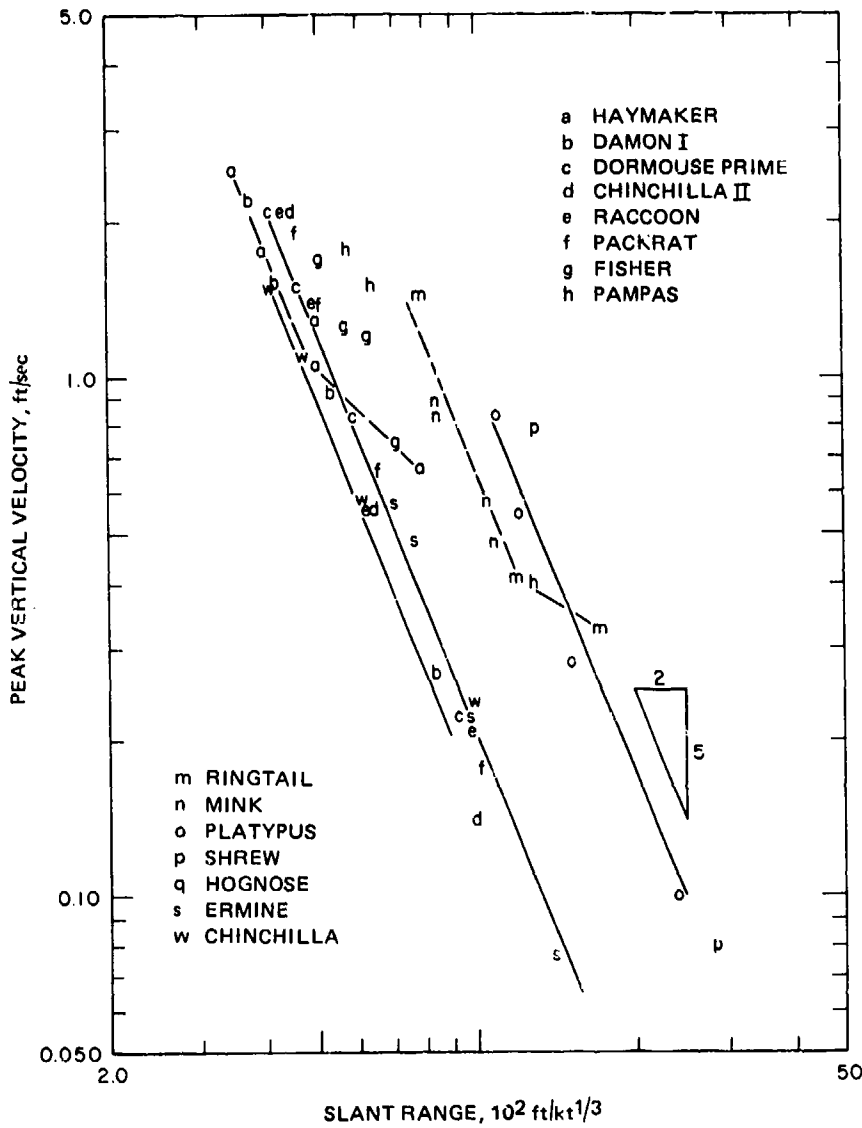


Figure IV-2.37. Magnitude of first pulse of vertical velocity, scaled to 1 kt, as a function of distance along the surface for detonations in NTS alluvium.

strong support to the 2.5 power rule. Data from the HAYMAKER detonation attenuate at a lesser rate due to refraction of energy as previously discussed in connection with the attenuation of peak vertical acceleration. The datum at the greatest range on RINGTAIL is unaccountably larger than expected.

In both Figures IV-2.35 and IV-2.37 the spread of data between detonations is due to differences in surface-zero velocities. It is believed that surface zero data differ from a constant multiple of the free-field radial velocity because of

variations in material properties rather than from a failure of scaling. These differences in properties are reflected in the spread between detonations as shown in Figures IV-2.35 and IV-2.37. Note that due to the difference in attenuation rate between surface-zero and non-surface-zero velocities, even for a constant set of material properties, the vertical velocity versus slant range correlation will depend on the depth of burst.

IV-2.5.3 Peak Vertical Displacement

The peak vertical displacement, d , of the ground surface under spalling conditions is the sum of the displacement up to the time spalling begins, d_0 , and the displacement due to the spall being in free fall,

$$d = d_0 + \frac{v^2}{2g} \quad (\text{IV-2.46})$$

where v is the maximum spall velocity.* For the surface-zero of GNOME, the second term of Equation IV-2.46 accounts for approximately 95 percent of the maximum displacement. For surface-zero of HARDHAT, the second term of Equation IV-2.46 exceeds the measured maximum displacement. For the surface-zero of RAINIER and ANTLER, the second term accounts for approximately 75 percent of the maximum displacement. On the other hand, on surface-zero motions for detonations in alluvium the first term of Equation IV-2.46 predominates, with the second term accounting for less than 40 percent of the total displacement.

The initial displacement, d_0 , may be evaluated by subtracting the second term of Equation IV-2.46 from the total displacement. For a homogeneous medium the initial displacement should be a scalable quantity provided the depth of spall is not influenced by gravity. The lithostatic stress due to gravity would of course be important if the spall mechanism depended upon the net tensile stress in the medium. The validity of scaling the initial vertical displacement is shown in Figures IV-2.38a and IV-2.38b. It should be remarked that the values shown in Figure IV-2.38 assume that all shots are at the same scaled depth of burst. In Figure IV-2.38a there appears, with the exception of MINK and PLATYPUS, a fair degree

*The maximum spall velocity is the initial velocity of the spalled material as it leaves the earth's surface. This velocity is assumed to be directed normal to the ground surface.

of correlation with no difference in trend noted between the "A" and "B" groups of Figure IV-2.38. Unfortunately, these two exceptions are the smallest yield detonations. Moreover, they do not exhibit the second pulse of acceleration characteristic of the remaining data. It is not known if this is due to lithologic conditions or to the yield or both; if due to yield, low yield and large slant range would result in weak waves. Therefore, the failure of data from these two detonations to fall into juxtaposition with the remaining data contributes no argument favoring one scaling method over another.

Data on initial displacement for detonations in NTS tuff (Figure IV-2.38b) are of little help in answering the question of the small difference in yield between ANTLER and RAINIER. It is interesting to note that initial displacements in the spalling region for all the detonations in the non-alluvial materials are surprisingly similar in magnitude. Although the initial vertical displacements in these media are about 20 times those observed in alluvium, the larger maximum velocity for detonations in rock makes the initial displacement of lesser importance compared to displacement due to the spall in free-fall.

In alluvium, and in the various rocks, the attenuation of initial vertical displacement has been tentatively determined to be at the rate of inverse fourth power of surface range. Power law relationships for the scaled initial displacements are, for detonations in NTS alluvium:

$$d_0/W^{1/3} = 9.4 \times 10^{10} \left(\frac{R}{W^{1/3}} \right)^{-4} \quad (\text{IV-2.47})$$

and for detonations in NTS granite and tuff and in salt

$$d_0/W^{1/3} = 1.5 \times 10^{12} \left(\frac{R}{W^{1/3}} \right)^{-4} \quad (\text{IV-2.48})$$

where d_0 is in inches, W is in kilotons, and R is in feet.

IV-2.5.4 Rules for Predicting Vertical Surface Motion

A rational procedure for predicting peak vertical motion on the surface above

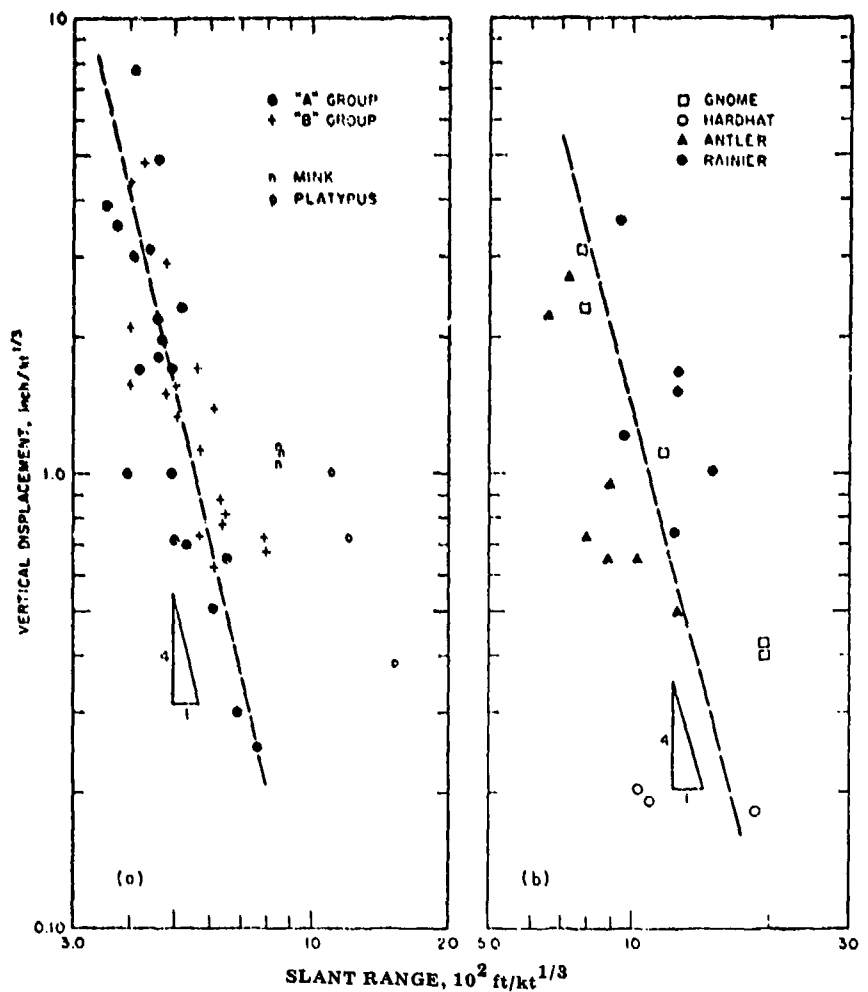


Figure IV-2.38. Magnitude of vertical displacement prior to spalling, scaled to 1 kt, as a function of distance along the surface. (a) detonations in NTS alluvium; (b) detonations in salt (GNOME), in NTS granite (HARDHAT) and tuff.

underground nuclear detonations based on the preceding sections is to establish first the magnitude of motion at surface zero using the free-field radial motion multiplied by an apparent reflection factor or using Figures IV-2.28 through IV-2.31. Selection of an apparent reflection factor for peak vertical acceleration equal to that for peak vertical velocity appears to result in an error less than 30 percent. However, the reflection factors themselves may vary by factors of 3 to 3-1/2 for detonations in the same medium. This variation in apparent reflection

factors can be reduced if account is taken of variations in seismic impedance in the lithologic structure above the shot point.

Having determined the peak acceleration at surface zero, the acceleration should then be attenuated as the inverse cube of the slant range. This rate of attenuation differs from the approximately inverse square attenuation of vertical component of acceleration suggested in Reference IV-2.46. The choice of this lesser rate of attenuation appears to be strongly influenced by peak accelerations resulting from refractions of energy at large slant ranges. Also, the regression equations of Reference IV-2.46, determined by statistical means, are dimensionally inconsistent; the power of yield so determined is consistent with an inverse cube attenuation rather than with an inverse square attenuation as postulated in the reference. Thus an inverse cube attenuation is preferred.

Although confined to attenuation of the first peak of vertical velocity, the inverse 2.5 power rule of surface range attenuation may be applied without serious error in finding the maximum vertical velocities. For the NTS alluvium (except for one case) the error introduced by this procedure is less than 50 percent in the estimation of peak vertical velocity. This is less than the error associated with the selection of an apparent reflection factor.

The maximum vertical displacement may then be evaluated using Equations IV-2.46 through IV-2.48. For detonations in the more competent materials, the error involved in estimating the peak displacement will be approximately the square of the error in estimating the peak velocity because of the predominance of the second term in Equation IV-2.46 for these media. For alluvium the error will be somewhat larger than the deviations noted in Figure IV-2.38 because of the predominance of the first term in Equation IV-2.46.

IV-2.6 OVERVIEW OF GROUND MOTION FROM SUBSURFACE HIGH EXPLOSIVE EVENTS

The overview of recent ground motion experiments with underground high-explosive detonations presented in this section is short and covers a period from 1972 to 1975. It does not deal with the subject over the stated period in any depth as that would make this section rather voluminous. The content is presented in the form of abstracts derived from the references listed. The reader is urged to consult these references for further specific information. This section is intended only to provide the interested readers with a place to start their search. For those interested in acquiring an understanding of the physical development and

the chemical processes of an HE detonation, the physics and chemistry of detonations and their computations, they should consult Reference IV-2.87.

Sauer and Kochly reported (Reference IV-2.88) on the DIAMOND MINE Event. It was an underground detonation of 985 pounds of nitromethane executed to compare the coupling factor associated with an overdriven shot cavity with that associated with the DIAMOND DUST Event (an underground nuclear event with an overdriven cavity of the same size with an heat sink). The purpose of the test was to record the detonation-induced free-field ground motion in the elastoplastic and elastic regions of the material to provide data to be used in evaluating the decoupling mechanism and to verify numerical calculations. Four instrument lines were installed, emanating radially from the cavity. One instrument line terminated in the access drift to the shot cavity and three instrument lines terminated in the main drift of the tunnel. Three motion-measuring instruments were used: crescent particle velocity gauges located 90 feet from the cavity surface, Kistler velocimeters, and diaphragm accelerometers located from 40 feet to 175 feet from the cavity. Measured maximum particle velocities varied from 54 ft/sec at the cavity wall to 0.5 ft/sec at the 145-ft range. Good agreement was obtained between maximum particle velocity determined by the crescent gauges, the Kistler velocimeters and the integrals of accelerograms. Close to the cavity wall, the maximum particle velocities were in agreement with those observed on DIAMOND DUST. However, the particle velocities on DIAMOND MINE attenuated more rapidly with ground range than those on DIAMOND DUST. Measurement of maximum transient displacement was obtained by integrating 23 velocity gauge records. While these measurements of displacement scattered to a greater extent than observations made on DIAMOND DUST, the DIAMOND MINE displacements were approximately a factor of 2 less than those for DIAMOND DUST.

Hendron published a report in 1973 (Reference IV-2.89) in which he reviewed a large number of motion measurements from contained explosions in various rock media. He interpreted these data in terms of dimensional analysis and other constraints necessary for dynamic consistency to give scaling relations for estimating peak motions in various rock media. He presented suggestions for estimating ground motions from directly induced ground shock resulting from a surface burst on rock. However, this method does not work well.

Jones and Green (Reference IV-2.90) calculated peak stresses from two contained 1000 pound nitromethane explosions in nearly saturated Nevada Test Site

(NTS) tuff and found agreement with measured values to within about 20 percent, over a pressure range of 1 to 20 kilobars. The total impulse measured at a given location was in good agreement with calculated values for piezoelectric gauges but about 50 percent less than the calculated values for the piezoresistive gauges (ytterbium). Improved correlation was obtained with the most recent Stanford Research Institute calibration data for ytterbium gauges stress unloading history. Many laboratory tests were conducted on small core samples from each site to provide an adequate representation of materials. Over the pressure range of interest (down to about 1 kilobar) the shear strength of the tuffs is not significant to the mechanical response, and therefore the model used needed only to fit volume and energy requirements. Measurement of stresses and velocities in the multi-kilobar pressure range was accomplished with piezoresistive stress gauges (ytterbium) and piezoelectric velocity gauges (quartz and ceramic).

Project ESSEX (see, for example, Reference IV-2.91) was formulated as a five-year research program in early 1972 to determine the effects of stemming (backfill) variations, depth-of-burial (DOB), and soil properties on the crater size and shape, obstacle effectiveness of the resulting crater and ejecta area, and collateral effects (airblast, nuclear fallout, etc.) produced by the subsurface detonation of a low-yield nuclear cratering source. The nuclear effects of interest are being modeled by high-explosive effects generated by high-explosive charges. The HE yield and geometry is determined from hydrodynamic calculations by assuming similarity between nuclear and high-explosive sources. The assumption of similarity implies similarity of ground shock, permanent ground displacements, ground shock induced airblast, ejecta distributions, and crater size and shape. The nuclear fallout from venting is modeled by an inert nonradioactive tracer suspended in the HE charge.

In August 1974, Sisemore, Burton and Bryan (Reference IV-2.93) released a report presenting results of close-in measurements of Project DIAMOND ORE, Phase IIA. This series of multiton cratering experiments was conducted at Fort Peck, Montana in October 1971. Three cratering charges, each approximately 9000 kg of sand contaminated slurry explosive, were detonated. Two of these charges were at a DOB of 12.5 m with one unstemmed detonation (DO IIA-1) and one stemmed detonation (DO IIA-2). The third charge (DO IIA-3) was detonated at a DOB of 6 m and was stemmed. These detonations were highly instrumented to provide data for code development work. Moreover, these experiments were conducted to provide a

first look at the effects of stemming in multiton yields. Other measurements and technical programs were directed toward comparing the effects of different stemming plans and DOB's on the resulting craters and determining collateral effects. These measurement programs included high-speed photography of each detonation, airblast measurements, ground shock measurements, and preshot and postshot aerial mapping of the craters.

In November 1974, Vortman and Beyeler (Reference IV-2.95) of Sandia Laboratories released a document dealing with the ground motion and airblast measurements conducted during ESSEX 1, Phase 1. During this experiment, four high-explosive charges were detonated in saturated soil to simulate employment of atomic demolition munitions (ADMs). Two 10-ton charges were buried 12 meters deep, one stemmed and one with a small open hole. Another 10-ton stemmed charge and one 8.5-ton unstemmed charge were detonated at a depth of 6 meters. On each shot, instruments measured shock propagation above the charge, shock stress and ground acceleration at one position at half-shot depth and at three shot-depth positions, ground-surface acceleration at four to five positions, shock pressure in the open holes of the unstemmed shots, and above-ground airblast at several distances. Ground-surface displacement was measured with high-speed photography. Peak stresses ranged from 0.05 to 3 kilobars. These measurements were made to provide information on effects of charge burial depth and stemming, as well as physical data that could be used to verify the hydrodynamic codes being used for numerical simulation of ADM explosions. An internally consistent set of measurements of all parameters was obtained on each shot. The measurements were especially well suited to the objectives but soil inhomogeneity obscured subtle effects of stemming differences and detracted from the precision with which codes can be verified from measured data. Airblast measurements on five 1000-pound surface and near-surface detonations showed that differences in meteorology on the different ways the shots were fired obscured subtle differences that could be attributed to charge position.

Reference IV-2.96 describes measurements of airblast and ground motion on shot 6M of the DIAMOND ORE Phase IIB Series. This particular shot was intended to evaluate the high explosives/nuclear explosives model of System, Science, and Software's design of a nitromethane detonation in clay shale. It was instrumented to gather data for determination of the effects that an open-hole geometry would have on crater formation. The charge contained 17 tons of nitromethane buried at

a depth of 5.85 meters. This reference reports on measurements of shock velocity up a vertical hole from the charge depth to the surface, airblast overpressure at the ground surface, radial earth stresses, and vertical and horizontal particle velocity.

IV-2.7 SOME ANALYTICAL MODELS FOR PREDICTING GROUND MOTION PHENOMENA

In this section we present a description of some useful models for the prediction of ground motion and related phenomena associated with the detonation of buried nuclear or high explosives. The first model is almost entirely graphical and very simple to use and, therefore, lends itself quite well to quick systems evaluation. It not only predicts ground motion but also allows the user to determine a number of other parameters such as, for example, cavity radius, chimney size, radial displacement, peak radial stresses and other quantities. The accuracy of the model is reasonable and for the most part within the experimental uncertainties. The graphs are the results of computer calculations based on an extensive data base and experimental data.

The next model is an analytic one but also simple to use. The user can easily obtain results on a pocket computer. Moreover, the modeling is simple enough to be easily programmed in almost any language. Unlike the other model, the predictions of this model are restricted to ground motion phenomena only. As will be shown below its accuracy is quite remarkable considering the assumption that went into building this model.

Finally, a semiempirical model using the methods of geometrical optics will be briefly discussed.

A general statement of caution is in order here: these models are not meant as substitutes for thoroughgoing analyses using detailed computer codes. They are rather intended for preliminary analysis, and to be used as supplement to detailed computations.

IV-2.7.1 The Butkovich and Lewis Model

As stated in the introduction this model summarizes in a graphical form, useful relationships for computing the effects on the surrounding media of underground nuclear explosions. The types of parameters considered include the device yield, the depth of burst, cavity volume and radius, chimney height, effects as a function of distance from shot point, fracture radius, mass of rock in the chimney, in situ and grain density, porosity, water content, compressional velocity, Poisson's

ratio, overburden pressure, radius of vaporization, radial stress and displacement, particle velocity and acceleration, ground-surface acceleration and displacement, and temperature increase. The complete model is described in Reference IV-2.97. An abbreviated version of Reference IV-2.97 is given below.

Computer codes designed specifically for predicting effects from underground nuclear explosions are available and may be used to improve the estimates made from the graphs discussed here. This would be desirable when information about a site (for example, rock properties) is accurate enough to justify detailed calculations. However, for preliminary planning and systems analysis purposes the estimates made from these graphs should be adequate.

In 1973 Butkovich and Lewis made the statement that:

Some aspects of underground nuclear explosion phenomenology are not well understood. Certain types of data are relatively scarce because of the high costs of drilling and instrumentation. Data on fracture porosity and permeability are particularly lacking. In spite of shortcomings such as this, the relationships reported here should prove valuable in estimating some of the various effects of an underground nuclear explosion on its surroundings.

This statement is by and large true today. They point out, for example, in a discussion of underground nuclear explosion phenomenology that if enough energy is deposited in a volume element in the cavity, the material is totally vaporized and expands as a gas. Butkovich reports calculations showing that approximately 70 metric tons of silicate rock per kiloton of yield are completely vaporized by the shock wave. Beyond the totally vaporized region, sufficient energy is deposited to shock-melt the rock and vaporize the water in the rock. Radiochemistry measurements on melt samples recovered during reentry drilling below the shot point seem to indicate that the total amount of melt present is between 1000 and 2000 metric tons per kiloton of yield and is a decreasing function of the rock density at the shot point. This amount of melt includes not only rock melted by the shock but also rock melted subsequently by redistribution of heat from superheated material. Beyond the melt zone the rock is heated, displaced, and fractured to some distance that depends on the device yield and the strength properties of the rock. The rock and included water that becomes vaporized expands as a gas and forms a growing cavity. If the depth of burst is greater than about $350 W^{1/3}$

ft ($106.7 W^{1/3}$ m), where W is the yield in kilotons, the gases will be contained. There have been a number of incidents in which small amounts of radioactivity have escaped into the atmosphere at slightly greater scaled depths of burst. In these instances, venting of a small fraction of the cavity gases has occurred through cableways and stemming materials, and certain precautions can be taken to eliminate this problem. For depths of burst of less than $200 W^{1/3}$ ft ($61 W^{1/3}$ m), cratering process begins to occur. In this case, the cavity expands asymmetrically toward the free surface, forming a mound and rupturing the surface. Optimum crater dimensions occur at a depth of burst of about $120 W^{1/3.4}$ ft ($36.6 W^{1/3.4}$ m). The empirically derived $W^{1/3.4}$ scaling rule indicates that higher yield explosions will be contained at shallower depths than the assumed $W^{1/3}$ scaling rule would indicate.

In the contained case, with which this model is primarily concerned, cavity growth continues until the cavity pressure is somewhat greater than the overburden pressure—between 1.4 and 2 times the overburden. The strength of the rock is affected by the presence of water and hence the cavity size. Thus, nuclear explosions in high-water-content rocks will form larger cavities not only from the enhancement of pressure due to the expansion of the noncondensable steam but also because wet rock is weak. Cavity growth is generally assumed to be spherical. However, calculations indicate that nearly spherical cavities are formed only when nuclear detonations occur at sufficient depths or in strong dry rock.

After cavity growth stops, the rock above the cavity usually collapses into the void, forming a chimney. As the pieces of broken rock fall, they rotate randomly so that the broken rock packs more loosely occupying more volume than it did before fracture. The upward growth of the chimney continues until it bulks full or until the rock can support an arch, leaving a void at the apex of the chimney. In many cases, particularly for high-energy yields in strong rock, and for almost all alluvium detonations, the chimney growth progresses until the collapse reaches the ground surface and a collapsed crater is formed. To facilitate the understanding of some of the graphs that are included in this discussion we proceed with the discussion of the modeling details.

Relationships between in-situ density (ρ_0), porosity (ϕ), volume-fraction saturation (S), and weight-fraction water (Z), for rocks of various grain densities (ρ_g) can be developed from the following equations:

$$\rho_0 = \frac{\rho_d}{1 - z} \quad (\text{IV-2.49})$$

$$\rho_g = \frac{\rho_d}{1 - \phi} \quad (\text{IV-2.50})$$

$$\rho_0 = \rho_g \left(\frac{1 - \phi}{1 - z} \right) \quad (\text{IV-2.51})$$

$$\phi = 1 - \frac{\rho_0(1 - z)}{\rho_g} \quad (\text{IV-2.52})$$

$$s = \frac{\rho_0 z}{\phi} \quad (\text{IV-2.53})$$

where ρ_d is the dry density.

The grain densities of common rock mineral components have been measured. For rocks with very low porosity, the rock density approaches the grain density. A table included in Reference IV-2.97 gives the grain densities of some common rock minerals and rock densities are given in another table of the same reference which may be used to approximate grain densities.

A number of figures such as Figure IV-2.39 are given to show the relationship between in-situ density, porosity, volume-fraction saturation, and water content (by weight) for rocks of grain density between 2.2 and 3.0 g/cm³. These plots may be used to check the internal consistency of the measurements on a given rock.

An example of the application of Figure IV-2.39 is as follows. Consider a rock with a grain density of 2.2 g/cm³, an in-situ density of 1.5 g/cm³, and a porosity of 0.40 (40 percent). Using this graph one can find that the water content is 0.12 weight fraction and the volume-fraction saturation is about 0.44. If this rock were then compressed until all the air-filled porosity were eliminated, the density would be about 1.925 g/cm³ and the porosity would be about 0.23 (23 percent).

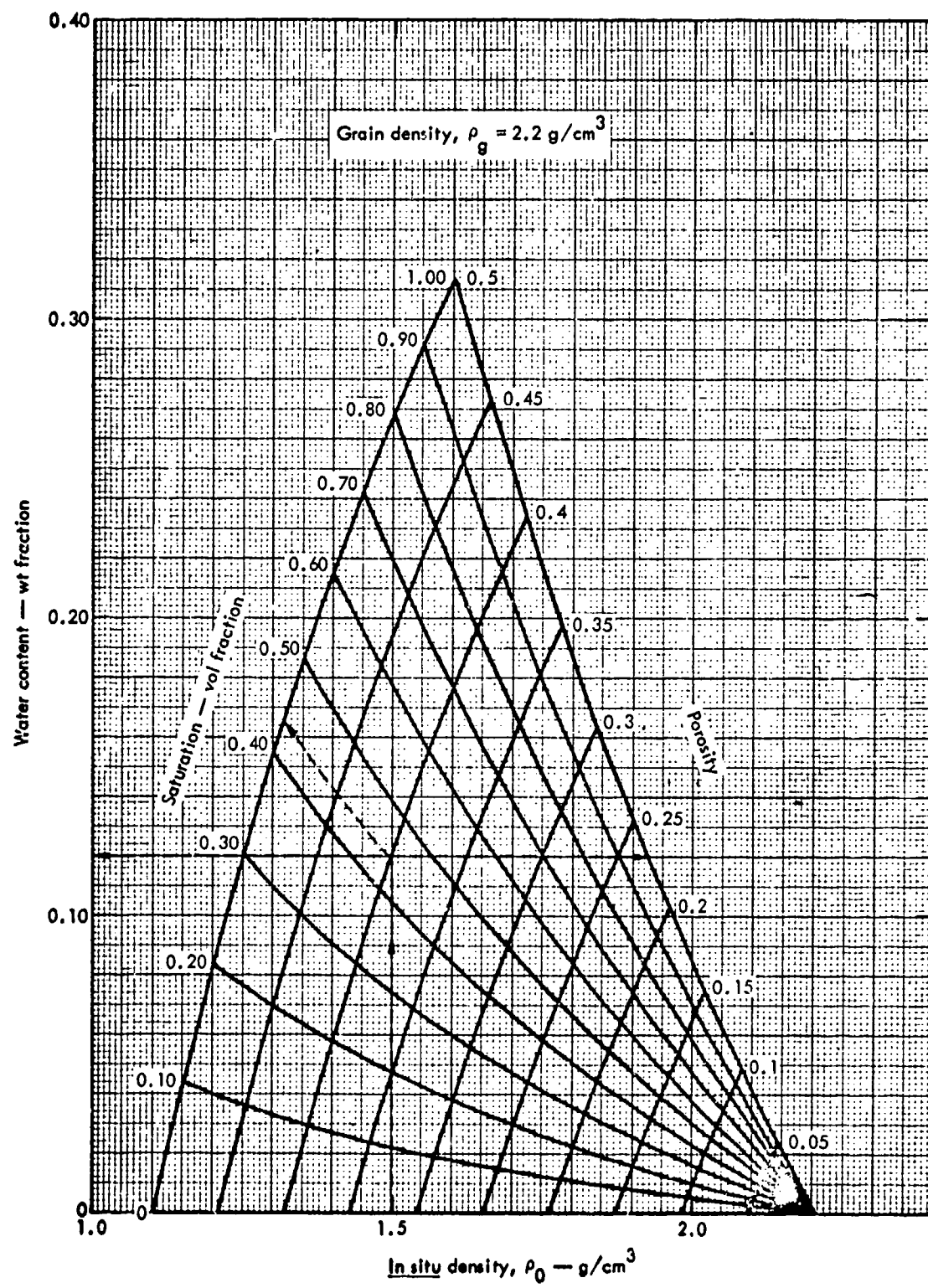


Figure IV-2.39. In-situ density, porosity, saturation, and water content for rocks of grain density 2.2 g/cm^3 . The other figures given in Reference IV-2.97 cover grain densities from 2.3 to 3.0 g/cm^3 .

This information is obtained by moving horizontally from the original point given to the volume-fraction saturation curve and reading the new density and porosity values.

Figure IV-2.40 shows the in-situ density as a function of compressional velocity for common test and collapse media at the Nevada Test Site. The equation giving the best fit to the data is

$$C_p = 10,232\rho_0 - 9,190 \quad (\text{IV-2.54})$$

where C_p is the compressional wave velocity in ft/sec and ρ_0 the in-situ density in g/cm³. It should be noted that the water table at NTS is abnormally deep. Much of these data were taken above the water table in unsaturated rocks and may, therefore, not be representative of rocks in other locations.

Figure IV-2.41 is an example of the types of curves given in Reference IV-2.97 showing the overburden pressure as a function of depth for various average overburden densities. The overburden pressure is equivalent to the lithostatic pressure. Also included is hydrostatic head of water as a function of depth.

Figures IV-2.42 through IV-2.45 are given as examples of the type of useful graphs contained in the model. They give information on underground nuclear explosion phenomenology obtained by measurement or calculation. The mass of rock vaporized by a nuclear explosion depends on the energy yield and the enthalpy for vaporization for the rock, which varies with rock type. Butkovich assumed a simple silicate approximation for silicate rocks and calculated that approximately 70 metric tons of rock per kiloton of device yield is vaporized by the shock wave. A similar calculation for salt and water gives 107 and 150 metric tons per kiloton, respectively, for their enthalpies of vaporization. Figure IV-2.42 shows the radius of vaporization (R_v) as a function of device yield in kilotons for various in-situ rock densities. This figure assumes 70 metric tons per kiloton for silicate rock.

Figure IV-2.43 gives the peak radial stress (σ_r) as a function of yield (W) and distance (R) from the shot point. These curves were obtained from best fit to the data from four different test materials. The equation giving the best fit to the data is

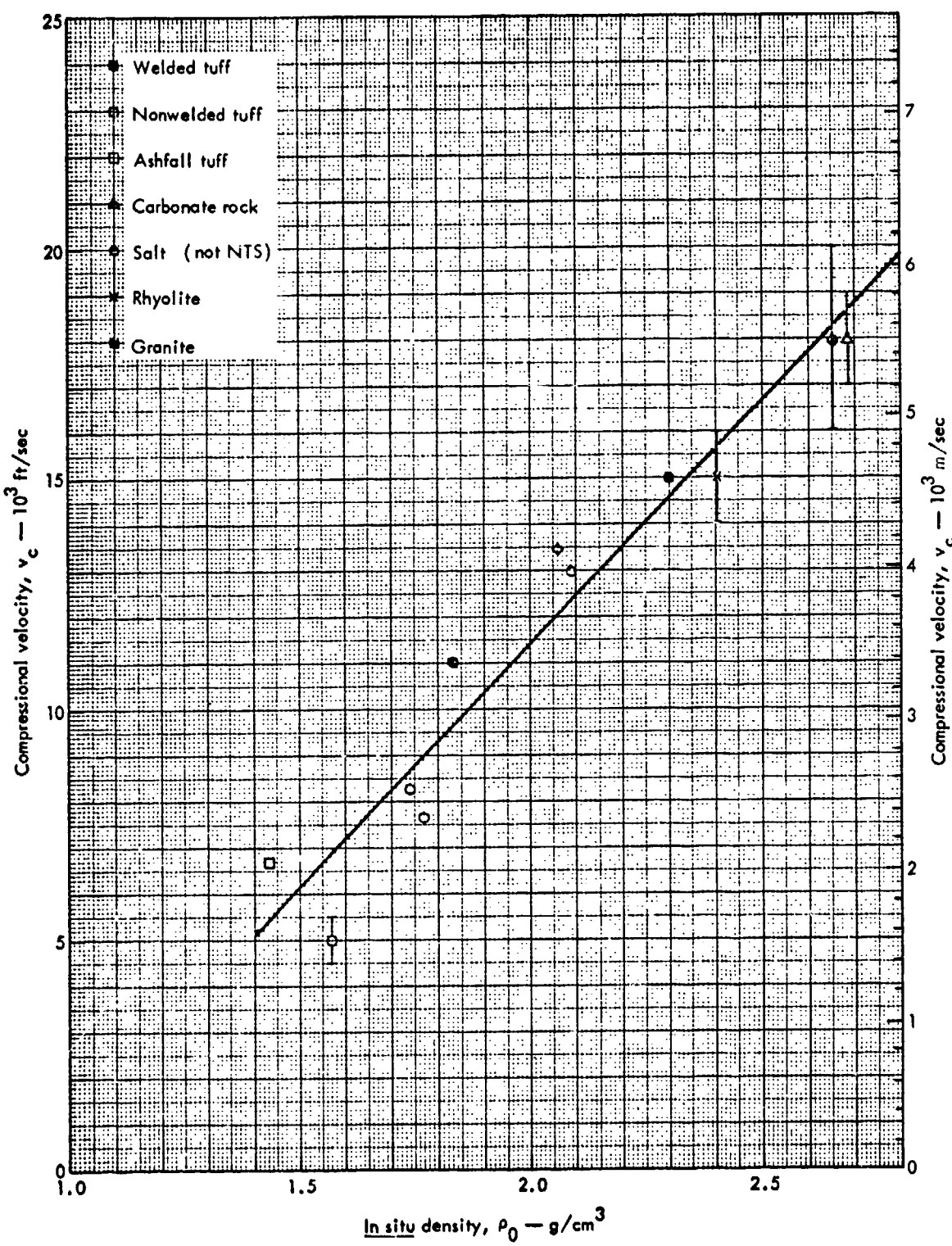


Figure IV-2.40. In-situ density as a function of compressional velocity for common test and collapse media (rock) at the Nevada Test Site.

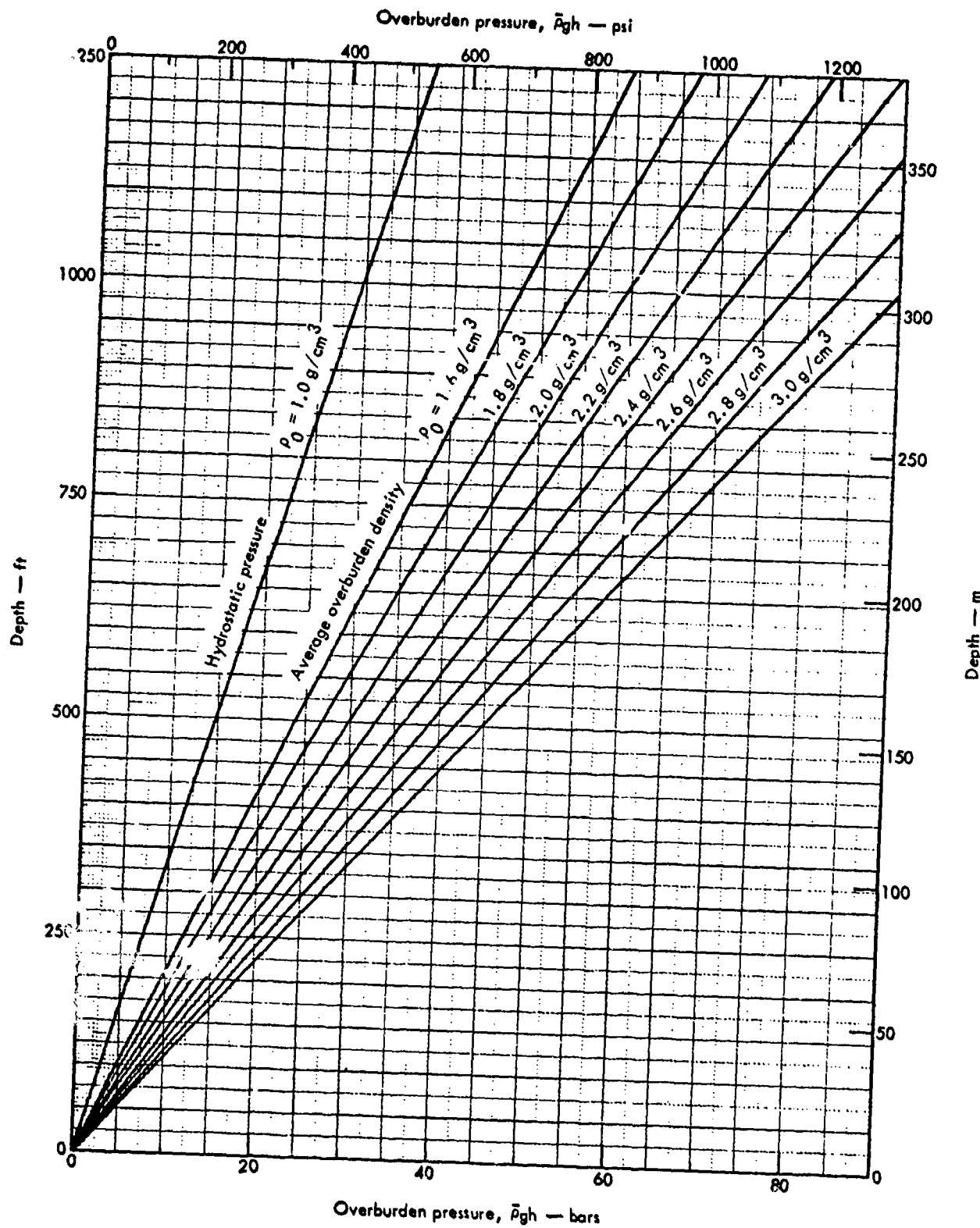


Figure IV-2.41. Overburden pressure as a function of depth (to 1250 ft) for various average overburden densities. Another curve is given in Reference IV-2.97 for the extension of these curves to depths of 10,000 ft.

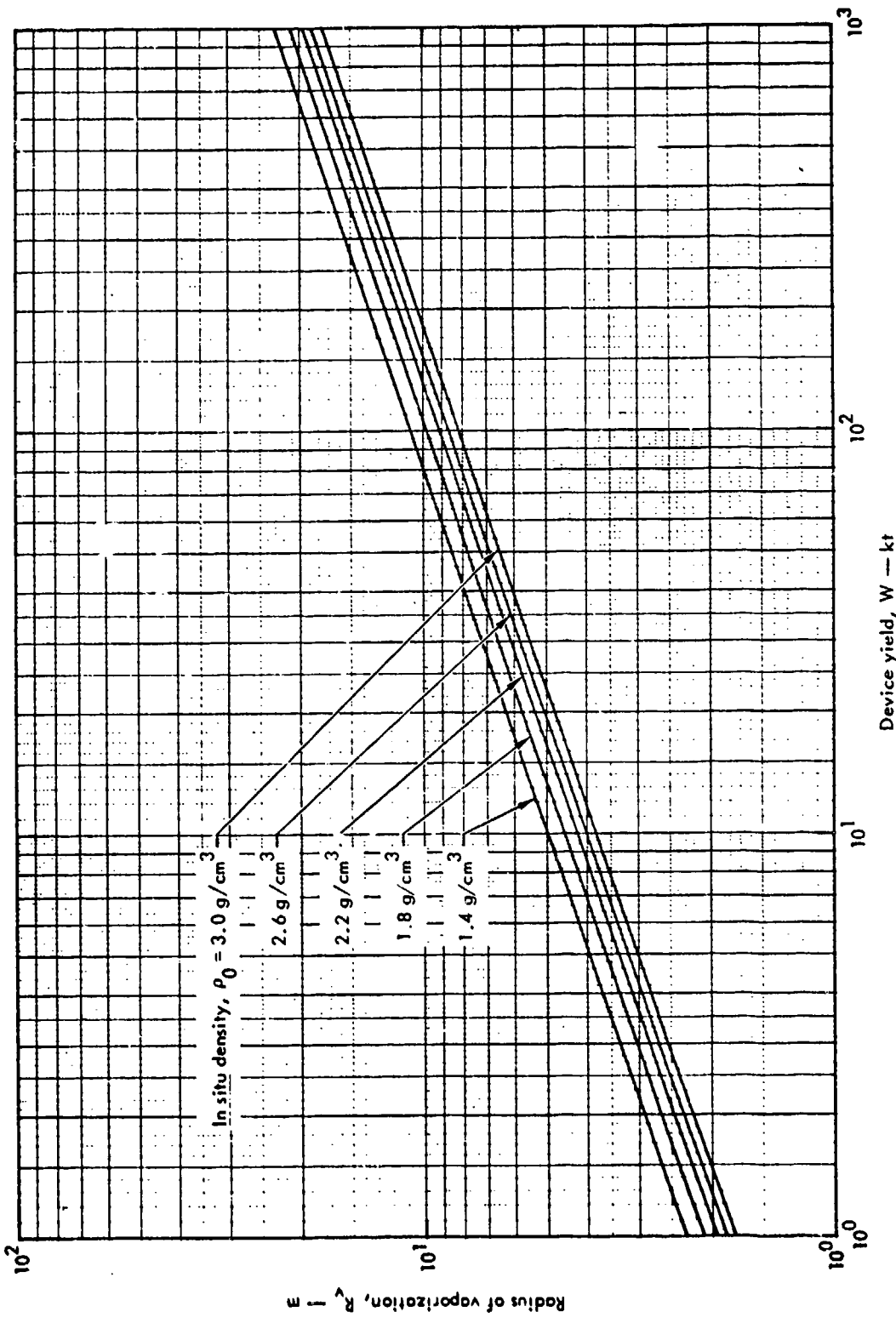


Figure IV-2-42. Radius of vaporization as a function of device yield for various in-situ shot-point rock densities.

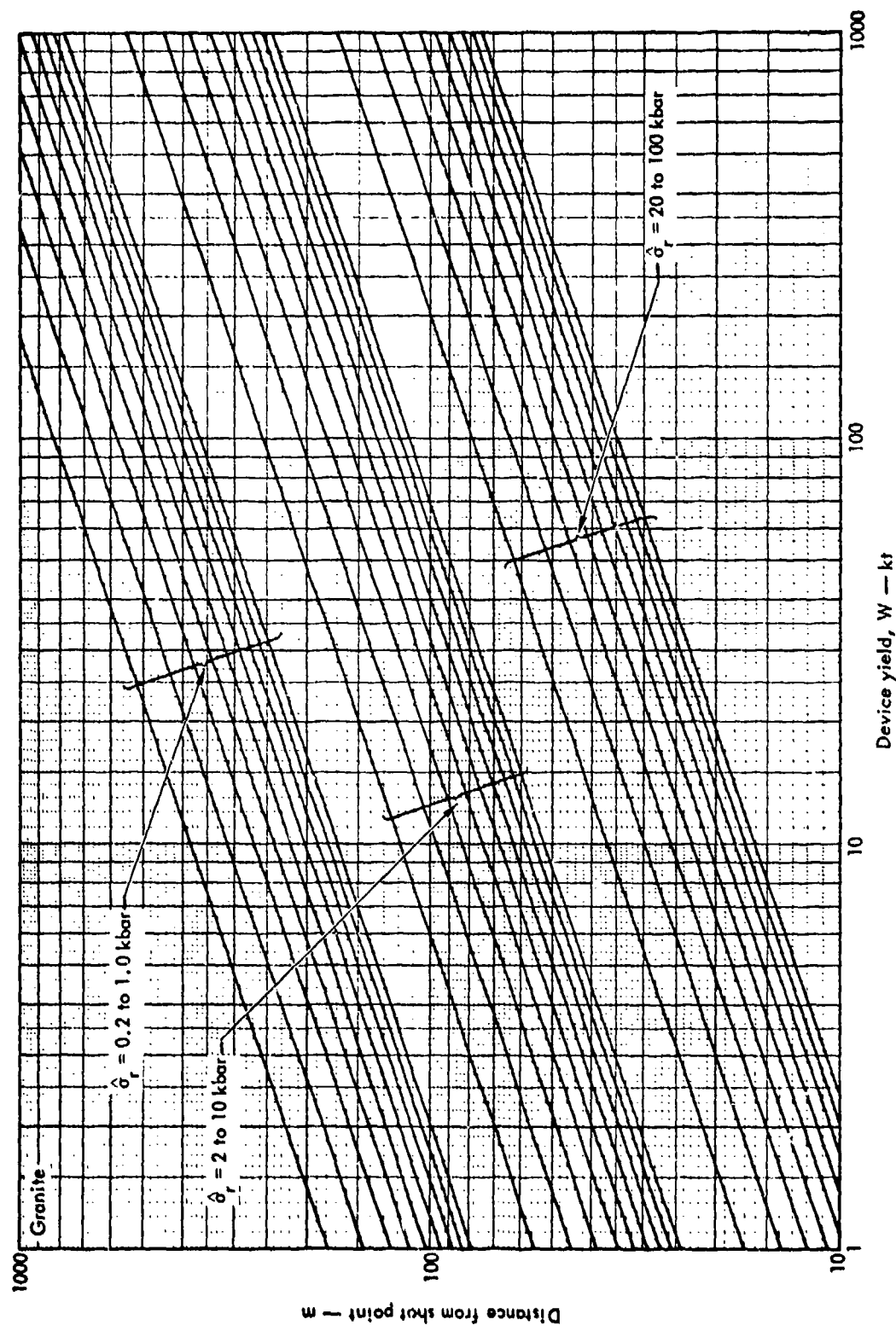


Figure IV-2-43. Peak radial stress (σ_r) as a function of device yield and distance from the shot point in granite.

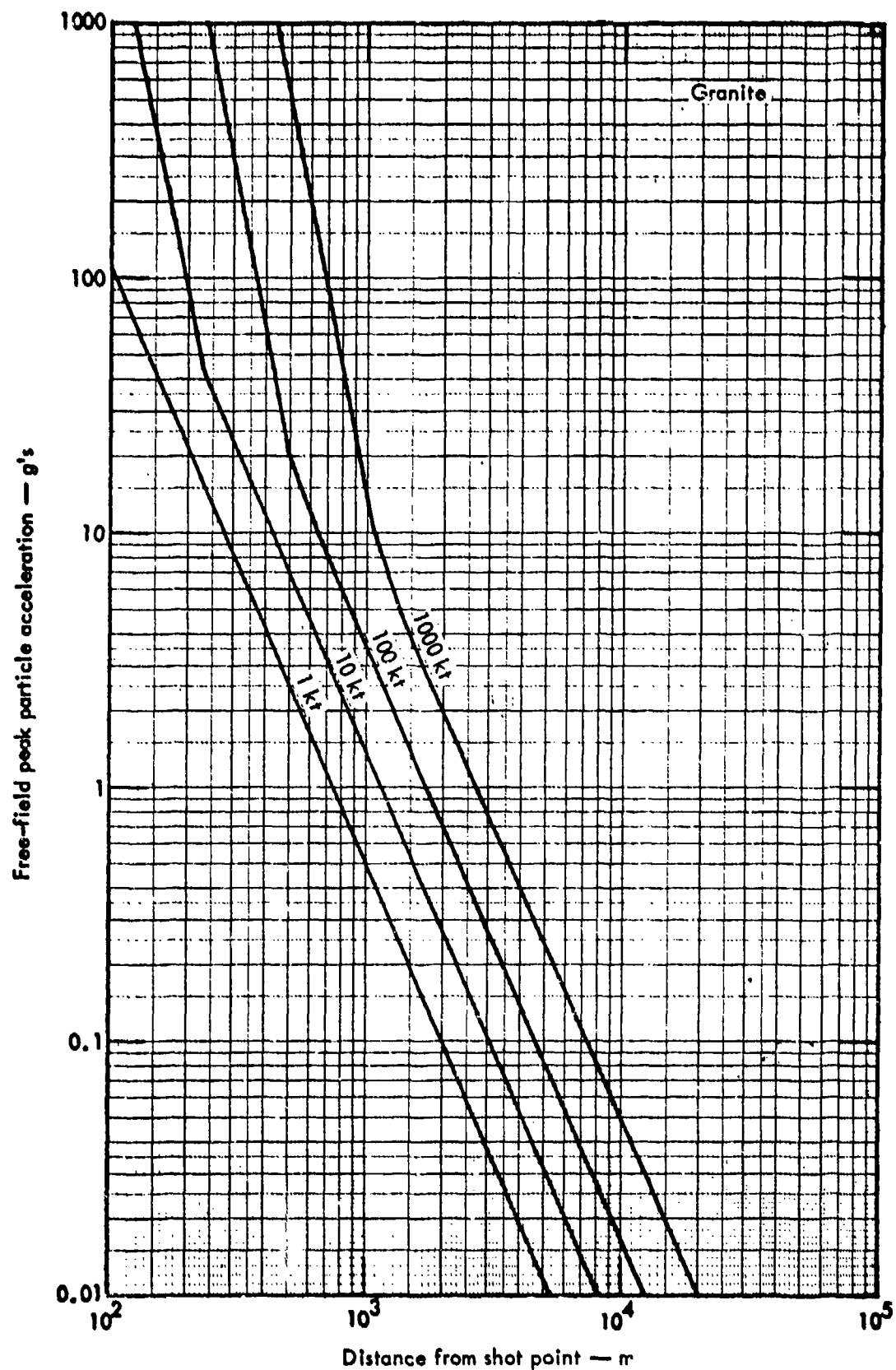


Figure IV-2.44. Free-field peak particle acceleration as a function of distance from the shot point in granite.

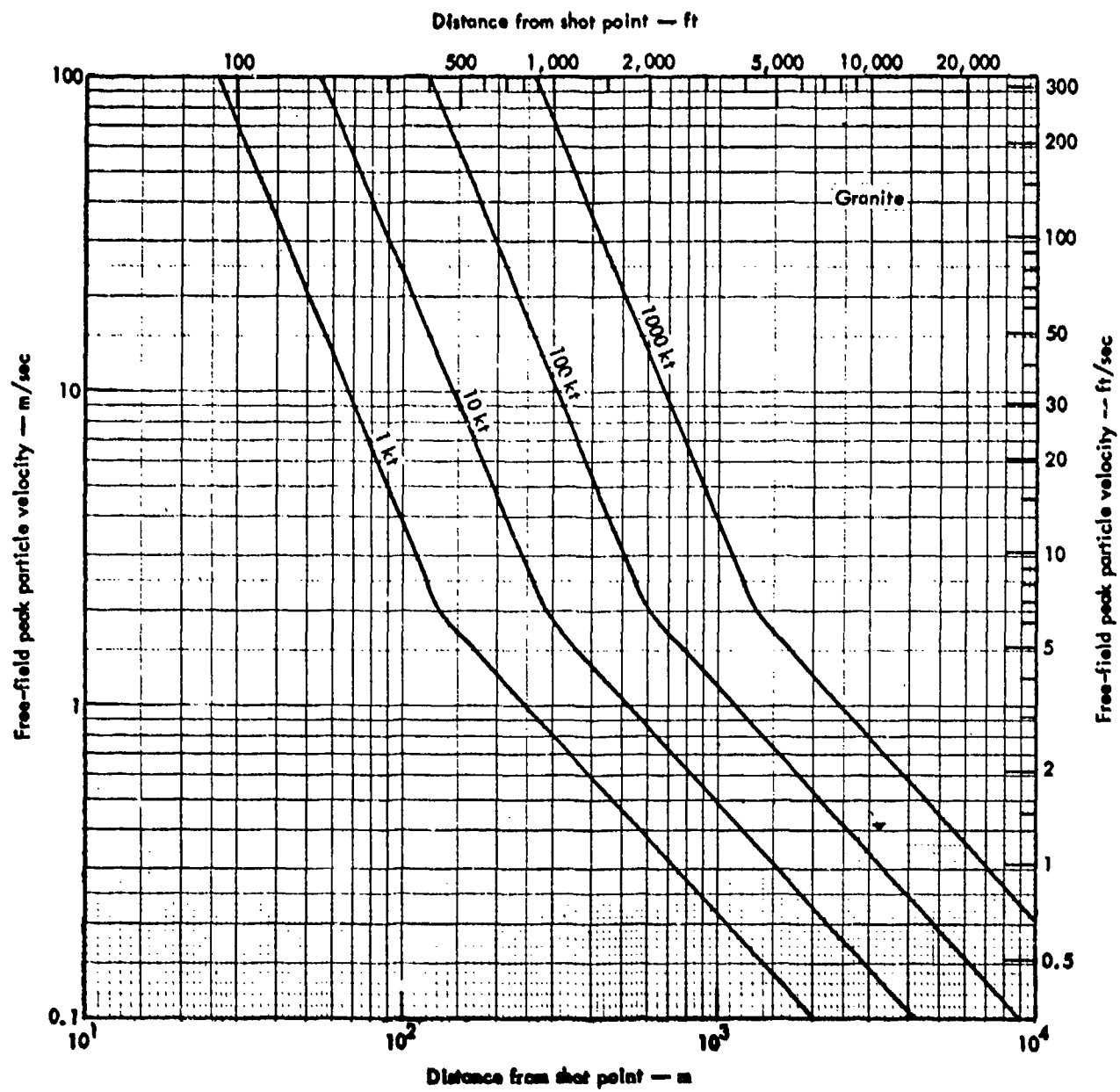


Figure IV-2.45. Free-field peak particle velocities as a function of distance from the shot point in granite.

$$\sigma_r = 5216 \left(\frac{R}{W^{1/3}} \right)^{-1.9625} \quad (\text{IV-2.55})$$

for granite. There are three more graphs and equations giving the peak radial stress for tuff, alluvium and salt. Here σ_r is in kilobars, R is in meters, and W in kilotons.

The stress wave emanating from the explosion center produces particle motion in the surrounding medium. This motion is termed free-field particle motion. Maximum particle acceleration is attained during the initial rise in stress, and maximum velocity is obtained at the time of peak stress. Knowledge of the peak radial stress components of particle motion in the first half-cycle of the stress wave is often used to assess the potential for damage from underground detonations. Figure IV-2.44 is an example that gives the peak free-field particle acceleration and Figure IV-2.45 is an example that gives the peak free-field particle velocity as functions of radial distance from the explosion center. These plots were derived from measurements in granite, salt, and alluvium.

Figure IV-2.46 gives the peak ground-surface acceleration for detonations in hard rock saturated to the surface, and Figure IV-2.47 is an example of the type of graphs that give the peak vertical free-surface displacement as a function of peak free-surface velocity calculated from

$$S = \frac{V_{fs}^2}{2g}, \quad (\text{IV-2.56})$$

where S is the displacement, V_{fs} the peak free-surface velocity, and g the acceleration of gravity.

The radius and volume of the cavity formed by the nuclear explosion depend on the medium. Butkovich and others have shown that the measured cavity radii depend on the yield (W), the average overburden density ($\bar{\rho}$), the depth of burst (h), and the weight fraction of water in the medium at the shot point. The relationship developed is

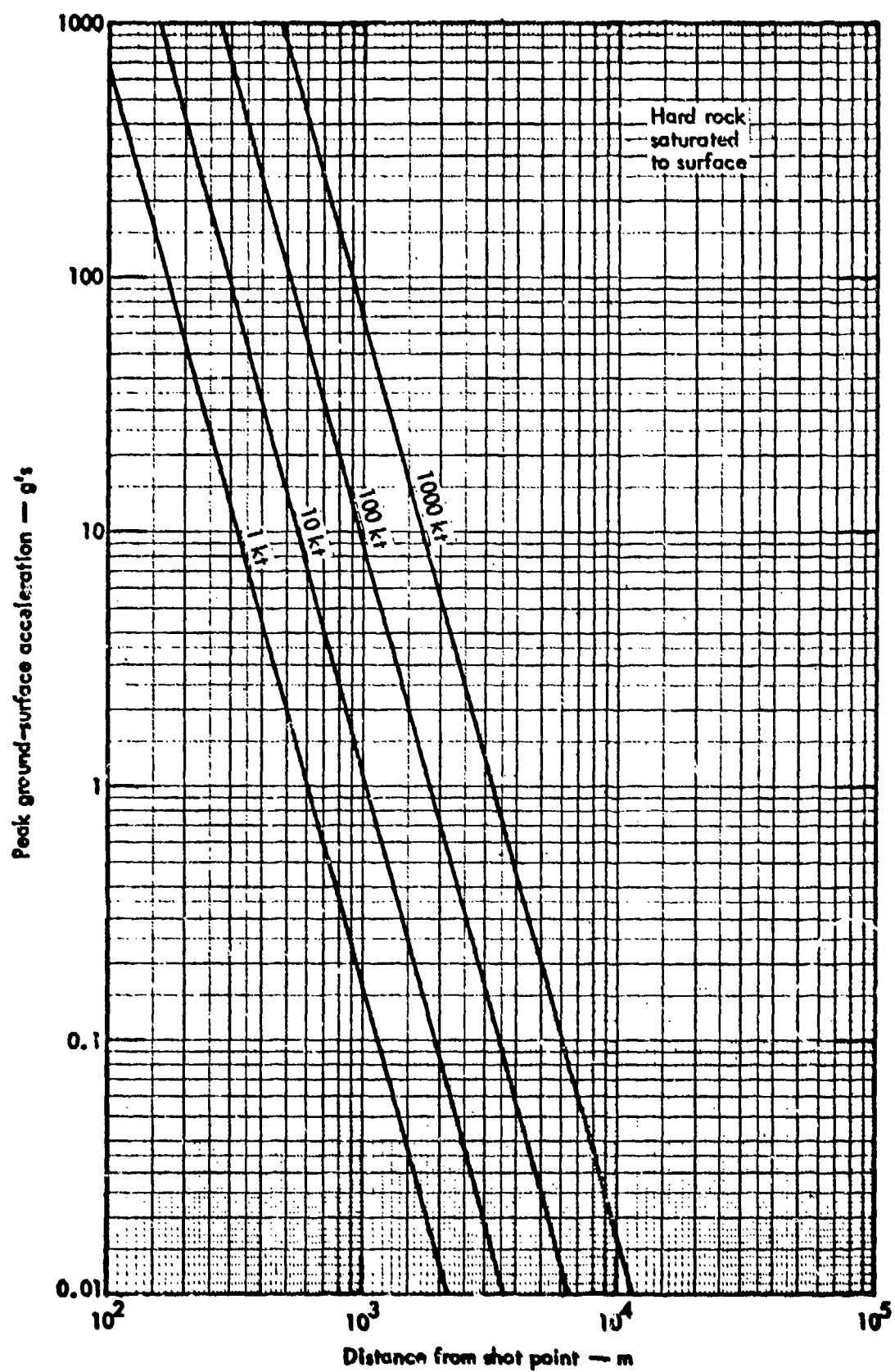


Figure IV-2.46. Peak ground-surface acceleration as a function of distance from the shot point in hard rock saturated to the surface.

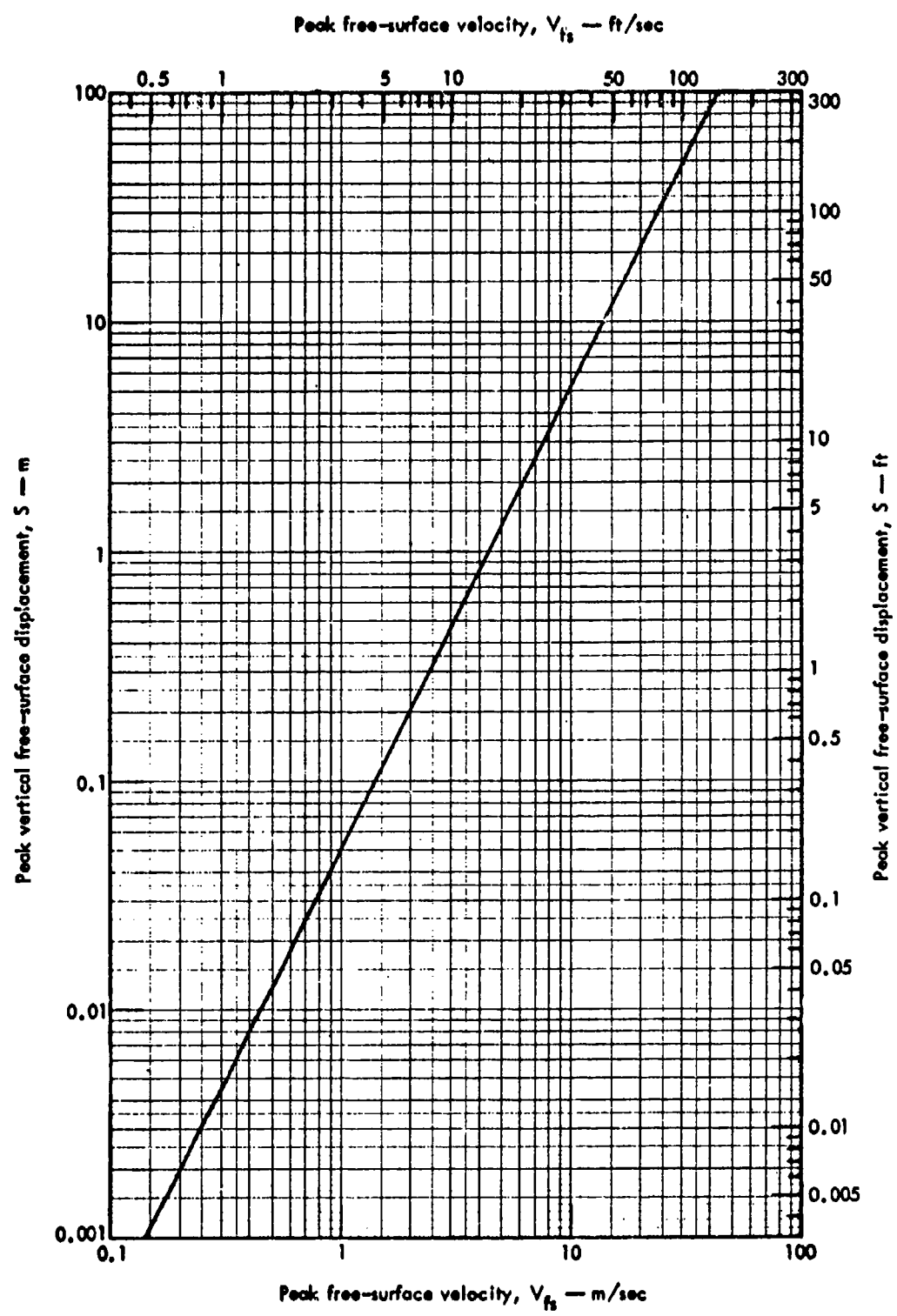


Figure IV-2.47. Peak vertical free-surface displacement as a function of peak free-surface velocity.

$$R_C = \frac{CW^{1/3}}{(\bar{\rho}h)^\alpha}, \quad (IV-2.57)$$

where R_C is the cavity radius in meters, W is in kilotons, $\bar{\rho}$ is in g/cm^3 , and h is in meters. The exponent α depends on the water content, while C is a constant equal to about 100 using this set of units. Figure IV-2.48 is an example of a number of graphs in Reference IV-2.97 that were obtained from the above relationship assuming spherical cavities. However, some cavities are aspherical for shallow depths of burst in weak wet rock. Figure IV-2.49 gives the radial displacement as a function of cavity radius at various distances from the shot point. The curves were calculated assuming spherical symmetry and noncompactable rock using the equation

$$D = \left[R^3 + R_C^3 \right]^{1/3} - R, \quad (IV-2.58)$$

where D is the radial displacement and R is the radial distance from the shot point. Figure IV-2.50 gives the horizontal and vertical components of displacement at various distances from the cavity boundary.

For the horizontal displacement, X is

$$X = \left\{ \left[R^3 + R_C^3 \right]^{1/3} - R \right\} \cos \theta \quad (IV-2.59)$$

and for the vertical displacement the value of Y is

$$Y = X \tan \theta \quad (IV-2.60)$$

where θ is the angle measured from the horizontal as shown in Figure IV-2.50. Any water-saturated rock or rock of low gas-filled porosity can be considered to be

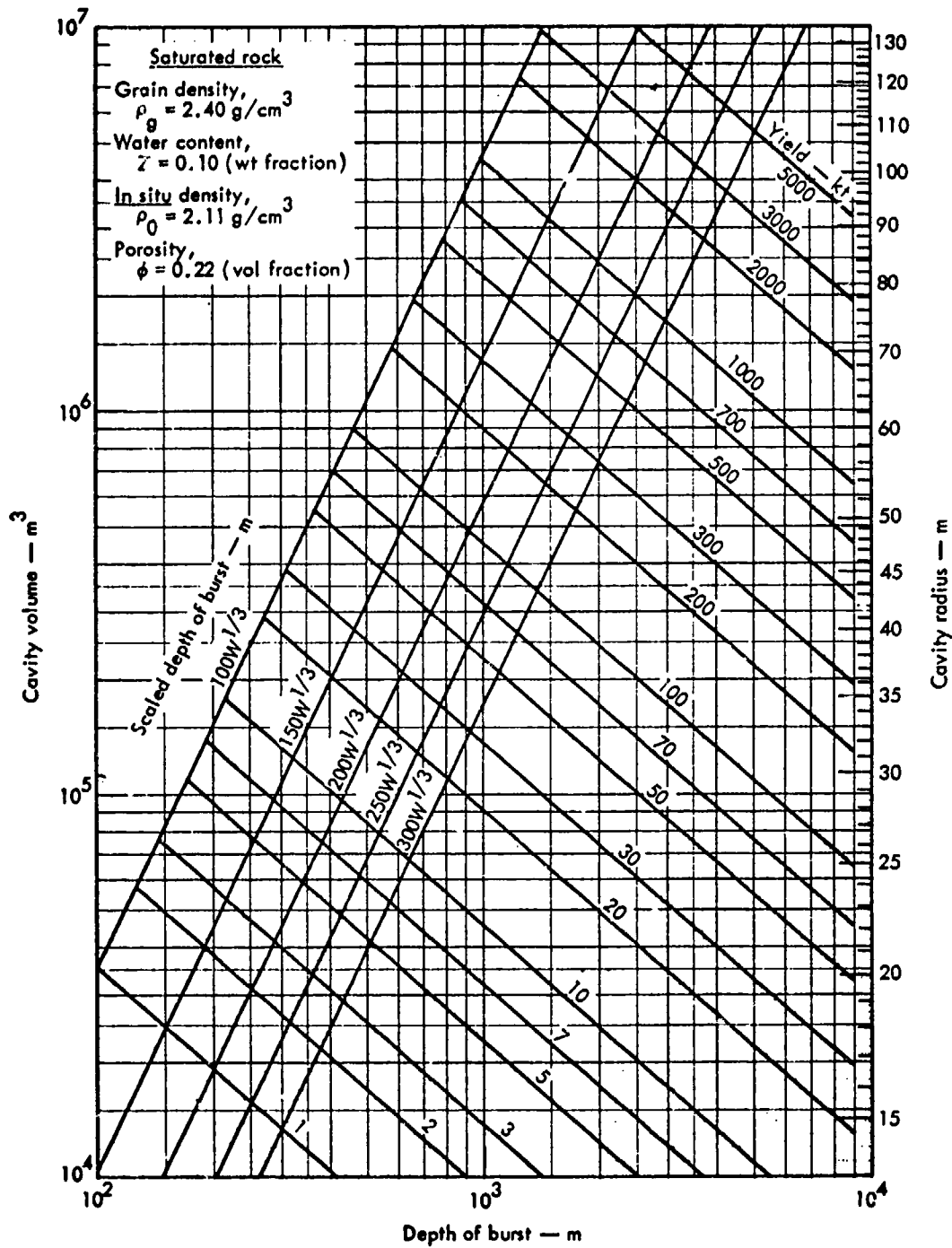


Figure IV-2.48. Cavity volume and radius as a function of device yield (W), and scaled depth of burst for a saturated rock with grain density and in-situ density equal to 2.4 g/cm^3 . It is assumed that the in-situ density equals the average overburden density. The other figures in Reference IV-2.97 cover other densities, water contents, and porosities for both saturated and unsaturated rock.

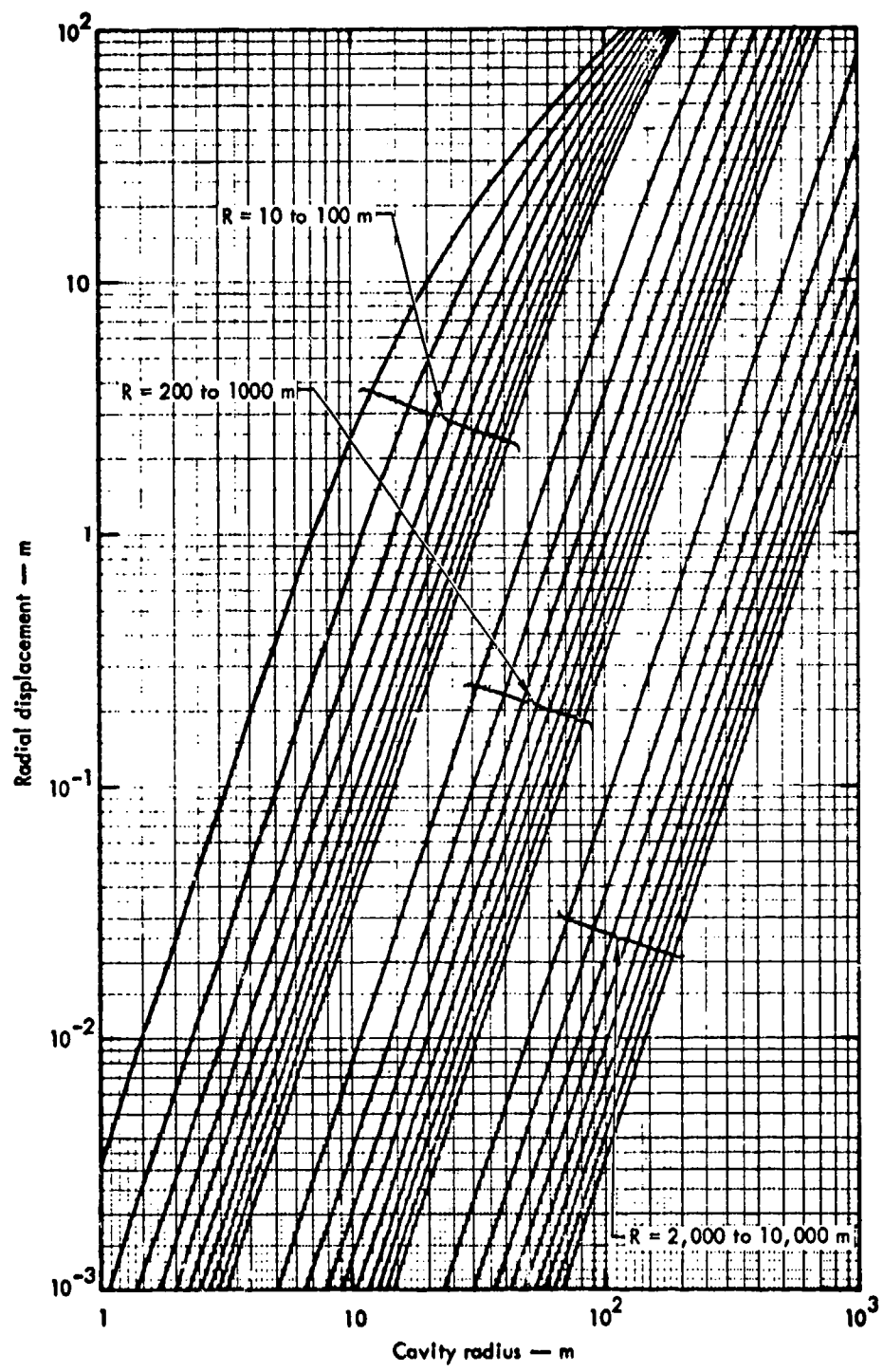


Figure IV-2.49. Radial displacement as a function of cavity radius at various distances (R) from the shot point for noncompactable rock.

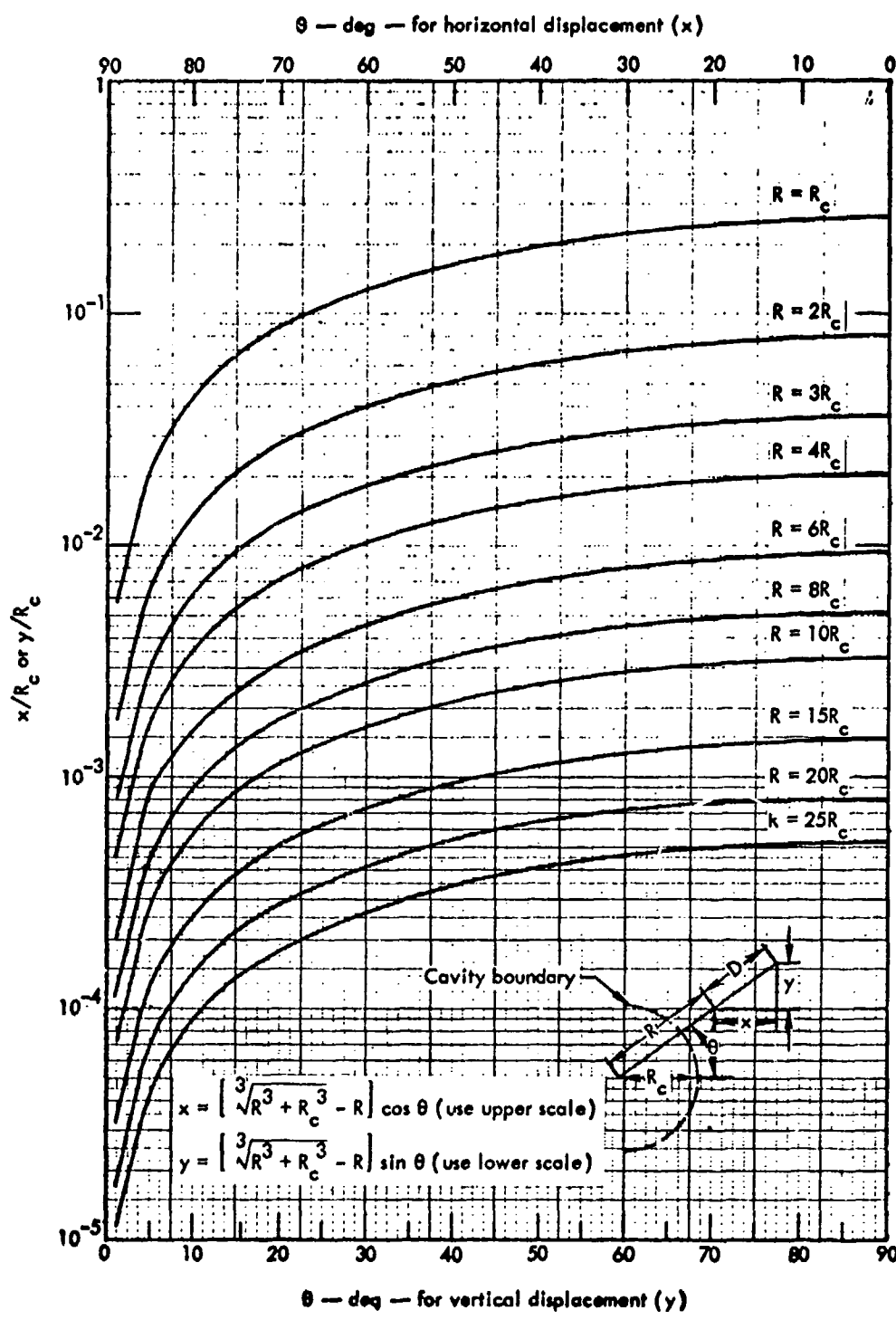


Figure IV-2.50. Horizontal (X) and vertical (Y) components of displacement at various distances from the cavity boundary.

noncompactable. Rock is not homogeneous on a large scale and local displacements along preexisting fractures may occur that exceed this estimate.

Figure IV-2.51 is an example of the type of graphs that give peak radial stress as a function of scaled radial displacement at various depths of burst and at distances from the shot point that are multiples of the cavity radius.

The details of the type of cavities that can form and the methods available for computing their content together with uncertainties associated with such computations can be found in Reference IV-2.97.

Energy deposition due to the passage of the shock wave is the primary method by which the energy is distributed. Since this deposition is very difficult to measure, a calculational technique was used to produce estimates of temperature increase as a function of distance from the explosion center. A one-dimensional hydrodynamic code that keeps track of the energy as a function of time was used to obtain the temperature increase after the energy had been distributed. Using a curve for the heat content of granite as a function of temperature, a relationship connecting the change in temperature (ΔT) as a function of the predisplacement distance from the center of detonation (R_i) was obtained. Butkovich has shown that the temperature distribution is also a function of the material properties. A compressible rock requires more $P\Delta V$ work than one that is less compressible; therefore, more energy is deposited in a compressible rock at a higher temperature close to the detonation. Since lower density rocks are generally more compressible than rocks of higher density, a relationship relating temperature (T) and in-situ density (ρ_0) was derived from the hydrodynamic calculations. This expression is

$$T = \frac{8.9 \times 10^5}{\rho_0^{3.156}} \left[\frac{R_i(-4.576/\rho_0^{0.411})}{W^{1/3}} \right] \quad (\text{IV-2.61})$$

where W is the yield in kilotons, and ΔT is the increase in temperature above ambient (assumed to be 25°C). To obtain the mass, M, of rock heated to temperature T or above, spherical symmetry is again assumed, so that the mass

$$M = \frac{4}{3} \pi R_i^3 \rho_0 \quad (\text{IV-2.62})$$

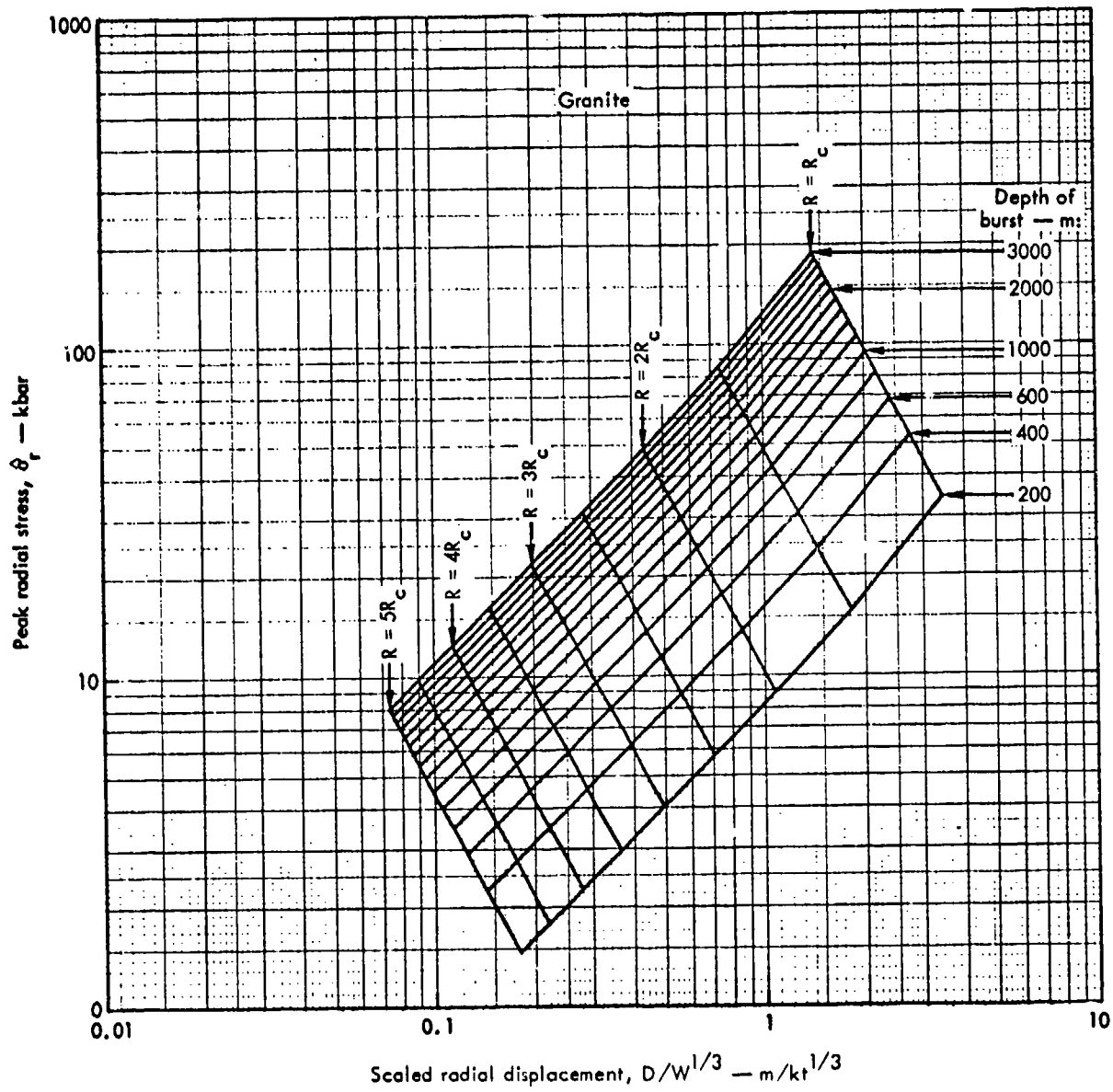


Figure IV-2.51. Peak radial stress as a function of scaled radial displacement at various depths of burst and distances from the shot point in granite.

becomes

$$M = \frac{4}{3} \pi p_0 W \left(\frac{\Delta T p_0^{3.156}}{8.9 \times 10^5} \right) \left[-\rho_0^{0.411} / 1.5253 \right] \quad (\text{IV-2.63})$$

Previous estimates of the amount of melt produced assumed a value of 70 tons per kiloton of energy released. Butkovich's work indicates that the amount of melt depends on the bulk density and can exceed this value by a factor of 2 for high-density, low-porosity rocks and by a factor of 3 or more for low-density, highly compressible rocks. Radiochemistry measurements support the higher values.

Figure IV-2.52 shows an example of the ΔT isotherms measured from the cavity wall at R_c meters from the center of detonations. Each plot given in Reference IV-2.97 is for a different energy yield and pertains to a different cavity radius. These curves were obtained assuming $p_0 = 2.81$. These figures should be useful for estimating the positions of isotherms for events in all relatively dry, dense rocks.

IV-2.7.2 The BOTE Model

The acronym BOTE stands for "Back-of-the-Envelope." This model is an analytic one developed by Kurtz of Lawrence Livermore Laboratory (Reference IV-2.98). Unlike the model of Butkovich and Lewis, results can be obtained using a pocket calculator or any programmable computer. Programming of the equations is straightforward. Moreover, this model is designed only to predict ground motion from underground nuclear explosions and is, therefore, not as comprehensive as the model of Butkovich and Lewis. However, what it lacks in comprehensiveness is offset by its greater flexibility for ground motion prediction.

Because Reference IV-2.98 was published in the open literature and, therefore, protected by copyright laws we can only describe its content without providing any supporting graphs to show how well its predictions agree with experimental data. The readers interested in this model should avail themselves of Reference IV-2.98.

The model is based upon a linear combination of the forms used to describe the extremes of stress wave lifetime: a strong shock at early time and a simple elastic wave at late times. Specifically, the assumption is made that the position and velocity of the stress wave can be expressed by the following functions:

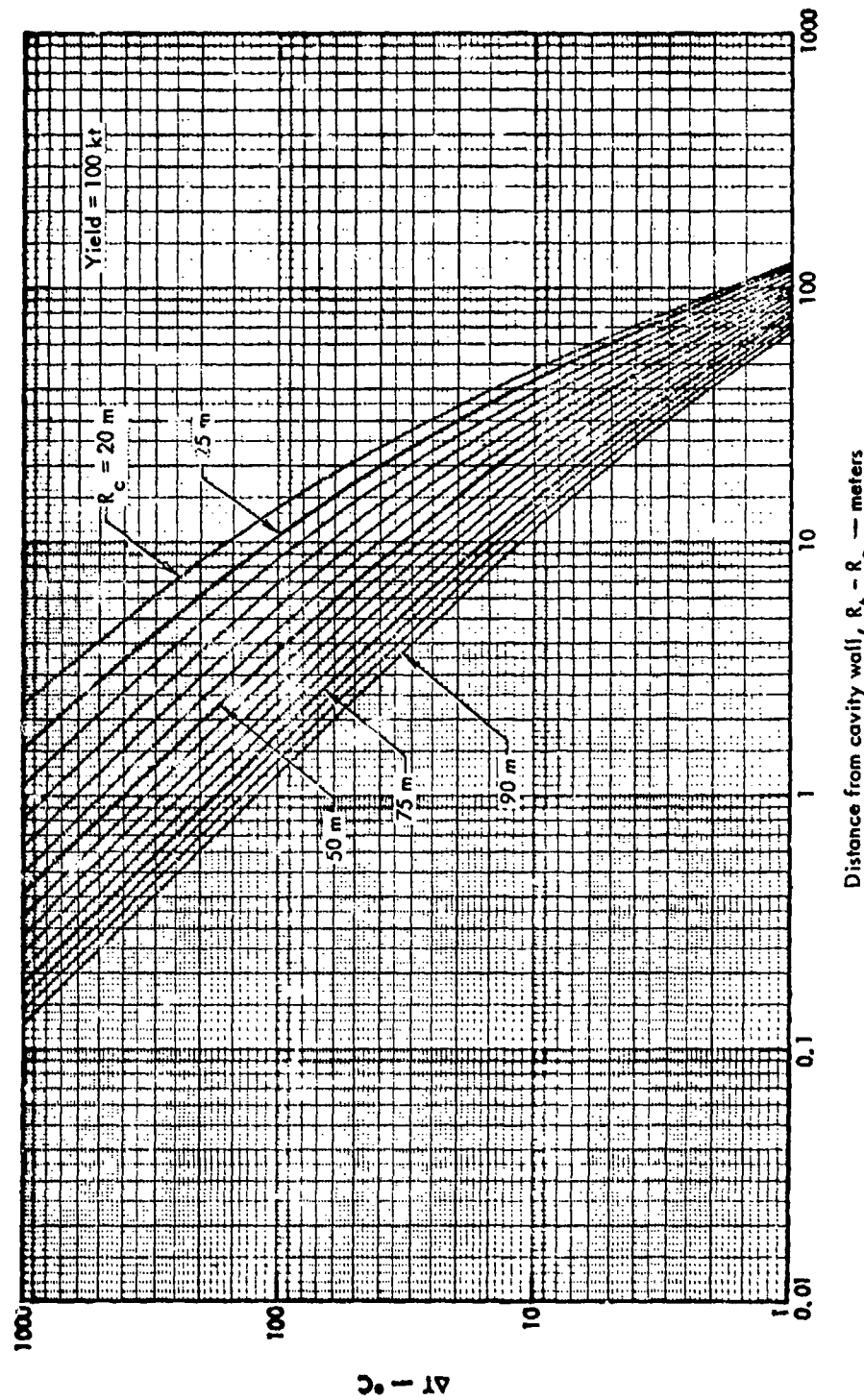


Figure IV-2-52.

Positions of isotherms (lines of constant temperature increase) resulting from the energy deposited by the shock wave generated by a nuclear explosion in relatively dry high-density silicate rock as a function of cavity radius (R_c) for an energy yield of 100 kt. Other figures in Reference IV-2-97 cover yields from 1 to 1000 kt.

$$r_s = r_{s_0} + Ct \quad (\text{IV-2.64})$$

$$v_s = v_{s_0} + C \quad (\text{IV-2.65})$$

where r_s and v_s are the position and velocity, respectively, predicted by a simple strong shock model, C is the sound speed, and t is time. The model development proceeds by assuming that the pressure in the medium surrounding an underground explosion can be expressed by

$$P = (\gamma - 1)\rho I \quad (\text{IV-2.66})$$

where P is the pressure, ρ is the density, I is the specific internal energy, and γ is a dimensionless constant, Kurtz argues that this form of the pressure equation is justified on the grounds that it is similar in form to the Grüneisen equation of state commonly used to describe shock propagation in solids. Kurtz then goes on to show that

$$\gamma = \Gamma_0 + 1 \quad (\text{IV-2.67})$$

where Γ_0 is the Grüneisen coefficient at normal density ρ_0 . For wet porous materials

$$\Gamma_0 = W\Gamma_{OW} + (1 - W)\Gamma_{OR} \quad (\text{IV-2.68})$$

where W is the weight fraction of water, Γ_{OW} is the Grüneisen coefficient for water, and Γ_{OR} is the Grüneisen coefficient for porous rock. Combining an explicit value for Γ_{OW} and Γ_{OR} he shows that

$$\gamma = W(2S_W - 2) + (1 - W) \left\{ \frac{2S_R}{(1 - W)} \left(\frac{\rho_g}{\rho_0} \right) - 1 \right\} \left\{ \frac{(1 - W)\rho_0}{\rho_g} \right\}^5 + 1 \quad (\text{IV-2.69})$$

where S_W is the slope of the shock velocity, particle velocity Hugoniot for water, and ρ_g is the grain density. Thus, with the use of Equation IV-2.69 into Equation IV-2.66 one can compute the pressure in rock. A table is provided in Reference IV-2.98 for the value of S_R for a number of soil materials.

The next step is to treat the transition from one pressure regime to the next. The assumption is now made that the loading curve in the P-V diagram can be divided into three basic regimes. The rock is assumed to behave elastically up to the elastic limit pressure P_E . As the pressure continues to increase above P_E , the voids in the medium begin to collapse. This begins the crush-up regime. At a pressure P_c , all voids in the rock have been crushed out and the rock itself begins to compress and deform plastically. This plastic pressure regime at higher pressures merges into the Hugoniot curve of the medium. Kurtz then uses Butkovich's empirical method of finding the values of P_c and P_E for rocks of varying water content and gas-filled porosity applicable to those media in which underground nuclear explosions are usually conducted. The functional relationships used in the model are then

$$P_c = 5 \quad , \quad W \leq 0.01 \quad (\text{IV-2.70a})$$

$$P_c = 0.065 W^{-0.944} \quad , \quad W > 0.01 \quad (\text{IV-2.70b})$$

$$P_E = 100 \exp(16.579 \phi_g - 6.908), \quad W < 0.05 \quad (\text{IV-2.71a})$$

$$P_E = 100 \exp(-4.859 \phi_g - 8.112), \quad 0.05 \leq W < 0.10 \quad (\text{IV-2.71b})$$

$$P_E = 100 \exp(-3.869 \phi_g - 8.805), \quad W \geq 0.10 \quad (\text{IV-2.71c})$$

where P_c and P_E are in gigapascals* and ϕ_g is the initial gas-filled porosity defined by

$$\phi_g = 1 - (1 - W) \frac{\rho_0}{\rho_g} - \rho_0 W \quad (\text{IV-2.72})$$

assuming the water density to be approximately unity.

The BOTE model assumes that the sound speed for each pressure-regime can be represented by a single value. For example, when the stress wave pressure is greater than P_c the sound speed is assumed to be equal to the bulk sound speed C_B for the medium. For pressures between P_c and P_E , the sound speed is assumed to be a "crushing" bulk sound speed C_{BC} . If the pressure is less than P_E , the sound speed is assumed to be equal to the elastic sound speed C_0 in the undisturbed medium. The following expressions are used where data is unavailable:

$$C_B = \left\{ \frac{B_0}{\rho_0} \left[\frac{(1 - W)\rho_0}{\rho_g} \right]^5 \right\}^{1/2} \quad (\text{IV-2.73})$$

$$C_{BC} = \left[(1 - W) \frac{\rho_0}{\rho_g} \cdot \frac{1}{S_R} \right]^{1/2} C_B \quad (\text{IV-2.74})$$

*One pascal = 10^{-5} bars = 1.45×10^{-4} psi = 7.5×10^{-3} torr. 1GPa = 10 kbars.

where the sound speed is expressed in m/msec, the densities in gm/cm³, and the zero-pressure bulk modulus B_0 for a dry nonporous rock material is in gigapascals. For the case of unavailable elastic sound speed data the following formula is used:

$$C_0 = 3.11871\rho_0 - 2.80355 \quad (\text{IV-2.75})$$

The equations for position, velocity, and pressure for a diverging stress wave in the BOTE model is based on the approximate solution for spherical blast wave developed by Chernyi discussed in Reference IV-2.31*. Kurtz gives a detailed description of the reasons for using Chernyi's theory particularly as it concerns the propagation of a strong shock moving with the velocity v_s at early times and decaying to a simple acoustic wave moving at velocity C_0 . The model uses relationships connecting device yield, in-situ density, time, pressure and velocity of propagation. Thus, explicit functions of the type

$$r_s = r_{s0} f(\gamma, \rho_0, t) \quad (\text{IV-2.76})$$

$$v_s = v_{s1} h(\gamma, \rho_0, r_s) \quad (\text{IV-2.77})$$

$$p_s = p_{s1} g(\gamma, \rho_0, r_s \text{ or } t) \quad (\text{IV-2.78})$$

are used.

The BOTE model goes beyond the simple predictive capability of a simple blast wave model by assuming that the outgoing stress wave velocity can be represented by a linear combination of the strong shock wave and a sound velocity term. Moreover, it takes account of the fact that the outgoing wave velocity is given by the

*It is suggested that the interested readers familiarize themselves with this theory as the details will not be given here.

derivative with respect to time of the position function of the wave. These assumptions lead to Equations IV-2.64 and IV-2.65. In these equations C is either C_B , C_{BC} or C_0 . Also, the functional Equations IV-2.76 and IV-2.77 can be substituted directly into Equations IV-2.64 and IV-2.65. By noting that the pressure in a stress wave cannot decay to less than the local overburden pressure P_0 , the value of P_S is rewritten as

$$P_S = P_S + P_0 \quad (\text{IV-2.79})$$

where P_S is given by the functional Equation IV-2.78. The equations used to define P_0 depend upon whether uphole, downhole, or horizontal stress information is needed. Kurtz recommends the following expressions for these cases:

$$\text{Uphole: } P_0 = \rho_0 g(H - r_S) \quad (\text{IV-2.80})$$

$$\text{Downhole: } P_0 = \rho_0 g(H + r_S) \quad (\text{IV-2.81})$$

$$\text{Horizontal: } P_0 = \rho_0 g H \quad (\text{IV-2.82})$$

where g is the acceleration due to gravity and H is the depth of burst.

Kurtz in Reference IV-2.98 then goes on to discuss results he obtained with the BOTE model and compares these results with experimental data. These results show good agreement for times ranging from tens of microseconds to tens of milliseconds for distances out to a scaled range of $10^7 \text{ m}/\text{kt}^{1/3}$ and for pressures to the order of 10^5 pascals. Moreover, Kurtz states that:

We feel that the BOTE model has some distinct advantages over other techniques that can be used to give the same results. It is quicker and less expensive to use than are large computer codes. Unlike simple scaling laws, it does not have to be used

in an interpolative manner or within the realm of previous experience to be completely trustworthy. We feel that the BOTE model could be used with good results in areas where data for scaling laws are either sparse or nonexistent. And we feel that the BOTE model is simply easier to use than are earlier attempts at using analytic solutions, ..., to describe the propagation of stress waves through solids and porous materials.

The paper concludes on a note of caution to preclude the generation of physically meaningless results.

IV-2.7.3 The Cooper and Seamon Model

Cooper and Seamon (Reference IV-2.99) developed a semiempirical technique, utilizing the methods of geometrical optics, to examine the effect of geologic layering on the surface peak particle velocity associated with the direct compressional wave produced by underground nuclear explosions. This geometric technique is different from former "ray" techniques in that it accounts for the curvature of the wave front, that is, the divergence of the rays, as well as the distance the wave travels. Data from contained nuclear explosions in "homogeneous" media are used to determine the relationship between the peak particle velocity and the divergence of the rays. This empirical relationship is then used for layered media, where the divergence of the rays is determined by the methods of geometrical optics, to predict the free-surface peak particle velocity. The required transmission and reflection factors are currently taken from the theory of elastic wave propagation. Several parametric studies and comparisons with data from experiments in layered media are presented in Reference IV-2.99. It is found that a number of previously unexplained departures from what was measured and what might intuitively be expected are qualitatively and sometimes quantitatively predicted by this technique. It is emphasized that layering between the source and the free surface (which usually occurs) can have a profound and deceiving effect on the surface motion, and, therefore, it should not be neglected in any prediction technique. The FORTRAN listing of the program developed is given in the Appendix of Reference IV-2.99.

IV-2.8 REFERENCES

- IV-2.1 Bass, R. C., A. J. Chabai, and H. L. Hawk, Project Shual, Hydrodynamic and Plastic Shock Studies, VUF 1003, Sandia Laboratory, Albuquerque, New Mexico, March 1966.
- IV-2.2 Chabai, A. J., and R. C. Bass, Measurements on a Spherical Shock Wave in a Granite Medium, SC-4741(RR), Sandia Laboratory, Albuquerque, New Mexico, December 1963.
- IV-2.3 Chabai, A. J., R. C. Bass, and H. L. Hawk, Close-in Phenomenon of Buried Explosions, DASA 1382, Defense Documentation Center, Cameron Station, Alexandria, Virginia, May 1963.
- IV-2.4 Day, J. D., and D. W. Murrell, Ground and Water Shock Measurements, Project 1.01 Vela Uniform Program, Long Shot Event, VUF 2701, U.S. Army Engineer Waterways Experiment Station, March 1967.
- IV-2.5 Eisler, J. D., and H. V. Hoffman, Free-Field Particle Motion from a Nuclear Explosion in Salt, Part II, Vela Uniform Program, Project Dribble, Salmon Event, VUF 3013, Stanford Research Institute, May 1969.
- IV-2.6 Perret, W. R., Surface and Subsurface Strong Motion Measurements, Projects 26.2 and 26.10, Operation Hardtack II, Evans Event, ITR 1703, Sandia Corporation, August 1959.
- IV-2.7 Perret, W. R., Subsurface Motion from a Confined Underground Detonation-Part I, Project 26.4b, Operation Plumbbob, Rainier Event, WT-1929, Sandia Corporation, May 1961.
- IV-2.8 Perret, W. R., Free-Field Ground Motion in Granite, Project 1.2a, Operation Flint Lock, Pile Driver Event, POE 4001, Sandia Laboratory, September 1968.
- IV-2.9 Perret, W. R., Gasbuggy Seismic Source and Surface Motion, Plowshare Program, Gasbuggy Event, PNE-1002, Sandia Laboratories, April 1970.
- IV-2.10 Perret, W. R., Ground Motion in a Multilayered Earth, Part I, Nuclear Explosion in Hardrock, Project 1.1/1.2, Operation Whetstone, Handcar/Painted Pony Event, POR 2800, Sandia Laboratories, June 1970.

- IV-2.11 Perret, W. R., Ground Motion in a Multilayered Earth, Part II, Nuclear Explosion in Tuff, Project 1.1/1.2, Operation Whetstone, Mud Pack Event, POR 2900, Sandia Laboratories, June 1970.
- IV-2.12 Perret, W. R., Free-Field and Surface Motion from a Nuclear Explosion in Alluvium: Merlin Event, SC-RR-69-334, Sandia Laboratories, November 1971.
- IV-2.13 Perret, W. R., "Seismic-Source Energies of Underground Nuclear Explosions," Bulletin of the Seismological Society, 62, pp. 763-774, June 1972.
- IV-2.14 Perret, W. R., Ground Motion in the Vicinity of the Cannikin Nuclear Explosion, SLA-73-0043, Sandia Laboratories, September 1973.
- IV-2.15 Perret, W. R., and D. R. Breding, Ground Motion in the Vicinity of an Underground Nuclear Explosion in the Aleutian Islands: Milrow Event, SC-RR-71-0668, Sandia Laboratories, May 1972.
- IV-2.16 Perret, W. R., A. J. Chabai, J. W. Reed, and L. J. Vortman, Project Scooter, Plowshare Program, SC-4602(RR), Sandia Corporation, October 1963.
- IV-2.17 Perret, W. R., and K. B. Kimball, Ground Motion Induced by a Contained Nuclear Explosion, Project 1.1a/1.2a, Operation Flint Lock, Discus Thrower Event, POR 6400, Sandia Laboratories, March 1971.
- IV-2.18 Preston, R. G., and V. E. Wheeler, Response of the Line-of-Sight Pipe to Ground Shock in the Hupmobile Nuclear Effects Test, Lawrence Radiation Laboratory (Unpublished).
- IV-2.19 Randolph, P. L., R. G. Preston, and V. E. Wheeler, Preliminary Report Ground Motion and Postshot Collapse Studies in the Vulcan Event, Lawrence Radiation Laboratory (Unpublished).
- IV-2.20 Swift, L. M., Intermediate Range Earth Motion Measurements, Plowshare Program, Gnome Event, PNE-111F, Stanford Research Institute, October 1962.
- IV-2.21 Swift, L. M., Measurement of Close-In Earth Motion, Project 1.2, Operation Nougat, Hard Hat Event, Stanford Research Institute (Unpublished).
- IV-2.22 Swift, L. M., and D. C. Sachs, Surface Motion from an Underground Detonation, Project 26.4a, Operation Plumbbob, Rainier Event, WT-1528, Stanford Research Institute, April 1959.

- IV-2.23 Swift, L. M., D. C. Sachs, and W. M. Wells, Earth Motion Measurements, Part I, Seismic Studies and Cavity Studies, Project 26.1, Operation Hardtack II, Evans Event, WT-1702, Stanford Research Institute, January 1959.
- IV-2.24 Weart, W. D., Particle Motion near a Nuclear Detonation in Halite, Projects 44.1 and 1.1, Plowshare Program, Gnome Event, PNE-108F, Sandia Corporation, February 1963.
- IV-2.25 Weart, W. D., Free-Field Earth Motion and Spalling Measurements in Granite, Project 1.1, Vela Uniform Program, Shoal Event, VUF 2001, Sandia Corporation, February 1965.
- IV-2.26 Wheeler, V. E. and R. G. Preston, Response of the Pipe and Ground in the Packard Nuclear Effects Test, UCRL-51112, Lawrence Livermore Laboratory, August 1971.
- IV-2.27 Perret, W. R., and R. C. Bass, Free-Field Ground Motion Induced by Underground Explosions, Sandia Laboratory, SAND74-0252, Reprinted November 1975.
- IV-2.28 Glasstone, S., The Effects of Nuclear Weapons, Revised Edition, Reprinted February 1964, USAEC, April 1962.
- IV-2.29 Johnson, G. W., G. H. Higgins, and C. E. Violet, "Underground Nuclear Detonations," J. Geophys. Res. 64, 1457 (1959).
- IV-2.30 Latter, A. L., R. E. LeLevier, E. A. Martinelli, and W. G. McMillan, "Method of Concealing Underground Nuclear Explosions," J. Geophys. Res. 66, 943 (1961).
- IV-2.31 Zel'dovich, Ya.B., and Yu. P. Raizer, Physics of Shock Waves and High-Temperature Hydrodynamic, Volume I and Volume II, Academic Press, 1967.
- IV-2.32 Rodean, H. C., "Nuclear-Explosion Seismology," AEC Critical Review Series, AEC Report No. TID-25572, 1971.
- IV-2.33 Heckman, R. A., Deposition of Thermal Energy by Nuclear Explosives, USAEC Report UCRL-7801, Lawrence Radiation Laboratory, 1964.
- IV-2.34 Tolstoy, I., Wave Propagation, McGraw-Hill Book Company, 1973.
- IV-2.35 Kolsky, H., Stress Waves in Solids, Dover Publications, Inc., New York, 1963.

- IV-2.36 Ewing, W. M., W. S. Jardetzky, and F. Press, Elastic Waves in Layered Media, McGraw-Hill Book Company, New York, 1957.
- IV-2.37 Lindsay, R. B., Mechanical Radiation, McGraw-Hill Book Company, New York, 1960.
- IV-2.38 Nakano, H., "On Rayleigh Waves," Jap. J. Astr. Geophys. 2, 233 (1925).
- IV-2.39 Chaszyka, Studies of Surface and Underground Nuclear Explosions, ARF Final Report 4195, February 1961.
- IV-2.40 Latter, A. L., R. E. LeLevier, E. A. Martinelli, and W. G. McMillan, A Method of Concealing Underground Nuclear Explosions, The RAND Corporation, Report No. R-348, 1959.
- IV-2.41 Latter, A. L., E. A. Martinelli, and E. Teller, "A Seismic Scaling Law for Underground Explosions," The Physics of Fluids, Vol. 2, No. 3, 280-283 (1959).
- IV-2.42 Carder and Mickey, Seismic Ground Effects from Coupled and Decoupled Shots in Salt, USC & GS, Final Report, Project Cowboy, December 1960.
- IV-2.43 Cherry, J. T., T. C. Bache, and D. F. Patch, The Teleseismic Ground Motion Generated by a Nuclear Explosion Detonated in a Tunnel and Its Effects on the M_s/m_b Discriminant, DNA Final Report, DNA 3645F, May 1975.
- IV-2.44 Davies, D., Seismic Methods for Monitoring Underground Explosions, Almqvist & Wiksell, Stockholm, 1969.
- IV-2.45 Adams, W. M., R. G. Preston, P. L. Flanders, D. C. Sachs, and W. R. Perret, "Summary Report of Strong-Motion Measurements, Underground Nuclear Detonations," J. of Geophys. Res. 66, No. 3, (March 1961).
- IV-2.46 Adams, W. M., P. L. Flanders, W. R. Perret, R. G. Preston, and D. C. Sachs, Summary Report of Strong Motion Measurements, Underground Nuclear Detonations, Operation Hardtack, Prepared for DASA and the AEC by LRL, SRI, and Sandia Corporation, ITR-1711, May 20, 1960.
- IV-2.47 Wells, W. M., Tunnel Dynamics-Madison Event, Stanford Research Institute (Unpublished).
- IV-2.48 Wells, W. M., Tunnel Dynamic-Platte Event, Stanford Research Institute (Unpublished).

- IV-2.49 Wells, W. M., Tunnel Dynamics-Des Moines, Stanford Research Institute (Unpublished).
- IV-2.50 Wells, W. M., Tunnel Dynamics-Yuba Event, Stanford Research Institute (Unpublished).
- IV-2.51 Swift, L. M., Nougat Series, Antler Event - Project 1.2: Measurement of Close-In Earth Motion, Stanford Research Institute, Report No. VUP-2100, October 1961.
- IV-2.52 Swift, L. M., Nougat Series, Hard Hat Event - Project 1.2: Measurement of Close-In Earth Motion, Stanford Research Institute, Report No. VUP-2101, March 1962.
- IV-2.53 Swift, L. M., and J. D. Eisler, Nougat Series, Antler and Hard Hat Events - Project 1.2: Measurement of Close-In Earth Motion, Stanford Research Institute, Report No. VUF-2100, May 1965.
- IV-2.54 Swift, L. M., and J. D. Eisler, Nougat Series, Clearwater Event - Project 1.2: Measurement of Close-In Earth Motion, Stanford Research Institute (Unpublished).
- IV-2.55 Swift, L. M., and J. D. Eisler, Vela Uniform Explosion Series - Project 1.2: Measurement of Close-In Earth Motion, Clearwater Event, Stanford Research Institute (Unpublished).
- IV-2.56 Weart, W. D. Particle Motion Near A Nuclear Detonation in Halite, Project Gnome, Carlsbad, New Mexico, Sandia Corporation, Final Report PNE-108F, December 10, 1961.
- IV-2.57 Swift, L. M., Intermediate Range Earth Motion Measurements, Project Gnome, Carlsbad, New Mexico, Stanford Research Institute, Final Report PNE-111F, December 10, 1961.
- IV-2.58 Perret, W. R., Free-Field Ground Motion Studies in Granite, Operation Nougat, Hardhat Event, Project 3.3, Sandia Corporation, Report No. POR-1803, April 1963.
- IV-2.59 Perret, W. R., Ground Motion Near Nuclear Explosions in Desert Alluvium, Projects 1.1 and 1.2, Vela Uniform Program, Operation Nougat, Fisher, Ringtail, Hognose, and Haymaker Events, Sandia Laboratories (Unpublished).

- IV-2.60 Carder, D. S., W. K. Cloud, L. M. Murphy, and J. H. Hershberger, Surface Motion from an Underground Explosion, U.S. C. and GS., Operation Plumbbob, WT-1530, November 14, 1958.
- IV-2.61 Hoffman, H. V., and F. M. Sauer Operation Flintrock, Shot Pile Driver, Free-Field and Surface Motions, WT-4000, June 3, 1969.
- IV-2.62 Perret, W. R., Vela Uniform Program, Project Dribble, Salmon Event, Final Report, VUF-3012, Sandia Laboratories, New Mexico, November 1967.
- IV-2.63 Perret, W. R., Free-Field Ground Motion Study, Project Sterling, Sandia Laboratory, Report SC-RR-68-410, October 1968.
- IV-2.64 Werth, G. C., The Handcar Nuclear Explosion in Dolomite, Report No. UCRL-50951, October, 1970.
- IV-2.65 Werth, G. C. and R. F. Herbst, Comparison of Amplitudes of Seismic Waves from Nuclear Explosions in Four Media, Lawrence Radiation Laboratory, Livermore, California, Report No. UCRL-6962, June 1962.
- IV-2.66 Perret, W. R. Subsurface Motion from a Confined Underground Detonation - Part I, Sandia Corporation, Operation Plumbbob, WT-1529, August 1, 1961.
- IV-2.67 Swift, L. M., and D. C. Sachs, Surface Motion from an Underground Detonation, Stanford Research Institute, Operation Plumbbob, WT-1428, March 31, 1960.
- IV-2.68 Swift, L. M., D. C. Sachs, and W. M. Wells, Earth Motion Measurements, Stanford Research Institute, Operation Hardtack-II, WT-1702, August 23, 1961.
- IV-2.69 Swift, L. M., Analysis of ERDL Photographic Records of Ground Motion-HE and Tamalpais Shots, prepared for Engineer Research and Development Laboratories, Fort Belvoir, Virginia, Stanford Research Institute Final Report, SRI-2897-5 (F), June 30, 1960.
- IV-2.70 Patterson, Scaling Curves for Peak Particle Motion for Nuclear Explosions in Four Media, Memorandum DPSI, Lawrence Radiation Laboratory, Livermore, California, April 8, 1963.
- IV-2.71 Patterson, Extension of Scaling Curves for Nuclear Explosions in Four Media, Letter of December 19, 1963 referencing Memorandum DPSI of April 8, 1963, Lawrence Radiation Laboratory, Livermore, California.

- IV-2.72 Murphy, Particle Motions Near Explosions in Halite, Project Cowboy, Sandia Corporation, Report No. SC-4440 (RR), June 1960.
- IV-2.73 Perkins, B., and A. A. Thompson, Preliminary Report on Medium Studies, BRL, Operation Hardtack-II, Report No. ITR-1709, August 10, 1959.
- IV-2.74 Swift, L. M., and W. M. Wells, Close-In Earth Motions, Project Hobo, prepared for Albuquerque Operations Office, U.S. Atomic Energy Commission and Lawrence Radiation Laboratory, Livermore, California by Stanford Research Institute, Report No. UCRL 6397, March 28, 1961.
- IV-2.75 Adams, W. M. and L. M. Swift, "The Effect of Shot-Point Medium on Seismic Coupling," J. Geophys., XXVI, No. 6, 765-771, December 1961.
- IV-2.76 Hake, L., High Explosives, Arming and Systematics, Project Cowboy, Final Report, Sandia Corporation, Report No. SC-4823 (RR), June 30, 1960.
- IV-2.77 Tockey, R. J., High Explosives, Arming, and Firing, Project Hobo, Report to Test Director, Sandia Corporation, Report No. SC-4824 (RR), August 1960.
- IV-2.78 Brode, H., Cavity Explosion Calculations for the Cowboy Program, RAND Corporation Research Memorandum 2624-AEC, August 5, 1960.
- IV-2.79 Morris, R. H. and R. C. Schneiderhan, Earth Motion Studies, EG&G, Operation Hardtack-II, Report No. ITR-1706, May 22, 1959.
- IV-2.80 Rice, M. H., R. G. McQueen, and J. M. Walsh, "Compression of Solids by Strong Shock Waves," Solid State Physics, Vol. 6, pp. 1-63, Academic Press, New York, 1958.
- IV-2.81 Bass, R. C., Additional Hugoniot Data for Geologic Materials, Sandia Laboratory, Albuquerque, New Mexico, Report No. SC RR-66-848, October 1966.
- IV-2.82 Bass, R. C., H. L. Hawk, and A. J. Chabai, Hugoniot Data for Some Geologic Materials, Sandia Laboratory, Albuquerque, New Mexico, Report No. SC-4903 (RR), June 1963.
- IV-2.83 Lombard, D. B., The Hugoniot Equation of State of Rocks, Lawrence Livermore Laboratory, Livermore, California, Report No. UCRL-6311, February 1961.
- IV-2.84 Chabai, A. J. and R. C. Bass, Measurements on a Spherical Shock Wave in a Granite Medium, Sandia Laboratory, Albuquerque, New Mexico, Report No. SC-4741 (RR), December 1963.

- IV-2.85 Long, J. W., The Round Robin Program: Ground Motion in the Vicinity of the Latir Event, Sandia Laboratories, Albuquerque, New Mexico, Report No. SAND 75-0596, January 1976.
- IV-2.86 Long, J. W., The Round Robin Program: Ground Motion in the Vicinity of the Tybo Event, Sandia Laboratories, Albuquerque, New Mexico, Report No. SAND 75-0572, January 1976.
- IV-2.87 Cook, M. A., The Science of High Explosives, Robert E. Krieger Publishing Co., Inc., Huntington, New York, 1971.
- IV-2.88 Sauer, F. M., and J. A. Kochly, Operation Diamond Mine Ground Motion Measurements - Final Report, Physics International Company, Report No. POR 6573, October 1972.
- IV-2.89 Hendron, A. J., Jr., Scaling of Ground Motions from Contained Explosions in Rock for Estimating Direct Ground Shock from Surface Bursts on Rock, Omaha District, Corps of Engineers, Technical Report No. 15, January 1973.
- IV-2.90 Jones, A. H., and S. J. Green, The Role of Material Properties in Determining Ground Motion from High Energy Detonations, Terra Tek, Inc., Report No. DNA 3056F, April 1973.
- IV-2.91 Harvey, W. T., Essex-Diamond Ore Research Program; Preliminary Results Report - Essex-I, Phase 1: Nuclear Cratering Device Simulation (Project Essex), DNA Report No. DNA PR 0002, WES TR E-74-1, 23 April 1974.
- IV-2.92 Harvey W. T., Summary Report, Essex I, Phase 1: Nuclear Cratering Simulation, WES (Unpublished).
- IV-2.93 Sisemore, C. J., D. E. Burton, and J. B. Bryan, Project Diamond Ore, Phase IIA: Close-In Measurement Program, Lawrence Livermore Laboratory Report No. UCRL-51620, August 28, 1974.
- IV-2.94 O'Connor, J. M., Numerical Modeling Calculations and Results of Unstemmed Cratering Experiments: Nuclear Cratering Device Simulation (Project Diamond Ore), WES/EERL (Unpublished).
- IV-2.95 Vortman, L. J., and J. A. Beyeler, Results of Ground Motion and Air Blast Measurements, Project Essex I, Phase I, Volumes 1 and 2, Sandia Laboratories, Report No. SLA-73-0918 (DNA PR 0006), November 1974.

- IV-2.96 Vincent, C. T., Ground Motion and Airblast Measurements on Shot 6M of Diamond Ore, (PIFR-436), U.S. Army Engineer Waterways Experiment Station, Explosive Excavation Research Laboratory, Livermore, California, Contract Report E-74-1, December 1974.
- IV-2.97 Butkovich, T. R., and A. E. Lewis, Aids for Estimating Effects of Under-ground Nuclear Explosions, Lawrence Livermore Laboratory, Report No. UCRL-50929 Rev. 1, February 23, 1973.
- IV-2.98 Kurtz, S. R., "A Back-of-the-Envelope Approach to Predicting Ground Motion Phenomena," J.G.R., Vol 80, No. 32, pp 4449-4460 (November 1975).
- IV-2.99 Cooper, H. F., Jr., and J. B. Seamon, A Geometric Technique for Studying Surface Motions from Underground Nuclear Explosions in Real Geologic Layered Media, Air Force Weapons Laboratory, Albuquerque, New Mexico, Report No. AFWL TR-66-123, January 1967.

DISTRIBUTION LIST

DEPARTMENT OF DEFENSE

Assistant to the Secretary of Defense
Atomic Energy
ATTN: Executive Assistant

Defense Advanced Rsch Proj Agency
ATTN: T10

Defense Intelligence Agency
ATTN: DB-4C2, C. Wiehle
ATTN: RDS-3A
ATTN: DB-4C2, B. Morris
ATTN: DB-4C3
ATTN: DB-4C1

Defense Nuclear Agency
ATTN: STSP
2 cy ATTN: SPSS
2 cy ATTN: SPAS
4 cy ATTN: TITL

Defense Technical Information Center
12 cy ATTN: DD

Field Command
Defense Nuclear Agency
ATTN: FCT
ATTN: FCPR
ATTN: FCTMOF

Field Command
Defense Nuclear Agency
Livermore Branch
ATTN: FCPRL

Field Command Test Directorate
Defense Nuclear Agency
ATTN: FCTC

Interservice Nuclear Weapons School
ATTN: TTV

Joint Strat Tgt Planning Staff
ATTN: NRI-STINFO Library
ATTN: DOXT
ATTN: JLA
ATTN: JLW-2
ATTN: XPFS

NATO School (SHAPE)
ATTN: U.S. Documents Officer

Undersecretary of Def for Rsch & Engrg
ATTN: Strategic & Space Sys (OS)

DEPARTMENT OF THE ARMY

BMD Advanced Technology Center
Department of the Army
ATTN: 1CRDABH-X
ATTN: ATC-T

BMD Systems Command
Department of the Army
ATTN: BMDSC-H, N. Hurst

DEPARTMENT OF THE ARMY (Continued)

Chief of Engineers
Department of the Army
ATTN: DAEN-RDL
ATTN: DAEN-MCE-D

Construction Engineering Rsch Lab
Department of the Army
ATTN: CERL-SOI-L

Deputy Chief of Staff for Ops & Plans
Department of the Army
ATTN: DAMO-NC

Deputy Chief of Staff for Rsch Dev & Acq
Department of the Army
ATTN: DAMA-CSS-N

Engineer Studies Center
Department of the Army
ATTN: DAEN-FES, LTC Hatch

Harry Diamond Laboratories
Department of the Army
ATTN: DELHD-I-TL
ATTN: DELHD-N-P

U.S. Army Armament Material Readiness Cmd
ATTN: MA Library

U.S. Army Ballistic Research Labs
ATTN: DRDAR-BLT, C. Kingery
ATTN: DRDAR-BLT, W. Taylor
ATTN: DRDAR-BLT, A. Picchiazz
ATTN: DRDAR-BLV
ATTN: DRDAR-BLT, J. Keefer
ATTN: Tech Library

U.S. Army Communiciations Command
ATTN: Tech Reference Division

U.S. Army Concepts Analysis Agency
ATTN: CSSA-ADL

U.S. Army Engineer Center
ATTN: ATZA

U.S. Army Engineer Div, Huntsville
ATTN: HNDED-SR

U.S. Army Engineer Div, Ohio River
ATTN: ORDAS-L

U.S. Army Engineer School
ATTN: ATZA-DTE-ADM
ATTN: ATZA-CDC

U.S. Army Foreign Science & Tech Ctr
ATTN: DRXST-SD

U.S. Army Mat Cmd Proj Mngr for Nuc Munitions
ATTN: DRCPM-NUC

DEPARTMENT OF THE ARMY (Continued)

U.S. Army Engr Waterways Exper Station
ATTN: WESSE, L. Ingram
ATTN: WESSD, J. Jackson
ATTN: J. Strange
ATTN: J. Zelasko
ATTN: F. Brown
ATTN: Library
ATTN: WEssa, W. Flathau
ATTN: WESSS, J. Ballard

U.S. Army Material & Mechanics Rsch Ctr
ATTN: DRXMR, J. Mescall
ATTN: DRXMR-TE, R. Shea
ATTN: Technical Library

U.S. Army Materiel Dev & Readiness Cmd
ATTN: DRCDE-D, L. Flynn
ATTN: DRXAM-TL

U.S. Army Missile R&D Command
ATTN: RSIC
ATTN: DRDMI-XS

U.S. Army Mobility Equip R&D Cmd
ATTN: DRDME-HT, A. Tolbert
ATTN: DRDME-WC

U.S. Army Nuclear & Chemical Agency
ATTN: Library

U.S. Army War College
ATTN: Library

U.S. Military Academy
Department of the Army
ATTN: Document Library

DEPARTMENT OF THE NAVY

Marine Corps
Department of the Navy
ATTN: POM

David Taylor Naval Ship R&D Ctr
ATTN: Code 1700, W. Murray
ATTN: Code 177, E. Palmer
ATTN: Code 2740
ATTN: Code 1740, R. Short
ATTN: Code 1740.5
ATTN: Code L42-3

Marine Corp Dev & Education Command
Department of the Navy
ATTN: DO91, J. Hartneady

Naval Construction Battalion Center
ATTN: Code L51, J. Crawford
ATTN: Code L51, S. Takahashi
ATTN: Code L51, W. Shaw
ATTN: Code L51, R. Odello

Naval Electronic Systems Command
ATTN: PME 117-21

Naval Electronics Systems Command
ATTN: Commander

Naval Explosive Ord Disposal Fac
ATTN: Code 504, J. Petrousky

DEPARTMENT OF THE NAVY (Continued)

Naval Facilities Engineering Command
ATTN: Code 04B

Naval Material Command
ATTN: MAT 08T-22

Naval Ocean Systems Center
ATTN: Code 013, E. Cooper
ATTN: Code 4471

Naval Postgraduate School
ATTN: Code 1424 Library
ATTN: G. Lindsay

Naval Research Laboratory
ATTN: Code 2627
ATTN: Code 8404, H. Pusey
ATTN: Code 8403, R. Belsham
ATTN: Code 8440, G. O'Hara

Naval Sea Systems Command
ATTN: SEA-09G53
ATTN: SEA-033
ATTN: SEA-06J, R. Lane
ATTN: SEA-0351
ATTN: SEA-9931G

Naval Surface Weapons Center
ATTN: Code F31
ATTN: Code R10
ATTN: Code R14
ATTN: Code U401, M. Kleinerman

Naval Surface Weapons Center
ATTN: Tech Lib & Info Svcs Br
ATTN: W. Wishard

Naval War College
ATTN: Code E-11

Naval Weapons Center
ATTN: Code 266, C. Austin
ATTN: Code 233
ATTN: Code 3263, J. Bowen

Naval Weapons Evaluation Facility
ATTN: Code 10
ATTN: R. Hughes

Office of Naval Research
ATTN: Code 474, N. Perrone

Office of the Chief of Naval Operations
ATTN: OP 982
ATTN: OP 982E, M. Lenzini
ATTN: OP 981
ATTN: OP 654C3, R. Piacesi
ATTN: OP 09878
ATTN: OP 03EG

Strategic Systems Project Office
Department of the Navy
ATTN: NSP-272
ATTN: NSP-273
ATTN: NSP-43

DEPARTMENT OF THE AIR FORCE

Aerospace Defense Command
Department of the Air Force
ATTN: XPX

Air Force Armament Laboratory
ATTN: DLYV, J. Collins

Air Force Geophysics Laboratory
ATTN: LWW, K. Thompson

Air Force Institute of Technology
ATTN: Library
ATTN: Commander

Air Force Office of Scientific Research
ATTN: NA, B. Wolfson

Air Force Systems Command
ATTN: DLW
ATTN: R. Cross

Air Force Weapons Laboratory
Air Force Systems Command
ATTN: NTES-C, R. Henny
ATTN: NTE, M. Plamondon
ATTN: SUL
ATTN: NTED
ATTN: NTES, J. Lee
ATTN: NTES, R. Jolley

Assistant Chief of Staff
Intelligence
Department of the Air Force
ATTN: IN

Ballistic Missile Office
Air Force Systems Command
ATTN: DEB

Ballistic Missile Office
Air Force Systems Command
ATTN: MNN
ATTN: MNNX
ATTN: MNNXH

Deputy Chief of Staff
Research, Development, & Acq
Department of the Air Force
ATTN: AFRDQI
ATTN: R. Steere

Deputy Chief of Staff
Logistics & Engineering
Department of the Air Force
ATTN: LEEE

Foreign Technology Division
Air Force Systems Command
ATTN: SDBF, S. Spring
ATTN: TQTD
ATTN: NIIS Library
ATTN: SDBG

Rome Air Development Center
Air Force Systems Command
ATTN: TSLD
ATTN: RBES, R. Mair
ATTN: Commander

DEPARTMENT OF THE AIR FORCE (Continued)

Strategic Air Command
Department of the Air Force
ATTN: NRI-STINFO Library
ATTN: XPFS

United States Air Force Academy
ATTN: DFCEM, W. Fluhr

DEPARTMENT OF ENERGY

Department of Energy
Albuquerque Operations Office
ATTN: CTID

Department of Energy
ATTN: OMA/RD&T

Department of Energy
Nevada Operations Office
ATTN: Mail & Rec for Tech Library

OTHER GOVERNMENT AGENCIES

Central Intelligence Agency
ATTN: OSWR/NED
ATTN: OSR/SE/F

Department of the Interior
Bureau of Mines
ATTN: Tech Lib

Department of the Interior
U.S. Geological Survey
ATTN: D. Roddy

Federal Emergency Management Agency
ATTN: Hazard Eval & Vul Red Div

NASA
AMES Research Center
ATTN: R. Jackson
ATTN: F. Nichols

U.S. Nuclear Regulatory Commission
ATTN: R. Whipp for Div of Sec for L. Shao

DEPARTMENT OF ENERGY CONTRACTORS

Lawrence Livermore National Lab
ATTN: L-200, T. Butkovich
ATTN: L-90, R. Dong
ATTN: Tech Info Dept Library
ATTN: J. Goudreau
ATTN: M. Fernandez
ATTN: T. Gold
ATTN: H. Glenn
ATTN: L-205, J. Hearst
ATTN: L-437, R. Schock
ATTN: L-90, D. Norris
ATTN: L-7, J. Kahn

Los Alamos National Scientific Lab
ATTN: MS 364
ATTN: A. Davis
ATTN: R. Sanford
ATTN: M/S 632, T. Dowler
ATTN: MS 670, J. Hopkins
ATTN: G. Spillman

DEPARTMENT OF ENERGY CONTRACTORS (Continued)

Oak Ridge National Laboratory
ATTN: Central Research Library
ATTN: Civil Def Res Proj

Sandia National Laboratories
Livermore National Laboratory
ATTN: Library & Sec Class Div

Sandia National Lab
ATTN: 3141
ATTN: L. Vortman

DEPARTMENT OF DEFENSE CONTRACTORS

Acurex Corp
ATTN: J. Stockton
ATTN: C. Wolf

Aerospace Corp
ATTN: L. Selzer
ATTN: P. Mathur
ATTN: H. Mirels
2 cy ATTN: Tech Info Services

Agbabian Associates
ATTN: C. Bagge
ATTN: M. Agbabian

Analytic Services, Inc
ATTN: G. Hesselbacher

Applied Research Associates, Inc
ATTN: H. Auld
ATTN: N. Higgins
ATTN: J. Bratton

Applied Theory, Inc
ATTN: J. Trulio

Artic Associates, Inc
ATTN: S. Gill

AVCO Research & Systems Group
ATTN: W. Broding
ATTN: Library A830
ATTN: J. Atanasoff
ATTN: D. Henderson

BDM Corp
ATTN: A. Lavagnino
ATTN: T. Neighbors
ATTN: Corporate Library

BDM Corp
ATTN: R. Hensley

Bell Telephone Labs
ATTN: J. White

Boeing Co
ATTN: M/S 42/37, R. Carlson
ATTN: Aerospace Library
ATTN: R. Holmes
ATTN: R. Hager
ATTN: R. Dyrdahl
ATTN: J. Wooster

Boeing Co
ATTN: M/S 42/37, K. Friddell

DEPARTMENT OF DEFENSE CONTRACTORS (Continued)

California Institute of Technology
ATTN: T. Ahrens

California Research & Technology, Inc
ATTN: K. Kreyenhagen
ATTN: Library
ATTN: M. Rosenblatt
ATTN: S. Schuster

California Research & Technology, Inc
ATTN: D. Orphal

Calspan Corp
ATTN: Library

Center for Planning & Rsch, Inc
ATTN: R. Shnider

University of Denver
ATTN: J. Wisotski

Effects Technolog., Inc
ATTN: K. Narasimhan

EG&G Washington Analytical Svcs Ctr, Inc
ATTN: Library
ATTN: Director

Electric Power Research Institute
ATTN: G. Sliter

Electromechanical Sys of New Mexico, Inc
ATTN: R. Shunk

Eric H. Wang
Civil Engineering Rsch Fac
University of New Mexico
ATTN: N. Baum
ATTN: D. Calhoun

Franklin Institute
ATTN: Z. Zudans

Gard, Inc
ATTN: G. Neidhardt

General Dynamics Corp
ATTN: R. Dibrell

General Electric Co
ATTN: M. Bortner

General Electric Co
ATTN: A. Ross

General Electric Company—TEMPO
ATTN: DASIAC

General Research Corp
ATTN: TIO

Geocenters, Inc
ATTN: E. Marram

H-Tech Labs, Inc
ATTN: B. Hartenbaum

Honeywell, Inc
ATTN: T. Helvig

DEPARTMENT OF DEFENSE CONTRACTORS (Continued)

IIT Research Institute
ATTN: A. Longinow
ATTN: Documents Library

Institute for Defense Analyses
ATTN: Classified Library
ATTN: Director

J. H. Wig Co, Inc
ATTN: J. Collins

Kaman AviDyne
ATTN: G. Zartarian
ATTN: Library
ATTN: R. Ruetenik
ATTN: N. Hobbs

Kaman Sciences Corp
ATTN: Library
ATTN: F. Shelton
ATTN: D. Sachs

Karagozian and Case
ATTN: J. Karagozian

Lockheed Missiles & Space Co, Inc
ATTN: B. Almroth
ATTN: T. Geers

Lockheed Missiles & Space Co, Inc
ATTN: TIC-Library

Management Science Associates
ATTN: K. Kaplan

Martin Marietta Corp
ATTN: G. Fotieo
ATTN: A. Cowan

Martin Marietta Corp
ATTN: J. Donathan

University of Massachusetts
ATTN: W. Nash

McDonnell Douglas Corp
ATTN: R. Halprin

Merritt CASES, Inc
ATTN: Library
ATTN: J. Merritt

Meteorology Research, Inc
ATTN: W. Green

Mitre Corp
ATTN: Director

Nathan M. Newmark Consult Eng Svcs
ATTN: J. Haitiwanger
ATTN: W. Hall
ATTN: N. Newmark

University of New Mexico
ATTN: G. Triandafalidis

University of Oklahoma
ATTN: J. Thompson

DEPARTMENT OF DEFENSE CONTRACTORS (Continued)

Pacific-Sierra Research Corp
ATTN: H. Brode

Pacifica Technology
ATTN: R. Bjork
ATTN: Tech Library
ATTN: G. Kent

Physics Applications, Inc
ATTN: C. Vincent

Physics International Co
ATTN: L. Behrmann
ATTN: Technical Library
ATTN: J. Thomsen
ATTN: E. Moore
ATTN: F. Sauer

University of Pittsburgh
ATTN: M. Williams, Jr

R & D Associates
ATTN: P. Rausch
ATTN: J. Lewis
ATTN: W. Wright, Jr
ATTN: A. Field
ATTN: R. Port
ATTN: Tech Info Center
ATTN: P. Haas

Rand Corp
ATTN: A. Laupa
ATTN: C. Mow
ATTN: Library

Science Applications, Inc
ATTN: Tech Library

Science Applications, Inc
ATTN: S. Oston

Science Applications, Inc
ATTN: D. Bernstein
ATTN: D. Maxwell
ATTN: R. Hoffmann

Science Applications, Inc
ATTN: W. Layson
ATTN: J. Cockayne
ATTN: B. Chambers III
ATTN: G. Binninger

Southwest Research Institute
ATTN: W. Baker
ATTN: A. Wenzel

SRI International
ATTN: G. Abrahamson
ATTN: W. Wilkinson

Systems, Science & Software, Inc
ATTN: K. Pyatt
ATTN: D. Grine
ATTN: R. Sedgewick
ATTN: T. McKinley
ATTN: T. Riney
ATTN: T. Cherry
ATTN: Library

DEPARTMENT OF DEFENSE CONTRACTORS (Continued)

TeleDyne Brown Engineering
ATTN: J. Ravenscraft

Terra Tek, Inc
ATTN: A. Abou-Sayed
ATTN: Library
ATTN: S. Green
ATTN: A. Jones

Tetra Tech, Inc
ATTN: L. Hwang

Texas A & M University System
ATTN: H. Coyle

Weidlinger Assoc, Consulting Engineers
ATTN: J. McCormick
ATTN: M. Baron

DEPARTMENT OF DEFENSE CONTRACTORS (Continued)

TRW Defense & Space Sys Group
ATTN: P. Bhutta
ATTN: B. Sussholtz
ATTN: A. Narevsky
ATTN: D. Jortner
ATTN: A. Feldman
ATTN: Tech Info Center
2 cy ATTN: N. Lipner

TRW Defense & Space Sys Group
ATTN: F. Pieper
ATTN: G. Hulcher
ATTN: E. Wong
ATTN: P. Dai

Weidlinger Assoc, Consulting Engineers
ATTN: J. Isenberg